Synthesis and Certification of Lanthanum Oxide Extracted from Monazite Sand

Samin[1,*], Suyanti[1], Susanna Tuning Sunanti[1], and Wisnu Ari Adi[2]

[1]*Department of Process Technology, Center for Science and Accelerator Technology BATAN, Jl. Babarsari, Kotak Pos 6101 ykbb, Yogyakarta 55281, Indonesia*

[2]*Department of Science and Advanced Materials, Center for Science and Technology of Advanced Materials BATAN, Kawasan PUSPITEK, Serpong, Tangerang Selatan, Banten, 15310, Indonesia*

* ***Corresponding author:***

tel: +62-8156882743
email: samin@batan.go.id

Received: March 19, 2019
Accepted: March 29, 2020

DOI: 10.22146/ijc.44327

Abstract: *Synthesis and certification of lanthanum oxide extracted from monazite sand have been carried out. This research aimed to increase the added value of monazite sand and obtain the lanthanum oxide in-house certified reference material (CRM). Synthesis of lanthanum oxide consists of several stages, namely: monazite sand digestion, rare-earth elements hydroxide [$REE(OH)_3$] precipitation, Ce separation, Nd separation, lanthanum oxalate precipitation, and calcination. Certification of lanthanum oxide was carried out by determining the average concentration of the oxides and its uncertainty from the seven accredited laboratories by the ISO 35-2006 statistical method. Two other minerals in the lanthanum oxide analyzed by the XRD method were cerium hydroxide [$Ce(OH)_3$] and neodymium yttrium oxide fluoride ($Nd_2Y_2O_3F_{16}$). Lanthanum oxide certified contains ten oxides, with the two highest concentrations of La_2O_3 (91.662 ± 0.007)% and Nd_2O_3 (3.949 ± 0.002)%. Lanthanum oxide has met the qualification in-house CRM since it contained water less than 1%, homogeneous, stable, and certified. La_2O_3 concentration in the lanthanum oxide in-house CRM from CSAT-BATAN, Indonesia was not significantly different in comparison to that from the Department of Chemical Engineering, Srinakharinwirot University, Thailand. Lanthanum oxide extracted from monazite sand can be used as reference material in determining the lanthanum oxide quality from the pilot plant process.*

Keywords: *synthesis; certification; lanthanum oxide; monazite sand*

■ INTRODUCTION

The synthesis and certification of lanthanum oxide extracted from the natural resources were not found, and the lanthanum oxide certified reference material also does not yet exist. Certified reference material (CRM) is a reference material characterized by a metrologically valid procedure for one or more specified properties. It is accompanied by a certificate, its associated uncertainty, and a statement of metrological traceability [1-3]. CRM is essential used for calibration, testing, and method validation [1-3].

The added value of monazite as a natural resource can be improved by processing monazite sand into lanthanum oxide in-house CRM [1,4]. Lanthanum oxide (La_2O_3) is a potentially useful material for various optical and electronic applications, such as high gate dielectric material, capacitors, non-volatile memories, optical filters, and waveguides [5]. Lanthanum oxide has a bandgap of 4.3 eV and the lowest lattice energy with a high dielectric constant [6]. Lanthanum oxide is a solid, odorless, white, and insoluble in water, but it is soluble in the dilute acids [7]. Nano-lanthanum oxide can be used for the preparation of organic chemical products catalysts and in automobile exhaust catalyst [8]. Trace analysis techniques applications based on the lanthanide spectroscopy have been found to detect many compounds up to parts per trillion (ppt) levels [9]. Lanthanum oxide is used widely in the film industry for studio lighting and projection [10]. The lanthanum oxide nanoscale can be used as a superconductor, exhaust gas converter, and hydrogen storage material [11].

Since lanthanum oxide has a high economic value, the research has emerged on how to get lanthanum oxide from minerals. Monazite is a mineral that has the form of phosphate bonds with Th and rare earth metals. In general, the chemical formula of monazite is (REE, Th)PO_4 [12]. The processing of monazite sand to obtain lanthanum oxide was carried out through several stages. Monazite sand was fused with sulfuric acid, to obtain REE-sulfate, thorium-sulfate, and phosphoric acid. The REE-sulfate was melted with NaOH, then REE-OH will be collected. REE-OH was dissolved with nitric acid and oxidized with oxidizing agents, so all rare earth metals will be oxidized and change oxidation state from II to III, except Ce, from oxidation state II to IV. The rare-earth was precipitated by using NH_4OH at a specific pH, so the rare earth metal was obtained individually. Lanthanum was precipitated as lanthanum oxalate, then calcined to obtain lanthanum oxide [13-14]. The steps for synthesis of the lanthanum oxide CRM are the preparation of lanthanum oxide, homogeneity study, stability study, characterization, and evaluation of uncertainty [1,15]. Certification of lanthanum oxide determines the average oxide concentration and the uncertainty by using the ISO 35-2006 statistical method [2,16,18]. It is expected that lanthanum oxide in-house CRM can be used as reference material to determine the quality of lanthanum oxide from the pilot plant process.

■ EXPERIMENTAL SECTION

Materials

Indonesian monazite sand sample was obtained from Bangka Island. Chemicals including ammonia, sodium hydroxide, oxalic acid, hydrochloric acid, and nitric acid in the technical grade were purchased from Sodawaru Sidoarjo Indonesia without prior treatment and concentrated sulfuric acid, $KBrO_3$, and lanthanum oxide standard were obtained from E-Merck, Germany.

Instrumentation

Instruments used included XRF Spectrometer Ortex 7010 (USA), XRD PANalytical X'Pert PRO PW3040/X0 (Netherlands), XRF Spectrometer Thermo Scientific ARL 9900 (Netherlands), and ball mill type Fritsch 05.4021522 (Germany).

Procedure

Synthesis of lanthanum oxide from monazite sand

Precipitation of rare-earth elements hydroxide [REE$(OH)_3$] from monazite sand. Monazite sand was crushed until the particle size escapes 325 mesh. Monazite sand 50 kg was digested in the pilot plant using NaOH 96.43 kg at 140 °C for 4 h to dissolve the phosphate. Phosphate containing filtrate was stored for further processing, while the residue was washed using hot water then fed to a partial dissolution reactor. The residue was dissolved with 51.22 L HCl 32% at pH 3.7 and 80 °C for 2 h. Ammonia 15% (450.4 kg) was added into the filtrate to precipitate U and Th. The filtrate was fed to the sedimentation reactor, and then NH_4OH was added up to pH of 9.8 at room temperature for 1 h, to form REE $(OH)_3$ precipitate. The REE$(OH)_3$ precipitate was filtered and dried in the oven at 110 °C for 24 h.

Synthesis of lanthanum oxide from REE$(OH)_3$. REE$(OH)_3$ (5 kg) was dissolved with 18.02 L of 63% technical HNO_3 solution, 0.25 kg $KBrO_3$, and heated at 135 °C for 1 h, then 40 L water was added to the solution, so the REE-nitrate solution was obtained. NH_4OH solution was added into the REE-nitrate solution to obtain a pH of 4, then Ce was precipitated as Ce-hydroxide. Further addition of NH_4OH solution into the filtrate of the REE-nitrate solution until pH 8, then Nd was precipitated as Nd-hydroxide.

A 3 kg of technical $H_2C_2O_4$ was added into the filtrate of $La(NO_3)_3$ solution to obtain the La-oxalate precipitate. The $La_2(C_2O_4)_3$ precipitate was filtered and dried in the oven at 110 °C for 10 h, Then the product was calcined at 1000 °C for 4 h, to produce lanthanum oxide powder.

Preparation of lanthanum oxide in-house CRM. Lanthanum oxide (350 g) was dried at 110 °C for 6 h, crushed with a ball mill until the particle size escaped 200 mesh, and sieved for 2 × 6 h. Lanthanum oxide was homogenized for 6 h to obtain 300 g of the lanthanum oxide powder. Lanthanum oxide was tested for water content, homogeneity, stability, and then certification. The water content of lanthanum oxide was determined by the gravimetric method. The homogeneity test and the stability test of lanthanum oxide were carried out

with the ISO 13528 statistical method. Certification of lanthanum oxide was carried out by the ISO 35-2006 statistical method [16,18].

Lanthanum oxide powder was already qualified as the in-house CRM if the water content was less than 1%, homogeneous, stable, and certification [1,16,18].

The water content test in lanthanum oxide

The container was heated in an oven at 110 °C for 1 h, cooled in a desiccator for 1 h, and weighed at room temperature. The weighing was carried out repeatedly until a constant weight was obtained. Lanthanum oxide sample 2.8 g was put into the container, heated in an oven at 110 °C for 1 h, cooled in a desiccator for 1 h and weighed at room temperature. The weighing was carried out repeatedly until a constant weight was obtained. Water content in lanthanum oxide was calculated from the wet weight minus the dry weight.

The homogeneity test of lanthanum oxide

Ten subsamples of lanthanum oxide were selected randomly. The weight of each subsample was 0.5 g. Ten subsamples were analyzed for macroelement (La) and microelements (Sm, Y) in duplicate by the XRF method. All subsamples were analyzed by the same analyst with the same instrument on the same day and the same laboratory. Standard deviations between samples (Ss) of the ten subsamples duplo analysis data were processed with the ISO 13528 statistical method by the formula, as reported previously [16,18].

Lanthanum oxide was homogeneous if $Ss \leq 0.3\ \sigma$, where σ was the standard deviation for proficiency assessment (SDPA), σ can be established through CV Horwitz [16,18].

Stability test of lanthanum oxide

The stability tests can be carried out if lanthanum oxide has been stored for 3–6 months. The stability test was carried out in the same laboratory and the same analysis method as the homogeneity test. Lanthanum oxide was selected g ($g \geq 3$) subsamples randomly. The weight of each subsample was 0.5 g. Three subsamples were analyzed for macroelement (La) and microelements (Sm, Y) in duplicate by the XRF method. The average concentration of each element in the stability test (Y_T) was calculated from the first test (Y_A) and the second test (Y_B). The average stability test value (Yr) was calculated from the Y_T value of three subsamples. The absolute value of the difference between the average homogeneity test value (Xr) and the average stability test value (Yr), $|Xr - Yr|$ was calculated. Lanthanum oxide must be stable if $|Xr - Yr| \leq 0.3\ \sigma$ [16,18].

Characterization of lanthanum oxide

The characterization of lanthanum oxide was carried out by the XRD method. Lanthanum oxide was characterized by the XRD PANalytical X'Pert PRO with the serial number of PW3040/X0. The scanning process of the lanthanum oxide sample was done at the angle of $2\theta = 0–4000°$.

Certification of lanthanum oxide

The lanthanum oxide subsamples were distributed to the seven accredited laboratories, namely: Laboratory of Geological Survey Center Bandung, Laboratory of tekMIRA Center Bandung, Laboratory of PSTNT BATAN Bandung, Laboratory of PTBGN BATAN Jakarta, Laboratory of PSTBM BATAN Serpong, Laboratory of NAA PSTA BATAN Yogyakarta, and Laboratory of XRF PSTA BATAN Yogyakarta for testing the concentration and its uncertainty of the oxides.

The average oxide concentration and its uncertainty in lanthanum oxide from the seven laboratories were processed by the ISO 35-2006 statistical method as following [16,18]:

The calculation of the average oxide concentration ($\bar{X}$) was used the equation:

$$\bar{X} = \sum WiXi \quad (1)$$

$$Wi = \frac{W'}{\sum_{i=1}^{p} Wi'} \quad (2)$$

$$W' = \frac{1}{\mu^2} \quad (3)$$

The calculation of the oxide concentration measurement uncertainty (μ) was performed with the equation:

$$\mu(\bar{x}) = \sqrt{\sum W_i^2 \mu_{xi}^2} \quad (4)$$

$\bar{X}$: the average oxide concentration, X_i: the oxide concentration of each laboratory, W: the weight of the

Table 1. The composition of Indonesian monazite sand from Bangka [16], the number of replication (n) = 4–7 laboratories

No	Oxide	Concentration (%)	No	Oxide	Concentration (%)
1	CeO_2	31.506 ± 0.075	11	Dy_2O_3	1.029 ± 0.011
2	La_2O_3	13.165 ± 0.038	12	SiO_2	1.295 ± 0.021
3	Nd_2O_3	11.025 ± 0.062	13	U_3O_8	0.298 ± 0.005
4	ThO_2	6.283 ± 0.022	14	Fe_2O_3	0.770 ± 0.012
5	Y_2O_3	3.931 ± 0.024	15	TiO_2	0.043 ± 0.001
6	Pr_6O_{11}	2.984 ± 0.022	16	Yb_2O_3	0.310 ± 0.004
7	P_2O_5	19.109 ± 0.102	17	Er_2O_3	0.412 ± 0.005
8	SnO_2	1.034 ± 0.004	18	Al_2O_3	0.826 ± 0.021
9	Sm_2O_3	1.956 ± 0.005	19	CaO	0.219 ± 0.006
10	Gd_2O_3	1.981 ± 0.003	20	ZrO_2	0.177 ± 0.005

oxide and μ: the oxide concentration measurement uncertainty.

■ RESULTS AND DISCUSSION

It was necessary to know the composition of monazite sand as raw material for the synthesis of lanthanum oxide in the pilot plant. The composition of Indonesian monazite sand from Bangka was presented in Table 1. It was observed that the major components of monazite sand were CeO_2, La_2O_3, Nd_2O_3, and P_2O_5. Monazite sand contains CeO_2: 31.506%, La_2O_3: 13.165%, Nd_2O_3: 11.025% and P_2O_5: 19.109%. So monazite sand can be processed into $REE(OH)_3$ and then lanthanum oxide.

Synthesis of Lanthanum Oxide from Monazite Sand

Precipitation of REE(OH)3 from monazite sand

The composition of $REE(OH)_3$ resulting from monazite sand was presented in Table 2. From the data in Table 2, $REE(OH)_3$ contains major components of Ce: 28.711%, La: 16.274%, and Nd: 4.633%, while P and Th were not detected. The Ce element was the most dominant, so firstly Ce must be separated from $REE(OH)_3$, then followed by separation of Nd so that a higher La concentration was obtained.

Table 2. The composition of $REE(OH)_3$ processed from monazite sand, the number of replication (n) = 3

No	Element	Concentration (%)
1	Ce	28.711 ± 0.073
2	La	16.274 ± 0.013
3	Nd	4.633 ± 0.016
4	Pr	1.847 ± 0.009
5	Y	1.449 ± 0.008
6	Gd	1.391 ± 0.009
7	Sm	0.664 ±0.038
8	Dy	0.293 ± 0.006
9	Er	0.171 ± 0.001

Separation of Ce from REE(OH)₃

For the separation of Ce, REE $(OH)_3$ was dissolved with nitric acid, in the $REE(NO_3)_3$ solution was added with NH_4OH solution to obtain a pH of 4. Ce was precipitated as Ce-hydroxide.

The reaction of rare earth elements hydroxide with nitric acid is shown below [13,19,21]:

$$(REE)(OH)_3 + 3HNO_3 \rightarrow (REE)(NO_3)_3 + 3H_2O \quad (5)$$

Separation of Nd from the REE-nitrate solution

The next step was the separation of Nd. The filtrate of the REE-nitrate solution was added with NH_4OH solution to obtain a pH of 8, then Nd was precipitated as neodymium hydroxide. The precipitation reaction of neodymium hydroxide [13,21]:

$$Nd(NO_3)_3 + 3\ NH_4OH \rightarrow Nd(OH)_3 \downarrow + 3\ NH_4NO_3 \quad (6)$$

Precipitation of lanthanum oxalate from the lanthanum nitrate solution

After Ce and Nd were separated, oxalic acid was added to the lanthanum nitrate solution, and the white precipitate formed was lanthanum oxalate.

Synthesis of lanthanum oxide

Lanthanum oxalate processed from monazite sand

was calcined at 1000 °C for 4 h, then lanthanum oxide powder was obtained.

The Water Content Test in Lanthanum Oxide

Based on the data in Table 3, the water content in lanthanum oxide was 0.181% to obtain water content less than 1%. The powder of lanthanum oxide has been qualified for certification. So the homogeneity test and the stability test could be done.

Homogeneity Test of Lanthanum Oxide

The homogeneity test of lanthanum oxide can be seen in Supplement 1 (S-1), Supplement 2 (S-2), and Supplement 3 (S-3). Lanthanum oxide was homogeneous if $Ss \leq 0.3\ \sigma$, both for the macroelement (La) and the microelements (Sm, Y). The concentration of La, Sm, and Y has been homogeneous as shown in supplement 1, 2, and 3, respectively.. Based on the homogeneity test of the macroelement (La), and the microelements (Sm, Y), lanthanum oxide has been homogenous.

Stability Test of Lanthanum Oxide

The stability test of lanthanum oxide can be seen in Supplement 4 (S-4), Supplement 5 (S-5), and Supplement 6 (S-6). Lanthanum oxide is stable if $|Xr - Yr| \leq 0.3\ \sigma$, both for macroelement (La) and microelements (Sm, Y). In Supplement 4, the concentration of La, Sm, and Y was found to be stable as given in supplement 4, 5, and 6, respectively. Based on the stability test of macroelement (La) and microelements (Sm, Y), lanthanum oxide has been stable.

Characterization of Lanthanum Oxide

The characterization results of lanthanum oxide made in CSAT BATAN and lanthanum oxide made in E-Merck Germany by using the XRD method were presented in Fig. 1. Lanthanum oxide produced in CSAT BATAN (a) contains the minerals of cerium hydroxide [$Ce(OH)_3$], lanthanum oxide (La_2O_3), neodymium yttrium oxide fluoride ($Nd_2Y_2O_3F_{16}$), yttrium oxide (Y_2O_3), and potassium barium niobium uranium oxide

Table 3. Water content test in lanthanum oxide by gravimetric method

La_2O_3 sub-sample	Wet weight (g)	Dry weight (g)	Water content (%)	Average water content (%)
1	2.879	2.882	0.104	
2	2.799	2.803	0.143	
3	2.838	2.844	0.211	
4	2.891	2.897	0.208	0.181 ± 0.046
5	2.856	2.862	0.210	
6	2.886	2.892	0.208	

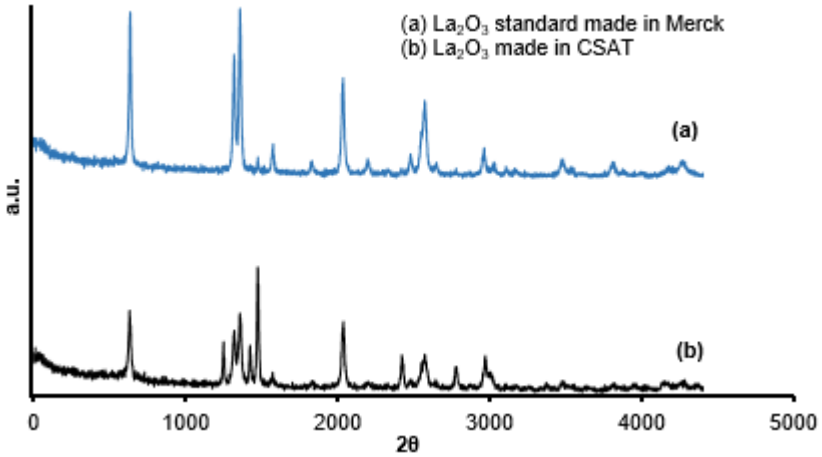

Fig 1. The XRD patterns of (a) lanthanum oxide made in CSAT BATAN and (b) lanthanum oxide made in E-Merck Germany

Table 4. The determination of the average La_2O_3 concentration and its uncertainty in the lanthanum oxide from the seven laboratories, the number of replication (n) = 3

Laboratory	Xi (%)	μi (%)	Wi'	Wi	Wi Xi	$Wi^2\mu i^2$
A	92.573	0.227	19.4065	0.1350	12.5005	9.4×10^{-4}
B	91.705	0.118	71.8184	0.4997	45.8271	3.5×10^{-3}
C	91.957	2.394	0.1745	0.0012	0.1117	8.5×10^{-6}
D	94.167	0.903	1.2265	0.0085	0.8037	5.9×10^{-5}
E	91.190	0.140	51.0204	0.3550	32.3731	2.5×10^{-3}
F	95.112	8.327	0.0144	0.0001	0.0096	7.0×10^{-7}
G	93.352	4.233	0.0558	0.0004	0.0363	3.0×10^{-6}
Total			**143.7165**			
$X_{average}$					**91.6620**	
μ_x						**7.0×10^{-3}**

($Nb_{7.6}U_{2.4}Ba_{5.2}K_8O_{30}$). Lanthanum oxide made in E-Merck Germany (b) contains the minerals of lanthanum deuteriohydroxide [$La(OD)_3$], cerium (Ce), scandium strontium fluoride ($ScSr_{1.56}F_{6.1}$) and zirconium iron antimonide ($ZrFe_{0.68}Sb$).

Certification of Lanthanum Oxide

The certification of lanthanum oxide such as the determination of the average oxide concentration and its uncertainty from the seven laboratories accredited was processed by the ISO 35-2006 statistical method [1,16,18]. The average oxide concentration ($X_{average}$) was determined using Eq. 1, 2, and 3, while the determination of the uncertainty (μ) was using Eq. 4. The determination of the average La_2O_3 concentration and uncertainty from the seven laboratories that were processed by the ISO 35-2006 statistical method were presented in Table 4.

From the data in Table 4, La_2O_3 concentrations in the lanthanum oxide from the seven laboratories were varied from 91.190% to 95.112%. With the ISO 35-2006 statistical method, the average La_2O_3 concentration was obtained 91.662% with an uncertainty of 0.007%.

The average concentration and other oxide uncertainties from the seven laboratories were determined in the same method. Certificate of the average oxide concentration and its uncertainty in the lanthanum oxide was presented in Table 5.

Based on the data in Table 5, certificate of the lanthanum oxide consists of ten oxides i.e., La_2O_3, Nd_2O_3, CeO_2, Pr_6O_{11}, Y_2O_3, Sm_2O_3, Tb_4O_7, CaO, SiO_2, and Al_2O_3. The concentration of La_2O_3 was obtained (91.662 ± 0.007)%, while ThO_2 and U_3O_8 were not detected.

The evaluation of data was obtained that lanthanum oxide has been homogeneous, stable, water content less than 1%, and certificated. So the lanthanum oxide powder was already qualified as the in-house CRM. From the data in Table 6, the major oxides in lanthanum oxide in-house CRM products from CSAT-BATAN, Indonesia were La_2O_3: 91.662%, Nd_2O_3: 3.949%, CeO_2: 2.426%, and Pr_6O_{11}: 1.217%. The major oxide in the lanthanum oxide product from the Department of Chemical Engineering, Srinakharinwirot University (DCE, SU), Thailand was La_2O_3: 95.360% only,

Table 5. Certificate of the average oxide concentration and its uncertainty in the lanthanum oxide

No	Oxide	Average Concentration (%)	Uncertainty (%)
1	La_2O_3	91.662	0.007
2	Nd_2O_3	3.949	0.002
3	CeO_2	2.426	0.040
4	Pr_6O_{11}	1.217	0.003
5	Y_2O_3	0.114	0.002
6	Sm_2O_3	0.144	0.007
7	Tb_4O_7	0.106	0.005
8	CaO	0.199	0.004
9	SiO_2	0.074	0.003
10	Al_2O_3	0.061	0.002
	Total	**99.952**	

Table 6. The comparison of the lanthanum oxide in-house CRM (La-oxide CRM) from CSAT-BATAN Indonesia, the lanthanum oxide (La-oxide) from DCE-SU Thailand, and REE-oxide from DRI-ME Myanmar by precipitation methods

No	Composition	Concentration (%)		
		La-oxide CRM from CSAT-BATAN, Indonesia	La-oxide from DCE-SU, Thailand [22]	REE-oxide from DRI-ME, Myanmar [17]
1	La_2O_3	91.662 ± 0.007	95.360	25.173
2	Nd_2O_3	3.949 ± 0.002	0.250	14.215
3	CeO_2	2.426 ± 0.040	0.940	51.530
4	Pr_6O_{11}	1.217 ± 0.003	n.d	3.204
5	Y_2O_3	0.114 ± 0.002	n.d	0.547
6	Sm_2O_3	0.144 ± 0.007	n.d	0.737
7	Tb_4O_7	0.106 ± 0.005	n.d	n.d
8	Gd_2O_3	n.d	n.d	0.381
9	ThO_2	n.d	n.d	n.d
10	U_3O_8	n.d	n.d	n.d
11	CaO	0.199 ± 0.004	2.290	n.d
12	SiO_2	0.074 ± 0.003	< 0.010	n.d
13	Al_2O_3	0.061 ± 0.002	0.334	n.d

and the major oxides in REE-oxide products from the Department of Research and Innovation, Ministry of Education (DRI-ME), Myanmar were La_2O_3: 25.173%, Nd_2O_3: 14.125%, CeO_2: 51.530%, and Pr_6O_{11}: 3.204%.

Based on the lanthanum oxide composition test data from the seven laboratories, it was found that the uncertainty of each component varied from 0.002–0.040%, so the lanthanum oxide can be used as reference material in determining the lanthanum oxide quality from the pilot plant process.

■ CONCLUSION

Lanthanum oxide certified contained ten oxides, and four oxides with the highest concentration included La_2O_3 (91.662 ± 0.007)%, Nd_2O_3 (3.949 ± 0.002)%, CeO_2 (2.426 ± 0.040)%, Pr_6O_{11} (1.217 ± 0.003)%. Two other minerals in the lanthanum oxide by the XRD method were cerium hydroxide [$Ce(OH)_3$] and neodymium yttrium oxide fluoride ($Nd_2Y_2O_3F_{16}$). Lanthanum oxide was already qualified as the in-house CRM since it contained water less than 1%, homogeneous, stable, and certified. La_2O_3 concentration in the lanthanum oxide in-house CRM from CSAT-BATAN, Indonesia was not significantly different compared to that from the Department of Chemical Engineering, Srinakharinwirot University, Thailand (the difference level was 3.70%). The lanthanum oxide extracted from monazite sand can be used as reference material in determining the lanthanum oxide quality from the pilot plant process.

■ ACKNOWLEDGMENTS

The author thanks Dr. Susilo Widodo who has agreed to the 2017 Budget (DIPA) of the Center for Science and Accelerator Technology-BATAN to financing this research. The authors are also grateful to Sutanto WW, Bambang Irianto, Dwi Purnomo, Suhardi, and Mulyono, who have helped with this research.

■ REFERENCES

[1] Guimarães, E.F., do Rego, E.C.P., Cunha, H.C.M., Rodrigues, J.M., and Figueroa-Villar, J.D., 2014, Certified reference material for traceability in environmental analysis: PAHs in toluene, *J. Braz. Chem. Soc.*, 25 (2), 351–360.

[2] Quan, C., Yao, H., and Hou, C., 2013, Certification and uncertainty evaluation of flavonoids certified reference materials, *Agric. Sci.*, 4 (9B), 89–96.

[3] Samin, and Sunanti, S.T., 2018, Analysis methods for development of certified reference materials (CRM) zircon minerals synthesis, *Indones. J. Chem.*, 18 (3), 448–456.

[4] Satusinprasert, P., Suwanmance, U., and Rattanaphra, D., 2015, Separation of light and middle-heavy rare earth from nitrate medium by

liquid-liquid extraction, *Kasetsart J. (Nat. Sci.)*, 49 (1), 155–163.

[5] Karthikeyan, S., and Selvapandiyan, M., 2017, Synthesis of nanocrystalline lanthanum oxide La_2O_3 powder at reflux routes, *Int. J. Comput. Sci. Commun. Netw.*, 7 (3), 70–78.

[6] Lim, S.R., Lee, S.D., Kim, H.S., Simanjuntak, F.S.H., and Lee, H., 2014, Lanthanum oxide–catalyzed transesterification of dimethyl carbonate with glycerol: Effect of surfactant, *Bull. Korean Chem. Soc.*, 35 (11), 3163–3168.

[7] Ammary, E., and Kangarlou, H., 2016, Investigation of the optical properties of lanthanum oxide, using density functional theory and LSDA and WC approximations, *Int. J. Pharm. Res. Allied Sci*., 5 (2), 436–441.

[8] Saravani, H., and Khajehali, M., 2016, Synthesis and characterization of lanthanum oxide and lanthanum oxide carbonate nanoparticles from thermalizes of La(acacen)(NO_3) (H_2O) complex, *Orient. J. Chem.*, 31 (4), 2351–2357.

[9] Shah, M.S., and Jan, G.M., 2016, Lanthanum oxide nanoparticles synthesis and their luminescent property, *Indo Am. J. Pharm. Sci.*, 3 (1), 81–85.

[10] Hastiawan, I., Firmansyah, F., Juliandri, Rakhmawaty, D., and Noviyanti, A.R., 2016, Pemisahan lanthanum dari limbah hasil pengolahan timah dengan menggunakan metode pengendapan bertingkat, *Chimica et Natura Acta*, 4 (2), 93–96.

[11] Xue, S., Wu, W., Bian, X., Wang, Z., and Yang, Z., 2014, Synthesis of lanthanum oxide using lanthanum chloride by hydrogen-oxygen flame pyrolysis route, *Appl. Mech. Mater.*, 633-634, 499–503.

[12] Bahri, C.N.A.C.Z., Al-Areqi, W.M., Ab Majid, A., and Mohd Ruf, M.I.F., 2016, Production of rare earth elements from Malaysian monazite by selective precipitation, *Malays. J. Anal. Sci.*, 20 (1), 44–50.

[13] Purwani, M.V., and Suyanti, 2005, Pengaruh HNO_3 dan $KBrO_3$ pada pembuatan konsentrat Ce, La dan Nd dari pasir monasit, *Prosiding PPI-PDIPTN 2005,* 194–202.

[14] Rodliyah, I., Rochani, S., and Wahyudi, T., 2015, Extraction of rare earth metals from monazite mineral using the acid method, *Indones. Min. J.*, 18 (1), 39–45.

[15] Gong, N., Guo, Y., Yang, N., Gao, Z., Du, G., and Lu, Y., 2012, Preparation and characterization of new certified reference material of puerarin (GBW09511), *Anal. Methods*, 4 (10), 3443–3447.

[16] Samin, Sunanti, S.T., and Setiawan, K., 2018, The synthesis and certification of in-house monazite sand certified reference materials, *AIP Conf. Proc.*, 2014, 020148.

[17] Tar, A.T., Myo, T.Z., Hlaing, T.M., and Win, B.B.M., 2017, Study on the processing of rare earth oxide from monazite, Mongmit Myitsone region, *ASRJETS*, 27 (1), 43–51.

[18] Samin, Suyanti, and Sunanti, S.T., 2018, The synthesis and certification of cerium oxide certified reference materials (CRM) as a processed result of monazite sand, *AIP Conf. Proc.*, 2014, 020049.

[19] Purwani, M.V., Trinopiawan, K., Poernomo, H., Suyanti, Pusporini, N.D., and Amiliana, R.A., 2019, Separation of Ce, La and Nd rare-earth hydroxide (REOH) by oxidation with potassium permanganate and precipitation, *J. Phys. Conf. Ser.*, 1198 (3), 032003.

[20] Purwani, M.V., Triyono, Suprihati, Sudibyo, R., and Suyanti, 2018, Pemisahan lantanum, cerium dan neodimium melalui dekomposisi termal dan leaching memakai HNO_3 encer, *Prosiding PPI–PDIPTN 2018*, 171–1778.

[21] Pusporini, N.D., Suyanti, Amiliana, R.A., and Poernomo, H., 2020, Processing, and refining of tin tailing mining, *J. Phys. Conf. Ser.*, 1436, 012136.

[22] Lerdtrakulwong, O., Prucksawan, E., Suwanmanee, U., and Rattanaphra, D., 2013, Synthesis of lanthanum oxide powder by precipitation method, *Burapha University International Conference*, Pattaya, Thailand, 4-6 July 2013.

Batik Wastewater Treatment Using Simultaneous Process of Electrocoagulation and Electro-Assisted Phytoremediation (EAPR)

Rudy Syah Putra[1,2,*], Aprilia Dwi Annisa[1], and Sigit Budiarjo[1]

[1]*Department of Chemistry, Faculty of Mathematics and Natural Sciences, Universitas of Islam Indonesia, Jl. Kaliurang km. 14, Yogyakarta 55584, Indonesia*

[2]*Environmental Remediation Research Group, Faculty of Mathematics and Natural Sciences, Universitas Islam Indonesia, Jl. Kaliurang km. 14, Yogyakarta 55584, Indonesia*

* ***Corresponding author:***

tel: +62-274-895920
email: rudy.syahputra@uii.ac.id

Received: August 26, 2019
Accepted: January 20, 2020

DOI: 10.22146/ijc.47898

Abstract: *The aims of the study are to identify the effectiveness of wastewater treatment from the Batik industry using a simultaneous of electrocoagulation (EC) and electro-assisted phytoremediation (EAPR). Rough horsetail (*Equisetum hyemale*) was used as an accumulator plant in the EAPR system. Electrocoagulation was conducted for 1 h at a constant voltage of 20 V in 10 L solution, while EAPR was processed for 7 day at a constant voltage of 5 V in 17 L solution. The chemical oxygen demand (COD) of water was determined by closed reflux of colorimetric methods and heavy metal concentration was determined by flame-atomic absorption spectrophotometer. The results showed that the COD decreased by 69.6% after 1 h of electrocoagulation process and up to 80.9% after the EAPR process. The concentration of Cr and Pb decreased as much as 25% and 8.52%, respectively in the similar process. The simultaneous process could extend the heavy metal removal up to 0.28 mg/L for Cr and 0.09 mg/L for Pb in liquid wastewater from the initial concentration. These results showed that the levels of COD and heavy metal concentration in Batik wastewater have reduced in accordance with the Ministry of Environment Decree No. 5/2014 Republic of Indonesia regarding various industries wastewater standard with the threshold limit of 150 mg/L for COD and 1.0 mg/L for Cr on textile industry and 0.1 mg/L for Pb on Class I for another wastewater standard. The estimated cost of operation was US$ 1.509 m^{-3} indicating the viability of Batik industry wastewater treatment.*

Keywords: *electrocoagulation; EAPR;* Equisetum hyemale*; phytoremediation; batik wastewater*

■ INTRODUCTION

Batik industry (i.e. an ingenious traditional textile in Indonesia) has potentially contributed hazardous pollutants to the environment. Direct discharge or unproper treatment of wastewater produced from these industries can be detected easily by a physical form in the environment, such as smell, and turbid color of water [1]. The largest pollutant from the Batik industry is from the dyeing process. Dye substances are usually non-biodegradable organic compounds, which are source of environmental pollution. Naturally, dyes compound in aquatic environments can be decomposed by photo-degradation. However, these processes occurred in a slow chemical reaction which impacted on the accumulation of dye compounds in the aquatic environment faster than the ability of photo-degradation process [2].

Today, there are many methods to process the Batik or other textiles wastewater such as coagulation, adsorption using activated carbon, and electrocoagulation [2]. However, those techniques are less effective and relatively complex process, so that it is needed a new method that is more effective and environmentally friendly. When compared with

activated carbon, the electrocoagulation has several advantages including environmental-friendly, non-toxic process, and less residue. Many studies showed that electrocoagulation was an efficient technique for discharging the pollutants at surface water in the lowlands [3], urban wastewater [4], restaurant's waste [5], chromium metal waste [6], and industrial wastewater [7]. Those studies have consistently shown that the electrocoagulation is one of the most promising techniques for wastewater treatment with the efficiencies between 70 and 95% in terms of COD and BOD respectively and less sludge products than other alternative procedures [8].

Presently, phytoremediation is an effective and affordable technological that use plant process to extract, remove, degrade, or render harmless hazardous materials including metals and metal pollutants present in the soils, sediments, and groundwater [9-10]. This technology is environmentally friendly and potentially cost-effective toward conventional water clean-up techniques. However, its application has limitations since the clean-up depth is strictly determined by the length of the plant roots. The transport of contaminants is minimal to the aboveground harvestable, and the movement of contaminants is induced exclusively by slow plant root suction. Therefore the efficiency of contaminant removal is depending on the extension of the plant roots in the soil and water surface [11].

Electro-assisted phytoremediation (EAPR) is an enhancement method to phytoremediation, requiring electrically assistance to overcome the weaknesses of phytoremediation itself [12]. The methods had been extensively reported on the improvement of soil [13-15] and aquatic phytoremediation [16-19] for the removal of heavy metals using various aquatic accumulator plants such as *Lemna minor*, *Lactuta sativa*, water hyacinth (*Eichornia crassipes*) and water lettuce (*Pistia stratiotes*).

The main objective of this study was to determine the optimal operation conditions and operating cost of effluent treatment from the Batik industry using a simultaneous electrocoagulation and EAPR system. Therefore, in this study, two major issues were addressed. First, the development and evaluation of a simultaneous process of electrocoagulation and EAPR was investigated. In addition, the assessment of rough horsetail (*Equisetum hyemale*) that is used in the electrical enhancement of aquatic phytoremediation treatment of the Batik wastewater was performed. Second, the survival strategy of growing plants in wastewater was assessed by (i) evaluation of the survival indicator to determine the COD level and heavy metal tolerance; (ii) determination of stressing indicator using total chlorophyll content and chlorophyll a/b ratio. In addition, the feasibility of operating cost on the effluent treatment of Batik wastewater was calculated.

■ EXPERIMENTAL SECTION

Batik Wastewater Sampling

Batik wastewater was collected before the rainy season from the Batik workshop in Mantrijeron, Yogyakarta, Indonesia, at the discharged point (GPS 7°49'06.7"S 110°22'00.3"E). The collected wastewater was directly used without preserved. The characteristics of wastewater such as COD, pH, and heavy metals (Pb and Cr) were shown in Table 1. The high COD concentration in the Batik wastewater occurred due to the presence of chemical substances used in these industries such as sodium silicate, sodium salt and sodium alginate [20-21]. In this study, the Batik wastewater has initial COD

Table 1. Profiles of Batik wastewater compared with the Ministry of Environment decree No. 5/2014 Republic of Indonesia regarding various industries wastewater standard

Characteristics	Batik Wastewater	Water Quality Standards			Unit
		Textile Industry	Other Quality		
			Class I	Class II	
COD	214.8	150	100	300	mg/L
Pb	0.47	N/A	0.1	1.0	mg/L
Cr (VI)	0.16	1.0	0.5	1.0	mg/L
pH	8.60	6-9	6-9	6-9	N/A

concentration of 214.8 mg/L. Usually the Batik or textile industry effluent contains high COD concentration than BOD [20,22-23].

Plant Collection

Rough horsetail (*Equisetum hyemale*) was collected based on a similar phytomorphology characteristic, which has the same number of stem segments and root density. Before being used in the EAPR system, the plants were undergoing the acclimation process to adapt the laboratory environment. Acclimation was proceeded in two steps. Initially, the plant was acclimated in a fresh water for 3 days and then the solution was changed to a Hoagland solution for the next 3 days. Hoagland solution contains the essential elements required by the plant for growth. 1 L of Hoagland solution was prepared by mixing of 0.00676 g KH_2PO_4, 0.252 g KNO_3, 0.59 g $Ca(NO_3)_2{\cdot}4H_2O$, and 0.20 g $MgCl_2{\cdot}6H_2O$ according to elsewhere publication [12].

Electrocoagulation Process

The wastewater was flown into the electrocoagulation reactor with the dimension of 35 (L) cm × 20 (W) cm × 20 (H) cm and filled with a volume of 10 L. The process was carried out for 1 h at constant voltage of 20 V (DC power supply, 60 V/10 A, SANFIX, Taiwan). The electrode used in the experiment was aluminum as anode and stainless-steel sheets as cathode for each consisted of 3 sheets with a dimension of 30 (L) cm × 20 (W) cm and 3 mm thickness. This process was intended to decrease the COD concentration in the wastewater. The solution was then continued to the EAPR reactor for the removal of the remaining heavy metal concentration. Fig. 1 shows the schematic diagram of the simultaneous processes. At first, wastewater from the equalization tank was treated by electrocoagulation process and then continued by EAPR treatment to decrease high COD and heavy metal concentration. The performance of electrocoagulation and EAPR process were evaluated by removal efficiency (%) of COD and heavy metal concentration as shown in Eq. (1).

$$\text{Removal efficiency}(\%) = \frac{C_o - C_f}{C_o} \times 100 \quad (1)$$

where, C_o was the initial concentration before treatment, and C_f was the final concentration after treatment.

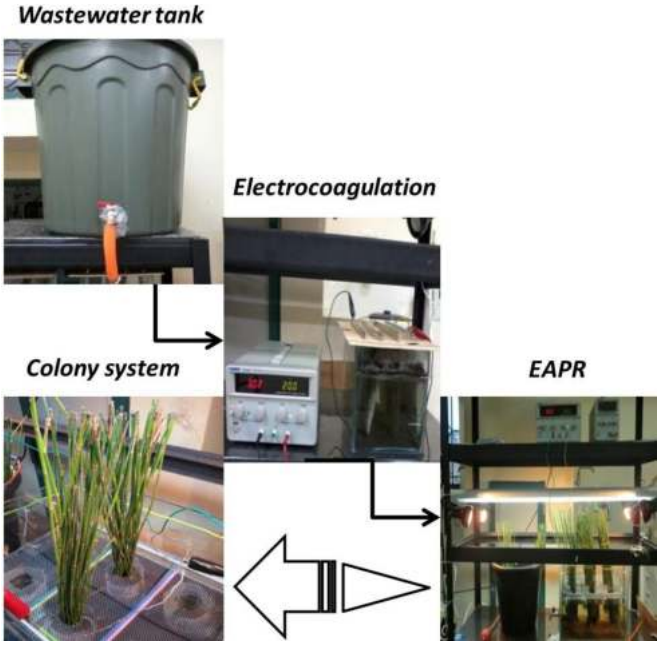

Fig 1. Simultaneous electrocoagulation process and EAPR treatment by which electrodes cathode of colony system. Rough horsetail (*Equisetum hyemale*) was used as an accumulator plant in the EAPR system

EAPR Process

After the electrocoagulation process, the wastewater then continued to flow into the EAPR reactor (40 (L) cm × 30 (W) cm × 30 (H) cm) for 17 L volume, equipped with Ti as anode (Ø 6 mm × 25 (L) cm, Nilaco, Japan) and stainless steel U316 (net wire: 10 mesh, 30 (L) × 20 (W) cm; and bar: 3 mm thick, 30 (L) × 1 (W) cm) as cathode electrode. The process was carried out for 7 days at a constant voltage of 5 V (DC power supply, 30 V/5 A, SANFIX, Taiwan) using rough horsetail (*Equisetum hyemale*) as the accumulator plant. The light source was provided by fluorescent tubes (40 W, Philips, Indonesia) and incandescent lamps (20 W, Osram Duluxstar PAR 38, China) which was controlled by an intra–matrix timer to provide 16/8 h light/dark cycle. In this process, a designed cathode-pot was used as electrode according to elsewhere publications [18-19].

Water and Plant Tissues Analysis

Six bundles of rough horsetail (*Equisetum hyemale*) were used in the EAPR system and for every two bundles was harvested consecutively at the 3rd, 5th

and 7th day of plantation. Those plants were weighed, washed thoroughly with running tap water and then separated into shoot and root. The shoot and root were cut into small pieces, dried for 5 days at 60 °C in an oven. Approximately 1.0 g of samples was digested in 10 mL concentrated HNO_3 overnight and then evaporated for 15 mins on a hot plate until half of the initial volume. All solutions were adjusted to the final volume of 10 mL with deionized water. Heavy metal (Pb and Cr) concentration was then measured by a flame atomic absorption spectrophotometer (Buck Scientific 202, USA). The concentrations of the element in this study were reported on a dry matter basis. The COD concentration in the water sample was determined by closed reflux of colorimetric methods according to SNI 6989.2:2009 with the reference method of 5220 D [24].

Chlorophyll Analysis

The changes of the plants morphology were observed and monitored every day. The chlorophyll content of the plants was measured according to Moran and Porath [25]. A sample of 200 mg plant shoots was cut into 0.5 cm segments and incubated in acetone for 24 h at 4 °C in a dark room. The absorbance of the supernatant was measured by a spectrophotometer (Hitachi 2000, Japan) at wavelengths (λ) of 645 and 663 nm. Chlorophyll concentrations ($mg.mL^{-1}$) were calculated by using the following Eq. (2) to Eq. (4).

$$[\text{Chl a}]=[12.7\times\lambda 663]-[2.69\times\lambda 645] \quad (2)$$

$$[\text{Chl b}]=[22.9\times\lambda 645]-[4.68\times\lambda 663] \quad (3)$$

$$[\text{Total Chl}]=[8.02\times\lambda 663]-[20.2\times\lambda 645] \quad (4)$$

Operating Cost

Under the experimental studied, there are two main operating costs to be considered. The first process was the electrocoagulation and the second was the EAPR process. The operating cost for the electrocoagulation process was mainly from the electrodes wear and electric energy costs [26], while the EAPR process was only from the electric energy consumption [27]. In addition, there were some factors in both processes that should be considered such as labor, maintenance, sludge dewatering and disposal as well as fixed costs. The calculations of electrode wear [28], electric energy consumption, and operating cost were calculated by using the following Eq. (5) to Eq. (7).

$$m_{el}=\frac{i.t.M}{F.z} \quad (5)$$

$$C_{en}=\frac{U.i.t}{V} \quad (6)$$

$$C_{op}=a.C_{en}+b.C_{el} \quad (7)$$

where m_{el} = electrode wear, C_{en} = energy consumption, C_{op} = operating cost, i = Current (Ampere), t = Time (sec or h), M = molar mass (g), F = Faraday constant, z = Number of electrons, U = Electric tension (Voltage), V = Volume (m^3), a = Energy cost, C_{en} = Energy consumption, b = cost of the plate, C_{el} = Electrode consumption.

■ RESULTS AND DISCUSSION

Electrocoagulation Process

Table 2 shows the concentrations of COD and heavy metal (Pb and Cr) in the wastewater after 1 h of electrocoagulation process. The result showed that the electrocoagulation has decreased the COD concentration by 69.8%, and the removal efficiencies of heavy metal was 8.5% and 25.0% for Pb and Cr respectively from the initial concentration. It is known that the removal of organic matter (i.e. COD) using electrocoagulation may involve electrochemical oxidation, adsorption by electrostatic attraction and physical entrapment [23]. In this step, the wastewater was treated only by electrochemical oxidation without further treatment, so that the resulted-effluent solution from this step still contained high organic matter. Therefore, the process was continued by the EAPR system to increase the removal of COD from wastewater. In this study, the aluminum electrode was used as an anode and stainless steel as a cathode. If the electric current passes through to the Al electrode, the Al^{3+} ions were generated electrochemically

Table 2. Profiles of COD and heavy metal (Pb and Cr) concentration after 1 h of electrocoagulation process

Condition	COD (mg/L)	Heavy metal (mg/L)	
		Pb	Cr
Initial	214.8	0.47	0.16
After 1 h process	65.3	0.43	0.12

at the anode, and coagulant agents $Al(OH)_3$ were formed as shown in the following Eq. (8) to Eq. (10). The formation of coagulant agent could decrease the heavy metal concentration together with organic substances in the wastewater. In this process, metal hydroxide has occurred because of hydroxyl ion production at the cathode during the electrocoagulation treatment. The solubility of a certain metal reaches a minimum at a specific alkaline condition, which has a characteristic value for each metal [23]. The pH of wastewater changed from 8.60 to 8.86 during the electrocoagulation treatment indicating more alkaline pH developed in the wastewater since hydroxyl (OH^-) ions were continuously produced in the solution as shown in Eq. (9) to Eq. (10).

$$\text{Anode}: Al_{(s)} \rightarrow AL^{3+}{}_{(aq)} + 3e^- \quad (8)$$

$$\text{Cathode}: 3H_2O_{(aq)} + 3e^- \rightarrow 3/2\, H_{2(g)} + 3OH^-{}_{(aq)} \quad (9)$$

$$\text{Hydrolysis}: Al^{3+}{}_{(aq)} + 3OH^- \rightarrow Al(OH)_{3(aq)} \quad (10)$$

EAPR Process

Fig. 2 shows the decreasing of COD concentration on the EAPR system for the 7 days process. The feed water for the EAPR treatment process (i.e. EA 1st to 7th) resulted in the effluent from 1 h after electrocoagulation treatment (i.e. EC1) by which the COD concentration has been decreased by 69.8% from the initial concentration of wastewater. In the EAPR treatment process, the COD concentration continued to decrease until 80.4% (i.e. EA1 to EA7). In general, the simultaneous process of electrocoagulation (i.e. EC) and EAPR (i.e. EA) have been successfully performed to decrease the COD concentration in the wastewater from 214.8 mg/L to 42.2 mg/L. The decreasing of COD in the phytoremediation process of Batik wastewater was a time consuming and the removal efficiency was depending on the plant used in the study. For example, degradation of COD using *Egeria densa* and *Salvinia molesta* achieved 95% and 99% respectively for the 17 days process [29]. Therefore, the electro-assisted system aimed to extend the phytoremediation process on the removal of organic matter could simultaneously decrease the heavy metal concentration in the Batik wastewater [30]. A significant decreased of heavy metal concentration in the wastewater

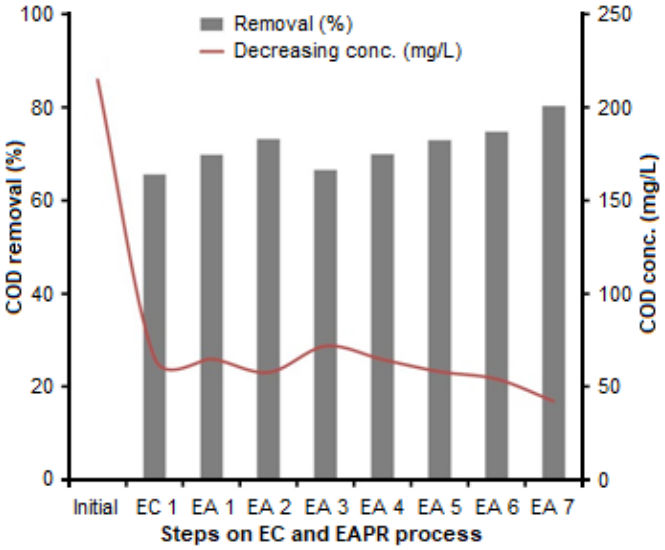

Fig 2. Profiles of decreasing COD concentration after electrocoagulation and continuing with the EAPR process on the treatment of Batik wastewater. EC1 indicates 1 h of electrocoagulation process and EA 1 to EA 7 indicates from 1st to 7th day of EAPR process

occurred from 3rd to 7th day of the EAPR process (Fig. are not shown). The removal of Pb and Cr concentration in the EAPR process decreased by 0.09 mg/L and 0.28 mg/L, respectively. The decrease of lead and chromium concentration in the wastewater indicates the absorption of heavy metal by rough horsetail through an electro-assisted process to the plants that occurred intensively. An acidified solution occurred around the anode when water hydrolyzed to form hydrogen ions (H^+). This acidic environment extended the lead ions (Pb^{2+}) migration toward the cathode and precipitated as metal-hydroxide around the cathode-pot electrode in the EAPR system as shown in Eq. (11) and Eq. (12). Moreover, those reactions have produced oxygen and hydrogen gas in the solution.

$$\text{Anode}: H_2O_{(aq)} \rightarrow O_{2(q)} \rightarrow O2(q) + 2H^+{}_{(aq)} + 2e^- \quad (11)$$

$$\text{Cathode}: 2H_2O_{(aq)} + 2e^- \rightarrow H_{2(g)} + OH^-{}_{(aq)} \quad (12)$$

Heavy Metal Concentration in the Plant

Phytoremediation takes advantage of the unique and selective uptake capabilities of plant root systems, together with the translocation, bioaccumulation, and contaminant degradation abilities of the entire plant

body [31]. In the EAPR system, the heavy metal absorption by plants was assisted by electrical migration of metal ions from the anode to cathode pot around the plant root which accelerated the plant to uptake ions from aquatic media [18-19]. Table 3 shows the accumulation profiles of Pb and Cr in shoot and root of rough horsetail plant. For hyper-accumulator plants, high translocation of the heavy metal from the root system would occur to the aerial part of plants, such as shoots and leaves [9]. In this study, despite the high level of lead and chromium concentration in the root, the ability of rough horsetail to translocate heavy metal from roots to shoots has low concentration for each treatment. Besides, heavy metal concentration in the plant tissues increased with the elevated EAPR process. The removal ability of heavy metal from the solution by the EAPR system was different (see Table 3). For example, a high uptake of lead was observed than that of chromium by rough horsetail (*Equisetum hyemale*). Regardless of chromium source in the environment, the potential of the plant species tested in phytoremediation was limited because high chromium concentration in the shoots was toxic to plants. Therefore, the most tolerant plant species accumulated the least amount of chromium. For example, metal-tolerant species like coastal Bermudagrass did not accumulate Cr more than 2 mg/Kg plant mass with 500 mg/Kg of soil [32-33]. In this study, chromium was still being measured after the treatment process even though the metal concentration was very low in the wastewater (see Table 1) because chromium has been recognized as a toxic, mutagenic and carcinogenic metal.

Plant Stress Tolerance

Plant appearance was observed, and chlorophyll content was measured to assess the tolerance of plants to heavy metal during the EAPR process. Total chlorophyll content and chlorophyll a/b ratio are parameters for photosynthetic activity and often used as indicators of stress in plants. These parameters have been used for detecting and assessing the exposure of plants to environmental contaminants [34-35]. Fig. 3 shows the total chlorophyll and chlorophyll a/b ratio in the plant after the EAPR process.

In general, for plant treatments with the EAPR process at all harvesting time, the total chlorophyll contents significantly decreased except the plant harvested at 5th day after cultivation. Similar results also showed that the chlorophyll a/b ratio of the treated plant decreased compared to the control plant. Those results concluded that the plants exposed by the EAPR process were not under toxic chemical stressing which was confirmed by negative visual characteristics of phytotoxic symptoms (e.g. discoloration, pigmentation, yellowing, and withering). Regarding the pigment content, heavy metal-exposed plants showed a remarkable decrease of chlorophyll. Therefore, the rate of photosynthesis decreased significantly in response to the elevated heavy metal concentration. In other words, any changes in chlorophyll synthesis and activity used as the index of direct toxic effects of heavy metals [36].

Calculation of the Operating Cost

The calculation of electrode wear that was consumed during the electrocoagulation process was shown in Eq. (5) with the molar mass of aluminum is 26.982 g mol^{-1} and the oxidation number of the element is 3.

$$m_{el} = \frac{5 \times 3600 \times 26.982}{96485 \times 3} = 1.6779\,\text{g Al} \quad (13)$$

Table 3. Heavy metal concentration in the rough horsetail plant after EAPR process

Cultivation periods	Shoot		Root	
	Pb (mg/Kg)	Cr (mg/Kg)	Pb (mg/Kg)	Cr (mg/Kg)
EA 3	53.3	12.3	274.2	111.5
EA 5	68.9	21.1	287.0	116.2
EA 7	83.3	23.5	312.9	109.7
Control	52.5	27.2	226.0	117.4

EA 3, EA 5 and EA 7 indicate the cultivation period after 3rd, 5th and 7th day of cultivation. At 7th day was the last experimental time in the EAPR system before the plant was harvested. The control plant was phytoremediation without wastewater. All data were the average value from two replication.

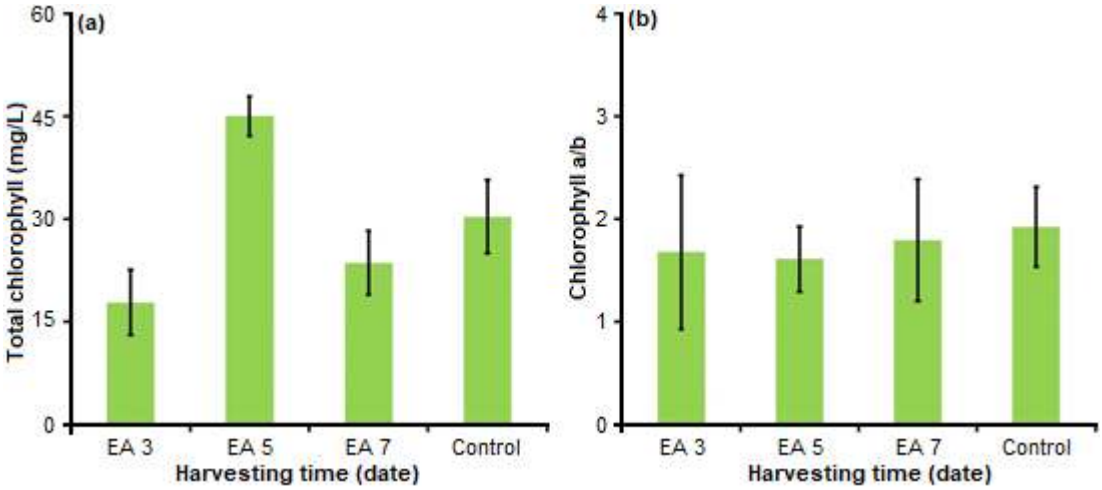

Fig 3. Total chlorophyll content (a) and chlorophyll a/b ratio (b) in the plants after EAPR process for lead (Pb) remediation (n = 3). Chlorophyll in the control plant defined as the plant that grew in phytoremediation. EA 3, EA 5 and EA 7 indicate the cultivation period after the 3rd, 5th and 7th day of cultivation

The energy consumption during the electrocoagulation (EC) and the EAPR process were calculated according to Eq. (6).

$$C_{en}(EC) = \frac{20\times5\times1}{0.01} = 10000\,Whm^{-3} = 10\,kWhm^{-3} \quad (14)$$

$$C_{en}(EAPR) = \frac{5\times5\times1}{0.017} = 1470.59\,Whm^{-3} = 1.47\,kWhm^{-3} \quad (15)$$

The operating cost of the batch reactor in the simultaneous of EC and EAPR system can be calculated using Eq. (7). The estimated value of 1.0 kg of aluminum plate is US$ 2.30, but the mass estimated cost of a small plate (200 g) used in the experiment is US$ 0.46. While, the value of industrial electrical energy in Indonesia (> 30000 kVA/October 2019) is US$ 0.0643 kWh (1 US$ = IDR 15,500).

$$C_{op} = 0.0643(10+1.47)+(0.46\times1.6779) = US\ \$1.509\,m^{-3} \quad (16)$$

The daily generation of effluent at the Batik industry was approximately 40 m^3 per day [37]. Therefore, the monthly value was estimated by US$ 1,811.

■ CONCLUSION

The results have demonstrated that the simultaneous process of electrocoagulation and EAPR process has been used to reduce significantly the concentration of COD and heavy metal (Pb and Cr) in the Batik wastewater. In addition, rough horsetail (*Equisetum hyemale*) was able to grow well in the EAPR system while treating the Batik wastewater. According to the total chlorophyll and chlorophyll a/b ratio, the plants were able to grow in Batik wastewater without showing a toxic chemical stressing. The results showed that the levels of COD and heavy metal (i.e. Pb and Cr) concentration in Batik wastewater has reduced in accordance to the Ministry of Environment Decree No. 5/2014 Republic of Indonesia regarding of various industries wastewater standard with the threshold limit of 150 mg/L COD and 1.0 mg/L Cr for textile industry and 0.1 mg/L Pb for another wastewater standard (Class I). The operating cost of mainly energy and electrode consumption was calculated as US$ 1.509/m^3 treated wastewater.

■ ACKNOWLEDGMENTS

The author would like to thank the Ministry of Research, Technology and Higher Education (KEMENRISTEKDIKTI), the Republic of Indonesia for their financial support through Excellence Higher Education Institution Research (PTUPT) 2017-2018 (Research contract: 041/HB-LIT/IV/2017 and Ministry of Research, Technology and Higher Education contract: 663/M/KP/XII/2015). Furthermore, financial support from the Directorate of Talent Development and Student Welfare of Universitas Islam Indonesia to A.D.A and S.B. are also gratefully acknowledged.

■ REFERENCES

[1] Wardhana, W.A., 2001, *Dampak Pencemaran Lingkungan*, Andi Offset, 10–12.

[2] Pereira, L., and Alves, M., 2012, "Dyes-Environmental impact and remediation" in *Environmental Protection Strategies for Sustainable Development*, Eds. Malik, A., and Grohmann, E., Springer, Netherlands, 111–162.

[3] Jiang, J.Q., Graham. N., André, C., Kelsall, G.H., and Brandon, N., 2002, Laboratory study of electrocoagulation-flotation for water treatment, *Water Res.*, 36 (16), 4064–4078.

[4] Smoczyński, L., Kalinowski, S., Ratnaweera, H., Kosobucka, M., Trifescu, M., and Pieczulis-Smoczyńska, K., 2017, Electrocoagulation of municipal wastewater - A pilot-scale test, *Desalin. Water Treat.*, 72, 162–168.

[5] Adegoke, A.T., and Abayomi, E.T., 2020, A preliminary study on the treatment of restaurant wastewater using electrocoagulation technique, *J. Degrade. Min. Land Manage.*, 7 (2), 2029–2033.

[6] El-Taweel, Y.A., Nassef, M.E., Elkheriany, I., and Sayed, D., 2015, Removal of Cr(VI) ions from wastewater by electrocoagulation using iron electrode, *Egypt. J. Pet.*, 24 (2), 183–192.

[7] Butler, E., Hung, Y.T., Yeh, R.Y.L., and Al Ahmad, M.S., 2011, Electrocoagulation in wastewater treatment, *Water*, 3, 495–525.

[8] Barrera-Díaz, C., Linares-Hernández, I., Roa-Morales, G., Bilyeu, B., and Balderas-Hernández, P., 2009, Removal of biorefractory compounds in industrial wastewater by chemical and electrochemical pretreatments, *Ind. Eng. Chem. Res.*, 48 (3), 1253–1258.

[9] Raskin, I., 2000, *Phytoremediation of Toxic Metals: Using Plants Clean Up the Environment*, Eds. Raskin, I., and Ensley, B.D., Wiley, New York.

[10] Terry, N., and Banuelos, G.S., *Phytoremediation of Contaminated Soil and Water*, Lewis Publisher, Boca Raton.

[11] Hodko, D., Van Hyfte, J., Denvir, A., and Magnuson, J.W., 2000, *Methods for enhancing phytoextraction of contaminants from porous media using electrokinetic phenomena*, US Patent No. 6145244A.

[12] Putra, R.S., Ohkawa, Y., and Tanaka, S., 2013, Application of EAPR system on the removal of lead from sandy soil and uptake by Kentucky bluegrass (*Poa pratensis* L.), *Sep. Purif. Technol.*, 102, 34–42.

[13] O`Connor, C.S., Lepp, N.W., Edwards, R., and Sunderland, G., 2003, The combined use of electrokinetic remediation and phytoremediation to decontaminate metal-polluted soils: a laboratory-scale feasibility study, *Environ. Monit. Assess.*, 84, 141–158.

[14] Aboughalma, H., Bi, R., and Schlaak, M., 2008, Electrokinetic enhancement on phytoremediation in Zn, Pb, Cu, and Cd contaminated soil using potato plants, *J. Environ. Sci. Health. Part A Environ. Sci. Health Part A Environ. Sci. Eng.*, 43 (8), 926–933.

[15] Zhou, D.M., Chen, H.F., Cang, L., and Wang, Y.J., 2007, Ryegrass uptake of soil Cu/Zn by EDTA/EDDS together with a vertical direct-current electrical field, *Chemosphere*, 67 (8), 1671–1676.

[16] Bi, R., Schlaak, M., Siefert, E., Lord, R., and Connolly, H., 2011, Influence of electrical fields (AC and DC) on phytoremediation of metal polluted soils with rapeseed (*Brassica napus*) and tobacco (*Nicotiana tabacum*), *Chemosphere*, 83 (3), 318–326.

[17] Kubiak, J.J., Khankhane, P.J., Kleingeld, P.J., and Lima, A.T., 2012, An attempt to electrically enhance phytoremediation of arsenic contaminated water, *Chemosphere*, 87 (3), 259–264.

[18] Putra, R.S., Cahyana, F., and Novarita, D., 2015, Removal of lead and copper from contaminated water using EAPR system and uptake by water lettuce (*Pistia stratiotes* L.), *Procedia Chem.*, 14, 381–386.

[19] Putra, R.S., Novarita, D., and Cahyana, F., 2016, Remediation of lead (Pb) and copper (Cu) using water hyacinth (*Eichornia crassipes* (Mart.) Solms) with electro-assisted phytoremediation (EAPR), *AIP Conf. Proc.*, 1744, 020052.

[20] Khalik, W.F., Ho, L.N., Ong, S.A., Wong, Y.S., Yusoff, N.A., and Ridwan, F., 2015, Decolorization and mineralization of Batik wastewater through the solar photocatalytic process, *Sains Malays.*, 44 (4), 607–612.

[21] Şahinkaya, S., 2013, COD and color removal from synthetic textile wastewater by ultrasound assisted electro-Fenton oxidation process, *J. Ind. Eng. Chem.*, 19 (2), 601–606.

[22] Holkar, C.R., Jadhav, A.J., Pinjari, D.V., Mahamuni, N.M., and Pandit, A.B., 2016, A critical review on textile wastewater treatments: Possible approaches, *J. Environ. Manag.*, 182, 351–366.

[23] Kabdaşli, I., Arslan-Alaton, I., Ölmez-Hancı, T., and Tünay, O., 2012, Electrocoagulation applications for industrial wastewaters: a critical review, *Environ. Technol. Rev.*, 1 (1), 2–45.

[24] Anonymous, 2009, *Air dan air limbah – Bagian 2: Cara uji kebutuhan oksigen kimiawi (Chemical Oxygen Demand/COD) dengan refluks tertutup secara spektrofotometri*, SNI 6989.2, Badan Standarisasi Nasional (BSN), Indonesia.

[25] Moran, R., and Porath, D., 1980, Chlorophyll determination in tissue using *N,N*-dimethylforamide, *Plant Physiol.*, 65 (3), 478–479.

[26] Kobya, M., Demirbas, E., and Akyol, A., 2009, Electrochemical treatment and operating cost analysis of textile wastewater using sacrificial iron electrodes, *Water Sci. Technol.*, 60 (9), 2261–2270.

[27] da Mota, I.O., de Castro, J.A., Casqueira, R.G., and de Oliveira Junior, A.G., 2015, Study of electroflotation method for treatment of wastewater from washing soil contaminated by heavy metals, *J. Mater. Res. Technol.*, 4 (2), 109–113.

[28] Geraldino, H.C.L., Simionato, J.I, de Souza Freitas, T.K.F., Garcia J.C., de Carvalho Júnior, O., and Correr, C.J., 2015, Efficiency and operating cost of electrocoagulation system applied to the treatment of dairy industry wastewater, *Acta Sci. Technol.*, 37(3), 401-408.

[29] Tangahu, B.V., and Putri, A.P., 2017, The degradation of BOD and COD of Batik industry wastewater using *Egeria densa* and *Salvinia molesta, JSTL*, 9 (2), 82–91.

[30] Tangahu, B.V., Ningsih, D.A., Kurniawan, S.B., and Imron, M.F., 2019, Study of BOD and COD removal in batik wastewater using *Scirpus grossus* and *Iris pseudacorus* with intermittent exposure system, *J. Ecol. Eng.*, 20 (5), 130–134.

[31] Viehweger, K., 2014, How plants cope with heavy metals, *Bot. Stud.*, 55 (1), 35.

[32] Shahandeh, H., and Hossner, L.R., 2000, Plant screening for chromium phytoremediation, *Int. J. Phytorem.*, 2 (1), 31–51.

[33] Kale, R.A., Lokhande, V.H., and Ade, A.B., 2015, Investigation of chromium phytoremediation and tolerance capacity of a weed, *Portulaca oleracea* L. in a hydroponic system, *Water Environ. J.*, 29 (2), 236–242.

[34] Aldoobie, N.F., and Beltagi, M.S., 2013, Physiological, biochemical and molecular responses of common bean (*Phaseolus vulgaris* L.) plant to heavy metals stress, *Afr. J. Biotechnol.*, 12 (29), 4614–4622.

[35] Rastgoo, L., Alemzadeh, A., Tale, A.M., Tazangi, S.E., and Eslamzadeh T., 2014, Effects of copper, nickel and zinc on biochemical parameters and metal accumulation in gouan, *Aeluropus littoralis*, *Plant Knowl. J.*, 3 (1), 31–38.

[36] Rastgoo, L., and Alemzadeh, A., 2011, Biochemical responses of gouan (*Aeluropus littoralis*) to heavy metals stress, *AJCS*, 5 (4), 375–383.

[37] Indrayani, L., 2018, Pengolahan limbah cair industri batik sebagai salah satu percontohan IPAL batik di Yogyakarta, *Ecotrophic*, 12 (2), 173–184.

An Investigation on the Effect of Solvent and Heat to Clay Minerals in Shaly Sandstone

Wan Zairani Wan Bakar[1,2,*], Ismail Mohd Saaid[2], Mohd Riduan Ahmad[3], Husna Hayati Jarni[1], and Siti Qurratu' Aini Mahat[2]

[1]*Oil and Gas Department, Faculty of Chemical Engineering, Universiti Teknologi MARA, 40450 Shah Alam, Selangor, Malaysia*

[2]*Department of Petroleum Engineering, Universiti Teknologi PETRONAS, 32610 Seri Iskandar, Perak, Malaysia*

[3]*Onyx Engineering Sdn Bhd, Jl. Perusahaan 4, 68100 Batu Caves, Selangor, Malaysia*

** **Corresponding author:***

tel: +60-192636695
email: zairani@uitm.edu.my

Received: July 23, 2019
Accepted: December 30, 2019

DOI: 10.22146/ijc.48010

Abstract: *Core cleaning could be complicated for samples that contain a high amount of clays. Some clays are delicate and exposure to solvent and heat would damage or alter its properties. In this study, we investigated the effect of direct exposure of solvent and heat to clay mineral properties based on petrographical data from X-Ray Diffraction (XRD), Fourier Transform Infrared Spectroscopy (FTIR), Field Emission Scanning Electron Microscope (FESEM) and Energy Dispersive X-Ray (EDX). Experiments were performed on sidewall core samples taken in a shaly sand zone. The FTIR data did not show any changes at the molecular level to the clay mineral after direct contact with the selected solvent. The FESEM images showed some illite floccules collapse in the samples exposed to oven-drying at 60 °C.*

Keywords: *clay minerals; core cleaning; petrography; solvent; heat exposure*

■ INTRODUCTION

Core analysis data is an important source of information for understanding formation characteristics as well as for calibrating with down hole well log data. Therefore, the information should be obtained from core samples that are representative of their native states and free from contaminants. Drilling mud and its additives are well-known sources of contamination that occur during drilling. It may alter rock surface chemistry and consequently affected important rock properties. These contaminants must be removed prior to any other measurement. However, the removal of these contaminants could be complicated especially from tight and delicate samples. Unsuitable techniques and solvent used in the cleaning process might lead to undesirable measurements as a result of the alteration of native rock properties. It has been reported that properties such as porosity, permeability and wettability are highly affected by the technique and solvent used in cleaning [1-4]. For samples with high clay content, the usage of solvent and exposure to heat might alter the electrochemical properties of the minerals.

Clay minerals are phyllosilicates with the tetrahedral layer and octahedral layer as the basic building block. The tetrahedral layer consists of either Si or Al bonding with the basal oxygen in tetrahedral coordination while the octahedral layer consists of cations (Si, Al or Mg) bonding with the basal oxygen in octahedral coordination. The structure of the clay determines its physical, electrochemical, rheological and thermal properties [5-6]. The alumino-silicates minerals appear as layering either in 2:1 or 1:1 ratio. In 1:1 clay minerals, the repetition of tetrahedron-octahedron (T–O) sheets in one layer disallows for alkali metal cations or water molecules to exist between them. In 2:1 structure the repetition of tetrahedron-octahedron-tetrahedron (T–O–T) sheets in one layer provides space for cations occupancy [7]. Smectite and illite are examples of 2:1 phyllosilicate (2 tetrahedral and 1 octahedral layer) and kaolinite is a 1:1 phyllosilicate. The 2:1 clay minerals only contain siloxane surfaces while the 1:1 clay minerals contain both the siloxane and hydroxyl surfaces [8]. The siloxane surface allows isomorphous substitutions by cations of lower valance at octahedral

sites, leaving the surface with positive charge deficiency. The charge deficiency is balanced by hydrated interlayer cations, which are easily released in water and exchanged with other cations, which contributes to electrical conductivity. Water can be bonded to the exchangeable cations or directly to the clay mineral surface.

Soxhlet extraction is one of the normal procedures used in core cleaning. In the Soxhlet procedure heat is introduced to vaporize the solvent, which also exposed the samples to heat. The samples were exposed to another heat by oven drying to remove pore water after cleaning. Nevertheless, earlier studies have been reported that exposure to heat during cleaning and drying would have impacted the rock properties. Bush and Jenkins [9] reported increasing errors in dry porosity and permeability for decreasing the values of the parameters. This was due to the removal of adsorbed water on the clay surface when exposed to heat in a Soxhlet procedure. From the study, it was suggested that at least one to two layers of adsorbed water on the clay surfaces should be retained when measuring the permeability and porosity of cores. Soeder et al. [4] claimed that unhumidified drying could cause a significant increase in permeability as a result of hydration water removal and the collapse of clay minerals.

A study by Pallatt et al. [10] exhibited that dehydration and shrinkage of clay minerals due to oven-dried had produced much higher permeability as compared to the wet and preserved state. Since clay minerals is a material that originally has a hydrophilic character due to the presence of the surface hydroxyl (–OH) groups that link easily to water molecules, hydration due to heat might affect the bonding to water molecules. This will consequently affect its electrical properties, which is related to the electrical current flow through hydrated clay surfaces. As an alternative, solvent flush cleaning without vapor is recommended for samples with delicate clays but this method incurs high cost and Soxhlet is preferable.

The use of solvent and heat in core cleaning is common to effectively remove mud contamination and pore fluid prior to the measurement of other rock properties. The possible effect of solvent to rock properties is balanced with the need to remove the contaminants in order to bring back the rock sample to its native state. Other than the effect of heat discussed earlier on, other studies also reported the effect of some organic solvent of varying polarities and dielectric to clay structure at a molecular level [11]. In this study, we analyzed any changes that might occur to the clay mineral structure as a result of the cleaning process. The mineral was analyzed X-Ray Diffraction (XRD), Fourier Transform Infra-Red (FTIR), Field Emission Scanning Electron Microscope (FESEM) and Energy Dispersive X-Ray (EDX).

■ EXPERIMENTAL SECTION

Materials

Laboratory analysis was performed on fresh samples taken in the Malay Basin where high compaction was expected. The sample was cored in the shaly sand zone on top of a gas reservoir and was preserved at low temperatures from the well site to protect from heat and keep the moisture. Gamma Ray from good log shows high reading indicating high shale content. As synthetic oil based mud was used during drilling, high resistivity reading at the near borehole wall as shown by induction log data indicates high mud contamination. The sample was carefully handled and preserved from the well site. Therefore, it was expected that any changes that would be observed after cleaning is due to response to the solvent and heat; and not from the surrounding effects.

Procedure

XRD

Relative mineral content was analyzed using the Empyrean XRD equipment. The mineralogical analysis using XRD was performed in a few steps involving bulk clays, glycolation, and heating at 350 and 550 °C. For first evaluation of the relative amount of bulk clays, a powdered sample was scanned over a 2θ range of 2–70° with CuKα radiation (1.5406) at a scan step time 148.92 and step width of 0.0260°. The generator was set at 40 mA and 45 kV. The proportion of clay minerals in the sample was further analyzed at clay size < 2 μm. 1.5g of the powdered sample was mixed with 3 drops of calgon

in a small tube to further break down the sample particles. Thirty milliliter distilled water was added and the mixture was well shaken before entering the ultrasonic bath for 10 min. Sample slurry was left for 24 h before air-dried on glass slides. The sample was then scanned using the same configuration as for bulk measurement. Ethylene glycol was used to detect the swelling components and estimate the illite-smectite composition. Sample on the glass slide was put side by side with ethylene glycol in a container and put in the oven at 80 °C for 30 min before scanned again. The sample was heated to 350 and 550 °C for 30 min before scanned again to distinguish kaolinite from chlorite.

FTIR, FESEM, and EDX

Two types of FTIR equipment were used to analyze the mineral content and structural change. The quantitative analysis was performed using bench top FTIR while Perkin Elmer FTIR Spectrometer was used to generate the spectrum in the range between 400 to 4000 cm^{-1}. Both types of equipment used the attenuated total reflection (ATR) method. The mid-range of infrared frequency was chosen as many minerals exhibit vibration modes within this range. For sample preparation, four offcuts from the sample were cleaned with four different types of solvent; methanol, toluene, chloroform and azeotrope (70% chloroform and 30% methanol). The effluent was checked every day until no further changes in the color were observed. The effluent was analyzed using Gas chromatography–mass spectrometry (GCMS) to study the component of contaminants being removed. Three types of drying were used for the samples cleaned with toluene; ambient, 60 °C with 40% humidity and 60 °C oven dry. Samples were ground to fine powder form prior to FTIR analysis. The powdered samples were also analyzed using Quanta FEG 450 FESEM and EDX.

■ RESULTS AND DISCUSSION

XRD Analysis

XRD data indicates the mineral constituents of the sample are consist of illite, kaolinite, chlorite, and quartz (Fig. 1). Characteristic reflection related to 10 Å periodicity that remains unchanged after ethylene glycol treatment indicates the presence of illite. Further confirmation is achieved with unchanged reflection after 350 and 550 °C treatment. Kaolinite and chlorite were identified from the reflection related to 7 Å that remains unchanged following ethylene glycol treatment. There are no changes in the reflection after 550 °C ignition indicates the presence of kaolinite rather than chlorite. Residual reflection identified at 7 Å is corresponding to kaolinite whereas chlorite would be destroyed at 450 °C heat [7]. However, the unchanged reflection after 550 °C heating could also indicate the existence of antigorite together with kaolinite. The presence of chlorite is indicated by the

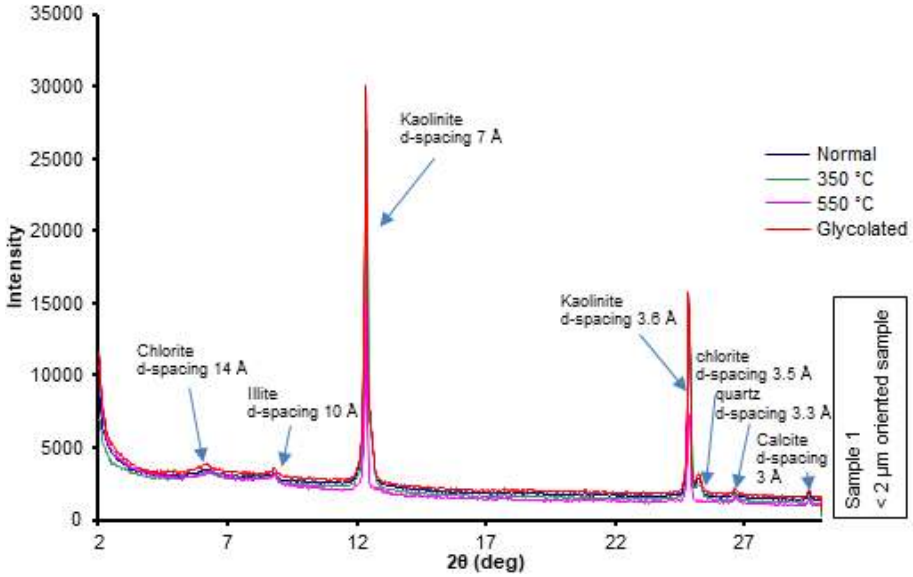

Fig 1. X-Ray Diffractogram of the sample

reflection at 14 Å periodicity that is unaltered following glycolation. The reflection slightly collapsed after 550 °C heating shows the presence of vermiculite alongside with the other minerals. Quartz was identified based on reflection related to 3 Å periodicity in the data.

EDX

The quantitative EDX analysis (Table 1) suggested O and Si as dominant elements in the sample. These elements are common in both quartz and clay minerals. Al and K, which are common in illite and kaolinite are found in smaller quantities. Fe also found in small quantities, which confirms the presence of illite as indicated by XRD and FTIR data. Minor concentrations of Na and Mg were also found in the sample. Mg is common is illite but Na is usually found in smectite. Since the XRD data did not indicate the presence of smectite, Na found in the EDX data could be attributed to residual impurities.

FTIR

Using the benchtop FTIR the mineral spectrum of the samples was automatically compared to a spectral library stored in the equipment. The mineral content in the samples was produced as a percentage as in Fig. 2. Consistent with the XRD result, FTIR data also recorded the presence of quartz, illite, kaolinite and chlorite. For the purpose of analysis, 10% tolerance is accepted for comparison of mineral content in each sample. Samples from toluene and chloroform recorded the same amount of quartz, illite, kaolinite and chlorite (within the acceptable tolerance). Samples from methanol and azeotrope recorded more quartz and less illite. Kaolinite and chlorite also presence in a smaller amount. The difference could be due to inefficient cleaning by methanol as inferred by the effluent's color. It had been observed that the effluent from samples in methanol was clear while effluent from toluene and chloroform were blackish. Effluent from azeotrope showed lighter color as compared to toluene and chloroform. This indicates that toluene and chloroform provide efficient cleaning while methanol is not suitable for this type of mud. This is supported by a study by Gupta et al. [2], who reported that toluene and chloroform have similar cleaning efficiencies. On the other hand, methanol is more suitable for removing polar components and dissipated salt [1]. The presence of mud contamination could have concealed the actual spectrum. The GCMS result indicates an abundance of alkane hydrocarbon (tridecane, undecane, ethyl, cyclopentane) and acid (oxalic and sulfuric) and no traces of components from

Table1. EDX result

No	Element	Weight %	Atomic %
1	O	56.53 ± 1.54	70.52
2	Na	0.24 ± 0.12	0.21
3	Mg	0.29 ± 0.12	0.24
4	Al	5.44 ± 0.25	4.02
5	Si	32.52 ± 0.95	23.11
6	K	1.39 ± 0.17	0.71
7	Ca	0.36 ± 0.14	0.18
8	Ti	0.27 ± 0.16	0.11
9	Fe	2.37 ± 0.38	0.85
10	U	0.58 ± 0.5	0.05
	Total	100	100

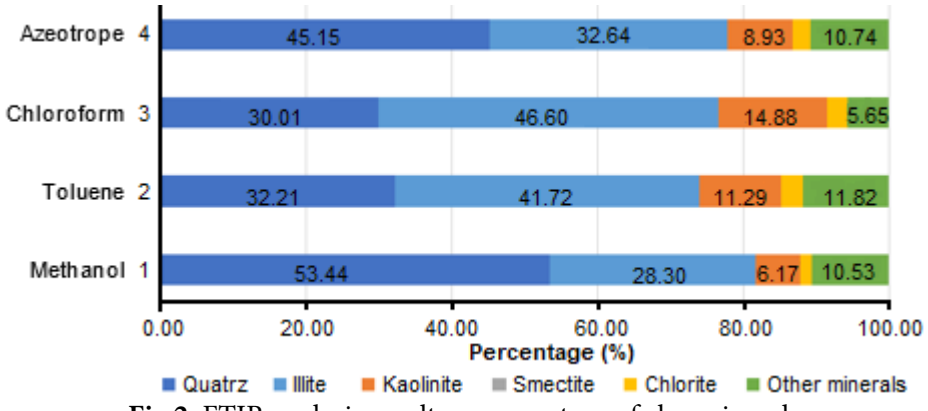

Fig 2. FTIR analysis result on percentage of clay minerals

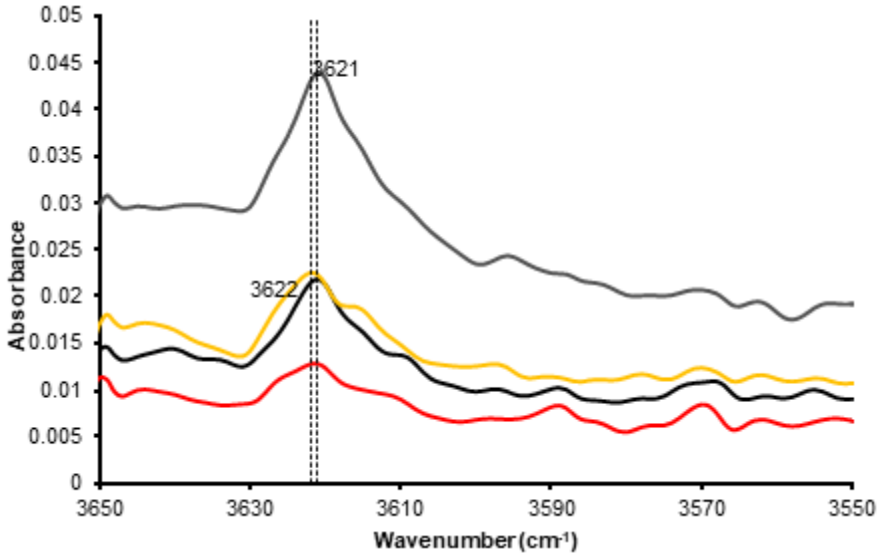

Fig 3. From top to bottom; FTIR spectrum for samples cleaned with chloroform, azeotrope, toluene, and methanol for 3600 to 3500 cm^{-1}

quartz minerals (O, Si). This excluded the possibility that quartz has been removed by toluene and chloroform.

The FTIR spectrum of the samples was further analyzed to study any changes to the mineral structure. FTIR spectrum for all samples shows absorbance in the 1200-400 cm^{-1} region and vibration at near 3620 cm^{-1} (Fig. 3 and 4). The 3620 cm^{-1} bands are corresponding to the stretching vibration of an inner hydroxyl group, lying between the tetrahedral and octahedral sheets [12]. The band is found in pure kaolinite and also in smectite that has a high amount of Al in the octahedral [12-13]. We believed that this energy bend represents kaolinite since smectite was unidentified by XRD analysis. The hydroxyl groups in kaolinite are bonded to octahedral cations, but residing largely within the plane of apical oxygen atoms that link the tetrahedral and octahedral sheets. The stretching region of samples cleaned with toluene, chloroform and azeotrope had shifted to higher energy band by 1 cm while the samples cleaned with methanol had shifted to higher energy band by 2 cm from the common band of pure kaolinite. Methanol is an intermediate polarity organic solvent, which has the ability to interact with clay surface oxygen and structural hydroxyl groups while toluene and chloroform are non-polar molecules that have a low influence on clay structure. Some other solvent with a very high polarity such as formamide had shown very strong nonbonding interaction with Na-montmorillonite structure that consequently affect its hydraulic conductivity [11]. However, very low energy shifting indicated that the hydroxyl stretching is able to return to its original energy band. The shifting to 3622 cm^{-1} in methanol exhibits an energy band as in dickite. Dickite is a 1:1 phyllosilicate that has identical chemical composition and structure of the individual layer to kaolinite but differs in the layer stacking arrangement. Kaolinite has a single-layer structure instead of double-layer polytype.

The energy band between 1200–400 cm^{-1} in the samples are corresponding to stretching and bending of Si-O and bending of OH from several minerals. The vibrations at 1116, 1029, 996, 935 and 908 cm^{-1} are closed to kaolinite with shifting to lower energy within 3 to 15 cm. These vibrations are attributes to Si-O stretching. The 908 cm^{-1} energy band is closed to the inner surface OH groups bending region of kaolinite at 913 cm^{-1}. All samples exhibited the same vibrations pattern that shows all solvent had a similar influence on the clay structure of the sample. 1029 cm^{-1} energy band is close to Si-O stretching vibrations in illite at 1030 cm^{-1} and muscovite at 1028 cm^{-1}. The lower energy bands at 522, 463 and 422 cm^{-1} carry almost similar patterns to those found in illite. No shifting in energy has been observed from all the samples.

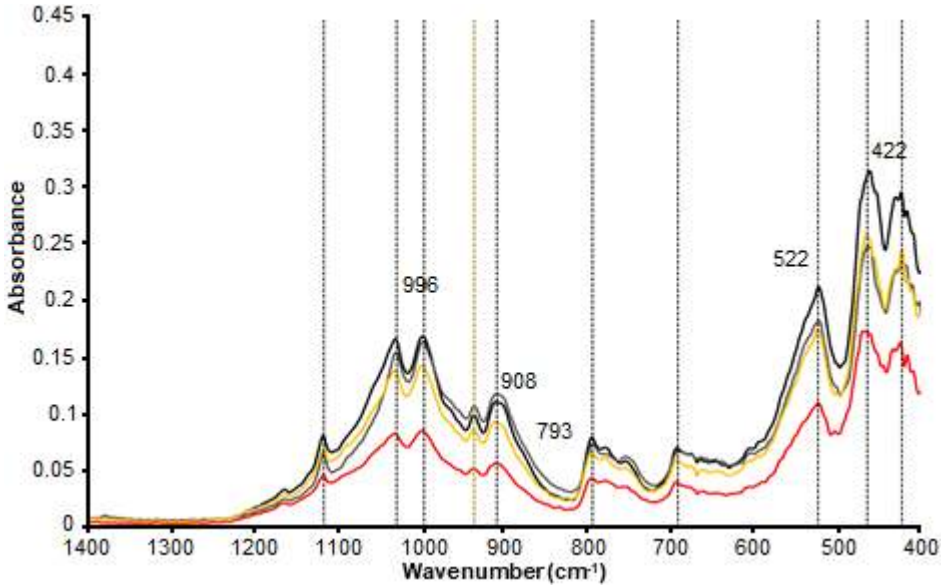

Fig 4. From top to bottom; FTIR for samples cleaned with toluene, chloroform, azeotrope and methanol for 1200 to 400 cm^{-1}

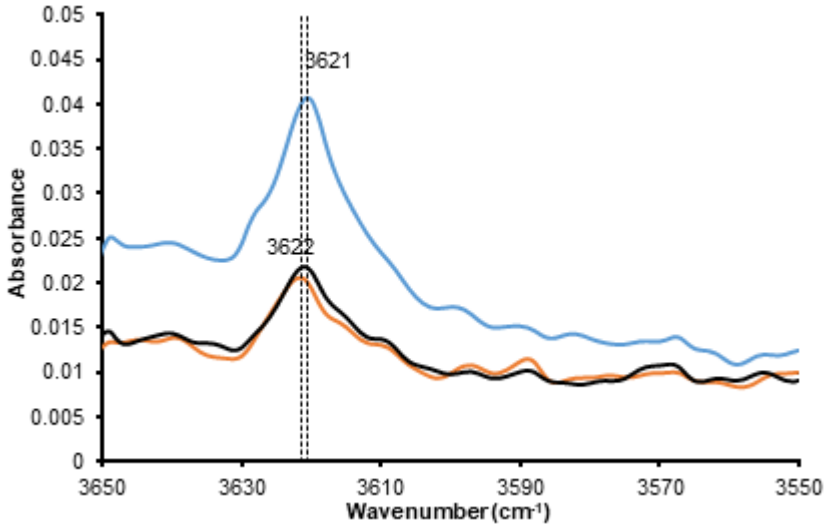

Fig 5. From top to bottom; the FTIR spectrum for samples dried at ambient, 60 °C humidity and 60 °C oven-dried for 3600 to 3500 cm^{-1}

The FTIR data for samples dried at ambient, 60 °C humidity and 60 °C oven-dried also shows a slight effect on the clay structure based on energy shifting in Fig. 5 and 6. All samples exhibited the same pattern with insignificant shifting in the energy band between 1200 to 400 cm^{-1}.

FESEM

FESEM images indicate that the clay minerals in the sample are dominated by kaolinite and illite (Fig. 7). The ragged appearance of the flat platelets exhibited that the illite is detrital in origin [14]. These two types of clay minerals are common in the Malay Basin. Illite flocculation of typical edge-face cardhouse orientation has been observed in the sample after toluene cleaning and dried at ambient temperature (Fig. 8). Flocculation happens when clumps of electrostatically charged clay flakes sink in ion-enriched salty water and form a "cardhouse" structure of individual edge-face or edge-edge–oriented flakes and/or domains of face-face–oriented flakes. This may generate pores, which when

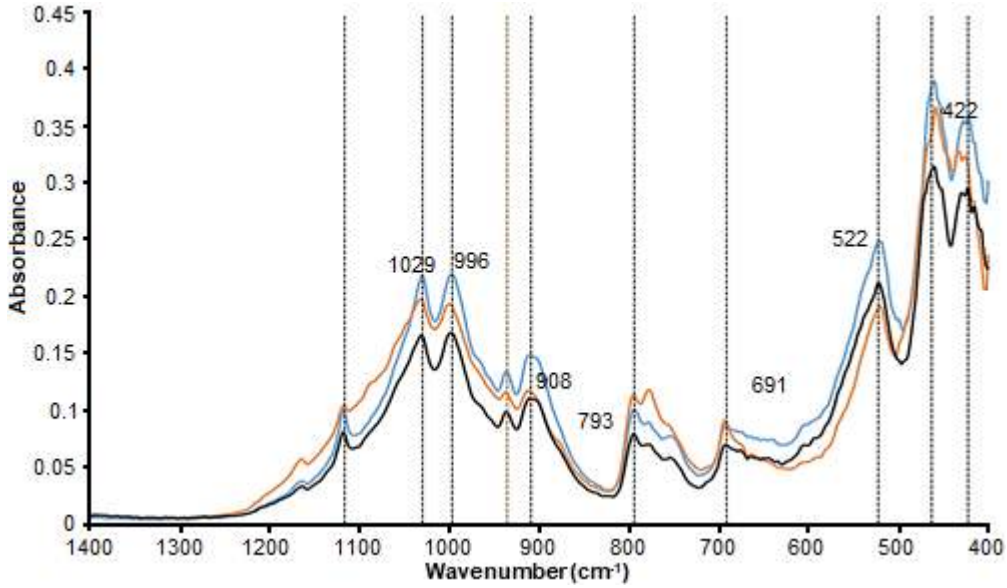

Fig 6. From top to bottom; the FTIR spectrum for samples dried at ambient, 60 °C humidity and 60 °C oven-dried for 1200 to 400 cm^{-1}

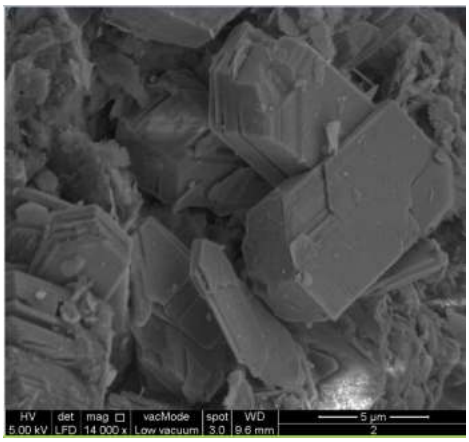

Fig 7. Kaolinite surrounded by illite

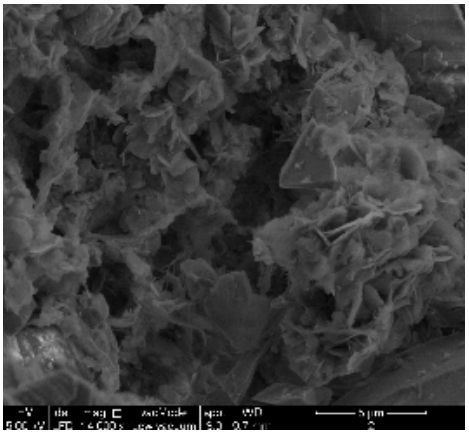

Fig 8. FESEM image of illite flocculation for sample dried at ambient temperature

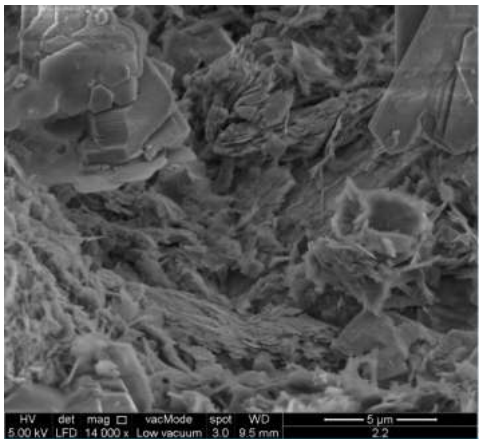

Fig 9. FESEM image of the sample after oven-dried at 60 °C

interconnected will form permeability pathways. The edge-face and face-face flocculation is common in clay aggregates and happens in the presence of either fresh or salt water [15]. The illite floccules and kaolinite structures show that the mineral survived and less affected by toluene cleaning.

Floccules collapsed (Fig. 9) has been observed in the sample after 60 °C oven-dried. The collapse of the floccules structure might be due to dehydration upon oven-heating. A similar effect in a different type of illite clays had been observed in an earlier study by Pallatt et al. [10]. The SEM photograph of filamentous diagenetic

illite clays in the report showed that the open mesh was compacted against pore walls due to oven-drying. This had created a larger path for fluid to flow and increased permeability.

GCMS

The Gas chromatography–mass spectrometry (GCMS) result of effluent from methanol, toluene or chloroform cleaning shows no traces of clay mineral components being removed or dissolved in the solvents (Fig. 10(a) to (b)). The effluent from toluene shows a high amount of hydrocarbon component and acid, which is expected from the drilling mud contamination. This shows that toluene interacts well with hydrocarbon

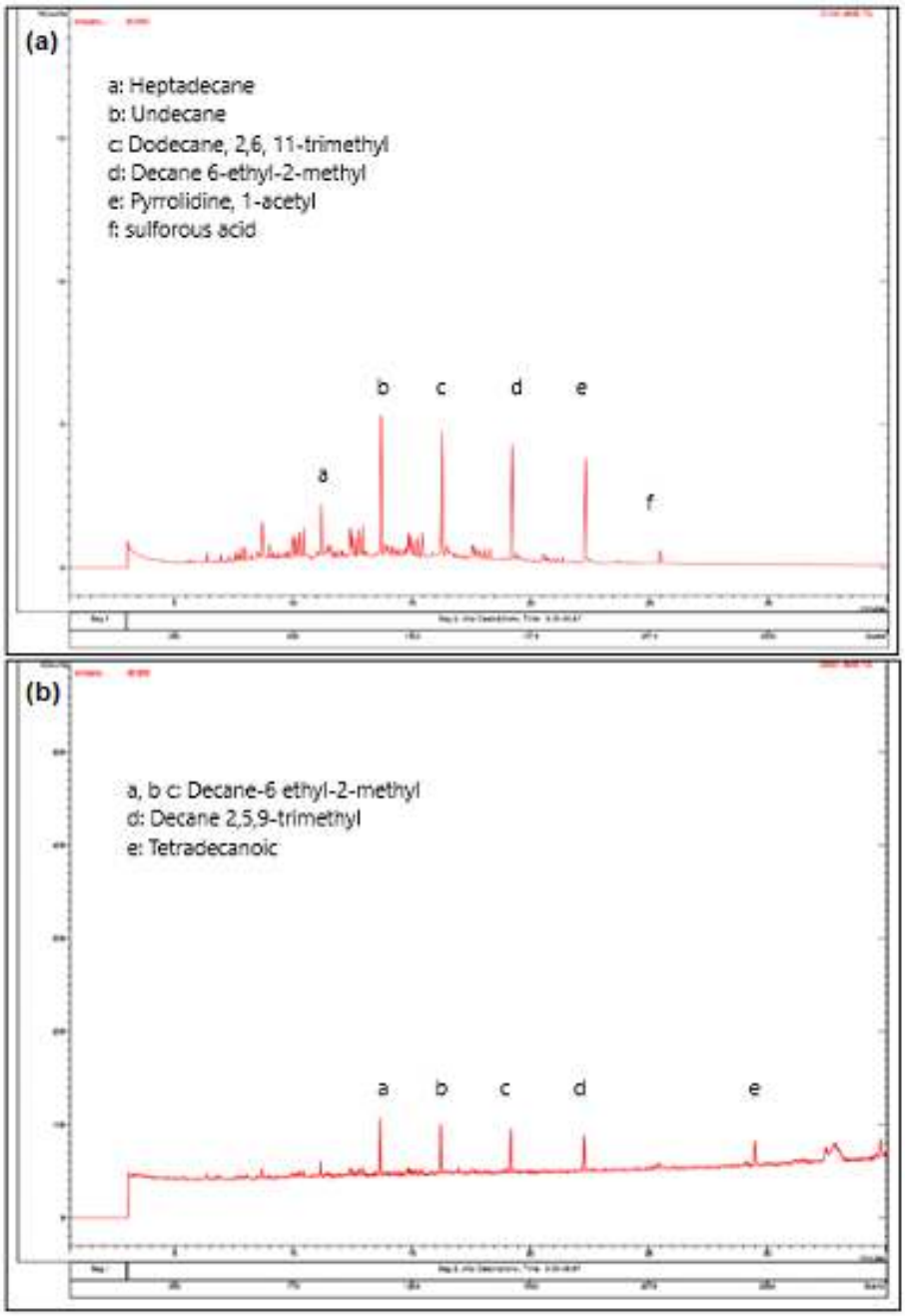

Fig 10. (a) chromatogram for effluent from toluene cleaning and (b) chromatogram for effluent from methanol cleaning

in drilling mud but does not give any effect to the clay mineral. A lesser amount of hydrocarbon component was recorded in the effluent from methanol cleaning showing that methanol alone is less efficient to remove the contaminants but better interaction with water and salt. We did not manage to get the result for effluent from chloroform cleaning due to evaporation prior to the test.

■ CONCLUSION

The FTIR result showed that direct contact with the selected solvent does not give any impact at the molecular level to the clay minerals in the sample. Toluene and chloroform are very-low polarity solvents that do not have a strong ability to interact with water or negatively charged clay sheets but only with the hydrocarbon component from the synthetic based mud. Methanol is an intermediate polarity solvent that can interact with water and oxygen on the clay surface but the kaolinite, illite and chlorite constituted in the sample are a type of non-expandable clay minerals, which have a tight crystal structure and low bonding with water. Kaolinite and illite have been reported to release the physically bound water at temperatures 55 and 72 °C respectively [16] but the effect had not been observed from FTIR data in this study.

The illite floccules collapse from the FESEM images could possibly due to the heat exposure during oven-drying. This could lead to enlargement of the fluid flow path and consequently increase porosity and permeability. The impact of these two parameters was not investigated here but should be further studied alongside with the impact of other parameters such as wettability and electrical properties.

■ ACKNOWLEDGMENTS

This research is supported by YUTP 0153AA-H05 and FRGS 5/3 (322/2019). The author also acknowledges the sponsorship of the program from the Ministry of Higher Education (MOHE), Malaysia (SLAI Fellowship Scheme), together with Universiti Teknologi MARA (UiTM), Malaysia. The author would also like to thank Onyx Engineering Sdn Bhd for their technical support.

■ REFERENCES

[1] Gant, P.L., and Anderson, W.G., 1988, Core cleaning for the restoration of native wettability, *SPE Form. Eval.*, 3 (1), 131-138.

[2] Gupta, I., Rai, C., Tinni, A., and Sondergeld, C., 2017, Impact of different cleaning methods on petrophysical measurements, *Petrophysics*, 58 (6), 613–621.

[3] Jennings, H.Y., 1957, Effect of Laboratory Core Cleaning on Water-Oil Relative Permeability, *Fall Meeting of the Society of Petroleum Engineers of AIME,* 6-9 October 1957, Dallas, Texas, SPE-897-G.

[4] Soeder, D.J., 1986, Laboratory drying procedures and the permeability of tight sandstone core, *SPE Form. Eval.*, 1 (1), 16–22.

[5] Cho, D.W., Chon, C.M., Kim, Y., Jeon, B.H., Schwartz, F.W., Lee, E.S., and Song, H., 2011, Adsorption of nitrate and Cr(VI) by cationic polymer-modified granular activated carbon, *Chem. Eng. J.*, 175, 298–305.

[6] Kloprogge, J.T, 1998, Synthesis of smectites and porous pillared clay catalysts: A review, *J. Porous Mater.*, 5 (1), 5–41.

[7] Grim, R.E., and Joitns, W.D., 1954 Clay mineral investigation of sediments in the northern Gulf of Mexico, *Clays Clay Miner.*, 2, 81–103.

[8] Djomgoue, P., and Njopwouo, D., 2013, FT-IR spectroscopy applied for surface clays characterization, *J. Surf. Eng. Mater. Adv. Technol.*, 3 (4), 275–282.

[9] Bush, D.C., and Jenkins, R.E., 1970, Proper hydration of clays for rock property determinations, *J. Pet. Technol.*, 22 (7), 800–804.

[10] Pallatt, N., Wilson, J., and McHardy, B., 1984, The relationship between permeability and the morphology of diagenetic illite in reservoir rocks, *J. Pet. Technol.*, 36 (12), 2–225.

[11] Amarasinghe, P.M., Katti, K.S., and Katti, D.R., 2009, Nature of organic fluid–montmorillonite interactions: An FTIR spectroscopic study, *J. Colloid Interface Sci.*, 337 (1), 97–105.

[12] Madejová, J., 2003, FTIR techniques in clay mineral studies, *Vib. Spectrosc.*, 31 (1), 1–10.

[13] Vaculíková, L., and Plevová, E., 2005, Identification of clay minerals and micas in sedimentary rocks,

Acta Geodyn. Geomater., 2 (2), 167–175.

[14] Huggett, J.M., 1995, Formation of authigenic illite in palaeocene mudrocks from the central North Sea: A study by high resolution electron microscopy, *Clays Clay Miner.*, 43 (6), 682–692.

[15] O'Brien, N.R., 1971, Fabric of kaolinite and illite floccules, *Clays Clay Miner.*, 19 (6), 353–359

[16] Kubliha, M., Trnovcová, V., Ondruška, J., Štubňa, I., Bošák, O., and Kaljuvee, T., 2017, Comparison of dehydration in kaolin and illite using DC conductivity measurements, *Appl. Clay Sci.*, 149, 8–12.

[17] Madejová, J., and Komadel, P., 2001, Baseline studies of the clay minerals society source clays: Infrared methods, *Clays Clay Miner.*, 49 (5), 410–432.

[18] Pironon, J., Pelletier, M., De Donato, P., and Mosser-Ruck, R., 2003, Characterization of smectite and illite by FTIR spectroscopy of interlayer NH_4^+ cations, *Clay Miner.*, 38 (2), 201–211.

The Effect of Red Palm Oil Concentration towards Characteristics and Biodegradability of PLA-Starch Film

Siti Fatma Abd Karim*, Nur Aliah Adilla Mohammad Asri, Rabiatul Adawiyah Abdol Aziz, and Ummi Kalthum Ibrahim

Faculty of Chemical Engineering, Universiti Teknologi MARA, 40450 Shah Alam, Selangor, Malaysia

** Corresponding author:*

tel: +6017-7789215
email: sitifatma9633@uitm.edu.my

Received: August 2, 2019
Accepted: December 26, 2019

DOI: 10.22146/ijc.48453

Abstract: *Polylactic acid (PLA) is a biodegradable polymer that had been used as a substitute for conventional petroleum based plastics. Plasticizers were added into the solution of PLA and starch (PLA/S) to increase the flexibility and degradability of the produced film. PLA/S films need plasticizers that able to improve the degradation process. Red palm oil (RPO) were incorporated into PLA/S blends. The films were casted into petri dish via casting method. The films were characterized based on the color, thickness and chemical composition (Fourier-transform infrared spectroscopy). The performance of the films was analyzed based on tensile strength and biodegradation percentage. The films were yellowish in color with the addition of RPO. The FTIR shows that the increment of RPO concentration modified the intermolecular interaction between the PLA/S molecules. The tensile strength of PLA decreased with the addition of starch. The biodegradability test was done by using soil burial method where the samples were buried in peaty soil for 12 days. The films produced from these combinations resulted in a good biodegradable activity. The films with high concentration of RPO and presence of starch degraded 100% within 12 days. RPO can be used as the plasticizer with further improvement.*

Keywords: *film packaging; polylactic acid; red palm oil; starch*

■ INTRODUCTION

Active film packaging had been developed in food industry to increase the shelf life of the food. The main goal in this area is to ensure that the food quality is in its best condition and can be maintained for the long term. Traditionally, petroleum-based food packaging is used as the food packaging. However, due to its low degradability and harmful features, biodegradable and edible film packaging using natural ingredients had been developed [1]. Polylactic acid (PLA) is a type of polymers used to produce food packaging. PLA had caught people attention as it can be chemically synthesized from agricultural resources [2]. PLA is a biodegradable thermoplastic that can be derived from the natural resources or through fermentation or chemical synthesis of lactic acid monomer [3]. Starch is a natural polymer that consists of linear polysaccharides and branched molecules that can promote the elastic properties that needed in the development of the thermoplastic. Starch based films had been one of the materials used in the film packaging production. This is due to its physical characteristics that similar to synthetic polymers which are odorless, tasteless, transparent and resistant to the O_2 passage [4-5]. Combination of PLA and starch (PLA/S) blends produced brittle film. Moreover, PLA/S films causes deterioration in terms of mechanical strength. According to Wang et al. [6], large and rigid particles cannot toughen the polymer matrix. From previous studies, it had been shown that a very poor interfacial adhesion between the hydrophobic PLA and hydrophilic starch [6]. Therefore, additives were added to toughening the blends. Researchers had found some methods that can toughen the combination matrix including addition of plasticizers. Plasticizers are commonly used as an ingredient to increase the flexibility of the polymers and improving their process ability [7] by improving the mechanical properties of the starch film. Sufficient amount of plasticizer will increase

the molecular mobility and increase the elongation at break point of the film [8-9]. PLA requires plasticizer to increase its ability to plastic deformation. Palm oil consists of triglycerides and unsaturated fatty acid which favors to be used as the plasticizer. In this study, red palm oil (RPO) were added as a plasticizer to improve the PLA and starch-based food packaging. By the addition of these materials, the quality of the produced film increased and can be commercialized. The objectives of this study was to develop and characterized a film food packaging from PLA/S/RPO blends and analyze the mechanical properties and biodegradability of the films.

■ EXPERIMENTAL SECTION

Materials

Polylactic Acid (PLA) resin was used (NatureWorks®). Red Palm Oil (RPO) used from IKO natural product with purely refined of 100% natural crude palm oil. The potato starch used from Bendosen with pH value at 6.7. The starch has white and crystal luster appearance. Chloroform with molecular weight of 119.380 g/mol and density of 1.490 g/cm^3 was used as a solvent to dissolve the PLA resins. Chloroform was gained from R&M chemicals.

Procedure

Preparation of the film

As for the PLA/starch/RPO films, PLA solution was mixed with the starch powder and stirred for 4 h or until the starch was completely dissolved. Then, different volume of RPO was added into the solution. The optimum volume of plasticizer into the PLA film was 5% of the PLA volume [10]. The solution was stirred for another 4 h before being casted in the glass petri dish with a radius of 70 mm. The samples were left to dry at room temperature for 24 h before being peeled and stored in a sealable plastic bags to avoid contamination. Eight samples were prepared consisting of PLA pure, PLA/RPO (0.25 mL, 0.5 mL and 1 mL), PLA/S and PLA/S/RPO (0.25 mL, 0.5 mL and 1 mL).

The thickness and color of the film

The thickness was measured using digimatic micrometer by Mitutoyo at room temperature. The thickness was measured for five different areas before calculating the average thickness. The color of each produced films were tested using the chromameter. Three readings were taken for each sample at different areas. The average value was used to determine the final color placement in the color chart.

Fourier transform infrared spectroscopy (FTIR)

The FTIR spectra of control and blend films were recorded at 8 cm^{-1} resolution and in the range between 400 to 4000 cm^{-1} at room temperature. FTIR analysis used to determine the stretching vibrations of the bonds and the components of each sample.

Tensile properties (tensile strength and elongation at break)

The samples were cut lengthwise and cross direction 60 mm × 15 mm. For tensile strength, the load range and appropriate grip of testing machine. The extensometer measured the load versus extension was recorded. The testing speed was at 500 mm/min with using load cell of 2.5 kN. The distances between the two anchorages was 40 mm. The maximum load, width and thickness were recorded. Tensile strength represents the film resistance to elongation. The following formula was used to calculate the tensile strength and percentage of elongation.

$$\text{Tensile strength} = \frac{\text{maximum load}}{\text{width}(\text{cm}) \times \text{thickness}(\text{cm})} \quad (1)$$

$$\%\,\text{elongation} = \frac{\text{break distance}}{\text{gauge length}} \times 100\% \quad (2)$$

Biodegradability test

The soil was prepared with soil samples from peaty soil from a palm tree plantation in Kuala Selangor. Films of 4 cm^2 were scaled and the initial weight of the samples were measured. Four sets of samples were prepared for this test. The samples then being put into soil at a depth of 8 cm from the soil surface. Sixty mL of water was added to the samples daily. The biodegradation tests were performed at the ambient temperature. The samples were retrieved after 12 days. The samples were cleaned with a brush and cleaned using distilled water to remove the soil debris. Then, it was dried in an oven at 80 °C for 24 h. after drying, the weights of the samples

were measured and recorded to assess the average weight loss (%WL) [11].

■ RESULTS AND DISCUSSION

Films Thickness and Color

Fig. 1 shows the average thickness of the films. The thickness of the film increased when the RPO concentration increased. However, there is a slight reduction of thickness at 0.5 mL RPO. Film with starch shows higher thickness compared to film without starch. The addition of starch into the film blends will increase the thickness of the films due to the domain structure of immiscible polymer blend [12]. The result obtained at 0.5 mL RPO for both films with and without starch showed the lowest thickness perhaps due to less plasticization effect occur at lowest concentration.

Fig. 2 shows the color produced by the films. Addition of RPO into the PLA/S solution had affected the color of the film. The film appears to be yellowish-colored. This is due to the nature of RPO which is red-orange color and the presence of beta-carotene in the oil. PLA/RPO 0.5 mL yielded more luminous which resulted higher DeltaE* value. The data gained from the chromameter being analyzed by using the color chart. Pure PLA film performed clear and transparent color while film of PLA/S blends in group of white color. Starch reduces the transparency of the film. Plasticizer affected the opacity and physical appearance of the film [8]. Higher concentration of RPO may had increased the PLA film luminosity [13]. Thus, performing more luminous film packaging.

Fourier Transform Infrared Spectroscopy (FTIR)

Fig. 3 shows the FTIR for PLA/RPO films and Fig. 4 shows the result for PLA/S/RPO film. Peaks 1080 cm^{-1} indicate the C-O stretching as according to Sanyang et al.,

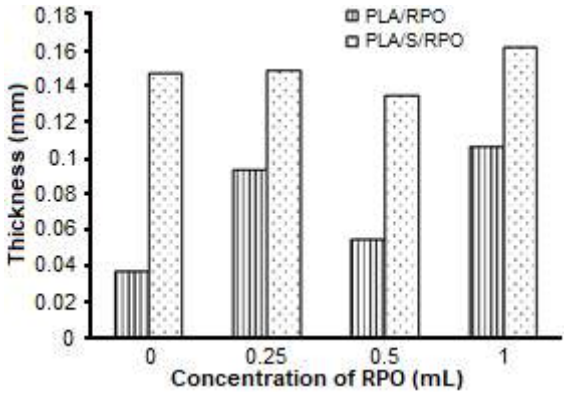

Fig 1. Thickness of the films

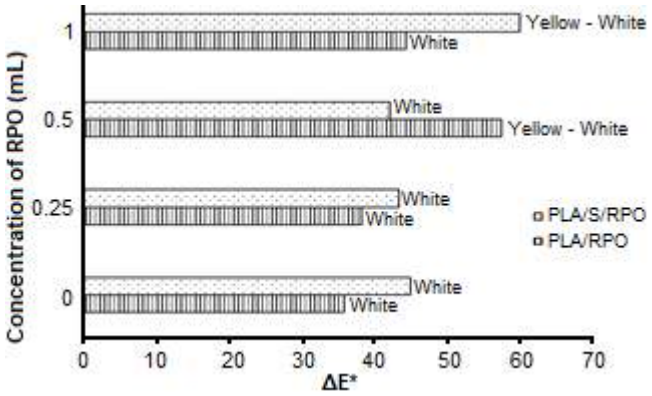

Fig 2. The color of the films

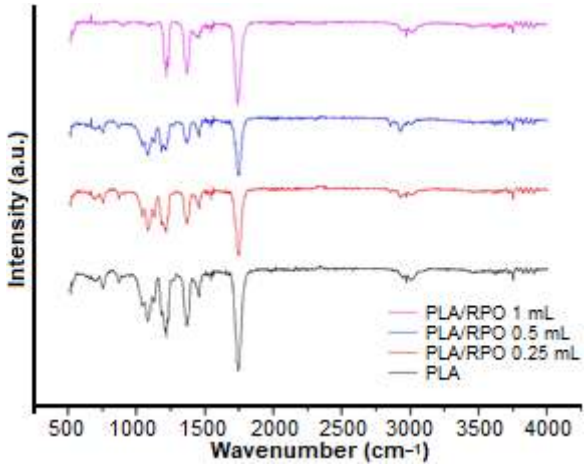

Fig 3. FTIR spectrum for PLA/RPO films

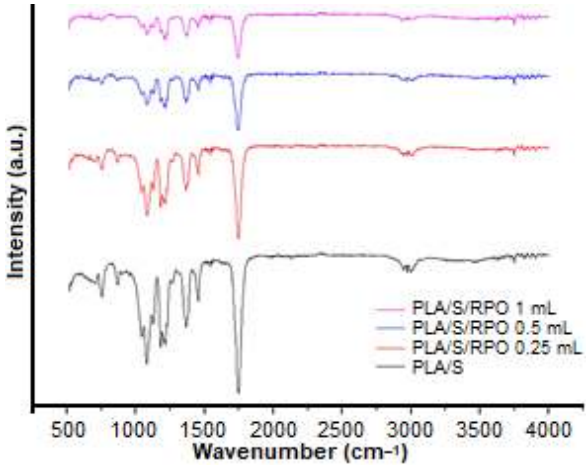

Fig 4. FTIR spectrum for PLA/S/RPO films

the peaks attributed to this bonds are range from 1100–950 cm^{-1} [14]. This also had been reported by Ref [15-16]. PLA/S blends showed the absorption spectra at 1082 cm^{-1} due to the saccharide structure. The peak corresponded to the –C-H deformation is at 1380 cm^{-1}. RPO are mainly consists of 50% saturated and 50% of unsaturated fatty acids. A significant increment for –C-H deformation in the PLA blends film. The absorbance peak at 1290–1180 cm^{-1} shows the esters stretching vibrations. The peak decreases as the concentration of RPO increases. The value of percentage of transmittance decreases from 1287 cm^{-1} to 1272 cm^{-1}. This shows that the ester molecular bonds, O=C-OR being interrupted and loosen its intermolecular bond [17]. Small alteration of peak from 1078 cm^{-1} (pure PLA film) to 1085 cm^{-1} (PLA/RPO 1 mL). This alteration in the absorption peak indicates that the miscibility and interaction of PLA and RPO. The peaks at 1500 to 1000 cm^{-1} indicates the region of oil. This has also reported by previous researchers [18-19].

The absorption band at 1745 cm^{-1} shows –C=O bonds stretching vibrations of carbonyl. Based on the obtained result, all of the samples shows the absorbance peak at 1738–1745 cm^{-1} which represented the C=O bonds stretching. This represents the stretching vibrations of carbonyl on ester group in PLA. The absorbance decreases as the concentration of RPO increases. The FTIR spectra shows at 1746 cm^{-1} that indicates the triglyceride ester linkage. This shows that PLA, starch and RPO link to each other in the film. There is a change in the FTIR spectra was observed at 1747 to 1740 cm^{-1} when RPO was added representing C=O stretching contributed by triglyceride ester presence in RPO. The intermolecular interactions of PLA and PLA/S were affected by the increment of RPO concentration. PLA is hydrophobic in nature; it is sensitive to moisture. This will affect the result in self-hydrolysis of carboxylic acid end groups present in PLA.

Tensile Properties (Tensile Strength and Elongation Break)

Fig. 5 shows the tensile strength of the films while Fig. 6 represent the elongation at break point of each produced film. Pure PLA possessed 40.4 MPa for its tensile strength and exhibited 4.96% at the elongation at break point. Addition of starch into PLA reduces the tensile strength from 40.4 MPa to 20.6 MPa. The tensile strength decreases with the increases concentration of RPO.

Theoretically, increase of tensile strength will decrease the elongation at break point. This is greatly opposite with the result by previous researchers [20-21]. According to Chieng et al. pure PLA typically rigid and brittle. Pure PLA had a high tensile strength but very limited elongation at break point. Adding plasticizers weakens the intermolecular forces in the film and reduce the brittleness and rigidity of the film [8] at once weaken the tensile strength. Low elongation at break point of PLA/RPO films may due to the insufficient amount of plasticizer to increase the molecular mobility and obtain more elongable film [8,22]. From the result, it can be seen that the ratio of PLA: RPO was not at optimum.

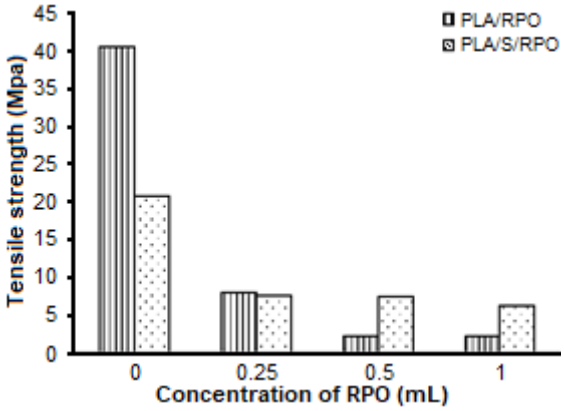

Fig 5. Tensile strength of the films

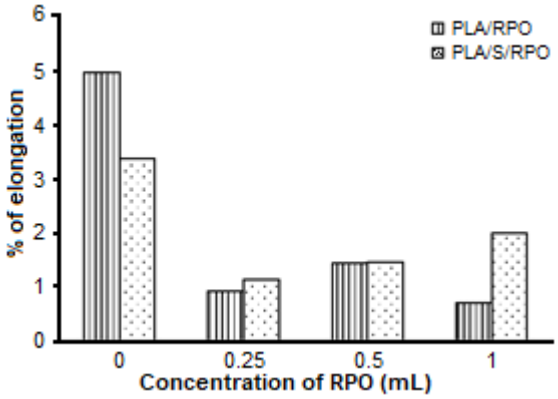

Fig 6. Elongation at break point of the films

Biodegradability Test

Fig. 7 shows biodegradability percentage of PLA/RPO and PLA/S/RPO films. Pure PLA did not degrade throughout the process. The percentage degradation of PLA/RPO films increased when the concentration of RPO increased. After 12 days, 100% degradation occurred for PLA/S/RPO 1 mL. As for PLA/RPO films, only PLA with 0.25 mL of RPO degrade 100% while the other films degrade 31%, 50% and 46%, respectively. This shows that good biodegradable activity occurred during the degradation process. Film consisting of starch and higher concentration of RPO blends degrade greatly. The degradation process and mechanism in soil are complex and unclear as it depends on the environmental conditions. Pure PLA film requires more time than the other samples [23]. The degradation of PLA begins with hydrolysis induced by the diffusion of water into the materials, followed by the microorganisms attack and the break-down of polymer chain [11]. PLA/S/RPO films exhibited aggressive changes on degradation. The collected samples were in pieces and no complete films were collected except for the PLA/S film. The most degraded films were PLA/S/RPO 1 mL. This proved that with the presence of starch and RPO accelerated the degradation process. Comparing to the fracture surface done by pure PLA, the structure remained unchanged even after day-12. This had been discussed by Tokiwa [23], PLA is susceptible to microbial attack in natural environment than other aliphatic polyesters [23]. This is due to the sparsely distributed PLA-degrading microorganisms in natural environment which leads to slow degradation process.

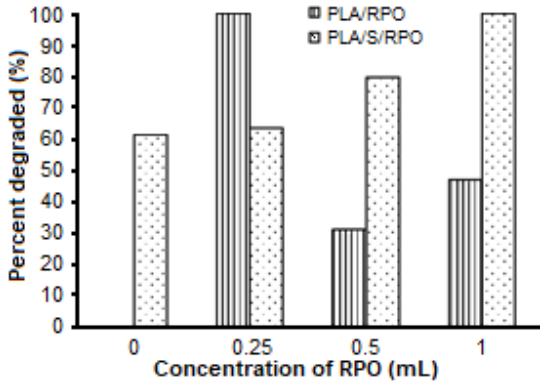

Fig 7. Biodegradation percentage of the films

■ CONCLUSION

This study was conducted to produce a film packaging by combining PLA, starch and RPO. The characteristics and biodegradability properties of film were analyzed. PLA film with high concentration of RPO resulting a glossy and shiny film while addition of starch reducing the opacity of the film. The thickness of the films increases as the concentration of RPO increases and presence of starch. The FTIR results show that the structure of the PLA being altered with the presence of RPO. The addition of RPO did not positively impact the tensile strength and the elongation at break point of the films. The blends of PLA/RPO ratio did not achieve the optimum value. PLA/S with 1 mL of RPO degrade 100% in 12 days. These findings show that the films are a biodegradable film which fulfilled the objectives. The methods used in the film formation need to be improved. A longer mixing time are needed in order to perform a thin and clear layer of PLA/RPO film.

■ ACKNOWLEDGMENTS

Thank you to Fakulti Kejuruteraan Kimia, Universiti Teknologi Mara and special appreciation to Kementerian Pendidikan Malaysia for the budget approval under RMI file number: 600-RMI/ST/FRGS 5/3/FST (37/2011).

■ REFERENCES

[1] Kaya, M., Khadem, S., Cakmak, Y.S., Mujtaba, M., Ilk, S., Akyuz, L., Salaberria, A.M., Labidi, J., Abdulqadir, A.H., and Deligöz, E., 2018, Antioxidative and antimicrobial edible chitosan films blended with stem, leaf and seed extracts of *Pistacia terebinthus* for active food packaging, *RSC Adv.*, 8 (8), 3941–3950.

[2] Gan, I., and Chow, W.S., 2018, Antimicrobial poly(lactic acid)/cellulose bionanocomposite for food packaging application: A review, *Food Packag. Shelf Life*, 17, 150–161.

[3] Tawakkal, I.S.M.A., Cran, M.J., Miltz, J., and Bigger, S.W., 2014, A review of poly(lactic acid)-based materials for antimicrobial packaging, *J. Food Sci.*, 79 (8), R1477–R1490.

[4] Cano, A., Jiménez, A., Cháfer, M., Gónzalez, C., and Chiralt, A., 2014, Effect of amylose: Amylopectin ratio and rice bran addition on starch films properties, *Carbohydr. Polym.*, 111, 543–555.

[5] Vásconez, M.B., Flores, S.K., Campos, C.A., Alvarado, J., and Gerschenson, L.N., 2009, Antimicrobial activity and physical properties of chitosan-tapioca starch based edible films and coatings, *Food Res. Int.*, 42 (7), 762–769.

[6] Wang, J., Zhai, W., and Zheng, W., 2012, Poly (ethylene glycol) grafted starch introducing a novel interphase in poly(lactic acid)/poly(ethylene glycol)/ starch ternary composites, *J. Polym. Environ.*, 20 (2), 528–539.

[7] Koh, J.J., Zhang, X., and He, C., 2018, Fully biodegradable poly(lactic acid)/starch blends: A review of toughening strategies, *Int. J. Biol. Macromol.*, 109, 99–113.

[8] Maniglia, B.C., Tessaro, L., Ramos, A.P., and Tapia-Blácido, D.R., 2019, Which plasticizer is suitable for films based on babassu starch isolated by different methods?, *Food Hydrocolloids*, 89, 143–152.

[9] Piorkowska, E., Kulinski, Z., Galeski, A., and Masirek, R., 2006, Plasticization of semicrystalline poly(l-lactide) with poly(propylene glycol), *Polymer*, 47 (20), 7178–7188.

[10] Zulkifli, W.N.F.M., 2017, Bioplasticiser and palm oil, *Palm Oil Dev.*, 67, 16–19.

[11] Lv, S., Zhang, Y., Gu, J., and Tan, H., 2018, Physicochemical evolutions of starch/poly(lactic acid) composite biodegraded in real soil, *J. Environ. Manage.*, 228, 223–231.

[12] Fathima, P.E., Panda, S.K., Ashraf, P.M., Varghese, T.O., and Bindu, J., 2018, Polylactic acid/chitosan films for packaging of Indian white prawn (*Fenneropenaeus indicus*), *Int. J. Biol. Macromol.*, 117, 1002–1010.

[13] Sanyang, M.L., Sapuan, S.M., Jawaid, M., Ishak, M.R., and Sahari, J., 2015, Effect of plasticizer type and concentration on tensile, thermal and barrier properties of biodegradable films based on sugar palm (*Arenga pinnata*) starch, *Polymers*, 7 (6), 1106–1124.

[14] Sanyang, M.L., Sapuan, S.M., Jawaid, M., Ishak, M.R., and Sahari, J., 2016, Development and characterization of sugar palm starch and poly(lactic acid) bilayer films, *Carbohydr. Polym.*, 146, 36–45.

[15] Chieng, B.W., Ibrahim, N.A., Then, Y.Y., and Loo, Y.Y., 2014, Epoxidized vegetable oils plasticized poly(lactic acid) biocomposites: Mechanical, thermal and morphology properties, *Molecules*, 19 (10), 16024–16038.

[16] González, A., and Alvarez Igarzabal, C.I., 2013, Soy protein - Poly (lactic acid) bilayer films as biodegradable material for active food packaging, *Food Hydrocolloids*, 33 (2), 289–296.

[17] Tee, Y.B., Talib, R.A., Abdan, K., Chin, N.L., Basha, R.K., and Yunos, K.F.M., 2014, Toughening poly(lactic acid) and aiding the melt-compounding with bio-sourced plasticizers, *Agric. Agric. Sci. Procedia*, 2, 289–295.

[18] Man, Y.B.C., Haryati, T., Ghazali, H.M., and Asbi, B.A., 1999, Composition and thermal profile of crude palm oil and its products, *J. Am. Oil Chem. Soc.*, 76 (2), 237–242.

[19] Jusoh, E.R., Ismail, M.H.S., Abdullah, L.C., Yunus, R., and Rahman, W.A.W.A., 2012, Crude palm oil as a bioadditive in polypropylene blown films, *BioResources*, 7 (1), 859–867.

[20] Mir, S.A., Dar, B.N., Wani, A.A., and Shah, M.A., 2018, Effect of plant extracts on the techno-functional properties of biodegradable packaging films, *Trends Food Sci. Technol.*, 80, 141–154.

[21] Mohd Amin, A.M., Mohd Sauid, S., So'aib, M.S., Musa, M., and Ku Hamid, K.H., 2017, Mechanical and thermal properties of thermoplastic film from *Tacca leontopetaloides* starch reinforced with rice husk biochar, *Mater. Sci. Forum*, 890, 188–191.

[22] Zhang, Y., 2010, "Hydrothermal liquefaction to convert biomass into crude oil" in *Biofuels from Agricultural Wastes and Byproducts*, Eds. Blaschek, H.P., Ezeji, T.C., and Scheffran, J., Wiley-Blackwell, Oxford, UK, 201–232.

[23] Tokiwa, Y., and Calabia, B.P., 2006, Biodegradability and biodegradation of poly(lactide), *Appl. Microbiol. Biotechnol.*, 72 (2), 244–251.

Metabolic Changes in the Trichomes of *Cannabis sativa* var. *bedrobinol* Analyzed by ^{1}H-NMR-Based Metabolomics

Nizar Happyana[1,2,*] and Oliver Kayser[2]

[1]*Organic Chemistry Division, Chemistry Study Program, Faculty of Mathematics and Natural Sciences, Bandung Institute of Technology, Jl. Ganesha No. 10, Bandung 40132, West Java, Indonesia*

[2]*Department of Technical Biochemistry, Technical University of Dortmund, Emil-Figge-Str. 66, 44227 Dortmund, Germany*

* ***Corresponding author:***

tel: +62-222502103
email: nizar@chem.itb.ac.id

Received: August 15, 2019
Accepted: December 4, 2019

DOI: 10.22146/ijc.48765

Abstract: *Trichomes of* Cannabis sativa *are the main tissue for synthesizing and storing cannabinoids, the most interesting compounds in this plant. In this report, metabolic changes in the trichomes of* C. sativa *var.* bedrobinol *were investigated by* ^{1}*H-NMR-based metabolomics over the flowering session. Three cannabinoids, including* Δ^9*-tetrahydrocannabinolic acid (THCA), cannabichromenic acid (CBCA), and* Δ^9*-tetrahydrocannabinol (THC), were successfully identified in the chloroform extracts of the* Cannabis *trichomes. Meanwhile, 20 non-cannabinoid compounds, including sugars, amino acids, and other acidic constituents, were detected in the water extracts. Metabolic changes of the* Cannabis *trichomes during the monitoring time were successfully revealed using the models of partial least squares discriminant analysis (PLSDA) and* ^{1}*H-NMR quantitative analysis. Score plots of the PLSDA models classified metabolomes based on the harvest time. Discriminant metabolites for the differentiation were detected in the loading plots of the models. THCA was found as an important discriminant compound in the chloroform extracts, while all quantified water-soluble compounds were detected, contributing to the metabolic changes of the water extracts. The obtained results shed more light on the biosynthesis of metabolites in the* Cannabis *trichomes over the flowering season.*

Keywords: Cannabis*; cannabinoids;* ^{1}*H-NMR-based metabolomics; trichomes*

■ INTRODUCTION

Cannabis sativa L. (Cannabaceae) is an annual flowering plant that has been cultivated for thousands of years ago. The *Cannabis* cultivation method was written in ancient Chinese literature, and this method had been used for a thousand years [1]. The plant has been used by humankind for medicine, food, clothing, and purposes of recreation and spiritual [2-3]. This plant originally comes from Central and Eastern Asia region [4] and then spread around the world, including Indonesia. Since *Cannabis* is often misused as a recreational drug, this plant is categorized as a dangerous narcotic in most countries, including Indonesia. However, some drugs derive from *Cannabis* are available for medication, including Marinol® and Sativex®. Marinol® is used for the treatments of HIV/AIDS-induced anorexia and chemotherapy-induced nausea and vomiting [5]. Meanwhile, Sativex® can be used for the treatment of neurologic disorders, including multiple sclerosis [6].

The responsible compounds for bioactivities of *Cannabis* are cannabinoids. More than 100 cannabinoids had been successfully detected in *Cannabis* [7]. Δ^9-tetrahydrocannabinol (THC) is the most interesting cannabinoid since it is mainly responsible for the psychoactive properties of *Cannabis*. This cannabinoid presents in the plant on its acidic form (Δ^9-tetrahydrocannabinolic acid, THCA). Based on the concentrations of THC and cannabidiol (CBD), *Cannabis* can be categorized in 3 types, namely THC type (THC >> CBD), CBD type (THC << CBD) and intermediate type (THC ≈ CBD). Cannabinoids are predominantly synthesized and deposited in the

trichomes of *Cannabis*. At least there are 3 types of trichomes in *Cannabis*, including capitate-stalked, capitate-sessile, and bulbous trichomes. Based on our previous works, capitate-stalked trichomes contain more cannabinoids compare to the others [8].

Metabolomics as one of the emerging omics tools has been applied for studying *Cannabis*. Gas chromatography-based metabolomics had been applied to classify *Cannabis* cultivars based on their varieties [9]. This method had been also used to discriminate *Cannabis sativa* from *Cannabis indica* [10]. HPLC-based metabolomics had successfully been employed to study the impact of domestication on *Cannabis* metabolomes [11]. The same method had been applied to study the terpene profiles in different *Cannabis* cultivars [12]. HPLC-ESIHRMS/MS based-metabolomics was used to evaluate the chemical composition of *Cannabis* medicinal extracts [13]. ^{1}H-NMR based-metabolomics as one of the advance metabolomic methods was employed in *Cannabis* study as well. This method had been successfully used to differentiate *Cannabis* cultivars [14]. Moreover, ^{1}H-NMR based-metabolomics had been applied to study the impact of elicitation in cell suspension cultures of *Cannabis* [15-16]. Our previous work also applied ^{1}H-NMR-based metabolomics that combined with real time PCR (RT-PCR) technique for studying cannabinoid biosynthesis of *Cannabis* cultivars over flowering season [17]. This combined method was used to differentiate *Cannabis* metabolome based on their organs [18]. Recently, we used the same approach for monitoring cannabinoid biosynthesis in the trichomes of *Cannabis* during the flowering period [19].

The sample used in our previous work [19] was *C. sativa* var. *bediol*, intermediate type *Cannabis* containing almost equal concentrations of THC and CBD. It elucidated cannabinoid biosynthesis in the trichomes of intermediate type *Cannabis*. However, to the best of our knowledge, the changes in metabolite profiles in THC-type *Cannabis* during the flowering period is still unclear. Therefore, in continuation of our studies on this plant, here we report ^{1}H-NMR-based metabolomics in the trichomes of *C. sativa* var. *bedrobinol*. This variety is THC type *Cannabis* containing high THC and almost zero CBD. The purpose of this report is to study metabolic change and to differentiate metabolomes of trichomes of *C. sativa* var. *bedrobinol* over the last flowering weeks.

■ EXPERIMENTAL SECTION

Materials

The standardized *C. sativa* var. *bedrobinol* was obtained from Bedrocan BV (Veendam, Netherlands). Chloroform and methanol used in the extraction were obtained from Carl Roth GmbH (Karlsruhe, Germany). Tetramethylsilane (TMS), trimethylsilane propionic acid sodium salt (TSP), sodium deuteroxide, deuterated chloroform, and deuterated water that required for the NMR measurement were bought from Carl Roth GmbH (Karlsruhe, Germany). Anthracene, as the quantitative standard compound, was purchased from Sigma-Aldrich GmbH (Darmstadt, Germany). Reference THCA and THC were obtained from THC Pharm GmbH (Frankfurt, Germany).

Instrumentation

An Eppendorf 5415D centrifuge (Eppendorf AG, Hamburg, Germany) was used to centrifuge the samples. A Buchi rotary evaporator (BÜCHI Labortechnik AG, Flawil, Switzerland) was applied to remove the solvents on the sample extracts. A Bruker Avance DRX 500 spectrometer (Bruker BioSpin GmbH, Rheinstetten, Germany) was used to record ^{1}H-NMR spectra of the *Cannabis* trichomes.

Procedure

Trichomes isolation

All plant handling and experiment procedures in this research were performed based on license No. 4584989 issued by the Federal Institute for Drugs and Medical Devices (BfArM), Germany. All experiments were carried out in the Laboratory of Technical Biochemistry, Technical University of Dortmund, Germany. The trichomes of *C. sativa* var. *bedrobinol* were isolated based on previous reports [19-20]. The floral leaves and the stigma of the fresh *Cannabis* flowers were removed using forceps. A 5–10 g of the flower was moved into a 50 mL centrifuge tube and placed for a while in a tank containing liquid nitrogen. A finely

powdered dry ice was added into the tube. Immediately, the tube was loosely capped and vortexed for 1 min. During the vortex process, the trichomes were released from the *Cannabis* flower. Afterward, the flower was removed from the tube. The trichomes were collected by filtering other materials from the tube with a 140 μm nylon net filter (Merck Millipore). In this work, the *Cannabis* trichomes were isolated at 4 different weeks over the flowering season, including weeks 5, 6, 7 and 8.

Extraction

The fresh trichomes of *C. sativa* var. *bedrobinol* in a centrifuge tube (200 mg) was extracted by 2 mL of water-methanol solvent (1:1) and 2 mL of chloroform. The tube was vortexed for 1 min and sonicated for 1 min. Afterward, the sample was incubated at a shaker machine (200 rpm) for 1 h at 30 °C. The water phase was separated from the chloroform phase by pipetting. The chloroform fraction was separated from the trichomes by filtering. The chloroform fraction was dried by a rotary evaporator at 30 °C and 31 mbar. Meanwhile, the water fraction was dried in a freeze-drying machine.

NMR measurements

Dry chloroform extracts of *Cannabis* trichomes were dissolved in deuterated chloroform. Tetramethylsilane (TMS) was used as an internal standard, while anthracene (1 mg/sample) was used as a quantitative standard compound. 128 scans of 64 K data points are recorded with a spectral width of 12531.32 Hz, the acquisition time of 5.23 sec and a relaxation delay of 5 sec. Dried water extracts of *Cannabis* trichomes were dissolved in deuterated water containing phosphate buffer (pH 6) and trimethylsilane propionic acid sodium salt (TSP, 0.01%, w/v) as an internal standard. ^{1}H-NMR spectra of the water extracts were recorded using a presaturation method. 128 scans of 32 K data points are recorded with a spectral width of 12019.23 Hz, the acquisition time of 2.72 sec and a relaxation delay of 2 sec. The free-induction decay (FID) NMR data were processed with ACD/Labs 12.0 software (Advanced Chemistry Development, Inc., Toronto, Canada). This software was also used for referencing, phasing, baseline correction of the ^{1}H-NMR spectra.

Quantitative analysis

^{1}H-NMR quantitative analysis was applied to determine concentrations of some identified metabolites semi-quantitatively. The identified cannabinoid was quantified based on a previous report [21]. The concentration of cannabinoids was determined by comparing the signal of the targeted cannabinoids with the singlet signal of anthracene (δ 8.45 ppm). Meanwhile, the quantification of the identified metabolites in the water extracts was carried out by comparing the corresponding signal area to the TSP signal.

Multivariate data analysis

Alignment and bucketing of the ^{1}H-NMR spectra were performed using ACD/Labs 12.0 software (Advanced Chemistry Development, Inc., Toronto, Canada). ^{1}H-NMR spectra of the chloroform extracts were scaled to TMS. Bucketing was carried out by integrating regions of equal width (0.02 ppm) within δ 0.50–13.00 ppm and performed with an intelligent bucketing option. The region δ 7.24–7.27 ppm was removed from the analysis because of the chloroform signal. The region of anthracene signals (δ 7.44–7.48, 7.96–8.06, and 8.42–8.48 ppm) were excluded from the analysis. ^{1}H-NMR spectra of the aqueous extracts were scaled to TSP. Bucketing of these spectra was performed by integrating regions of equal width (0.02 ppm) from δ 0.50–10.00 ppm. The residual water signal at δ 4.73–5.22 ppm was excluded from the data analysis. The processed data sets extracted from the ^{1}H-NMR spectra were imported into SIMCA-P version 13.0 (Umetrics, Umeå, Sweden) for the multivariate statistical analysis. Partial Least Squares Discriminant Analysis (PLSDA) was applied as the primary method for extracting maximum separation among samples.

■ RESULTS AND DISCUSSION

Metabolite Identification

For identifying metabolites present in the trichomes of *C. sativa* var. *bedrobinol*, the ^{1}H-NMR spectra of both extracts were investigated. Δ^9-tetrahydrocannabinolic acid (THCA) and its neutral form, Δ^9-tetrahydrocannabinol

(THC), were successfully identified in the ^{1}H-NMR spectra of the chloroform extracts. Other identified cannabinoid in the spectra was cannabichromenic acid (CBCA). The proton signals belong to THCA were clearly distinguishable in the ^{1}H-NMR spectra, indicating this compound was a major metabolite in the *Cannabis* trichomes. Four methyl groups of THCA were detected in the spectra at δ 0.90 (H-5', m), 1.12 (H-13, s), 1.45 (H-12, s), and 1.69 ppm (H-11, s). Other aliphatic proton signals belong to THCA were identified at δ 1.33 (H-3', m), 1.33 (H-4', m), 1.55 (H-2', m), 2.79 (H-1a', m), 2.92 (H-1b', m) and 3.23 ppm (H-10a, brd, J = 10.9). Two aromatic protons of THCA were recorded at δ 6.25 (H-4, s) and δ 6.39 ppm (H-10, s). Meanwhile, one chelating proton signal belongs to the carboxyl group of THCA was detected at δ 12.20 ppm (COOH, s). THC and CBCA were identified by identifying their characteristic signals in the ^{1}H-NMR spectra of the chloroform extracts. However, the signals of THC and CBCA in the spectra were low, indicating both are minor compounds in the trichomes. The characteristic proton signals of THC were identified at δ 6.13 (H-2, brs), 6.28 (H-4, s) and 6.30 ppm (H-10, brs). Meanwhile, the signals of CBCA were recorded at δ 5.49 (H-7, d, J = 10.1), 6.23 (H-4, s) and 6.74 ppm (H-8, d, J = 10.1). The signals of CBCA were further verified by comparison with published data [22]. Proton signals of THCA and THC in the ^{1}H-NMR spectra were further verified by comparing the data with their reference spectra. Structures of identified cannabinoids are depicted in Fig. 1.

Investigation of ^{1}H-NMR spectra of the water extracts successfully identified amino acids, sugar compounds, and other organic compounds. The fingerprint signals of alanine (δ 1.48 ppm, H-3, d, J = 7.2), asparagine (δ 2.87, H-3b, dd, J = 16.9, 7.6; δ 2.96, H-3a, dd, J = 16.9, 4.3; δ 4.01 ppm, H-2, dd, J = 16.9, 4.3), glutamine (δ 2.07, H-4, m; δ 2.38 ppm H-3, m), glutamic acid (δ 2.14 H-4, m; δ 2.46 ppm, H-3, m), glycine (δ 3.58 ppm, H-2, s), leucine (δ 0.95, H-5, d, J = 6.6; δ 0.97 ppm, H-6, d, J = 6.6), proline (δ 2.35, H-3, m; δ 4.06 ppm, H-2, m), threonine (δ 1.33 ppm, H-5, d, J = 6.6) and valine (δ 1.00, H-3, d, J = 6.8; δ 1.05 ppm, H-4, d, J = 6.8) were successfully recorded in the spectra within the δ 0.8–4.0 ppm region. Meanwhile, in the δ 4.0–6.0 ppm region, the proton signals of α-glucose (δ 5.23 ppm, H-1, d, J = 3.8), β-glucose (δ 4.64 ppm, H-1, d, J = 7.9), β-mannose (δ 4.99 (H-1, d, J = 7.9), fructose (δ 4.06 ppm, H-1, d, J = 3.5), inositol (δ 3.25, H-5, t, J = 9.3; δ 3.49, H-1, dd, J = 9.9, 2.9; δ 3.61; H-4 , t, J = 9.3) and sucrose (δ 4.22, H-1', d, J = 8.6), δ 5.42 ppm, H-1, d, J = 3.8) were detected as well. Further investigation of the obtained ^{1}H-NMR spectra revealed other organic acids, including acetic acid (δ 1.91 ppm, s), formic acid (δ 8.46 ppm, s), fumaric acid (δ 6.59 ppm, s), succinic acid (δ 2.45 ppm, s) and choline (δ 3.21 ppm, s). All the fingerprint signals of the identified compounds were further verified with the data from reported works [14,23-25].

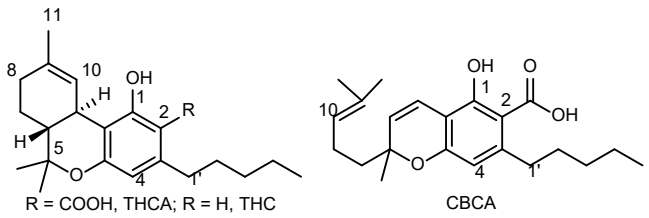

Fig 1. Chemical structures of identified cannabinoids

^{1}H-NMR Quantitative Analysis

The concentrations of some identified metabolites were determined semi-quantitatively by ^{1}H-NMR technique. According to the analysis of chloroform extracts of the trichomes of *C. sativa* var. *bedrobinol*, concentrations of THCA in weeks 5 and 6 did not vary too much as described in Table 1. Nevertheless, the concentrations of these compounds increased significantly in week 7 and enhanced slightly in the following week. Meanwhile, concentrations of CBCA and THC increased over the monitoring time.

Besides, as the main site for synthesizing secondary metabolites, trichomes are well known as the main place for storing secondary metabolites, including cannabinoids [26]. Although THCA and CBCA could be decarboxylated by heat into their neutral forms (THC and CBC) [27], however, both are the end products of cannabinoid biosynthesis [28-29]. Therefore, concentrations of cannabinoids that quantified in the ^{1}H-NMR analysis, were the accumulated concentrations of THCA, CBCA, and THC, which produced from the initial cannabinoid

biosynthesis till the harvesting. It was confirmed by the results of the quantitative analysis that showed the concentration enhancement of the cannabinoids over the flowering period as depicted in Table 1.

The amounts of alanine, asparagine, choline, fructose, glucose, glutamine, glutamic acid, inositol, sucrose, threonine, and valine in the water extracts of the trichomes of *C. sativa* var. *bedrobinol* were successfully determined. Their concentrations were diverse during the monitoring period. These quantified metabolites are primary metabolites that directly involved in the normal growth, development, and maintenance of the cellular functions of the plant. Besides that, these metabolites are also precursors or intake compounds in the biosynthesis of secondary metabolites. The diverse concentrations of the quantified compounds over monitoring time were probably correlated to their functions as primary metabolites. The recorded production patterns of the quantified metabolites over monitoring time are described in Table 1.

Multivariate Data Analysis

In this research, the extracted data of the ^{1}H-NMR spectra were further analyzed with multivariate data analysis for investigating metabolite profiles of the trichomes of *C. sativa var. bedrobinol* over the last flowering weeks. In the first step, the extracted data were treated with principal component analysis (PCA) method, an unsupervised pattern-recognition approach. However, this method could not give enough separations (data not shown); thus, the analysis was continued further with partial least square discriminant analysis (PLSDA) method, supervised pattern-recognition approach. This method applies a discrete class matrix and is based on the partial least squares (PLS) model [30].

PLSDA modeling of the chloroform extract data set resulted in the good separation of the trichomes of *C. sativa var. bedrobinol* based on their harvesting time. This PLSDA model had 6 components, 74.8% of cross validation coefficient (Q2), and explained 83.0% and 91.2% of total variations (R2X and R2Y, respectively). This model was further validated by the permutation test (300 permutations). The test produced the regressions of Q2 line that intersects the y-axis at points below zero [Q2 = (0.00, -0.0741); R2 = (0.00, 0.392)]. This result validated the PLSDA model statistically. The best separation model of the chloroform extracts was obtained when combining the first (34.7%) and the second (18.8%) PLSDA components. This score plot successfully illustrated metabolic discrimination of the trichomes of *C. sativa var. bedrobinol* based on their harvesting time,

Table 1. Concentrations of quantified compounds in the trichomes of *C. sativa* var. *bedrobinol*, over the last flowering weeks

Compound	Concentration (mg/g of fresh trichomes weight ± SD)			
	Week 5	Week 6	Week 7	Week 8
CBCA (δ 6.74)	0.60 ± 0.10	0.77 ±0.12	0.92 ± 0.30	1.12 ± 0.40
THCA (δ 6.39)	45.27 ± 2.29	45.90 ± 3.04	64.39 ± 6.39	67.65 ± 7.19
THC (δ 6.13)	0.09 ± 0.01	0.19 ± 0.08	0.38 ± 0.09	0.99 ± 0.06
Alanine (δ 1.48)	1.39 ± 0.19	1.42 ± 0.26	1.54 ± 0.38	1.66 ± 0.68
Asparagine (δ 2.87)	11.80 ± 1.74	13.66 ± 2.16	16.38 ± 2.16	15.30 ± 3.80
Choline (δ 3.21)	2.11 ± 0.15	2.22 ± 0.18	2.34 ± 0.41	1.65 ± 0.20
Fructose (δ 4.06)	10.33 ± 1.49	11.84 ± 0.63	11.97 ± 0.63	9.43 ± 0.35
Glucose (δ 5.23)	1.36 ± 0.22	1.57 ± 0.48	2.28 ± 0.84	1.28 ± 0.32
Glutamic acid (δ 2.46)	1.94 ± 0.25	2.08 ± 0.21	2.66 ±0.43	2.22 ± 0.58
Glutamine (δ 2.07)	1.49 ± 0.22	1.54 ± 0.31	1.33 ± 0.29	1.25 ± 0.19
Inositol (δ 3.61)	4.52 ± 0.49	5.45 ± 1.10	5.13 ± 0.64	5.44 ± 2. 47
Sucrose (δ 4.22)	8.75 ± 1.82	10.31 ± 1.65	10.72 ± 1.63	10.90 ± 2.88
Threonine (δ 1.33)	7.31 ± 1.29	4.56 ± 0.59	2.84 ± 0.59	3.84 ± 0.89
Valine (δ 1.05)	0.36 ± 0.07	0.52 ± 0.10	0.47 ± 0.14	0.43 ± 0.07

as depicted in Fig. 2(a). For investigating the responsible compounds in the classification, the loading plot of the first PLSDA component was analyzed. As described in Fig. 2(b), THCA was identified as the most discriminant compound in the classification of the metabolic trichomes based on their harvesting time.

In our previous work, we found that THCA and cannabidiolic acid (CBDA) were detected as important discriminant compounds in the classification of trichome metabolomes of *C. sativa* var. *bediol* during the flowering period [19]. *C. sativa* var. *bediol* is intermediate-type *Cannabis* containing almost equal concentrations of THC (a neutral form of THCA) and CBD (a neutral form of CBDA). Meanwhile, in this report, we detected THCA as the most discriminant compound in the classification. It was possibly due to the sample used in this report is categorized as THC-type *Cannabis* containing high THC and almost zero CBD. However, this result confirmed THCA as the crucial cannabinoid that synthesized in high amounts in the trichomes of *Cannabis* over flowering weeks and had an important role in the metabolome differentiation.

PLSDA model of the water extracts successfully classified the trichomes of *C. sativa var. bedrobinol* according to the collecting times. This model possessed 9 PLS with R2X = 62.0%, R2Y = 99.6%, and Q2 = 67.7%. The model validation was carried out by the permutation test (300) resulting the regressions of Q2 lines intersected the y-axis at points below zero [Q2 = (0.00, -0.399); R2 = (0.00, 0.301)]. The score plot consisting of the first component (13.1%) and the third component (5.1%) revealed four well-separated groups, as seen in Fig. 3(a). Based on the loading plot investigation of the first component (Fig. 3(b)), all quantified water-soluble

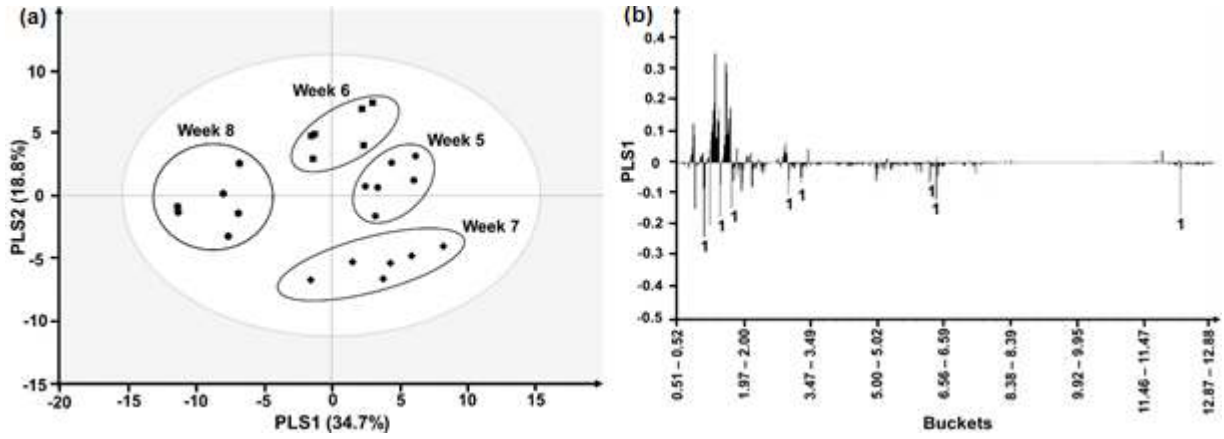

Fig 2. PLSDA score (a) and loading (b) plots from the ^{1}H-NMR spectra of chloroform extracts of *bedrobinol* trichomes 1: THCA

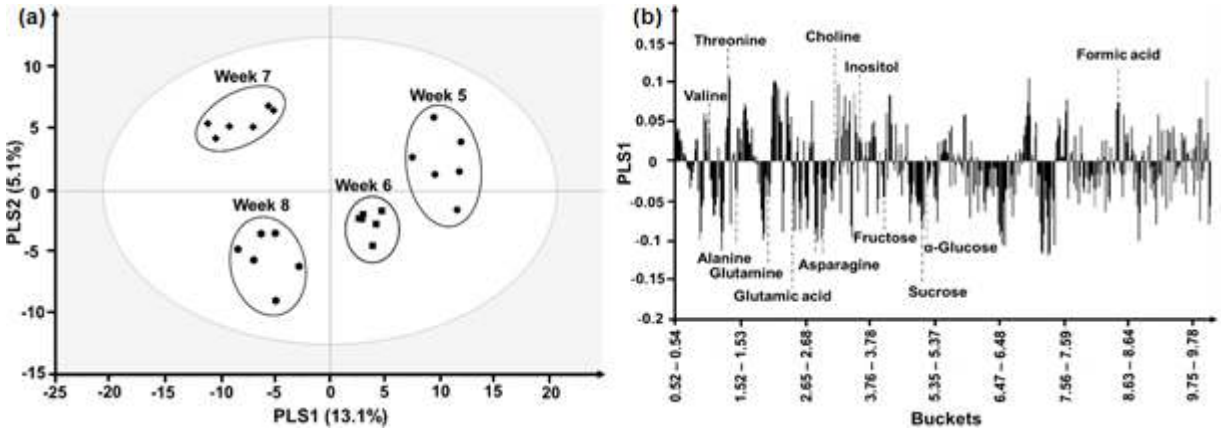

Fig 3. PLSDA score (a) and loading (b) plots from ^{1}H-NMR spectra of water extracts of *bedrobinol* trichomes

metabolites, were found contributing to the discrimination of the metabolic trichomes. Beside those, formic acid, an unquantified metabolite, was also detected giving a contribution in the loading plot. These results indicated that concentrations of these compounds were diverse over the flowering weeks and confirmed the results of the quantitative analysis as explained before.

The results of multivariate data analysis revealed that the trichome metabolomes of *C. sativa* var. *bedrobinol*, which is the THC-type, were varied during the last 4 weeks of the flowering period. These results were similar to the trichome metabolomes of *C. sativa* var. *bediol* which is the intermediate-type [19]. Thus, it indicated that during the flowering period, the metabolite production either in the trichomes of the THC-type *Cannabis* or the intermediate-type depends on the time.

C. sativa possesses 2 growth periods, vegetative and generative or flowering. The plant grows rapidly in the first period and then synthesizes cannabinoids in a large amount in the flowering period. The previous report showed that cannabinoid production in the flower of *C. sativa* var. *bediol* and *bedrobinol* grew under the standardized condition and genetic homogeneity, increased with the time of flowering and achieved the highest level over the last 4 flowering weeks [17]. The responsible tissue in the *Cannabis* flower for producing cannabinoids is the trichome [26]. The pattern of cannabinoid biosynthesis in the trichomes of *C. sativa* var. *bediol* over the second period had been analyzed previously using the ^{1}H-NMR-based metabolomics combined with the real-time PCR analysis [19]. Meanwhile, the pattern of cannabinoid production in the trichomes of THC-type *Cannabis*, var. *bedrobinol*, during the flowering stage was explained in this work using ^{1}H-NMR based metabolomics approach. Therefore, this report may lead to a better understanding of the cannabinome.

■ CONCLUSION

In this report, metabolite profiles of the trichomes of *C. sativa* var. *bedrobinol* over the last 4 weeks of the flowering season were successfully monitored by ^{1}H NMR-based metabolomics. The trichomes of *C. sativa* var. *bedrobinol* during the flowering period biosynthesized metabolites in different amounts depending on the time. Moreover, THCA was found as the most crucial discriminant compound in the classification. This report sheds more light on metabolite profiles of the trichomes of THC-type *Cannabis* during the flowering period.

■ ACKNOWLEDGMENTS

Doctoral Scholarship Program of the Directorate General of Higher Education, Indonesia, is gratefully acknowledged for the support of Nizar Happyana. The authors also thank Bedrocan BV (Tjalling Erkelens and Freerk Bruining) for providing the *Cannabis* samples.

■ REFERENCES

[1] Li, H.L., 1974, An archeological and historical account of *Cannabis* in China, *Econ. Bot.*, 28 (4), 437–448.

[2] Chopra, G.S., 1969, Man and marijuana, *Int. J. Addict.*, 4 (2), 215–247.

[3] Fleming, M.P., and Clarke, R.C., 2008, Physical evidence for the antiquity of *Cannabis sativa* L., *J. Int. Hemp Assoc.*, 5 (2), 80–92.

[4] de Candolle, A., 1886, *Origin of Cultivated Plants*, 2nd Ed., Paul Trench, London.

[5] Badowski, M.E., 2017, A review of oral cannabinoids and medical marijuana for the treatment of chemotherapy-induced nausea and vomiting: A focus on pharmacokinetic variability and pharmacodynamics, *Cancer Chemother. Pharm.*, 80 (3), 441–449.

[6] Koppel, B.S., Brust J.C.M., Fife, T., Bronstein, J., Youssof, S., Gronseth, G., and Gloss, D., 2014, Systematic review: Efficacy and safety of medical marijuana in selected neurologic disorders, *Neurology*, 82 (17), 1558–1563.

[7] ElSohly, M.A., and Slade, D., 2005, Chemical constituents of marijuana: The complex mixture of natural cannabinoids, *Life Sci.*, 78 (5), 539–548.

[8] Happyana, N., Agnolet, S., Muntendam, R., Van Dam, A., Schneider, B., and Kayser, O., 2013, Analysis of cannabinoids in laser-microdissected trichomes of medicinal *Cannabis* sativa using

LCMS and cryogenic NMR, *Phytochemistry*, 87, 51–59.

[9] Fischedick, J.T., Hazekamp, A., Erkelens, T., Choi, Y.H., and Verpoorte, R., 2010, Metabolic fingerprinting of *Cannabis sativa* L., cannabinoids and terpenoids for chemotaxonomic and drug standardization purposes, *Phytochemistry*, 71 (17-18), 2058–2073.

[10] Hazekamp, A., Tejkalova, K., and Papadimitriou, S., 2016, *Cannabis*: From cultivar to chemovar II—A metabolomics approach to *Cannabis* classification, *Cannabis Cannabinoid Res.*, 1 (1), 202–215.

[11] Mudge, E.M., Murch, S.J., and Brown, P.N., 2018, Chemometric analysis of cannabinoids: chemotaxonomy and domestication syndrome, *Sci. Rep.*, 8, 13090.

[12] Mudge, E.M., Brown, P.N., and Murch, S.J., 2019, The terroir of *Cannabis*: terpene metabolomics as a tool to understand *Cannabis sativa* selections, *Planta Med.*, 85 (9-10), 781–796.

[13] Citti, C., Battisti, U.M., Braghiroli, D.B., Ciccarella, G., Schmid, M., Vandelli, M.A., and Cannazza, G., 2018, A metabolomic approach applied to a liquid chromatography coupled to high-resolution tandem mass spectrometry method (HPLC-ESIHRMS/MS): Towards the comprehensive evaluation of the chemical composition of *Cannabis* medicinal extracts, *Phytochem. Anal.*, 29 (2), 144–155.

[14] Choi, Y.H., Kim, H.K., Hazekamp, A., Erkelens, C., Lefeber, A.W.M., and Verpoorte, R., 2004, Metabolomic differentiation of *Cannabis sativa* cultivars using ^{1}H NMR spectroscopy and principal component analysis, *J. Nat. Prod.*, 67 (6), 953–957.

[15] Flores-Sanchez, I.J., Peč, J., Fei, J.N., Choi, Y.H., Dušek, J., and Verpoorte, R., 2009, Elicitation studies in cell suspension cultures of *Cannabis sativa* L., *J. Biotechnol.*, 143 (2), 157–168.

[16] Peč, J., Flores-Sanchez, I.J., Choi, Y.H., Verpoorte, R., 2010, Metabolic analysis of elicited cell suspension cultures of *Cannabis sativa* L. by ^{1}H-NMR spectroscopy, *Biotechnol. Lett.*, 32, 935–941.

[17] Muntendam, R., Happyana, N., Erkelens, C., Bruining, F., and Kayser, O., 2012, Time dependent metabolomics and transcriptional analysis of cannabinoid biosynthesis in *Cannabis sativa* var. Bedrobinol and Bediol grown under standardized condition and with genetic homogeneity, *Online Int. J. Med. Plant Res.*, 1 (2), 31–40.

[18] Happyana, N., and Kayser, O., 2016, ^{1}H NMR-based metabolomics differentiation and real time PCR analysis of medicinal *Cannabis* organs, *Acta Hortic.*, 1125, 25–32.

[19] Happyana, N., and Kayser, O., 2016, Monitoring metabolite profiles of *Cannabis sativa* L. trichomes during flowering period using ^{1}H NMR-based metabolomics and real-time PCR, *Planta Med.*, 82 (13), 1217–1223.

[20] Yerger, E.H., Grazzini, R.A., Hesk, D., Coxfoster, D.L., Craig, R., and Mumma, R.O., 1992, A rapid method for isolating glandular trichomes, *Plant Physiol.*, 99 (1), 1–7.

[21] Hazekamp, A., Choi, Y.H., and Verpoorte, R., 2004, Quantitative analysis of cannabinoids from *Cannabis sativa* using ^{1}H NMR, *Chem. Pharm. Bull.*, 52 (6), 718–721.

[22] Lee, Y.R., and Wang, X., 2005, Concise synthesis of biologically interesting (+/-)-cannabichromene, (+/-)-cannabichromenic acid, and (+/-)-daurichromenic acid, *Bull. Korean Chem. Soc.*, 26 (12), 1933–1936.

[23] Kirk, H., Cheng, D., Choi Y.H., Vrieling, K., and Klinkhamer, P.G., 2012, Transgressive segregation of primary and secondary metabolites in F2 hybrids between *Jacobaea aquatica* and *J. vulgaris*, *Metabolomics*, 8 (2), 211–219

[24] Abreu, I.N., Choi, Y.H., Sawaya, A.C.H.F., Eberlin, M.N., Mazzafera, P., and Verpoorte, R., 2011, Metabolic alterations in different developmental stages of *Pilocarpus microphyllus*, *Planta Med.*, 77 (3), 293–300.

[25] Ali, K., Maltese, F., Fortes, A.M., Pais, M.S., Choi, Y.H., and Verpoorte, R., 2011, Monitoring biochemical changes during grape berry development in Portuguese cultivars by NMR spectroscopy, *Food Chem.*, 124 (4), 1760–1769.

[26] Lewis, G.S., and Turner, C.E., 1978, Constituents of *Cannabis sativa* L. XIII: Stability of dosage form

prepared by impregnating synthetic (-)-Δ^9-*trans*-tetrahydrocannabinol on placebo *Cannabis* plant material, *J. Pharm. Sci.*, 67 (6), 876–878.

[27] Petri, G., Oroszlan, P., and Fridvalszky, L., 1988, Histochemical detection of hemp trichomes and their correlation with the THC content, *Acta Biol. Hung.*, 39 (1), 1, 59–74.

[28] Taura, F., Morimoto, S., Shoyama, Y., and Mechoulam, R., 1995, First direct evidence for the mechanism of Δ^1-tetrahydricannabinolic acid biosynthesis, *J. Am. Chem. Soc.*, 117 (38), 9766–9767.

[29] Morimoto, S., Komatsu, K., Taura, F., and Shoyama, Y., 1998, Purification and characterization of cannabichromenic acid synthase from *Cannabis sativa*, *Phytochemistry*, 49 (6), 1525–1529.

[30] Westerhuis, J.A., van Velzen, E.J.J., Hoefsloot, H.C.J., Smilde, A.K., 2010, Multivariate paired data analysis: Multilevel PLSDA versus OPLSDA, *Metabolomics*, 6 (1), 119–128.

Characterization and Prediction of the Non-Bonded Molecular Interactions between Racemic Ibuprofen and α-Lactose Monohydrate Crystals Produced from Melt Granulation and Slow Evaporation Crystallization

Zulfahmi Lukman, Nornizar Anuar*, Noor Fitrah Abu Bakar, and Norazah Abdul Rahman

Faculty of Chemical Engineering, Universiti Teknologi MARA, 40450 Shah Alam, Selangor, Malaysia

* ***Corresponding author:***

email: nornizar@uitm.edu.my

Received: August 21, 2019
Accepted: February 7, 2020

DOI: 10.22146/ijc.48912

Abstract: *Granulation of racemic ibuprofen (±IBP) and α-lactose monohydrate (ALM) at a slightly lower (±IBP) melting point is an efficient method of binding the active pharmaceutical ingredients (API) and excipient in a binderless condition. However, the co-crystals may be formed from recrystallization of ±IBP on ALM. The objective of this study is to evaluate the tendency of co-crystal formation of granules (3:7 w/w ratio of ±IBP:ALM) by melt granulation process. Second, investigate the recovery of crystals from polyethylene glycol (PEG) 300 solutions containing ±IBP-ALM mixtures. Characterizations of the samples were performed using Fourier Transform Infrared (FTIR) spectroscopy, Differential Scanning Calorimetry (DSC) and Powder X-Ray Diffraction (PXRD) system of the ±IBP-ALM granules produced from melt crystallization and harvested crystals from PEG 300 solution which is produced using slow evaporation crystallization. Crystal analysis of solution containing ±IBP-ALM mixtures revealed that the crystals formed were not co-crystals. Molecular interactions assessment through binding prediction between ±IBP and ALM terminating surfaces was conducted using molecular modelling technique. The result showed that the favorable binding sites of ±IBP molecules were on the surfaces of (0-20), (1-10), (001) and (011) ALM crystals. Successful binding prediction by the attachment energy method has proven that the co-crystal formation between these molecules is theoretically possible.*

Keywords: *surface chemistry; hydrogen bond; lattice energy; melt crystallization; binding prediction*

■ INTRODUCTION

In recent years, there has been increasing interest in melt granulation [1-4], apart from dry granulation and wet granulation. Melt granulation employs molten binder such as PEG and Gelucire [2-6]. The process skips the drying stage which is a part of routine stages in wet granulation. Drying stage in wet granulation consumes a lot of time and energy to dry the solvent (such as water) and volatile solvents, such as ethanol and isopropanol [3,5,7]. This becomes compelling when melt granulation involves racemic ibuprofen (±IBP) and a widely used excipient, α-lactose monohydrate (ALM). Ibuprofen is a highly potential active pharmaceutical ingredients (API) of non-steroidal anti-inflammatory drugs (NSAIDs) [8] and cannot afford to have residual solvents in the formulations [9]. However, there are limited reports focusing on racemic ibuprofen in melt granulation [5,10].

Melt spherical granules of α-lactose monohydrate and racemic ibuprofen can be prepared using a pressure swing granulation (PSG) technique in a fluidized bed [4,10]. Three types of granule products can be produced namely core, coated and heated granules. It has been proven that racemic ibuprofen can be acted as an API and binder simultaneously. The granule products have enough strength to handle processes before tableting. Enhanced strength was recorded for both coated and heated granules due to solidification of melting ibuprofen, which binds α-lactose monohydrate particles in the granules and results in no requirement for any

other type of binders [10]. Application of this technique also solved the tendency of high sublimation of racemic ibuprofen [10-11] by blocking the diffusion of racemic ibuprofen out of the granules through the coating with 2 wt.% α-lactose monohydrate layer. Coating naked tablets of ibuprofen mixture with cooling crystallization sucrose produces uniform and crystalline coating, but analysis of sublimation of ibuprofen was not carried out yet [12]. However, Abu Bakar and co-workers [10] characterized only physical properties of the granules. Walker et al. investigate racemic ibuprofen-α-lactose monohydrate-PVP-PEG 600 granules determined the nature of the crystals formed during the process [5-6]. The granules were produced by fluidized hot melt granulation method. A mixture of 300 g of granulated racemic ibuprofen, α-lactose monohydrate, PVP and PEG 600 was heated at 100 °C for predetermined period, before cooling to ambient air for 30 sec [5]. However, the properties of solidified ibuprofen in the granules form remain unclear [10]. It is postulated that the ±IBP recrystallizes on α-lactose monohydrate particles, especially when the melt granulation approximately has the same principle with melt crystallization [13], which can form co-crystal [14]. Thus, formation co-crystal of racemic ibuprofen-α-lactose monohydrate is possible. Co-crystal is a molecular complex which contains two or more different molecules in the same crystal lattice [15]. Ibuprofen co-crystal is desired because it has shown significant improvement in dissolution, compactability and compressibility of the co-crystals [16] compared to pure ibuprofen crystals. The pure racemic ibuprofen crystals are undesired because it has high cohesivity, adhesivity and hydrophobicity in nature [17]. Various attempts were made to produce co-crystals, such as racemic ibuprofen-2-aminopyrimidine by solvent-free grinding and slow evaporation of acetonitrile solution [18]. Meanwhile, racemic ibuprofen-nicotinamide co-crystal was produced by Kofler mixed fusion and slow evaporation of methanol or ethanol solution [19]. An alternative proposed technique to produce the racemic ibuprofen-nicotinamide co-crystal is by simultaneous agglomeration via hot melt extrusion [16]. Only fusion method forms amorphous granule of racemic ibuprofen-gelucire [20]. Measurement using Fourier Transform Infrared Spectroscopy (FT-IR) showed that the racemic ibuprofen has the tendency to produce co-crystal with PEG via hydrogen bonding interactions [21]. The attempts showed that different racemic ibuprofen recrystallized methods from racemic ibuprofen mixtures will differ in final product of recrystallization. Therefore, the investigation of properties of racemic ibuprofen crystals in granules subjected to the granulation conditions is imperative.

The interactions between crystal surfaces and molecules in the bulk solution have been predicted using molecular modelling technique in previously reports [22-25]. Some of computational techniques such as docking/grid search are commonly used to assess the wettability of the crystal surface. These methods rely on the finding a suitable attachment site between a free molecule in the solution to the surface. Another application of grid search is to calculate solvent-dependent morphologies of organic material. For example; the grid-based search for crystal surface of racemic ibuprofen terminating surfaces of (100), (001) and (011) and the solvents (ethanol, ethyl acetate, acetonitrile and toluene) showed that the solute racemic ibuprofen molecules has the strongest interaction with the capping (011) morphology, followed by the side (0 0 1) and the weakest with the top (1 0 0) crystal surface [26]. The molecular modelling study on the effect of additives on the crystal growth of methyl paraben has shown that acetaminophen, *p*-methyl acetanilide and acetanilide selectively adsorbed on the growth surfaces of methyl paraben and induced the change in methyl paraben crystal habit [27]. The work on assessment of additives on the *p*-toluamide crystal surface also has showed that additive molecule was capable to promote the growth of specific crystal faces by repelling the solvent molecules and eliminating the negative influence of the solvent on the surface diffusion of *p*-toluamide [28].

In this article, the tendency of co-crystal formation of racemic ibuprofen-ALM in granules produced through melt crystallization; and in crystals produced from PEG 300 solutions through slow evaporation crystallization are studied.

Assessment of co-crystal formation was carried out using an X-Ray Powder Diffraction (XRPD), Differential Scanning Calorimetry (DSC) and Fourier Transform Infrared (FTIR) spectroscopy. A molecular modelling work was conducted to predict first the binding preference of racemic ibuprofen on the α-lactose monohydrate surfaces and second to predict the possibility on the co-crystal formation.

■ EXPERIMENTAL SECTION

Materials

Form I polymorphic form of racemic ibuprofen, (±)-IBP, (±)-2-(4-isobutylphenyl) propanoic acid, $C_{13}H_{18}O_2$ (PhEur) of 99.9% purity CAS 15687-27-1 were obtained from Shasun Pharmaceutical Limited, India. (±)-IBP is a white, crystalline powder and has a characteristic odor. The compound is insoluble in water, but soluble in most organic solvents. Its molecular weight is 206.29 g/mol and conforms to Ph.Eur. The α-lactose monohydrate (ALM) ($C_{12}H_{22}O_{11}$) powder (Pharmatose 450M, DMV) with 99.99% of purity, was purchased from Sigma Aldrich. The white or almost white α-lactose monohydrate crystalline powder is soluble in water, but insoluble in ethanol and non-polar solvents. Its molecular weight is 342.30 g/mol. Polyethylene glycol 300 ($C_{2n}H_{4n+2}O_{n+1}$) (PEG 300) of CAS 25322-68-3, Ph.Eur was obtained from Sigma-Aldrich, Germany. The viscous, clear solvent is soluble in water with an average molecular weight of 300 g/mol.

Crystal Structure

The molecular structures of racemic ibuprofen and α-lactose monohydrate were shown in Fig. 1(a) and (b), respectively. Ibuprofen has an aromatic ring, a methyl, and a carboxyl functional group in its structure, whilst α-lactose monohydrate has two pyranose rings and a water molecule, forming a dimer in its structure. An α-lactose monohydrate is built from a moiety of β-D-galactose and α-D-galactose, joined by a 1,4 glycosidic bond between C1 of galactose and C4' of the glucose unit [29,31-33]. Fig. 2(ai–aiii) showed the α-lactose monohydrate structure in its crystal lattice, viewed from x-, y- and z-axis direction. The structure was packed in monoclinic lattice with space group P_{21}, in which consisted of two α-lactose monohydrate molecules of the same conformation and two water molecules in a unit cell. One asymmetric unit of α-lactose monohydrate consisted of a pair of α-lactose monohydrate and water molecule. The cell parameters were a = 4.7830, b = 21.540, c = 7.7599 Å, and α = γ = 90°, β = 105.911°. The packing involved a complex 3D hydrogen bond network, in which each α-lactose was intermolecularly bonded with its neighboring atoms with 14 hydrogen bonds. Meanwhile, each water molecule was hydrogen-bonded to four different α-lactose molecules [29,34]. Fig. 2(b) showed the α-lactose monohydrate crystals grown in PEG 300 solution and Fig. 2(c) showed the predicted morphology of α-lactose monohydrate crystals in vacuum using PCFF force field and Hirshfield atomic charges. The calculated lattice energy was -41.9 kcal/mol [30]. Most of the terminating surfaces of α-lactose monohydrate were monopolized by the hydroxyl functional groups, which can act as binding sites for attachment of other molecules in solution, due to the presence of H-bond acceptors and H-bond donors on the surfaces.

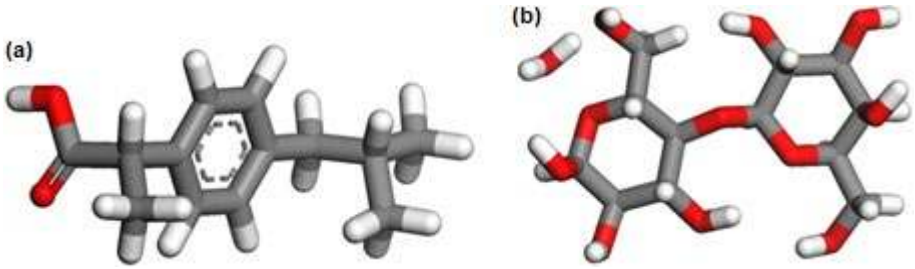

Fig 1. (a) A racemic ibuprofen molecule, and (b) An α-lactose monohydrate molecule

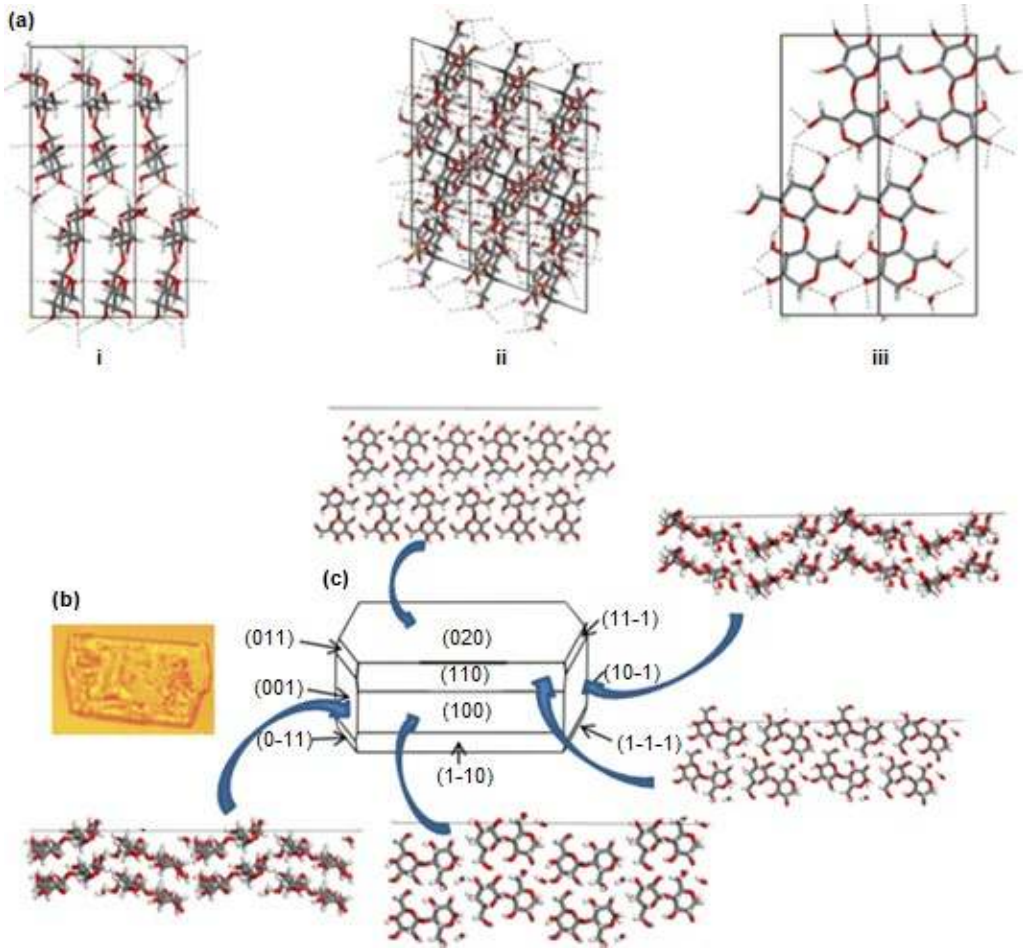

Fig 2. (a) The α-lactose monohydrate crystal lattice, showing the hydrogen bond network, in the order of: (i) view from x-direction, (ii) view from y-direction and (iii) view from z-direction [29], (b) α-lactose monohydrate crystal grown in PEG 300 solution (top view); and (c) morphology prediction of α-lactose monohydrate in vacuum, showing an elongated hexagonal crystal shape and selected surfaces of the crystal. Images were adopted from [30]

Procedure

Granules produced from pressure swing granulation (PSG) technique

Detail description of the employed pressure swing granulation (PSG) technique were detailed out by Ab Ghani et al. [4]. Granules of (±)-IBP-ALM was produced according to methods and conditions underlined by Abu Bakar et al. [10]. A 70 wt.% milled lactose and 30 wt.% milled ibuprofen were fed to the PSG at the ambient temperature for the production of core granules. A batch size of 120 g of well mixed (±)-IBP-ALM sample was fed into the PSG fluidized bed through a rotating sieve with aperture size of 840 μm. The gas velocity used to produce the granules was 0.364 m/s. The duration of fluidization was 15 sec and the duration for compaction was 1 sec. The compaction pressure used was 0.03 MPa and with the vibration frequency of 40 Hz. The total granulation time was 240 min. The granules then further coated with 2 wt.% of fine lactose particles in the fluidized bed at 70 °C for 1 h.

Crystals produced from slow evaporation crystallization

Crystallization experiments involved three separate systems, namely α-lactose monohydrate, ibuprofen and (±)-IBP-ALM mixtures, crystallized in PEG 300 solution. Crystallization experiment was conducted by trial and error method in which substrates and water were added successively into PEG 300

solutions to produce supersaturated solution in a 100 mL beaker. The methods used to prepare the supersaturated solution were as follow: (1) for α-lactose monohydrate supersaturation: A 0.2 g of α-lactose monohydrate and a 2 mL of water were added successively to a 5 mL PEG 300, (2) for Ibuprofen supersaturation: 6.48 g of ibuprofen were added to a 5 mL of PEG 300 solution, and (3) for (±)-IBP-ALM supersaturation: A mixture of 0.123 g ibuprofen and 0.2 g α-lactose monohydrate (1:1 molar ratio, 1:1.62 w/w ratio of (±)-IBP-ALM) were added successively to a 5 mL of PEG 300 solution. The solutions were heated at 70 °C and mixed at 1100 rpm using a magnetic stirrer on a hot plate. The solutions were cooled to the ambient temperature, with the top of the beakers capped with an aluminium foil with punctured holes, so that water vapor could escape from the solution. The crystals were harvested from the solution when the crystals have grown in the solution (after being left to stand for 3 days). The crystals were filtered from the solution using a filter paper. Then, the crystals were dried in a dryer at 40 °C for 4 days.

Solid state characterization of granules and crystals of (±)-IBP-ALM

The granules and crystals produced in this work were characterized using a Fourier Transform Infrared (FTIR) spectroscopy, X-Ray Powder Diffraction (XRPD) system and Differential Scanning Calorimetry (DSC). Transmission from the FTIR spectroscopy was recorded on a Perkin-Elmer Spectrum One spectrometer (Perkin-Elmer Instruments, USA). The Attenuated Total Reflection (ATR) samples disk was scanned four times from 400 to 4000 cm^{-1} with a resolution 4 cm^{-1}. The XRPD diffractograms at 25 °C were collected by Rigaku D/Max-2000 (Rigaku, Japan) to provide information for the identification and crystallinity of materials. The source of XRPD was Cu Kα (λ = 1.542 Å). The diffractometer was operated at 40 kV, 40 mA with scan speed 0.6°/min, sampling step 0.02° and the range at 2θ between 3 and 40°. The DSC was used to analyze solid transformation and to identify melting temperatures in the materials. Indium standard of high purity was used to calibrate the DSC temperature and enthalpy scale. Thermal analytical data of the samples (between 2–4 mg) in a 40 μL perforated aluminium crucible were collected by a Mettler Toledo DSC 1 (Mettler-Toledo, Germany). The heating rate used was 10 °C/min, heated from 25 to 300 °C, under a constant flow rate of 50 mL/min nitrogen gas purge.

Molecular computational technique details

In this work, molecular modelling software, Material Studio 4.4 from Accelrys was used for the prediction of the α-lactose monohydrate morphology. Crystal structures of α-lactose monohydrate molecules (CCDC ID: LACTOS10) and racemic ibuprofen (CCDC ID: IBPRAC03) were obtained from Cambridge Crystallographic Data Centre. The simulation was carried out in a vacuum environment. The lattice energy and the attachment energy of each facets of α-lactose monohydrate were obtained from Lukman et al. [30]. In their work, the predicted lattice energies (obtained from the morphology prediction) were compared to the experimental data which was calculated by using Eq. (1).

$$E_{latt} = \Delta H_{sub} - 2RT \quad (1)$$

Where ΔH_{sub} is the sublimation energy of α-lactose monohydrate and the 2RT represents a correction factor, for the difference between the gas enthalpy and the vibrational contribution to the crystal enthalpy [35-37]. The attachment energy, E_{att} used as a reference in this work, was obtained as the difference between the lattice energy and the slice energies, E_{slice} of each habit facet, and as shown by the Eq. (2);

$$E_{att} = E_{latt} - E_{slice} \quad (2)$$

The values of E_{att} for the terminating surfaces tested in this work were also obtained from Lukman et al. [30].

Binding prediction

All visible surfaces of the facetted morphology of α-lactose monohydrate were cleaved to a depth of 323 Å and a periodic superstructure was constructed from a unit cell. A 60-Å thick vacuum slab was built above the crystal slice. Attachment method was used between a guest molecule (either (±)-IBP or ALM) and a host surface (ALM) for the binding prediction work. Binding prediction between ibuprofen and α-lactose monohydrate was first conducted as it gave a preliminary indication on the facet suitability for (±)-IBP binding. Only then the appropriate facets were

selected for self-binding simulation between an α-lactose monohydrate molecule and an α-lactose monohydrate surface (as a host facet). The selected ALM surface molecules were locked to its Cartesian coordinates while a relaxed guest molecule was given a reasonable initial position, so that the molecule possibly formed hydrogen bond with the layers of α-lactose monohydrate.

The guest molecule was relaxed, which allows flexibility of molecular structure to interact with the rigid hkl surface. The molecular dynamics calculation allows the simulation of a relaxed guest molecule to move under the influence of computed forces. Hence, the calculation determines the best orientation of guest molecule on the rigid host slice. Both molecule and the rigid layers were then relaxed to achieve the minimum energies in optimization stage. Ewald summation method was used to compute electrostatics and van der Waals forces. Modified attachment energy, E_{att}^{mod} was calculated by using Eq. (3) [36];

$$E_{att}^{mod} = E_{att} - \frac{E_{att} \cdot \Delta b}{E_b^{host}} \quad (3)$$

Attachment energy, E_{att} for each facet of α-lactose monohydrate was obtained from Lukman et al. [30]. Binding energy difference, Δb was calculated for both host and guest molecule. In cases where $\Delta b < 0$ (preferred interaction with guest molecule), E_{att}^{mod} will be smaller and growth rate becomes slower, contributing to morphological important face, and vice versa [36].

■ RESULTS AND DISCUSSION

Characterization of Solid Granules from Melt Crystallization

Both α-lactose monohydrate and ibuprofen (polymorph I) were used as received from the manufacturer and used to compare the characteristic of feed materials with the granules produced using the PSG. The FTIR spectra of ibuprofen, the (±)-IBP-ALM granules and α-lactose monohydrate are shown in Fig. 3.

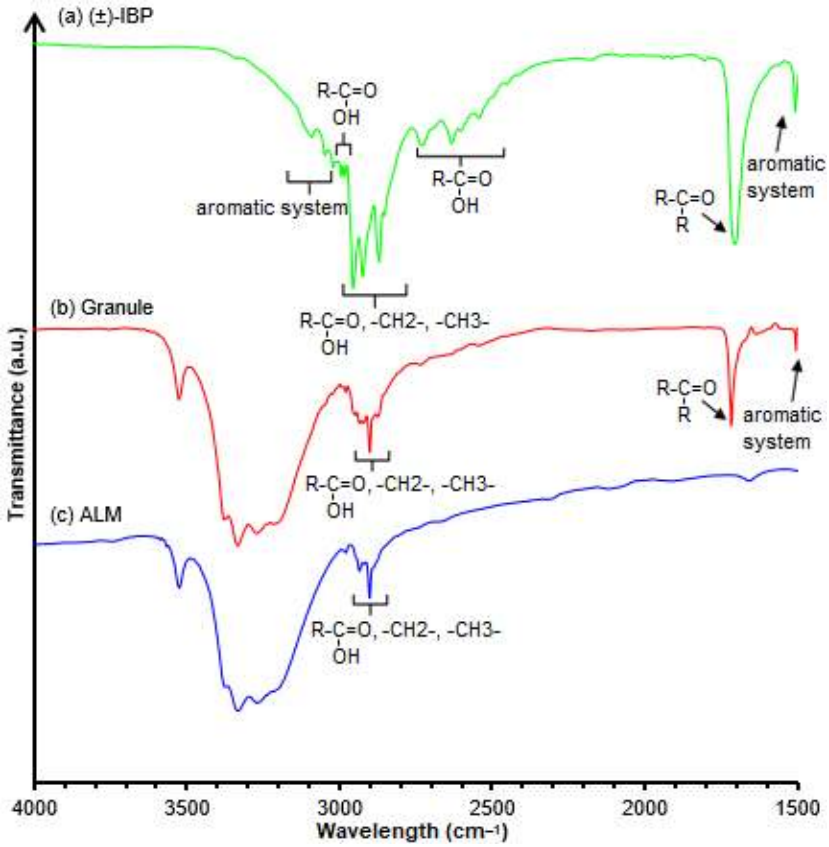

Fig 3. FTIR spectra of (a) pure ibuprofen, (b) granules of (±)-IBP-ALM produced from melt crystallization, and (c) pure α-lactose monohydrate

Based on the FTIR analysis, due to H-bridge and crystal water band are observed, it can be concluded that the pressure swing fluidization procedure did not produce anhydrous α-lactose monohydrate granules to become anhydrous, proven by the H-bridge and crystal water band present in the FTIR spectra.

The FTIR spectrum of the (±)-IBP-ALM granules is dominated by α-lactose monohydrate, except for the carboxylic group and aromatic system bands which are the identifying bands for ibuprofen. The carbonyl absorptions were observed at 1714 cm^{-1} for granules, whilst at 1705 cm^{-1} for ibuprofen (Fig. 3(a) and (b)). From the work of Chan and Kazarian [21], the shift of carbonyl stretching at 22 °C from 1705 (ibuprofen) to 1732 cm^{-1} (pure ibuprofen dispersed in PEG 1500) is due to H-bonding of PEG 1500 (hydroxyl group) and pure (±)-IBP (carbonyl and hydroxyl groups). In this work, the shift of band (1714 cm^{-1}) for the granules from the ibuprofen of 1705 cm^{-1} probably indicates that the interaction between the carbonyl of ibuprofen and the hydroxyl groups of the α-lactose monohydrate. This band could be an indicator of the presence of a new phase, i.e. the co-crystals formed in the granules.

Differential scanning calorimetry (DSC) analysis shows that the melting points at notation 1 (78 °C, (±)-IBP) and notation 2 (76 °C, granules) indicate the presence of (±)-IBP in granules (Fig. 4). Both melting points of ibuprofen sample and granules are within the range as reported by previous researchers, from 71 to 78 °C [10-11,38-41]. The wide range of the melting points reported for ibuprofen could be due to the degree of crystallinity and nature of employed solvents in crystallization process [42]. The endotherm at notation (3) (131 °C, granules) and notation (4) (144 and 148 °C, ALM) are believed due to the dehydration of crystalline water. These values are within and over the range of 120

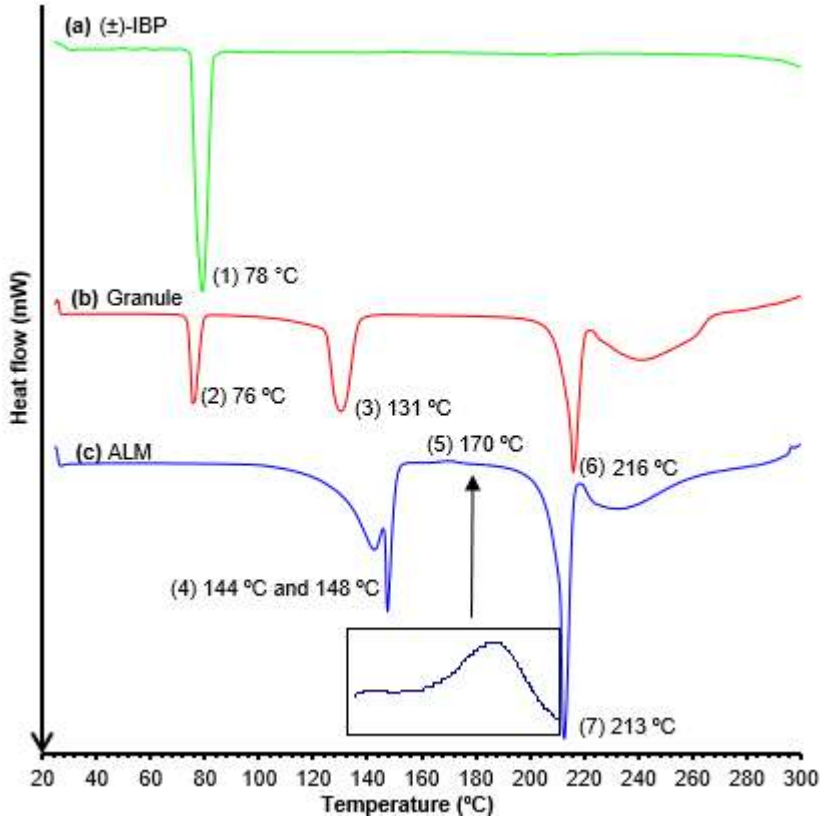

Fig 4. Comparison of DSC patterns between: (a) racemic ibuprofen (b) the granules, and (c) milled ALM. The notations are as follows: (1) 78 °C – melting temperature of racemic ibuprofen. (2) 76 °C – melting temperature of racemic ibuprofen. (3) 131 °C – loss of water. (4) 144 and 148 °C – loss of water, (5) 170 °C. (6) 216 °C – melting temperature of α-lactose monohydrate, and (7) 213 °C – melting temperature of α-lactose monohydrate

and 140 °C which were reported by previous researchers [43-48]. The lower value of 131 °C (notation 3, granules) relative to 144 and 148 °C (notation 4, ALM) might be due to partial water evaporation during heat treatment at 70 °C during granulation process by PSG [49]. The α-lactose monohydrate sample (Fig. 4(c)) and α-lactose monohydrate in granules sample (Fig. 4(b) become anhydrous due to the dehydration of α-lactose monohydrate. This is supported by Garnier et al. [34], who reported that α-lactose monohydrate could become anhydrous α-lactose by losing its water molecule after 100 °C. The small exotherm at notation 5 (170 °C, ALM) is similarly found in α-lactose monohydrate by Gombás et al. [44] and Garnier et al. [34]. However, the close-up (the small insertion of notation 5) shows that it is not preceded by a small endotherm [50]. This exotherm might be the recrystallization of anhydrous α-lactose to β-lactose. This recrystallization is proved by temperature-resolved XRPD which revealed that, at 170 °C, α-lactose monohydrate composed of both anhydrous α-lactose and β-lactose [50]. In fact, the presence of β-lactose in α-lactose monohydrate was also detected at 100 °C [50]. However, the granules do not show the same exotherm (notation 5), even though the granules are composed of mixtures of both α-lactose monohydrate and ibuprofen. The endotherms at notation (6) (216 °C, granules) and notation (7) (213 °C, ALM) correspond to the melting point of α-lactose monohydrate. These values are slightly lower than those reported by the researchers [39,46] which were in between 217 and 218 °C. The presence of an endothermic peak at 213 °C (notation (7)) indicates that the samples (Fig. 4(b)) contains α-lactose monohydrate only [47] which contradicts the finding by Garnier et al. [50]. α-Lactose monohydrate starts to degenerate at a temperature higher than 220 °C [45,47,51]. The presence of a co-crystal normally can be detected from the presence of a new melting peak in the DSC endotherm [52-53]. In this work, no new peak was detected, which could indicate that the granulation of (±)-IBP-ALM mixture in PSG does not produce a co-crystal.

The XRPD patterns shown in Fig. 5 are for ibuprofen, granule, and α-lactose monohydrate. The result

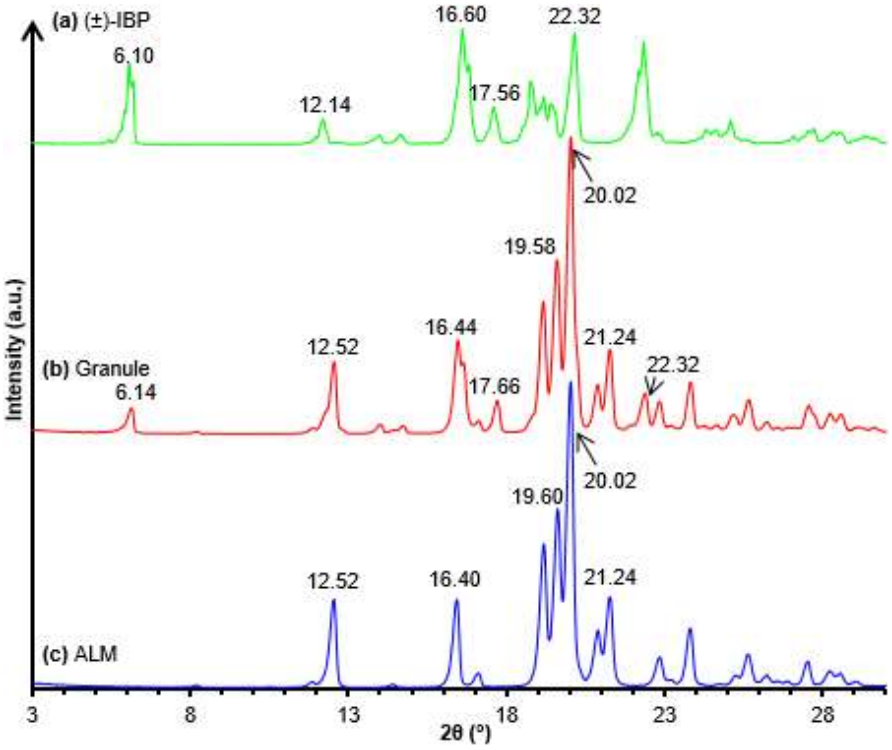

Fig 5. Comparison of XRPD patterns between (a) racemic ibuprofen (b) granules, and (c) α-lactose monohydrate, showing the important diffraction angle peaks which indicate that the granules produced using the PSG method contains mixtures of ibuprofen and α-lactose monohydrate only, and no co-crystal was produced

shows that the granule contains a mixture of peaks from both ibuprofen (polymorph I) and α-lactose monohydrate. However, there was no new peak observed for the granules, which indicates that no co-crystal was formed in the granules produced from the PSG process. The absence of new crystalline phase in granule might be due to structural difference between the ibuprofen and α-lactose monohydrate molecules. Nevertheless, high structural similarity between the host molecule and additive does not guarantee co-crystal formation. These are consistent with the finding that there was no incorporation of structurally related additives (SRAs) in ALM layers based on HPLC analyses although strong morphological changes were observed [34].

Characterization of Racemic Ibuprofen-Alpha Lactose Monohydrate Crystals Grown in PEG 300 Solutions

In this work, all the crystals (ibuprofen, α-lactose monohydrate, and crystals from (±)-IBP-ALM mixtures) were grown in PEG 300 solution. Both the ibuprofen and α-lactose monohydrate produced from PEG 300 were compared with the pure form of these components (feed materials) using the XRPD. The results show that both ibuprofen and α-lactose monohydrate crystallized from PEG 300 are of the same polymorphs as the feed materials. Comparison of FTIR spectra of the crystals grown in the PEG 300 solution using slow evaporation method are shown in Fig. 6. The spectrum of (±)-IBP-ALM (Fig. 6(b)) is composed of moieties of (±)-IBP (carboxyl) and ALM (hydroxyl). This indicates that both compounds are present in (±)-IBP-ALM crystal sample. The carbonyl band at 1651 cm^{-1} was recorded by both α-lactose monohydrate (Fig. 6(c)) and (±)-IBP-ALM (Fig. 6(b)). Nevertheless, ibuprofen recovered from PEG 300 solution in Fig. 6(a) recorded higher carbonyl stretching, 1713–1651 cm^{-1} which is similarly to the band recorded for granule in Fig. 3(b). This shift of carbonyl stretching from 1705–1651 cm^{-1} of pure ibuprofen (Fig. 3(a)) to 1713–1651 cm^{-1} (Fig. 6(a)) might indicate that the ibuprofen is in a monomer state and could interact with carboxyl moiety of PEG 300 [21,53]. However, the shift of peak could also indicate that a new crystalline phase (such as a co-crystal) has formed [52-53].

The showed ibuprofen crystal in Fig. 7(a) was grown in PEG 300 solution, and the melting temperature recorded by the DSC has shown that the ibuprofen has a

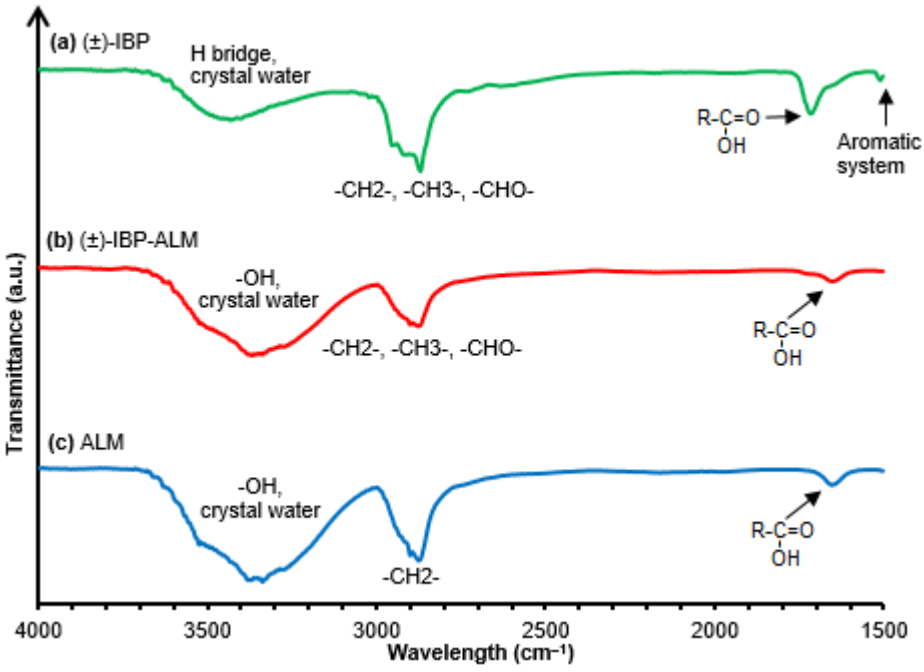

Fig 6. FTIR spectra of crystals grown in PEG 300 solution: (a) ibuprofen, (b) crystals from (±)-IBP-ALM mixtures, and (c) α-lactose monohydrate

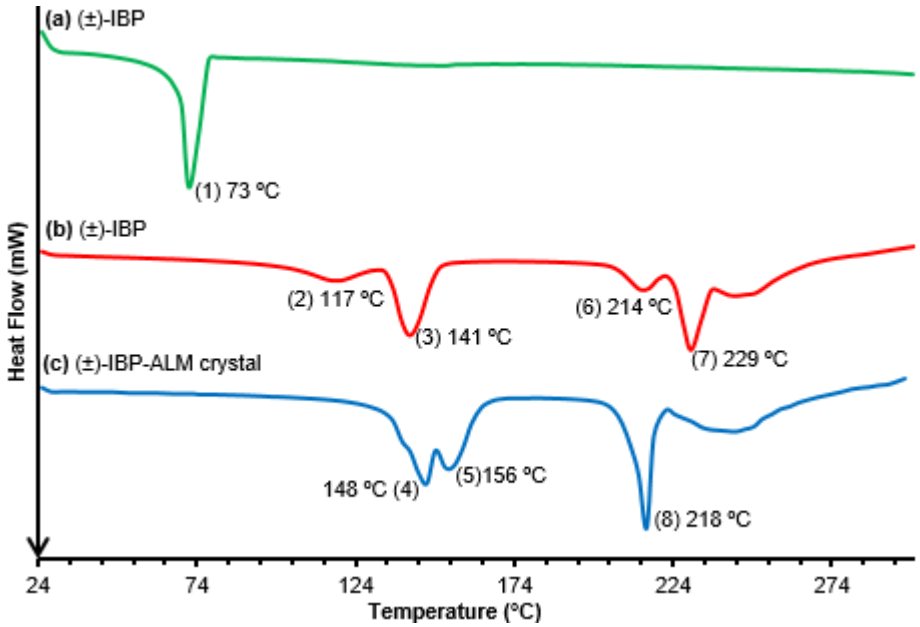

Fig 7. Comparison of DSC patterns of product crystals recovered from PEG 300 solutions between (a) ibuprofen (b) crystals from (±)-IBP-ALM mixtures (c) α-lactose monohydrate. The notations are as follow: (1) 73 °C – melting of (±)-IBP. (2) 117 °C – loss of water. (3) 141 °C – loss of water. (4) 148 °C – loss of water. (5) 156 °C – loss of water. (6) 214 °C – melting of α-lactose monohydrate. (7) 229 °C and (8) 218 °C – melting of α-lactose monohydrate

lower melting point, at 73 °C (notation 1) than that of ibuprofen (78 °C) in Fig. 4(a), but within the range of values recorded by other researchers from 71 to 78 °C [10-11,38-41]. Both patterns of the crystals recovered from the solution containing (±)-IBP-ALM (Fig. 7(b)) and α-lactose monohydrate (Fig. 7(c)) are similar, with no endotherm of ibuprofen detected in the crystal. This result shows that crystallization of (±)-IBP-ALM mixture in PEG 300 solution yields only α-lactose monohydrate. The endotherms at notation (2) 117 °C, (3) 141 °C and notation (4) 148 °C, (5) 156 °C are believed due to the dehydration of crystalline water. These values are within and over the range of 120–140 °C, as previously reported by researchers [43-48]. The endotherms at notation (6) 214 °C, (7) 229 °C and (8) 218 °C are believed correspond to the melting point of α-lactose monohydrate, which are somewhat higher than reported by the previous researchers [46-47], i.e., between ~217 °C and 218 °C. α-Lactose monohydrate starts to degenerate after 220 °C [45,47,51], nevertheless, in this work, the (±)-IBP-ALM crystals (Fig. 7(b)) start to degenerate at a temperature higher than 229 °C. As there is no new endotherm in (±)-IBP–ALM, and the peaks are identical to the peaks of pure ALM and (±)-IBP, this might indicate no co-crystal is formed.

Fig. 8 depicts the XRPD diffractogram of the crystal of (±)-IBP-ALM mixtures grown in PEG 300 solution and the result shows that the 2-theta peaks (Fig. 8(b)) resembles that of α-lactose monohydrate (Fig. 8(c)). This phenomenon indicates that only α-lactose monohydrate crystallized from (±)-IBP-ALM mixtures, and this result confirms that no co-crystal has been successfully formed from the slow evaporation method adopted in this work.

In other similar work, Mohammad et al. [54] found that a mixture of sucrose-indomethacin analyzed using a DSC to have two distinct endotherms, which belong to melting endotherms of sucrose and indomethacin; respectively, due to a lack of miscibility and no co-crystal formation. The same phenomena were also observed in this work (Fig. 7 and 4), which have separate melting endotherms for both ibuprofen and α-lactose monohydrate. Sucrose and maltose were found to not co-crystallize with ibuprofen through co-evaporation of ethanol solutions at 65 °C ((±)-IBP:sugar 4:1 w/w [55]). Through XRPD analysis, the co-evaporated crystals have

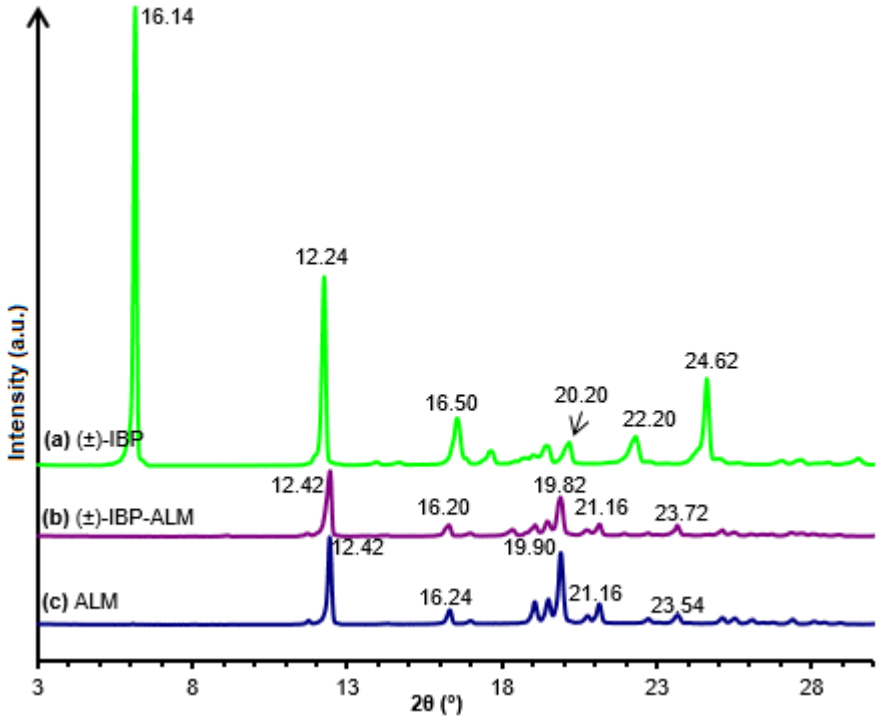

Fig 8. Comparison of powder XRD diffractogram between product crystals recovered from PEG 300 solution: (a) ibuprofen (b) (±)-IBP - ALM and (c) α-lactose monohydrate

patterns which are almost identical to that of ibuprofen. This trend was also observed in Fig. 5 and 8, in which XRPD pattern of crystals produced from the (±)-IBP-ALM mixtures resembles that of α-lactose monohydrate. This might be due to the separate crystallization of (±)-IBP and sugar [55], or (±)-IBP, and in this case the α-lactose monohydrate molecules.

Binding Process Analysis

In this work, cleaved surfaces, and corresponding attachment energy, E_{att} of the predicted facetted morphology of α-lactose monohydrate from Lukman et al. [30] was calculated using PCFF potential function and Hirshfeld charge set. Table 1 shows the changes in the differential binding energy, Δb between guest molecules of α-lactose monohydrate and ibuprofen attached to different habit facet of α-lactose monohydrate and the corresponding modified attachment energy, E_{att}^{mod} calculated using Eq. (3). Table 1 also shows the distribution of E_{att} due to the van der Waals interaction and E_{att} due to the Coulombic interaction, which indicate that the Coulombic interaction comprise only about 5% to 18% of the total attachment energy for the respective crystal facets, and the interactions were dominated by the van der Waals interactions. According to Dressler et al. [36] favorable binding (forming co-crystal) with the additive (i.e., racemic ibuprofen) for a given facet occurs when $\Delta b < 0$, in which the binding predicted between ibuprofen molecule and the α-lactose monohydrate surface is more negative compared to the binding energy between the α-lactose monohydrate molecule with its self-crystal surface. In other words, the presence of ibuprofen on the α-lactose monohydrate surface prevents the binding of the α-lactose monohydrate molecule as a growth unit to the surface and suppresses the growth of that facet. This results in E_{att}^{mod} becomes less negative to that of attachment energy, E_{att} of pure habit facet (i.e., α-lactose monohydrate). From Table 1, there are four habit facets ((0 -2 0), (1 -1 0), (0 0 1), and (0 1 1)) which were predicted to have favorable binding with ibuprofen as it fulfilled the condition set by Dressler et al. [36]. These results are agreeing well with the prediction on the possibility of binding sites based on the premise of low electrostatic energy, E_{stat} carried out by Lukman et al. [30].

Table 1. Binding energy difference, Δb and modified attachment energy, E_{att}^{mod} between α-lactose monohydrate and ibuprofen with the corresponding attachment energy, E_{att} of pure α-lactose monohydrate surfaces. The recorded lattice energy for α-lactose monohydrate was -41.9 kcal/mol [30]. All energies are in kcal/mol

ALM facets	E_{att}	E_{att} (vdW)	$E_{att(Est)}$	Δb_{total}		$\Delta b_{non\text{-}bonded}$	
						Δb (vdW)	Δb (E_{stat})
(0 2 0)	-12.09	-11.49	-0.60	-	-	-	-
(0 -2 0)	-12.09	-11.49	-0.60	-2590.41	-4.36	3.59	-2608.78
(1 0 0)	-17.38	-13.68	-3.71	460.90	-18.76	-	-
(1 1 0)	-18.25	-15.00	-3.24	106.81	-18.67	-	-
(1 -1 0)	-18.25	-15.00	-3.24	-884.32	-12.82	-1.70	-882.06
(1 0 -1)	-27.9	-26.30	-1.60	254.46	-29.73	-	-
(0 0 1)	-29.4	-26.90	-2.50	-236.83	-28.09	5.02	-241.70
(1 1 -1)	-29.2	-27.40	-1.80	296.75	-29.22	-	-
(1 -1 -1)	-29.2	-27.40	-1.80	-1876.25	-29.22	-	-
(0 1 1)	-30.5	-28.00	-2.50	-185.66	-29.43	9.58	3169.19
(0 -1 1)	-30.5	-28.00	-2.50	566.89	-35.18	-	-

This work helps to pinpoint the specific habit facet favoring binding with ibuprofen, which possibly is an indication that the co-crystal formation could form. Prediction of successful binding is illustrated in Fig. 9 which shows that ibuprofen becomes either both H-bond donor and acceptor or just H-acceptor. In this work, ibuprofen is represented by carboxyl (COOH) and carbonyl (CO) moieties which make up the carboxylic acid dimer (COOH·COOH) while hydroxyl (OH) is represented by α-lactose monohydrate. The working binding prediction as illustrated in Fig. 9 clearly shows that either carboxyl or carbonyl moieties must be complemented by hydroxyl via H-bond, forming a hetero-synthon. The attachment preserves the complex

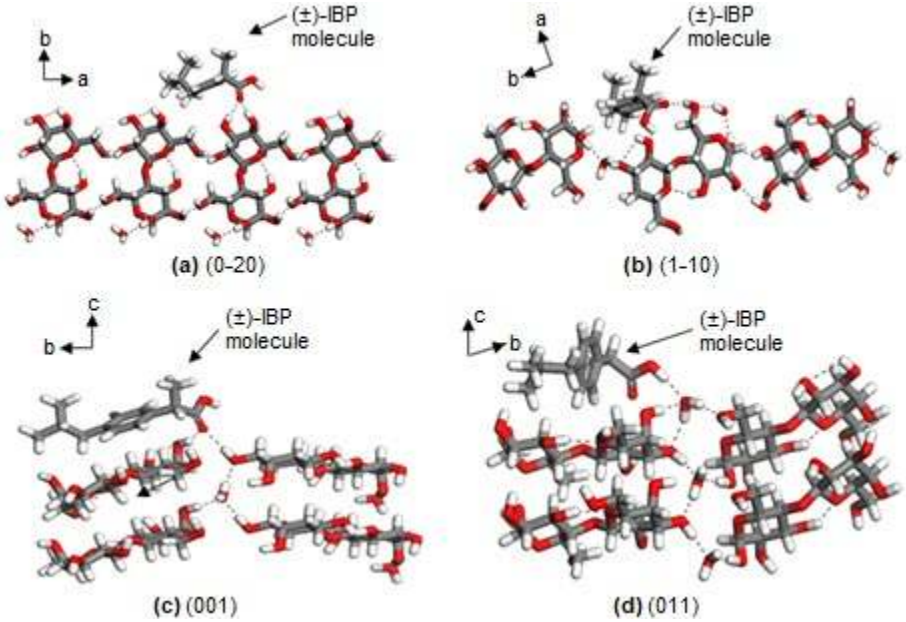

Fig 9. The most favorable position of the ibuprofen molecule on the host slice of α-lactose monohydrate for the respective crystal surfaces from the molecular dynamics simulation; illustrating possible interaction of ibuprofen molecule with the crystal surface that can suppress the growth of α-lactose monohydrate surface. These also can be taken as a possible interaction between the two compounds for the formation of the cocrystal

3D hydrogen bond network of α-lactose monohydrate by comparing with corresponding surfaces in Lukman et al. [30]. It was observed from facets in Fig. 9(a–c) that ibuprofen molecule is positioned with its phenyl group facing downward towards the α-lactose monohydrate surface while its isobutyl and methyl group projected upwards. This is probably due to high repulsive van der Waals forces compared to other facets in Fig. 9(d) to ensure that the position of the concerned groups can fully minimize van der Waals repulsive effects. Furthermore, the hydrocarbon part of ibuprofen cannot be fitted into the gap between the α-lactose monohydrate molecules because of the presence of carbon and hydrogen atoms of α-lactose monohydrate on both sides which interact via van der Waals forces and steric effects. Interestingly, the phenyl, isobutyl and methyl groups recede downward to the (0 1 1) facets (Fig. 9(d)). This might be the case due to the van der Waals forces dominating the facets. For (0 -2 0), (1 -1 0) and (0 0 1) surfaces, (Fig. 9(a–c)), the phenyl ring is oriented parallel with the α-lactose monohydrate surfaces, probably so that it can maximize van der Waals attractive forces. This favorable binding prediction is consistent with prediction using superimposition method, reported by Garnier et al. [34]. Four (α-glucosamine hydrochloride, maltitol, α-galactose and β-cellobiose) out of six structurally related additives (SRAs) (including sucrose and β-glucuronamide) are predicted to be incorporated successfully into α-lactose monohydrate layers, either disrupting or preserving H-bonds formation.

This successful binding could also be contributed by the geometrically optimized ibuprofen and α-lactose monohydrate individual structures, in which minimum energies were achieved for stabilization. Furthermore, it also depends on exact orientations of (±)-IBP positioned centrally on the exact surface sites of the α-lactose monohydrate facets during the stage of molecular dynamics and geometrical optimization of (±)-IBP-ALM [13].

■ CONCLUSION

The evaluation of cocrystal tendency in this work has shown that ALM-(±)-IBP cocrystals has not been successfully formed in both solid granules from melt granulation and in crystals formed from through slow evaporation technique. Analysis of the crystals has revealed that the crystals formed in the granules were a mixture of pure components of ibuprofen and α-lactose monohydrate, even though the mixtures have been granulated and heated in the pressure wing granulator. In the case of the mixture of ibuprofen and α-lactose monohydrate crystallized in PEG 300 solution, the crystals harvested was of α-lactose monohydrate only, with ibuprofen remained dissolved in the solution. Molecular modelling work undertaken in this study reflected the phenomenon in melt crystallization of the (±)-IBP-ALM, and has shown that ibuprofen is capable to form favorable interactions with the (0 -2 0), (1 -1 0), (0 0 1), and (0 1 1) terminating surfaces of α-lactose monohydrate crystals, reflecting that the co-crystal formation between these molecules is theoretically possible.

■ ACKNOWLEDGMENTS

The authors would like to express their gratitude to the Ministry of Education (MOE), Malaysia for funding of this work, which was carried out at Universiti Teknologi MARA (UiTM), Shah Alam, Malaysia. This work is part of grant 600-RMI/FRGS 5/3 (92/2013) and grant 600-RMI/ERGS 5/3 (29/2012).

■ REFERENCES

[1] Pauli-Bruns, A., Knop, K., and Lippold, B.C., 2010, Preparation of sustained release matrix pellets by melt agglomeration in the fluidized bed: Influence of formulation variables and modelling of agglomerate growth, *Eur. J. Pharm. Biopharm.*, 74 (3), 503–512.

[2] Vilhelmsen, T., Eliasen, H., and Schaefer, T., 2005, Effect of a melt agglomeration process on agglomerates containing solid dispersions, *Int. J. Pharm.*, 303(1-2), 132–142.

[3] Yang, D., Kulkarni, R., Behme, R.J., and Kotiyan, P.N., 2007, Effect of the melt granulation technique on the dissolution characteristics of griseofulvin, *Int. J. Pharm.*, 329 (1-2), 72–80.

[4] Ab Ghani, S., Abu Bakar, N.F., Abu Bakar, M.R., Yusof, Y.A., and Abd Rahman, N., 2018, Granulation

of mefenamic acid and poly-ethylene glycol (PEG) using pressure swing granulation (PSG) technique in fluidized bed, *Malays. J. Anal. Sci.*, 22 (2), 318–325.

[5] Walker, G.M., Bell, S.E.J., Andrews, G., and Jones, D., 2007, Co-melt fluidized bed granulation of pharmaceutical powders: Improvements in drug bioavailability, *Chem. Eng. Sci.*, 62 (1-2), 451–462.

[6] Walker, G.M., Andrews, G., and Jones, D., 2006, Effect of process parameters on the melt granulation of pharmaceutical powders, *Powder Technol.*, 65 (3), 161–166.

[7] Ghorab, M.K., and Adeyeye, M.C., 2001, Enhancement of ibuprofen dissolution via wet granulation with β-cyclodextrin, *Pharm. Dev. Technol.*, 6 (3), 305–314.

[8] Pacheco, D.P., Manrique, Y.J., and Martínez, F., 2007, Thermodynamic study of the solubility of ibuprofen and naproxen in some ethanol + propylene glycol mixtures, *Fluid Phase Equilib.*, 262 (1-2), 23–31.

[9] Passerini, N., Albertini, B., González-Rodríguez, M.L., Cavallari, C., and Rodriguez, L., 2002, Preparation and characterization of ibuprofen-poloxamer 188 granules obtained by melt granulation, *Eur. J. Pharm. Sci.*, 15 (1), 71–78.

[10] Abu Bakar, N.F., Mujumdar, A., Urabe, S., Takano, K., Nishii, K., and Horio, M., 2007, Improvement of sticking tendency of granules during tabletting process by pressure swing granulation, *Powder Technol.*, 176 (2-3), 137–147.

[11] Perlovich, G.L., Kurkov, S.V., Hansen, L.K., and Bauer-Brandl, A., 2004, Thermodynamics of sublimation, crystal lattice energies, and crystal structures of racemates and enantiomers: (+) and (±)-ibuprofen, *J. Pharm. Sci.*, 93 (3), 654–666.

[12] Mameri, F., Koutchoukali, O., Bouhelassa, M., Hartwig, A., Nemdili, L., and Ulrich, J., 2017, The feasibility of coating by cooling crystallization on ibuprofen naked tablets, *Front. Chem. Sci. Eng.*, 11, 211–219.

[13] Myerson, A.S., 2002, *Handbook of Industrial Crystallization*, 2nd Ed., Butterworth-Heinemann, Boston, 312.

[14] Chen, J., Sarma, B., Evans, J.M.B., and Myerson, A.S., 2011, Pharmaceutical crystallization, *Cryst. Growth Des.*, 11 (4), 887–895.

[15] Stahly, G.P., 2007, Diversity in single- and multiple-component crystals. The search for and prevalence of polymorphs and cocrystals, *Cryst. Growth Des.*, 7 (6), 1007–1026.

[16] Dhumal, R.S., Kelly, A.L., York, P., Coates, P.D., and Paradkar, A., 2010, Cocrystalization and simultaneous agglomeration using hot melt extrusion, *Pharm. Res.*, 27 (12), 2725–2733.

[17] Rasenack, N., and Müller, B.W., 2002, Ibuprofen crystals with optimized properties, *Int. J. Pharm.*, 245 (1-2), 9–24.

[18] Alshahateet, S.F., 2011, Synthesis and X-ray crystallographic analysis of pharmaceutical model *rac*-ibuprofen cocrystal, *J. Chem. Crystallogr.*, 41, 276–279.

[19] Berry, D.J., Seaton, C.C., Clegg, W., Harrington, R.W., Coles, S.J., Horton, P.N., Hursthouse, M.B., Storey, R., Jones, W., Friščić, T., and Blagden, N., 2008, Applying hot-stage microscopy to co-crystal screening: A study of nicotinamide with seven active pharmaceutical ingredients, *Cryst. Growth Des.*, 8 (5), 1697–1712.

[20] Rajanikant, P., Nirav, P., Patel, N.M., and Patel, M.M., 2010, A novel approach for dissolution enhancement of Ibuprofen by preparing floating granules, *Int. J. Res. Pharm. Sci.*, 1 (1), 57–64.

[21] Chan, K.L.A., and Kazarian, S.G., 2006, High-throughput study of poly(ethylene glycol)/ibuprofen formulations under controlled environment using FTIR imaging, *J. Comb. Chem.*, 8 (1), 26–31.

[22] Hammond, R.B., Pencheva, K., Ramachandran, V., and Roberts, K.J., 2007, Application of grid-based molecular methods for modeling solvent-dependent crystal growth morphology: Aspirin crystallized from aqueous ethanolic solution, *Cryst. Growth Des.*, 7 (9), 1571–1574.

[23] Anuar, N., Daud, W.R.W., Roberts, K.J., Kamarudin, S.K., and Tasirin, S.M., 2012, Morphology and associated surface chemistry of L-isoleucine crystals modeled under the influence of L-leucine additive molecules, *Cryst. Growth Des.*, 12 (5), 2195–2203.

[24] Rosbottom, I., Ma, C.Y., Turner, T.D., O'Connell, R.A., Loughrey, J., Sadiq, G., Davey, R.J., and Roberts, K.J., 2017, Influence of solvent composition on the crystal morphology and structure of *p*-aminobenzoic acid crystallized from mixed ethanol and nitromethane solutions, *Cryst. Growth Des*., 17 (8), 4151–4161.

[25] Abdul Mudalip, S.K., Adam, F., and Abu Bakar, M.R., 2019, Evaluation of the intermolecular interactions and polymorphism of mefenamic acid crystals in *N,N*-dimethyl formamide solution: A molecular dynamics simulation and experimental study, *C.R. Chim.*, 22 (11-12), 771–778.

[26] Rosbottom, I., Pickering, J.H., Etbon, B., Hammond, R.B., and Roberts, K.J., 2018, Examination of inequivalent wetting on the crystal habit surfaces of RS-ibuprofen using grid-based molecular modelling, *Phys. Chem. Chem. Phys.*, 20 (17), 11622–11633.

[27] Cai, Z., Liu, Y., Song, Y., Guan, G., and Jiang, Y., 2017, The effect of tailor-made additives on crystal growth of methyl paraben: Experiments and modelling, *J. Cryst. Growth*, 461, 1–9.

[28] Wu, H., Wang, J., Li, F., Liu, Q., Zong, S., Bi, J., Wang, N., Shan, G., and Hao, H., 2019, Investigations on growth intensification of *p*-toluamide crystals based on growth rate analysis and molecular simulation, *CrystEngComm*, 21 (36), 5519–5525.

[29] Fries, D., Rao, S.T., and Sundaralingam, M., 1971, Structural chemistry of carbohydrates. III. Crystal and molecular dtructure of 4-*O*-β-D-galactopyranosyl-α-D-glucopyranose monohydrate (α-lactose monohydrate), *Acta Crystallogr., Sect. B: Struct. Sci.*, 27 (5), 994–1005.

[30] Lukman, Z., Anuar, N., Abu Bakar, N.F., and Abd Rahman, N., 2018, Alpha lactose monohydrate morphology: Molecular modelling and experimental approach, *Int. J. Eng. Technol.*, 7 (4.18), 107–112.

[31] Dincer, T.D., Parkinson, G.M., Rohl, A.L., and Ogden, M.I., 1999, Crystallization of α-lactose monohydrate from dimethyl sulfoxide (DMSO) solutions: Influence of β-lactose, *J. Cryst. Growth*, 205 (3), 368–374.

[32] MacFhionnghaile, P., Svoboda, V., McGinty, J., Nordon, A., and Sefcik, J., 2017, Crystallization diagram for antisolvent crystallization of lactose: Using design of experiments to investigate continuous mixing-induced supersaturation, *Cryst. Growth Des.*, 17 (5), 2611–2621.

[33] Smith, J.H., Dann, S.E., Elsegood, M.R.J., Dale, S.H., and Blatchford, C.G., 2005, α-Lactose monohydrate: A redetermination at 150 K, *Acta Crystallogr., Sect. E: Struct. Rep. Online,* 61(8), 2499–2501.

[34] Garnier, S., Petit, S., and Coquerel, G., 2002, Influence of supersaturation and structurally related additives on the crystal growth of α-lactose monohydrate, *J. Cryst. Growth*, 234 (1), 207–219.

[35] Bisker-Leib, V., and Doherty, M.F., 2001, Modeling the crystal shape of polar organic materials: Prediction of urea crystals grown from polar and nonpolar solvents, *Cryst. Growth Des*., 1 (6), 455–461.

[36] Dressler, D.H., Hod, I., and Mastai, Y., 2008, Stabilization of α-L-glutamic acid on chiral thin films–A theoretical and experimental study, *J. Cryst. Growth*, 310 (7-9), 1718–1724.

[37] Poornachary, S.K., Chow, P.S., and Tan, R.B.H., 2008, Impurity effects on the growth of molecular crystals: Experiments and modeling, *Adv. Powder Technol.*, 19 (5), 459–473.

[38] Dwivedi, S.K., Sattari, S., Jamali, F., and Mitchell, A.G., 1992, Ibuprofen racemate and enantiomers: Phase diagram, solubility and thermodynamic studies, *Int. J. Pharm.*, 87 (1-3), 95–104.

[39] Uchida, H., Yoshida, M., Kojima, Y., Yamazoe, Y., and Matsuoka, M., 2005, Measurement and correlation of the solid-liquid-gas equilibria for the carbon dioxide + *S*-(+)-ibuprofen and carbon dioxide + *RS*-(±)-ibuprofen systems, *J. Chem. Eng. Data*, 50 (1), 11–15.

[40] Romero, A.J., Savastano, L., and Rhodes, C., 1993, Monitoring crystal modifications in systems containing ibuprofen, *Int. J. Pharm.*, 99 (2-3), 125–134.

[41] Xu, F., Sun, L.X., Tan, Z.C., Liang, J.G., and Li, R.L., 2004, Thermodynamic study of ibuprofen by adiabatic calorimetry and thermal analysis, *Thermochim. Acta*, 412 (1-2), 33–57.

[42] Lerdkanchanaporn, S., and Dollimore, D., 1997, A thermal analysis study of ibuprofen, *J. Therm. Anal.*, 49, 879–886.

[43] Lefort, R., Caron, V., Willart, J.F., and Descamps, M., 2006, Mutarotational kinetics and glass transition of lactose, *Solid State Commun.*, 140 (7-8), 329–334.

[44] Gombás, Á., Szabó-Révész, P., Kata, M., Regdon, G.Jr., and Erõs, I., 2002, Quantitative determination of crystallinity of α-lactose monohydrate by DSC, *J. Therm. Anal. Calorim.*, 68, 503–510.

[45] Listiohadi, Y., Hourigan, J.A., Sleigh, R.W., and Steele, R.J., 2008, Moisture sorption, compressibility and caking of lactose polymorphs, *Int. J. Pharm.*, 359 (1-2), 123–134.

[46] Genina, N., Räikkönen, H., Heinämäki, J., Antikainen, O., Siiriä, S., Veski, P., and Yliruusi, J., 2009, Effective modification of particle surface properties using ultrasonic water mist, *AAPS PharmSciTech*, 10 (1), 282–288.

[47] Kaialy, W., Martin, G.P., Ticehurst, M.D., Royall, P., Mohammad, M.A., Murphy, J., and Nokhodchi, A., 2011, Characterisation and deposition studies of recrystallised lactose from binary mixtures of ethanol/butanol for improved drug delivery from dry powder inhalers, *AAPS J.*, 13 (1), 30–43.

[48] Raut, D.M., Allada, R., Pavan, K.V., Deshpande, G., Patil, D., Patil, A., Deshmukh, A., Raut, D.M., Sakharkar, D.M., Bodke, P.S., and Mahajan, D.T., 2011, Dehydration of lactose monohydrate: Analytical and physical characterization, *Der Pharm. Lett.*, 3 (5), 202–212.

[49] Perissutti, B., Rubessa, F., Moneghini, M., and Voinovich, D., 2003, Formulation design of carbamazepine fast-release tablets prepared by melt granulation technique, *Int. J. Pharm.*, 256 (1-2), 53–63.

[50] Garnier, S., Petit, S., and Coquerel, G., 2002, Dehydration mechanism and crystallization behaviour of lactose, *J. Therm. Anal. Calorim.*, 68, 489–502.

[51] Dhumal, R.S., Biradar, S.V., Paradkar, A.R., and York, P., 2008, Ultrasound assisted engineering of lactose crystals, *Pharm. Res.*, 25 (12), 2835–2844.

[52] Abd Rahim, S., Tan, C.C., and Ramle, N.A., 2016, Carbamazepine-fumaric acid co-crystal screening using solution based method, *MATEC Web Conf.*, 69, 03003.

[53] Othman, M.F., Jamburi, N., Anuar, N., Abd Rahim, S., and Rohalim, N.H., 2016, Ibuprofen-amino acids co-crystal screening via co-grinding methods, *MATEC Web Conf.*, 69, 03002.

[54] Mohammad, M.A., Alhalaweh, A., and Velaga, S.P., 2011, Hansen solubility parameter as a tool to predict cocrystal formation, *Int. J. Pharm.*, 407 (1-2), 63–71.

[55] Greenhalgh, D.J., Williams, A.C., Timmins, P., and York, P., 1999, Solubility parameters as predictors of miscibility in solid dispersions, *J. Pharm. Sci.*, 88 (11), 1182–1190.

Application of Titanium-Silica-Graphite Composite Material for Photocatalytic Process of Methylene Blue

Lia Destiarti* **and Risya Sasri**

Department of Chemistry, Universitas Tanjungpura, Jl. Prof. Dr. Hadari Nawawi, Pontianak 78114, West Kalimantan, Indonesia

** **Corresponding author:***

tel: +62-81345208035
email: lia.destiarti@chemistry.untan.ac.id

Received: August 25, 2019
Accepted: April 29, 2020

DOI: 10.22146/ijc.48998

Abstract: *The use of TiO_2 in the slurry system for the photocatalytic process has disadvantages. It causes the resistance of UV transmission because it is cloudy and the difficulty for obtaining the catalyst at the end of the process. Therefore, an attempt to overcome this was conducted by compositing TiO_2 on SiO_2. Furthermore, carbon material can be used as a support material for TiO_2-SiO_2, so that the mixed materials can be used as a photocatalyst. The method of synthesis of the material was a sol-gel method by varying the composition of TiO_2-SiO_2/graphite, which was 1:1; 1:2; and 2:1. The material obtained was characterized by FTIR, DRUV, XRD, and SEM. Photocatalytic activity of the synthesized material was tested in methylene blue solution, whereas the quantitative data derived from UV-Vis spectrometry measurement. Photocatalyst activity was carried out by varying the degradation time of 30–180 min. The FTIR spectrum showed that O-H (~3400 cm^{-1}) and C-O (~1100 cm^{-1}) are the major groups in the synthesized materials. The value of bandgap energy (E_g) were 4.15, 4.20, 5.22, and 5.19 eV for TiO_2-SiO_2, TiO_2-SiO_2/G (1:1; 1:2; and 2:1) composites, respectively. The XRD pattern of TiO_2-SiO_2 showed that the highest peaks of 2θ were observed at 25.32, 37.71, and 47.91°. Graphite identity appeared at 2θ = 59.87°. The micrograph of SEM showed a homogenous dispersion of spherical particles in the materials. Photocatalytic test results showed that TiO_2-SiO_2/G with a composition of 2:1 has the highest percentage of methylene blue degradation, which reached 94% at 180 min.*

Keywords: *titanium dioxide; silica; graphite; photocatalytic; methylene blue*

■ INTRODUCTION

Methylene blue is a chemical used in the textile and painting industry. Industrial dye and textile dye are one of the largest groups of toxic organic compounds [1]. Methylene blue becomes the primary source of environmental contamination. The degradation and conversion of them into harmless substances is an important issue [2]. Physical and chemical methods are used to solve this problem. However, the complexity of the organic compound becomes a severe problem. The conventional method only transfers the pollution from a phase to another phase and concentrate them, and also are non-destructive processes. In recent years, the Advanced Oxidation Process (AOPs) techniques become more popular than conventional methods. An example of AOPs is photocatalytic using titanium dioxide (TiO_2) as a catalyst.

Titanium dioxide is widely known as a photocatalyst in the photocatalytic method. This method has the advantage of being able to degrade organic matter with complex structures. However, the use of TiO_2 in the photocatalytic process has a disadvantage. The turbidity generated in aqueous solution by TiO_2 dispersion will inhibit UV light transmission as an activator of TiO_2 catalysts. Also, TiO_2 in the form of slurry will make difficulties in separating TiO_2 at the end of the photocatalytic process [3-5].

A photocatalytic reaction occurs when TiO_2 photocatalyst is irradiated with energy equal or greater than the bandgap energy, the electron moves to the conduction band to generate positive holes in the

valence band. The positive holes can react with adsorbed H_2O to form hydroxyl radicals while the electrons react with O_2 to form superoxide radicals. The OH and O_2 radicals can oxidize the pollutants in solution with adsorbed contaminants. Otherwise, these electron and hole pairs can recombine and restrict the efficiency of TiO_2 photocatalyst [6]. Thus, much effort has been made to overcome this problem. One of them is to combine TiO_2 into other materials.

Titania-carbon nanotubes composite was used to degrade organic pollutants in aqueous solutions. This composite can increase UV radiation adsorption compared to pure TiO_2. Doping TiO_2 with nonmetal elements has received much attention, especially for carbon element, whereas the C element did not enter the TiO_2 lattice but deposited on the surface of TiO_2 grains [7]. Another example of photocatalyst material is graphite/$PbTiO_3$ composite that can be used for photocatalysis and photoelectrocatalysis of organic matter [8]. The combination of TiO_2 with carbonaceous nanomaterials can increase photocatalytic activity [9]. Carbon nanotubes are used as TiO_2 supports, and it can increase electron-hole recombination time as electron catchers [10]. Besides that, rGO-ZnO-Fe_3O_4 nanocomposite was made using the solvothermal method and tested its photocatalytic activity on rhodamine B samples [11]. The results of this study indicate that the dye could be degraded to 90%, and the nanocomposite was quickly recovered with magnetic fields. This recovery method can occur because of the presence of Fe_3O_4 in the synthesis material. Magnetic photocatalysts containing TiO_2 nanocrystals have been synthesized, and the result is that the catalyst can be separated easily from the wastes. Photocatalytic activity of Fe_3O_4/TiO_2-Co has been tested to degrade methylene blue, and the catalyst can be separated magnetically [5].

Titanium dioxide can also be applied to carbon-based materials. Photocatalysis using TiO_2-biochar (biomass charcoal) can be used to degrade sulfamethoxazole [12]. Biochar is used as a cheap and efficient TiO_2 support to reduce the electron-hole recombination rate during the photocatalysis process, efficient insertion of TiO_2, to increase adsorption capacity, and to make the separation of photocatalysts from samples after use can be conducted efficiently. Granule activated carbon plays a useful role in the process of photocatalysis of carbofuran [13]. The results of this study indicate that 100% of carbofuran can be degraded.

The structure and chemical composition of TiO_2-SiO_2 nanopowder composites changed the photocatalyst activity [14]. The silica doped in the titania matrix can increase the photocatalytic activity because the silica doping decreases particle size and also increase the specific area. The catalytic activity of TiO_2-SiO_2 is better than TiO_2 and SiO_2 [3,15]. The structure of the synthesis material can change with the calcination process. Also, the composition of SiO_2 in TiO_2-SiO_2 composites determines its photocatalyst activity. The TiO_2/SiO_2-functionalized carbon nanotubes are among the most promising photocatalytic candidates for the degradation of emerging pollutants [16].

In this study, the synthesis of TiO_2, TiO_2-SiO_2, and TiO_2-SiO_2/G composites will be carried out using the sol-gel method. The composite materials obtained were analyzed using FTIR, DRUV, SEM, and XRD. The materials were then tested on the industrial waste model, methylene blue dye, to determine the photocatalytic activity (time variation). The profile of methylene blue reduction is done by observing the UV-Vis spectrum profile.

■ EXPERIMENTAL SECTION

Materials

Titanium tetraisopropoxide (TTIP) and tetraethylorthosilicate (TEOS) were obtained from Aldrich. Sodium hydroxide (NaOH), nitric acid (HNO_3), ammonium hydroxide (NH_4OH), ethanol (C_2H_6O), and methylene blue were acquired from Merck. Hydrochloric acid (HCl) was derived from Mallinckrodt. Used dry battery cells was taken for graphite source, and DI water was used to make all solution.

Instrumentation

In this research, the instrumentations used were a photocatalytic reactor and UV-Vis Spectrophotometer (Shimadzu 1280). Instrumentations used for

characterization of composites were FTIR Prestige 21 (Shimadzu), X-Ray Diffraction (*XRD* X'PERT POWDER PW 30/40), and Diffuse Reflectance Ultra Violet Spectrophotometer (Shimadzu DR UV 2450), Scanning Electron Microscope-SEM Hitachi SU3500, using Au coating.

Procedure

Preparation of graphite

Carbon powder was taken from used dry battery cells. The powder was ground and soaked in 250 mL of 0.1 M nitric acid solution for 24 h. The suspension was separated into filtrate and residue. The residue was washed with distilled water and dried at 80 °C for 3 h. Carbon powder was sifted; the carbon used was the particle with size ≤ 100 mesh.

Preparation of TiO_2-SiO_2

Five milliliters of TEOS was mixed to ethanol by 1:6 comparison. TEOS was added to ethanol dropwise. Then, HCl 0.05 M was added drop-by-drops to the solution until the pH of the mixture solution was 2, continued by stirring for 2 h. The product from this step was called SiO_2 solution.

Titanium tetraisopropoxide was dissolved in DI water by comparison (1:14). The solution was stirred until homogeneous for 2 h, and SiO_2 solution was poured to 75 mL TTIP solution. It was stirred for 24 h. An amount of 0.05 M NH_4OH was added to adjust the pH solution. The solution of Ti-Si was stirred until homogeneous and heated at 65 °C for ± 1 h to obtain sol-gel. For the aging process, the sol-gel was heated at 100 °C for 2 h.

Preparation of TiO_2-SiO_2/G composite

The method is a modification of Purnawan et al. [8]. First step: 5 mL of TEOS was added dropwise into 30 mL ethanol while the solution was stirred continuously. It was added by 2 mL of 0.05 M HCl slowly to the system until the pH of the solution was two and stirred for 2 h. Second step: 5 mL TTIP was dissolved in 70 mL of DI water. It was continued by mixing process until homogeneous, and then added by the solution derived from the first step, and stirred for 24 h. An amount of 0.05 M NH_4OH was added to adjust the pH then stirred until homogeneous. The graphite powder was combined with variations of 1:2, 1:1, and 2:1 %w/w (TiO_2-SiO_2/G). The suspension was heated at 65 °C for 1 h. The sol form was heated at 150 °C for 2 h to have an aging process. The sol-gel of TiO_2-SiO_2/G was calcinated at 400 °C for 2 h, to produce TiO_2-SiO_2/G composite.

Photocatalytic of methylene blue

The photocatalytic activity of the TiO_2-SiO_2, TiO_2-SiO_2/G = 1:1, TiO_2-SiO_2/G = 1:2, TiO_2-SiO_2/G = 2:1, and graphite was evaluated by observing the degradation process of methylene blue (MB) solution, as a model of industrial waste. The initial concentration of MB was 14 mg/L, and the sample solution volume was 200 mL. The mass of the loading catalyst was 1 g/L. The reactor was irradiated with a 6 × 10 W UV black light lamp. The starting point (t = 0) of the reaction was defined as the point where the concentration of the sample solution was recorded as C_o. Afterward, 3 mL of each mixture was taken at regular intervals of 30, 60, 90, 120, 120, and 105 min. The powders were separated using a 0.45 membrane filter. The dye concentration in the solution (filtrate) was measured as a function of the irradiation time. The measurement was conducted using a UV-Vis spectrophotometer. The spectral range was investigated at λ = 665 nm. The degradation capacity (η%) was calculated as $\eta(\%) = (1-C/Co) \times 100\%$ [5,8,17].

■ RESULTS AND DISCUSSION

The sol-gel and hydrothermal method have been considered as an alternative for Si-Ti preparation due to no requirement of high temperature. The precursor of Ti and Si were derived from TTIP and TEOS, respectively. The hydrolysis starts when the precursor reacts with water and follows by the condensation process that changes the solution to become the sol. After solvent vaporization, the gel will be formed, and after the drying process, the silica-titania mixture is obtained.

The criteria of adsorbents in integrated photocatalyst system are high adsorption capacity yet moderate affinity to the target compound and reasonable transparency to UV-Vis light. Other requirements of the materials are high surface area with acceptable pore size, acting as support material which

inhibits leaching of photocatalyst, and good stability with solvent and reusability [18]. Graphite is chosen in this research as the adsorbent.

FTIR Analysis

FTIR spectroscopy was used to characterize the interaction between graphite, titania, and silica. Fig. 1 shows the FTIR spectra of the graphite and titanium dioxide. The dominant peaks that are commonly present in graphitic material such as 1008, 1579, and 2922 cm^{-1} correspond to the stretching of C-O, asymmetric stretching vibration of C=C, and stretching of C-H. This data is supported by Basheer [6]. The broad peak related to the vibration of the hydroxyl (–OH) group also can be seen at a wavenumber of 3425 cm^{-1}. The IR spectra of TiO_2 show a broad and strong band at 3408 and 1631 cm^{-1} that can be identified as –OH groups from the adsorbed water on the surface of titania indicating stretching and bending vibration, respectively.

Fig. 2 shows the comparison of the IR spectrum between TiO_2-SiO_2/G in various compositions. The pattern of TiO_2-SiO_2/G and TiO_2-SiO_2 is quite similar. The peak observed at ~1100 cm^{-1} corresponds to Si-O-Si asymmetric stretching vibration. The Si-O-Ti vibrates at ~960 cm^{-1}. The more the graphite added into the mixture of titania-silica, the lower the intensity of the OH band became. The data was supported by Riazian, [14], and Yaseen et al. [15]. Further characterization is needed to determine the effect of graphite addition to the TiO_2-SiO_2 composites.

DRUV Analysis

Fig. 3 shows the DRUV spectra of synthesized materials. This characterization was conducted to measure the band gap energy of materials. The value of band gap energy (E_g) was determined using the Tauc plot of the Kubelka Munk equation. The E_g of materials were 4.15, 4.20, 5.22, and 5.19 for TiO_2-SiO_2, TiO_2-SiO_2/G = 1:1, TiO_2-SiO_2/G = 1:2, and TiO_2-SiO_2/G = 2:1, respectively. Based on this data, the lowest band gap energy is TiO_2-SiO_2. The addition of graphite to TiO_2-SiO_2 can increase the number of band gap energy. The more the number of graphite added to the Ti-Si makes the E_g becomes higher than the others.

XRD Characterization

There are three crystalline forms of TiO_2 which are anatase, brookite, and rutile. The anatase phase is reported

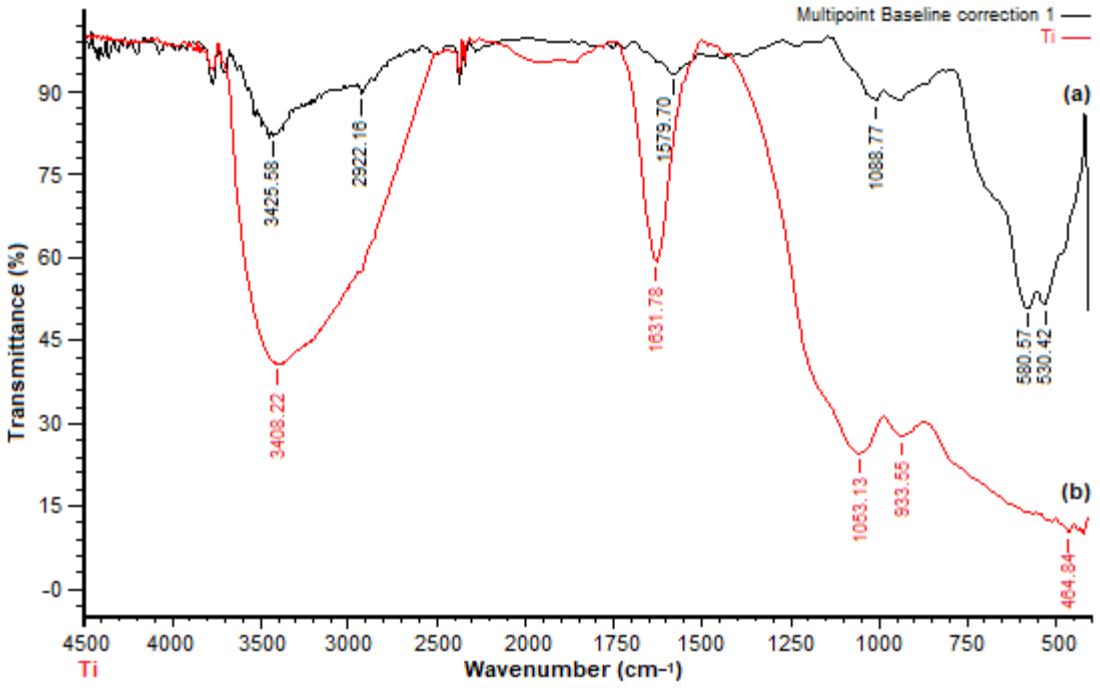

Fig 1. FTIR spectrum of graphite (a) and titanium dioxide (b)

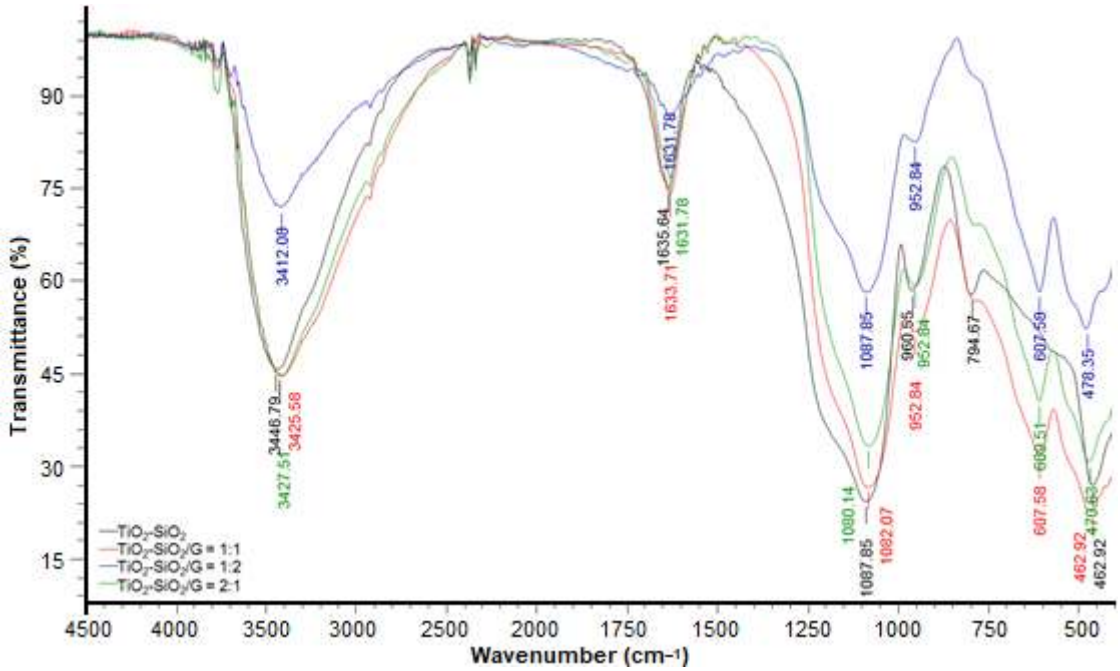

Fig 2. FTIR spectrum of synthesized materials

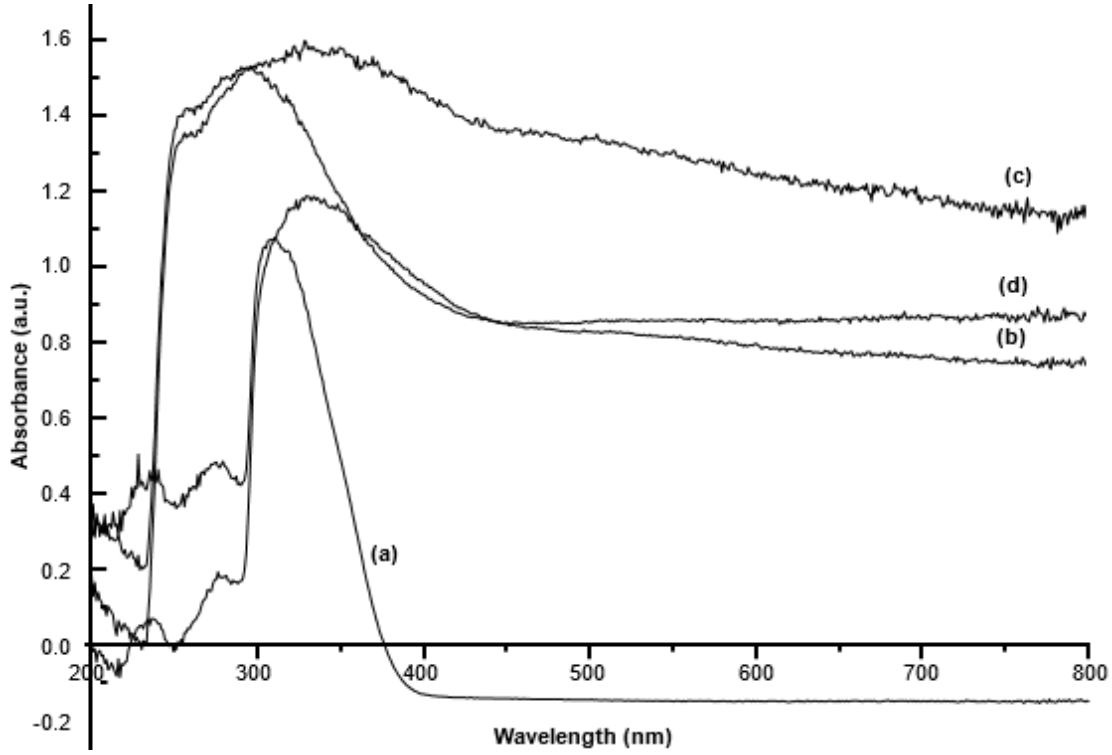

Fig 3. DR-UV Visible spectra of TiO_2-SiO_2 (a), TiO_2-SiO_2/G=1:1 (b), TiO_2-SiO_2/G=1:2 (c), and TiO_2-SiO_2/G=2:1 (d)

to give the best combination of photoactivity and photostability. The TiO_2-SiO_2 has the highest peak at 2θ = 25.32; 37.71 and 47.91°. The data reported was compared to the TiO_2 standard (JCPDS No. 01-075-2546) and SiO_2 standard (JCPDS No. 01-070-2535). It can be seen that the TiO_2-SiO_2 diffraction pattern follows the dominant characteristics of TiO_2, while the amorphous SiO_2 influences the intensity of the composite diffraction

pattern. The composite characteristics of TiO_2-SiO_2 also show a similar pattern with TiO_2 crystals, which can be seen in Table 1. The identity of SiO_2 appeals at 2θ of 53.70 and 62.54°, which corresponds to (022) and (113) planes, respectively.

Fig. 4 shows the XRD pattern of TiO_2-SiO_2 and three formula of TiO_2-SiO_2/G. The diffractogram shows the presence of graphite, TiO_2, and SiO_2 in the sample. A characteristic angle shift occurs for TiO_2-SiO_2 after interaction with graphite. However, the diffraction pattern of TiO_2 appears at 2θ of 25.32 and 37.71°, which corresponds to (101) and (004) planes. The SiO_2-G characteristic was confirmed at 2θ =59.87°, which was concluded by comparison with the standard graphite

Table 1. d Spacing of TiO_2 and TiO_2-SiO_2 lattices

Samples	h	k	L	2θ (deg)	d_{hkl} (Å)	Assigned Peak of
TiO_2	1	0	1	25.47	3.49	NA
	0	0	4	37.75	2.38	NA
	2	0	0	47.96	1.89	NA
TiO_2-SiO_2	1	0	1	25.32	3.51	TiO_2
	0	0	4	37.71	2.38	TiO_2
	2	0	0	47.91	1.89	TiO_2
	0	2	2	53.70	1.71	SiO_2
	1	1	3	62.54	1.48	SiO_2

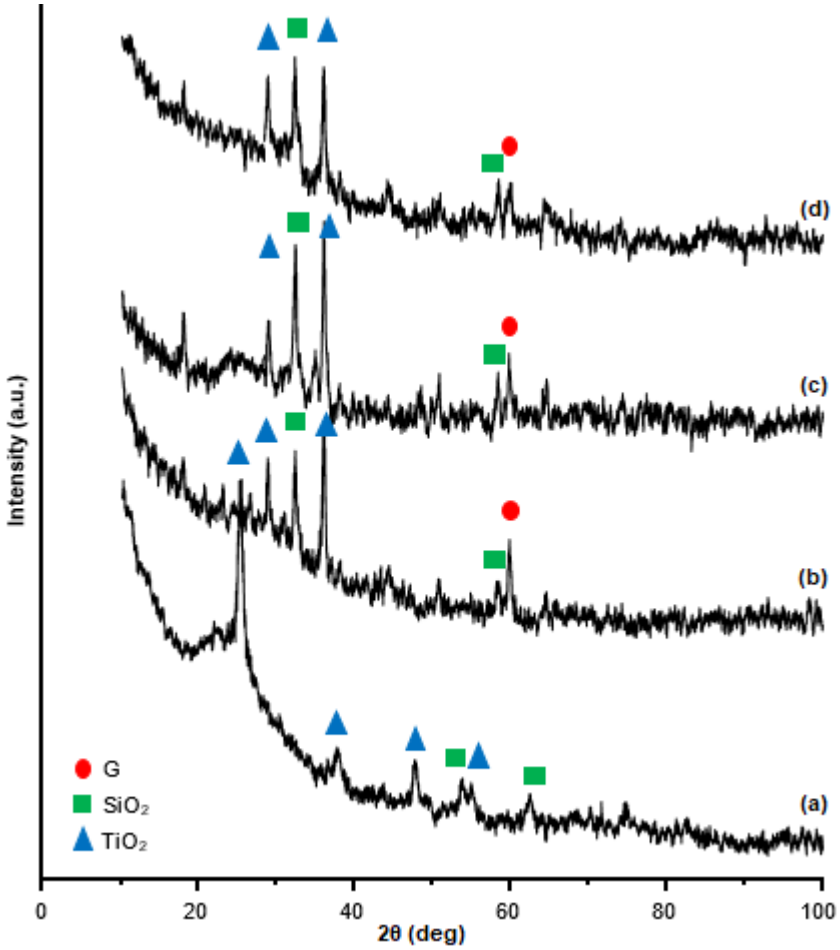

Fig 4. Diffractogram of TiO_2-SiO_2 (a), TiO_2-SiO_2/G=1:1 (b), TiO_2-SiO_2/G=1:2 (c), and TiO_2-SiO_2/G=2:1 (d)

Table 2. Comparison of 2θ and d_{hkl} of synthesized materials

Samples	h	K	L	2θ (deg)	d_{hkl} (Å)	Assigned Peak of
TiO_2-SiO_2	1	0	1	25.32	3.51	TiO_2 (A)
	0	0	4	37.71	2.38	TiO_2 (A)
	2	0	0	47.91	1.89	TiO_2
	0	2	2	53.70	1.71	SiO_2
	1	1	3	62.54	1.48	SiO_2
TiO_2-SiO_2/G = 1:1	1	1	0	28.85	3.09	TiO_2 (R)
	1	1	0	32.33	2.77	SiO_2
	0	0	4	36.04	2.49	TiO_2 (A)
	1	2	1	58.54	1.58	SiO_2
	1	0	3	59.87	1.54	G
TiO_2-SiO_2/G = 1:2	1	1	0	28.84	3.09	TiO_2 (R)
	1	1	0	32.34	2.77	SiO_2
	0	0	4	36.03	2.49	TiO_2 (A)
	1	0	3	59.90	1.54	G
TiO_2-SiO_2/G = 2:1	1	1	0	28.87	3.09	TiO_2 (R)
	1	1	0	32.33	2.77	SiO_2
	0	0	4	36.02	2.49	TiO_2 (A)
	1	2	1	58.47	1.58	SiO_2
	1	0	3	59.80	1.54	G

diffractogram (JCPDS No 03-065-6212). Interestingly, when graphite was added to TiO_2-SiO_2, the characteristic of the two diffraction angles for TiO_2 shifted from 2θ = 25.32° to ~28.85° and 2θ = 37.71° to ~36.04° after the composite was formed. This phenomenon reveals that there was a change of TiO_2 form; anatase becomes rutile. Some publications stated that dopant could be a reason for anatase to rutile transition, size, and strain of materials as the factors [19-20]. This result is supported by Rahmawati et al., the character of 2 theta of SiO_2-TiO_2/Graphite is labeled as rutile rises in 37.53° [21]. The transformation in its publication is due to the use of high temperature in the calcination process. Anatase and rutile phases are easier to differentiate since the first two reflection peaks are well separated. The 2 theta of anatase is 25.28° for d_{101} while the rutile gives 27.44° for d_{110} [22]. This research indicates that graphite tends to change the phase of TiO_2 in TiO_2-SiO_2 but not entirely, so the TiO_2 becomes a mixture of rutile-anatase.

The identity of graphite shows that the d_{103} peak presents at 59.8° with a value of 1.54 Å. To look deep that the character of Si in TiO_2-SiO_2 is 53.7, and 62.54° become 32.33 and 58.54° in TiO_2-SiO_2/G. The peak at value d_{121} of 58.80° disappears when the formula with more graphite than the TiO_2-SiO_2 (TiO_2-SiO_2/G = 1:2). This phenomenon proves that the composite has a different phase composition when the formula is changed.

SEM Analysis

The SEM images of TiO_2-SiO_2, TiO_2-SiO_2/G = 1:1, TiO_2-SiO_2/G = 1:2, and TiO_2-SiO_2 = 2:1 are shown in Fig. 5(a–d). As can be seen in Fig. 5, there is an increasing roughness throughout the surface of the TiO_2-SiO_2/G with the increase of loaded TiO_2-SiO_2. The aggregates on the images indicate the existence of interaction of the titanium dioxide layers on the particle surface (graphite). The uniform of a homogenous dispersion of spherical particles is the outcome of synthesis that takes place during the condensation stage [23]. This data supports the XRD analysis that Ti-O-Si was formed. This structure can provide significant surface area contact between TiO_2-SiO_2 and graphite particles, and also have a good potential for carrier transport, related to the photocatalytic activity.

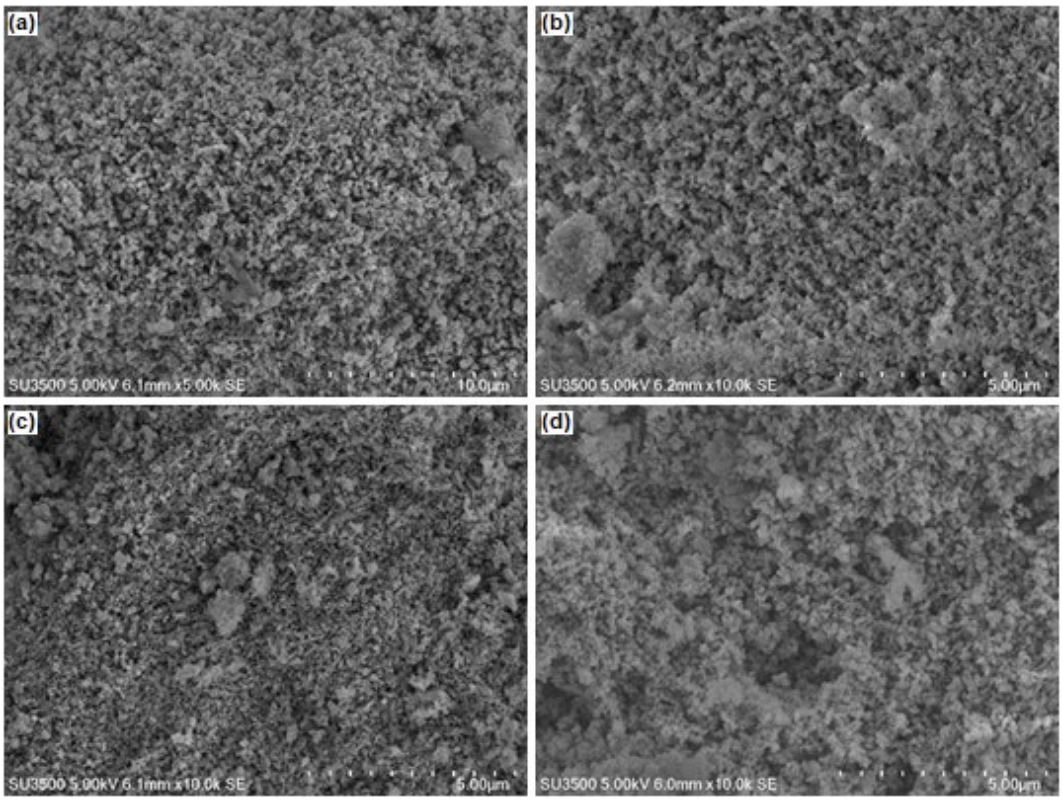

Fig 5. Micrograph SEM of TiO_2-SiO_2 (a), TiO_2-SiO_2/G= 1:1 (b), TiO_2-SiO_2/G = 1:2 (c), and TiO_2-SiO_2/G= 2:1 (d)

Photocatalytic Activity

The TiO_2 itself as the photocatalyst faces several problems, (1) the difficulty in separating the powder from the solution after the reaction is complete, (2) aggregation of particles in suspensions, and (3) difficulty in an application for continues flows system [9]. The graphite can provide a high-surface-area structure over which TiO_2 particles may be distributed and immobilized. The role of SiO_2 is as electron trapper for the excited electron from the valence band of TiO_2, and this mechanism can reduce the possibility of electron-hole recombination [21].

The combination of TiO_2-SiO_2 material already proved to give an increase in photocatalytic activity. The combination of TiO_2-SiO_2 as a catalyst in the photocatalytic process showed an excellent activity to degrade organic compound, phenol, and linear alkyl benzenesulfonate [3]. Also, graphite silica was used by Ikeda et al. to the photocatalytic process to produce hydrogen [24]. The GS successfully combined with TiO_2, and as the results, the photocatalytic activity increases significantly.

The photocatalytic activities of graphite and TiO_2-SiO_2/G composites were evaluated by degradation of a hazardous textile dye (methylene blue, MB). Absorbance spectra of MB aqueous solution were measured using a UV-Vis spectrophotometer at 500–750 nm are shown in Fig. 6. The spectra were taken after irradiation of MB solution for specific irradiation time (0, 30, 60, 90, 120, 150, and 180 min). Generally, it can be seen clearly that absorbance peaks at 665 nm decreased with increasing of irradiation time (Fig. 6(a–e).

The photocatalytic activities of all materials on the degradation process of MB were shown via the plot of degradation efficiency as a function of time (Fig. 6(f)). The data demonstrated that photocatalytic activity by applying the graphite itself has an efficiency value of 14%, the lowest value than other composites. After using the TiO_2-SiO_2/G as the photocatalyst, the efficiency can increase sharply where the range of the value is 65–94%. The photocatalytic ability by applying TiO_2-SiO_2 gave an efficiency value of 83%, higher than TiO_2-SiO_2/G = 1:1 (76%) and TiO_2-SiO_2/G = 1:2 (65%). By having more

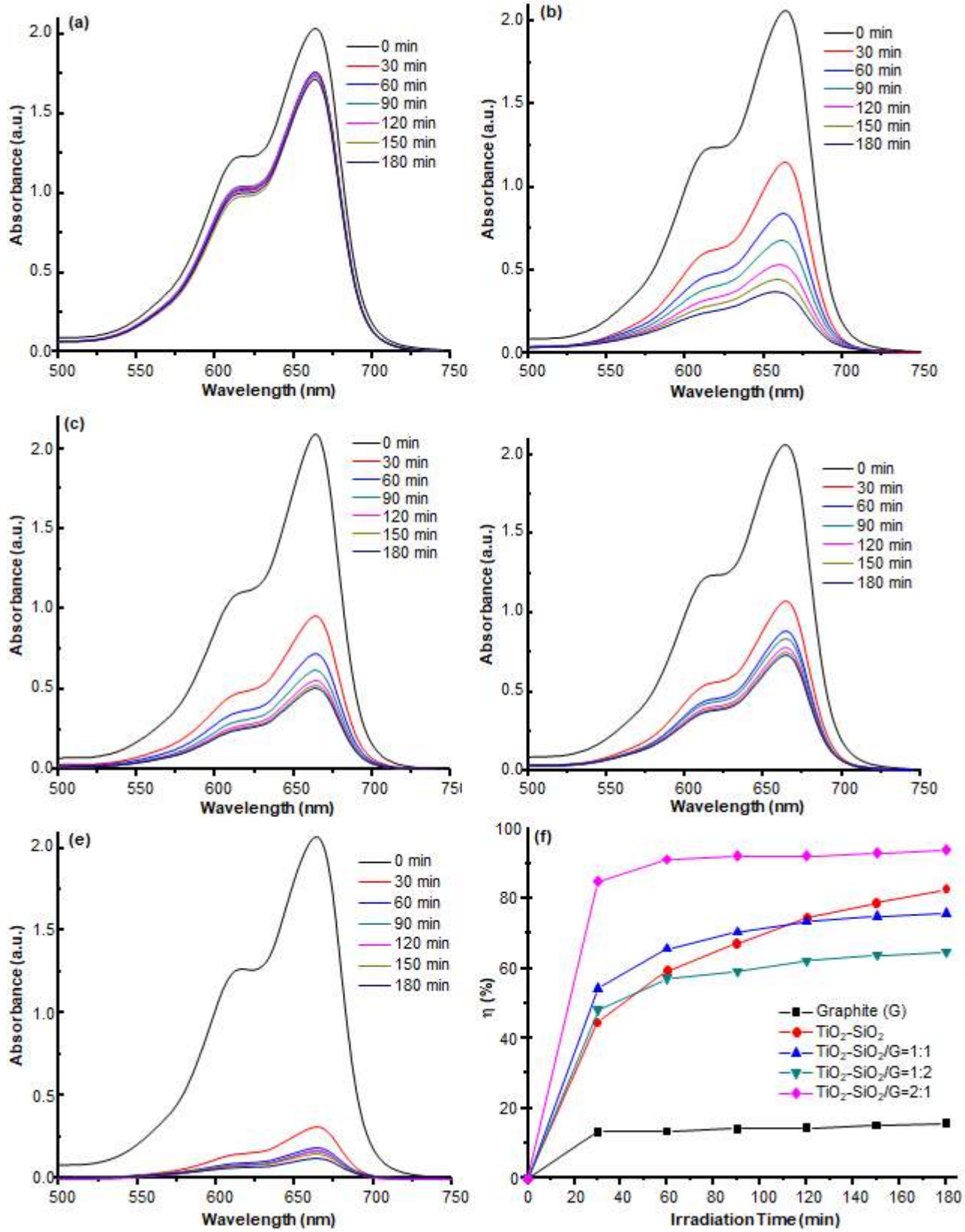

Fig 6. The degradation profile of MB using synthesized materials (a-e) and the efficiency of degradation versus irradiation time using all synthesized materials (f)

graphite in TiO_2-SiO_2, the efficiency become lower. On the contrary, while TiO_2-SiO_2 had been added with G in a ratio formula of 2:1, the data give 11% increase from the activity of TiO_2-SiO_2, to be 94%. It can be concluded that the role of graphite can increase the activity of TiO_2-SiO_2 in a particular formula. The result of this research has an agreement with Lang and Matejka [25] and Andriantsiferana et al. [26].

The existence of graphite in the TiO_2-SiO_2 composite may increase the rate of MB photodegradation. Guidetti et al. reported that graphite can decrease the charge recombination rate, and increases the efficiency of the reactive species photo-production, so that the photocatalytic activity can increase [27]. The photocatalytic of anatase is higher than rutile. This performance is attributed to a higher density of localized states and consequent surface-adsorbed hydroxyl radicals and slower charge recombination in anatase relative to rutile [20]. Even though, based on this data, the composition of G in TiO_2-SiO_2 composite role significant effect on photocatalytic power. The bandgap of TiO_2-SiO_2/G has a broad band gap, which is 4.1–5.2 eV allows the adsorption of the photon to excite an electron from the conductance band to the valence band. When the excitation happens, electron-hole is generated. The electron reacts with an O_2 molecule creating an unstable$\cdot O_2^-$ molecule. At the same time, the photogenerated holes (h^+) with strong oxidation ability could react with H_2O to produce radical hydroxyl (•OH). The generated species can degrade the MB and other organic complex dyes [28].

■ CONCLUSION

The titanium-silica-graphite composites were successfully synthesized by the sol-gel method. The precursors are TTIP, TEOS, and graphite from the used battery. The character of the FTIR spectrum showed that O-H (~3400 cm^{-1}) and C-O (~1100 cm^{-1}) are the major groups in the synthesized materials. The value of band gap energy is increasing by the addition of graphite. The Diffractogram of XRD shows the identity of Ti, Si, and graphite. The micrograph of SEM showed the uniform of a homogenous dispersion of spherical particles in the materials. Photocatalytic test results with these synthesis materials as a catalyst to degrade methylene blue showed that TiO_2-SiO_2/G with a composition of 2:1 has the highest percentage of degradation, which reached 94% at 180 min.

■ ACKNOWLEDGMENTS

This research was funded by Mathematics and Natural Sciences Faculty, Universitas Tanjungpura Pontianak, under DIPA UNTAN Grant No. SP DIPA-042.01.2.400955/2018. The authors express great gratitude for that support.

■ REFERENCES

[1] Ajmal, A., Majeed, I., Malik, N., Idriss, H., and Nadeem, M.A., 2014, Principles and mechanisms of photocatalytic dye degradation on TiO_2 based photocatalysts: A comparative overview, *RSC Adv.*, 4 (70), 37003–37026.

[2] Dariani, R.S., Esmaeili, A., Mortezaali, A., and Dehghanpour, S., 2016, Photocatalytic reaction and degradation of methylene blue on TiO_2 nano-sized particles, *Optik*, 127 (18), 7143–7154.

[3] Destiarti, L., Tjokronegoro, R., Rakhmawaty, D., and Rudiyansyah, R., 2015, The use of TiO_2-SiO_2 in photocatalytic process to degrade toxic and dangerous waste, *Makara J. Sci.*, 19 (1), 1–6.

[4] Lin, J., Luo, Z., Liu, J., and Li, P., 2018, Photocatalytic degradation of methylene blue in aqueous solution by using ZnO-SnO_2 nanocomposites, *Mater. Sci. Semicond. Process.*, 87, 24–31.

[5] Kunarti, E.S., Kartini, I., Syoufian, A., and Widyandari, K.M., 2018, Synthesis and photoactivity of Fe_3O_4/TiO_2-Co as a magnetically separable visible light responsive photocatalyst, *Indones. J. Chem.*, 18 (3), 403–410.

[6] Basheer, C., 2013, Application of titanium dioxide-graphene composite material for photocatalytic degradation of alkylphenols, *J. Chem.*, 2013, 456586.

[7] Chen, L., Chen, F., Shi, Y., and Zhang, J., 2012, Preparation and visible light photocatalytic activity of a graphite-like carbonaceous surface modified TiO_2 photocatalyst, *J. Phys. Chem. C*, 116 (15), 8579–8586.

[8] Purnawan, C., Wahyuningsih, S., and Kusuma, P.P., 2016, Photocatalytic and photoelectrocatalytic degradation of methyl orange using graphite/$PbTiO_3$ composite, *Indones. J. Chem.*, 16 (3), 347–352.

[9] Leary, R., and Westwood, A., 2010, Carbonaceous nanomaterials for the enhancement of TiO_2 photocatalysis, *Carbon*, 49 (3), 741–772.

[10] Cao, Q., Yu, Q., Connell, D.W., and Yu, G., 2013, Titania/carbon nanotube composite (TiO_2/CNT) and its application for removal of organic pollutants, *Clean Technol. Environ. Policy*, 15, 871–880.

[11] You, J., Xiang, Y., Ge, Y., He, Y., and Song, G., 2017, Synthesis of ternary rGO-ZnO-Fe_3O_4 nanocomposites and their application for visible light photocatalytic degradation of dyes, *Clean Technol. Environ. Policy*, 19 (8), 2161–2169.

[12] Kim, J.R., and Kan, E., 2016, Heterogeneous photocatalytic degradation of sulfamethoxazole in water using a biochar-supported TiO_2 photocatalyst, *J. Environ. Manage.*, 180, 94–101.

[13] Vishnuganth, M.A., Remya, N., Kumar, M., and Selvaraju, N., 2016, Photocatalytic degradation of carbofuran by TiO_2-coated activated carbon: Model for kinetic, electrical energy per order and economic analysis, *J. Environ. Manage.*, 181, 201–207.

[14] Riazian, M., 2014, Dependence of Photocatalytic activity of TiO_2-SiO_2 nanopowders, *J. Nanostruct.*, 4, 433–441.

[15] Yaseen, M., Shah, Z., Veses, R.C., Dias, S.L.P., Lima, E.C., dos Reis, G.S., Vaghetti, J.C.P., Alencar, W.S.D., and Mahmood, K., 2017, Photocatalytic studies of TiO_2-SiO_2 nanocomposites xerogels, *J. Anal. Bioanal. Tech.*, 8 (1), 348.

[16] Rasheed, T., Adeel, M., Nabeel, F., Bilal, M., and Iqbal, H.M.N., 2019, TiO_2/SiO_2 decorated carbon nanostructured materials as a multifunctional platform for emerging pollutants removal, *Sci. Total Environ.*, 688, 299–311.

[17] Nguyen, D.C.T., Cho, K.Y., and Oh, W.C., 2017, Synthesis of mesoporous SiO_2/Cu_2O–graphene nanocomposites and their highly efficient photocatalytic performance for dye pollutants, *RSC Adv.*, 7 (47), 29284–29294.

[18] Yahya, N., Aziz, F., Jamaludin, N.A., Mutalib, M.A., Ismail, A.F., Salleh, W.N.W., Jafar, J., Yusof, N., and Ludin, N.A., 2018, A review of integrated photocatalyst adsorbents for wastewater treatment, *J. Environ. Chem. Eng.*, 6 (6), 7411–7425.

[19] Anita, Yadav, A.K., Khatun, N., Kumar, N., Tseng, C.M., Biring, S., and Sen, S., 2017, Size and strain dependent anatase to rutile phase transition in TiO_2 due to Si incorporation, *J. Mater. Sci. - Mater. Electron.*, 28, 19017–19024.

[20] Hanaor, D.A.H., and Sorrell, C.C., 2011, Review of the anatase to rutile phase transformation, *J. Mater. Sci.*, 46, 855–874.

[21] Rahmawati, F., Wahyuningsih, S., and Irianti, D., 2014, The photocatalytic activity of SiO_2-TiO_2/graphite and its composite with silver and silver oxide, *Bull. Chem. React. Eng. Catal.*, 9 (1), 45–52.

[22] Scarpelli, F., Mastropietro, T.F., Poerio, T., and Godber, N., 2018, "Mesoporous TiO_2 thin films: State of the art" in *Titanium Dioxide - Material for a Sustainable Environment*, Eds. Yang, D., IntechOpen, Rijeka, Croatia.

[23] Fajriati, I., Mudasir, and Wahyuni, E.T., 2014, Photocatalytic decolorization study of methyl orange by TiO_2-chitosan nanocomposites, *Indones. J. Chem.*, 14 (3), 209–218.

[24] Ikeda, M., Kusumoto, Y., Somekawa, S., Ngweniform, P., and Ahmmad, B., 2006, Effect of graphite silica on TiO_2 photocatalysis in hydrogen production from water-methanol solution, *J. Photochem. Photobiol., A*, 184 (3), 306–312.

[25] Lang, J., and Matějka, V., 2013, Graphite/titanium dioxide composite, *Proceedings of The 5th International Conference NANOCON 2013*, Brno, Czech Republic, 16-18 October 2013.

[26] Andriantsiferana, C., Mohamed, E.F., and Delmas, H., 2013, Photocatalytic degradation of an azo-dye on TiO_2/activated carbon composite material, *Environ. Technol.*, 35 (1-4), 355–363.

[27] Guidetti, G., Pogna, E.A.A., Lombardi. L., Tomarchio, F., Polischuk, I., Joosten, R.R.M., Ianiro, A., Soavi. G., Sommerdijk, N.A.J.M.,

Friedrich, H., Pokroy, B., Ott, A.K., Goisis, M., Zerbetto, F., Falini, G., Calvaresi, M., Ferrari, A.C., Cerullo, G., and Montalti, M., 2019, Photocatalytic activity of exfoliated graphite-TiO_2 nanoparticle composites, *Nanoscale*, 11 (41), 19301–19304.

[28] Salgado, B.C.B., and Valentini, A., 2019, Evaluation of the photocatalytic activity of SiO_2@TiO_2 hybrid spheres in the degradation of methylene blue and hydroxylation of benzene: Kinetic and mechanistic study, *Braz. J. Chem. Eng.*, 36 (4), 1501–1518.

Structure of the Cyclic, Cationic Antimicrobial Peptide (KKWWKF) in Octanol Solution: *in silico* Approach

Seyed Hassan Mortazavi, Mohammad Reza Bozorgmehr*, and Mohammad Momen Heravi

Department of Chemistry, Mashhad Branch, Islamic Azad University, Mashhad, Iran

* ***Corresponding author:***

tel: +98-511-8797022
email: bozorgmehr@mshdiau.ac.ir

Received: September 1, 2019
Accepted: November 12, 2019

DOI: 10.22146/ijc.49190

Abstract: *Understanding the mechanism of antimicrobial activity of cyclopeptides helps to design new drugs based on these compounds. A common aspect of the mechanisms provided for the creation of antimicrobial activity of cyclopeptides is their interaction with cell membranes. On the other hand, the octanol/water system is a good mimic of the water/membrane interface. Here, the conformational structure of the very short sequences cationic hexapeptide cyclo (Lys-Lys-Trp-Trp-Lys-Phe) has been studied in different concentrations of octanol by molecular dynamics simulation. The concentration of alcohol in the range of experimental concentrations of octanol was considered. The results obtained from calculating the radial distribution function show that the interaction of the peptide with octanol is a mixed of interactions between charged residues with octanol and the interaction of aromatic residues with octanol. These results are in agreement with experimental observations. Also, Lys5 plays a greater role than Lys1 and Lys2 in the interactions with octanol.*

Keywords: *cyclopeptide; lipophilic solvents; octanol; membrane*

■ INTRODUCTION

Antimicrobial peptides are among the new therapeutic compounds [1]. These compounds are the main components of the immune system against invading pathogens [2]. Structurally, antimicrobial peptides have low molecular masses, usually less than 10 kDa. Also, they have amphipathic, cationic nature and different sequences and lengths [3]. For two main reasons, the tendency of research on antimicrobial peptides has increased: First, bacteria are resistant to existing drugs. Second, the development of new antibiotics has been restricted [4]. The range of activity of these peptides is extensive and includes Gram-positive bacteria, Gram-negative bacteria, yeast, viruses, and fungi [5]. Although the activity of antimicrobial peptides is low, however, the resistance of the bacteria against them is less observed [6].

A better understanding of the molecular basis of the mechanism of action of antimicrobial peptides helps to design new drugs based on these peptides. The proposed mechanisms for the antimicrobial function of antimicrobial peptides are divided into two major categories such as membrane degradation and elimination of the intracellular cytoplasmic targets [7]. The common aspect of these mechanisms is the interaction of the antimicrobial peptides with the membrane, whether to degrade the membrane or to pass through it and enter the cell. The interactions of the antimicrobial peptides with the membrane occur through regular adhering and the formation of a cavity in the membrane. Another pathway is irregularly adhering to the membrane and unstable membrane, or a mixture of two methods [7-8]. It has also been noted that antimicrobial peptides bind to the membrane through the interactions of positive charges of arginine or lysine residues with negative charges of the membrane surface. During this interactions, the side chain of aromatic residues orientates and enters the membrane [9]. Maintaining the peptide backbone, the orientation of the side chain of aromatic sequences and the electrostatic interactions of charged residues with membranes are important aspects of these mechanisms. In spite of many studies on the activity of antimicrobial peptides, their mechanism of action is not well understood [10]. For example, by replacing L-amino acid with D-amino acid

in antimicrobial peptides, in most cases, the activity is not completely eliminated. The fact that it is unlikely about a particular receptor [11]. On the other hand, despite the fact that the membrane surface of most mammals is not charged, positive charged antimicrobial peptides interact with it [12]. The experimental study of the interactions of antimicrobial peptides with membranes has some limitations, for example the complex structure of the membrane, the irregularity of the membrane surface and the alteration of the structure of the membrane when labeled in fluorescence methods [13-14]. Hence, in many cases, molecular dynamics simulations have been used to study the mechanisms of action of antimicrobial peptides [15-17].

Here, the structure of the very short sequences cationic hexapeptide cyclo (Lys-Lys-Trp-Trp-Lys-Phe) (c-AMP) has been studied by molecular dynamics simulation. To investigate the effect of hydrophobic forces on this peptide, molecular dynamics simulation was performed at different concentrations of octanol.

■ COMPUTATIONAL DETAILS

The initial structure of c-AMP was taken from the protein database with the code 1skk [18]. 9 simulation boxes were designed. The peptide was placed in the center of the box. In 8 boxes, the number of octanol molecules were added, thus different concentrations of 5, 10, 15, 20, 25, 30, 35 and 40% of alcohol were prepared. Each box was assigned as OCTx, (x = 0, 5, 10, 15, 20, 25, 30, 35 and 40%). The detail information of simulation systems were reported in Table 1.

The octanol molecules were randomly placed in the box. Each simulation box was neutralized with chlorine ions. Gromacs software version 5.1.2 [19] and the Gromos 43a1 force field [20] were used for the calculations. To eliminate bad contacts between atoms, steepest descent algorithm was used to minimize simulation systems. Then extensive equilibrations in NVT and NPT were run for 5 ns. Finally, the configuration of simulated systems were sampled for 500 ns. The V-rescale and Berendsen algorithms were used to control the temperature and pressure of the system components, respectively. For these weak-coupling algorithms, a coupling time of 1.0 ps was considered. The PME algorithm with 1.4 nm cutoff was used to calculate the electrostatic charge. The chemical bonding of non-solvent components was fixed with the LINCS algorithm [21] and chemical bonding of solvent molecules with SETTLE algorithm [22]. Therefore, the simulation time step was set to 2 fs. To avoid any dependency on the initial conditions all simulations were repeated.

■ RESULTS AND DISCUSSION

The key aspects of mechanism of antimicrobial activity of cyclopeptides are the interaction strength of residues and membrane [9]. Therefore, these criteria were studied in this works. To study the interaction of c-AMP residues with solvent in simulated systems, the radial distribution function (RDF) was used. The RDF between particles of type A and B is defined as follow:

$$g_{AB}(r) = \frac{\langle \rho_B(r) \rangle}{\langle \rho_B \rangle_{local}} = \frac{1}{\langle \rho_B \rangle_{local}} \frac{1}{N_A} \sum_{i \in A}^{N_A} \sum_{j \in B}^{N_B} \frac{\delta(r_{ij} - r)}{4\pi r^2} \quad (1)$$

Table 1. The dimensions of the designed simulation boxes with the number of solvent molecules

System	Box dimensions (nm^3)	Number of water molecules
OCT0	3.05*4.06*3.07	1214
OCT5	3.04*4.04*3.06	952
OCT10	3.04*4.04*3.06	701
OCT15	3.04*4.05*3.07	489
OCT20	3.11*4.05*3.07	319
OCT25	3.47*4.49*3.50	546
OCT30	3.67*4.71*3.71	606
OCT35	3.85*4.85*3.87	638
OCT40	4.07*5.09*4.09	819

which $\langle \rho_B(r) \rangle$ is the particle density of type B at a distance r around A, and $\langle \rho_B \rangle_{local}$ is the particle density of type B averaged over all spheres around particles A. The c-AMP peptide has six residues which are lysine, lysine, tryptophan, tryptophan, lysine and phenylalanine, respectively. The c-AMP residues are divided into two groups of charged residues and aromatic residues. The graphs of the RDF of the water's oxygen atoms surrounding the N_ζ atom of the lysine's side chain are shown in the Fig. 1.

In this figure, the black, red and green colors are denoted for Lys1, Lys2 and Lys5, respectively. According to the Fig. 1, in the absence of alcohol, the height of the first peak in RDF is similar for the three lysine residues. In system OCT0, the height of the first peak of the RDF is slightly increased relative to the height of the first peak of the Lys1's RDF However, the overall shape of the RDF is not changed. In system OCT10, the height of the first peak of the RDF is increased relative to the height of the first peak of the RDF in systems OCT0 and OCT5. The

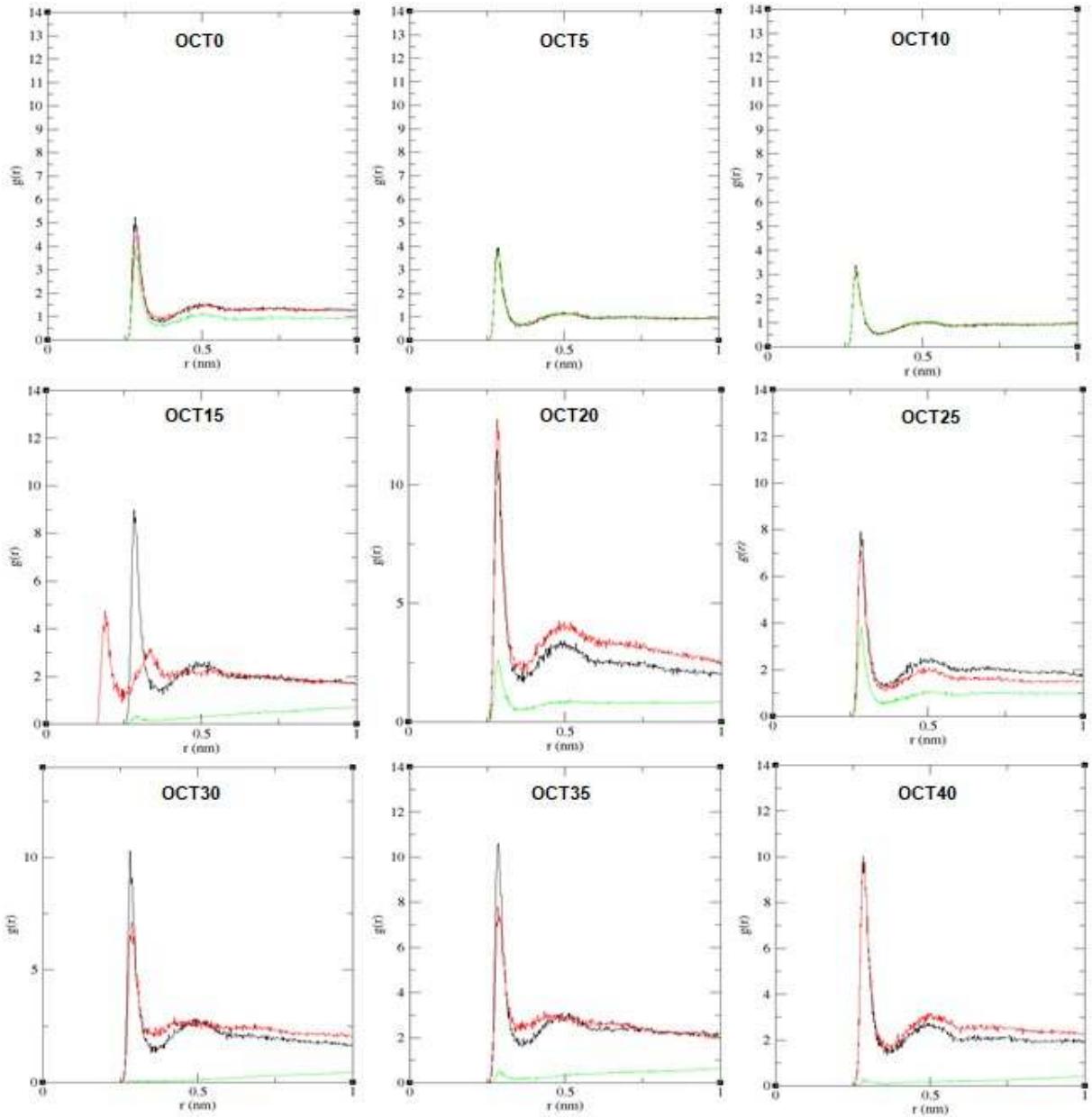

Fig 1. The plots of radial distribution function for N_ζ–Lys….O (water). Black: Lys1, Red: Lys2 and Green: Lys5

height of the first peak of the RDF for Lys1 and Lys2 increases in system OCT20 and reaches its maximum value in this system. But in the case of Lys5, all of systems with increasing concentration of octanol (OCT25 and OCT40) the height of first peak decreases. Therefore, the interaction of Lys5 with water is decreased. According to the c-AMP sequence, Lys5 is located between two aromatic residues, while Lys1 and Lys2 are bounded by the aromatic residue and charged residue. In Fig. 2, the obtained c-AMP structure from the last simulation step in systems OCT0 and OCT40 is shown.

As can be seen from Fig. 2, the side chain of Lys5 in the system OCT40 is oriented upward, approximately perpendicular to the peptide ring axis and surrounded by the side chain of Trp4 and Phe6. However, in OCT0 system, the side chain of Lys5 is oriented toward the bottom and is somewhat distant from the side chain of Trp4 and Phe6. The graph of the RDF of the water's oxygen atoms surrounding the C_ζ atom of the phenylalanine's side chain and the C_η atom of the tryptophan's side chain is shown in the Fig. 3.

Atoms C_ζ and C_η are the outermost atoms in the side chain of phenylalanine and tryptophan, respectively. Compared to Fig. 1, it is observed that the height of the peak in the RDF is considerably lower. This means that the intensity of the interaction of the aromatic residues with water is greater than the intensity of interactions of the charged residues with water. It is also observed that changes in the interaction of aromatic residues with water molecules due to an increase in the concentration of octanol. The changes in the interaction of charged residues with water molecules due to the increase in concentration of octanol is much lower. This finding agrees with experimental data that indicates that the interaction of charged residues with membranes is greater [8,23-24]. With respect to Fig. 3, it is observed that the Phe6 behavior has changed in 25% concentration of octanol and its interaction with water molecules is more than that of Trp3 and Trp4. Therefore, according to Fig. 1 and 3, the orientations of the aromatic residues change the behavior of the charged residues and affects their interactions with the octanol. It is also observed that the effect of alcohol on aromatic residues varies in different concentrations. At higher concentrations of octanol, Trp4 is more affected. This is consistent with the experimental data reported by Dathe et al. [25].

In order to elaborate more detail on other structural aspects, the coordination numbers on c-AMP residues were calculated by integrating the radial distribution function according to the relation $(r)=4\pi\rho\int^{r}_{0}g(r)r^2dr$. In this relation, g (r) is a radial distribution function. The respective coordination number for N_ζ–Lys, C_ζ–Phe and C_η–Trp are presented in Table 2.

Based on Table 2, it is seen that the coordination number around the carbon atom of aromatic residues decreases with increasing concentration in most cases. A peculiar behavior is observed for of the nitrogen atom of lysine. These results are in agreement with the results obtained in similar simulations [26].

In Fig. 4, the calculated RMSF values for c-AMP residues in simulated systems have been reported. RMSF is a measure of the flexibility of the peptide residues [27-28]. In Fig. 4, for a better comparison of the effect of alcohol, the difference between the amounts of RMSF in

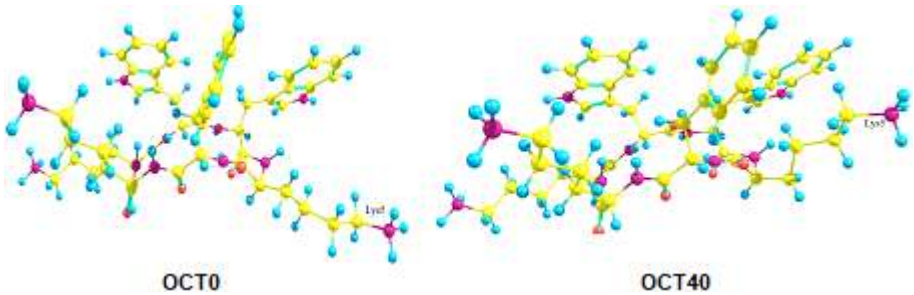

Fig 2. The c-AMP structure obtained from the last simulation step in systems OCT0 and OCT40. Water and octanol molecules eliminate for clarity

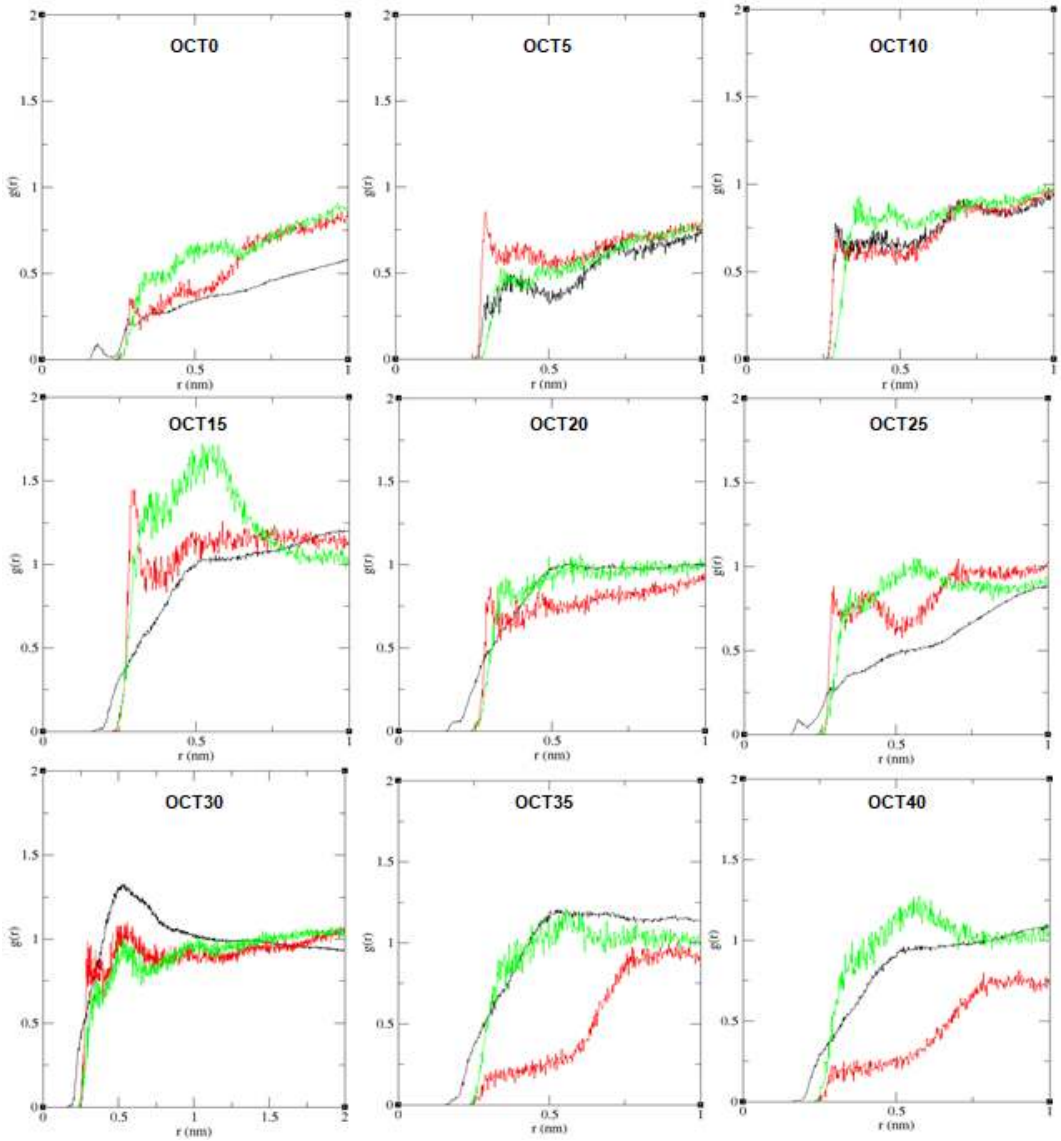

Fig 3. The plots of radial distribution function for C_ζ–Phe….O (water) and C_η–Trp….O (water). Black: Trp3, Red: Trp4 and Green: Phe6

Table 2. The number of water molecules around atoms N_ζ–Lys, C_ζ–Phe and C_η–Trp

	OCT0	OCT5	OCT10	OCT15	OCT20	OCT25	OCT30	OCT35	OCT40
Lys1	3.041	3.035	4.034	3.052	5.038	3.048	4.062	3.039	5.046
Lys2	2.055	3.061	4.053	2.049	3.062	4.052	3.066	3.048	5.039
Trp3	2.035	3.037	4.039	5.004	5.146	5.547	5.749	5.850	6.002
Trp4	2.037	3.038	3.541	3.944	4.046	4.748	5.149	5.552	5.957
Lys5	3.146	3.642	3.951	4.355	3.762	3.448	4.049	4.050	5.156
Phe6	3.036	3.441	3.946	4.449	4.555	4.959	5.166	5.367	5.770

the presence and/or absence of octanol. Regarding Fig. 4, it is observed that the flexibility of the residues is not much affected by octanol.

According to Fig. 4, the range of RMSF changes is about 0.15 nm. In fact, this change value for a peptide with 6 residues is not high. In other words, the backbone

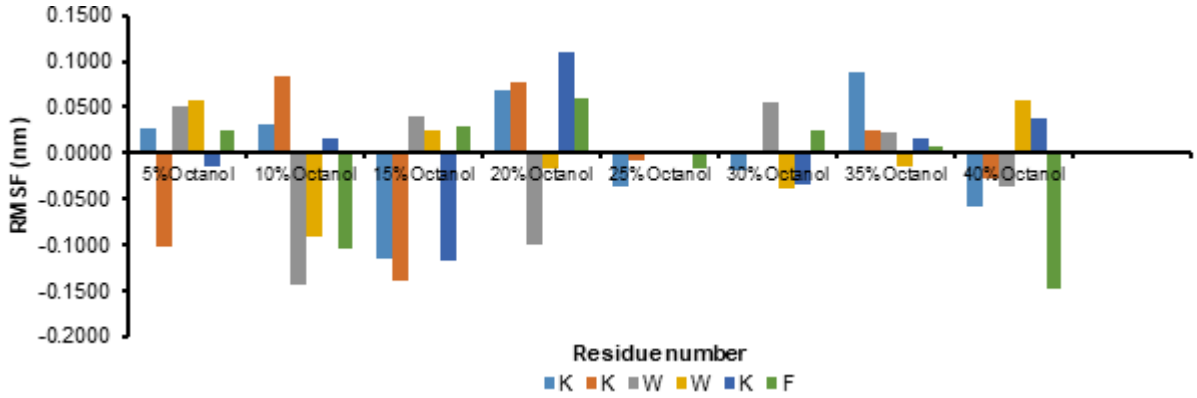

Fig 4. The values of the RMSF difference curve of the c-AMP residues in the systems with the octanol and in the absence of the octanol

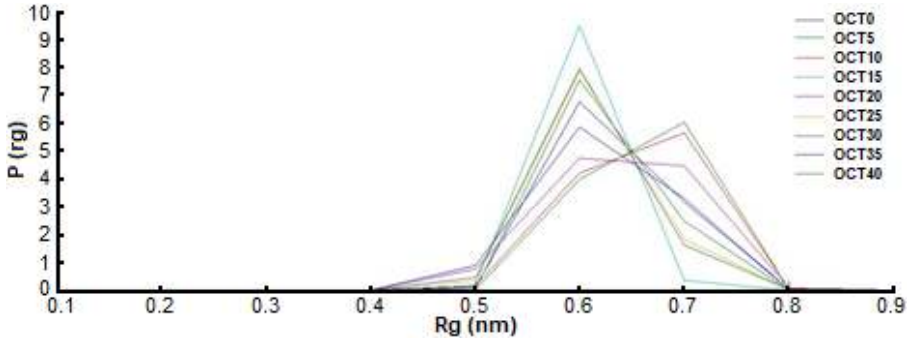

Fig 5. The probability distribution of the radius of gyration in different simulation systems

of c-AMP is maintained when interacting with octanol. This is consistent with experimental evidence that the peptide backbone should be maintained in the interaction of the cyclopeptide with the membrane to preserve the antimicrobial activity [9,29]. A remarkable point in Fig. 4 is at 25% octanol, the RMSF shows the smallest values. This is consistent with the findings of the radial distribution function in Fig. 1 and 3. To examine the overall shape of the c-AMP, the distribution of the peptide radius of gyration was calculated in various simulated systems. The results are shown in Fig. 5.

Based on Fig. 5, the amplitude of the change in the radius of gyration is about 0.1 nm, thus the presence of alcohol does not affect the overall shape of the peptide. Finally, to investigate the effect of alcohol on peptide dynamics, the respective diffusion coefficients in different systems was calculated. The diffusion coefficient is a criterion of motion of a molecule in a solvent. As the diffusion coefficient value increases, the mobility of the molecule increases [30]. Einstein relation was used to calculate the diffusion coefficient of c-AMP in all simulated systems:

$$D = \frac{1}{6}\lim_{t\to\infty}\frac{d}{dt}\langle|r_i(t) - r_i(0)|^2\rangle \quad (2)$$

where r_i is the atom coordinate vector and the term inside the angle brackets is the mean square displacement (MSD). In this approach, the self-diffusion coefficient (D) is proportional to the slope of the MSD as a function of time in the diffusional regime [31]. The

Table 3. Calculated values of Amyloid β-peptide (1-42) diffusion coefficient

System	Diffusion coefficient ($D*10^{-5}$ cm^2/s)
OCT0	0.1473 (± 0.0830)
OCT5	0.1180 (± 0.1779)
OCT10	0.0466 (± 0.0749)
OCT15	0.0515 (± 0.0467)
OCT20	0.0255 (± 0.0142)
OCT25	0.0168 (± 0.0321)
OCT30	0.0013 (± 0.0147)
OCT35	0.0007 (± 0.0004)
OCT40	0.0003 (± 0.0001)

diffusion coefficient values of c-AMP listed in Table 3.

Based on Table 3, it can be concluded that increasing alcohol concentration will reduce the mobility of the peptide.

■ CONCLUSION

The structure of cationic hexapeptide cyclo (Lys-Lys-Trp-Trp-Lys-Phe) (c-AMP) was investigated in the presence of different concentrations of octanol. The c-AMP shows conformational stability in the presence of octanol. Also, the obtained results show that the interaction of c-AMP with octanol from the beginning occurs through charged residues and then through aromatic residues. These findings results are in good agreement with experimental results. The results obtained from the radial distribution function indicate that the water molecules around the lysine residues are more structurally than in the aromatic residues.

■ REFERENCES

[1] Hancock, R.E., and Sahl, H.G., 2006, Antimicrobial and host-defense peptides as new anti-infective therapeutic strategies, *Nat. Biotechnol.*, 24 (12), 1551–1557.

[2] Reddy, K.V.R., Yedery, R.D., and Aranha, C., 2004, Antimicrobial peptides: Premises and promises, *Int. J. Antimicrob. Agents*, 24 (6), 536–547.

[3] Yount, N.Y., and Yeaman, M.R., 2004, Multidimensional signatures in antimicrobial peptides, *Proc. Natl. Acad. Sci. U.S.A.*, 101 (19), 7363–7368.

[4] Appelt, C., Schrey, A.K., Söderhäll, J.A., and Schmieder, P., 2007, Design of antimicrobial compounds based on peptide structures, *Bioorg. Med. Chem. Lett.*, 17 (8), 2334–2337.

[5] Marr, A.K., Gooderham, W.J., and Hancock, R.E., 2006, Antibacterial peptides for therapeutic use: Obstacles and realistic outlook, *Curr. Opin. Pharmacol.*, 6 (5), 468–472.

[6] Zasloff, M., 2002, Antimicrobial peptides of multicellular organisms, *Nature*, 415 (6870), 389–395.

[7] Fjell, C.D., Hiss, J.A., Hancock, R.E., and Schneider, G., 2012, Designing antimicrobial peptides: Form follows function, *Nat. Rev. Drug Discovery*, 16 (11), 37–51.

[8] Finger, S., Kerth, A., Dathe, M., and Blume, A., 2015, The efficacy of trivalent cyclic hexapeptides to induce lipid clustering in PG/PE membranes correlates with their antimicrobial activity, *Biochim. Biophys. Acta, Biomembr.*, 1848 (11), 2998–3006.

[9] Chan, D.I., Prenner, E.J., and Vogel, H.J., 2006, Tryptophan- and arginine-rich antimicrobial peptides: Structures and mechanisms of action, *Biochim. Biophys. Acta, Biomembr.*, 1758 (9), 1184–1202.

[10] Hale, J.D., and Hancock, R.E., 2007, Alternative mechanisms of action of cationic antimicrobial peptides on bacteria, *Expert Rev. Anti Infect. Ther.*, 5 (6), 951–959.

[11] Wessolowski, A., Bienert, M., and Dathe, M., 2004, Antimicrobial activity of arginine-and tryptophan-rich hexapeptides: The effects of aromatic clusters, D-amino acid substitution and cyclization, *J. Pept. Res.*, 64 (4), 159–169.

[12] Lai, Y., and Gallo, R.L., 2009, AMPed up immunity: how antimicrobial peptides have multiple roles in immune defense, *Trends Immunol.*, 30 (3), 131–141.

[13] Shai, Y., 1999, Mechanism of the binding, insertion and destabilization of phospholipid bilayer membranes by α-helical antimicrobial and cell non-selective membrane-lytic peptides, *Biochim. Biophys. Acta, Biomembr.*, 1462 (1-2), 55–70.

[14] Marchal, D., Boireau, W., Laval, J.M., Moiroux, J., and Bourdillon, C., 1998, Electrochemical measurement of lateral diffusion coefficients of ubiquinones and plastoquinones of various isoprenoid chain lengths incorporated in model bilayers, *Biophys. J.*, 74 (4), 1937–1948.

[15] Shepherd, C.M., Vogel, H.J., and Tieleman, D.P., 2003, Interactions of the designed antimicrobial peptide MB21 and truncated dermaseptin S3 with lipid bilayers: Molecular-dynamics simulations, *Biochem. J.*, 370 (1), 233–243.

[16] Jean-François, F., Elezgaray, J., Berson, P., Vacher, P., and Dufourc, E.J., 2008, Pore formation induced

by an antimicrobial peptide: Electrostatic effects, *Biophys. J.*, 95 (12), 5748–5756.

[17] Wang, Y., Schlamadinger, D.E., Kim, J.E., and McCammon, J.A., 2012, Comparative molecular dynamics simulations of the antimicrobial peptide CM15 in model lipid bilayers, *Biochim. Biophys. Acta, Biomembr.*, 1818 (5), 1402–1409.

[18] Appelt, C., Wessolowski, A., Söderhäll, J.A., Dathe, M., and Schmieder, P., 2005, Structure of the antimicrobial, cationic hexapeptide cyclo (RRWWRF) and its analogues in solution and bound to detergent micelles, *ChemBioChem*, 6 (9), 1654–1662.

[19] Abraham, M.J., van der Spoel, D., Lindahl, E., Hess, B., and the GROMACS development team, 2016, *GROMACS User Manual version 5.1.2*, www.gromacs.org.

[20] van Gunsteren, W.F., Billeter, S., Eising, A.A., Hunenberger, P.H., Krüger, P., Mark, A.E., Scott, W.R.P., and Tironi, I.G., 1996, *Biomolecular simulation: The GROMOS96 manual and user guide*, Hochschulverlag AG an der ETH Zürich, Zürich, Switzerland.

[21] Hess, B., Bekker, H., Berendsen, H.J.C., and Fraaije, J.G.E.M., 1997, LINCS: A linear constraint solver for molecular simulations, *J. Comput. Chem.*, 18 (12), 1463–1472.

[22] Miyamoto, S., and Kollman, P.A., 1992, Settle: An analytical version of the SHAKE and RATTLE algorithm for rigid water models, *J. Comput. Chem.*, 13 (8), 952–962.

[23] Arouri, A., Dathe, M., and Blume, A., 2009, Peptide induced demixing in PG/PE lipid mixtures: A mechanism for the specificity of antimicrobial peptides towards bacterial membranes?, *Biochim. Biophys. Acta, Biomembr.*, 1788 (3), 650–659.

[24] Wadhwani, P., Epand, R.F., Heidenreich, N., Bürck, J., Ulrich, A.S., and Epand, R.M., 2012, Membrane-active peptides and the clustering of anionic lipids, *Biophys. J.*, 103 (2), 265–274.

[25] Dathe, M., Nikolenko, H., Klose, J., and Bienert, M., 2004, Cyclization increases the antimicrobial activity and selectivity of arginine-and tryptophan-containing hexapeptides, *Biochemistry*, 43 (28), 9140–9150.

[26] Jahanbin, F., Bozorgmehr, M.R., Morsali, A., and Beyramabadi, S.A., 2019, The effect of different alcohols on the Asp23-Lys28 and Asp23-Ala42 salt bridges of the most effective peptide in Alzheimer's disease: Molecular dynamics viewpoints, *J. Mol. Graphics Modell.*, 86, 199–208.

[27] Bozorgmehr, M.R., and Monhemi, H., 2015, How can a free amino acid stabilize a protein? Insights from molecular dynamics simulation, *J. Solution Chem.*, 44 (1), 45–53.

[28] Housaindokht, M.R., Bozorgmehr, M.R., and Monhemi, H., 2012, Structural behavior of *Candida antarctica* lipase B in water and supercritical carbon dioxide: A molecular dynamic simulation study, *J. Supercrit. Fluids*, 63, 180–186.

[29] Almeida, P.F., and Pokorny, A., 2009, Mechanisms of antimicrobial, cytolytic, and cell-penetrating peptides: From kinetics to thermodynamics, *Biochemistry*, 48 (34), 8083–8093.

[30] Brune, D., and Kim, S., 1993, Predicting protein diffusion coefficients, *Proc. Natl. Acad. Sci. U.S.A.*, 90 (9), 3835–3839.

[31] Frenkel, D., and Smit, B., 2002, *Understanding Molecular Simulation: From Algorithms to Applications*, 2nd Ed., Academic Press, San Diego, CA.

Comparative Study of Various Kinetic Models on Leaching of NCA Cathode Material

Soraya Ulfa Muzayanha[1,2], Cornelius Satria Yudha[1], Luthfi Mufidatul Hasanah[1], Linggar Tungga Gupita[1], Hendri Widiyandari[3], and Agus Purwanto[1,*]

[1]*Department of Chemical Engineering, Faculty of Engineering, Universitas Sebelas Maret, Jl. Ir. Sutami 36 A, Surakarta 57126, Central Java, Indonesia*

[2]*Pertamina Research & Technology Center, PT. PERTAMINA, Jl. Raya Bekasi Km. 20, Pulogadung, Jakarta 13920, Indonesia*

[3]*Department of Physics, Faculty of Mathematic and Natural Science, Universitas Sebelas Maret, Jl. Ir. Sutami 36 A, Surakarta 57126, Central Java, Indonesia*

* ***Corresponding author:***

tel: +62-271-632112
email: aguspur@uns.ac.id

Received: September 9, 2019
Accepted: April 4, 2020

DOI: 10.22146/ijc.49412

Abstract: *The kinetics study of NCA leaching in the HCl system was proposed. Various kinetic models such as shrinking core, logarithmic rate law, and Avrami equation were used to find out the most appropriate kinetic models for this process. The effect of HCl concentrations, leaching temperatures, solid to liquid (S/L) ratio, and leaching duration were observed. The optimum conditions of NCA leaching were at HCl concentration of 4 M, temperature of 80 °C, S/L ratio of 100 g/L, and leaching time of 1 h. The result shows that shrinking core model with diffusion control process of residue layer describes well the leaching mechanism in this research, which is indicated by the good fitting of coefficient values of correlation (R^2) and confirmed by the activation energy values of Ni, Co, Al that were less than 40 kJ/mol.*

Keywords: *NCA cathode waste; kinetics study; recycle; hydrometallurgical; Li-ion batteries*

■ INTRODUCTION

Nowadays, the popularity of Lithium-ion batteries (Libs) increases as a result of the high demands of Libs in portable electronics like phones, power banks, laptops, and electric vehicles. One of the most popular cathode material used for Libs is $Li_{0.8}Co_{0.15}Al_{0.05}O_2$ (NCA) [1]. NCA batteries have some features of high capacity and high energy density of cathode material, which is beneficial for Libs, especially for electric vehicle applications [2-3]. Due to its high demand, the usage of NCA material is predicted to increase from 2015 to 2025 [4]. As a consequence, waste such as cathode scrap or spent libs can be generated in which the recycling process is indispensable.

Hydrometallurgical is one of recycling method via leaching step using acids or base to leach out the valuable metal contained in material [5-8] which provide more advantages such as simple, low energy consumption, and high purity of product [9-10]. From our previous study, we focused on the investigation of re-synthesis NCA material via hydrometallurgical with various strong acids (HCl, HNO_3, H_2SO_4) in the leaching system [11]. The result showed that the re-synthesis of NCA material from cathode waste has been succeeded and showed that the HCl leaching system is the most efficient process to recover the valuable metals in cathode waste. The recycled-NCA material had a comparable performance with commercial NCA, and it is promising to be adapted for large-scale production [11]. However, there are no reports about the study of leaching kinetics of ternary metals (nickel, cobalt, aluminum) using HCl from NCA waste, which is important for scaling up the production of recycled NCA.

Hence, the present novel aspect is the study of leaching kinetic from NCA scrap using HCl. The various modeling equation is applied to predict the most appropriate modeling for kinetic study of NCA leaching. The effects of various HCl concentrations, temperatures, solid to liquid ratio (S/L), and leaching time were

investigated to obtain the optimized conditions of leaching. The study of NCA waste leaching kinetics in the HCl system is needed considering scale up production of the recycling process.

■ EXPERIMENTAL SECTION

Materials

NCA scrap used in this research was obtained from a Battery Manufacturing Facility (Sebelas Maret University, Indonesia). NaOH was purchased from Asahi, Cilegon, Indonesia. Analytical grade of HCl (Merck, Darmstadt, Germany) was used in this research.

Instrumentation

The concentration of metals was measured using Atomic Absorption Spectroscopy (AAS/PinAAcle 900T Perkin Elmer, Waltham, MA, USA). The structure and morphology of NCA before and after leaching were analyzed using X-ray Diffraction (XRD) with a 2θ range of 10–70° (D2 Phaser Bruker, Germany) and Scanning Electron Microscopy (Jeol JSM-6510LA, Tokyo, Japan), respectively.

Procedure

Pre-treatment

NCA scrap still consists of Aluminum foil (Al foil), binder (Polyvinylidene Difluoride/PVDF), conducting agent (Acetylene Black/AB), and active material contained valuable metals. NaOH dissolution was employed to separate the powder from Al foil. First, the collected 50 g of NCA scrap was cut into smaller size and then immersed with agitation in 200 mL of 5 M NaOH solution for 2 h. The Al foil reacted spontaneously with NaOH solution to form sodium aluminate then the powder can be detached from Al foil. The slurry was filtered to obtain the powder, which will be washed using demineralized water to eliminate the remaining NaOH during the dissolution process. The collected powder was heated in an oven at a temperature of 80 °C. Then, the PVDF and AB were burned via heat treatment at a temperature of 800 °C for 4 h. The powder was then minimized by grounding into smaller sizes to enhance the surface area of powder, which can be beneficial during the leaching process.

Leaching process

Determination of the optimum conditions. The leaching process was conducted in a 500 mL three-necked batch reactor of Pyrex involving a water bath to maintain the specified temperature. The leaching conditions were performed at HCl. The leachate was then filtered to separate the filtrate from the residue. In order to find out the total concentrations of valuable metals (Ni, Co, Al), the powder was completely leached out in concentrated HCl. The filtrate was analyzed using Atomic Absorption Spectroscopy (AAS) to determine the concentrations of metals. The effect of acid concentrations, various temperatures, solid to liquid ratio (S/L ratio), and time of leaching were observed to find out the optimized conditions in this leaching process. The leaching efficiency was calculated using Eq. (1):

$$X = \frac{Ct - C}{Ct} \times 100\% \quad (1)$$

where X is leaching efficiency of Ni, Co, Al (%), Ct is the total concentration of Ni, Co, Al (g/L), and C is the concentration of Ni, Co, Al at certain conditions (g/L).

Kinetics. The shrinking core model, logarithmic rate law, and Avrami equation were studied to elucidate the suitable leaching kinetics during the process.

Characterization of NCA waste before and after leaching

The NCA powder before leaching and the residue of the leaching were analyzed using X-ray Diffraction (XRD) to investigate the structure of NCA before and after the leaching process. Scanning Electron Microscopy (SEM) was also employed to observe the morphology of NCA waste.

■ RESULTS AND DISCUSSION

Leaching Process

HCl was used as a leaching agent during the leaching process. In order to evaluate the optimum conditions of the leaching process using HCl for recycling of NCA scrap, the various conditions of HCl concentrations, leaching time, S/L ratio, and temperatures during leaching were shown in Fig. 1. As shown in Fig. 1(a), the leaching efficiency of Ni, Co, Al increased up to concentrations of 3 M and tended to be

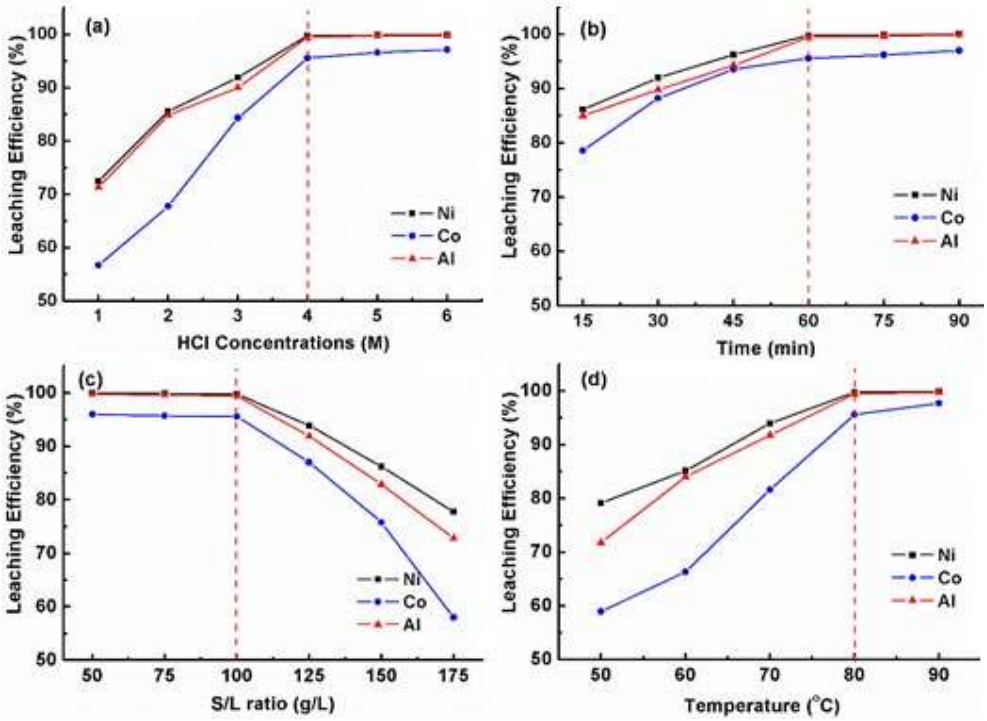

Fig 1. Effect of (a) HCl concentrations, (b) leaching duration, (c) S/L ratio, and (d) temperatures on NCA waste leaching

constant from 4 M to 6 M. The increasing concentrations of HCl from 5 M to 6 M did not present a significant effect on leaching efficiencies after 60 min. It means that a continued increase in acid concentrations can impede the diffusion of metal ion and inhibit the reaction during the leaching process [12]. Therefore, the acid concentration of 4 M was selected.

Fig. 1(b) presents the effect of reaction time (15–75 min) on the leaching efficiencies of Ni, Co, and Al at 100 g/L S/L ratio, 80 °C. At high temperatures, the reaction between metals and HCl was rapid. As a result, the leaching efficiencies enhanced slightly with time. However, the leaching efficiencies of Ni, Co, and Al increased with the increasing duration of the reaction. Fig. 1(c) shows the effect of S/L ratio (g/L) towards the leaching efficiencies of Ni, Co, Al. There was an insignificant difference in leaching efficiencies from 50 g/L to 100 g/L. Still, the increasing of S/L ratio after 100 g/L lead to the leaching efficiencies of metal ions decreases. It can be caused by the higher S/L ratio lead to a more viscous solution that can slow the reaction during leaching and resulted in low efficiency [12]. Next, the effects of leaching temperature are shown in Fig. 1(d). It can be seen that leaching temperature from 50–70 °C has a significant impact on the leaching efficiencies of Ni, Co, and Al, but tends to constant after 80 °C. This high temperature (80 °C) increases the reactivity of metal ions, which promote reaction acceleration during leaching [12]. However, a further increase in temperature (90 °C) resulted in the leaching efficiency near to the temperature of 80 °C. Also, it was difficult to control the leaching system at a temperature of 90 °C. Consequently, the temperature of 80 °C was selected. Therefore, the optimum leaching conditions in this study were chosen at the concentration of 4 M HCl, temperature of 80 °C, S/L ratio of 100 g/L, and leaching time of 60 min.

Fig. 2 presents the leaching behavior at the optimum conditions of leaching. The result shows that the rapid reaction during the leaching process occurred at the beginning (0–15 min), then the reaction became slow, which is indicated from the curve that tends to be constant. The reactivity of HCl towards metals is very high, as reported in the previous study [11]. The metal oxides are converted from trivalent to divalent states of Ni and Co during reaction on the leaching process [11].

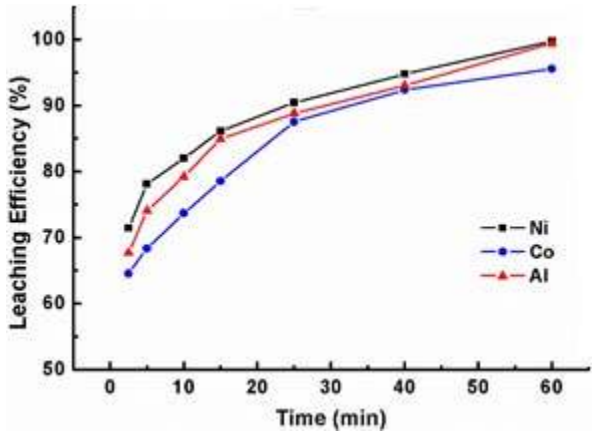

Fig 2. Leaching behavior of Ni, Co, Al at optimum condition

The reaction occurred during the leaching process between HCl and NCA scrap is explained in Eq. 2 [11].

$$3HCl_{(aq)} + LiNi_{0.80}Co_{0.15}Al_{0.05}O_{2(s)} \rightleftarrows LiCl_{(aq)} + 0.8NiCl_{2(aq)} + 0.15CoCl_{2(aq)} + 0.05AlCl_{3(aq)} + 1.5H_2O_{(liq)} + 0.5O_{2(g)} \quad (2)$$

The Kinetics Study of Leaching

In this study, the leaching process involves the reaction between NCA and HCl as a solid phase and liquid phase, respectively. The leaching kinetic models possible occurred are shrinking core, logarithmic rate law, and Avrami equation. The equations of leaching kinetic were presented below [12-13]:

Shrinking core model

$$X = k.t \quad (3)$$

$$1-(1-X)^{1/3} = k.t \quad (4)$$

$$1-\frac{2}{3}X-(1-X)^{2/3} = k.t \quad (5)$$

Logarithmic rate law

$$(-\ln(1-X))^2 = k.t \quad (6)$$

Avrami equation

$$\ln(-\ln(1-X)) = \ln k + n \ln t \quad (7)$$

In Eq. (3–7), X is the efficiency of leaching, k is the constant in the reaction rate (1/min for Eq. (3–4) and 1/(min^n) for Eq. (7)) that is the slope of the plotted line, t is the time required for the leaching process (min). The activation energy of leaching using HCl can be calculated by the Arrhenius equation that presents the relationships between temperature and k value. The Arrhenius equation is shown in Eq. (8).

$$k = Ae^{-Ea/RT} \quad (8)$$

where, k: Kinetic constant rate, 1/min; A: Frequency factor, 1/min; Ea: Activation energy, J/mol; R: Gas constant, (8.3145 J/mol K).

Shrinking core

The first prediction of leaching kinetic models in this study was the shrinking core model. The kinetic models for a shrinking core feature several forms of control: mass transfer process control of the liquid layer (Eq. 3), chemical reaction process control of the surface (Eq. 4), and diffusion process control of the residue layer (Eq. 5) [14].

Shrinking core Eq. (3): $X = k.t$. In this kinetic equation of the shrinking core model, the leaching process is controlled by the mass transfer process of the liquid layer. The plotted of X vs. t and Ea for Ni, Co, Al, respectively, is shown in Fig. 3(a-c). Some of the coefficient values of correlation (R^2) for each metal are below 0.95, which indicated poor fitting of this equation.

In this study, due to the high temperature and HCl concentration of leaching conditions, the high solubility of the metal ions that lead to rapid release into the bulk solution occurred. Also, the high speed of stirring (800 rpm) was used. Thus, the mass transfer process runs fast and can be ignored, according to the results of R^2 values in the curves [12].

Shrinking core Eq. (4): $1-(1-X)^{1/3} = k.t$. Previously, this kinetic model was successfully applied in the recycling of mixed spent Libs [15]. In this equation, the leaching process is controlled by the chemical reaction process of the surface. The kinetic and Ea curves of Ni, Co, and Al in this study are presented in Fig. 4. However, the R^2 values of each curve have a low fitting degree (< 0.95). This may be caused by the high reactivity of HCl towards metal oxide during leaching, resulting in fast reaction kinetics. As a consequence, the chemical reaction process of the surface can be negligible in this study.

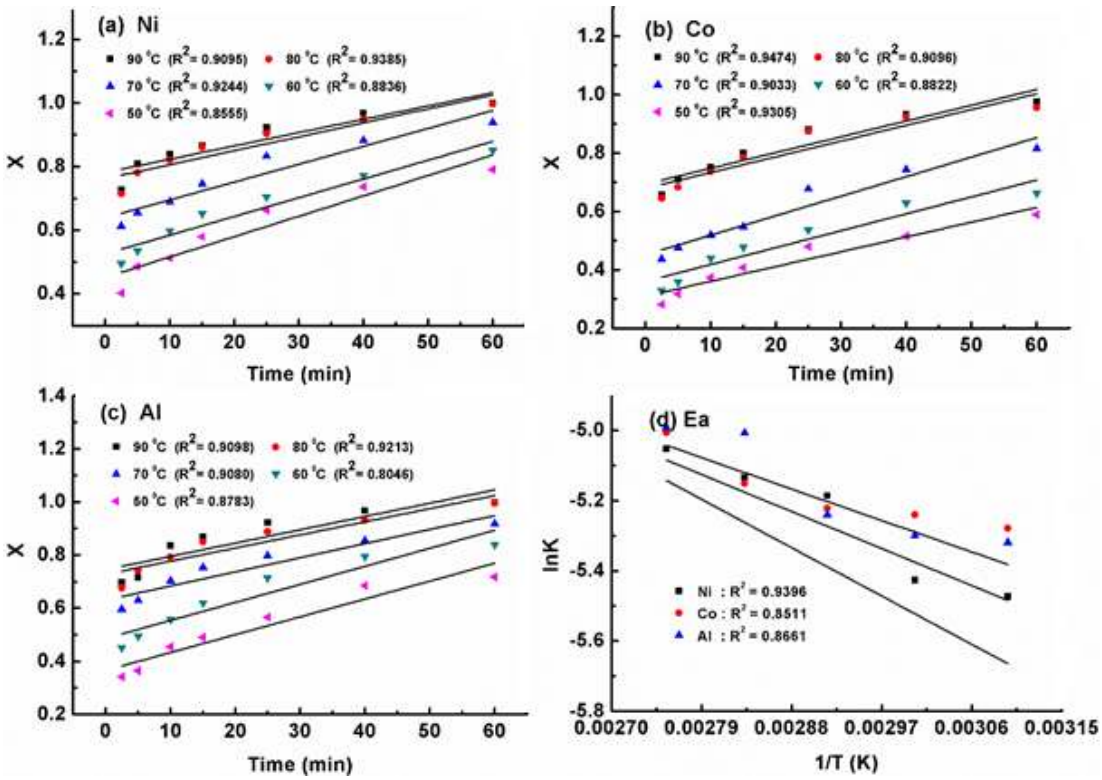

Fig 3. The kinetic curve of (a) Ni, (b) Co, and (c) Al using shrinking core (Eq. 3). (d) the Arrhenius plot of Ni, Co, Al using shrinking core (Eq. 3)

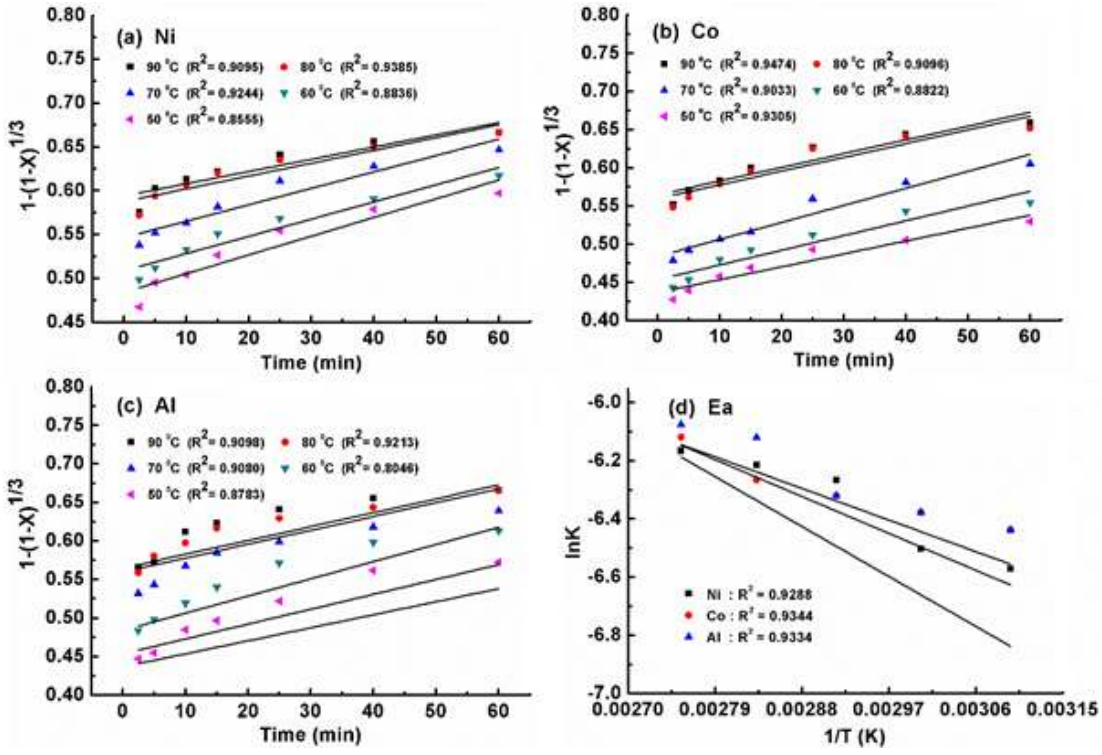

Fig 4. The kinetic curve of (a) Ni, (b) Co, and (c) Al using shrinking core (Eq. 4). (d) the Arrhenius plot of Ni, Co, Al using shrinking core (Eq. 4)

Shrinking core Eq. (5): $1-\frac{2}{3}X-(1-X)^{2/3}=k.t$. The last shrinking core model is controlled by the diffusion process of the residue layer and has been applied successfully in the previous study [14,16]. Fig. 5 represents the curves of the kinetic equation and Ea of Ni, Al, and Al. All curves have high values of R^2 (> 0.95), suggesting a high fitting degree of this kinetic model.

Logarithmic rate law

Another kinetic model for the leaching process is the logarithmic rate law model. Based on our previous study, the logarithmic rate law was successfully applied for the leaching process of valuable metals [17-20]. In this study, the plots of the logarithmic rate law model (Eq. (6)) are shown in Fig. 6. The curves exhibit a poor fitting of R^2 values (< 0.95). Chen et al. have selected this kinetic model due to the difference in leaching behaviors of valuable metals (Li and Co) [17]. In this case, the leaching behaviors of Ni, Co, and Al are similar (see Fig. 2); therefore, this kinetic equation is irrelevant to this study.

Avrami model

Kinetic equation related to leaching phenomena is the Avrami model. During the HCl leaching process, the NCA waste was nearly dissolved in HCl without the formation of a solid phase, which is the opposite of the crystallization process. Zhuang et al. have used this equation for the recycling process of $LiNi_{0.5}Co_{0.2}Mn_{0.3}O_2$ using mixed acids of phosphoric and citric acids [21]. Other researchers reported that the Avrami equation had been succeeded in explaining the leaching kinetics of multi-metals [22-24]. Thus, the implementation of the Avrami model is appropriate to be used in this study.

The curves of using the Avrami equation (Eq. 7) for Ni, Co, and Al are shown in Fig. 7. The R^2 values are less than 0.95, which indicates the invalid fitting by this equation. The result showed that the value of n, which suggests the leaching behavior of metals, is obtained to be around 0.3-0.46. In our previous study [21], we have found that the leaching reaction initially occurred rapidly after several minutes, and then the reaction starts

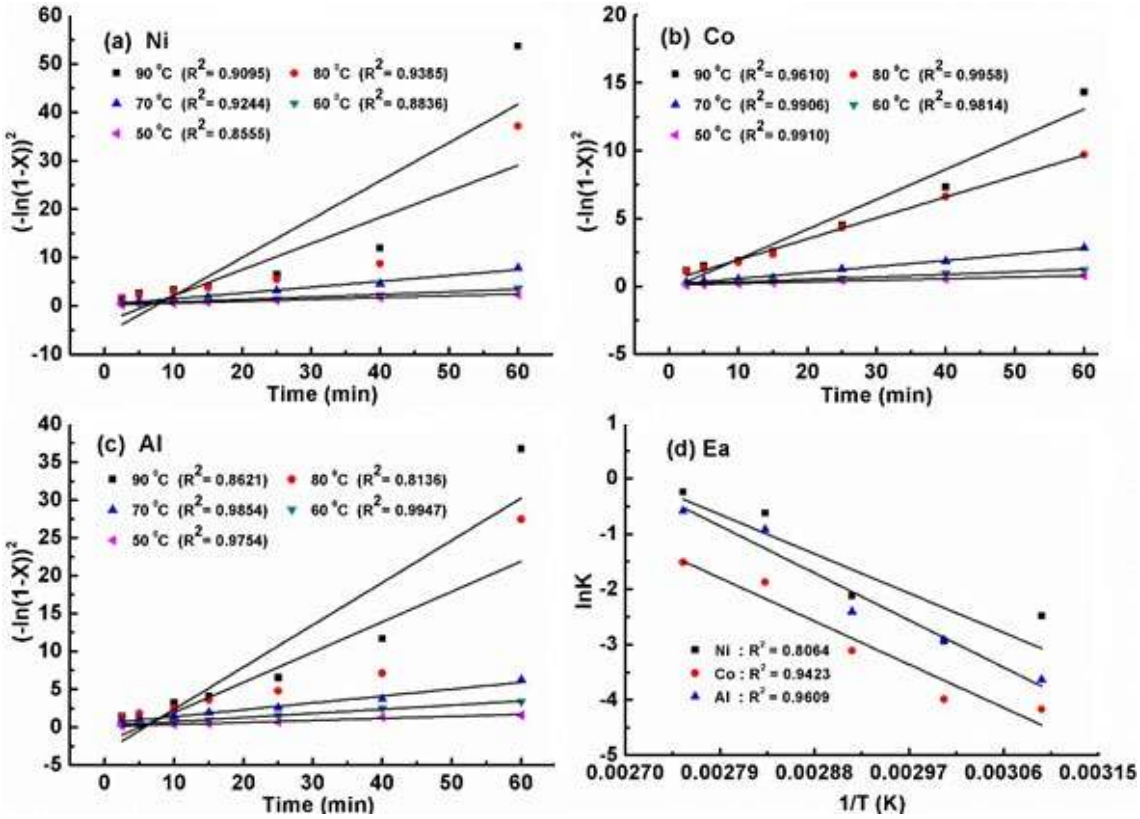

Fig 6. The kinetic curve of (a) Ni, (b) Co, and (c) Al using logarithmic rate law (Eq. 6). (d) the Arrhenius plot of Ni, Co, and Al using logarithmic rate law (Eq. 6)

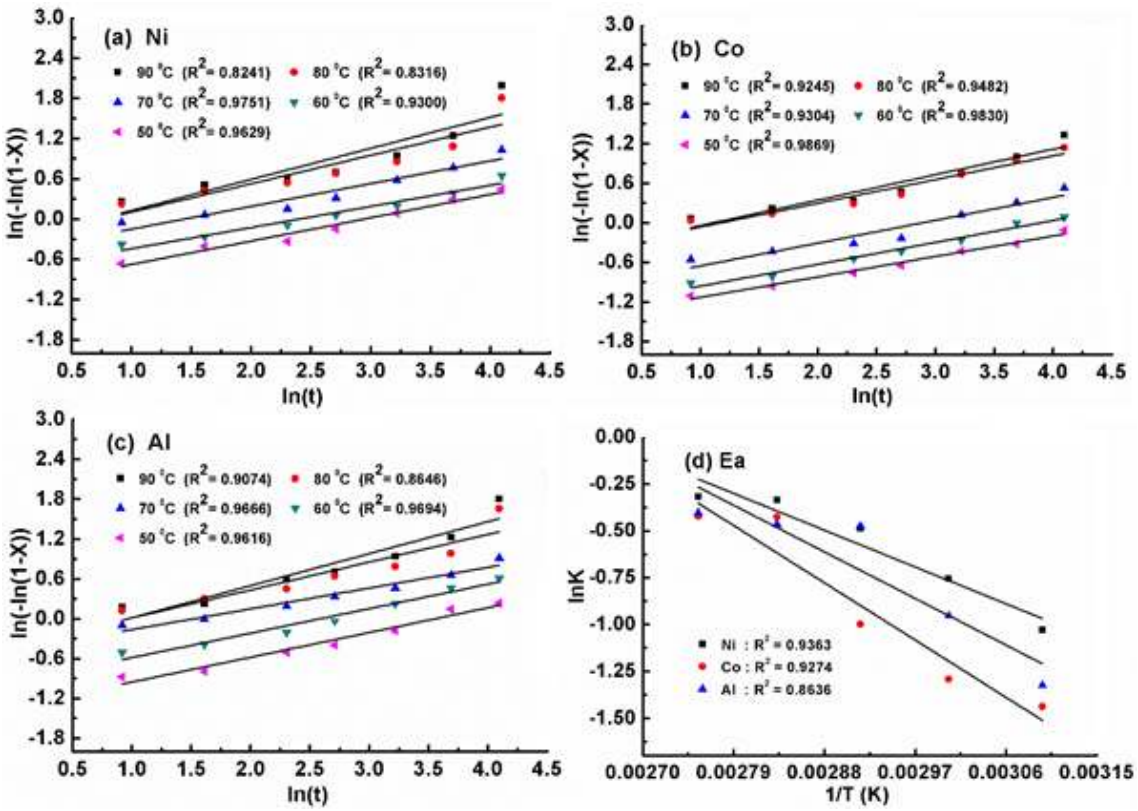

Fig 7. The kinetic curve of (a) Ni, (b) Co, and (c) Al using the Avrami model (Eq. 7). (d) the Arrhenius plot of Ni, Co, and Al using the Avrami model (Eq. 7)

to slow down. Based on previous studies, the value of n is in the range of 0.5–1 [21]. Therefore, it is predicted that the leaching mechanism in this study does not behave like the reverse crystallization mechanism proposed by the Avrami model.

The summary of the activation energy calculation proposed by shrinking core, logarithmic rate law, and Avrami equation was presented in Table 1. The result exhibits that the most appropriate kinetics model of the HCl leaching process for NCA waste was the shrinking core, where the diffusion process is controlled by the residue layer (Eq. 3). From Table 1, it is marked that all curves of shrinking core Eq. (5) show good fitting lines higher than 0.95. Also, the results of activation energy (Ea) for Ni, Co, and Al were 21.75, 38.09, and 26.07 kJ/mol, respectively. The Ea values of all metals were lower than 40 kJ/mol, confirmed that the leaching step was controlled by the diffusion process of the residue layer [25-26]. In this study, the Ea of Ni had the lowest value than Co and Al, indicating that the extraction process of Ni is easier than other metal, which is consistent with the leaching behavior in Fig. (2-5) [14].

Table 1. Summary of activation energy from various kinetic equations

Metals	Ea (kJ/mol)									
	Shrinking Core Eq. (3)		Shrinking Core Eq. (4)		Shrinking Core Eq. (5)		Logarithmic Rate Law		Avrami Equation	
	value	R^2	value	R^2	value	R^2	value	R^2	value	R^2
Ni	11.0915	0.9495	10.7640	0.9288	21.7549	0.9569	65.7386	0.8064	18.1406	0.9363
Co	6.1195	0.9121	7.2413	0.9344	38.0962	0.9751	72.1931	0.9423	28.2402	0.9274
Al	9.1792	0.8745	9.5450	0.9334	26.0726	0.9642	78.7092	0.9609	22.9780	0.8636

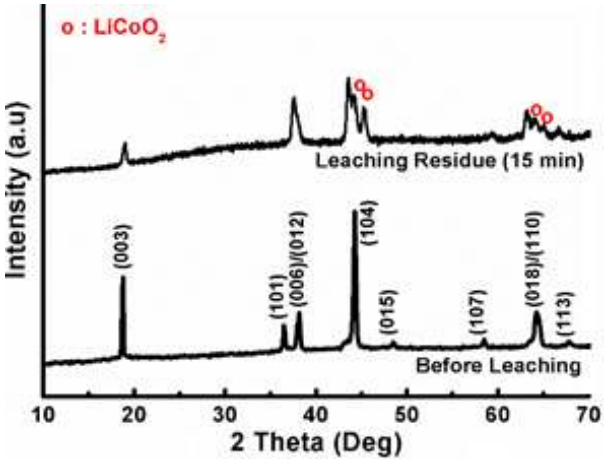

Fig 8. XRD patterns of NCA waste before and after leaching for 15 min

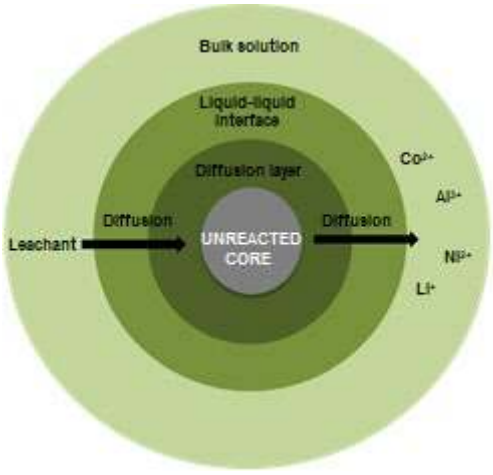

Fig 10. The mechanism of the leaching process using a shrinking core model

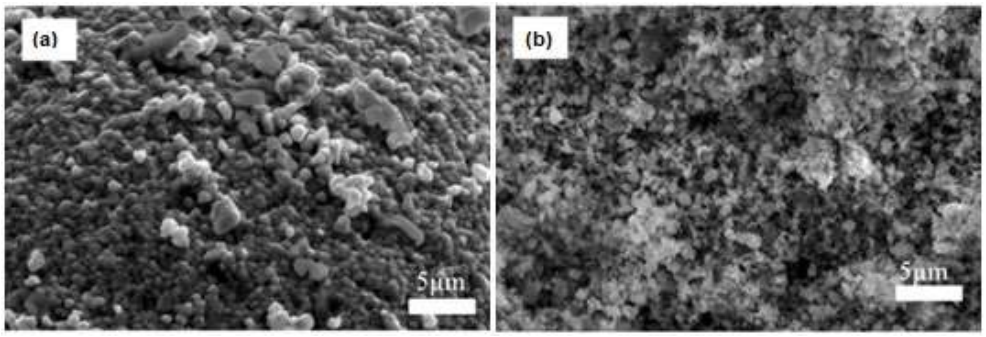

Fig 9. SEM images of NCA waste (a) before and (b) after leaching for 15 min

Material Characterization Before and After Leaching

The comparison of XRD patterns between powder before and after leaching of 15 min is shown in Fig. 8. The XRD patterns of samples exhibit the structure of hexagonal α-$NaFeO_2$ with space group R3m. There is no other crystalline chemical detected, indicating that only the dissolution of metals has occurred and no precipitates form during the leaching process [21]. However, the $LiCoO_2$ phase found on the peaks of (104) and (018)/(110) suggests that the reduction of Co occurs during leaching [20].

The morphology of NCA waste before and after leaching (15 min) is shown in Fig. 9. It can be seen that the morphology of leaching residue is more amorphous due to the dissolution of the metal. Moreover, the loose particles originate from dense spherical particles which confirm the shrinking core phenomena due to acid leaching. The mechanism of the leaching process using a shrinking core model in Fig. 10 is following these steps:

1st step: The diffusion process of leachant molecules from the bulk solution to the liquid-liquid interface.

2nd step: The diffusion process whereby molecules are leached from the liquid-liquid interface via the diffusion layer to the unreacted core surface.

3rd step: The reaction between leachant molecules and the solid core at the solid-liquid interface. The metal ions are dissolved and released into the bulk solution.

4th step: The process of diffusing metal ions via the diffusion layer into the liquid-liquid interface.

5th step: The process of the diffusion of metal ions into the bulk solution.

■ CONCLUSION

This study focused on the optimization and kinetic study of the NCA leaching process using HCl. The

optimum condition of leaching was at 4 M HCl concentration, 80 °C, S/L ratio of 100 g/L for 1 h. Various kinetic equation models were plotted to determine the suitable kinetic model in this study. The shrinking core model with diffusion process control of the residue layer could describe well the leaching mechanism and exhibited a good fitting line on the curve with R^2 higher than 0.95. The activation energy of this process was higher than 40 kJ/mol, which reveals that the leaching process was controlled by the residue layer.

■ ACKNOWLEDGMENTS

This paper is funded by Indonesia Endowment Fund for Education (LPDP/Lembaga Pengelola Dana Pendidikan) through Pendanaan Riset Inovatif Produk (Rispro) Invitasi grant no.PRJ-31/LPDP/2018 and supported by the Indonesian Ministry of Research, Technology, and Higher Education under the WCU program managed by Institut Teknologi Bandung (ITB).

■ REFERENCES

[1] Purwanto, A., Yudha, C.S., Ubaidillah, U., Widiyandari, H., Ogi, T., and Haerudin, H., 2018, NCA cathode material: Synthesis methods and performance enhancement efforts, *Mater. Res. Express*, 5 (12), 122001.

[2] Nitta, N., Wu, F., Lee, J.T., and Yushin, G., 2015, Li-ion battery materials: Present and future, *Mater. Today*, 18 (5), 252–264.

[3] Yudha, C.S., Muzayanha, S.U., Widiyandari, H., Iskandar, F., Sutopo, W., and Purwanto, A., 2019, Synthesis of $LiNi_{0.85}Co_{0.14}Al_{0.01}O_2$ cathode material and its performance in an NCA/graphite full-battery, *Energies*, 12, 1886.

[4] Pillot, C., 2017, *Lithium-ion battery raw material Supply & demand 2016-2025*, Avicenne Energy, Information for Growth, Mainz, Germany, 30 January 2017.

[5] Li, L., Dunn, J.B., Zhang, X.X., Gaines, L., Chen, R.J., Wu, F., and Amine, K., 2013, Recovery of metals from spent lithium-ion batteries with organic acids as leaching reagents and environmental assessment, *J. Power Sources*, 233, 180–189.

[6] Zheng, X., Gao, W., Zhang, X., He, M., Lin, X., Cao, H., Zhang, Y., and Sun, Z., 2017, Spent lithium-ion battery recycling – Reductive ammonia leaching of metals from cathode scrap by sodium sulphite, *Waste Manage.*, 60, 680–688.

[7] Chen, Y., Liu, N., Hu, F., Ye, L., Xi, Y., and Yang, S., 2018, Thermal treatment and ammoniacal leaching for the recovery of valuable metals from spent lithium-ion batteries, *Waste Manage.*, 75, 469–475.

[8] Zou, H., Gratz, E., Apelian, D., and Wang, Y., 2013, A novel method to recycle mixed cathode materials for lithium-ion batteries, *Green Chem.*, 15 (5), 1183–1191.

[9] Chen, W.S., and Ho, H.J., 2018, Recovery of valuable metals from lithium-ion batteries NMC cathode waste materials by hydrometallurgical methods, *Metals*, 8 (5), 3211.

[10] Joulié, M., Laucournet, R., and Billy, E., 2014, Hydrometallurgical process for the recovery of high value metals from spent lithium nickel cobalt aluminum oxide-based lithium-ion batteries, *J. Power Sources*, 247, 551–555.

[11] Muzayanha, S.U., Yudha, C.S., Nur, A., Widiyandari, H., Haerudin, H., Nilasary, H., Fathoni, F., and Purwanto, A., 2019, A fast metals recovery methods for the synthesis of lithium nickel cobalt aluminum oxide material from cathode waste, *Metals*, 9 (5), 615.

[12] Li, L., Bian, Y., Zhang, X., Guan, Y., Fan, E., Wu, F., and Chen, R., 2018, Process for recycling mixed-cathode materials from spent lithium-ion batteries and kinetics of leaching, *Waste Manage.*, 71, 362–371.

[13] Purwani, M.V., and Muzakky, 2019, Optimization and kinetics of zirconium oxychloride (ZOC) dissolution using HNO_3, *Indones. J. Chem.*, 19 (4), 928–935.

[14] Gao, W., Song, J., Cao, H., Lin, X., Zhang, X., Zheng, X., Zhang, Y., and Sun, Z., 2018, Selective recovery of valuable metals from spent lithium-ion batteries – Process development and kinetics evaluation, *J. Cleaner Prod.*, 178, 833–845.

[15] Nayl, A.A., Elkhashab, R.A., Badawy, S.M., and El-Khateeb, M.A., 2017, Acid leaching of mixed spent

Li-ion batteries, *Arabian J. Chem.*, 10 (Suppl. 2), S3632–S3639.

[16] Zheng, Y., Long, H.L., Zhou, L., Wu, Z.S., Zhou, X., You, L., Yang, Y., and Liu, J.W., 2016, Leaching procedure and kinetic studies of cobalt in cathode materials from spent lithium-ion batteries using organic citric acid as leachant, *Int. J. Environ. Res.*, 10 (1), 159–168.

[17] Chen, X., Xu, B., Zhou, T., Liu, D., Hu, H., and Fan, S., 2015, Separation and recovery of metal values from leaching liquor of mixed-type of spent lithium-ion batteries, *Sep. Purif. Technol.*, 144, 197–205.

[18] Kim, E., Kim, M., Lee, J., Jeong, J., and Pandey, B.D., 2011, Leaching kinetics of copper from waste printed circuit boards by electro-generated chlorine in HCl solution, *Hydrometallurgy*, 107 (3-4), 124–132.

[19] Meshram, P., Pandey, B.D., and Mankhand, T.R., 2015, Hydrometallurgical processing of spent lithium-ion batteries (LIBs) in the presence of a reducing agent with emphasis on kinetics of leaching, *Chem. Eng. J.*, 281, 418–427.

[20] Meshram, P., Pandey, B.D., and Mankhand, T.R., 2015, Recovery of valuable metals from cathodic active material of spent lithium-ion batteries: Leaching and kinetic aspects, *Waste Manage.*, 45, 306–313.

[21] Zhuang, L., Sun, C., Zhou, T., Li, H., and Dai, A., 2019, Recovery of valuable metals from $LiNi_{0.5}Co_{0.2}Mn_{0.3}O_2$ cathode materials of spent Li-ion batteries using mild mixed acid as leachant, *Waste Manage.*, 85, 175–185.

[22] Demirkiran, N., and Künkül, A., 2007, Dissolution kinetics of ulexite in perchloric acid solutions, *Int. J. Miner. Process.*, 83 (1-2), 76–80.

[23] Li, G., Rao, M., Jiang, T., Huang, Q., and Peng, Z., 2011, Leaching of limonitic laterite ore by acidic thiosulfate solution, *Miner. Eng.*, 24 (8), 859–863.

[24] Zhang, X., Cao, H., Xie, Y., Ning, P., An, H., and You, H., 2015, A closed-loop process for recycling $LiNi_{1/3}Co_{1/3}Mn_{1/3}O_2$ from the cathode scraps of lithium-ion batteries: Process optimization and kinetics analysis, *Sep. Purif. Technol.*, 150, 186–195.

[25] Espiari, S., Rashchi, F., and Sadrnezhaad, S.K., 2006, Hydrometallurgical treatment of tailings with high zinc content, *Hydrometallurgy*, 82 (1-2), 54–62.

[26] Ebrahimzade, H., Reza, G., and Mahin, K., 2018, Leaching kinetics of valuable metals from waste Li-ion batteries using neural network approach, *J. Mater. Cycles Waste Manage.*, 20, 2117–2129.

Imprinted Zeolite Modified Carbon Paste Electrode as a Selective Sensor for Blood Glucose Analysis by Potentiometry

Miratul Khasanah*, Alfa Akustia Widati, Usreg Sri Handajani, Muji Harsini, Bahrotul Ilmiah, and Irene Dinda Oktavia

Department of Chemistry, Faculty of Science and Technology, Universitas Airlangga, Campus C, Jl. Dr. Ir. H. Soekarno (MERR), Surabaya 60115, Indonesia

* ***Corresponding author:***

tel: +62-8123077233
email: miratul-k@fst.unair.ac.id

Received: September 19, 2019
Accepted: January 30, 2020

DOI: 10.22146/ijc.49820

Abstract: *Imprinted zeolite modified carbon paste (carbon paste-IZ) electrode had been developed as a sensor to analyze blood glucose content by potentiometry. The used zeolite was Lynde Type A (LTA) that synthesized with a mole ratio of Na_2O, Al_2O_3, SiO_2 and H_2O of 4:1:1.8:270, respectively while non-imprinted zeolite was prepared with a mole ratio of glucose/Si of 0.0306. Glucose was then extracted from the zeolite framework using hot water (80 °C) to produce imprinted zeolite (IZ). The carbon paste-IZ electrode prepared from activated carbon, paraffin pastilles, and IZ with a mass ratio of 5:4:1 showed the best performance. The modified electrode demonstrated the measurement range of 10^{-4}-10^{-2} M, the Nernst factor of 29.55 mV/decade, the response time less than 120 s, and the detection limit of 5.62×10^{-5} M. Ascorbic acid, uric acid, urea and creatinine did not interfere on the glucose analysis by potentiometry. Comparison test with spectrophotometry showed an accuracy of (90.7 ± 1.4)% (n = 5), while the application of the electrode to analyze five spiked serum samples showed recovery of (92.2 ± 1.3)% (n = 5). The electrode was stable for up to 9 weeks (168 times usage). Based on its performance, the developed electrode can be applied to analyze glucose in human serum sample and recommended for used in the medical field.*

Keywords: *blood glucose; carbon paste electrode; imprinted zeolite; potentiometric sensor*

■ INTRODUCTION

Diabetes mellitus has become a serious threat to human health because it can cause kidney failure, heart disease, and stroke. An increase in high blood glucose levels (> 200 mg/dL) is a major cause of diabetes mellitus [1]. In the body, normal blood glucose values are 60–100 mg/dL (3.3×10^{-3}–5.5×10^{-3} M), while serum glucose is 70–110 mg/dL (3.88×10^{-3}–6.1×10^{-3} M) [2]. Based on the effects that can be caused by high blood glucose levels, controlling the glucose level in the blood is necessary. The general method for determining glucose levels is spectrophotometry using chemical or enzymatic, such as hexokinase or glucose 6-phosphate dehydrogenase [3]. A few studies have reported about the use of some methods for glucose determination including GOx (glucose oxidase) based colorimetric methods [4-5], high performance liquid chromatography (HLPC) [6], liquid chromatography-mass spectrometry (LC-MS) [7], and potentiometry using modified carbon-based electrodes [8]. Modified carbon-based electrodes have previously been developed including zeolite-modified electrodes for the analysis of uric acid [9], Cr^{3+} ions [10], creatinine [11], creatine [12]; and polymer-based electrodes for phenol analysis [13]. Nanoparticle material has also been shown to increase the selectivity and sensitivity of electrodes to analytes [14].

In this study, an imprinted zeolite modified carbon paste electrode has been developed for potentiometric glucose detection. The zeolite used was LTA zeolite that synthesized from the basic materials of SiO_2, $NaAlO_2$, and water with a mole ratio of Na_2O, Al_2O_3, SiO_2, H_2O of 4:1:1.8:270 [15]. Glucose solution was added to the mixture of these materials to produce non imprinted zeolites (NIZ). Next, the glucose molecule was extracted, so that it leaves a mold on the zeolite framework called

imprinted zeolite (IZ). The imprinted is expected only match the size and shape to glucose molecules so that they can selectively detect glucose molecules when it is used for sample analysis.

Electrode performance was studied from the measurement range value, Nernst factor, detection limit, response time and the life time of the electrode. The use of electrodes was studied through the accuracy value compared with the spectrophotometry method as a standard method for determining blood glucose levels in the medical field. Electrode selectivity was investigated through the effect of another component in serum samples including ascorbic acid, uric acid, creatinine, and urea on the glucose analysis using the electrode.

■ EXPERIMENTAL SECTION

Materials

Chemicals used in this study were glucose (Sigma Aldrich, 99.5%), SiO_2 (Sigma Aldrich, Ludox 40%), sodium aluminate (Sigma Aldrich, 50%), sodium dihydrogen phosphate (Merck, 99%), disodium hydrogen phosphate (Merck, 99.5%), uric acid (Fluka, 98%), urea, creatinine, H_3PO_4, $AgNO_3$, Ag wire, *n*-hexane, paraffin pastilles and activated carbon with pore size of 3.835 nm. The sample used was blood serum from a clinical laboratory in Surabaya.

Instrumentation

The equipment used in this study was a Cyberscan 510 potentiometers with Ag/AgCl as a reference electrode, Fourier transform infrared (FTIR) spectrophotometer (Shimadzu IR Prestige 21), X-ray diffraction (PANalytical E'xpert Pro), Spectrophotometer (UV 1800 Pharmaspec), hotplate (Termolyne S46410-2), pH meter (Cyberscan Eutech pH 510), centrifuge (HITTECH EBA) 20, vacuum oven (NAPCO Model 5851), magnetic stirrer, polypropylene bottle, agate mortar, 1000 µL micropipette tip and glassware.

Procedure

Synthesis of zeolite, non-imprinted zeolite (NIZ), and imprinted zeolite (IZ)

The LTA zeolite was synthesized by mixing Na_2O, Al_2O_3, SiO_2, and H_2O with a mole ratio of 4:1:1.8:270 [15]. The mixture was stirred for 3 h. A one third part was heated in an oven at 100 °C for 45 h. Next, it is washed using distilled water with the help of a centrifuge. The remaining 2/3 parts of the mixture were added with glucose to produce a glucose/Si mole ratio of 0.0306. The obtained mixture was allowed to stand for 3 h so that glucose can be binded and trapped in the zeolite framework. A half part of the mixture was dried at 80 °C and the other part was added with hot water to extract glucose and form imprinted zeolite.

Fabrication of carbon paste-imprinted zeolite and pH optimization

The carbon paste electrodes were prepared by inserting Ag wires in a 1 mL micropipette tube. Three quarter part of the micropipette tip was filled with melted paraffin. Then a paste made from a mixture of activated carbon, solid paraffin, and IZ with various compositions (Table 1) was filled into the ¼ part remaining of the micropipette tube. The surface of the electrodes was rubbed on the HVS paper and immersed in a 10^{-2} M glucose solution overnight for conditioning.

Furthermore, each electrode was used to measure the glucose standard solution 10^{-8}–10^{-1} M pH 6 (without pH adjustment). Then a graph between the concentration and electrode potential was created and determined the value of the Nernst factor and linear measurement range. The composition of carbon paste-IZ electrodes that produce optimum performance is used as the basis for preparing zeolite-modified carbon paste electrodes (EZ) and NIZ-modified carbon paste electrodes (ENIZ). The performance of EZ and ENIZ were compared with carbon paste-IZ to observe the effect of glucose mold on the electrode performance. The effect of pH solution was

Table1. Composition of activated carbon, paraffin, and IZ on electrode fabrication

Electrode	% weight		
	Activated carbon	paraffin	IZ
E1	60	40	0
E2	55	40	5
E3	50	40	10
E4	45	40	15
E5	40	40	20

studied through the Nernst factor value and linear measurement range resulting from the measurement of glucose solution with varies pH.

Performance of the electrode and method validity

Parameters for expressing electrode performance and method validity in this study include linear measurement range, Nernst factor, detection limit, precision, accuracy, response time, life time and selectivity. The selectivity of the electrode was stated by the selectivity coefficient (K_{ij}) value determined by the matched potential method (MPM) [16]. The accuracy was determined through a comparison test with the results of blood glucose analysis using the spectrophotometric method as a commonly used method in the medical field.

■ RESULTS AND DISCUSSION

Synthesis and Characterization of Zeolite, NIZ, and IZ

The LTA zeolite is prepared through a sol-gel method using silica sol as the silica source and sodium aluminate as the aluminium source. The precursor solution is combined under vigorous stirring. The mixture is then sealed in polypropylene bottles for the hydrothermal process. The reactions that occur in zeolite synthesis are as shown in Eq. (1) and (2).

$$NaAlO_{2(s)} + 4H_2O_{(I)} \rightarrow Al(OH)_4^-{}_{(aq)} + NaOH_{(aq)} + H_3O^+_{(aq)} \quad (1)$$

$$Si(OH)_{4(aq)} + Al(OH)_4^-{}_{(aq)} \rightarrow (HO)_3 - Si - O - Al - (OH)_{3(aq)} + H_2O_{(I)} + e^- \quad (2)$$

SiO_2 was added to $NaAl(OH)_4$ solution dropwise and stirred for 1 h until it became a white gel. This process is an aging step which is the process of forming a zeolite crystal core [18]. The aging process aims the breaking of silica monomers into a stronger silica gel with the expected pore [19].

Furthermore, the mixture was heated hydrothermally at 100 °C for 45 h in a polypropylene bottle to accelerate the growth of zeolite crystals [20]. From this process, a white suspension is produced. A total of 1/3 parts of the suspension are centrifuged at 4000 rpm for 5 min. Then the precipitate was separated and washed with distilled water to remove the remaining NaOH and dried it in an oven at 80 °C for 24 h.

Non imprinted zeolite (NIZ) is zeolite which contains templates/mold in the pores. Non imprinted zeolite was prepared by taking as much as 2/3 parts of a mixture of SiO_2, $NaAlO_2$, and H_2O (after the hydrothermal process). Then the mixture was added with glucose solution dropwise and stirred with a magnetic stirrer for

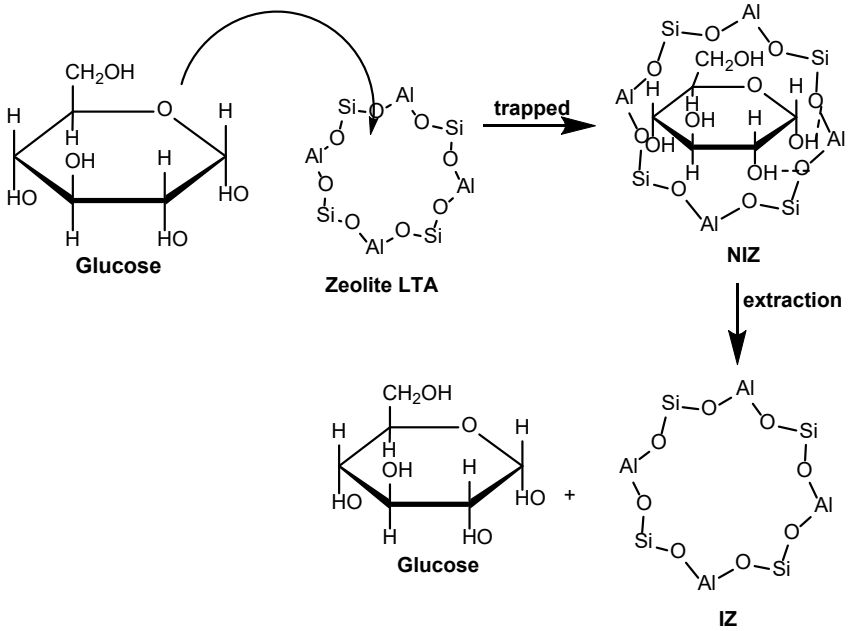

Fig 1. An illustration of trapping glucose molecules into a zeolite framework

30 min. An illustration of trapping glucose molecules into a zeolite framework can be seen in Fig. 1. The imprinted zeolite (IZ) was obtained by extracting glucose molecules from the NIZ framework using hot water. Benedict tests were performed to ensure that all glucose has been extracted from the NIZ framework (Fig. 2).

Characterization of zeolites by XRD was carried out to determine the formation of synthesized LTA zeolites. Fig. 3 is an X-ray diffraction pattern of LTA zeolites.

Based on the XRD pattern of Fig. 3, there is a peak with high intensity at position 2θ i.e. 7.23; 10.16; 12.46; 16.09; 21.67; 23.97; 27.11; 29.93; and 34.17°. At position 2θ 12.46°, it shows the orientation of the cubic structure of the LTA zeolite [22]. Furthermore, these peaks were compared with the LTA zeolite diffraction pattern in the Collection of Simulated XRD Powder Patterns for Zeolites International Zeolite Association (IZA) data base [21] and American Society for Testing and Materials (ASTM) standard no. 39-222 [23]. There is a similarity between the peaks of the synthesized zeolite with the zeolite diffractogram in the data base. (Table 2) It can be concluded that synthesized LTA zeolite has formed. The peak at 2θ 13.79° which is a typical peak of silicon dioxide (SiO_2), indicates that there is remaining unreacted SiO_2 to form zeolites.

Characterization with FTIR spectrophotometers produced the spectrum in Fig. 4. The wave number 1640 cm^{-1} shows the peak of bending vibrations –OH from Si-OH, Al–OH, and H_2O and the peak at wave number 990 cm^{-1} is the asymmetry stretching vibrations of Al-O and Si–O [24]. The peak at wave number 561 cm^{-1}

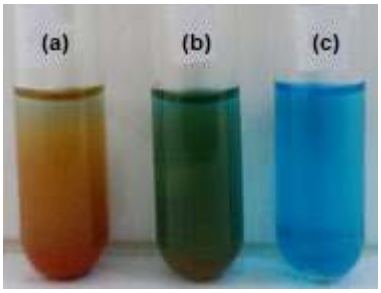

Fig 2. Benedict test on (a) glucose standard solution, (b) leached filtrate of NIZ, a (c) leached filtrate of IZ

Table 2. The data peak position of synthesized LTA zeolite and data base from IZA and ASTM

2θ (°)		
ASTM	Synthesized zeolite	IZA
7.18	7.23	7.18
10.16	10.16	10.17
12.45	12.46	12.46
-	13.79	-
16.09	16.09	16.11
21.65	21.67	21.67
23.97	23.97	23.99
27.09	27.11	27.11
29.92	29.93	29.94
34.16	34.17	34.18

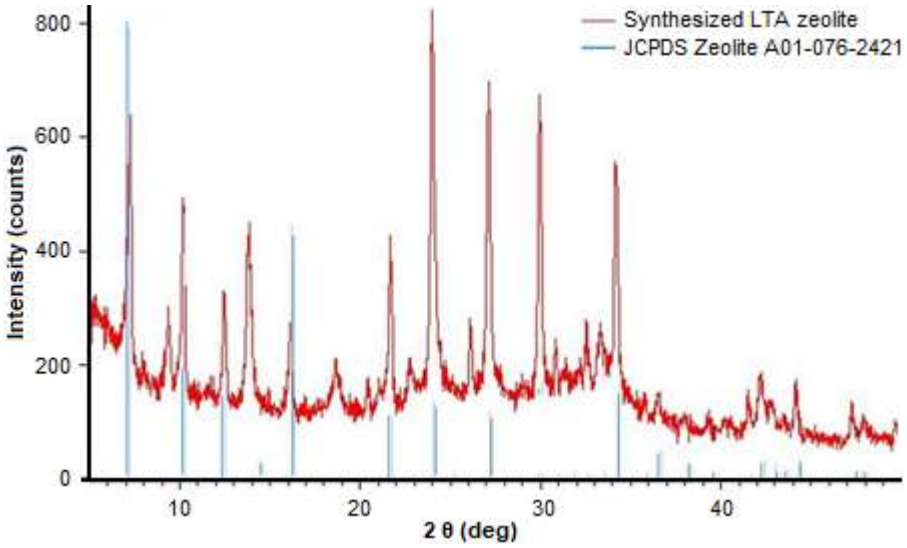

Fig 3. XRD-pattern of synthesized LTA zeolite and LTA zeolite on IZA [21]

indicates the crystallization of zeolites with a double ring [25] and the peak at wave number 440 cm^{-1} is a tetrahedral internal vibration of Si-O and Al–O [24]. The wavenumber at 3460 cm^{-1} in non imprinted zeolite spectrum is broader than the peak at zeolite or imprinted zeolite. This is due to the presence of stretching –OH from C–OH in glucose [26].

Optimization of Electrode Composition and pH Solution

The carbon paste-IZ electrodes are prepared from a mixture of activated carbon, paraffin and IZ. The presence of imprinted zeolite is expected to increase the electrode selectivity to glucose because IZ has a selective mold for glucose. The composition of activated carbon and IZ in the manufacture of electrodes may affect the performance of the electrodes, therefore the preparation of electrodes with variations in the composition of carbon and IZ were conducted. The resulted measurement range and Nernst factor from the measuring data of glucose solution using the carbon paste-IZ electrode with varies composition are shown in Table 3.

The electrode that exhibits a Nernstian graph on the electrode potential versus log [glucose] plot is the E3 (Table 3). The E3 electrodes also show good linearity in the measurement range of 10^{-4}–10^{-2} M. The carbon paste modified zeolite (EZ) and NIZ (ENIZ) were prepared by composition of activated carbon, paraffin and zeolite or NIZ similar to the composition of the E3 electrode to determine the effect of glucose mold on the electrode performance. NIZ-modified electrodes produce curves close to Nernstian, while zeolite-modified electrodes show the shape of sub-Nernstian curves. It is suspected that the presence of glucose molecules in NIZ enhances the electrodes to recognize free glucose molecules in solution. Thus, ENIZ functions like an ion selective electrode in recognizing glucose molecule.

The IZ modified electrode with the best performance was then used to measure the glucose solutions 10^{-8}–10^{-1} M at pH 4, 5, 6, 7, and 8. Measurement data was used to create a graph of log [glucose] versus

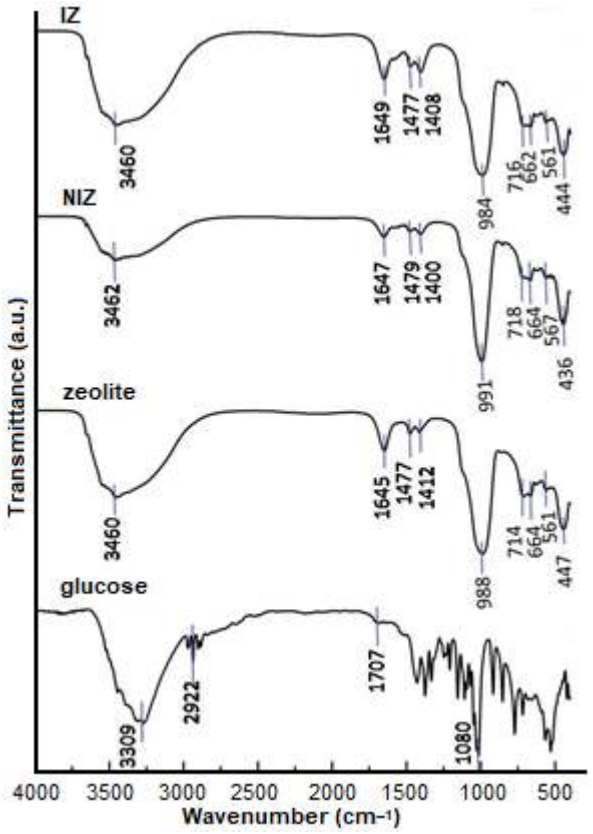

Fig 4. FTIR spectra of glucose, zeolite LTA, NIZ, and IZ

Table 3. Value of the electrode measurement range, Nernst factor and linearity of calibration graph in the glucose measurement (without pH adjustment)

Electrode	Nernst factor (mV/decade)	Linear measurement range (M)	Linearity (R^2)
E1	27.79	10^{-4}–10^{-2}	0.9549
E2	27.71	10^{-4}–10^{-2}	0.9512
E3	29.55	10^{-4}–10^{-2}	0.9924
E4	24.55	10^{-4}–10^{-2}	0.9434
E5	16.16	10^{-4}–10^{-2}	0.9604
EZ*	13.50	10^{-4}–10^{-2}	0.9720
ENIZ*	27.35	10^{-4}–10^{-2}	0.9147

*) similar composition with E3

electrode potential (Fig. 5) and determined the measurement range, linearity and the Nernst factor (Table 4).

Fig. 5 explained that the best performance of E3 is shown in the measurement of glucose solution without adjusting pH (pH 6). From these measurements obtained linear and Nernstian curve with the equation of y = 29.55x + 175.52 in the concentration range of 10^{-4}–10^{-2} M and non-linear curve with the equation of y = $-0.1x^2$–3.18 + 38.43. Based on the intersection of both lines, the detection limit value obtained was 5.62×10^{-5} M. The value is lower than the detection limit of the conductive polymer-based sensors developed previously [8]. Table 5 displayed the comparison data of the limit of detection (LOD) of our work with the previously reports.

With this low detection limit, carbon paste-IZ electrodes can be used for glucose analysis with concentrations up to 100 times lower than normal concentrations in the blood [2]. The linear curve describes the linear measurement range of the potentiometric method using the developed electrodes, which is 10^{-4}–10^{-2} M with a Nernst factor of 29.55 mV/decade. It shows that glucose has two valency molecules. This result is in agreement with the research report of [31] which fabricated the potentiometric glucose sensor based on glucose oxidase immobilized iron ferrite magnetic particle/chitosan composite modified gold coated glass electrode. They resulted in the Nernst factor of glucose about 27.3 mV/decade. A similar result also reported by [32] which stated glucose is a divalent molecule in the analysis of glucose using the voltammetry method. The valency of the molecule is constant in both analyses using potentiometry and voltammetry. The comparison of potentiometry and voltammetry method in the Ca^{2+} sensor is used as an analogue approach, whereas both of the methods found a similar Nernst factor value [33-34].

Table 4. Data of electrode measurement range, Nernst factor, and linearity on varies pH of glucose solution

pH	Measurement range (M)	Nernst factor (mV/decade)	Linearity (R^2)
4	10^{-3}–10^{-1}	1.40	0.8547
5	10^{-7}–10^{-4}	2.49	0.9208
6	10^{-6}–10^{-4}	1.25	0.9868
6*	10^{-4}–10^{-2}	29.55	0.9924
7	10^{-4}–10^{-1}	3.02	0.8341
8	10^{-6}–10^{-4}	3.35	0.9964

*) pH of glucose solution without pH adjustment

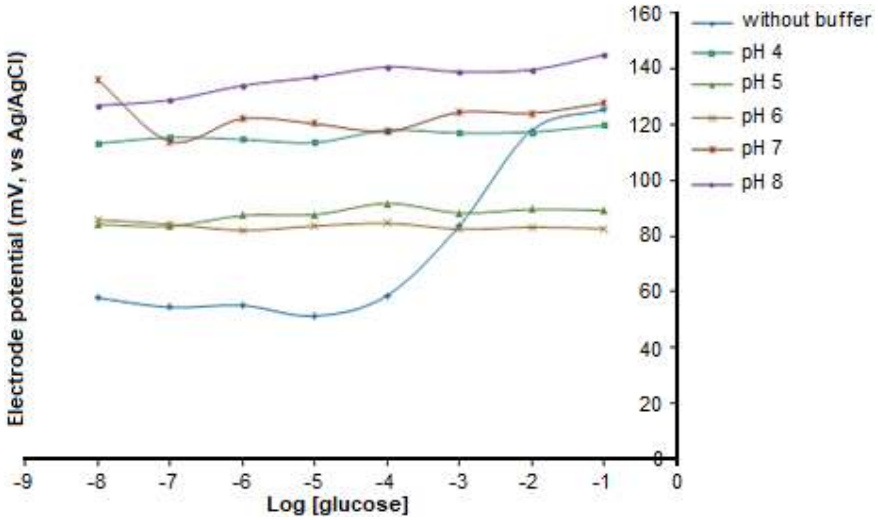

Fig 5. The plot of log [glucose] and electrode potential on varies pH

Table 5. The comparison data of the LOD of our work with the previously reports

Method	The material of the electrode	Linear range	LOD	Reference
Amperometry	Carbon paste/GOx silica	5×10^{-4}–9×10^{-3} M	1.5×10^{-4} M	[27]
Amperometry	Carbon paste/selenium nanoparticle-mesoporous silica composite (MCM-41)	1×10^{-5}–2×10^{-3} M	1×10^{-4} M	[28]
Potentiometry	Poly (3-aminophenyl boronic acid-co-3-octylthiophene)	5×10^{-3}–5×10^{-2} M	5×10^{-4} M	[8]
Potentiometry	Poly (terthiophene benzoic acid) (pTBA) layered-AuZn alloy oxide (AuZnOx)	1.6×10^{-3}–2.7×10^{-2} M	9.6×10^{-4} M	[29]
Potentiometry	Carbon nanotube on gold printed	10^{-3}–10^{-1} M	1×10^{-4} M	[30]
Potentiometry	Carbon paste/IZ	10^{-4}–10^{-2} M	5.6×10^{-5} M	This work

The coefficient of variation (CV) in the linear range is 0.42–2.20%. This value is within the limit of the CV value required by the Association of Analytical Chemist (AOAC) which is 5.3% for concentrations less than 10^{-2} M [35].

The Selectivity of the Electrode

Electrode selectivity to glucose molecules is expressed by the value of the selectivity coefficient (K_{ij}). This value is calculated using the matched potential method (MPM) [16]. Determination of K_{ij} is begun by measuring separately the glucose, ascorbic acid, uric acid, creatinine and urea solution with a concentration range of 10^{-4}–10^{-2} M using bare carbon paste and carbon paste-IZ electrode, then the selectivity coefficient value of each electrode is determined. The K_{ij} values of bare carbon paste and carbon paste-IZ electrode are shown in Table 6.

Data on Table 6 illustrates that the presence of ascorbic acid, uric acid, creatinine or urea did not interfere with glucose potentiometric analysis using imprinted zeolite modified carbon paste electrodes, while the bare carbon paste electrodes are disturbed by these components. It explains that the modification of electrodes using imprinted zeolite can increase electrode selectivity, due to the presence of specific molds for glucose molecules in the zeolite. The selectivity of carbon paste-IZ electrode is as good as the zeolite-based electrodes developed previously [11-12,36].

Method Comparison Test and Recovery

The stability of electrode was studied using a comparison test of the results of the analysis with the potentiometric method using a carbon paste-IZ electrode with a spectrophotometric method which is

Table 6. Data of K_{ij} value of bare carbon paste electrode and carbon paste-IZ electrode

Solution	Concentration (M)	Selectivity coefficient (K_{ij})	
		Bare carbon paste	Carbon paste-IZ
Ascorbic acid	10^{-4}	1.66	3.24×10^{-3}
	10^{-3}	2.59	3.48×10^{-3}
	0^{-2}	3.67	3.79×10^{-3}
Uric acid	10^{-4}	1.98	2.27×10^{-3}
	10^{-3}	2.70	2.64×10^{-3}
	10^{-2}	4.98	3.71×10^{-3}
Creatinine	10^{-4}	2.21	1.62×10^{-2}
	10^{-3}	3.01	1.77×10^{-2}
	10^{-2}	4.76	1.94×10^{-2}
Urea	10^{-4}	2.21	5.21×10^{-3}
	10^{-3}	3.19	6.25×10^{-3}
	10^{-2}	4.68	9.37×10^{-3}

Table 7. Data of accuracy and recovery value on the determination of blood serum glucose

Solution	Glucose concentration (M)		Accuracy (%)	Recovery (%)
	Potentiometry	Spectrophotometry*)		
Glucose 10^{-3} M	8.38×10^{-4}	-	-	-
Serum sample 1	4.19×10^{-3}	4.55×10^{-3}	92.02	-
Serum sample 1 + Glucose 10^{-3} M	4.97×10^{-3}	-	-	93.4
Serum sample 2	4.18×10^{-3}	4.72×10^{-3}	88.60	-
Serum sample2 + Glucose 10^{-3} M	4.94×10^{-3}	-	-	90.3
Serum sample 3	5.85×10^{-3}	6.38×10^{-3}	91.70	-
Serum sample 3 + Glucose 10^{-3} M	6.66×10^{-3}	-	-	92.5
Serum sample 4	8.11×10^{-3}	8.89×10^{-3}	91.20	-
Serum sample 4 + Glucose 10^{-3} M	8.89×10^{-3}	-	-	93.10
Serum sample 5	11.09×10^{-3}	12.22×10^{-3}	90.72	-
Serum sample 5 + Glucose 10^{-3} M	11.86×10^{-3}	-	-	92.18

*) data from clinical laboratory

standard method for determining blood glucose levels in the medical field. Sampling and handling of blood samples were carried out by a clinical laboratory in Surabaya. The recovery test is carried out to determine the influence of the matrix in the serum sample through standard addition techniques. Data on the accuracy and recovery resulted in blood glucose analysis are shown in Table 7.

Based on Table 7, the accuracy value obtained from the analysis of blood serum samples in this study is the range of accuracy received for a chemical analysis method according to AOAC, which is 80–110% [35]. This shows that the potentiometric method to analyze glucose in serum using the developed electrodes give in good agreement results from spectrophotometric method. Recovery value in this study illustrates that there are other components contained in serum samples that interfere with glucose analysis such as fructose, sucrose, maltose [37] and ions such as Na^+, Cl^-, K^+, PO_4^{3-}, SO_4^{2-}, NH_4^+ [38]. However, based on the obtained recovery value, the developed potentiometric method fulfill the requirements as a chemical analysis method. Thus, the developed method can be used as an alternative method for determining blood glucose levels in the medical field.

■ CONCLUSION

The carbon paste-IZ electrodes for potentiometric glucose analysis showed a measurement range of 10^{-4}–10^{-2} M, Nernst factor 29.55 mV/decade, and able to detect concentrations up to 100 times lower than normal concentrations of glucose in the blood serum. The electrode exhibited fast response and high selectivity against glucose molecules in solutions containing ascorbic acid, uric acid, creatinine, or urea. Potentiometry using developed electrodes shows high accuracy toward spectrophotometry as a standard method for blood glucose analysis in the medical field. Based on its performance, the potentiometric method using carbon paste-IZ electrodes is recommended as an alternative method for the analysis of blood glucose levels in the medical field.

■ ACKNOWLEDGMENTS

The authors thank the Ministry of Research, Technology and Higher Education, Indonesia for the financial support of this study through PDUPT Grant No. 713/UN3.14/LT/2019 Universitas Airlangga and for the Chemistry Department Universitas Airlangga for the laboratory facilities provided.

■ REFERENCES

[1] Tonyushkina, K., and Nichols, J.H., 2009, Glucose meters: A review of technical challenges to obtaining accurate results, *J. Diabetes Sci. Technol.*, 4 (3), 971–980.

[2] Kee, J.L., Hayes, E.R., and McCuistion, L.E., 2015, *Pharmacology: A Patient Centered Nursing Process Approach*, 8th Ed., Elsevier Saunders, St. Louis.

[3] Bishop, D.K., La Belle, J.T., Vossler, S.R., Patel, D.R., and Cook, C.B., 2010, A disposable tear

glucose biosensor-Part 1: Design and concept testing, *J. Diabetes Sci. Technol.*, 4 (2), 299-306.

[4] Yoo, E.H., and Lee, S.Y., 2010, Glucose biosensors: An overview of use in clinical practice, *Sensors*, 10 (5), 4558–4576.

[5] Galant, A.L., Kaufman, R.C., and Wilson, J.D., 2015, Glucose: Detection and analysis, *Food Chem.*, 188, 149–160.

[6] Odden, J., 2011, Determination of D-glucose in human blood serum using HPLC-PED, *Concordia Coll. J. Anal. Chem.*, 2, 58–66.

[7] Kamal, A.M., and Klein, P., 2011, Determination of sugar in honey by liquid chromatography, biomedical, and applied sciences, *Saudi J. Biol. Sci.*, 18 (1), 17–21.

[8] Çiftçi, H., Tamer, U., Teker, M.Ş., and Pekmez, N.Ö., 2013, An enzyme free potentiometric detection of glucose based on a conducting polymer poly (3-aminophenyl boronic acid-co-3-octylthiophene), *Electrochim. Acta*, 90, 358–365.

[9] Khasanah, M., Harsini, M., and Widati, A.A., 2013, Imprinting zeolite-modified glassy carbon as a voltammetric sensor for uric acid, *Indones. J. Chem.*, 13 (2), 108–113.

[10] Heidari, Z., and Masrournia, M., 2018, A novel modified carbon paste electrode for the determination of chromium(III) in water, *J. Anal. Chem.*, 78 (8), 824–831.

[11] Khasanah, M., Handajani, U.S., Widati, A.A., Abdulloh, A., and Rindarti, R.R., 2018, Construction and performance of creatinine selective electrode based on carbon paste-imprinting zeolite, *Anal. Bioanal. Electrochem.*, 10 (4), 429–438.

[12] Athiroh, A., Fadillah, T., Damayanti, D.F., Abdulloh, A., Widati, A.A., and Khasanah, M., 2019, Carbon paste electrode modified imprinted zeolite as a selective sensor for creatine analysis by potentiometry, *IOP Conf. Ser.: Earth Environ. Sci.*, 217, 012003.

[13] Rahmadhani, S., Setiyanto, H., and Zulfikar, M.A., 2018, Fabrication of carbon paste electrode modified with phenol imprinted polyaniline as a sensor for phenol analysis by potentiometric, *Mater. Sci. Forum*, 936, 71–76.

[14] Jiang, L.C., and Zhang, W.D., 2010, A highly sensitive non-enzymatic glucose sensor based on CuO nanoparticles-modified carbon nanotube electrode, *Biosens. Bioelectron.*, 25 (6), 1402–1407.

[15] Pera-Titus, M., Bausach, M., Lorens, J., and Cunnil, F., 2008, Preparation of inner-side tubular zeolite NaA membranes in a continuous flow system, *Sep. Purif. Technol.*, 59 (2), 141–150.

[16] Tohda, K., Dragoe, D., Shibata, M., and Umezawa, Y., 2001, Studies on matched potential method for determining selectivity coefficients of ion-selective electrode based on neutral ionophores: Experimental and theoretical verification, *Anal. Sci.*, 17 (6), 733–743.

[17] Baerlocher, C.H., McCusker, L.B., and Olson, D.H., 2007, *Atlas of Zeolite Framework Types*, 6th Ed., Elsevier Science, Amsterdam.

[18] Houssin, C.J.Y., 2003, Nanoparticles in Zeolite Synthesis, *Dissertation*, Technische Universiteit Eindhoven, Netherlands.

[19] Smitha, S., Shajesh, P., Aravind, P.R., Kumar, S.R., Pillai, P.K., and Warrier, K.G.K., 2006, Effect aging time and concentration of aging solution on the porosity characteristic of subcritically dried silica aerogels, *Microporous Mesoporous Mater.*, 91 (1-3), 286–292.

[20] Cundy, C.S., and Cox, P.A., 2005, The hydrothermal synthesis of zeolites: Precursors, intermediates and reaction mechanism-review, *Microporous Mesoporous Mater.*, 82 (1-2), 1–78.

[21] Treacy, M.M.J., and Higgins, J.B., 2001, *Collection of Simulated XRD Powder Patterns for Zeolites*, 4th Ed., Elsevier Science, Amsterdam.

[22] Huang, A., Wang, N., and Caro, J., 2012, Synthesis of multi-layer zeolite LTA membranes with enhanced gas separation performance by using 3-aminopropyl triethoxysilane as interlayer, *Microporous Mesoporous Mater.*, 164, 294–301.

[23] Selim, M.M., and Abd El-Maksoud, I.H., 2004, Hydrogenation of edible oil over zeolite prepared

from local kaolin, *Microporous Mesoporous Mater.*, 74 (1-3), 79–85.

[24] Rios, C.A., Wiliams, C.D., and Fulen, M.A., 2009, Nucleation and growth history of zeolite LTA synthesized from kaolinite by two different methods, *Appl. Clay Sci.*, 42 (3-4), 446–454.

[25] Alkan, M., Hopa, C., Yilmaz, Z., and Guler, H., 2005, The effect of alkali concentration and solid/liquid ratio on the hydrothermal synthesis of zeolite NaA from natural kaolinite, *Microporous Mesoporous Mater.*, 86 (1-3), 176–184.

[26] Silverstein, R.M., Webster, F.X., and Kiemle, D.J., 2005, *Spectrometric Identification of Organic Compounds*, 7th Ed., John Wiley & Sons, New York.

[27] Jedrzak, A., Rębiś, T., Klapiszewski, L., Zdarta, J., Milczarek, G., and Jesionowski, T., 2018, Carbon paste electrode based on functional GOx/silica-lignin system to prepare an amperometric glucose biosensor, *Sens. Actuators, B*, 256, 176–185.

[28] Yusan, S., Rahman, M.M., Mohamad, N., Arrif, T.M., Latif, A.Z.A., Mohd Aznan, M.A., and Wan Nik, W.S.B., 2018, Development of an amperometric glucose biosensor based on the immobilization of glucose oxidase on the Se-MCM-41 mesoporous composite, *J. Anal. Methods Chem.*, 2018, 2687341.

[29] Kim, D.M., Cho, S.J., Cho, C.H., Kim, K.B., Kim, M.Y., and Shim, Y.B., 2016, Disposable all-solid-state pH and glucose sensors based on conductive polymer covered hierarchical AuZn oxide, *Biosens. Bioelectron.*, 79, 165–172.

[30] Alhans, R.A., Singh, A., Singhal, C., Narang, J., Wadhwa, S., and Mathur, A., 2018, Comparative analysis of single-walled and multi-walled carbon nanotubes for electrochemical sensing of glucose on gold printed circuit boards, *Mater. Sci. Eng., C*, 90, 273–279

[31] Khun, K., Ibupoto, Z.H., Lu, J., AlSalhi, M.S., Atif, M., Ansari, A.A., and Wilander, M., 2012, Potentiometric glucose sensor based on the glucose oxidase immobilized iron ferrite magnetic particle/chitosan composite modified gold coated glass electrode, *Sens. Actuators, B*, 173, 698–703.

[32] Park, S., Boo, H., and Chung, T.D., 2006, Electrochemical non-enzymatic glucose sensors, *Anal. Chim. Acta*, 556 (1), 46–57.

[33] Mousavi, M.P.S., Ainla, A., Tan, E.K.W., Abd El-Rahman, M.K., Yoshida, Y., Yuan, L., Sigurslid, H.H., Arkan, N., Yip, M.C., Abrahamson, C.K., Homer-Vanniasinkam, S., and Whitesides, G.M., 2018, Ion sensing with thread-based potentiometric electrodes, *Lab Chip*, 18 (15), 2279–2290.

[34] Zhang, J., Harris, A.R., Cattral, R.W., and Bond, A.M., 2010, Voltammetric ion-selective electrodes for the selective determination of cations and anions, *Anal. Chem.*, 82 (5), 1624–1633.

[35] Taverniers, I., De Loose, M., and Van Bockstaele, E., 2004, Trends in quality in the analytical laboratory. II. Analytical method validation and quality assurance, *TrAC, Trends Anal. Chem.*, 23 (8), 535–552.

[36] Khasanah, M., Harsini, M., Widati, A.A., and Ibrani, P.M., 2017, The influence of ascorbic acid, creatine, and creatinine on the uric acid analysis by potentiometry using a carbon paste modified imprinting zeolite electrode, *J. Chem. Technol. Metall.*, 52 (6, 1039 –1044.

[37] Amani-Beni, Z., and Nezamzadeh-Ejhieh, A., 2017, A novel non-enzymatic glucose sensor based on the modification of carbon paste electrode with CuO nanoflower: Designing the experiments by response surface methodology (RSM), *J. Colloid Interface Sci.*, 504, 186–196.

[38] Guyton, A.C., and Hall, J.E., 2006, *Textbook of Medical Physiology*, 11th Ed., Elsevier, Philadelphia.

Synthesis, Characterization and Biological Efficacies from Some New Dinuclear Metal Complexes for Base 3-(3,4-Dihydroxy-phenyl)-2-[(2-hydroxy-3-methylperoxy-benzylidene)-amino]-2-methyl Propionic Acid

Shatha Mohammed Hassan Obaid[1], Jasim Shihab Sultan[1], Abbas Ali Salih Al-Hamdani[2,*]

[1]*Department of Chemistry, College of Education for Pure Science – Ibn Al-Haitham, University of Baghdad, Iraq*

[2]*Department of Chemistry, College of Science for Women, University of Baghdad, Baghdad, Iraq*

* ***Corresponding author:***

email: Abbas_alhamadani@yahoo.co.uk

Received: September 20, 2019
Accepted: January 20, 2020

DOI: 10.22146/ijc.49842

Abstract: *The reaction of methyldopa with o-vanillin in refluxing ethanol afforded Schiff base and characterized through physical analysis with a number of spectra also the study of biological activity. The geometry of the Schiff base was identified through using (C.H.N) analysis, Mass, ^{1}H-NMR, FT-IR, UV-Vis spectroscopy. Metal complexes of Cr^{3+}, Mn^{2+}, Co^{2+}, Ni^{2+}, Cu^{2+}, Zn^{2+}, Cd^{2+} and Hg^{2+} with Schiff base have been prepared in the molar ratio 2:1 (Metal:L), (L = Schiff base ligand) except Hg^{2+} at molar ratio 1:1 (Hg:L). The prepared complexes were characterized by using Mass, FT-IR and UV-Vis spectral studies, on other than magnetic properties and flame atomic absorption, conductivity measurements. According to the results a dinuclear octahedral geometry has been suggested for Cr^{3+}, Mn^{2+}, Co^{2+}, Ni^{2+}, Cu^{2+} and Zn^{2+} complexes, dinuclear tetrahedral for Cd^{2+} and mononuclear tetrahedral for Hg^{2+} complex. This work highlights the relevance of metal complexation strategy to stabilize the ligands and improve their bioactivity. Schiff base complexes have been screen for their antibacterial activity against Gram negative and positive bacteria and antifungal activity showing promising antibacterial and biological activity.*

Keywords: *methyldopa; o-vanillin; Schiff base complexes; spectral studies; biological efficacy*

■ INTRODUCTION

Schiff bases a special class of organic ligands with a variety of donor atoms revealing interesting coordination modes towards numerous metals [1-2]. These are the condensation product of an active carbonyl group acting as an electrophile and an amino group as a nucleophile. Due to their structural varieties and unique characteristics, these are the most versatile studied ligands in coordination chemistry. Among the Schiff base derivatives, those having phenol moiety have attracted considerable attention due to their wide range of biological activities Metal complexes such as Zn, Cd, Co, Ni, Pd, Ag, and Hg have different biological activities such as antimicrobial [3-4], antifungal [5-7], antioxidant [5,8] and anticancer [9-12]. These type complexes have also many different properties such as catalytic activity, porosity, magnetism, and conductivity [13-14]. C–C and C–N cross-coupling reactions are very important for natural products, drug design and industrial starting materials. For this reason, it is an important reaction group for organic chemistry. Among the Schiff base derivatives, those having carbonyl and phenol groups' moiety have attracted considerable attention due to their wide range of biological activities [15-16]. Methyldopa (M-dopa), the L-isomer of alpha-methyldopa, is levo-3-(3,4-dihydroxyphenyl)-2-methylalanine. Its empirical methyldopa is used in the clinical treatment of the following disorders: hypertension (or high blood pressure) gestational hypertension (or pregnancy-induced hypertension). Aldomet (L-methyldopa) is an antihypertensive drug and is an aromatic amino-acid de carboxyl's inhibitor in animals and man. A literature survey revealed that a little work has been reported on

metal complexes of Schiff bases derived from methyldopa derivative [17], Schiff bases derived from *o*-vanillin are well known for their interesting ligational properties and exclusive applications in different fields. The interaction of these donor ligands and metal ions gives complexes of different geometries, and a literature survey reveals that these complexes are potentially more biologically active. Thus, in recent years Schiff bases and their metal complexes have attained much attraction because of their extensive biological activities [18-19]. The authors reported the catalytic effects of the Schiff base. The present paper aims to prepare, characterize the chemical structure and to study the antibacterial activity and antifungal from Schiff base ligand prepared which is derived from methyldopa as well as *o*-vanillin and its metal complexes with Cr^{3+}, Mn^{2+}, Co^{2+}, Ni^{2+}, Cu^{2+}, Zn^{2+}, Cd^{2+} and Hg^{2+} are being reported.

■ EXPERIMENTAL SECTION

Materials

All the reagents used for the synthesis of methyldopa (Sigma-Aldrich), *o*-vanillin (Fluka), solvents such as aceton, chloroform as well benzene (Merck), but dimethyl sulfoxide also dimethylformamide (BDH), and inorganic salts such as $CrCl_3{\cdot}6H_2O$, $MnCl_2{\cdot}4H_2O$, $NiCl_2{\cdot}6H_2O$, $CuCl_2{\cdot}H_2O$ also $HgCl_2$ (Merck), $CoCl_2{\cdot}6H_2O$ (Riedial-Dehaen), $ZnCl_2$ (Aldrih) as well as $CdCl_2{\cdot}H_2O$ (Fluka) and were used as supplied.

Instrumentation

Melting points of the Schiff base ligand and all its metal complexes were determined by using Stuart Melting Point Apparatus. Metal contents to all compounds have been determined by using atomic absorption technicality by AA–680 Shimadzu. The conductometric measurements of the Schiff base ligand and metal complexes were carried out in DMSO solution using CON 510 Conductivity at room temperature. Vibrational spectra were recorded to the Schiff base ligand and all complexes using KBr pellets on FT-IR-600 FT-IR Spectrophotometer, in the region 4000–400 cm^{-1} range. ^{1}H-NMR for Schiff base ligand was registered on by NMR Bruker 400 MHz at DMSO-d_6 for TMS as the inner standard. Mass spectra to Schiff base ligand as well all its compounds have been registered by MS Model 5973 Network Mass Selection Technology (HP) with Triple–Axis Detector by the analyzer Quadrupole at 230 °C. Electronic spectral studies were performed on using Shimadzu-U.V-160 to the Schiff base ligand and its metal complexes as well as metal(II) complexes at DMSO (10^{-3} M) in the range (200–1100) nm. Magnetic susceptibility for prepared metal(II) complexes was measured on Auto Magnetic Susceptibility Balance Sherwood Scientific. In the chloride test with each complex (5×10^{-2} g) has been washed using concentrated nitric acid and diluted with water. To the resultant solution from the complexes, an aqueous solution of silver nitrate was added, a white precipitate of silver chloride was formed in the case of metals complexes has chloride content where as in the case of metals complexes [20], no precipitate was observed with all metal complexes.

Procedure

Prepare for Schiff base ligand [3-(3,4-dihydroxy-phenyl)-2-[(2-hydroxy-3-methylperoxy-benzylidene)-amino]-2-methyl propionic acid]

Schiff base ligand (L) has been prepared through adding 1mmol of (0.2112 g) of methyldopa (2-amino-3-(3,4-dihydroxy-phenyl)-2-methyl-propionic acid) with 25 mL) of ethanol with (1 mmol of 0.0040 g) of sodium hydroxide to the solution and was added (1 mmol, 0.1522 g) of *o*-vanillin (2-hydroxy-3-methoxy-benzaldehyde) dissolved of (25 mL) ethanol. The mixture was refluxed with stirring for (7 h). The resulting solution was evaporated to half volume and the precipitated produced was collected by filtration, washed twice with distilled water, and dried over anhydrous calcium chloride. The deep orange solid mass formed. Yield: 70%. %Calculated: C: 62.599%, H: 5.545%, N: 4.056%. Found: C: 61.511%, H: 4.056%, N: 3.609%. The condensation of methyldopa and *o*-vanillin in ethanol gives according to the following reaction in Scheme 1.

Preparation of the metal complexes

A general method has been used for prepare of all chelate complexes except the Hg^{2+} complex. A solution (0.3454 g, 1 mmol) of Schiff base ligand dissolved in (20 mL) of ethanol with (0.0040 g, 1 mmol) of sodium

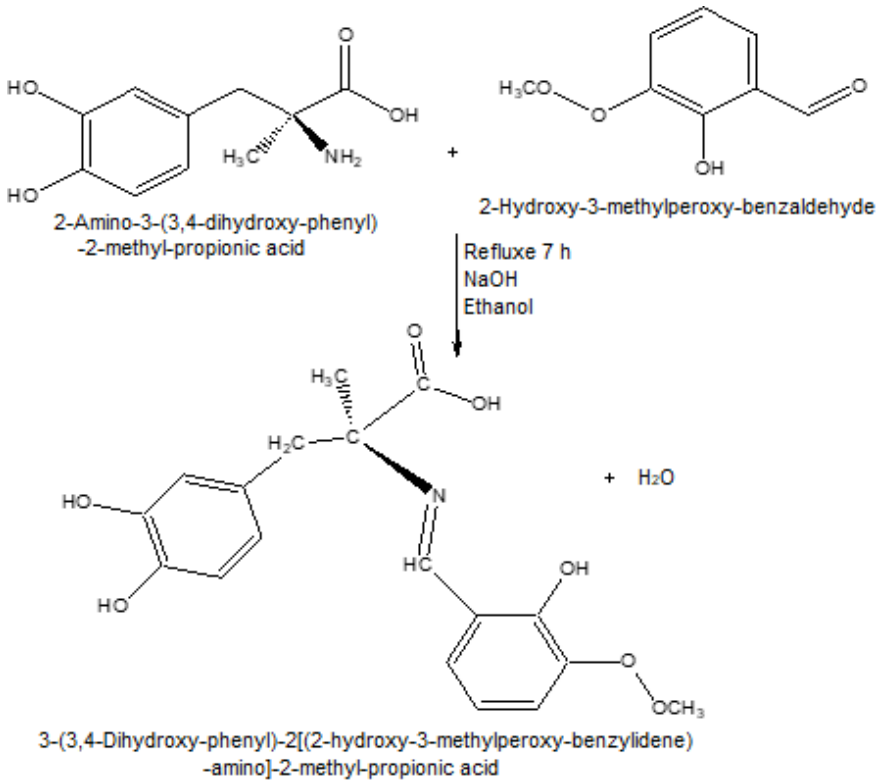

Scheme 1. Synthesis of Schiff base ligand (L)

hydroxide was added with stirring a stoichiometric amount (1:2) (ligand:metal) ratio for $CrCl_3{\cdot}6H_2O$ (0.4529 g, 2 mmol), $MnCl_2{\cdot}4H_2O$ (0.394 g, 2 mmol), $CoCl_2{\cdot}6H_2O$ (0.476 g, 2 mmol), $NiCl_2{\cdot}6H_2O$ (0.476 g, 2 mmol), $CuCl_2{\cdot}2H_2O$ (0.3410 g, 2 mmol), $ZnCl_2$ (0.372 g, 2 mmol) and $CdCl_2{\cdot}H_2O$ (0.402 g, 2 mmol). But the Hg^{2+} complex with a stoichiometric amount (1:1) (ligand:metal) ratio for $HgCl_2$ (0.2715 g, 1 mmol), dissolved with distilled water. Each mixture was refluxed for 3 h for each of the eight complexes. At room temperature on cooling, colored compounds deposited out in every case. They have been filtrated, washed for acetone as well as dried over anhydrous calcium chloride.

Biological activities

The biological activities of Schiff base ligand and its metal complexes have been studied for their antibacterial against four species of bacteria two strain from a gram positive as well two strain of a gram negative and antifungal against *Candida albicans* by diffusion method [21]. The screened compounds were dissolved individually in DMSO in order to make up a solution of 10^{-3} M concentration for each from these complexes. Discs have been placed at the exterior from agar solid nutrients dishes seeded through the examined bacteria and fungi. Diameters of inhibition zones (mm) have been measured on the end from a nursery period that was 24 h at 37 °C with bacteria and fungi.

■ RESULTS AND DISCUSSION

Elemental Analysis and Conductance Measurements

The reaction of the Schiff base ligand with the metal chloride (Cr^{3+}, Mn^{2+}, Co^{2+}, Ni^{2+}, Cu^{2+}, Zn^{2+}, Cd^{2+} as well Hg^{2+}) gave colored complexes at good yields. The analytical data along with some physical properties of the ligand and its metal complexes are summarized in Table 1. The Schiff base ligand, on interaction with Cr^{3+}, Mn^{2+}, Co^{2+}, Ni^{2+}, Cu^{2+}, Zn^{2+}, Cd^{2+}, and Hg^{2+}, yields compounds corresponding to the general formula $[M_2(L)(H_2O)_n]X_2{\cdot}H_2O$. [M = Cr^{3+}, n = 7, X = 2)], [M = (Mn^{2+}, Co^{2+}, Ni^{2+}, Cu^{2+}, Zn^{2+}), n = 7, X = 0], [M = Cd^{2+}, n = 3, X = 0] and [M = Hg^{2+}, n = 1, X = 0] Fig. 1. The analytical data show that the metal to ligand ratio of the

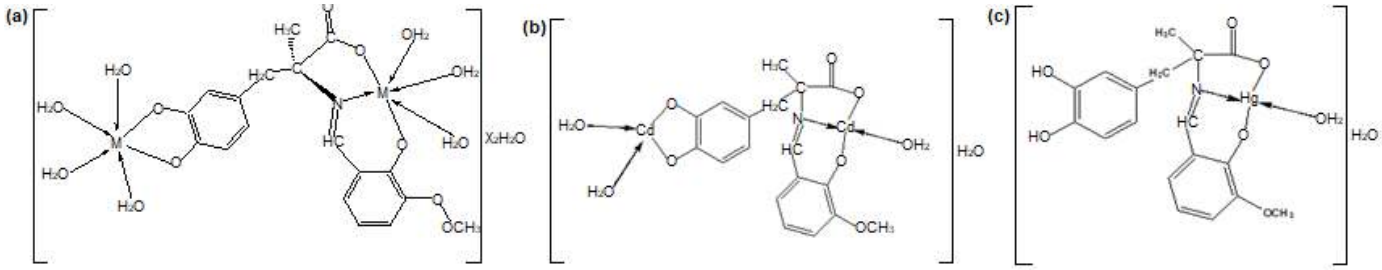

Fig 1. (a) Binuclear octahedral for Cr^{3+}, Mn^{2+}, Co^{2+}, Ni^{2+}, Cu^{2+} and Zn^{2+} complexes, (b) Binuclear tetrahedral for Cd^{2+}complex and (c) Mononuclear tetrahedral for Hg^{2+} complex

Table 1. Analytical and physical data for Schiff base ligand as well as its compounds

Compounds	MWt./g mol^{-1}	Empirical Formula	Color	MP °C	M% Calculate (Found)	Λ_m(ohm^{-1} cm^2 mol^{-1}) in DMSO, 10^{-3} M.
Schiff base ligand (L)	345.37	$C_{18}H_{19}NO_6$	Deep orange	120	-	-
$[Cr_2(L)(H_2O)_7]\cdot Cl_2H_2O$	660.27	$C_{18}H_{31}NO_{14}Cl_2Cr_2$	Deep green	> 350 dec.	15.75 (14.17)	52.30
$[Mn_2(L)(H_2O)_7]\cdot H_2O$ Valine(Val)	595.33	$C_{18}H_{31}NO_{14}Mn_2$	Deep green	> 350 dec.	18.46 (17.67)	25.64
$[Co_2(L)(H_2O)_7]\cdot H_2O$ $[Co(Ala)(Val)(H_2O)_2]H_2$	603.23	$C_{18}H_{31}NO_{14}Co_2$	Deep brown	> 350 dec.	19.54 (18.92)	27.14
$[Ni_2(L)(H_2O)_7]\cdot H_2O$	602.75	$C_{18}H_{31}NO_{14}Ni_2$	Deep brown	> 350 dec.	19.48 (18.19)	28.94
$[Cu_2(L)(H_2O)_7]\cdot H_2O$	612.46	$C_{18}H_{31}NO_{14}Cu_2$	Deep brown	> 350 dec.	20.75 (19.01)	27.14
$[Zn_2(L)(H_2O)_7]\cdot H_2O$	616.13	$C_{18}H_{31}NO_{14}Zn_2$	Pale green	> 350 dec.	21.22 (21.06)	23.44
$[Cd_2(L)(H_2O)_3]\cdot H_2O$	638.19	$C_{18}H_{25}NO_{10}Cd_2$	Pale green	> 350 dec.	35.23 (34.48)	24.04
$[Hg(L)(H_2O)]\cdot H_2O$	579.96	$C_{18}H_{21}NO_8Hg$	Pale brown	> 350 dec.	34.59 (33.73)	25.94

dec. = Decompose

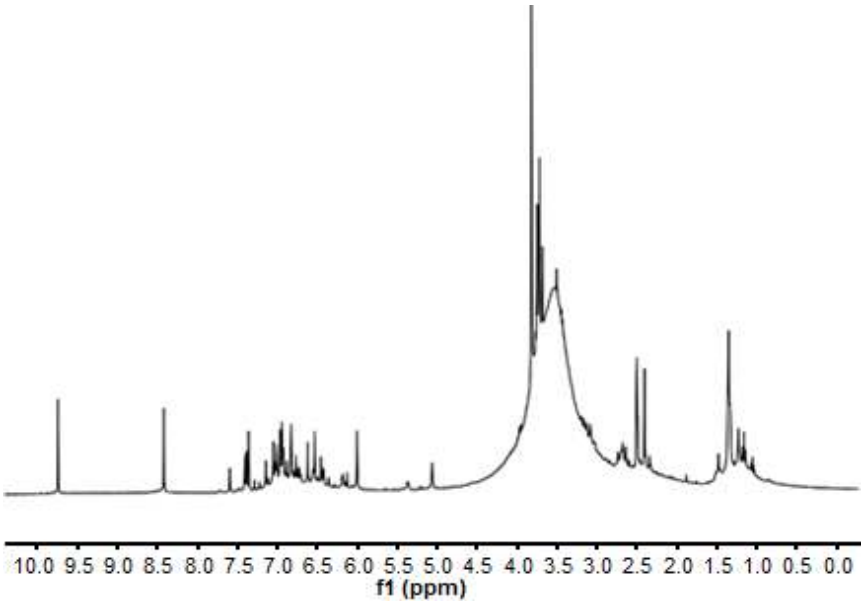

Fig 2. ^{1}H-NMR spectrum for Schiff base ligand

complexes is (2:1) except the Hg^{2+} complex is (1:1). The low molar conductance values of the complexes except the Cr^{3+} complex reveal their non-electrolytic nature [22]. All the complexes are no hygroscopic, stable, solid, stable in water except Cr^{3+} complex and at common organic solvents like acetone, chloroform, and benzene, but soluble at ethanol, methanol, DMSO and DMF.

^{1}H-NMR Spectra of the Schiff Base Ligand

^{1}H-NMR spectra for Schiff base ligand (L) at DMSO-d_6 solvent in Fig. 2, appears chemical shift at δ = 9.74 and 8.42 ppm due to –OH proton of the carboxyl and azomethane groups respectively. The spectrum displays various signals in δ = 6.00–7.58 ppm assigned into aromatic protons, the signals at δ = 5.21, 5.25 and 5.45 ppm lead to (–OH) of phenol. Resonance in δ = 2.73, 1.18, and 3.82 ppm due to protons of CH_2, CH_3 and methoxy groups sequences, the signals at δ = 2.50 ppm and δ = 3.50 indicated into DMSO-d_6 and water (H_2O) respectively [23-25].

UV-Visible Spectra and Magnetic Susceptibility Measurements

UV-Vis spectra for Schiff base ligand as well as its metal compounds dissolved at DMSO (10^{-3} M) have been obtained and listed in Table 2. The Schiff base ligand

Table 2. Electronic spectral of the Schiff base ligand and its metal complexes

Compounds	(λ nm)	ABS	w.n cm^{-1}	ϵ_{max} (L mol^1 cm^{-1})	Assignments	μ_{eff}(B.M.)	Suggested Structure
Ligand	279	1.019	35842	1019	π-π*	-	-
	342	0.486	29239	486	n-π*		
$[Cr_2(L)(H_2O)_7]\cdot Cl_2.H_2O$	276	2.202	36231	2202	L.F.	3.66	Octahedral
	364	0.947	27472	947	C.T.		
	449	0.634	22271	634	$^4A_2g \rightarrow {}^4T_1g(p)$		
	552	0.036	18115	36	$^4A_2g \rightarrow {}^4T_1g(F)$		
	670	0.028	14925	28	$^4A_2g \rightarrow {}^4T_2g(F)$		
$[Mn_2(L)(H_2O)_7]\cdot H_2O$	277	1.509	36101	1509	L.F.	6.05	Octahedral
	347	0.777	28818	777	C.T.		
	380	0.566	26315	566	C.T.		
	520	0.203	19230	203	$^6A_1g \rightarrow {}^4A_1g, {}^4Eg(G)$		
	809	0.027	12360	27	$^6A_1g \rightarrow {}^4T_2g(G)$		
					$^6A_1g \rightarrow {}^4T_1g(G)$		
$[Co_2(L)(H_2O)_7]\cdot H_2O$	276	2.347	36231	2347	L-F	5.25	Octahedral
	347	1.315	28818	1315	C.T.		
	374	0.855	26737	855	C.T.		
	502	0.207	19920	207	$^4T_1g(F) \rightarrow {}^4T_1g(P)$		
	730	0.074	13698	74	$^4T_1g(F) \rightarrow {}^4A_2g$		
	988	0.052	101121	52	$^4T_1g(F) \rightarrow {}^4T_2g(F)$		
$[Ni_2(L)(H_2O)_7]\cdot H_2O$	275	1.761	36363	1761	L-F.	2.89	Octahedral
	375	0.546	26666	546	C.T.		
	575	0.112	17482	112	$^3A_2g \rightarrow {}^3T_1g(P)$		
	750	0.063	13333	63	$^3A_2g \rightarrow {}^3T_1g(F)$		
	870	0.033	11494	33	$^3A_2g \rightarrow {}^3T_2g(F)$		
$[Cu_2(L)(H_2O)_7]\cdot H_2O$	279	1.770	34842	1770	L-F.	1.73	Octahedral
	370	0.553	27027	553	C.T.		
	827	0.025	12091	25	$^2Eg \rightarrow {}^2T_2g$		
$[Zn_2(L)(H_2O)_7]\cdot H_2O$	277	1.430	36101	1430	L.F.	Dia	Octahedral
	372	0.355	26881	355	C.T.		
$[Cd_2(L)(H_2O)_3]\cdot H_2O$	277	1.430	36101	1430	L-F.	Dia	Tetrahedral
	372	0.355	26881	355	C.T.		
$[Hg(L)(H_2O)]\cdot H_2O$	271	1.635	36900	1635	L-F.	Dia	Tetrahedral
	380	0.488	26315	488	C.T.		

the spectrum shows peaks at 279 and 342 nm lead to (π–π*) and (n–π*) electronic transition [26]. The spectrum of Cr^{3+} complex display two peaks at 276 and 364 nm described to ligand felid and charge transfer respectively, other three peaks at 449, 552 and 670 nm which were assigned to electronic transition type $^4A_2g \rightarrow {}^4T_1g(p)$, $^4A_2g \rightarrow {}^4T_1g(F)$ and $^4A_2g \rightarrow {}^4T_2g(F)$ respectively, also the value of the magnetic moment at 3.66 B.M may be taken as additional evidence for octahedral geometry [27]. The spectrum of Mn^{2+} complex displays three peaks at 277, 347 and 380 nm due to the ligand field and charge transfer. Peaks at 520 and 809 nm assigned to electronic transition type $^6A_1g \rightarrow {}^4A_1g$, $^4Eg(G)$, $^6A_1g \rightarrow {}^4T_2g(G)$ and $^6A_1g \rightarrow {}^4T_1g(G)$ respectively, the magnetic moment of this complex was found at 6.05 B.M which was so close for the octahedral environment [28-29]. The spectrum of Co^{2+} complex appears three peaks at 276, 347 and 374 nm which were described to ligand field and charge transfer, peaks at 502, 730 and 988 nm due to electronic transition type $^4T_1g(F) \rightarrow {}^4T_1g(P)$, $^4T_1g(F) \rightarrow {}^4A_2g$ and $^4T_1g(F) \rightarrow {}^4T_2g(F)$ respectively, also the value of the magnetic moment at 5.25 B.M may be taken as additional evidence for octahedral geometry [30]. The Ni^{2+} complex exhibited two absorption peaks at 275 and 375 nm due to the ligand field and charge transfer. The other three peaks at 572, 750 and 870 nm have been appointed in to electronic transition type $^3A_2g \rightarrow {}^3T_1g(P)$, $^3A_2g \rightarrow {}^3T_1g(F)$ and $^3A_2g \rightarrow {}^3T_2g(F)$ respectively. The magnetic moment for this compound was found in 2.89 B.M which was very close for octahedral geometry [31]. The Cu^{2+} complex appears two peaks at 279 and 370 nm due to the ligand field as well charge transfer, whilst the third peak at 827 nm described to electronic transition type $^2Eg \rightarrow {}^2T_2g$, the magnetic moment for this compound was found at 1.73 B.M which was octahedral geometry [32]. Electronic spectra for Zn^{2+}, Cd^{2+} and Hg^{2+} compounds do display the charge transfer, as well the magnetic susceptibility offers that three compounds have diamagnetic moments because the d-d transition is not possible subsequently electronic spectra did not give any productive information, at Zn^{2+} complex this result agrees with the previous work of octahedral geometry but the Cd^{2+} as well Hg^{2+} complexes for geometry are tetrahedral [33-34].

Infrared Spectra and Mode of Bonding

FT-IR spectra of Schiff base (L) and the prepared its metal complexes have been compared, and the data was recorded in Table 3 and Fig. 3, 4 for the ligand and its metal complexes, respectively. The FT-IR spectrum of Schiff base exhibited broad bands at (3230–3350) cm^{-1}, which have been appointed to the stretching vibration of

Fig 3. IR spectrum of ligand

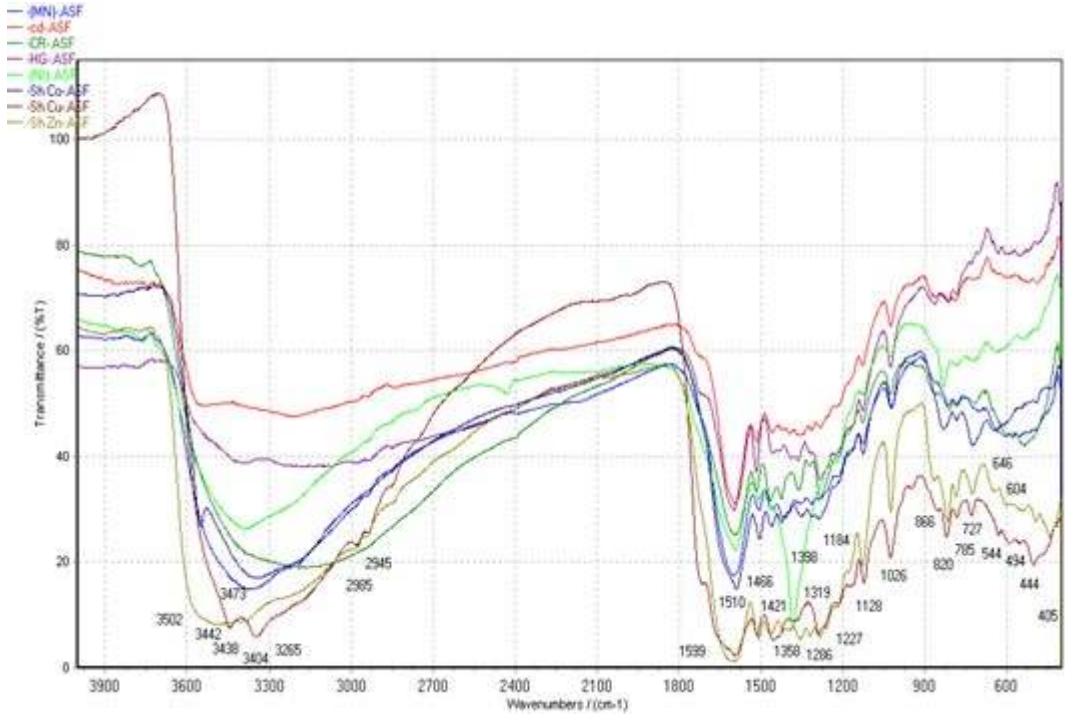

Fig 4. IR spectrum of all metal complexes

Table 3: Selected FT.IR Data (4000–400) cm^{-1} for Schiff base ligand as well its metal compounds

Compounds	υ (H_2O)hydrate and Coord.	υ (OH), υ(C=N)	$\upsilon_{asy,sy}(COO^-)$	δ(H_2O)	υ(M-N)	υ(M-O)
Schiff base (L)	-	3230-3350 br., 1674 s.	1520 sh., 1387 m.	-	-	-
$[Cr_2(L)(H_2O)_7]\cdot Cl_2H_2O$	3410 br., 3330 br.	-, 1596 s.	1518 sh., 1361 sh.	719 w.	602 w.	534 w.
$[Mn_2(L)(H_2O)_7]\cdot H_2O$	3352 br., 3372 br.	-, 1601 s.	1508 sh., 1358 m.	816 w.	609 w.	496 w.
$[Co_2(L)(H_2O)_7]\cdot H_2O$	3550 br., 3334 br.	-, 1589 s.	1504 sh., 1354 m.	727 w.	494 w.	436 w.
$[Ni_2(L)(H_2O)_7]\cdot H_2O$	3386 br., 3356 br.	-, 1593 s.	1510 sho, 1381 sh.	723 w.	544 w.	490 w.
$[Cu_2(L)(H_2O)_7]\cdot H_2O$	3442 br., 3346 br.	-, 1593 s.	1516 s., 1381 m.	731 w.	503 w.	465 w.
$[Zn_2(L)(H_2O)_7]\cdot H_2O$	3504 br., 3400 br.	-,1597 s.	1508 sh., 1358 m.	727 w.	523 w.	496 w.
$[Cd_2(L)(H_2O)_3]\cdot H_2O$	3545 br., 3360 br.	-, 1595 sh.	1516 sh., 1358 m.	708 w.	521 w.	485 w.
$[Hg(L)(H_2O)]\cdot H_2O$	3384 br., 3350 br.	3266 br., 1601 sh.	1518 sh., 1385 m.	733 w.	552 w.	486 w.

br.=broad, sh.-sharp, s.-strong, sho.=shoulder, w.=weak

υ(OH) carboxylic and phenol groups, these bands disappear in the all spectra of complexes described to coordinated these groups in coordination [35], except the Hg^{2+} complex the coordinated through the (OH) for carboxyl and phenol of *o*-vanillin. Band in (1674) cm^{-1} whom has been assigned into ν(C=N) group of Schiff

base ligand, suffered a great change to lower frequency was observed on complexation with a metal ion, lead to coordinated of this group at coordination [36].

The bands at 1520 and 1387 cm^{-1} have been appointed into stretching vibration for Schiff base ligand of ν(COO^-) asymmetric as well symmetric respectively, these bands were shifted into lower frequencies, may result to coordination with metal ions [37]. The presence of water hydrate at the scope (3352–3550) cm^{-1} and coordinated in the spectra of all complexes were suggested by the very broad absorption bands around (3330–3400) cm^{-1} and show peaks at (708–816) cm^{-1} due to stretching, rocking and wagging modes of coordination water molecules [38]. Some new bands' weak intensity observed in the regions around (436–609) cm^{-1} may be ascribed to ν(M-N) and ν(M-O) vibration respectively [39]. According to the result data the geometry has been suggested at.

Mass Spectra for Schiff Base Ligand as Well Its Metal Compounds

The mass spectra fragmentation patterns for free Schiff base (L) were in good agreement with the suggested structure in Fig. 5. The mass spectrum was characterized by an intense peak at (m/z = 345.37), which corresponding [M^+]. The mass spectra of Fig. 6 is for Co complex each

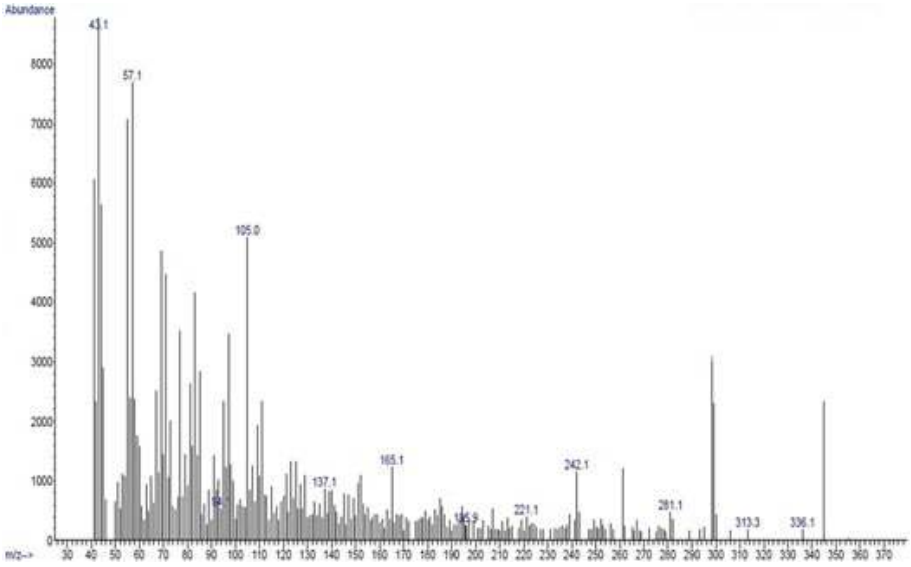

Fig 5. Mass spectral of the Schiff base

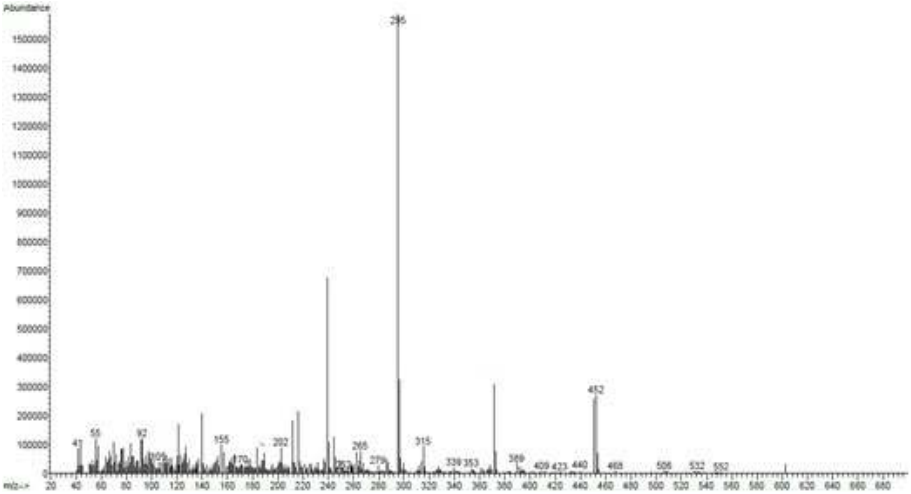

Fig 6. Mass spectral of the Co complex

spectrum of Cr^{3+}, Mn^{2+}, Co^{2+}, Ni^{2+}, Cu^{2+}, Zn^{2+}, Cd^{2+} and Hg^{2+} complexes, respectively. Displayed peaks referred in the molecular ions m/z at 660.27, 595.33, 603.23, 602.73, 612.46, 620.13, 638.19 and 579.96 M^+ into Cr^{3+}, Mn^{2+}, Co^{2+}, Ni^{2+}, Cu^{2+}, Zn^{2+}, Cd^{2+} and Hg^{2+} complexes, consecutively. That datum is at a good convention for the suggestion of molecular formulation into the complexes.

Antimicrobial Bioassay

Antibacterial and Antifungal activity of Schiff base ligand and its metal complexes were tested in vitro against bacteria such as *Steptococcus epidermidis*, *Staphylococcus aureus*, *Klebsiella sp*. and *Escherichia coli* and fungal *Candida albicans* (yeast) through paper disc plate method [40]. The compounds have been examined at condensation 10^{-3} in DMSO Shown in Table 4, Fig. 7 and Fig. 8. From Table 4, it is clear which the inhibition through metal chelates is higher than that with Cd^{2+} complex to the against bacteria *Steptococcus epidermidis*), *Staphylococcus aureus*, *Klebsiella sp.,* and *Escherichia.* Coli compared to Schiff base and other complexes and with Hg^{2+} complex to the versus fungal *Candida albicans* (yeast).

■ CONCLUSION

On the start of results got after portrayal and antibacterial, antifungal examinations clearly all the blended Schiff base metal complexes showed octahedral

Table 4. Antibacterial and antifungal activities for Schiff base ligand as well its metal compounds in the form of inhibition zone diameter (mm)

Compounds	*Steptococcus epidermidis* (G+ev)	*Staphylococcus aureus* (G+ev)	*Klebsiella sp.* (G-ev)	*Escherichia. ColiB*(G-ev)	*Candida albicans* (Yeast)
L	12	10	10	12	11
Cr-complex	-	11	-	12	-
Mn-complex	-	15	9	9	-
Co-complex	-	15	-	13	-
Ni-complex	-	-	-	11	-
Cu-complex	-	-	-	-	18
Zn-complex	12	25	14	13	22
Cd-complex	20	33	19	19	25
Hg-complex	22	30	15	21	29

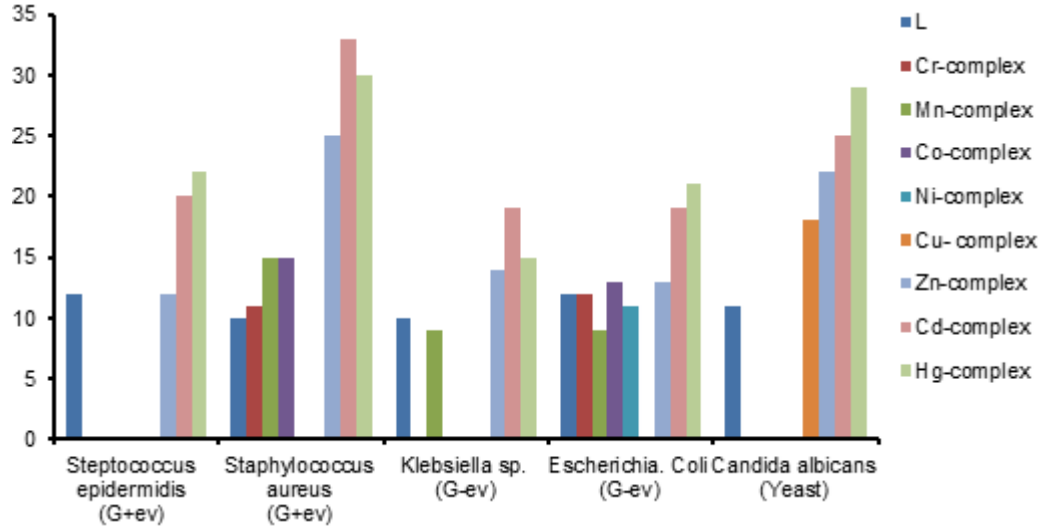

Fig 7. Results of antibacterial and antifungal screening for the Schiff base ligand and its metal compounds

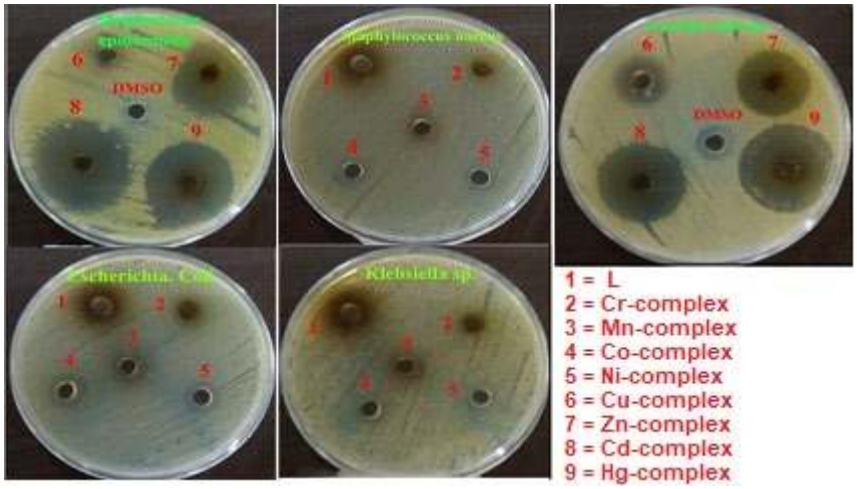

Fig 8. Antibacterial activity of investigated compounds against *Steptococcus epidermidis*, *Staphylococcus aureus*, *Klebsiella sp.* and *Escherichia coli* and antifungal activity evaluation against *Candida albicans (Yeast)* for Schiff base and its metal compounds

geometry and upgraded antibacterial, antifungal properties against chose microorganisms. These perceptions, as per diverse examinations, suggest that metal based drugs have potential as therapeutics. These preliminary outcomes, got from in vitro tries, might be enhanced by other more comprehensive studies in vivo, both in controlled conditions and in an open field for all intents and purposes assess the utilization of these complexes on the edge of biological applications.

■ REFERENCES

[1] Yousif, E., Majeed, A., Al-Sammarrae, K.., Salih, N., Salimon, J., and Abdullah, B., 2017, Metal complexes of Schiff base: Preparation, characterization and antibacterial activity, *Arabian J. Chem.*, 10 (Suppl. 2), S1639–S1644.

[2] Sarwar, A., Shamsuddin, M.B., and Lingtang, H., 2018, Synthesis, characterization and luminescence studies of metal-diimine complexes, *Mod. Chem. Appl.*, 6 (3), 1–7.

[3] Iniama, G.E., Iorkpiligh, I.T., and Alfred, A.I., 2018, Stereochemical characterization and antimicrobial activities of synthesized Ni(II), Cu(II) and Zn(II) Schiff base complexes derived from *p*-nitroaniline and salicylaldehyde, *IJST*, 6 (5), 52–56.

[4] Divya, K., Pinto, G.M., and Pint, A.F., 2017, Application of metal complexes of Schiff bases as an antimicrobial drug: A review of recent works, *Int. J. Curr. Pharm. Res.*, 9 (3), 27–30.

[5] Al Zoubi, W., Al-Hamdani, A.A.S., and Ko, Y.G., 2017, Schiff bases and their complexes: Recent progress in thermal analysis, *Sep. Sci. Technol.*, 52 (6), 1052–1069.

[6] Şabik, A.E., Karabörk, M., Ceyhan, G., Tümer, M., and Dığrak, M., 2012, Polydentate Schiff base ligands and their La(III) complexes: Synthesis, characterization, antibacterial, thermal, and electrochemical properties, *Int. J. Inorg. Chem.*, 2012, 791219.

[7] Tobriya, S.K., 2014, Biological applications of Schiff base and its metal complexes-A review, *Int. J. Sci. Res.*, 3 (9), 1254–1256.

[8] Prakash, A., and Ahmad, S., 2018, Synthesis and characterization of Schiff base complexes with Ti(III), Cr(III) and Ni(II), *Orient. J. Chem.*, 25 (4), 1035–1040.

[9] Al Zoubi, W., Al-Hamdani, A.A.S., Ahmed, S.D., and Ko, Y.G., 2018, Synthesis, characterization, and biological activity of Schiff bases metal complexes, *J. Phys. Org. Chem.*, 31 (3752), 1–13.

[10] Al-Hamdani, A.A.S., and Al Zoubi, W., 2015, New metal complexes of N_3 tridentate ligand: Synthesis, spectral studies, and biological activity, *Spectrochim. Acta, Part A*, 137, 75–89.

[11] Al-Hamdani, A.A.S., Al-Dulyme, N.K.G., Ahmed, S.D., and Basheer, H.M., 2017, Preparation, spectroscopic, bioactive and theoretical studies of mixed ligand complexes, *Al-Nahrain J. Sci.*, 20 (3), 49–59.

[12] Malik, A., Goyat, G., Vikas, K., Verma, K.K., and Garg, S., 2018, Coordination of tellurium(IV) with Schiff base derived from *o*-vanillin and 3-aminopyridine, *Int. J. Chem. Sci.*, 6 (1), 1–10.

[13] Ejidike, I.P., and Ajibade, P.A., 2015, Transition metal complexes of symmetrical and asymmetrical Schiff bases as antibacterial, antifungal, antioxidant and anticancer agents: Progress and prospects, *Rev. Inorg. Chem.*, 35 (4), 191–224.

[14] Borase, J.N., Mahale, R.G., and Rajput, S.S., 2017, Design, synthesis, and biological evaluation of a novel class of heterocyclic Schiff bases, *Eur. J. Biomed. Pharm. Sci.*, 4 (10), 842–845.

[15] Neelakantan, M.A., Esakkiammal, M., Mariappan, S.S., Dharmaraja, J., and Jeyakumarit, A., 2010, Synthesis, characterization and biocidal activities of some Schiff base metal complexes, *Indian J. Pharm. Sci.*, 72 (2), 216–222.

[16] Begum, N.T., Raju, J.A., Nageswara, R.G., and Sreeramulu, J., 2014, Spectroscopic characterization and biological evolution of ortho vanillin pramipexole Schiff base metal complexes, *Der Pharma Chem.*, 6 (2), 51–58.

[17] World Health Organization, 2013, *WHO Model List of Essential Medicines*, 18th list, October 2013, https://www.who.int/medicines/publications/essentialmedicines/en/, accessed on 22 April 2014.

[18] Jain, S., Jain, N.K., and Pitre, K.S., 2002, Electrochemical analysis of sparfloxacin in pharmaceutical formulation and biochemical screening of its Co(II) complex, *J. Pharm. Biomed. Anal.*, 29 (5), 795–801.

[19] Chandra, S., Shukla, D., and Gupta, L.K., 2008, Synthesis and spectroscopic studies of cobalt(II), nickel(II), and copper(II) complexes with N-donor (N4) macrocyclic ligand (DSLF), *J. Indian Chem. Soc.*, 85 (5), 800–806.

[20] Vogel, A.I.., 1978, *Text Book of Quantitative Inorganic Analysis*, 4th Ed., Longman, London, 694.

[21] Geary, W.J., 1971, The use of conductivity measurements in inorganic solvents for the characterization of coordination compounds, *Coord. Chem. Rev.*, 7, 81–122.

[22] Singh, B.K., Rajour, H.K., and Prakash, A., 2012, Synthesis, characterization and biological activity of transition metal complexes with Schiff bases derived from 2-nitrobenzaldehyde with glycine and methionine, *Spectrochim. Acta, Part A*, 94, 143–151.

[23] Silverstein, R.M., Webster, X.F., and Kiemle, D.J., 2005, *Spectrometric Identification of Organic Compounds*, 7th Ed., John Wiley & Son, Inc., Hoboken, New York.

[24] Khaleel, A.M.N., and Jaafar, M.I., 2017, Synthesis and characterization of boron and 2-aminophenol Schiff base ligands with their Cu(II) and Pt(IV) complexes and evaluation as antimicrobial agents, *Orient. J. Chem.*, 33 (5), 2394–2404.

[25] Al-Hamdani, A.A.S., Ahmed, S.D., Shake, S.H., and Hassan, Z.A., 2016, Synthesis and spectroscopic characterization for some metal ion complexes with 2-hydroxy-3-((5-mercapto-1,3,4-thiadiazol-2-yl)diazenyl)-1-naphthaldehyde, *Baghdad Sci. J.*, 13, 105–114.

[26] Al Zoubi, W., Al-Hamdani, A.A.S., Widiantara, I.P., Hamoodah, R.G., and Ko, Y.G., 2017, Theoretical studies and antibacterial activity for Schiff base complexes, *J. Phys. Org. Chem.*, 30 (12), e3707.

[27] Lever, A.B.P., 1968, *Inorganic Electronic Spectroscopy*, Elsevier, Amsterdam, 121.

[28] Ghanim, F.H., 2016, Synthesis, characterization and antibacterial activities of Mn(II), Fe(II), Co(II), Ni(II), Cu(II), Zn(II) and Cd(II) mixed-ligand complexes of 8-hydroxyquinoline and sulfamethoxazole, *Trans. Eng. Sci.*, 4 (2), 73–76.

[29] Shaker, S.A., Mohammed, H.A., and Al-Hamdani, A.A.S., 2010, Preparation, physico-chemical and spectroscopic investigation of thiacetazone and quinalizarin complexes with Mn(II), Fe(II), Co(II),

Ni(II), Cu(II), Zn(II), Cd(II) and Pb(II), *Aus. J. Basic Appl. Sci.*, 4 (10), 5178–5183.

[30] Raja, R., Verma, K.K., Solanki, K., and Bhojak, N., 2016, Synthesis, characterization and antimicrobial activity of cobalt(II) complexes with pyrimidine derivatives, *Res. J. Chem. Sci.*, 6 (3), 48–55.

[31] AL-Hamdani, A.A.S., and Shaker, S.A., 2011, Synthesis, characterization, structural studies, and biological activity of a new Schiff base- azo ligand and its complexation with selected metal ions, *Orient. J. Chem.*, 27 (3), 835–845.

[32] AL-Hamdani, A.A.S., Balkhi, A.M., Falah, A., and Shaker, S.A., 2015, New azo-Schiff base derived with Ni(II), Co(II), Cu(II), Pd(II) and Pt(IV) complexes: Preparation, spectroscopic investigation, structural studies, and biological activity, *J. Chil. Chem. Soc.*, 60 (1), 2774–2785.

[33] Al-Noor, T.H., Jarad, A.J., and Abo, S.B., 2015, Synthesis, spectral and antimicrobial activity of mixed ligand complexes of Co(II), Ni(II), Cu(II) and Zn(II) with 4-aminoantipyrine and tributylphosphine, *Int. J. Curr. Res.*, 7 (5), 15605–15609.

[34] Obaid, S.M.H., Al Naemi, H.A.S., Jarad, A.J., Al-Hamdani, A.A.S., and Fendi, W.J., 2017, Preparation, spectral studies and biological efficiency of metal (II) mixed ligand complexes Schiff base derived from (benzaldehyde and *o*-aminoaniline) with 8-hydroxyquinoline, *Res. J. Pharm. Biol. Chem. Sci.*, 8 (6), 179–189.

[35] Nakamoto, K., 1997, *Infrared and Raman Spectra of Inorganic and Coordination Compounds, Applications in Coordination, Organometallic, and Bioinorganic Chemistry*, 5th Ed., Wiley-Inter Science, New York.

[36] Silverstein, R.M., Bassler, G.C., and Morril, T.C., 1981, Spectroscopic Identification of Organic Compounds, 4th Ed., Wiley, New York.

[37] Obaid, S.M.H., Al Naemi, H.A.S., and Al-Hamdani, A.A.S., 2018, Synthesis, spectroscopic and antimicrobial studies of mixed ligand metal(II) complexes with three amino acids, *Res. J. Pharm. Biol. Chem. Sci.*, 9 (6), 1560–1571.

[38] Al Zoubi, W., Al-Hamdani, A.A.S., Ahmed, S.D., and Ko, Y.G., 2018, A new azo-Schiff base: Synthesis, characterization, biological activity and theoretical studies of its complexes, *Appl. Organomet. Chem.*, 32 (1), e3895.

[39] Abdulghani, A.J., and Hussain, R.K., 2018, Synthesis and characterization of Schiff base metal complexes derived from cefotaxime with 1*H*-indole-2,3-dione (Isatin) and 4-N,N-dimethyl-aminobenzaldehyde, *Open J. Inorg. Chem.*, 5 (4), 83–101.

[40] Al-Hamdani, A.A.S., Altayy, M.A.M., and Al-Dulyme, N.K.G., 2017, Synthesis, spectroscopic and theoretical studies of some new transition metal complexes with mixed ligands Schiff base and bipyridyl, *Ibn Al-Haitham J. Pure Appl. Sci.*, 30 (2), 69–83.

In-Situ Ionic Imprinted Membrane (IIM) Synthesis Based on Acetic Polyeugenoxy Acetyl Tiophen Methanolate for Gold(III) Metal Ion Transports

Muhammad Cholid Djunaidi*, Pardoyo, Didik Setiyo Widodo, Retno Ariadi Lusiana, and Anggun Yuliani

Department of Chemistry, Faculty of Science and Mathematics, Diponegoro University, Jl. Prof. Soedharto SH, Tembalang, Semarang 50275, Indonesia

* ***Corresponding author:***

tel: +62-81226328778
email: choliddjunaidi@live.undip.ac.id

Received: September 23, 2019
Accepted: February 3, 2020

DOI: 10.22146/ijc.49941

Abstract: *In this research, Polyeugenoxy Acetyl Tiophen Methanolate (PEATM)-Au ionic imprinted membrane (IIM) was synthesized. IIM is a PEATM based membrane that has Au(III) ion molds. The PEATM synthesis was analyzed using FTIR spectroscopy, and its relative molecular weight was determined by the viscometry method. To find out the presence of Au(III) templates on IIM, FTIR spectroscopy and SEM-EDX were used. The results of FTIR spectroscopy & SEM-EDX analysis prove the existence of Au(III) metal ion templates at IIM. Through FTIR spectra, it could be seen that the absorption area of the -OH group was widening. In the IIM, the CS group wave number (702.9 cm^{-1}) also shifted to a larger wavenumber (848.68 cm^{-1}), this is likely due to the presence of PEGDE as a crosslinker agent and PVA as a plasticizer on the membrane that interacts with PEATM-Au, which influences the shift of vibrational wavenumber of CS bonds. It was also found that the most effective pH of the feed phase for the transport was at pH 3, and the most optimum transport time was 24 h for IIM and 48 h for NIM. The transport of Au in binary mixture of Au/Cd, Au/Fe, and Au/Pb also proves that the presence of Au(III) ions in IIM makes IIM more selective to Au(III) metal ions than NIM when used for the transport process as it transports Au more than the other metals. These results were as expected by using the HSAB theory as its groundwork.*

Keywords: *ionic imprinted membrane; gold metal ion; transport; selectivity; binary metal ions*

■ INTRODUCTION

Gold is a precious metal that is widely applied in various fields. In the electronics field, gold is used as a coating material for electronic components because of its corrosion-resistant properties, and its conductivity is almost 100%. During this time, gold can be obtained from ore contained in nature with relatively small amounts, namely in 1 ton of gold ore, containing only about 5–30 g of gold metal [1]. Given the high demand for the gold metal, various attempts were made to find new sources of gold apart from panning for gold ore in nature. One promising source of gold is from electronic equipment waste. When compared with the concentration of gold in the ore, the concentration of gold in electronic waste is relatively higher at 200 g in each ton of electronic waste [2]. The process of recovering (recovering) gold from electronic waste is often done using hazardous materials, such as washing using cyanide salt of nitric acid and the amalgamation process using mercury (Hg) [3-4]. Besides requiring relatively high costs (for the management of secondary waste generated from the recovery process), this process is certainly dangerous. In acidic water, mercury can be converted to methyl mercury and can harm the fetus and can cause damage to the brain. Therefore, various attempts were made to find an environmentally friendly alternative method for the recovery of gold metal from electronic waste.

Supported Liquid Membrane (SLM) is one of the environmentally friendly methods that can be used for gold metal recovery from electronic waste. The

advantages of this SLM method are that it has high selectivity, a broad spectrum of separation, and is easy to do. The SLM method still has weaknesses, namely low stability against leakage of carrier compounds during the transport process, causing the source and receiver phases to mix; besides, SLM also has a short lifetime. One effort to overcome SLM weaknesses is by mixing a carrier compound with plasticizer and supporting polymer to be made into a solid membrane in the form of thin, stable, and flexible films. The separation mechanism of target compounds on this solid membrane is almost the same as the SLM method [5].

Ionic imprinted membrane (IIM) is a membrane-based on a functional polymer that has an ionic mold. The printed ion is used as a template that acts as a group to recognize the target ion. The existence of ion templates aims to make the membrane selective to the target ion when used for the transport process through a simple static adsorption mechanism of permeation [6-7]. Selectivity in transport can be achieved because during the process of removing template ions from the polymer matrix will cause the arrangement of ions printed polymer [8].

The ester derivative of the eugenol compound has been proven to be used as a liquid membrane carrier with selectivity, which can be adjusted depending on the functional group included [9]. In previous studies, esters of sulfur (E) functional group eugenol, namely thiophene-2-methyl-2-eugenoxy acetate as carrier compounds in liquid membranes for the recovery of soft metal Ag^+ (silver ions) [10]. The research is based on the theory of HSAB (Hard Soft Acid Base), so that sulfur functional groups in soft carrier compounds will bind soft metals (such as Cd^{2+}, Ag^+, and Au^{3+}) [11-10].

In this research, PEATM ionic imprinted membrane (IIM) synthesis was used using eugenol derivative polymer base, in the form of polyeugenoxy acetyl thiophene methanolate (PEATM). The PEATM IIM was applied as an Au(III) ion-selective transport membrane whose selectivity would be compared to NIM (as a control). PEATM was chosen as the base for IIM and NIM in this study due to its sulfur-containing functional group, 2-thiophenmethanol. The carrier used in this membrane was chosen according to the HSAB theory (grouping of acid-base based on hardness and softness), in which gold(III) as the targeted ion could be categorized into a soft acid metal ion that forms a stronger complex with soft base donor atoms (such as sulfur from 2-thiophenmethanol). The presence of the Au template on IIM synthesized in-situ is expected to increase membrane selectivity for the recovery of Au ions in solution. This research is the first research to use PEATM as an ionic imprinted membrane for selective transport of Au(III) known. Previous research about PEATM synthesis has been done as a new selective carrier using the bulk liquid membrane method. The PEATM was then used as a BLM carrier to separate a mixture of Cd^{2+}, Cr^{3+}, and Cu^{2+} [12]. Through this research, it is proven that PEATM-Au ionic imprinted membrane could be used to selectively remove Au(III) from its binary metal ions.

■ EXPERIMENTAL SECTION

Materials

The materials used in this research were Eugenol p.a. (Mv 169 g/mol), polyvinyl alcohol p.a. (Mv 130,000 g/mol), Na_2SO_4 p.a., Thionil chloride p.a., polyethylene glycol diglycidyl ether p.a. (Mv 500 g/mol), NMP p.a. from Sigma Aldrich, HCl p.a., Methanol p.a., NaOH p.a., $BF_3O(C_2H_5)_2$ p.a., 2-thiophenmethanol p.a., $NaHCO_3$ p.a., KCl p.a., $HAuCl_4$ p.a., $Fe(NO_3)_3$ p.a., $Pb(NO_3)_2$ p.a., $Cd(NO_3)_2$ p.a. from Merck and double-distilled water from Bratachem.

Instrumentation

The equipment used in this research were Standard research glass equipment, petri dish, analytical balance (Mettler-200), furnace, stirrer, desiccator, thickness meter, pH meter (HACH E C20), reflux apparatus, and pH indicator. AAS (Perkin Elmer Analyst 400), SEM-EDX (Phenom Pro X Desktop with EDX), and FTIR (Shimadzu Prestige 21) were used to analyze the PEATM ionic imprinted membrane.

Procedure

PEATM synthesis

PEATM was synthesized from polyeugenoxy acetic acid (POA) with 2-thiophenemethanol through an esterification reaction. A total of 3 g POA was refluxed

with 3 mL of thionyl chloride for 240 min at a temperature of 40 °C. 2 mL of 2-thiophenemethanol was then added to the mixture and reflux was continued at 40 °C for 6 h. After chilled, washing was done with chloroform and double-distilled water. The synthesized product was dried at room temperature.

Synthesis of PEATM-Au

PEATM-Au was synthesized by contacting 1 g of PEATM with 20 mL of 1000 ppm $HAuCl_4$. The contacting procedure was done by mixing the mixture for 24 h. Afterward, filtering was performed, and it was then analyzed with AAS. The sediment (PEATM-Au) was later dried and then analyzed using FTIR.

Synthesis of IIM and NIM

IIM and NIM were synthesized by in-situ method, by mixing 0.25 g PEATM-Au (for IIM synthesis) and 0.25 g PEATM (for NIM synthesis), 0.5 g PVA, 0.25 mL NaOH 0, 1 M, 0.3 mL PEGDE, and 2.5 mL NMP. The mixture was refluxed for 30 min at 90–110 °C until a hydrogel was formed. Once cooled, the gel was weighed and taken 3 g, mixed with 3 mL of NMP, then was refluxed for 30 min at a temperature of 110–130 °C. After it was homogeneous, the mixture was then poured into a mold and then heated at 80 °C until dry in the furnace. 2 M KCl was poured into the membrane mold until it was submerged and then allowed to stand for 15 min until the membrane could be removed from the mold. The membrane was washed using distilled water to remove excess KCl and was dried at room temperature afterward.

PEATM characterization

Synthesized PEATM-Au was characterized by FTIR to identify the functional group and using AAS to detect the remaining levels of Au^{3+} in the filtrate (after contacting).

Characterization of PEATM. The synthesized PEATM was FTIR to identify the functional group characterized by and molecular weight (Mv) measurement was done using the viscometry method.

Characterization of PEATM-Au. Synthesized PEATM-Au was characterized by an FTIR spectrophotometer to identify the functional group and using AAS to detect the remaining levels of Au^{3+} in the filtrate (after contacting).

Feed phase pH optimization

To determine the optimum pH of the feed phase, the transport was carried with variations of pH conditions in the feed phases, which are pH 1, 3, 5, 7, and 9. Transport was carried out for 24 h. 0.8 M thiourea was used as the transport receiving phase. The feed phase and the receiving phase after the transport were analyzed using AAS to determine the levels of Au^{3+} metals.

Transport time optimization

To determine the optimum time of the feed phase, the transport was carried out with variations in transport time of 0, 4, 8, 12, 16, 20, 24, and 48 h. Transport is carried out at the optimum pH that has been obtained. 0.8 M thiourea was used as the transport receiving phase. The feed phase and the receiving phase after transport were analyzed using AAS to determine the levels of Au^{3+} metals.

Selectivity test

Membrane selectivity (IIM and NIM) was tested through a binary metal ion transport (Au/Fe, Au/Cd, and Au/Pb). Transport is carried out at optimum time and pH conditions. 0.8 M Thiourea was used as the transport receiving phase. The feed phase and the receiving phase after transport were analyzed using AAS to determine the levels of Au^{3+} metals to prove the membrane selectivity.

■ RESULTS AND DISCUSSION

The synthesized IIM and NIM have a physical shape of a round flat sheet with a diameter of ± 4.5 cm, brownish-yellow color, an average thickness of 0.037 mm, not easily torn, and in a dry state are rigid. IIM is synthesized by an in-situ method. In-situ is a membrane synthesis method that begins with the manufacture of hydrogel polymers from a functional polymer mixture that has a metal ion template as a membrane base with cross-linker agents and solvents refluxed together until it thickens (formed sol), followed by cooling at room temperature until it forms gel solids [13].

In this study, PEATM-Au is used as a functional polymer of the Au^{3+} ion template. PVA was chosen as a polymer base membrane support and as a plasticizer because PVA is a polymer that is chemically stable,

hydrophilic, elastic, non-toxic, biodegradable, and not carcinogenic [14]. PEGDE is applied as a crosslinking agent as well as a plasticizer, which will increase the mechanical strength of the membrane. Based on previous studies, PEGDE crosslinked PVA based membranes have been shown to have good mechanical strength as indicated by the results of tensile strength tests [15-16].

Characterization of IIM FTIR

The success of the IIM synthesis was analyzed from the FTIR spectra in Fig. 1. The IIR FTIR spectra showed that the absorption area of the -OH group was widening; this indicates the increasing number of hydrogen interactions that made the vibration of the -OH group weaker [17]. In the IIM the CS group wave number (702.9 cm^{-1}) also shifted to a larger wavenumber (848.68 cm^{-1}), this is likely due to the presence of PEGDE as a crosslinker agent and PVA as a plasticizer on the membrane that experience interaction with PEATM-Au which influences the shift of vibrational wavenumber of CS bonds [17-18]. Based on the plank equation theory, which is the basis in the FTIR analysis, explains that energy is directly proportional to the wavenumber (E = h v), the greater the vibrational energy, the greater the peak of the wavenumber [19].

From the FTIR analysis data, the approximate chemical reactions that occur in IIM synthesis can be described, as shown in Fig. 2. To reassure whether the PEATM has been formed or not, ^{1}H-NMR spectroscopy could be done and is determined by the appearance of a new peak at δ 6.83–7.40 ppm (A) which indicates the presence of thiophene compounds and also at peak

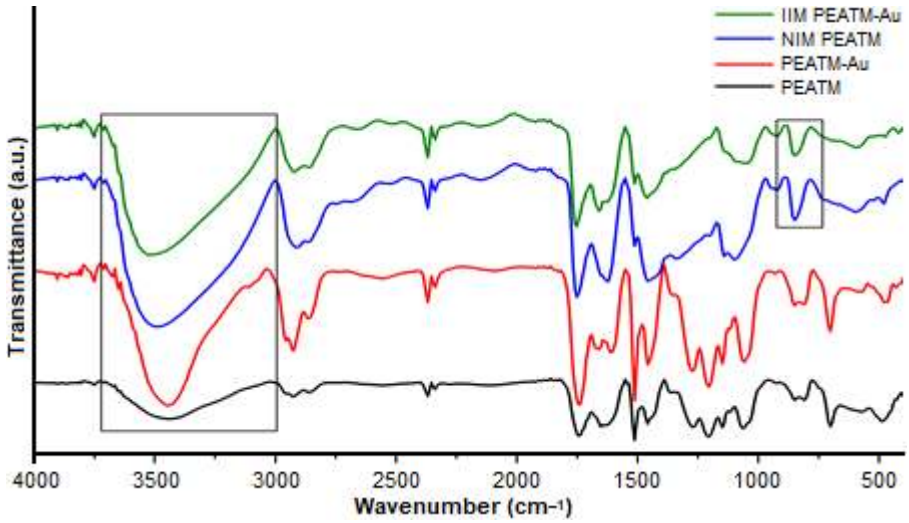

Fig 1. Comparison of IIM, NIM, PEATM-Au, and PEATM FTIR spectra

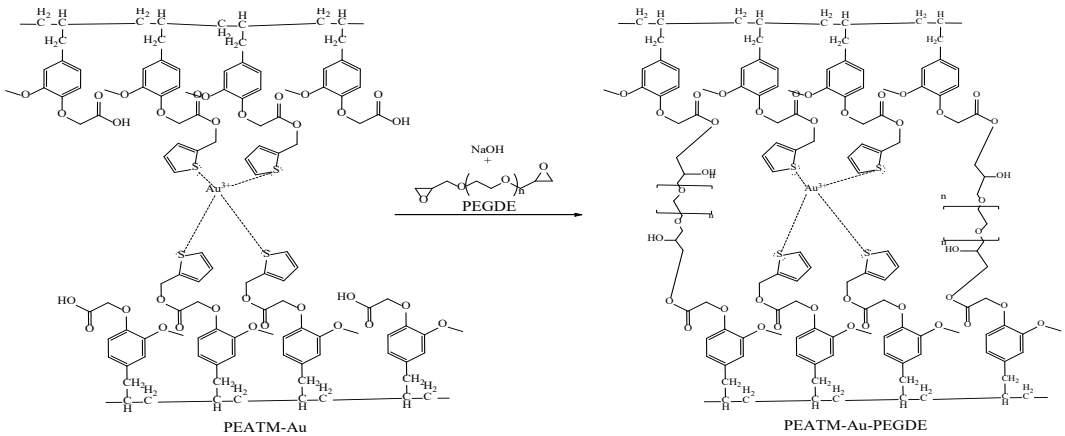

Fig 2. The estimated reaction of IIM synthesis

δ 4.46 ppm (D) and δ 4.89 ppm, which indicates the presence of a methylene (-CH2-) group [12]. PEATM molecular weight determination was also performed, and the results showed that PEATM synthesized has a molecular weight of 7333,791 g/mol with a polymerization degree of 23.

The crosslink reaction in the IIM manufacturing process here, in addition to adding polymer chains and increasing the mechanical strength of the membrane, also plays a role in locking the Au^{3+} metal ion template on the PEATM polymer, so that an appropriate imprint will be formed [16].

Analysis of SEM-EDX IIM and NIM

SEM-EDX results in Fig. 3 shows the porous membrane morphology, with an average NIM pore size of 1.80 μm and IIM of 1.29 μm. The pore size at IIM is more uniform and smaller, and this is presumably due to the influence of the printed Au metal ions on the membrane. In the state of the hydrated Au^{3+} ion species has a radius of 275 nm [20]. The presence of these Au metal ion molds is expected to increase the membrane affinity for Au^{3+} ions.

The EDX result for NIM and IIM before and after Au release could be seen in Table 1. From the EDX results obtained, the composition of elements in the membrane and its mass percent. Based on these results, since the Au on IIM before the release is 75.45% and after the release is 67.75%, it proves that the gold content (Au) on the membrane is reduced by 7.7% after removing the template.

Feed pH Optimation

The feed phase pH optimization can be determined from the transport percentage curve, as seen in Fig. 4.

The graph shows the optimum pH of transport with both IIM and NIM is pH 3. Optimization of this pH in terms of the feed phase. At pH 3, the remaining percent concentration of metal ions in the feed phase is the least when compared to pH 1, 5, 7, and 9. This proves that at pH 3, more Au^{3+} metal ions are being transported. When viewed from the receiving phase, the greater the pH, the ability to transport Au^{3+} metal ions will decrease. In a previous study, it was explained that transport to the membrane could occur if the phenolic component is in a dissociated state (the feed phase) and as a phenolate ion (the receiving phase). The acidity conditions in the feed phase affect the phenol transport process. The same thing happens with Au^{3+} ion transport. In the feed phase,

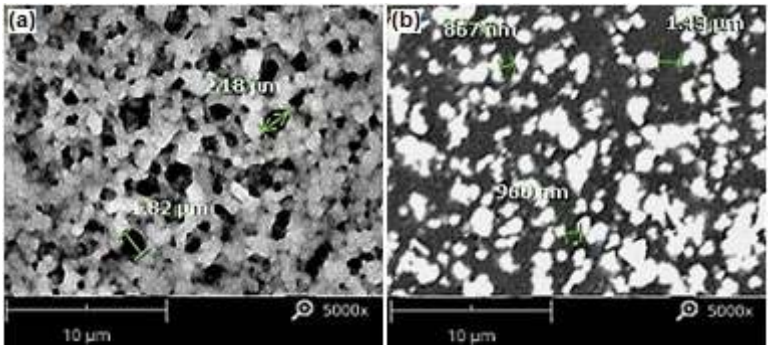

Fig 3. SEM morphology and pore size: (a) NIM, (b) IIM

Table 1. EDX results of NIM, IIM before Au release, and IIM after Au release

Elements	NIM	IIM before Au release	IIM after Au release
C	44.025%	16.75%	1.74%
O	28.875%	2.275%	2.725%
N	24.47%	2.6%	6.9125%
S	2.3%	1.575%	17.5125%
Au	-	75.45%	67.75%
K	< 1%	< 1%	-
Cl	< 1%	< 1%	-

the Au^{3+} ion species that will be transported to the receiving phase, in the receiving phase in the form of a thiourea solution in acidic pH of the Au^{3+} ion species are unstable but will be reduced by becoming Au^{1+} ions. Thiourea solution under acidic pH conditions was chosen as the catching phase because based on previous research showed that thiourea in acidic pH is effective for gold extraction and has several advantages, such as low environmental impact, easier reagent treatment, greater selectivity to gold and faster gold dissolution kinetics [21]. The thiourea solution will then react with Au^{1+} to produce cationic complexes or aurous ions.

$$Au^{+} + SC(NH_2)_2 \rightarrow Au[SC(NH_2)_2]^{2+}$$

The reduction reaction of Au^{3+} ions to Au^{+} in the receiving phase (thiourea) occurs because the Au^{+} complex with thiourea is more stable. The stability of the $Au[SC(NH_2)_2]^{2+}$ complex decreases as the pH of the solution increased, so that the pH conditions of the feed phases 1 and 3 will make the driving force of the transport of Au^{3+} metal ions become greater and will decrease with increasing pH (pH = 5, 7, and 9). Complex species changes if the pH of the solution is more than 3 also affects the transport of Au^{3+} metal ions. As described by Paclawski and Fitzner [22] in the distribution of Au^{3+} species under various pH conditions, at pH more than 3 the presence of hydroxyl ligands begins to replace Cl ligands so that at pH above 3 species will exist $[AuCl_3OH]^-$, $[AuCl_2(OH)_2]^-$, $[AuCl(OH)_3]^-$, and $[Au(OH)_4]^-$. The difference in Au^{3+} metal ion species influences the stability of the complex and causes the transport percentage to decrease as the pH of the feed phase increased.

Transport Time Optimization

The results of the optimization of transport time can be described from the transport percentage graph in Fig. 5. Based on the graph in Fig. 5, it showed that the longer the transport time, the transported percentage of

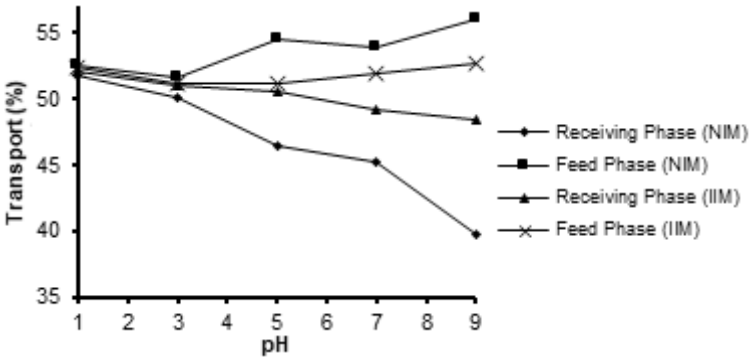

Fig 4. Curve of transport versus pH

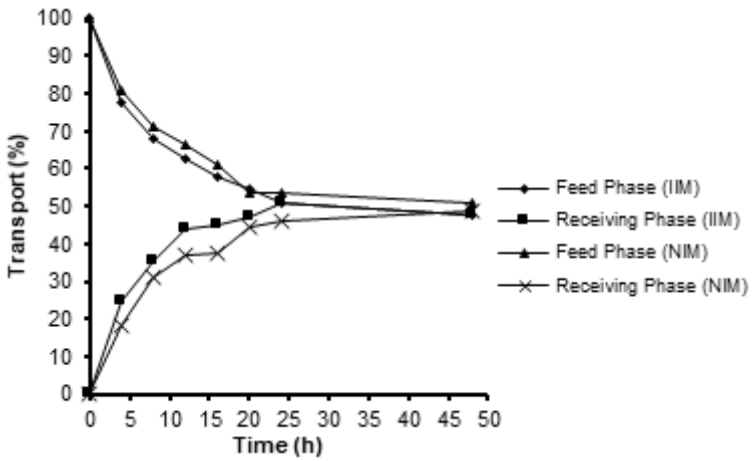

Fig 5. Curve of transport versus time

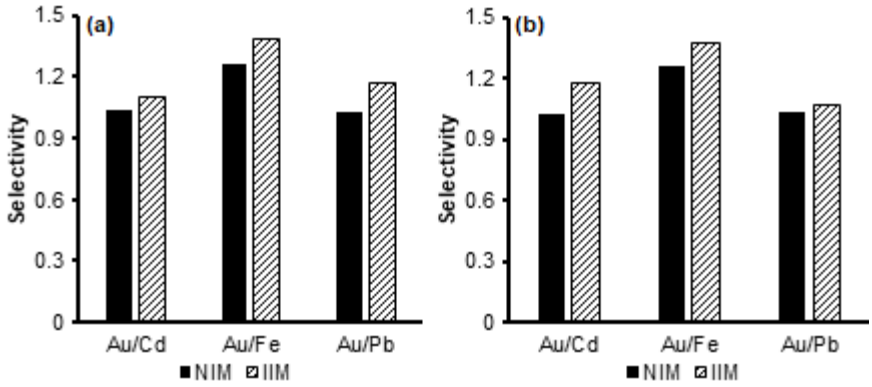

Fig 6. Comparison graph of IIM and NIM selectivity values: (a) Feed phase, (b) Receiving phase

Au^{3+} metal ions increased when viewed from the receiving phase and decrease when viewed from the feed phase.

This means that the longer the transport time, the greater the concentration of Au^{3+} metal ions transported. The optimum IIM transport time is achieved at 24 h and NIM at 48 h, which is indicated by the percent of the transport phase of the receiver, and the remaining percent of the transport phase of the feed is in one point (overlapping). At 24 h, the concentration of Au metal ions in the feed phase is almost the same as the concentration of Au metal ions in the receiving phase, so there is no driving force due to the effect of different concentrations of the feed phase and the receiving phase. After more than 24 h to 48 h, there was no change in transport percentages; this indicated that there was no longer a driving force for transport due to differences in the concentration of the feed phase and the receiving phase.

IIM Selectivity to Au^{3+} Ions

IIM transport selectivity to Au^{3+} metal ions is obtained through the transport of binary metal ions. The selectivity value is obtained from the ratio of the transported percentage of the target metal ion to the transported percentage of the competing metal ion. The membrane is said to be more selective about the target metal ion if the percentage of the transport of the target metal ion is greater than that of the competing metal ion, so the membrane selectivity value is more than 1 (selectivity > 1). According to the HSAB theory, Fe^{3+} is a hard acid, Pb^{2+} is a borderline while Cd^{2+} and Au^{3+} is a soft acid. Since the IIM was made to recognize Au^{3+} (a soft acid), so the IIM during transport will tend to draw a soft acid rather than those which are not. The results were as expected and can be seen in the graph in Fig. 6 that compares IIM and NIM selectivity values.

The graph in Fig. 6 showed that the selectivity of IIM transport for Au^{3+} metal ions in all competing metal ion mixture solutions is greater than NIM PEATM. In a solution of a mixture of Au^{3+}/Cd^{2+}, the selectivity IIM was 1.10, and NIM was 1.03. In a solution of a mixture of Au^{3+}/ Fe^{3+}, the selectivity of IIM was 1.39, and NIM was 1.26. In a solution of the Au^{3+}/Pb^{2+} mixture, the selectivity of IIM was 1.17, and NIM was 1.02. Supported by the selectivity data from the receiver phase in Fig. 6(b), the same thing is also shown. In a solution of a mixture of Au^{3+}/Cd^{2+}, the selectivity of IIM was 1.18, and NIM selectivity was 1.02. In a solution of a mixture of Au^{3+}/Fe^{3+}, the selectivity of IIM was 1.37, and NIM was 1.26. In a solution of the Au^{3+}/Pb^{2+} mixture, the selectivity of IIM was 1.07, and NIM was 1.03. Previous research on ionic imprinted membrane based on polyeugenol derivates also showed similar results, such as the same optimum pH condition of 3 and higher adsorption capacity towards Fe^{3+} when compared to its competitive metal [16]. Through this study, it is proven that IIM is more able to transport Au from its binary mixture selectively.

■ CONCLUSION

This research proves that the presence of S groups in PEATM makes NIM and IIM selective to Au^{3+} metal ions in accordance with the HSAB theory. The presence of ion templates on the membrane makes IIM have a higher selectivity to Au^{3+} metal ions compared to NIM.

The most effective condition for Au^{3+} metal transport was in pH 3, and the most optimum transport time for IIM is 24 h, while for NIM, it was 48 h. The results showed that IIM has better selectivity towards Au^{3+} in all mixtures of metal ions compared to NIM. Future studies will probably discuss the membrane applicability for extraction of Au^{3+} from real wastewater that contains Au^{3+} and also for the development of gold metal sensing devices.

■ REFERENCES

[1] Ogata, T., and Nakano, Y., 2005, Mechanisms of gold recovery from aqueous solutions using a novel tannin adsorbent gel synthesized from natural condensed tannin, *Water Res.*, 39 (18), 4281–4286.

[2] Lestari, P., 2017, Adsorpsi ion emas menggunakan asam humat tanah gambut di bawah radiasi sinar UV, *JST*, 6 (1), 168–177.

[3] Torre, M., Bachiller, D., Rendueles, M., Menéndez, C.O., and Díaz, M., 2006, Cyanide recovery from gold extraction process waste effluents by ion exchange I. Equilibrium and kinetics, *Solvent Extr. Ion Exch.*, 24 (1), 99–117.

[4] Rochat, D., Hagelüken, C., Keller, M., and Widmer, R., 2007, Optimal recycling for printed wiring boards (PWBs) in India, *R'07 World Congress - Recovery of Materials and Energy for Resource Efficiency*, 3-5 September 2007, Davos, Switzerland.

[5] Nghiem, L.D., Mornane, P., Potter, I.D., Perera, J.M., Cattrall, R.W., and Kolev, S.D., 2006, Extraction and transport of metal ions and small organic compounds using polymer inclusion membranes (PIMs), *J. Membr. Sci.*, 281 (1-2), 7–41.

[6] Yoshikawa, M., 2001, Molecularly imprinted polymeric membranes, *Bioseparation*, 10 (6), 277–286.

[7] Vatanpour, V., Madaeni, S.S., Zinadini, S., and Rajabi, H.R., 2011, Development of ion imprinted technique for designing nickel ion selective membrane, *J. Membr. Sci.*, 373 (1-2), 36–42.

[8] Buhani, Narsito, Nuryono, and Kunarti, E.S., 2013, Chemical stability of Cd(II) and Cu(II) ionic imprinted amino-silica hybrid materials in solution media, *Eksakta*, 13 (1-2), 1–10.

[9] Djunaidi, M.C., Khabibi, and Ulumudin, I., 2017, Separation of $Cu2^{+}$, Cd^{2+} and Cr^{3+} in a mixture solution using a novel carrier poly(methyl thiazoleethyl eugenoxy acetate) with BLM (bulk liquid membrane), *IOP Conf. Ser.: Mater. Sci. Eng.*, 172, 012032.

[10] Djunaidi, M.C., Wibawa, P.J., and Murti, R.H., 2018, Synthesis of a carrier compound thiazoethyl methyl eugenoxyacetate from eugenol and its use in the bulk liquid membrane technique, *Indones. J. Chem.*, 18 (1), 121–126.

[11] Qu, R., Sun, C., Wang, M., Ji, C., Xu, Q., Zhang, Y., Wang, C., Chen, H., and Yin, P., 2009, Adsorption of Au(III) from aqueous solution using cotton fiber/chitosan composite adsorbents, *Hydrometallurgy*, 100 (1-2), 65–71.

[12] Djunaidi, M.C., Lusiana, R.A., Pardoyo, Widodo, D.S., and Utami, T.W., 2019, Synthesis of polieugenoxy acetyl thiophene methanolate as a new selective carrier, *IOP Conf. Ser.: Mater. Sci. Eng.*, 509, 012068.

[13] Putrie, Z.M., 2013, Sintesis membran hibrida kitosan silika grafting silfonat sebagai proton exchange membran, *Master Thesis*, Department of Chemical Engineering, Institut Teknologi Sepuluh Nopember, Surabaya, Indonesia.

[14] Bolto, B., Tran, T., Hoang, M., and Xie, Z., 2009, Cross-linked poly(vinyl alcohol) membranes, *Prog. Polym. Sci.*, 34 (9), 969–981.

[15] Merle, G., Hosseiny, S.S., Wessling, M., and Nijmeijer, K., 2012, New cross-linked PVA based polymer electrolyte membranes for alkaline fuel cells, *J. Membr. Sci.*, 409-410, 191–199.

[16] Djunaidi, M.C., Jumina, J., Siswanta, D., and Ulbricht, M., 2015, Synthesis of Fe ionic-imprinted polyeugenol using polyethylene glycol diglycidylether as cross-linking agent for sorption of Fe(III), *Indones. J. Chem.*, 15 (3), 305–314.

[17] González, M.A.G., Edlund, U., Vidaurre, A., and Ribelles, J.L.G., 2017, Synthesis of highly swellable hydrogels of water-soluble carboxymethyl chitosan and poly(ethylene glycol), *Polym. Int.*, 66 (11), 1624–1632.

[18] Atkins, P.W., and de Paula, J., 2010, *Atkins' Physical Chemistry*, 9th Ed., Oxford University Press, Oxford, New York.

[19] Marcus, Y., 1991, Thermodynamics of solvation of ions. Part 5.–Gibbs free energy of hydration at 298.15 K, *J. Chem. Soc., Faraday Trans.*, 87 (18), 2995–2999.

[20] Groenewald, T., 1976, The dissolution of gold in acidic solutions of thiourea, *Hydrometallurgy*, 1 (3), 277–290.

[21] Nicol, M.J., Fleming, C.A., and Paul, R.L., 1992, "The chemistry of the extraction of gold" in *The Extractive Metallurgy of Gold*, Eds. Stanley, G.G., South African Institute of Mining and Metallurgy, Johannesburg, 831–905.

[22] Pacławski, K., and Fitzner, K., 2004, Kinetics of gold(III) chloride complex reduction using sulfur(IV), *Metall. Mater. Trans. B*, 35, 1071–1085.

Supplementary Data

This supplementary data is a part of paper entitled "Design of Catechin-based Carbon Nanodots as Facile Staining Agents of Tumor Cells".

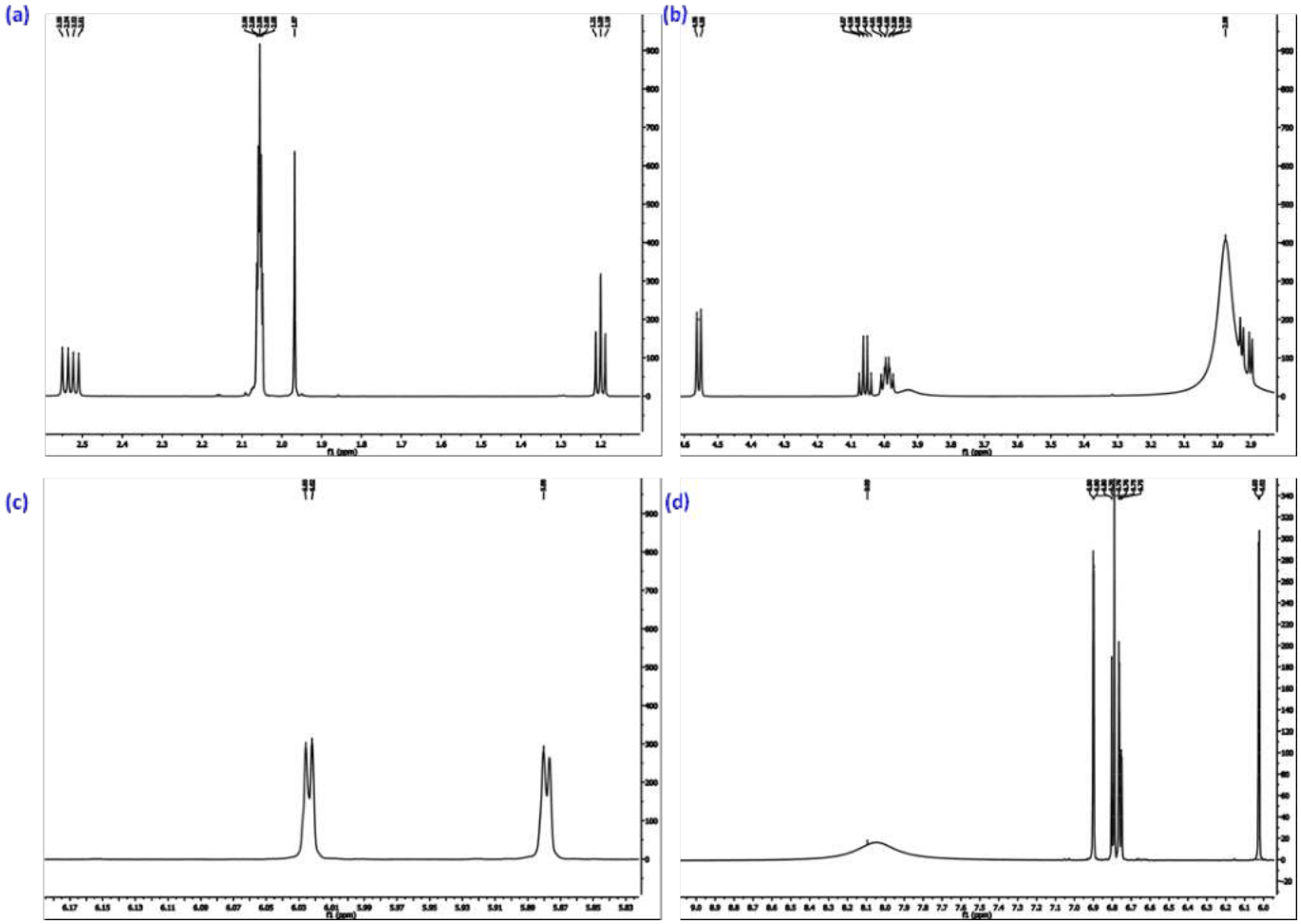

Fig S1. ^{1}H-NMR spectra of Catechin with δ from 1.1–2.6 ppm (a); 2.9–4.6 ppm (b); 5.81–6.19 ppm (c); and 6.0–9.1 ppm (d)

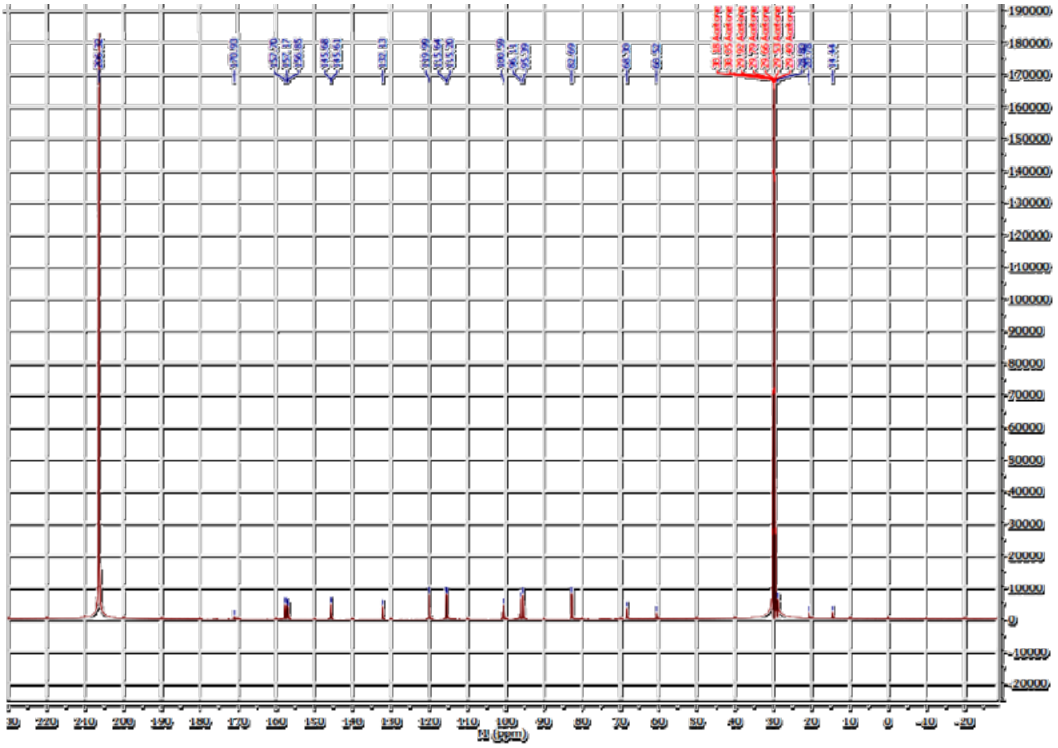

Fig S2. ^{13}C-NMR of Catechin

Design of Catechin-based Carbon Nanodots as Facile Staining Agents of Tumor Cells

Yaung Kwee[1,2], Alfinda Novi Kristanti[1], Nanik Siti Aminah[1], and Mochamad Zakki Fahmi[1,3,*]

[1]*Department of Chemistry, Airlangga University, Kampus C Mulyorejo, Surabaya 60115, Indonesia*

[2]*Department of Chemistry, University of Mandalay, University Drive, 73rd Mandalay, Myanmar*

[3]*Supramodification Nano-micro Engineering Laboratory, Airlangga University, Kampus C Mulyorejo, Surabaya 60115, Indonesia*

* ***Corresponding author:***

email: m.zakki.fahmi@fst.unair.ac.id

Received: October 2, 2019
Accepted: January 3, 2020

DOI: 10.22146/ijc.50327

Abstract: *Carbon nanodots (CNDs) have widely received great attention as a result of favorable optical, electrical, optoelectrical, biocompatible, and non-toxic properties that these nanoparticles possess. However, the exploration of nanoparticles from natural raw material is still limited. In the present work, carbon dots were produced from catechin isolated from* Uncaria gambir *through a simple and facile process. Carbon nanodots were produced by the pyrolysis process of catechin, which allowed it for carbonization. Owing to its unique properties, such as photoluminescence with an emission peak at 500 nm (λ_{ex} = 380 nm), average size diameter of about 5 nm and non-toxic properties, Cat-CNDs were incredibly potential for staining targeted tumor cells. The staining ability shown by confocal microscopy observations showed their green fluorescence images which meant that the CNDs easily penetrated HeLa cells via endocytosis. The resulting CNDs which were analyzed using several significant techniques proved that the prepared Cat-CNDs were tremendously dispersible and water-soluble, had good colloidal stability, excellent biocompatibility, favorable hydrophilicity, high photostability, and were non-toxic.*

Keywords: Uncaria gambir*; catechin; carbon nanodots; staining tumor cells*

■ INTRODUCTION

Gambir is one of the most important economical natural products in which Indonesia is the world's largest exporter, currently supplying 80% of the global market [1]. Moreover, it is a well-known and cost-effective plant, and considered as a promising medicinal plant that is found in Southeast Asian regions such as in West Sumatera of Indonesia and in the Peninsula of Malaysia. The family of the genus *Uncaria* is Rubiaceae, containing approximately 34 species, which abundantly grow in tropical regions of Southeast Asia, Africa, and South America [2-5]. The hooks of *Uncaria gambir* are conventionally prepared for the treatment of wounds, ulcers, fever, asthma, rheumatism, hyperpyrexia, hypertension, headaches, gastrointestinal illness, and bacterial or fungal infections [6-9]. Catechin, a polyphenolic compound, can be isolated from *Uncaria gambir* as a particular compound [10-11]. There have been reports on the pharmacological uses of catechin to enhance mental and behavioral symptoms of dementia that includes dementia with Lewy bodies, aggressiveness in patients with Alzheimers, agitation, hallucinations, and other forms of senile dementia [12-13].

In 2004, carbon dots (CDs) were accidentally discovered during the separation and purification of the single-walled carbon nanotubes and became a potentially new component of fluorescent carbon material with a diameter in the range of below 10 nm. Subsequently, many studies regarding the nature of CDs have been developing at a great rate [14]. Consequently, there are currently many exploratory methods for the potent fabrication of fluorescent CNDs, such as electrochemical oxidation, chemical oxidation, arc-discharge, pyrolysis method, laser ablation, hydrothermal method, and solvothermal method, which can simply be classified into top-down and bottom-up approaches [15]. However, in contrast with heavy-metal-based quantum dots, carbon nanoparticles are

considered more reliable, exhibiting great advantages such as low toxicity, good water dispersibility, favorable biocompatibility, and excellent photostability especially for several clinical applications [16-17]. Furthermore, carbon nanodots derived from natural products have received great reputation due to particular merits such as photostability, excellent biocompatibility, optoelectrical properties, additional luminescence, and non-toxic nature. In addition, specific hydrophobic sites on CDs allow the improvement of diagnostics and therapy in clinical applications [18-19].

Recently, a great deal of attention have been particularly given to the production of carbon dots (CDs/CNDs) derived from natural products since they have a large number of advantages such as being renewable and sustainable and also other advantages that have already been mentioned above, [20]. Furthermore, heteroatoms from natural products promote heteroatom-doped nanocarbon dots without the addition of any external heteroatom sources. There are many ways to synthesize carbon nanodots from natural products that are incredibly green and simple compared to conventional preparation methods of carbon quantum dots from artificial carbon sources [21]. There are many literature and reports of green carbon nanodots synthesized from organic products such as from plant extracts, fruits, leaves, fruit shells and peels, algae, and fruit juice for many applications. In contrast with past applications, carbon nanodots are currently considered to be applied in photothermal treatment, drug delivery systems, photoacoustic imaging, fluorescence imaging, sensing, and magnetic resonance imaging, and is recognized to be a beneficial eco-friendly alternative to semiconductor quantum dots [22]. Yallapa et al. reported that carbon nanodots with porous particles can be synthesized from OPL (Oil Palm Leaves) which contained several important organic products such as cellulose, lignin, and hemicelluloses. Those CNDs were conjugated with fluorescent dye for cellular imaging and targeted drug delivery to cancer cells [23]. Carbon nanodots synthesized from molecules or compounds with rigid and graphene-like structures showed strong fluorescence likely due to the presence of aromatic rings and hydroxyl groups, in which the aromatic rings were able to form co-planar structures and causing the hydroxyl group to become dehydrated and introduce oxygen defects [24]. As a promising cost-effective alternative, CNDs have recently been considered as a new quantum dot candidate. In addition, carbon nanodots synthesized from aromatic rings and abundant hydroxyl groups also have benefits of better surface grafting, stable photoluminescence, good solubility, and low toxicity, and thus making them promising materials [25-27].

There are several commonly used treatment methods for cancer such as chemotherapy, radiation, surgery, targeted treatments, and immunotherapy that are applied separately or in combination [28]. However, these treatment methods might bring about various side effects [29]. On the other hand, drug nanocarriers were reported to have improved cancer treatment efficacy and diminish side effects of the conventional methods [30-31]. Several studies have reported the application of CNDs on cancer treatment [32-34]. In the present study, we synthesized potential carbon nanodots (CNDs) from catechin as a natural product isolated from *Uncaria gambir*. The as-prepared nanoparticles (Cat-CNDs) from the organic product catechin has great biofunctions and can potentially be applied for staining specific tumor cells. The optimization of the synthesized Cat-CNDs was performed by characterizations of optical properties, spectroscopic properties, and bioassay tests using different analytical techniques. According to its unique properties discovered from the performed analysis, Cat-CNDs are highly expected to contribute to improving the method of cancer theranostics to a great extent. Furthermore, the synthesized Cat-CNDs are considered to be more biocompatible, have high cell uptake when diagnosing cancer cells, and great cell viability for staining specific tumor cells.

■ EXPERIMENTAL SECTION

Materials

The dried blocks of *Uncaria gambir* were collected from a commercial market in Surabaya, Indonesia. Some of the chemicals such as hydrochloric acid (97%, HCl),

sodium chloride (55.5%, NaCl), ethanol (99.9%), sodium hydroxide (98.5%, NaOH), and ethyl acetate (99.8%, EA) were purchased from Sigma-Aldrich, USA. The WST-8 reagent of [monosodium (2-(2-methoxy-4-nitrophenyl)-3-(4-nitrophenyl)-5-(2, 4-disulfophenyl) 2H-tetrazolium)] was bought from TCl, Japan. Phosphate-buffered saline (PBS) was from UniRegion, Biotech, Taiwan. All reagents were of analytical grade and used as received without any further purification.

Procedure

Isolation of catechin

The dried blocks of *Uncaria gambir* (350 g) were ground into fine powders using a mortar and pestle. To attain the uniform-sized raw powders, sieving was performed at 62 μm using a laboratory sieve. The fine powders were then collected for further work. The fine powders (300 g) were extracted with methanol for 24 h and then it was further extracted three more times. The methanol extract was then evaporated in order to obtain methanol crude extract. The methanol crude extract was then partitioned three times with *n*-hexane. After that, the methanol liquid extract was partitioned again three times with ethyl acetate in order to get the ethyl acetate crude extract. The ethyl acetate extract (12 g) was taken and separated by silica gel column chromatography with a gradient of *n*-hexane in EA (50:50, 40:60, 30:70, 20:80, 10:90, 0:100). The purified catechin (7 g) was isolated from solvent ratios of *n*-hexane: EA (2:8) and the structure was further confirmed by spectroscopic techniques.

Synthesis of carbon nanodots (CNDs)

The Cat-CNDs were derived from the isolated pure catechin through a single-step method of pyrolysis following a previous report [35]. Experimentally, 50 mg of the purified catechin was powdered and placed on the isolated reactor to avoid air flow, then pyrolyzed at 250 °C for 4 h in a furnace for the carbonization process. The resulting Cat-CNDs were dissolved in 1 M NaOH at 60 °C, subjected to dialysis process (MWCO 10.000 kDa) and collected by centrifugation (12.000 rpm, 2 h) for further use.

Cell culture

To culture human cervical (HeLa) tumor cells, Eagle's minimum essential medium (EMEM, containing 1.5 g L^{-1} sodium bicarbonate) was used, which was added for cell medium with the respective content of 1% of antibiotic-antimycotic formulation, 1% of non-essential amino acid, 1% of l-glutamine, 1% of sodium pyruvate, and 10% of fetal bovine serum. The cells treated were then put safely in a humidified incubator with 5% of CO_2 which was maintained at 37 °C.

Confocal imaging observation

For the exploration of the potential bioimaging and cellular distribution of Cat–CNDs, HeLa cells were implanted at a density of 5 × 104 cell mL^{-1} in 1 mL EMEM medium in 24-well plates. Hence, a newly medium containing varied and different concentrations of Cat–CNDs was attached to the corresponding dishes and was incubated for 1 h. Afterwards, the medium was washed twice with PBS and fixed with ethanol. Then, the samples were captured by using a laser scanning confocal microscopy (CLSM). CLSM images were obtained by irradiating the samples with inline Ar (488 nm) and He–Ne (503–680 nm and 588 nm) lasers.

Cytotoxicity assessment

The assessment of cell viability was evaluated using a WST-8 assay in HeLa tumor cells. HeLa cells, which were cultured in EMEM, were cultured in 24-well plates (15.000 cells per well) for 24 h. After rinsing with PBS to wash the proliferated cells and the cells were incubated with an adjusted concentration of Cat-CNDs for 24 h. After rinsing the plate twice with PBS, WST-8 reagent (1 mL, 500 mg mL^{-1}) was supplemented and incubated for 4 h. Afterwards, dimethyl sulfoxide (1 mL) was added to each well to dissolve formazan crystals, and the crystals' absorbance was determined at 570 nm using an Elisa reader (Biotech Powerwave XS). The greater the absorbance intensity, the more the number of live cells because more formazan was being absorbed.

$$\text{Cell viability} = \frac{\text{A570 in treated cell}}{\text{A570 in control sample}} \times 100\%$$

Characterization

The Nuclear Magnetic Resonance spectroscopy (NMR), Brucker Ultra shield Advance II 600 MHz was used to characterize the isolated catechin compound. Related spectroscopy methods of nuclear magnetic

resonance (NMR) such as heteronuclear single quantum coherence spectroscopy (HSQC) and heteronuclear multiple-bond coherence spectroscopy (HMBC) was also applied. Atomic force microscopic photographs were achieved using a scanning probe AFM5500M instrument (Hitachi Co., Japan) at ambient temperature. UV-Vis absorption spectra were determined using a JASCO V-670 spectrometer. By using a Rigaku 18 kW rotating anode source X-ray diffractometer with Cu Kα1 line radiation (λ = 1.54 Å), Powder X-ray diffraction (XRD) diagrams were analyzed. By using a PerkinElmer LS 55 spectrofluorometer equipped with a 20 kW xenon lamp, PL spectra were measured. Fourier transforms infrared (FTIR) spectra were observed with a Nicolet AVATAR 360 FTIR instrument. Raman analysis was performed using an MRS-320 Raman Instrument system (Horiba Ltd., Japan). Colloidal stability tests were performed in different pH (3–12), different temperatures (30–100 °C), and different concentrations of NaCl salts (0–0.5 M). All analyses were conducted at room temperature.

Statistical analysis

The statistical study, performed by determining the cytotoxic concentration that causes a 50% decrease in cell viability (IC_{50}), was conducted using dose-response mode on the nonlinear fitting curve in Origin software (version 8.0724, Origin Lab Inc., Northampton, MA). Means were calculated using a paired-sample t-test, and all presented data were achieved in triplicates.

■ RESULTS AND DISCUSSION

Extraction, Isolation, and Elucidation of Catechin

By the extraction process, the white crystals of catechin (7 g) were obtained. High purity of this compound was determined by performing a single spot analysis at R_f = 0.39 (eluent; Ethyl acetate:*n*-hexane = 8:2) and also determining its melting point at 125–126 °C. NMR analysis was conducted to confirm the catechin chemical structure (Fig. S1, supporting information). The analysis of the ^{1}H-NMR indicated the presence of nine protons (Fig. S1) with aromatic protons that indicated chemical shifts at 5.88–6.90 ppm. Besides that, non-aromatic cyclic protons exhibited chemical shifts at 4.06–4.56 ppm. The signal that appeared at 2.53–2.98 ppm corresponded to the secondary protons of methylene (-CH_2-). The aromatic protons appeared at δ_H 6.02 ppm (H_6, d, J = 2.3 Hz), δ_H 5.88 ppm (H_8, dd, J = 2.3 Hz), δH 6.90 ppm ($H_{2'}$, d, J = 2.1Hz), δ_H 6.8 ppm ($H_{5'}$, d, J = 6 Hz), and δ_H 6.76 ppm ($H_{6'}$, dd, J = 6 Hz, and J = 2.1 Hz). According to the three coupling constant values, the $H_{6'}$, $H_{5'}$, and $H_{2'}$ protons formed an ABX system on ring B, whereas H_6 was at meta position to H_8 on ring A. The non-aromatic cyclic protons appeared as a doublet at δ_H 4.56 ppm (H_2, d) and multiplet at δ_H 4.06 ppm (H_3, m). The last proton chemical shifts at δ_H 2.53 ppm (H_{4a}, dd) and δ_H 2.98 (H_{4b}, dd) were given by the secondary protons of methylene (-CH_2-).

The ^{13}C-NMR showed 15 signals which showed the number of carbons in the structure of the isolated pure catechin compound as demonstrated in Fig. S2. Through the DEPT 135 spectrum, it could be seen that the isolated compound included seven- tertiary carbons (δ_C, 68.30; 82.68; 95.38; 96.10; 115.19; 115.64 and 119.99 ppm), seven-quaternary carbons (δ_C, 100.60; 132.13; 145.60; 145.70;156.85; 157.70 and 157.17 ppm), and one-secondary carbon (δ_C 28.80).

The information about the correlation between directly-bonded ^{1}H on ^{13}C was obtained by the HMQC spectrum. Table 1 is the result of HMQC spectrum analysis. Moreover, the ^{1}H–^{1}H correlated spectroscopy (COSY) was used to analyze the correlation between proton and another proton in adjacent carbon. The correlation spectrum of ^{1}H–^{1}H COSY of isolated catechin compound was indicated in Fig. 1(a) and 1(b) as supplementary materials.

Moreover, the HMBC spectrum showed the presence of long-range correlations between protons and carbons that could be seen in Fig. 2(a) and 2(b) as supplementary material.

The spectrum data was made in contrast with the similar catechin compound which was isolated and identified from Acacia catechu Willdenow, reported by Acharya [36].

Synthesis and Characterization of Cat-CNDs

Pure catechin was used as raw materials to produce Cat-CNDs. The cyclohexane and benzene structure

owned by catechin was a basic reason for choosing this organic compound. By giving a thermal treatment at 250 °C, catechin will go through both dehydration and carbonization resulting in graphene like the structure of carbon dots as shown on Scheme 1. Thus, the preparation of Cat-CNDs was highlighted through a one-pot step method of pyrolysis.

To obtain solution form, the fabricated Cat-CNDs can be dissolved in polar solvents. The morphology of synthesized Cat-CNDs was firstly identified by the atomic force microscopy. The Cat-CNDs exhibited uniformly dispersible materials without any apparent aggregation. The diameter of Cat-CNDs supported its sizes between 2 and 5 nm (Fig. 3). The analysis of Cat-CNDs by AFM (Atomic Force Microscopy) is to assess the morphology, topography, and size distribution of the as-prepared CNDs. Fig. 3 also shows the characteristic AFM photographs of the

Table 1. ^{1}H, ^{13}C and HMBC NMR data of catechin in $CDCL_3$ (δ in ppm)

No. of Atom	δH (mult, J Hz)	δc
2	4.56, d	82.68
3	4.06, m	68.30
4	2.53, dd; 2.98, dd	28.80
10	-	100.60
5	-	157.17
6	6.02 (d, J = 2.3 Hz)	96.10
7	-	157.70
8	5.88 (dd, J = 2.3 Hz)	95.38
9	-	156.65
1’	-	132.13
2’	6.90 (d, J = 2.1 Hz)	115.19
3’	-	145.60
4’	-	147.70
5’	6.8 (d, J = 6 Hz)	115.64
6’	6.76 (dd 6.76 (dd, J = 6, & 2.1 Hz)	119.99

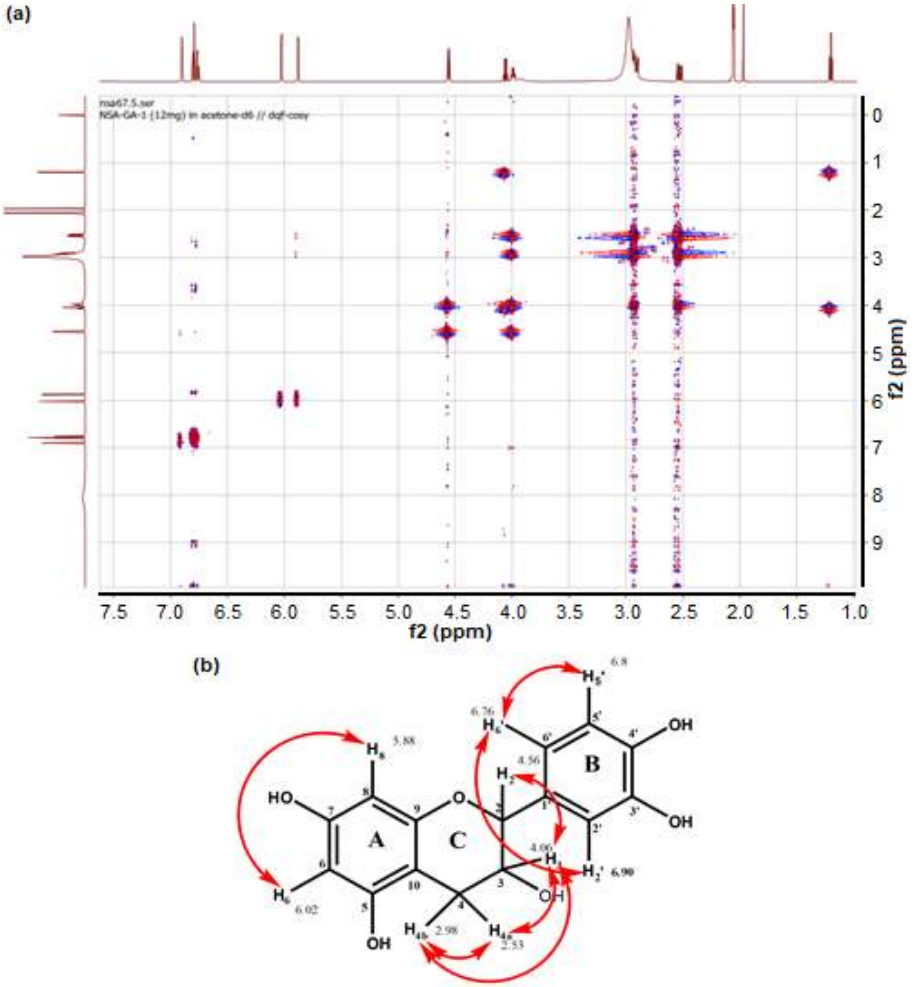

Fig 1. (a) The ^{1}H-^{1}H correlation spectrum of catechin, (b) The correlation of ^{1}H–^{1}H COSY of isolated compound

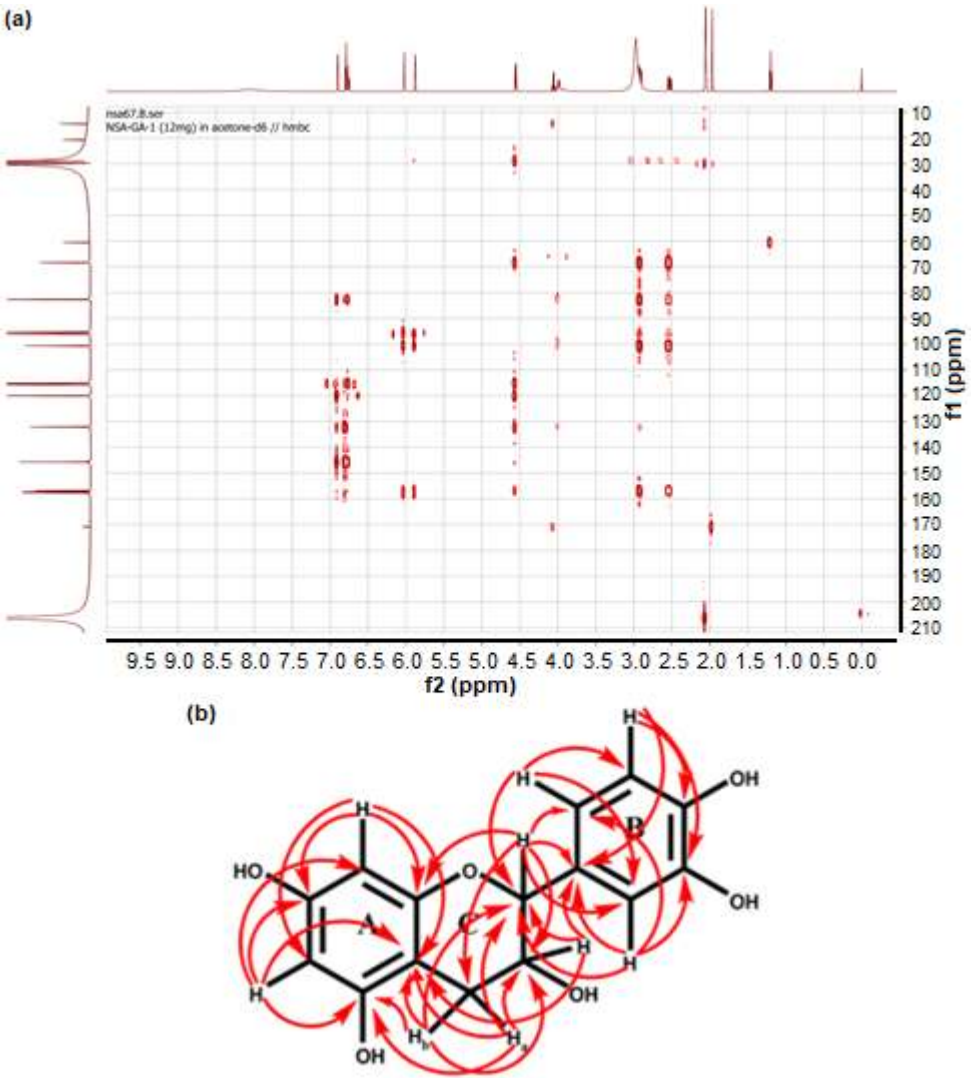

Fig 2. (a) The long-range correlation spectrum of ^{1}H-^{13}C HMBC of isolated catechin compound, (b) The correlation of HMBC in the isolated catechin compound

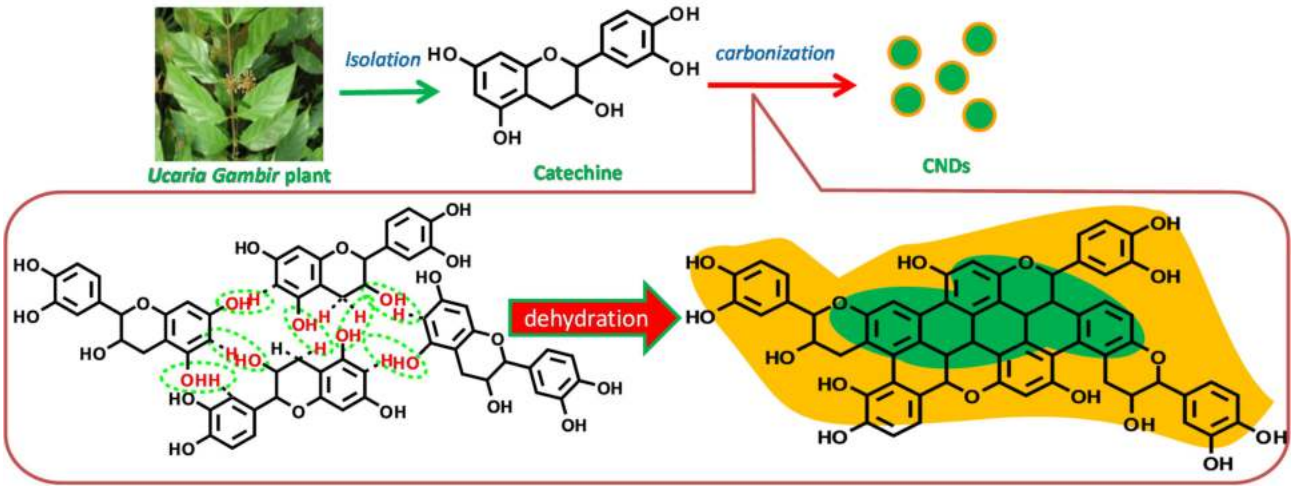

Scheme 1. Schematic illustration synthesis of Cat-CNDs from catechin

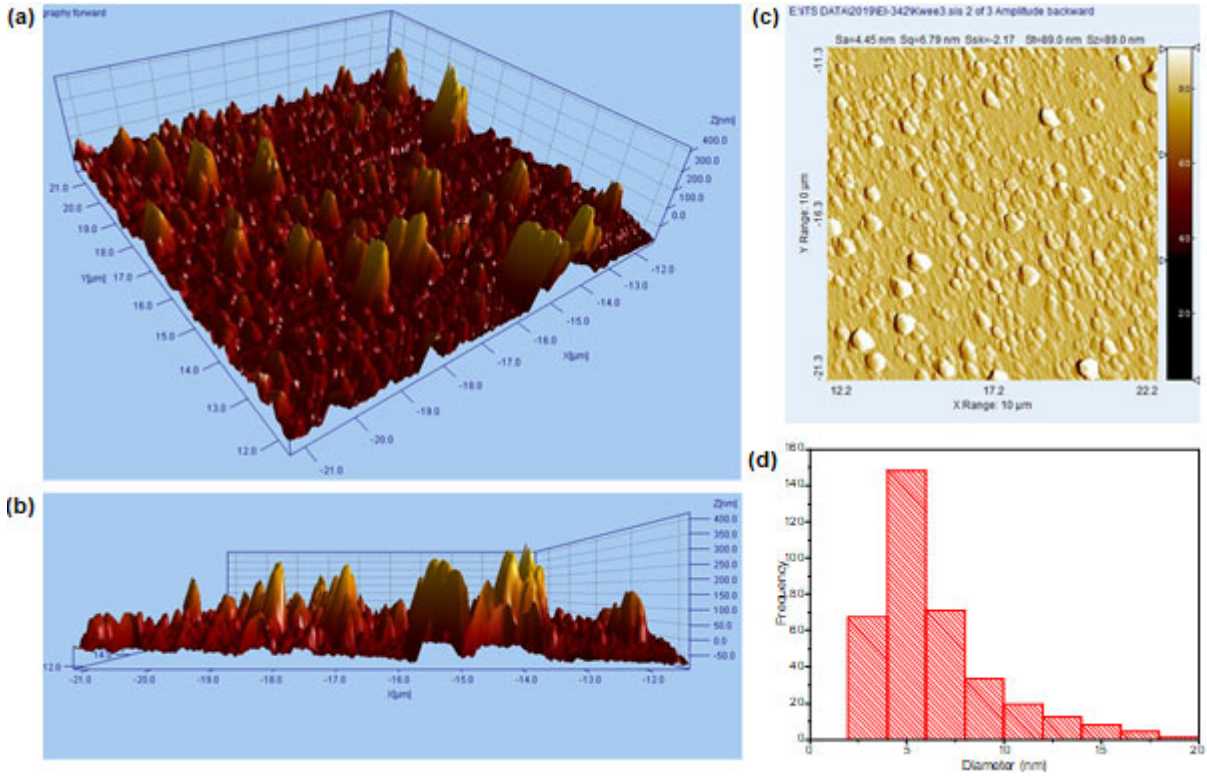

Fig 3. AFM photographs of Cat-CNDs on diagonal (a); vertical (b); top views (c); and its histogram (d)

as-synthesized CNDs solution. The height profile indicated that even though some particles had a size diameter of about 100 nm, the average size of these nanoparticles were about 5 nm supported by the histogram of the Cat-CNDs interpreted by the Image J software (Fig. 3(c)). Furthermore, it was revealed that the Cat-CNDs were well dispersed in the appropriate solvent and appeared in the spherical shape. The diameter of the CNDs was included in its size range which has been widely developed, which measures less than 10 nm in size [37].

Crystal characterization of the synthesized Cat-CNDs was investigated by XRD (Fig. 4). Its crystallinity was confirmed by a definite peak observed in the range of the shoulder diffractogram between 5 and 30°, confirming the peak of graphite carbon structure (based on crystal database JCPDS 74-2328). The XRD data also demonstrated interlayer spacing of Cat-CNDs on (003) plane at 11.15Å. The pyrolyzed CNDs performed weak XRD intensity, indicating nano-sized materials that matched with the supporting literature on nanostructure graphitic nature [38-39]. The average size of the crystalline CNDs with a 2θ position of 15.88 (FWHM = 7.2804°) was calculated to be 0.2 nm according to the Scherrer's equation.

Further observation focused on photo-physical properties of the CNDs that was acquired by using UV-Vis spectroscopy (Fig. 5(a)). The spectrum of pure catechin solution showed two absorption peaks that were

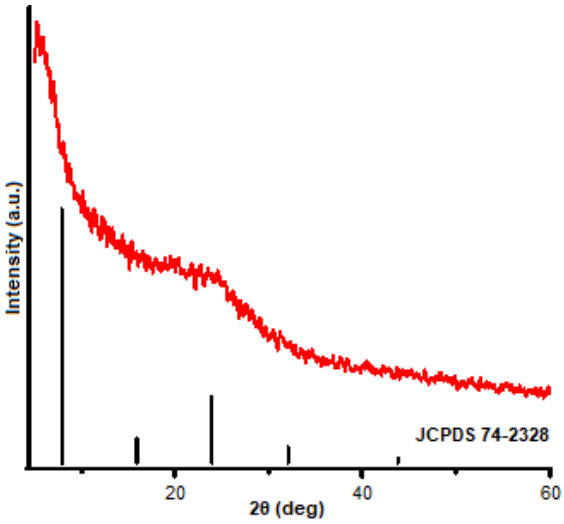

Fig 4. XRD pattern of Cat-CNDs

found at wavelengths of 267 and 318 nm corresponding to $\pi-\pi^*$ transitions of the aromatic ring. After the pyrolysis process, the synthesized Cat-CNDs possessed a nearly similar absorption spectrum to catechin. Furthermore, it was noticeable that two absorption peaks of Cat-CNDs appeared at around 267 nm, which was assigned to $\pi-\pi^*$, and 500 nm (blue shift emission) influencing electrostatic interactions between the aromatic rings within the catechin compound. The optical analysis of the as-prepared CNDs compared with bare catechin was further investigated (Fig. 5(b)). The data showed a strong fluorescent intensity presented as a broad peak (PL) at 500 nm, whereas pure catechin solution relatively exhibited a very weak fluorescent intensity centered at around 480 nm when both of the samples were exposed with excited wavelength at 380 nm (supported by the photograph in Fig. 5(b)). The photograph figures also show that Cat-CNDs had good solubility in water and hence having stronger fluorescence. For this reason, it was favorable for this material to be used as a staining agent for targeting tumor cells. Furthermore, it was noticed that the Cat-CNDs held excitation-dependent fluorescence on the complexity of the excited states of the CNDs, affecting the bandgap on the surface state of the carbon nanodots material [40].

Fig. 5(c) shows the Raman peak detected at 1590 cm^{-1} referring to a typical G band to the graphene (sp^2), due to the action of a double degenerated photo mode integrated with the symmetric E_{2g} in graphitic nature and the vibrations of the sp^2 were determined by the bonded carbon atoms in the two-dimension system of a hexagonal lattice [23]. The Raman data in Fig. 5(c) also show a peak at 1335 cm^{-1} described as the D band due to the disorder-induced nature in graphite of the sp^3 hybridization among carbon atoms which was inferred

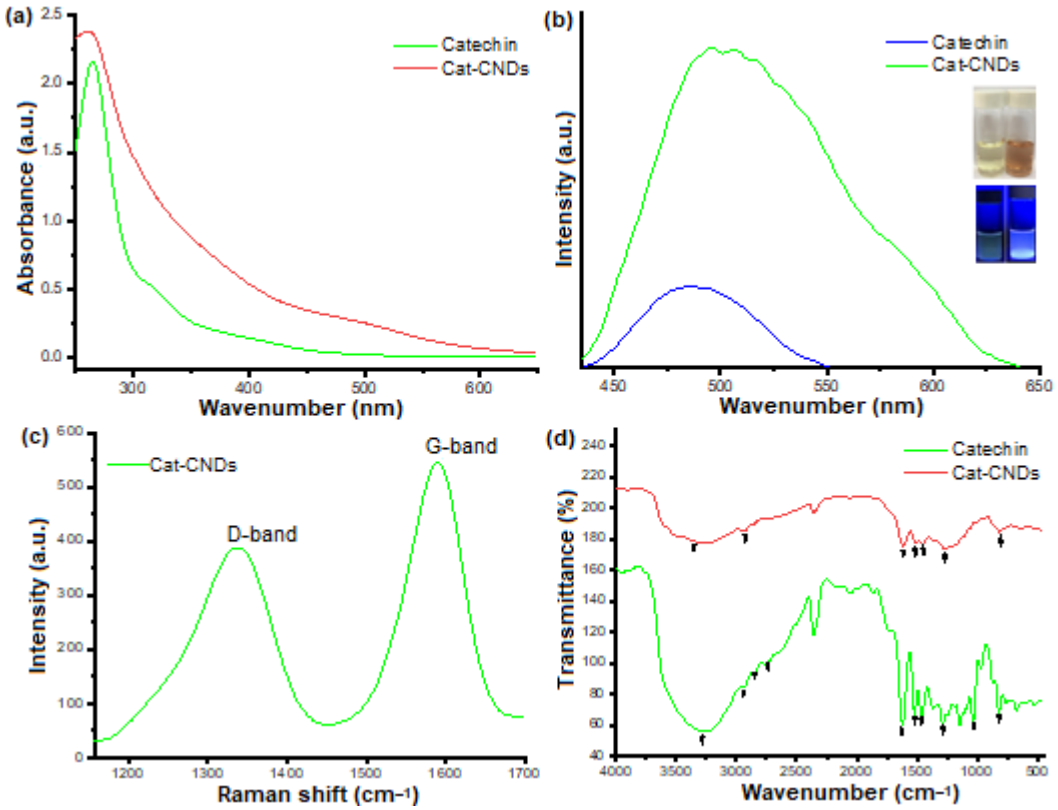

Fig 5. UV-Vis spectra of catechin (green solid line) and Cat-CNDs (red solid line) (a). PL spectra of catechin (blue solid line) and Cat-CNDs (red solid line). Inset: photographs of catechin and Cat-CNDs solutions under visible light and UV light (b). Raman spectra of Cat-CNDs (c). FTIR spectra of Cat-CNDs (red solid line) compared with bare Catechin (green solid line) (d)

to the A_{1g} mode [23]. These two bands are common bands of graphene or graphene oxide structure thus confirming the formation of a graphene oxide-like structure on the prepared Cat-CNDs. The calculation of the different intensity ratio of the D to G bands (I_D/I_G) resulted the value of 0.84, indicating the purity of graphitic formation. The CNDs sample with amorphous nature had a high ID/IG ratio whereas the CNDs sample with a high degree of graphitization was indicated by a relatively lower I_D/I_G ratio [41]. This means that the lower the intensity ratio of I_D/I_G, the more purified graphitic crystals were dominated. Therefore, the Raman spectrum confirmed a high purity of crystalline graphite in the carbon nanodots obtained from catechin.

As shown in Fig. 5(d), the functional groups of the Cat-CNDs were systemically analyzed with infra-red spectroscopy and compared with bare catechin.

For the catechin compound, a strong peak showed the stretching frequency of O–H bands at 3319 cm^{-1}, while C–H stretching of sp^2 hybridization was found at 2930 cm^{-1}, and C–H asymmetric and symmetric stretching vibrations of methane (–CH_2–) at 2871 and 2835 cm^{-1}, respectively. Furthermore, the bands between 1624 and 1525 cm^{-1} corresponded to the C=C stretching of the aromatic ring, while C–O/C–O–C stretching vibrations were found at 1285 cm^{-1} (symmetric band) and 1139 cm^{-1} (symmetric band), and C–H bending of CH_2 (out of plane) was found at 813 cm^{-1} [41]. In contrast the spectra for Cat-CNDs showed a broad peak at 3280 cm^{-1} that was attributed to the stretching vibration of a small number of residual hydroxyl groups that remained even after dehydrogenation, while the peak at 2926 cm^{-1} corresponded to C–H stretching vibration and aromatic ring stretching of the C=C vibration appeared at 1602, 1503, and 1450 cm^{-1}. The C–O–C stretching vibration was observed at 1280 cm^{-1}, and the broad peak at 810 cm^{-1} was attributed to the C=C–H out-of-plane bending. The synthesized carbon dots showed favorable hydrophilicity and good dispersion in water due to the polar functional groups on the surface site.

Stability Evaluation of Cat-CNDs

The colloidal stability analysis was carried out to assure the stability of Cat-CNDs. The stability of nanoparticles in aqueous solutions is vital for both biomedical and clinical uses. The first observation to study the pH effect on the CNDs, as shown in Fig. 6. The result showed that Cat-CNDs solution at pH 5 to 11 showed good stability up to 24 h after pH adjustment. However, Cat-CNDs at pH 3 and 4 showed precipitated particulates for the first 6 h. The change in appearance of the Cat-CNDs was observed at pH 12, where its color became bright brown. These conditions were likely due to the destruction of Cat-CNDs in extreme conditions. At low pH, the hydroxyl-abundant environment most likely caused the increase of hydrogen bonding of the CNDs [43], whereas structural destruction occurred when the CNDs were treated in high pH resulting in the color change. These findings were supported by UV-Vis spectra analysis (Fig. 6(b)), where π*–π excitation of CNDs at wavelength below 300 nm was disrupted by its electrostatic effect.

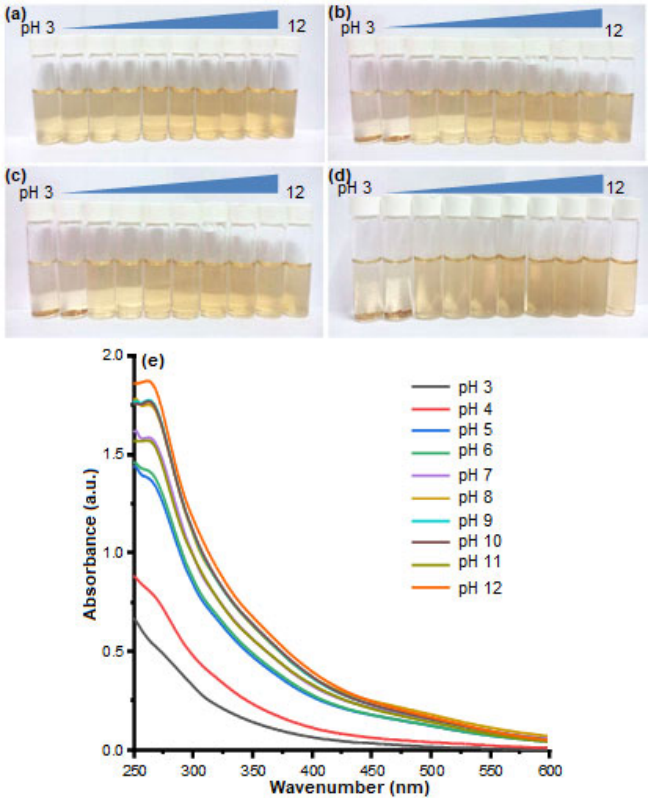

Fig 6. Photograph images of Cat-CNDs from pH 3 to pH 12 at (a) 0 h, (b) 6 h, (c) 12 h, and (d) 24 h. (e) The UV-Vis Spectra of Cat-CNDs from pH 3 to pH 12

The stability of CNDs was then observed against varied thermal treatment (30–100 °C). As a result, in Fig. 7(a), there were no coagulation and color change, while UV-Vis spectroscopy analysis revealed that all of the varied CNDs resulted similar absorption spectra. The synthesis of Cat-CNDs that reached up to 270 °C produced good thermal stability of this material and fulfilled the thermal stability requirement for materials that can be applied for the human body.

Further assessment was focused on Cat-CNDs stability on varied ionic strength by NaCl addition. This part was considered necessary due to the blood circulation in the human body that is affected by salt concentration. Thus, the effect of ionic strength on prepared Cat-CNDs was a crucial factor for further clinical applications. As shown in Fig. 8(a), the CNDs mixed with varying concentrations of NaCl salts (from 0.1 to 0.5 M) show similar conditions with the untreated Cat-CNDs, showing no coagulated solids even until 24 h.

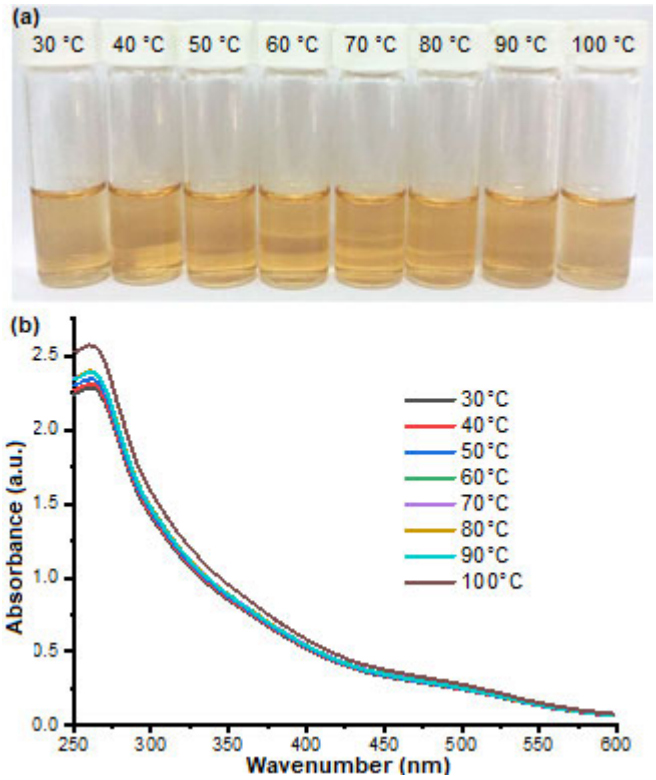

Fig 7. Photograph of Cat-CNDs on varied temperature assessment at 30, 40, 50, 60, 70, 80, 90, and 100 °C (a), The UV-Vis spectra of Cat-CNDs at varied temperatures treatment after 24 h (b)

This data is supported by the UV-Vis spectra (Fig. 8(e)), where the maximum wavelengths of the treated CNDs were similar to the untreated Cat-CNDs. Therefore, all these stability investigations prove the potential of this material for bio-applications and other fields of commercial purpose.

Confocal Observation

The fluorescence properties possessed by Cat-CNDs were the main factor to consider applying this material for tumor cell staining. Laser confocal scanning microscopy (LCSM) was used to improve the fluorescent properties as well as the cellular uptake and internalization of Cat-CNDs on the HeLa tumor cell. After 4 h of addition and incubation of Cat-CNDs onto HeLa (Fig. 9), its green emission was detected and localized in the cytoplasm of Hela tumor cells. This finding

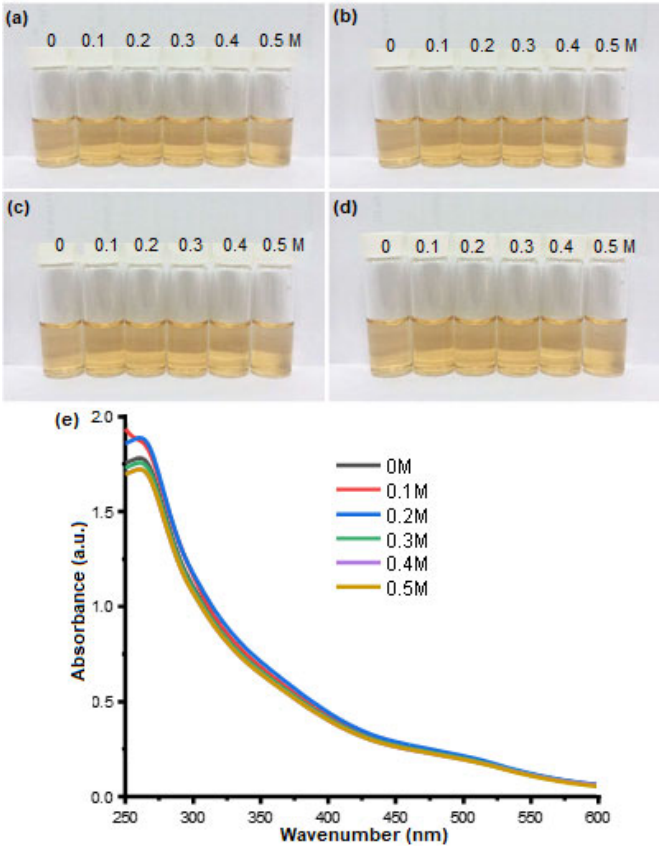

Fig 8. Photograph images of Cat-CNDs on varied NaCl concentration at 0 h (a), 6 h (b), 12 h (c), and 24 h (d). The UV-Vis spectra of Cat-CNDs at varied concentrations of NaCl after 24 h (e)

indicates that CNDs were successfully taken up by the cells.

The facile internalization of CNDs on the tumor cell was considered based on the basic properties of the catechin compound that possess high affinities to a variety of proteins expressed on the cell membrane by massive hydrogen bonding [44-45]. Further reports also stated that the insertion of catechin was founded by an association of membrane plasma by lipid rafts [46]. We speculate to that those reasons made the Cat-CNDs significantly appear on the cytoplasm. To ensure the position of Cat-CNDs on the cytoplasm, the Z stacking mode of CLSM was used (Fig. 10), where higher emission of the cell was found in the middle position. Therefore, these findings proved the potential and biocompatibility of Cat-CNDs while staining on a specific tumor cell and showed similar results with a previous report [46].

Cytotoxicity Test with CCK-8 Assay

Several studies have reported the anticancer potential of catechin derivatives, including the cytotoxicity of catechin when it is modified to nanoparticle form, which is an important aspect to verify its biocompatibility in biomedical and pharmaceutical applications. The cytotoxicity evaluation is conducted by

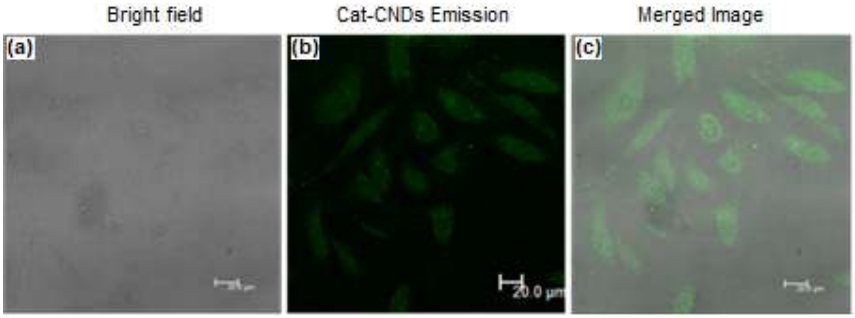

Fig 9. CLSM images of HeLa tumor cell after 4 h incubation with Cat-CNDs

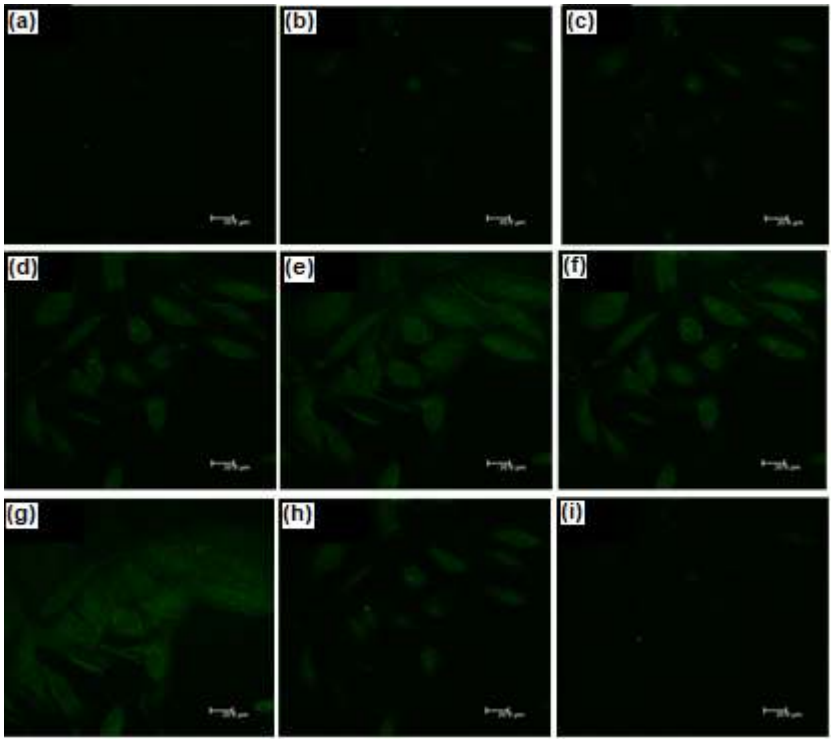

Fig 10. CLSM images of HeLa cells through z-stacking mode after 4 h treated with Cat-CNDs (a-i) Hela cells images captured by excitation at 488 nm

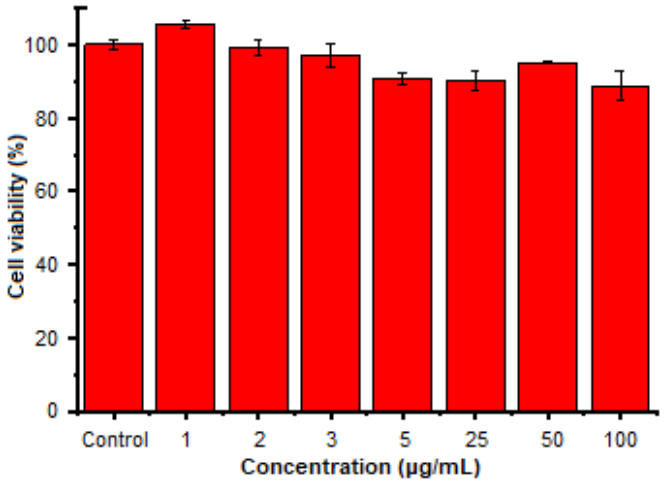

Fig 11. Cell viability assessed byWST-8 assay of Hela Cells after 24 h of treatment with Cat-CNDs. WST-8 data is shown as means ± SD with n = 3

incubating the adjusted concentration of Cat-CNDs on HeLa cells via WST-8 assay (Fig. 11). After being incubated for 24 h, the cell viability results showed that the cell had a high viability percentage of over 80% in concentrations of up to 400 µg mL^{-1} and IC_{50} of about 1815 µg mL^{-1}. This strongly indicated that Cat-CNDs have very low toxicity. Previous reports show that synthesized carbon nanodots are classified into non-toxic and low toxic categories if the percentage of cell viability is between 50.0–80.0% [47-48].

■ CONCLUSION

Catechin was successfully isolated from *Uncaria gambir* as raw material for the synthesis of Cat-CNDs through a single-step pyrolysis method and was later used for staining specific tumor cells. The resulting Cat-CNDs possess excellent optical properties. The average size of the Cat-CNDs was found to be below 5 nm with near-spherical shape and was crystalline in nature, which was confirmed by the analysis of the physicochemical properties. Moreover, the Cat-CNDs could be easily internalized into the tested Hela cancer cells and demonstrated excellent biocompatibility without any obvious toxicity. Due to their good biocompatibility, non-toxicity, strong photoluminescence, and eco-friendliness; this work strongly suggested that the as-synthesized Cat-CNDs have much potential to be applied for various biomedical applications specifically in targeted staining of specific tumor cells.

■ ACKNOWLEDGMENTS

Authors would like to thank Universitas Airlangga, Indonesia for research facilities and funding under contract 341/UN3.14/LT/2019.

■ REFERENCES

[1] Nandika, D., Syamsu, K., Arinana, A., Kusumawardani, D.T., and Fitriana, Y., 2019, Bioactivities of catechin from Gambir (*Uncaria gambir* Roxb.) against wood-decaying fungi, *BioResources*, 14 (3), 5646–5656.

[2] Davis, A.P., and Figueiredo, E., 2007, A checklist of the Rubiaceae (coffee family) of Bioko and Annobon (Equatorial Guinea, Gulf of Guinea), *Syst. Biodivers.*, 5 (2), 159–186.

[3] Anggraini, T., Tai, A., Yoshino, T., and Itani, T., 2011, Antioxidative activity and catechin content of four kinds of *Uncaria gambir* extract from West Sumatra, Indonesia, *Afr. J. Biochem. Res.*, 5 (1), 33–38.

[4] Amir, M., Mujeeb, M., Khan, A., Ashraf, K., Sharma, D., and Aqil, M., 2012, Phytochemical analysis and *in vitro* antioxidant activity of *Uncariagambir*, *Int. J. Green Pharm.*, 6 (1), 67–72.

[5] Ahmad, R., Hashim, H.M., Noor, Z.M., Ismail, N.H., Salim, F., Lajis, N.H., and Shaari, K., 2011, The Antioxidant and antidiabetic potential activity of Malaysian *Uncaria*, *Res. J. Med. Plant*, 5 (5), 587–595.

[6] Picking, D., Delgoda, R., Boulogne, I., and Mitchell, S., 2013, *Hyptis verticillata* Jacq: A review of its traditional uses extension, phytochemistry, pharmacology, and toxicology, *J. Ethnopharmacol.*, 147 (1), 16–41.

[7] Heitzman, M.E., Neto, C.C., Winiarz, E.,Vaisberg, A.J., and Hammond, G.B., 2005, Ethnobotany, phytochemistry, and pharmacology of *Uncaria* (Rubiaceae), *Phytochemistry*, 66 (1), 5–29.

[8] Gadkari, P.V., and Balaraman, M., 2015, Catechins: Sources, extraction, and encapsulation: A review, *Food Bioprod. Process.*, 93, 122–138.

[9] Zhang, Q., Zhao, J.J., Xu, J., Feng, F., and Qu, W., 2015, Medicinal uses, phytochemistry and pharmacology of the genus *Uncaria gambir*, *J. Ethnopharmacol.*, 173, 48–80.

[10] Melia, S., Novia, D., and Juliyarsi, I., 2015, Antioxidant and antimicrobial activities of gambir (*Uncaria gambir* Roxb) extracts and their application in *rendang*, *Pak. J. Nutr.*, 14 (12), 938–941.

[11] Ferdinal, N., 2014, A simple purification method of catechin from gambier, *IJASEIT*, 4 (6), 53–55.

[12] Fujiwara, H., Takayama, S., Iwasaki, K., Tabuchi, M., Yamaguchi, T., Sekiguchi, K., Ikarashi, Y., Kudo, Y., Kase, Y., Arai, H., and Yaegashi, N., 2011, Yokukansan, a traditional Japanese medicine, ameliorates memory disturbance and abnormal social interaction with anti-aggregation effect of cerebral amyloid β proteins in amyloid precursor protein transgenic mice, *Neuroscience*, 180, 305–313.

[13] Mizukami, K., Asada, T., Kinoshita, T., Tanaka, K., Sonohara, K., Nakai, R., Yamaguchi, K., Hanyu, H., Kanaya, K., Takao, T., Okada, M., Kudo, S., Kotoku, H., Iwakiri, M., Kurita, H., Miyamura, T., Kawasaki, Y., Omori, K., Shiozaki, K., Odawara, T., Suzuki, T., Yamada, S., Nakamura, Y., and Toba, K., 2009, A randomized cross-over study of a traditional Japanese medicine (kampo), yokukansan, in the treatment of the behavioural and psychological symptoms of dementia, *Int. J. Neuropsycho. Pharmacol.*, 12 (2), 191–199.

[14] Shen, J., Zhu, Y., Yang, X., and Li, C., 2012, Graphene quantum dots: Emergent nanolights for bioimaging, sensors, catalysis, and photovoltaic devices, *Chem. Commun.*, 48 (31), 3686–3699.

[15] Wang, X., Cao, L., Yang, S.T., Lu, F., Meziani, M.J., Tian, L., Sun, K.W., Bloodgood, M.A., and Sun, Y.P., 2010, Bandgap-like strong fluorescence in functionalized carbon nanoparticles, *Angew. Chem. Int. Ed.*, 49, 5310–5314.

[16] Sun, Y.P., Wang, X., Lu, F., Cao, L., Meziani, M.J., Luo, P.G., Gu, L., and Veca, L.M., 2008, Doped carbon nanoparticles as a new platform for highly photoluminescent dots, *J. Phys. Chem. C*, 112 (47), 18295–18298.

[17] Vandarkuzhali, S.A., Jeyalakshmi, V., Sivaraman, G., Singaravadivel, S., Krishnamurthy, K.R., and Viswanathan, B., 2017, Highly fluorescent carbon dots from pseudo-stem of banana plant: Applications as nanosensor and bio-imaging agents, *Sens. Actuators, B*, 252, 894–900.

[18] Namdari, P., Negahdari, B., and Eatemadi, A., 2017, Synthesis, properties and biomedical applications of carbon-based quantum dots: An updated review, *Biomed. Pharmacother.*, 87, 209–222.

[19] Zhang, Q., Xie, S., Yang, Y., Wu, Y., Wang, X., Wu, J., Zhang, L., Chen, J., and Wang, Y., 2018, A facile synthesis of highly nitrogen-doped carbon dots for imaging and detection in biological samples, *J. Anal. Methods Chem.*, 2018, 7890937.

[20] Himaja, A.L., Karthik, P.S., Sreedhar, B., and Singh, S.P., 2014, Synthesis of carbon dots from kitchen waste: Conversion of waste to value added product, *J. Fluoresc.*, 24 (6), 1767–1773.

[21] Das, R., Bandyopadhyay, R., and Pramanik, P., 2018, Carbon quantum dots from natural resource: A review, *Mater. Today Chem.*, 8, 96–109.

[22] Baguley, D.M., Humphriss, R.L., Axon, P.R., and Moffat, D.A., 2005, Change in tinnitus handicap after translabyrinthine vestibular schwannoma excision, *Otol. Neurotol.*, 26 (5), 1061–1063.

[23] Yallappa, S., Manaf, S.A.A., and Hegde, G., 2018, Synthesis of a biocompatible nanoporous carbon and its conjugation with florescent dye for cellular imaging and targeted drug delivery to cancer cells, *New Carbon Mater.*, 33 (2), 162–172.

[24] Wang, J., Cheng, C., Huang, Y., Zheng, B., Yuan, H., Bo, L., Zheng, M.W., Yang, S.Y., Guo, Y., and Xiao, D., 2014, A facile large-scale microwave synthesis of highly fluorescent carbon dots from benzenediol isomers, *J. Mater. Chem. C*, 2 (25), 5028–5035.

[25] Xiao, F.X., Miao, J., and Liu, B., 2014, Layer-by-layer self-assembly of CdS quantum dots/graphene nanosheets hybrid films for photoelectrochemical and photocatalytic applications, *J. Am. Chem. Soc.*, 136 (4), 1559–1569.

[26] Fahmi, M.Z., Sukmayani, W., Khairunisa, S.Q., Witaningrum, A.M., Indriati, D.W., Matondang,

M.Q.Y., Chang, J.Y., Kotaki, T., and Kameoka, M., 2016, Design of boronic acid-attributed carbon dots on inhibits HIV-1 entry, *RSC Adv.*, 6 (95), 92996–93002.

[27] Thoo, L., Fahmi, M.Z., Zulkipli, I.N., Keasberry, N., and Idris, A., 2017, Interaction and cellular uptake functions of surface-modified carbon dot nanoparticles by J774. 1 macrophages, *Cent. Eur. J. Immunol.*, 42 (3), 324–330.

[28] Yao, J., Feng, J., and Chen, J., 2016, External-stimuli responsive systems for cancer theranostic, *Asian J. Pharm. Sci.*, 11 (5), 585–595.

[29] Saneja, A., Kumar, R., Arora, D., Kumar, S., Panda, A.K., and Jaglan, S., 2018, Recent advances in near-infrared light-responsive nanocarriers for cancer therapy, *Drug Discovery Today*, 23 (5), 1115–1125.

[30] Xu, W., Qian, J., Hou, G., Suo, A., Wang, Y., Wang, J., Sun, T., Yang, M., Wan, X., and Yao, Y., 2017, Hyaluronic acid-functionalized gold nanorods with pH/NIR dual-responsive drug release for synergetic targeted photothermal chemotherapy of breast cancer, *ACS Appl. Mater. Interfaces*, 9 (42), 36533–36547.

[31] Huang, C.Y., Ju, D.T., Chang, C.F., Reddy, P.M., and Velmurugan, B.K., 2017, A review on the effects of current chemotherapy drugs and natural agents in treating non–small cell lung cancer, *BioMedicine*, 7 (4), 23.

[32] Feng, T., Ai, X., An, G., Yang, P., and Zhao, Y., 2016, Charge-convertible carbon dots for imaging-guided drug delivery with enhanced in vivo cancer therapeutic efficiency, *ACS Nano*, 10 (4), 4410–4420.

[33] Fahmi, M.Z., Chen, J.K., Huang, C.C., Ling, Y.C., and Chang, J.Y., 2015, Phenylboronic acid-modified magnetic nanoparticles as a platform for carbon dot conjugation and doxorubicin delivery, *J. Mater. Chem. B*, 3 (27), 5532–5543.

[34] Yan, T., Zhong, W., Yu, R., Yi, G., Liu, Z., Liu, L., Wang, X., and Jiang, J., 2019, Nitrogen-doped fluorescent carbon dots used for the imaging and tracing of different cancer cells, *RSC Adv.*, 9 (43), 24852–24857.

[35] Fahmi, M.Z., Haris, A., Permana, A.J., Wibowo, D.L.N., Purwanto, B., Nikmah, Y.L., and Idris, A., 2018, Bamboo leaf-based carbon dots for efficient tumor imaging and therapy, *RSC Adv.*, 8 (67), 38376–38383.

[36] Acharya, P.P., Genwali, G.R., and Rajbhandari, M., 2013, Isolation of catechin from *Acacia catechu* willdenow estimation of total flavonoid content in *Camellia sinensis* Kuntze and *Camellia sinensis* Kuntze var. *assamica* collected from different geographical region and their antioxidant activities, *Sci. World*, 11 (11), 32–36.

[37] Bhunia, S.K., Saha, A., Maity, A.R., Ray, S.C., and Jana, N.R., 2013, Carbon nanoparticle-based fluorescent bioimaging probes, *Sci. Rep.*, 3, 1473.

[38] Saravanan, K.R.A., Prabu, N., Sasidharan, M., and Maduraiveeran, G., 2019, Nitrogen-self doped activated carbon nanosheets derived from peanut shells for enhanced hydrogen evolution reaction, *Appl. Surf. Sci.*, 489, 725–733.

[39] Fei, H., Li, H., Li, Z., Feng, W., Liu, X., and Wei, M., 2014, Facile synthesis of graphite nitrate-like ammonium vanadium bronzes and their graphene composites for sodium-ion battery cathodes, *Dalton Trans.*, 43 (43), 16522–16527.

[40] Choi, J., Kim, N., Oh, J.W., and Kim, F.S., 2018, Bandgap engineering of nanosized carbon dots through electron-accepting functionalization, *J. Ind. Eng. Chem.*, 65, 104–111.

[41] Huang, C.C., Hung, Y.S., Weng, Y.M., Chen, W., and Lai, Y.S., 2019, Sustainable development of carbon nanodots technology: Natural products as a carbon source and applications to food safety, *Trends Food Sci. Technol.*, 86, 144–152.

[42] Sepperer, T., and Tondi, G., 2018, Fractioning of Industrial Tannin Extract in Different Organic Solvents, *Das 12. Forschungs forum der österreichischen Fachhochschulen (FFH)*, 4–5 April 2018, Campus Urstein, Salzburg, Austria.

[43] Jia, X., Li, J., and Wang, E., 2012, One-pot green synthesis of optically pH-sensitive carbon dots with up conversion luminescence, *Nanoscale*, 4 (18), 5572–5575.

[44] Rawangkan, A., Wongsirisin, P., Namiki, K., Iida, K., Kobayashi, Y., Shimizu, Y., Fujiki, H., and

Suganuma, M., 2018, Green tea catechin is an alternative immune checkpoint inhibitor that inhibits PD-L1 expression and lung tumor growth, *Molecules*, 23 (8), E2071.

[45] Yang, C.S., and Wang, H., 2016, Cancer preventive activities of tea catechins, *Molecules*, 21 (12), E1679.

[46] Negri, A., Naponelli, V., Rizzi, F., and Bettuzzi, S., 2018, Molecular targets of epigallocatechin—Gallate (EGCG): A special focus on signal transduction and cancer, *Nutrients*, 10 (12), E1936.

[47] Fahmi, M.Z., Wibowo, D.L.N., Sakti, S.C.W., Lee, H.V., and Isnaeni, 2020, Human serum albumin capsulated hydrophobic carbon nanodots as staining agent on HeLa tumor cell, *Mater. Chem. Phys.*, 239, 122266.

[48] Ansari, A.A., Hasan, T., Syed, N., Labis, J., and Alshatwi, A.A., 2017, *In-vitro* cytotoxicity and cellular uptake studies of luminescent functionalized core-shell nanospheres, *Saudi J. Biol. Sci.*, 24 (6), 1392–1403.

Isotope and Geochemistry Characterization of Hot Springs and Cold Springs of Sembalun – Rinjani Area, East Lombok, West Nusa Tenggara – Indonesia

Satrio Satrio[1,*], Rasi Prasetio[1], Boy Yoseph Cahya Sunan Sakti Syah Alam[2], Teuku Yan Waliyana Muda Iskandarsyah[2], Faizal Muhammadsyah[2], Mohamad Sapari Dwi Hadian[2], and Hendarmawan Hendarmawan[2]

[1]*Center for Isotopes and Radiation Application – BATAN, Jl. Lebak Bulus Raya No. 49, Jakarta 12440 Indonesia*

[2]*Faculty of Geological Engineering, Padjadjaran University, Jl. Raya Bandung Sumedang Km 21, Jatinangor, Sumedang 45363 Indonesia*

* ***Corresponding author:***

tel: +62-813-87609230
email: satrio@batan.go.id

Received: October 23, 2019
Accepted: March 18, 2020

DOI: 10.22146/ijc.50790

Abstract: *The presence of several hot springs in Sembalun – Rinjani, East Lombok, West Nusa Tenggara is an indicator of geothermal potential in the area. This study aims to determine the characteristics of hot springs and cold springs and also the geothermal potential in Sembalun – Rinjani area using isotopes and geochemistry methods. The result of $\delta^{18}O$ and $\delta^{2}H$ stable isotopes analysis shows that most of the hot springs are meteoric water. Except for Kalak hot spring, other hot springs are a mixing product of meteoric water and andesitic water, with meteoric water composition between 64 to 87%. While ^{14}C radioisotope suggests that the age of hot springs in the Sembalun area is about 10,000–12,000 years BP, the surrounding cold springs are mostly Modern except Jorong cold spring. The results of gas analysis (He, Ar, and Ne) also suggest the same origin of geothermal fluid, i.e., meteoric water origin. Based on chemical composition, Kalak hot spring is plotted as sulfate type water, while Sebau hot spring is plotted near mature water composition but not representing reservoir fluid due to its relatively low temperature and high Mg content. Na/K geothermometer calculation from Sembalun area shows that subsurface temperature is varied between 111–161 °C, while from Rinjani hot springs indicates higher subsurface temperature, i.e., 250–260 °C. It is estimated that reservoir fluid has high TDS with chloride content up to 4000 mg/L.*

Keywords: *geothermal; Sembalun – Rinjani; hot spring; cold spring; isotope; geochemistry; geothermometer*

■ INTRODUCTION

Sembalun is located on the east flank of Mount Rinjani, East Lombok Regency, Lombok Island – Indonesia. Geographically, Sembalun is surrounded by mountainous hills with elevation about 800–1100 m above sea level, around 60 km from Mataram, the capital city of West Nusa Tenggara Province. There are several cold springs in the valley of Sembalun that being uses by surrounded villagers for daily use and agricultural use, while some hot springs also emerge from this area, namely Kalak, Orok, and Sebau. Some hot springs with higher temperatures also emerge at a higher elevation, near Segara Anak Lake, a crater lake of Rinjani Mountain. The presence of several hot springs in the area is an indicator of geothermal energy potential, thus might be utilized to meet electricity demand in Lombok Island. Based on previous work, the Ministry of Energy and Mineral Resources has identified the prospective of the Sembalun area to be developed for its geothermal energy [1]. The aim of this current study is to determine the characteristics of hot springs and cold springs and asses its geothermal potential using isotopes and geochemistry data in the hydrogeological framework. The study utilized stable isotopes of water, i.e., ^{2}H and ^{18}O, to investigate the origin of fluids and its interaction with surrounding rocks [2-

3], while ^{14}C radioisotope is used to determine groundwater age [4-5]. In addition, a fluid geochemistry approach is used to determine the characteristics and temperature of the reservoir [6]. The result of this study will bring benefits as support for the development of Sembalun – Rinjani geothermal prospect, especially as electricity generation.

■ EXPERIMENTAL SECTION

Study Area

The study area is located at Suela, Aikmal and Sembalun Districts, East Lombok Regency, West Nusa Tenggara with geographical coordinate between 116°30'00" E to 116°35'00" E and 8°20'30" S to 8°30'00" S, covering 10 × 19 km^2 [7]. The location of sampling sites in the study area can be seen in Fig. 1.

Samples were taken in some thermal manifestations such as hot springs and gas bubbles, as well as groundwater and surface water as a comparison. During the sampling, field measurements were also conducted, i.e., temperature, pH, and electric conductivity.

Procedure

Water sampling

Water samples were taken at the discharge point of the spring. Samples for cation analysis were acidified with HNO_3, while samples for anion analysis were not acidified [8]. Samples for isotopes analysis (^{18}O and ^{2}H) were collected in 30 mL air-tight bottle with no air bubbles to minimize isotope fractionation [9]. Meanwhile, samples for groundwater dating (^{14}C analysis) were collected as much as 60 L, followed by in situ precipitation of carbonates using barium chloride and coagulation agent. The barium carbonate precipitation was then collected and brought to the laboratory [10].

Gas sampling

Gas sampling was done using the Giggenbach flask (Fig. 2), an evacuated glass-bottle filled with 4 N NaOH [11]. Steam from fumaroles is condensed inside the bottle, while acidic gases, i.e., CO_2 and H_2S, will be dissolved in NaOH solution as carbonate and sulfide. Other minor gases, i.e., H_2, He, Ar, O_2, N_2, CH_4, will occupy the headspace above NaOH solution. During the sampling, the glass bottle is connected with fumarole using silicone hose and titanium funnel or titanium tube. Clay was placed around the vent to minimize air contamination [12].

Analysis of stable isotopes of ^{2}H and ^{18}O

Analysis of stable isotopes was done by laser spectroscopic method, i.e., using LGR (Los Gatos Research) DLT-100 Liquid Water Isotope Analyzer. The

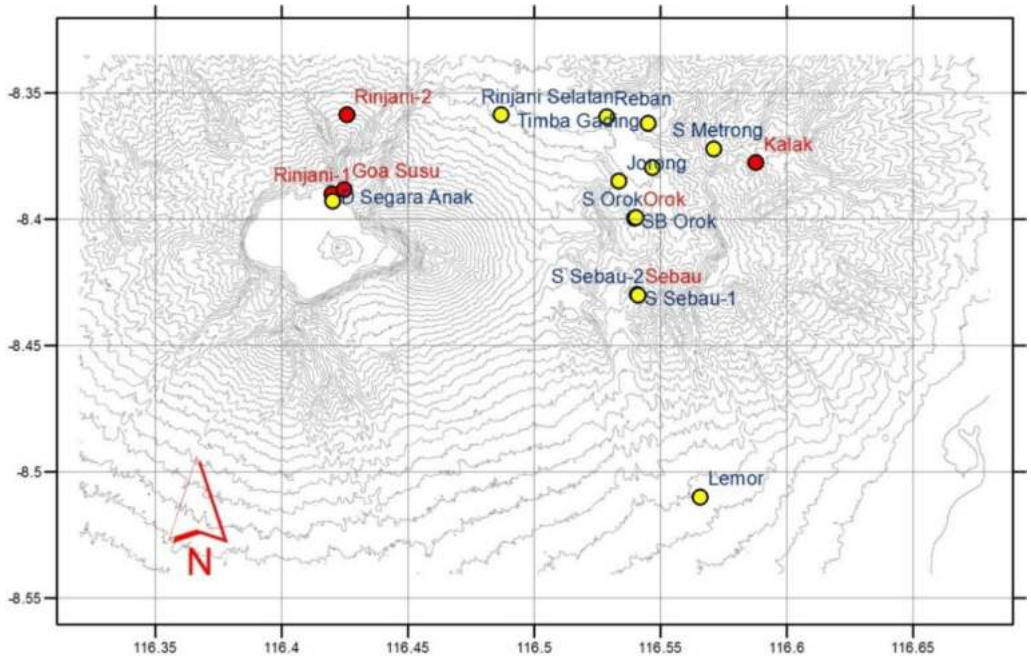

Fig 1. Sampling location at mount Rinjani and Sembalun area

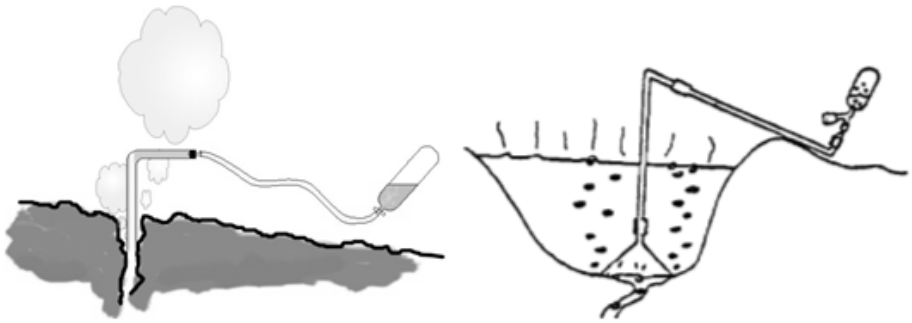

Fig 2. Sampling scheme

value of isotope composition (δ) is expressed in ‰ unit, i.e., relative deviation of isotope ratio of a sample against isotope ratio Standard Mean Oceanic Water (SMOW) as defined by the following equation [13-14]:

$$\delta = \frac{R_{Sample} - R_{SMOW}}{R_{SMOW}} \times 1000\ ‰$$

where, R_{Sample} = the isotope ratio (δ^2H or $\delta^{18}O$) of the sample; R_{SMOW} = the isotope ratio (δ^2H or $\delta^{18}O$) of the SMOW

Analysis of radiocarbon (^{14}C)

Radiocarbon dating was prepared by reacting $BaCO_3$ precipitation from a sample with 10% HCl in preparation line, producing CO_2 gas.

$$BaCO_3 + 2HCl \rightarrow BaCl_2 + H_2O + CO_2$$

The produced CO_2 is then absorbed using 30 mL of 1:1 Carbosorb-E and Permafluor-E [15] and counted using Liquid Scintillation Analyzer (LSA) Perkin Elmer Tri-Carb 2910TR.

Analysis of water chemistry

Analysis of water chemistry was done using several methods, i.e., acid-base titration for HCO_3^- using HCl as the titrant, while ion chromatography was used to analyze Cl^-, SO_4^{2-}, F^- and Na^+, K^+, Ca^{2+}, Mg^{2+}, Li^+. Silica was analyzed using a spectrophotometric method with ammonium molybdate reagent.

Analysis of non-condensable gases (NCG)

Analysis of some NCG, i.e., He, H_2, N_2, Ar, and CH_4, was done using Agilent 7890A gas chromatography equipped with porapak column and thermal conductivity detector, with N_2 and He as a carrier gas. Meanwhile, the analysis of CO_2 and H_2S were conducted by using a titration method [16].

■ RESULTS AND DISCUSSION

Physicochemical Characteristics

The summary of the physical properties during the dry season and rainy season are given in Table 1 and 2.

Sebau hot spring

Sebau hot spring is located in Sapit village, Sula regency, at an elevation of 1345 m. The temperature of the spring is 35.4 °C and neutral pH about 7.3 with blackish color and sulfuric odor. There is no significant change in temperature and pH between the rainy season and dry season. The river water was also taken as a comparison, i.e., as surface water end-member.

Kalak hot spring

Kalak hot spring is located in Sambelia area at an elevation of 1050 m. The pH of the hot spring is neutral, i.e., 7.2, while the temperature is 43.6 °C with an ambient temperature of 23.9 °C. There is also no significant change in temperature and pH between the rainy season and dry season in this area.

Orok warm spring and well bore

Orok is located in Sembalun Bumbung village, Sembalun regency, at an elevation of 1219 m. The temperature of the warm spring is 23.5 °C, and the well bore water is 23.8 °C (at a depth of 125 m) while the ambient air is 21.3 °C. The pH of the spring and well are neutral, i.e., 7.30 and 7.0, respectively. During the dry season, the well is dry.

Rinjani hot spring

There are some hot springs located on the slope of Mount Rinjani, i.e., Goa Susu, Rinjani-1, and Rinjani-2. Goa Susu hot spring is located at an elevation of 1891 m,

Table 1. Location and physical properties of springs during rainy season

No.	Location	Coordinate	Elevation (m)	T ambient (°C)	T sample (°C)	pH	EC (mS/cm)
1	Kalak hot spring	S: 9073907.93 E: 454634.22	1050	23.9	43.6	7.20	2.61
2	Kalak river	S: 9073907.93 E: 454634.22	1050	23.9	22.9	7.26	0.16
3	Sebau hot spring	S: 9068128.66 E: 449466.36	1345	28.0	35.4	7.30	2.02
4	Sebau-1 river	S: 9068190.01 E: 449402.07	1331	28.0	20.2	7.83	0.13
5	Orok wellbore	S: 9071472.94 E: 449395.16	1308	22.4	23.8	7.00	0.74
6	Orok river	S: 9071509.79 E: 449395.12	1291	22.4	20.3	7.00	0.19

Table 2. Location and physical properties of springs during dry season

No.	Location	Coordinate	Elevation (m)	T ambient (°C)	T sample (°C)	pH	EC (mS/cm)
1	Kalak hot spring	S: 9073907.93 E: 454634.22	1050	23.9	43.8	7.06	2.26
2	Sebau hot spring	S: 9068128.66 E: 449466.36	1345	26.5	35.3	7.35	2.02
3	Orok warm spring	S: 9071509.79 E: 449395.12	1291	21.3	23.5	7.33	0.80
4	Rinjani-1 hot spring	S: 9072534.25 E: 436143.50	2003	18.0	45.0	6.34	4.03
5	Goa Susu hot spring	S: 9072712.26 E: 436695.87	1891	18.0	42.0	7.00	3.65
6	Rinjani-2 hot spring	S: 9072575.80 E: 436207.36	1984	18.0	44.0	6.22	5.07
7	Segara Anak lake	S: 9073708.56 E: 450105.73	2020	18.0	20.8	7.94	3.18
8	Lemor cold spring	S: 9059290.29 E: 452216.09	450	24.1	22.2	6.20	0.16
9	Reban cold spring	S: 9075893.71 E: 448111.56	1297	22.5	21.2	8.01	0.20
10	Makem cold spring	S: 9075992.30 E: 448380.59	1152	22.5	22.2	6.65	0.26
11	Jorong cold spring	S: 9065445.52 E: 448653.11	1282	21.4	20.4	7.70	0.12
12	Rante Mas cold spring	S: 9073708.56 E: 450105.73	1205	22.5	20.9	7.01	0.13
13	Timba Gading cold spring	S: 9075638.18 E: 449926.74	1162	21.0	20.5	6.20	0.33
14	Sebau-1 river	S: 9068190.01 E: 449402.07	1331	26.5	18.3	7.90	0.13
15	Sebau-2 river	S: 9068117.96 E: 449509.18	1350	26.0	18.3	7.44	0.11
16	Orok wellbore	S: 9071472.94 E: 449395.16	1308	21.3	-	-	-
17	Orok river	S: 9071509.79 E: 449395.12	1291	21.3	20.1	7.76	0.18

while Rinjani-1 and Rinjani-2 are located at an elevation of 2003 m and 1984 m, respectively. The temperatures of these hot springs are 42 °C, 45 °C and 44 °C, respectively, while the ambient temperature is 18 °C. In addition, water from Segara Anak Lake (2020 m) was also taken as an end-member of meteoric water.

Cold spring and river

In addition, several cold springs and river samples were also taken as meteoric end-member. The temperature of these springs and rivers are varied at 20.2–22.2 °C, with a neutral pH between 6.20–8.01.

Isotopes Characteristics

The result of stable isotope analysis ($\delta^{18}O$, $\delta^{2}H$) during the rainy season and dry season and groundwater dating (^{14}C) can be seen in Table 3, 4, and 5, while a graphic of $\delta^{18}O$ versus $\delta^{2}H$ is provided in Fig. 3. Since the Local Meteoric Water Line of Lombok is not available, the Indonesian Meteoric Water Line (IMWL) is used to help isotope data interpretation [17]. All isotope ($\delta^{18}O$ and $\delta^{2}H$) data samples are plotted into the graph with reference to the Indonesian Meteoric Line. As a comparison, the Global Meteoric Water Line (GMWL) is also included in the graph. The isotopes ($\delta^{18}O$ and $\delta^{2}H$) data of water samples are a representation of meteoric water, so it should be referred to the Meteoric Water Line [18].

The isotopic ratio can represent some physical-chemical processes in the geothermal system, such as water-rock interaction, mixing process, and steam separation [19]. The isotope of $\delta^{18}O$ and $\delta^{2}H$ are also can be used as a tracer to infer the mechanism of geothermal fluid evolution [20].

Fig. 3 shows that all cold spring and river water plotted near the Indonesia Meteoric Water Line. Meanwhile, some hot springs, i.e., Sebau, Rinjani, and Segara Anak, are plotted along the mixing line between meteoric and andesitic water. Kalak hot spring is not showing a sign of significant evaporation or oxygen shift. Orok hot spring exhibits the influence of season on isotopic composition where during the dry season shows oxygen shift and mixing with andesitic water; on the contrary, during the rainy season shows the meteoric component. In general, all hot springs in Rinjani and Sembalun are meteoric origin with different evolution, which can be explained later by chemistry data.

Another isotope, which is used to determine the characteristics of springs in the Sembalun – Rinjani area, i.e., its age is ^{14}C radioisotope. The result of ^{14}C analysis is expressed in units of percent Modern Carbon (pMC)

Table 3. Result of stable isotope analysis ($\delta^{18}O$ and $\delta^{2}H$) during the rainy season

No.	Location	$\delta^{18}O$ (‰)	$\delta^{2}H$ (‰)
1	Kalak hot spring	−6.87	−49.76
2	Sebau hot spring	−5.41	−42.72
3	Orok well bore	−7.63	−48.38
4	Kalak river	−6.45	−45.84
5	Sebau river	−7.64	−45.90
6	Orok river	−6.36	−46.99

Table 4. Result of stable isotope analysis ($\delta^{18}O$ and $\delta^{2}H$) during the dry season

No.	Location	$\delta^{18}O$ (‰)	$\delta^{2}H$ (‰)
1	Kalak hot spring	−6.62	−49.30
2	Sebau hot spring	−5.50	−41.40
3	Orok warm spring	−5.59	−46.30
4	Rinjani-1 hot spring	−2.09	−34.10
5	Goa Susu hot spring	−3.65	−38.00
6	Rinjani-2 hot spring	−3.58	−38.10
7	Segara Anak lake	−1.96	−34.80
8	Lemor spring	−5.50	−35.50
9	Reban spring	−7.09	−47.30
10	Makom spring	−7.04	−46.90
11	Jorong spring	−6.73	−45.10
12	Rante Mas spring	−6.95	−48.80
13	Timba Gading spring	−6.58	−42.50
14	Sebau-1 river	−6.75	−43.70
15	Sebau-2 river	−6.58	−44.30
16	Orok river	−6.77	−47.00

Table 5. Analysis result of ^{14}C dating in Sembalun area

Location	pMC	Age (years BP)
Kalak hot spring	26.95	10,425
Sebau hot spring	22.18	12,030
Orok warm spring	24.41	11,240
Jorong cold spring	42.20	6,715
Timba Gading cold spring	93.50	140
Lemor cold spring	93.52	135

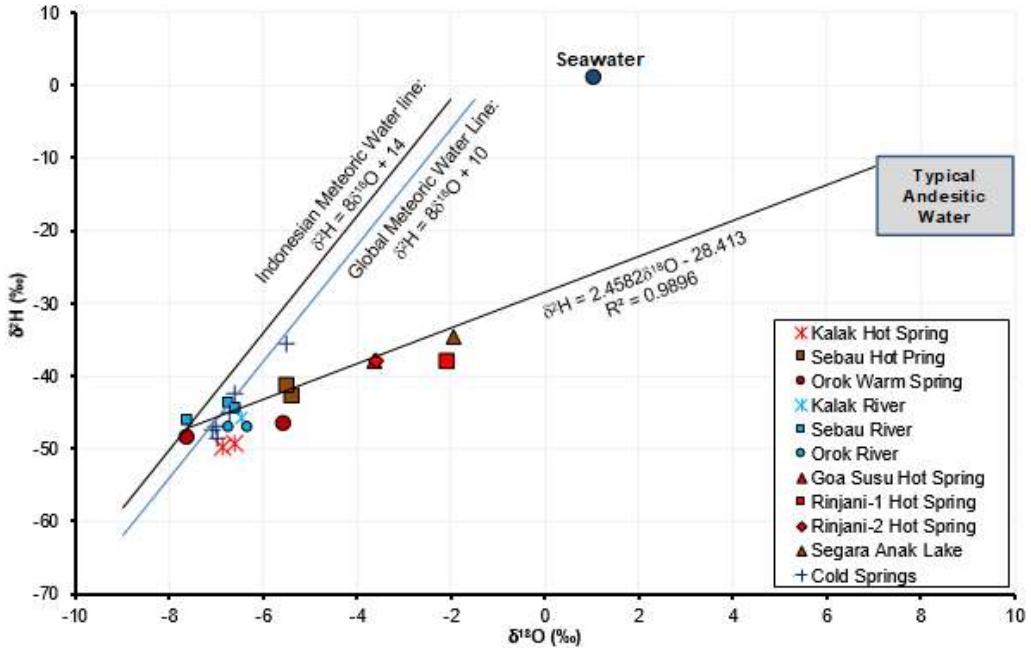

Fig 3. Graphic of δ^2H vs. $\delta^{18}O$ of the hot and cold spring in Sembalun – Rinjani area

and then converted into age (years BP) with the following equation [21]:

$$t = 8267 \ln\left(\frac{100}{A_{SN}}\right)$$

where, A_{SN} = the radioisotope ^{14}C activity of the sample (pMC); t = year BP (before present = before 1950)

The result of a radioisotope of ^{14}C (groundwater dating) shows that Sebau, Kalak, and Orok hot springs have relatively the same age between 10,000–12,000 year BP, where Kalak hot spring is younger than two other hot springs. This probably due to mixing with local shallow groundwater. Jorong cold spring is 6,751 years BP, which probably comes from the upper hillside, while Timba Gading and Lemor cold springs are young groundwater below 200 years BP. The information on groundwater age is important because the sustainability of geothermal exploitation depends on fluid presence.

Geothermal fluid fraction

The fraction of geothermal fluid can be calculated using the following equation [22-23]:

$$\delta_m O^{18} = \delta_{aw} O^{18} . x - \delta_{rw} O^{18} . (1 - x)$$

where x = fraction of andesitic water; $\delta_m O^{18}$ = ^{18}O composition of mixed groundwater and andesitic water (‰); $\delta_{aw} O^{18}$ = ^{18}O composition of andesitic water (‰); $\delta_{rw} O^{18}$ = ^{18}O composition of groundwater (‰)

Table 6. Fraction of fluid from hot springs at Sembalun – Rinjani area

No.	Location	Andesitic Water	Meteoric Water
Rainy season			
1	Sebau hot spring	0.14	0.86
2	Orok wellbore	0.00	1.00
Dry season			
1	Sebau hot spring	0.13	0.87
2	Rinjani-1 hot spring	0.35	0.65
3	Goa Susu hot spring	0.25	0.75
4	Rinjani-2 hot spring	0.26	0.74
5	Segara Anak lake	0.36	0.64

Table 6 shows the calculated geothermal fluid fraction from several hot springs in the Rinjani – Sembalun area. Generally, the geothermal fluid of Sembalun – Rinjani is dominated by meteoric water, where at Sebau meteoric water fraction is consistent during the rainy and dry season, i.e., 86–87%. Meanwhile, hot springs at Rinjani hillside and Segara Anak, the fraction of meteoric water is lesser, i.e., 64–75%.

Chemical Characteristics

The results of the chemical analysis of hot springs, cold springs, and river water samples in the Sembalun –

Rinjani area, West Nusa Tenggara, which were taken in two seasons, rain and dry, can be seen in Table 7 and 8.

Fluid characteristics

Table 7 and 8 show that hot springs are distinguished from cold springs (MAD) from its TDS, i.e., hot springs have higher TDS than cold springs. However, there are differences between the hot springs, i.e., its chloride and sulfate content. Kalak has lower chloride content than Sebau hot spring, i.e., 173 mg/L and 526 mg/L, respectively. On the contrary, sulfate content of Kalak is much higher than Sebau, i.e., 1114 mg/L and 78.1 mg/L, respectively, which also consistent with the previous study by Sundhoro et al. [24]. This difference can be seen clearly by a ternary diagram of Cl-SO_4-HCO_3 (Fig. 4), which also depicts the hydrochemistry classification of the hot springs.

From the diagram, it can be seen that Sebau hot spring is plotted closer to mature water or reservoir composition due to its dominant chloride; however, this is not the case. Sebau hot spring is high in Mg content, which infer more dominant groundwater end-member [25]. Meanwhile, Kalak hot spring is plotted at the sulfate corner, but it is not steam-heated water due to its neutral pH. Moreover, there is no steam vent or fumarole around Kalak hot spring. Thus, the high sulfate content in Kalak is not originated from geothermal H_2S oxidation but likely caused by leaching from a sulfur-bearing rock formation. Orok warm spring is plotted on

Table 7. Chemical composition (mg/L) during rainy season

No.	Location	Cation				Anion					
		K	Na	Ca	Mg	SiO_2	Cl	SO_4	F	HCO_3	B
1	Kalak hot spring	4.87	255.25	425.37	3.78	45.71	173.42	1114.52	0.47	147.46	2.13
2	Sebau hot spring	5.90	178.25	174.01	1.31	32.96	526.22	78.09	0.36	90.55	3.39
3	Orok well bore	11.50	88.10	93.25	48.17	54.09	34.44	81.37	0.28	550.66	1.10
4	Kalak river	3.86	8.54	32.25	8.76	38.05	3.02	11.64	0.14	128.66	n.d.
5	Sebau river	1.41	5.16	16.97	7.59	27.37	3.49	5.57	0.15	115.29	n.d.
6	Orok river	4.33	10.61	24.44	12.83	38.88	2.00	16.72	0.19	175.33	n.d.

n.d.: not detected

Table 8. Chemical composition (mg/L) during dry season

No.	Location	Cation				Anion					
		K	Na	Ca	Mg	SiO_2	Cl	SO_4	F	HCO_3	B
1	Kalak hot spring	3.45	164.42	216.02	13.67	60.05	109.06	811.92	0.34	141.38	1.85
2	Sebau hot spring	6.48	170.91	291.88	11.21	40.69	627.10	14.29	0.21	136.5	3.59
3	Orok hot spring	3.24	72.27	45.16	43.29	66.73	89.23	101.05	0.33	338.7	2.16
4	Rinjani-1 hot spring	49.67	357.95	388.66	362.91	120.08	470.89	2254.19	0.53	316.88	5.67
5	Goa Susu hot spring	47.77	346.11	215.72	31.63	144.34	477.02	313.62	0.50	782.34	6.12
6	Rinjani-2 hot spring	49.46	384.39	189.46	348.70	131.48	530.54	1028.21	0.69	1145.65	5.52
7	Segara Anak lake (DSA)	45.36	282.80	121.68	337.94	89.98	470.89	1033.63	1.53	582.58	3.43
8	Lemor cold spring	3.5	5.02	16.43	13.28	57.61	3.22	6.98	0.41	117.47	n.d.
9	Reban cold spring	3.83	6.27	12.38	15.19	53.20	5.28	9.36	0.48	130.38	0.11
10	Makom cold spring	8.19	10.98	14.83	14.76	53.87	3.34	17.75	0.6	152.82	n.d.
11	Jorong cold spring	3.26	4.39	10.96	9.95	49.80	2.07	n.d.	0.57	110.88	0.18
12	Rante Mas cold spring	2.31	3.24	10.74	5.73	44.90	1.99	3.98	0.14	74.82	n.d.
13	Timba Gading spring	7.90	17.36	25.05	27.63	59.39	8.59	23.7	0.61	202.26	0.1
14	Sebau-1 river	1.49	10.62	27.54	10.01	37.42	15.78	33.23	0.13	124.32	0.18
15	Sebau-2 river	2.61	3.27	15.87	8.23	34.66	1.11	15.8	0.12	99.44	n.d
16	Orok river	2.93	4.12	27.13	13.39	62.17	1.54	32.1	0.2	122.82	n.d

n.d.: not detected

bicarbonate corner clearly shows mixing with groundwater, as also indicated by its near ambient temperature. Rinjani hot springs are plotted spreading between sulfate and bicarbonate, while cold springs are plotted at bicarbonate corner.

The different characteristics between hot springs can be assessed by correlation graphs between Na vs. Cl and Na vs. SO_4 (Fig. 5).

Fig. 5 shows that there is no common linear relationship between Na and Cl of all hot springs but rather divided into three groups: Sebau-Orok, Rinjani, and Kalak groups. Meanwhile, the graph of Na vs. SO_4 shows a more random plot that indicates different genesis of fluids since SO_4 is not a conservative element. Thus, the SO_4 concentration is more likely influenced by rock mineral composition. On the other hand, Segara Anak shows unique chemical composition, i.e., high Cl and SO_4 concentration but with neutral pH, which is different from the typical volcanic lake that has high Cl and SO_4 concentration but with low pH as Kawah Ijen volcanic lake [26]. There are two possibilities of Segara Anak fluid genesis: (1) the fluid is the hydrothermal origin with high Cl content, leaching out sulfate from rocks, and later mixing with meteoric water, (2) Input of magmatic gas, neutralized during fluid-rock interaction and later mixing with meteoric water.

Origin of fluids

The fluid origin also can be inferred from Li-Cl-B ternary diagram (Fig. 6). The diagram shows that none of the hot springs is plotted near the Li corner, indicates dominant deep rock dissolution [27], while springs plotted near Cl corner are originated from absorption of low B/Cl steam.

Geothermometer

Estimation of reservoir temperature is based on temperature-dependent of specific equilibration reaction, i.e., isotopes, cation solubility, and gases, applied to the composition of discharge geothermal fluids, i.e., hot springs, production wells, fumaroles [28]. In this study, Na/K and SiO_2 geothermometer are applied to estimate reservoir temperature (Table 9) [29].

Based on Na/K geothermometer, subsurface temperature from Kalak hot spring is estimated at about 111–126 °C, while Sebau hot spring is higher around

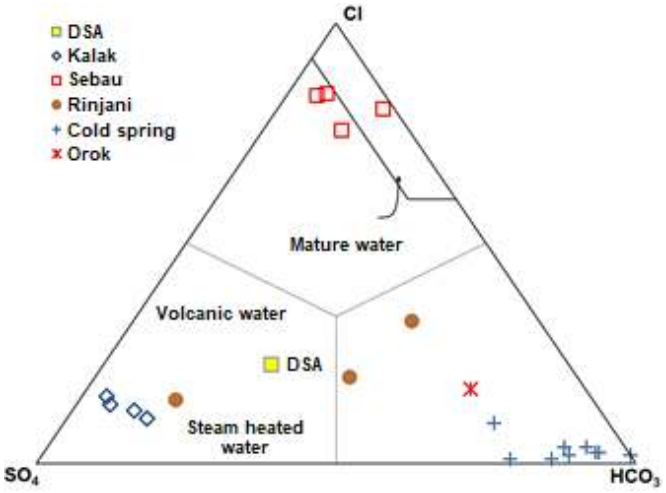

Fig 4. Ternary diagram of Cl-SO_4-HCO_3

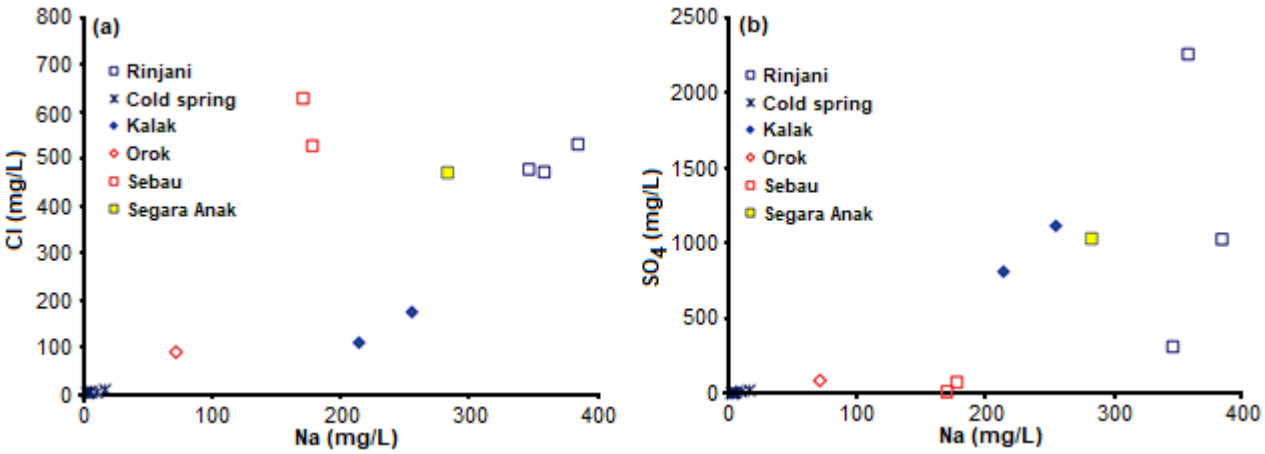

Fig 5. Correlation plot between: (a) Na vs. Cl and (b) Na vs. SO_4

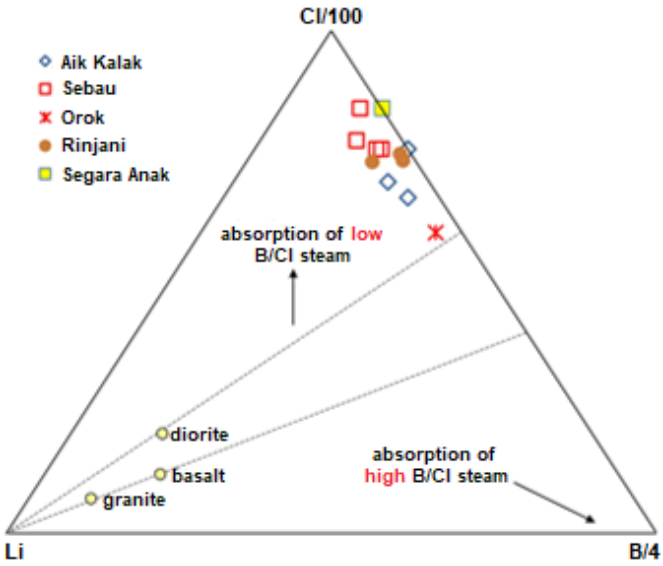

Fig 6. Ternary diagram of Li-Cl-B

148–161 °C. Rinjani hot spring indicates the highest reservoir temperature, i.e., 250–260 °C. Giggenbach ternary diagram (Fig. 7) shows that Kalak and Sebau hot springs are plotted at immature water composition where reservoir fluid is mixed with shallow water [30]. Calculation of silica quartz geothermometer indicates lower temperature, i.e., 98 °C, and 83 °C for Kalak, and Sebau hot springs, respectively. This low temperature is due to the fact that silica has a faster equilibrium rate compare to Na/K equilibrium; thus, this silica geothermometer indicates equilibrium temperature at shallower aquifer or mixing with aquifer with low silica content [31].

Gas composition

Relative composition of He, Ar, and N_2 can be utilized to distinguish the origin of volcanic and geothermal gases [32], i.e., meteoric, andesitic, or crustal origin [33]. Table 10 shows gas composition taken from bubbling pool at mount Rinjani slope. NCG (non-condensable gases) content is relatively high, i.e., 66% mol. Meanwhile, CO_2 and H_2S are dominant gases, reaching 90% mol and 8.6% mol from total NCG, respectively. This composition is slightly different from typical geothermal gas composition, where H_2S content is up to 15% [34]. This is possibly due to the conversion of H_2S into SO_4 by

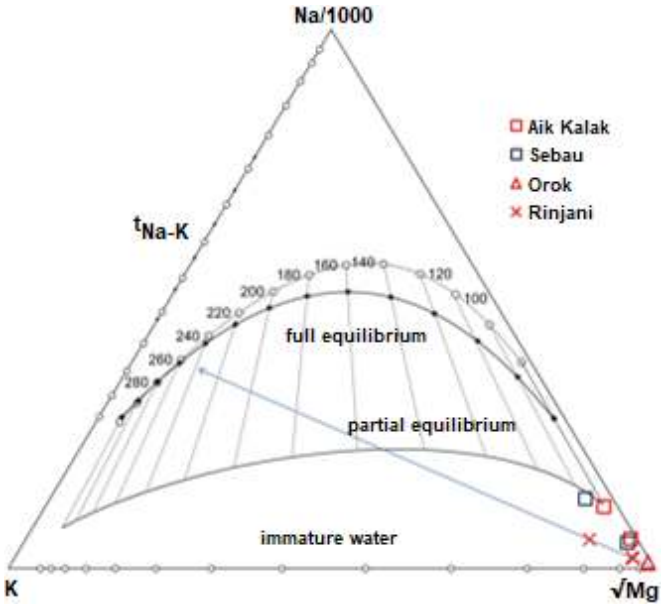

Fig 7. Giggenbach ternary diagram

Table 9. Calculation of Na/K and SiO_2 geothermometer

Location		Geothermometer (°C)		
		Na/K Fournier	Na/K GGB	SiO_2 Quartz
Kalak hot spring (rainy season)		112	127	98
Kalak hot spring (dry season)		109	124	111
	Average	111	126	105
Sebau hot spring (rainy season)		144	157	83
Sebau hot spring (dry season)		152	165	92
	Average	148	161	88
Orok hot spring		164	175	116
Rinjani-1 hot spring		257	260	148
Goa Susu hot spring		256	259	159
Rinjani-2 hot spring		250	253	153

Table 10. Gas composition of Rinjani-2

mmol								
CO_2	H_2S	He	H_2	N_2	O_2	Ar	CH_4	steam
95.667	1.011	0.0013	Ttd	9.2036	Ttd	0.1941	0.0682	54.43
% mol								
CO_2	H_2S	He	H_2	N_2	O_2	Ar	CH_4	total NCG
90.13	0.95	0.00	Ttd	8.67	Ttd	0.18	0.06	66.10

oxidation, as can be seen in SO_4 content of Rinjani hot spring [35].

The ratio of N_2/Ar is 47, which indicates that the fluid origin is meteoric, as also can be seen in the He-N_2-Ar ternary diagram (Fig. 8).

Reservoir fluid composition (mixing model)

Discharged fluid at hot springs is already altered from its reservoir composition due to physical-chemical interaction during ascending to surface. The actual reservoir composition, i.e., chloride and silica, can be estimated and traceback using silica-enthalpy and chloride-enthalpy mixing models [36], as can be seen in Fig. 9, which shows the curve of the quartz-geothermometer. It also shows that the mixing line is only passing through Orok and Rinjani samples and then intercept the curve at 450 mg/L silica and enthalpy of 850 kJ/kg, which is equivalent to 218 °C. Sebau and Kalak are not connected through the mixing line because the relation between silica and chloride in both samples is not positively correlated (Fig. 10), i.e., loss of silica from the fluid due to forming of secondary mineral [37-38]. Based on enthalpy of the reservoir, the composition of the reservoir's chloride can be estimated using the chloride-enthalpy diagram (Fig. 11). It is shown that the mixing

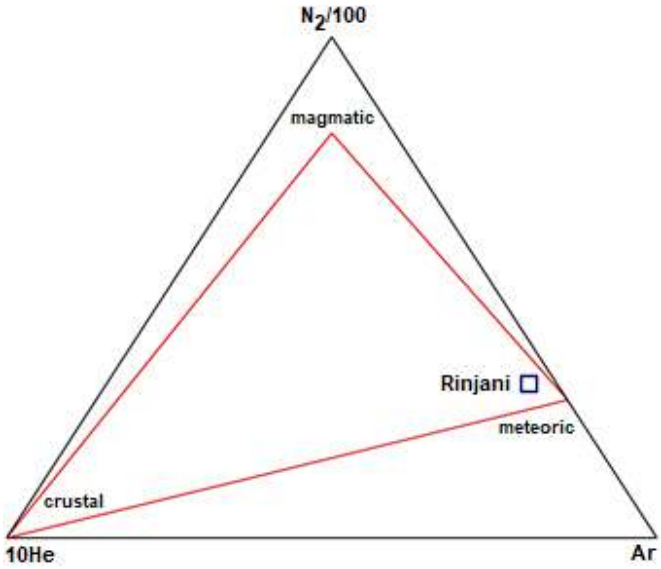

Fig 8. Ternary diagram of He-N_2-Ar

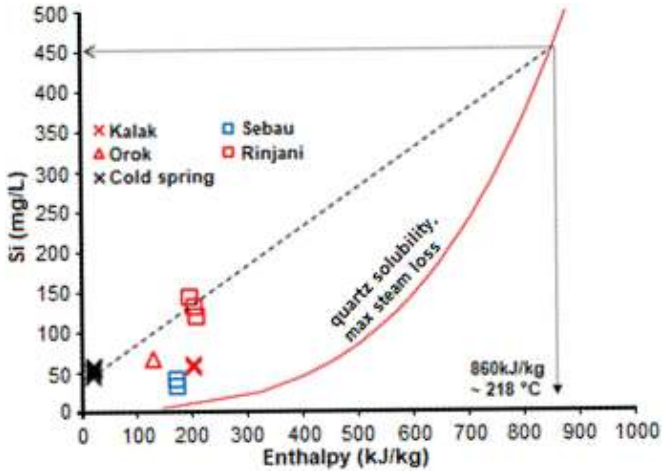

Fig 9. Mixing model of silica vs. enthalpy

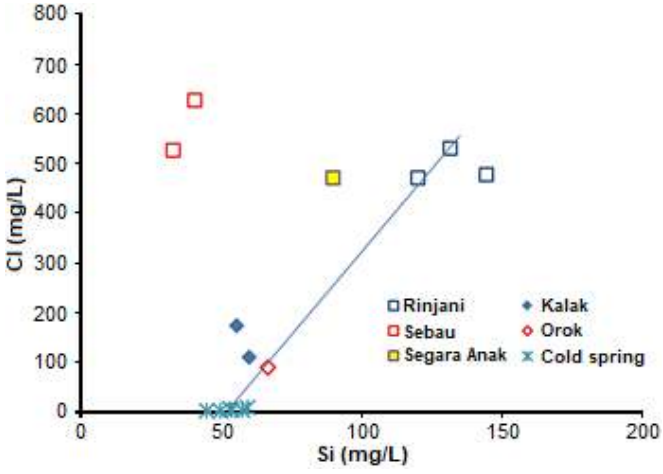

Fig 10. Correlation diagram of silica vs. chloride

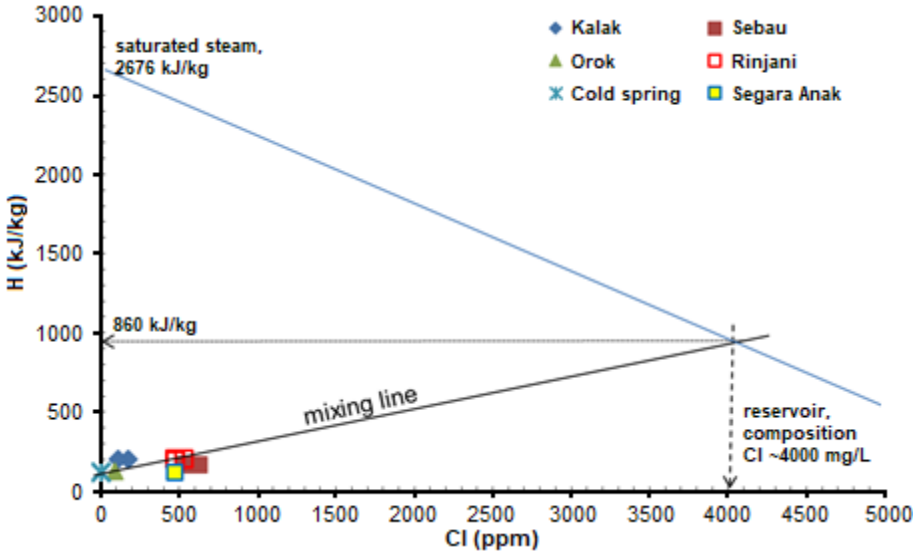

Fig 11. Mixing model of Cl vs. enthalpy

line with groundwater intercepts at enthalpy of 850 kJ/kg and chloride concentration at 40000 ppm, i.e., chloride concentration in the reservoir.

■ CONCLUSION

Based on stable isotopes content ($\delta^{18}O$, $\delta^{2}H$), it is found that all hot springs except Kalak, are the product of mixing between meteoric water and andesitic water with meteoric fraction about 0.64–0.87, while other surrounding springs are clearly meteoric water. Gas content, i.e., He, Ar, N_2, also indicates that fluid origin is meteoric water. The ^{14}C dating of Kalak hot spring shows 10,425 years BP of age. Sebau and Orok hot springs have an older groundwater age than Kalak hot spring, i.e. 12,030 years BP and 11,240 years BP, respectively, while surrounding cold springs are mostly modern except Jorong cold spring. Although Kalak hot spring is plotted on the sulfate corner, it does not have acidic properties; thus, it is not steam-heated waters. The high sulfate content in Kalak is not coming from H_2S oxidation but probably caused by leaching of sulfur-bearing minerals. Although Sebau hot spring is plotted at mature water composition with dominant chloride content, the hot spring does not represent reservoir fluid considering its low temperature and high Mg content.

Based on Na/K geothermometer, subsurface temperature for Kalak is estimated between 111–126 °C, while for Sebau is higher, i.e., between 148–161 °C. The highest temperature estimation is found in Rinjani, i.e. 250–260 °C. The geothermal fluid of the Sembalun area is calculated having brine composition with chloride content about 4000 mg/L, thus scaling can be a potential problem in the future.

■ REFERENCES

[1] Sundhoro, H., Kasbani, Yushantarti, A., and Hadi, M.N., 2007, Penyelidikan geologi dan geokimia daerah panas bumi Sembalun, Kabupaten Lombok Timur - Nusa Tenggara Barat, *Proceeding Pemaparan Hasil Kegiatan Lapangan dan Non Lapangan Tahun 2007*, Pusat Sumber Daya Geology, 1–7.

[2] Chenaker, H., Houha, B., and Valles, V., 2017, Isotope studies and chemical investigations of hot springs from North-Eastern Algeria, *J. Mater. Environ. Sci.*, 8 (12), 4253–4263.

[3] Mwangi, S.M., 2013, Application of geochemical methods in geothermal exploration in Kenya, *Procedia Earth Planet. Sci.*, 7, 602–606.

[4] Cabrera, A., Blarasin, M., and Maldonado, L., 2017, Groundwater age and hydrothermalism of confined aquifers in the Argentine Pampean plain, *Geotherm. Energy*, 5, 6.

[5] Bouchaou, L., Warner, N.R., Tagma, T., Hssaisoune, M., and Vengosh, V., 2017, The origin

of geothermal waters in Morocco: Multiple isotope tracers for delineating sources of water-rock interactions, *Appl. Geochem.*, 84, 244–253.

[6] Hou, Y., Shi, Z., and Mu, W., 2018, Fluid geochemistry of fault zone hydrothermal system in the Yidun-Litang area, eastern Tibetan Plateau geothermal belt, *Geofluids*, 2018, 6872563.

[7] Hadi, M.N., Yushantarti, A., Suhanto, E., and Sundhoro, H., 2007, Survei panas bumi terpadu (geologi, geokimia dan geofisika) daerah Sembalun, Kabupaten Lombok Timur - NTB, *Proceeding Pemaparan Hasil Kegiatan Lapangan dan Non Lapangan Tahun 2007*, Pusat Sumber Daya Geology, 1–14.

[8] Clark, I.D., and Fritz, P., 1997, *Environmental Isotopes in Hydrogeology*, CRC Press, Boca Raton, Florida, 285.

[9] Wijatna, A.B., Kayyis, M., Satrio, and Pujiindiyati, E.R., 2019, Study of seawater intrusion in deep aquifers of Semarang coast using natural isotopes and hydrochemical, *Indones. J. Geosci.*, 6 (1), 17–28.

[10] Aggarwal, P.K., Araguas-Araguas, L., Choudhry, M., van Duren, M., and Froehlich, K., 2013, Lower groundwater ^{14}C age by atmospheric CO_2 uptake during sampling and analysis, Groundwater, 52 (1), 20–24.

[11] Joseph, E.P., Fournier, N., Lindsay, J.M., Robertson, R., and Beckles, D.M., 2013, Chemical and isotopic characteristics of geothermal fluids from Sulphur Springs, Saint Lucia, *J. Volcanol. Geotherm. Res.*, 254, 23–36.

[12] Marini, L., 2000, *Geochemical techniques for the exploration and exploitation of geothermal energy*, Department for the Study of Territory and its Resources, University of Genoa, Corso Europa 26, 16132, Genoa, Italy, 1–82.

[13] Muhammad, S.B., and Sadiq, U., 2014, Analysis of stable isotopic composition of precipitation in Katsina State in Nigeria as an indication of water cycle, *Adv. Phys. Theor. Appl.*, 33, 28–34.

[14] Hendriksson, N., Karhu, J., and Niinikoski, P., 2014, *^{18}O, ^{2}H and ^{3}H Isotopic Composition of Precipitation and Shallow Groundwater in Olkiluoto*, Working Report 2014-69, Posiva Oy, FI-27160 Eurajoki, Finland, 1–48.

[15] Canducci, C., Bartolomei, P., Magnani, G., Rizzo, A., Piccoli, A., Tositti, L., and Esposito, M., 2013, Upgrade of the CO_2 direct absorption method for low-level ^{14}C liquid scintillation counting, *Radiocarbon*, 55 (2), 260–67.

[16] Armannsson, H., and Olafsson, M., 2007, Geothermal sampling and analysis, *Short Course II on Surface Exploration for Geothermal Resources*, UNU-GTP and KenGen, Lake Naivasha, Kenya, 2-17 November 2007, 1–8.

[17] Bungkus, P., and Satrio, 2014, Garis meterorik Indonesia, *Prosiding Seminar Nasional Geologi untuk Meningkatkan Kesejahteraan Masyarakat*, Faculty of Geological Engineering, Universitas Padjadjaran, Bandung, 24 May 2014.

[18] Geyh, M., 2000, *Environmental Isotopes in the Hydrological Cycle: Principles and Applications, Volume IV. Groundwater – Saturated and Unsaturated Zone*, Eds. Mook, W.G., International Hydrological Programme, UNESCO/IAEA Series.

[19] Güleç, N., 2013, "Isotope and gas geochemistry of geothermal systems" in *Geothermal Exploration Best Practices – Geology, Exploration Drilling, Geochemistry, Geophysics*, Eds. Bracke, R., Harvey, C., and Rueter, H., IGA Academy Report, Bochum, Germany, 0112-2013.

[20] Arvanitis, A., Dotsika, E., and Kolios, N., 2016, Geochemical characteristics of the geothermal fluids in the Akropotamos area (Macedonia, Northern Greece), *BGSG*, 50 (2), 596–605.

[21] IAEA, 2013, *Isotope Methods for Dating Old Groundwater*, International Atomic energy Agency, Vienna, Austria, 39–40.

[22] Porowski, A., 2014, "Isotope hydrogeology" in *Handbook of Engineering Hydrology: Fundamentals and Applications*, Eds. Eslamian, S., CRC Press, Boca Raton, Florida, 346–377.

[23] Abuharara, A., 2017, Using isotopes to understand the origin of water and the effect of reinjection in the Los Azufers geothermal field in Mexico, *Thesis*, Department of Earth and Environmental Sciences,

University of Waterloo, Canada.

[24] Sundhoro, H., Nasution, A., and Simanjuntak, J., 2000, Sembalun Bumbung geothermal area, Lombok Island, West Nusa Tenggara, Indonesia: An integrated exploration, *Proceedings World Geothermal Congress,* Kyushu–Tohoko, Japan, 28 May-10 June, 2000, 1785–1790.

[25] Cruz, V., Vargas, V., Matsuda, K., and Soeda, Y., 2013, Geochemical characterization of the Calacoa geothermal zone, *Procedia Earth Planet. Sci.*, 7, 859–862.

[26] Delmelle, P., Bernard, A., Kusakabe, M., Fischer, T.P., and Takano, B, 2000, Geochemistry of the magmatic–hydrothermal system of Kawah Ijen volcano, East Java, Indonesia, *J. Volcanol. Geotherm. Res.*, 97 (1-4), 31–53.

[27] Torbehbar, A.K., and Sattari, S.M., 2015, Geochemistry and isotope study of discharged geothermal fluids, NW Sabalan geothermal field, NW Iran, *Proceeding World Geothermal Congress 2015*, Melbourne, Australia, 19-25 April 2015, 1–9.

[28] Besser, H., Mokadem, N., Redhaounia, B., Hadji, R., Hamad, A., and Hamed, Y., 2018, Groundwater mixing and geochemical assessment of low-enthalpy resources in the geothermal field of southwestern Tunisia, *EMJE*, 3 (16), 1–15.

[29] Óskarsson, F., and Ármannsson, H., 2015, Geochemical methods in geothermal surface exploration, *Short Course X on Exploration and Development of Geothermal Resources*, UNU-GTP, GDC and KenGen, Lake Bogoria and Lake Naivasha, Kenya, 9 November-1 December, 2015.

[30] Wentao, B., and Bo, L., 2017, Hydrochemical and geochemical characteristics of geothermal water in Gedong area of Guizhou Province, *J. Environ. Anal. Toxicol.*, 7, 488.

[31] Wishart, D.N., 2013, Geothermometry and shallow circulation of a low enthalpy system: The bath geothermal reservoir, Jamaica, *Proceeding Thirty-Eighth Workshop on Geothermal Reservoir Engineering,* Stanford University, California, 11-13 February, 2013.

[32] Giggenbach, W.F., 1992, The composition of gases in geothermal and volcanic systems as a function of tectonic setting, *Proc. Int. Symp. Water-Rock Interact.*, 873–878.

[33] Tian, J., and Pang, Z., 2017, Geochemical characteristics of gases from typical high-temperature geothermal systems in China, *Procedia Earth Planet. Sci.*, 17, 500–503.

[34] Haklidir, M., and Haklidir, F.S.T., 2010, Hydrogen production from geothermal sources in Turkey, *Proceedings World Congress 2010*, Bali, Indonesia, 25-29 April 2010.

[35] Masoumi, R., Calagari, A.A., Siahcheshm, K., and Porkhial, S., 2017, Evaluation of hydrogeochemical and isotopic properties of the geothermal waters in the east of Mount Sabalan, NW Iran, *Turk. J. Earth Sci.*, 26, 441–453.

[36] Strelbitskaya, S., 2005, *Interpretation of chemical composition of geothermal fluid from the geothermal field of Baransky volcano, Iturup Island, Russia*, United Nations University, UNU Geothermal Training Programme, Orkustofnun, Grensásvegur 9, IS-108 Reykjavík, Iceland.

[37] Wang, X., Wang, G.L., Gan, H.N., Liu, Z., and Nan, D.W., 2018, Hydrochemical characteristics and evolution of geothermal fluids in the Chabu high-temperature geothermal system, southern Tibet, *Geofluid*, 2018, 8532840.

[38] Kemboi, E., 2015, Evaluation of groundwater hydrogeochemical characteristics and mixing behaviour in Olkaria geothermal systems, Naivasha Kenya, *Proceedings World Geothermal Congress 2015*, Melbourne, Australia, 19-25 April 2015.

Hydrochemical Evolution in Ciliwung River – Java, Indonesia: Study of Sea Water Mixture and Mineral Dissolution

Evarista Ristin Pujiindiyati[1,*], Paston Sidauruk[1], Tantowi Eko Prayogi[2], and Faizal Abdillah[2]

[1]*Center for Isotopes and Radiation Application – National Nuclear Energy Agency, Jl. Lebak Bulus Raya No. 49, Jakarta 12440, Indonesia*

[2]*Groundwater Conservation Center, Geological Agency, Ministry of Energy and Mineral Resources, Jl. Tongkol No. 4 Pademangan, Jakarta Utara 14430, Indonesia*

* ***Corresponding author:***

email: ristinpi@batan.go.id

Received: October 28, 2019
Accepted: March 10, 2020

DOI: 10.22146/ijc.50962

Abstract: *The chemical characteristics of the Ciliwung River were analyzed to understand hydrochemical evolution. A fraction of sea water mixture and kinds of mineral controlling for chemicals were also determined. During three year investigations in 2015, 2016, and 2018, electrical conductivity increased with decreasing elevations. Two hydrochemical facies had been identified for the Ciliwung river water; those were Ca-Mg-HCO_3 and Ca-Na-HCO_3. The river water mixing with seawater was recognized in the Mangga Dua site in which its water type had shifted to Na-Ca-HCO_3-Cl. Based on Na-Cl contents, the fraction of sea water into the Ciliwung River reached 2% in the Mangga Dua site during the dry season and decreased to 0.7% during the rainy season in 2015. The much higher monthly rainfall during the dry season in 2016 and 2018 had washed out invading seawater from the Mangga Dua site; its fraction of sea water was less than 0.4%. Saturation indexes with respect to calcite, dolomite, and gypsum minerals showed an increasing trend related to the decreasing elevations. All water samples were undersaturated with respect to gypsum. Meanwhile, saturation indexes with respect to calcite and dolomite mostly indicated undersaturated, except in the Mangga Dua site that was saturated (during the rainy season in 2015 and dry season in 2018) and supersaturated during the dry season in 2015.*

Keywords: *Ciliwung River; hydrochemical; sea water mixture; saturation index*

■ INTRODUCTION

The catchment area of the Ciliwung River is originated from the slope of the Gede Pangrango Mountain (3000 m above sea level) – West Java. This river flows from mountainous areas to the low land through Bogor, Depok, and empties in Jakarta Bay. The Ciliwung River is the largest, and the most important of thirteen rivers flowing through the coastal region of Jakarta with length from upstream to the estuary is approximately 117 km and covers an area 387 km^2 [1]. Geographically, the Ciliwung catchment area is located at latitude ranges from 6°06'12" to 6°34'56" and longitude ranges from 106°47'43" to 107°0'15'. Flat slope (8%) dominates in downstream, whereas the middle area has slope range between 8%–15%, and steep slope only occurs in upstream. The catchment area of Ciliwung is bordered by the Cisadane catchment area in the northern part and Citarum catchment area in the eastern part [2-3]. In the Ciliwung catchment area, there is a forested mountainous part in the headwater, urbanized Bogor city area in the middle part and heavily urbanized Jakarta metropolitan area at the lower most part of the catchment [4].

Hydrologically, the flow rate of the Ciliwung River varies depending on the average annual precipitation in a watershed. There are two seasons influencing the amount of precipitation coming from two wind regimes. The northwest monsoon season is the dry season occurring from May to October; the flow rate is low. Meanwhile, the southeast monsoon season is from November to April that is the rainy season; the flow rate

is very high such that flooding often occurs. The geological condition of the Ciliwung catchment area is formed by volcanic rocks from two volcanic mountains. They are Pangrango Mountain that contains tuff breccia rocks, and Salak Mountain that contains alluvial deposits and alluvial fan. The surface is mostly covered by alluvial deposits comprising soil, sand, and gravel. Those main geological compositions produce the kind of fertile soil. Upstream of Ciliwung is dominated by tertiary sediment and intrusive rock fraction, whereas the type of rock in the middle is precipitated quarter [2,5].

The great importance of the Ciliwung River for Jakarta District had paid some researcher's attention to study for various aspects such as its water quality [3,4], hydrology, and hydrogeology [1,5,6]. However, fewer studies about chemicals contained in the Ciliwung River had been reported in the public domain. Irawan et al. [7] concluded that there were closed connections between the river water and groundwater.

Major dissolved chemicals such as Na^+, K^+, Ca^{2+}, Mg^{2+}, Cl^-, SO_4^{2-} and HCO_3^- are an important parameter in the investigation of river water formation and geochemical evolution along with the flow. The well understanding of the geochemical evolution of river water is needed for achieving proper management of the important resources and for the protection of river water quality and its river ecology. The most common pathway of geochemical evolution or the introduction of salinity into the freshwater system is an enrichment of salts such as NaCl and $CaSO_4$ by evaporation, rock weathering, or dissolution of minerals, wash out or flushing of salts by precipitation, cation exchange, mixing of different water and input from anthropogenic sources. However, in a different section of the river, the main processes could be different [8]. The river water formations had become an interesting topic and intensively studied around the world [8-13]. Rothwell et al. [13] studied the spatial and seasonal pattern of river water chemistry in Northwest England and found that there was a clear distinction between uplands and lowlands in water quality.

In this Ciliwung River study, major dissolved ions of Na^+, K^+, Ca^{2+}, Mg^{2+}, Cl^-, SO_4^{2-} and HCO_3^- as well as some physical parameters such as pH, Electrical conductivity (EC) and temperatures were intensively observed for the periods of 2015, 2016 and 2018. The aims of this study were to understand the signatures of the Ciliwung River system responding to a natural process such as mineral dissolution and sea water mixture.

■ EXPERIMENTAL SECTION

Location and Sampling

Collecting water samples was conducted in three years of 2015, 2016, and 2018 in which each year was scheduled in two sampling periods, the rainy and dry seasons. Ciliwung River samples were taken at surface water, starting from the upper stream at Telaga Warna Lake in National Park of Gede Pangrango Mountain - Bogor – West Java with an elevation around 1485 m a.s.l to the mouth of Jakarta Bay in Mangga Dua with an elevation around 5 m a.s.l. Those sites were defined with red points, while the region of the Ciliwung catchment area was defined with the yellow area, as mapped in Fig. 1. Sampling site with its ID codes and its elevations were performed in Table 1. For analysis of cations, as much as 0.5 L water samples were put in a plastic bottle and added a few drops of HNO_3 solution to preserve water samples from precipitation. While for anion analysis, the same amount of water was put in a separate plastic bottle

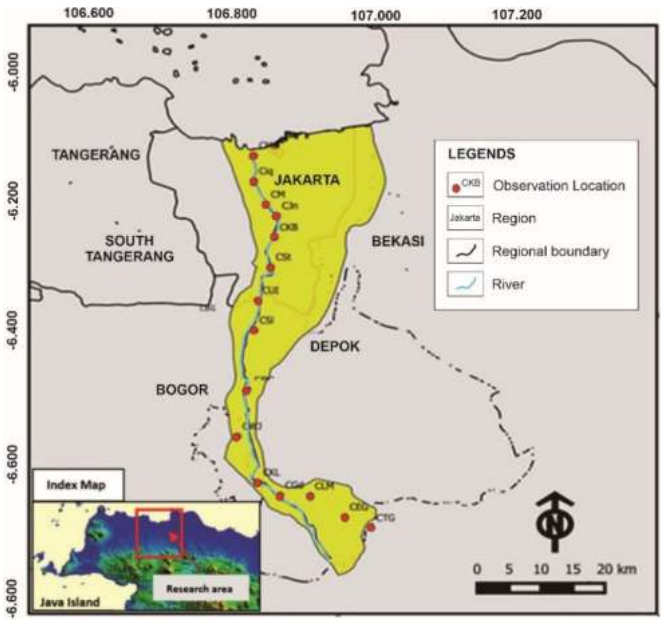

Fig 1. Observation locations of Ciliwung River

Table 1. Observation locations for Ciliwung River and its elevations

No	Observation location	ID	Elevation (m asl)
1	Telaga Warna	CTG	1485
2	Evergreen	CEG	945
3	Leuwi Malang	CLM	637
4	Gadog	CGd	457
5	Katulampa	CKL	351
6	Warung Jambu	CWJ	183
7	Bojong Gede	CBG	116
8	Siliwangi	CSl	72
9	Univ. Indonesia	CUI	50
10	Simatupang	CSt	33
11	Kalibata	CKB	19
12	Jatinegara	CJn	15
13	Manggarai	CM	11
14	Istiqlal	Ciq	7
15	Mangga Dua	CMD	5

without any special treatments. Some physical parameters such as pH, temperature, electrical conductivity (EC) were measured directly in the fields.

Materials

IC Multi element standard VII for cations from Merck (Certipur®; HC 84849022; Na, K, Ca, M: 95–105 mg/L; accuracy: 5%) and multi anion standard 1 for IC from Sigma Aldrich (TraceCERT®; Lot: BCBSO420V; CRM: Cl 10 mg/L, SO_4 20 mg/L) were used in this investigation. Eluent solution for cation analysis was a mixture of 0.7 mmol/L of Pyridine-2,6-dicarboxylic acid (for synthesis, Merck) and 1.7 mmol/L of nitric acid (HNO_3 65%, Merck) whereas that for anion analysis was a mixture of 3.2 mmol/L of sodium carbonate (Na_2CO_3, M = 84.01 g/mol, Merck), 1 mmol/L of sodium hydrogen carbonate ($NaHCO_3$, M = 105.99 g/mol, Merck) and 20 mL acetone (CH_3COCH_3, Merck). A suppressor solution of 50 mmol/L of sulfuric acid (H_2SO_4 95–97%, Merck) was needed for Cl^- and SO_4^{2-} analysis. Other materials were hydrochloric acid (HCl 37%, Merck), Natrium tetraborate ($Na_2B_4O_7{\cdot}10H_2O$, Reidel-De Haen AG Seelze-Hannover), pH buffer solutions of 4.01; 7.01; 10.01 (Hanna® Instruments) and 0.45 µm pore size filter paper.

Instrumentation

The equipment used in this investigation were Ion Chromatography (IC), with its specification is 833 Basic IC plus Metrohm and Compact autosampler Metrohom 863. For anion chromatography, IC is equipped by Metrosep A supp 5 (150/4) column, whereas cation chromatography is equipped by Metrosep C4 (250/4.0) column. Other equipment was Automatic Potentiometric Titrator AT-710 KEM, data logger for pH, EC/TDS, Global Positioning System (GPS), and a set of vacuum water filtration.

Procedure

Analysis of cations and anions were conducted in the Laboratory of Hydrology – Center for Application of Isotopes and Radiation – National Nuclear Energy Agency (BATAN), which routinely participated in the proficiency test [14]. As much as 20 µL of each filtered water sample was injected separately to Ion Chromatography for analysis of major cations in water samples such as Na^+, K^+, Ca^{2+}, and Mg^{2+} as well as for analysis of anions of Cl^- and SO_4^{2-}. Column for anions could clearly separate Cl^- and SO_4^{2-} from water samples in different retention time, those were approximately 6 and 15 min, respectively. While column for cations could separate Na^+, K^+, Ca^{2+}, and Mg^{2+} in the retention time of around 6, 8, 16, and 20 min, respectively. To make standard calibration curve, a series of standard solutions consisting of different concentrations were also injected. The curve was used to calculate back the concentration of each element in water samples. For analysis of HCO_3^- concentration in water samples, the titration method was applied using a solution of 0.02 N HCl that was previously standardized by the borax solution.

■ RESULTS AND DISCUSSION

Physical characteristics of Ciliwung River

The pH measured in the Ciliwung River was found to be in the range of 6.63–7.71 for the dry season and 6.56–7.86 for the rainy season. The pH trendline during

the dry season, compared to the rainy season, showed more increase from the acidic pH at the highest upland of the Ciliwung River to the basic pH at the lowest land of Mangga Dua (CMD) as seen at Fig. 2. Rothwell et al. [13] explained that acidic pH in upland is due to vegetation covers, while in lowlands, both past and present human activities have a major impact on river water chemistry. The pH level at the Istiqlal Mosque site increased sporadically to 7.5 during the rainy season in 2015 that could be caused by detergent waste effluents from Cipto Mangunkusumo and Cikini Hospital at sampling time. The rising pH at Katulampa Dam (CKL) during periods of abundant rainfalls occurred, which could be mainly caused by the more rapid flushing or weathering carbonate minerals like calcite and dolomite consisted of limestone as materials in dam construction. Mostly, the pH level for Mangga Dua located nearest from the Java Sea indicated the highest value that was probably caused by mixing between freshwater of Ciliwung River and sea water, which has pH value around 8.2 as measured in Ancol Beach.

Temperatures measured in the Ciliwung River were performed in Fig. 3. The temperature increased from the upstream to the downstream with the range from 21.7 °C to 30.5 °C during the rainy season and 21.3 °C to 32.5 °C during the dry season. The highest temperature was recorded in Mangga Dua, which is measured during the dry season in 2015.

Electrical Conductivity (EC) measured in the Ciliwung River had increased from its upstream to the downstream, as seen in Fig. 4. Irawan et al. [7] found more increasing Total Dissolved Solid–TDS towards downstream, which indicated increasing enrichment and contamination. Kozaki et al. [15] investigated that EC

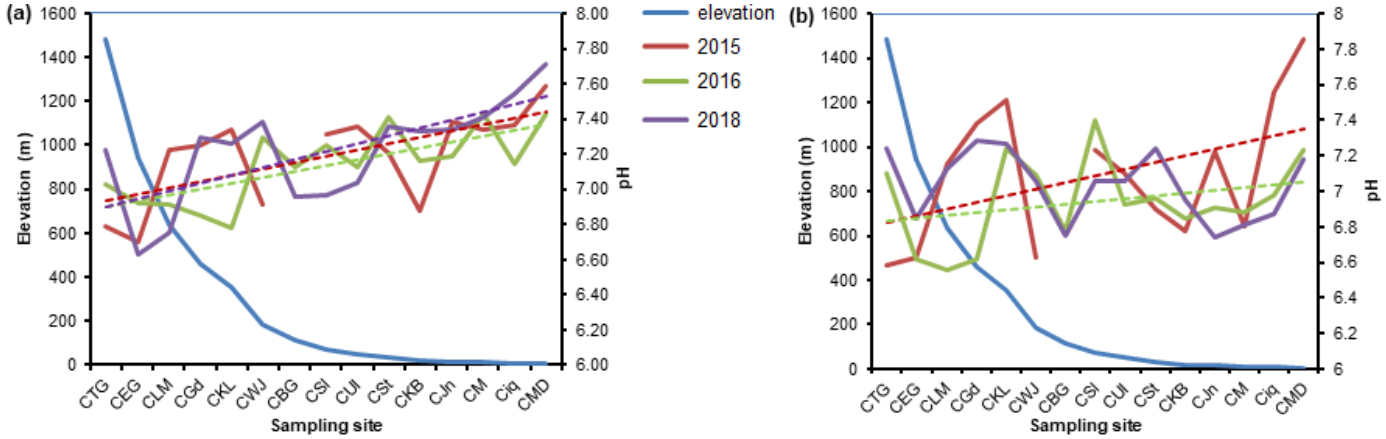

Fig 2. pH level measured in Ciliwung River in (a) the dry season and (b) the rainy season

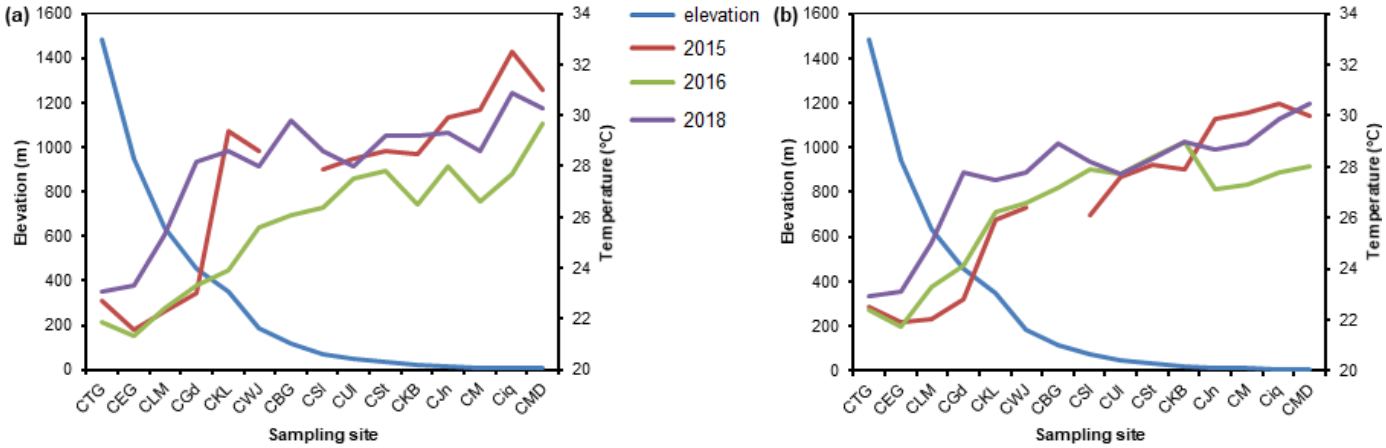

Fig 3. Temperature measured in Ciliwung River in (a) dry season and (b) the rainy season

values increased from 150 µS/cm in upstream of Ciliwung River to 666 µS/cm in downstream. The other large variations of EC values were supposed to be mainly due to water-rock interaction along the flow paths and proximity sampling locations to the coast [16]. The EC values in Mangga Dua were more variable depending on the seasons. When water samples were measured in the dry season, EC values increased greatly more than two order magnitude compared to those measured in the rainy season as occurred in 2015 and 2018. As seen in Fig. 5, rainfall in the dry seasons, starting from May to October, in 2015 (average rainfall = 89 mm) and 2018 (average rainfall = 155 mm) was less than those that occurred in 2016 (average rainfall = 302 mm) [17-19]. Duvert et al. [12] investigated that EC values steadily increased from Cisarua-Bogor to Jakarta during the dry season (from 450 to 890 µS/cm) but was lower and less variable during the wet season (from 90 to 140 µS/cm). Increasing EC values at Mangga Dua site compared to those at other sites indicated the effect of tides that enter the river, high EC values show a high salinity [20]. High evaporation in the river body in the dry season had taken a role part in the increasing EC values in most sites. Moreover, the decreasing flow rate of river water as a result of lower intensity of rainfall in the dry season could increase EC values due to the concentration of water chemistry in rivers resulted from intensive evaporation [21].

During the dry seasons, the most EC values from upper lands remained basically unchanged from CTG to CKL, except those were measured in 2016, having more constant EC values to CUI. From CWJ to CUI site, the EC values slightly increased, then elevated drastically at CSt to Ciq site for both seasons. In the later zone, the growth of population, markets, industries, and offices, as well as business centers, were fast increasing, and they produced a large volume of effluents that found their way into the Ciliwung River. For example, the wastewater effluents derived from surfactants in detergents contained the major element of Na^+, SO_4^{2}, SO_3, and NH_4OH, whereas those from textile processing consumed

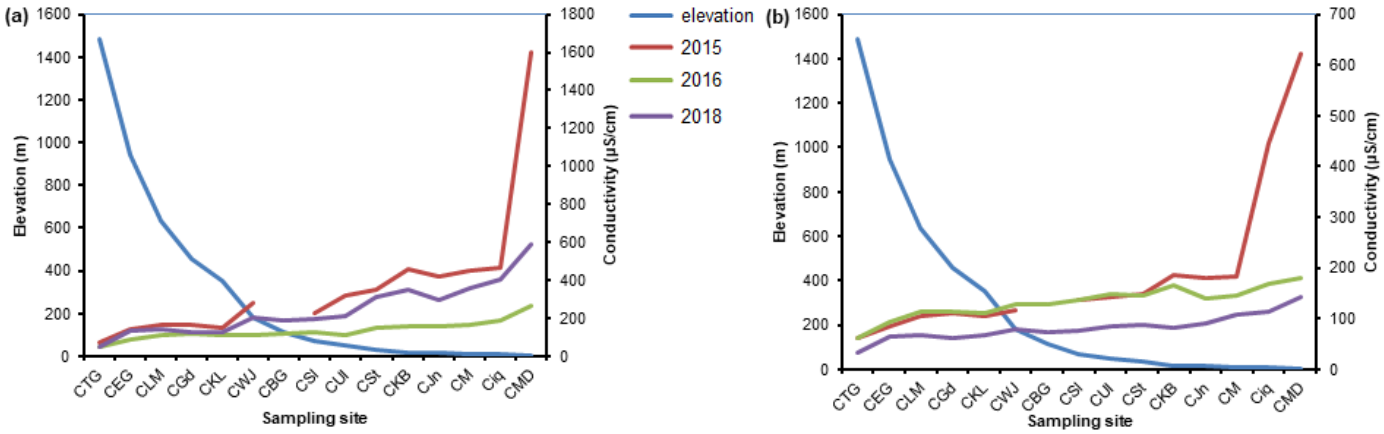

Fig 4. Electrical conductivity measured in Ciliwung River in (a) the dry season and (b) the rainy season

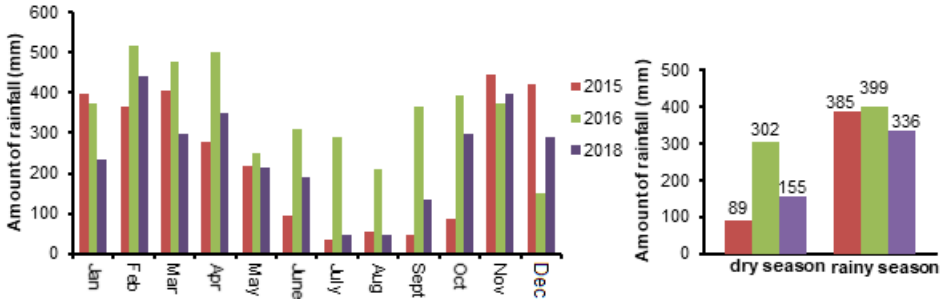

Fig 5. (a) Amount of monthly rainfalls and (b) average rainfalls in the dry and rainy season as recorded by Meteorological and Geophysical Agency in Bogor Regency [17-19]

amount of NaCl and KCl. Those dissolved salts could increase the salinity of the receiving water like a river. Degradation of organic nitrogen materials from municipal solid waste, leakage of the septic tank, and sewage sludge also produced ammonium. Under aerobic conditions, NH_4^+ is oxidized by the nitrification process to nitrate. The high nitrate concentration dissolved in water was also responsible for the increasing EC value. Organic carbon materials from domestic and dead vegetation accumulated within the soil would decay by aerobic bacteria and converted it back to CO_2. When waters infiltrated to the subsurface, the equilibration between water and soil CO_2 occurred and produced carbonic acid as well as bicarbonate, which increased the EC value. The highest EC value in Ciliwung River was reached at the Istiqlal site in the rainy season in 2015 with its value of about 450 µS/cm, following Mangga Dua. The rise of EC in this site could be from the accumulation of the waste effluents as additional of weathering minerals contained in the rocks.

The sporadically elevated EC value was found at CMD in both seasons, which reached 1600 µS/cm in the dry season in 2015 and reduced to 600 µS/cm in the rainy season. The decreasing EC during the dry season in 2016 and 2018 were probably caused by a higher intensity of rainfall in Bogor (as seen in Fig. 5) such that wash out and flushing of salts contained in rocks/soils were more diluted. The salinity depends on tidal height in the mouth of rivers and the discharge of freshwater in the upstream that vary on a seasonal basis. The changes in seasonal salinity patterns are also induced by mean sea level rise and freshwater flow reduction [22-23].

Hydrochemical Facies of Ciliwung River

River water evolution could be described through the piper diagram, which was plotting of concentration of major cations (Na^+, K^+, Ca^{2+}, and Mg^{2+}) and anions (Cl^-, SO_4^{2-} and HCO_3^-) [10]. Fig. 6, 7, and 8 showed piper diagrams for all water samples collected from the Ciliwung River during the rainy and dry seasons in 2015, 2016, and 2018, respectively. Based on the dominancy of those cation and anion species, the most hydrochemical facies in the Ciliwung River were identified as (1) Ca-Mg-HCO_3; and (2) Mixed Ca-Na-HCO_3^-. Both facies predominated, reflecting the main rock types in the Ciliwung River, where limestone [consists of calcite mineral ($CaCO_3$)] and dolomites [$CaMg(CO_3)_2$] were the most dominant formation.

In 2015, most samples were characterized as a mixed Ca-Na-HCO_3 water type, except the samples from the Mangga Dua site (CMD), which had been introduced by Cl^-. During the rainy season (Fig. 6(b)) the water samples tended to be more scattered as shown by Telaga Warna (CTG) and Evergreen (CEG) located in the highest upland, which belonged to Ca-SO_4-HCO_3 water type. During the dry season in the year of 2015, CTG belonged to Ca-HCO_3 water type while CEG, CGd, and CLM sites had shifted to Ca-Mg-Na-HCO_3. In the

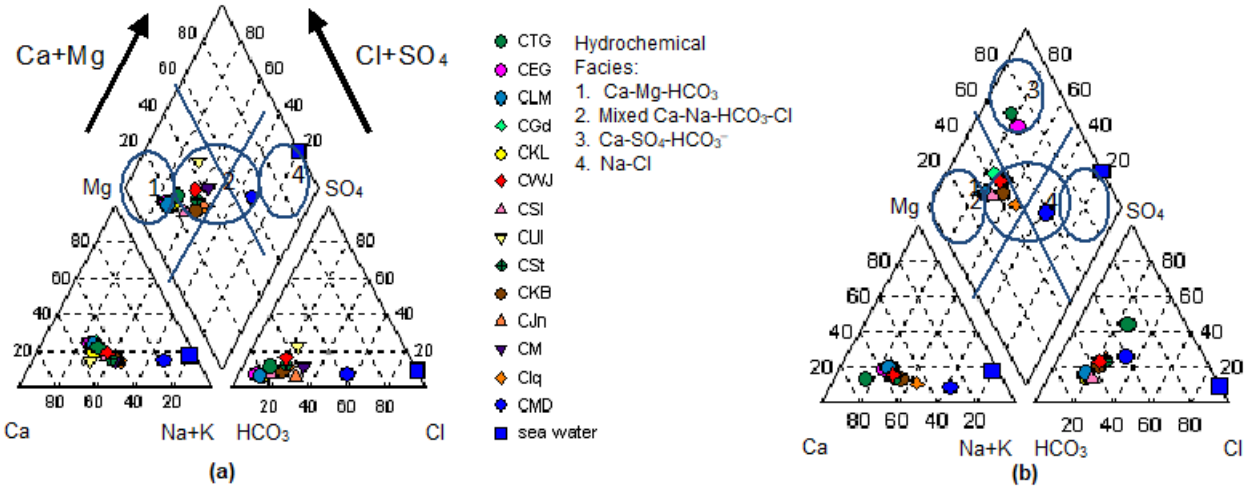

Fig 6. Water type of the Ciliwung River collected in (a) the dry season and (b) the rainy season 2015

next sites, Ca-Na-HCO_3 water type predominated Ciliwung River water until CIq, which belonged to Ca-Na-HCO_3-Cl and finally predominated by Na-Cl-HCO_3 in CMD as seen at Fig. 6(a). The point of Mangga Dua (CMD) that rather lied in the right side of the diamond shape in the piper diagram showed a tendency to Na-Cl water type as a characteristic of sea water due to the proximity of Mangga Dua site to Jakarta Bay. The salinization path due to sea water admixture toward CMD site also occurred in the rainy season 2015, which was predominated by Na-Ca-HCO_3-Cl.

In the case of water samples collected in the year 2016 and 2018, as described in Fig. 7 and Fig. 8, respectively, seemly Ca-Na-HCO_3 facies still predominated for all water samples in both seasons, including the Mangga Dua site. However, during the dry season, this site (CMD) slightly moved to Ca-Na-HCO_3-Cl facies, reflecting a few encroachments of chloride from sea water than that occurred in 2015. A higher amount of monthly rainfall (average = 302 mm) during the dry season in 2016 might have influenced to more rapid flushing of freshwater instead of sea water flush.

To have a more clear understanding of water chemistry evolutions, a Schoeller diagram for cation and anion concentrations for each water sample in the logarithmic scale was made. Those were described in

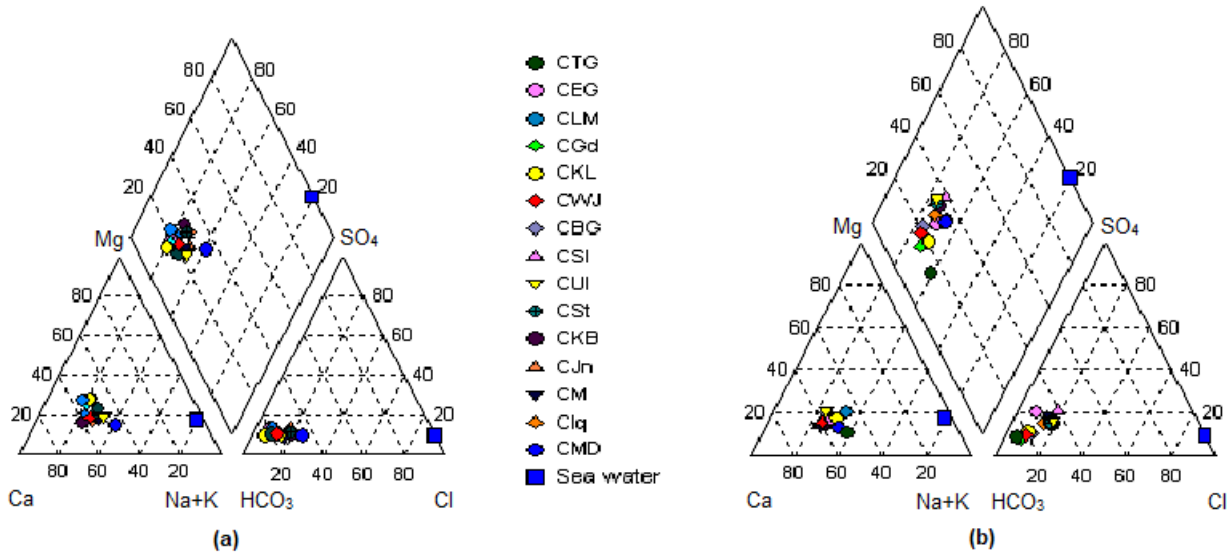

Fig 7. Water type of the Ciliwung River collected in (a) the dry season and (b) the rainy season 2016

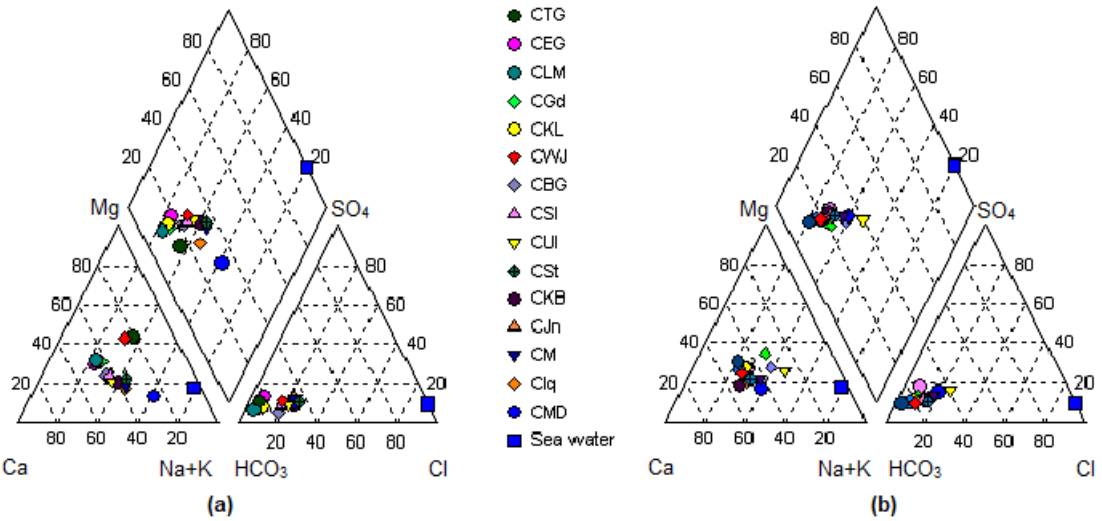

Fig 8. Water type of the Ciliwung River collected in (a) the dry season and (b) the rainy season 2018

Fig. 9, 10, and 11 for collecting samples in 2015, 2016, and 2018, respectively. During the dry season in 2015, all anion and cation concentrations tended to be higher than those in the rainy season. The presence of a high concentration of Mg^{2+}, Ca^{2+}, Na^{+}, Cl^{-}, SO_4^{2-}, in a coastal area, as shown in the Mangga Dua site, could be due to flushing of sea water which apparently increased during dry season 2015. However, that sporadic increasing trend of chemical concentration in the Mangga Dua site was not found during collecting samples in 2016 and 2018 in which the chemical concentrations were more constant in both seasons. The more rapid flushing of river water resulted from higher monthly rainfall during both seasons in 2016 and 2018 (as seen in Fig. 5) could be the reason for more constant chemical concentration at Mangga Dua site.

With the exception of CMD sites, generally, the major cations in Ciliwung river observed in 2015, 2016 and 2018 could be ranked in term of proportion (unit of meq/L) as follows: $Ca^{2+} > Na^{+} > Mg^{2+} > K^{+}$ and the major anions as $HCO_3^{-} > Cl^{-} > SO_4^{2}$. On the other hand, the CMD site observed during both seasons in 2015 showed the following rank: Na > Ca > Mg > K for cations and Cl > HCO_3 > SO_4 for anions. Those concentrations decreased significantly in flood season because of the increasing dilution effect.

In the highest elevation (1485 m) of Ciliwung River, most anion and cation compositions were distributed at the lowest concentration. Seemly, the higher monthly rainfall occurred during dry seasons in 2016 and 2018, as seen in Fig. 5(b) did not significantly influence hydrochemical compositions at the Telaga Warna site. A similar case also occurred during the dry season in 2015, even though its monthly rainfall was categorized as below normal condition [17]. In that season, Ca^{2+} (6 ppm) and

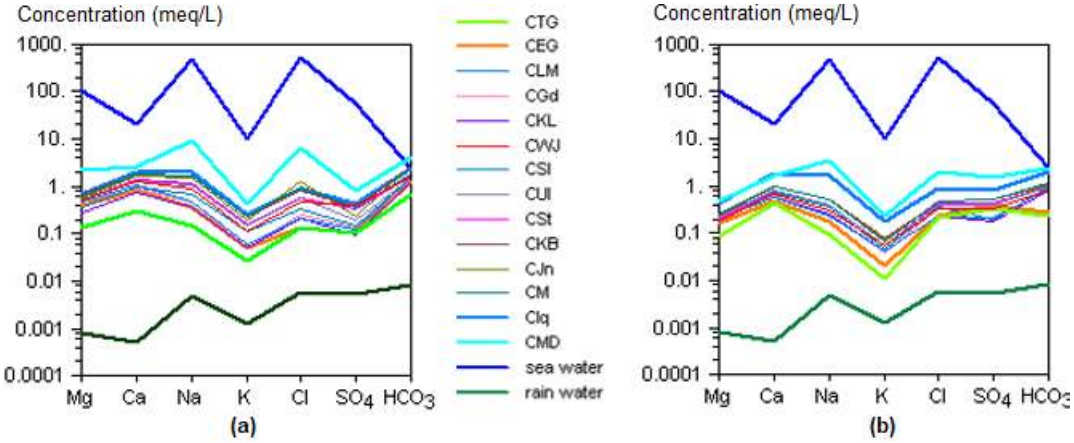

Fig 9. Chemical compositions for Ciliwung River in (a) the dry season and (b) the rainy season 2015

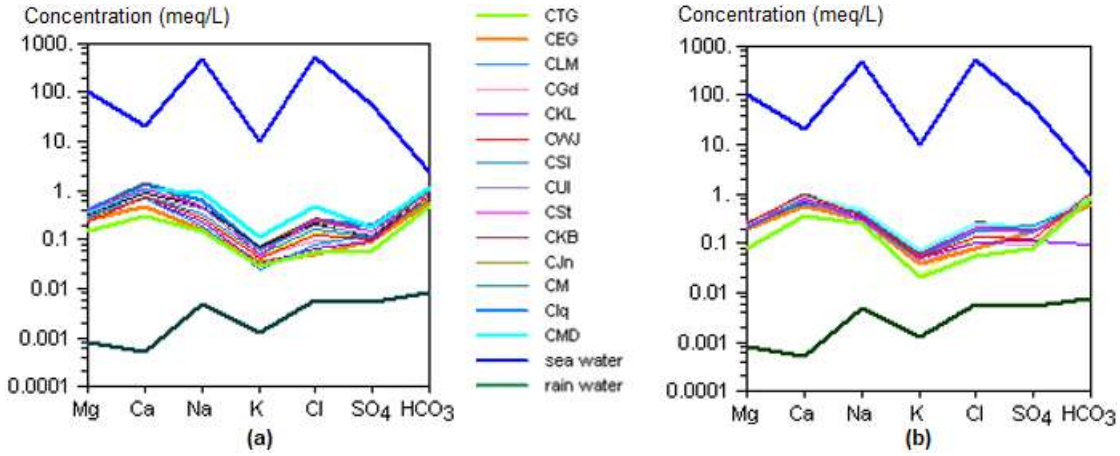

Fig 10. Chemical compositions for Ciliwung River in (a) the dry season and (b) the rainy season 2016

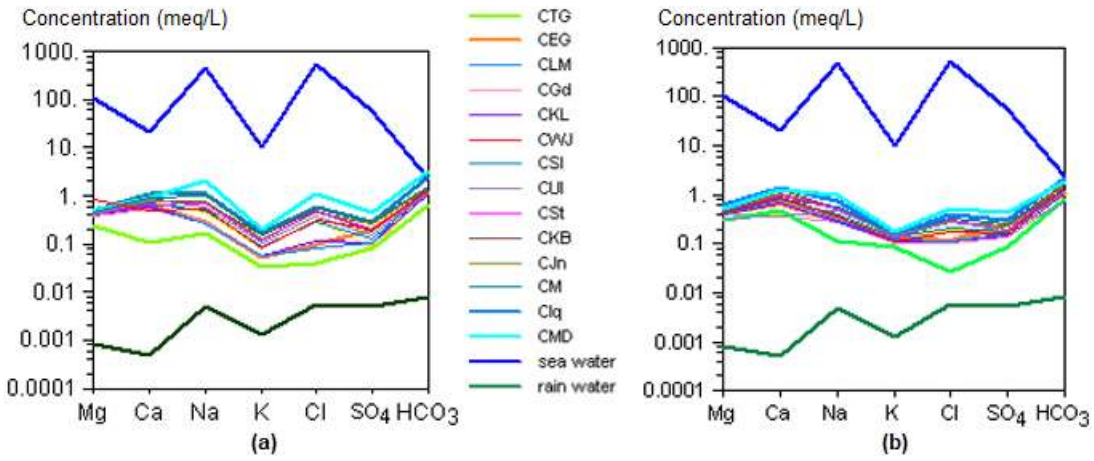

Fig 11. Chemical compositions for Ciliwung River in (a) the dry season and (b) the rainy season 2018

HCO_3^- (43 ppm) were the dominant constituents in Telaga Warna Lake, followed by Na^+ (4 ppm) and Mg^{2+} (2 ppm) for cations, as well as SO_4^{2-} (5 ppm) and Cl^- (4 ppm) for anions. Those concentrations increased along the flow path until to the mouth of Jakarta Bay, indicating that the dissolution of minerals had been still in progress.

The mineral dissolution process, together with river water evaporation during the dry season, could result in the extent of increasing anion and cation concentrations. Those constituents reached maximum concentration in the endpoint of the Ciliwung River flow at Mangga Dua. However, those orders clearly changed in which Na^+ as the dominant constituent (213 ppm) in coastal site replaced calcium (51 ppm) as the main constituent of the Ciliwung River in the highest upland. Besides mineral dissolution and evaporation, the common pathways of salinization into the freshwater system are mixing with sea water and cation exchange process in most coastal regions. However, chemical reactions like the cation exchange process effect little to the concentration of water chemistry compared to sea water mixing [8,16].

Mixing of Freshwater with Sea Water

Based on a mass balance model, mixing lines between two different water samples for a range of hydrochemical indicators can be calculated using a simple mixing equation through AQUACHEM program as follow: $C_{mix} = C_1 n + C_2(1\text{-}n)$, where C_{mix} is the ion concentration of mixture sample, C_1 is ion concentration of sea water, and C_2 is ion concentration of rainwater. Notation n represents a mixing fraction of sea water in river water, whereas 1-n is the fraction of rainwater [8,24]. Hence, increasing of Cl^- and Na^+ concentration for each step of mixing fraction could be calculated by the equation, and then the calculated admixtures were plotted in Na^+ versus Cl^- graph.

Fig. 12 showed that during the rainy season in 2015, the river water in Mangga Dua might be estimated as much as 0.7% of sea water composition. The less mixing fraction of sea water, about 0.3%, was signified at the Istiqlal site. When the river water was taken during the dry season, the mixing fraction of sea water in the Mangga Dua site increased to approximately 2%. The other sites starting from CWJ to Ciq showed a shifting of Na^+ and Cl^- concentrations to the higher mixing fraction of saline water. The increasing of Na^+ and Cl^- in this zone was compared well with the elevating of the EC values (see Fig. 4) that could be derived from past or present domestic or industrial waste. However, it was also considered that huge evaporation during water flow due to the hot landscape in the dry season became a dominant effect on the samples, which located far away from the shoreline.

During the dry season 2016 (Fig. 13), the mixing fraction of sea water into CMD site decreased to less than 0.2% that was still higher than that was taken in the rainy season. Rather similar evidence also occurred in dry season 2018 (Fig. 14) that had a mixing fraction of sea water as much as 0.4%. Their Na-Cl compositions were in the same clusters as other sites. For three year

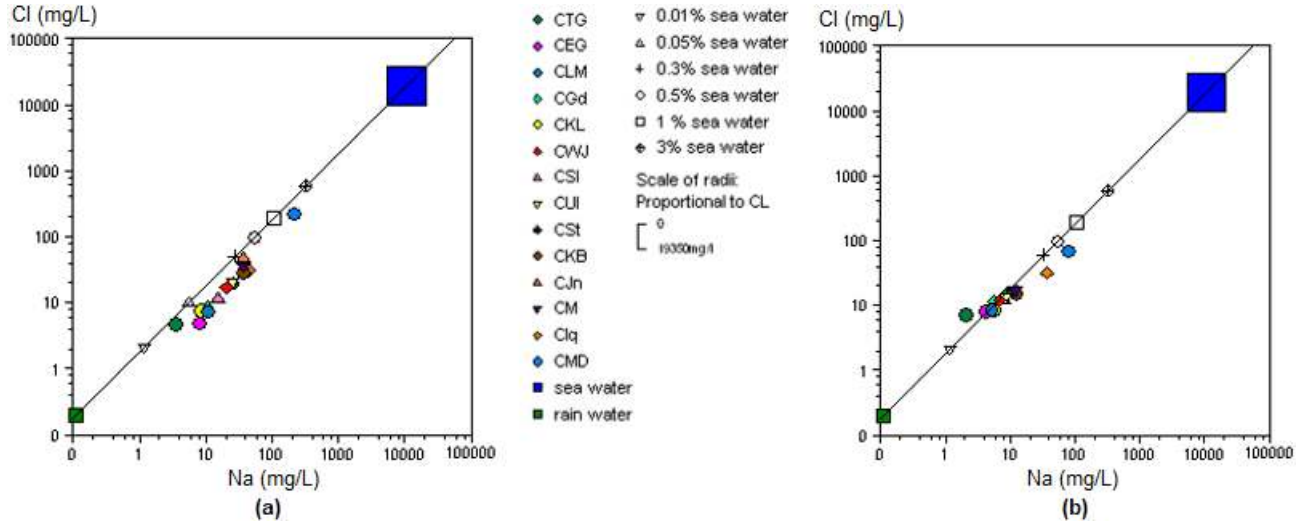

Fig 12. Mixing fraction of sea water into the river in (a) the dry season and (b) the rainy season 2015

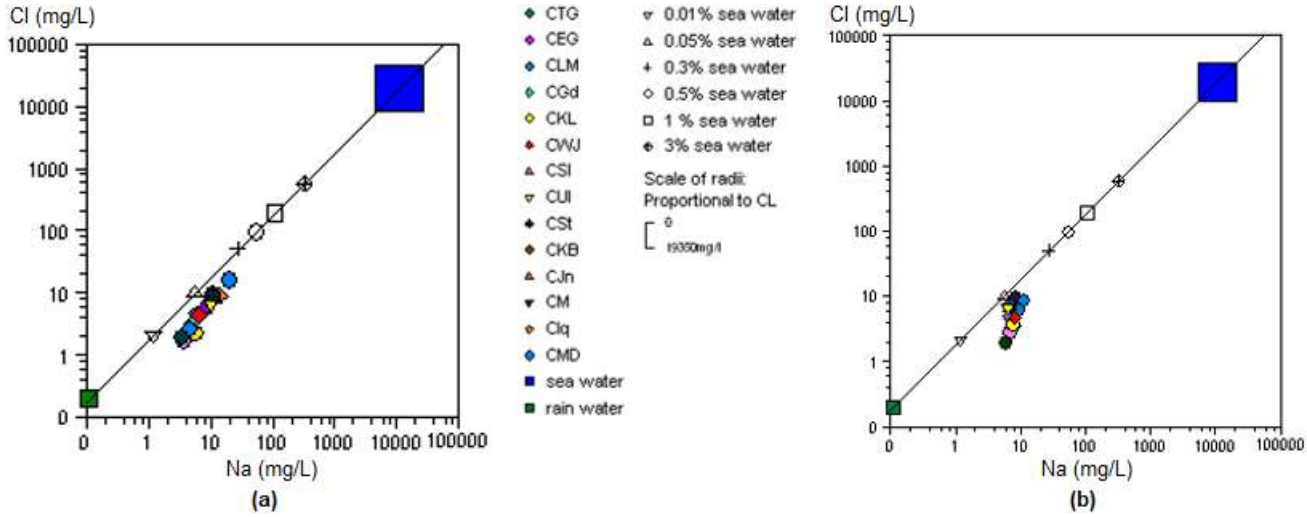

Fig 13. Mixing fraction of sea water into the river in (a) the dry season and (b) the rainy season 2016

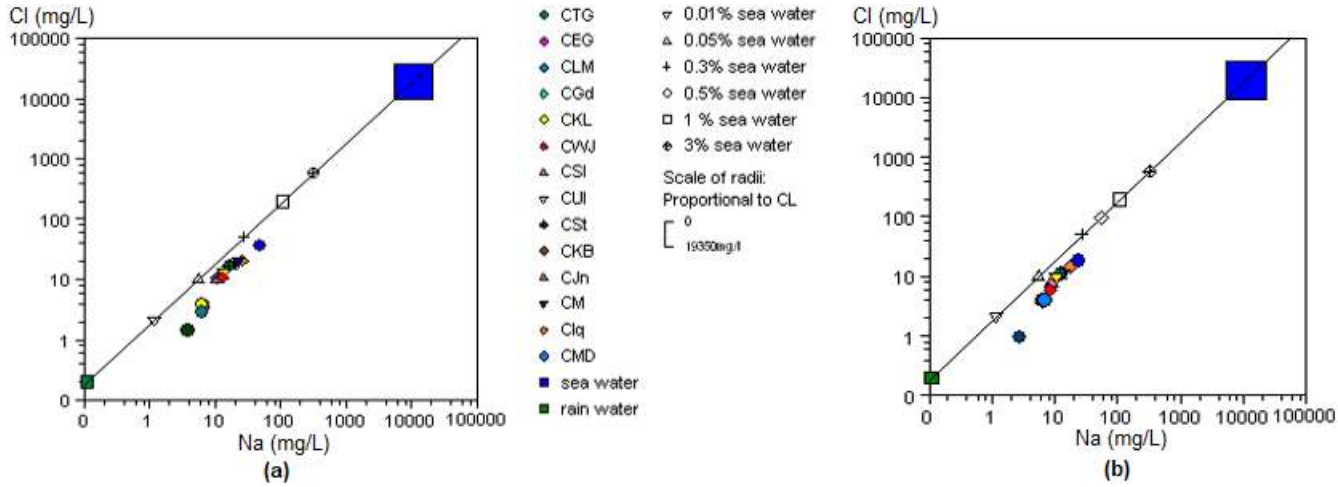

Fig 14. Mixing fraction of sea water into the river in (a) the dry season and (b) the rainy season 2018

investigations, the mixing fraction of sea water to the river located nearest to shoreline increased during the dry season. The important mechanisms forcing for flow and salt transport in the nearshore region are driven by tides, waves, their interaction with beach morphology and seasonal changes in the inland water table elevations [25].

Saturation Index (SI)

As mentioned above, most samples from the Ciliwung River were dominated by bicarbonate for anion showing interaction with carbonate rocks. Dissolving calcite ($CaCO_3$) and dolomite [$CaMg(CO_3)_2$] contained in carbonate rocks follows to these reactions [16]:

$$CaCO_3 + CO_2 + H_2O \rightleftarrows Ca^{2+} + HCO_3^-$$

$$CaMg(CO_3)_2 + 2CO_2 + 2H_2O \rightleftarrows Ca^{2+} + Mg^{2+} + 4HCO_3^-$$

Whereas for evaporating rocks of gypsum minerals ($CaSO_4\ 2H_2O$) follows the reaction [8]:

$$CaSO_4 + 2H_2O \rightleftarrows Ca^{2+} + SO_4^{2-} + 2H_2O$$

To evaluate the degree of equilibrium between water and minerals, the used parameter is the saturation index (SI), which was calculated using PHREEQC software. Changes in saturation state are useful to distinguish different stages of hydrochemical evolution and to identify which geochemical reaction is important in controlling water chemistry. The saturation index of minerals is obtained from the equation of SI = log (IAP/Kt). The term of IAP is the Ion Activity Product of the dissociated chemical species in solution. Kt is the equilibrium solubility product for the chemical involved at the sample temperature [16,26-27].

Fig. 15, 16, and 17 showed the SI for calcite, dolomite, and gypsum against the order of sampling locations of the Ciliwung River for sampling periods of 2015, 2016, and 2018, respectively. Along with river flow, SI with respect to calcite mineral was the highest value, among other minerals. All water samples had negative SI values in 2016 (Fig. 16) and during the rainy season 2018 (Fig. 17(b)). It suggested that all water samples were undersaturated with respect to calcite, dolomite, and gypsum minerals. Such an undersaturated

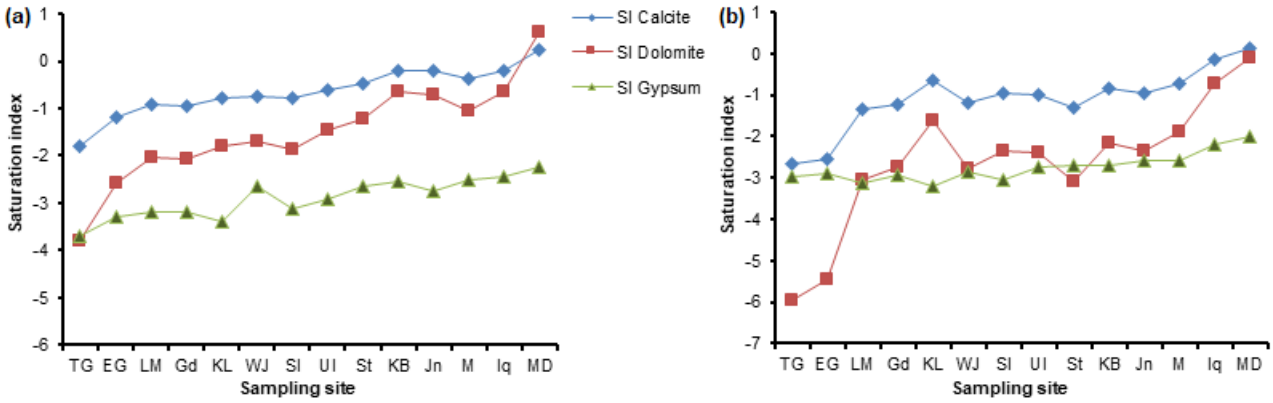

Fig 15. Saturation indexes for some minerals in (a) the dry season and (b) the rainy season 2015

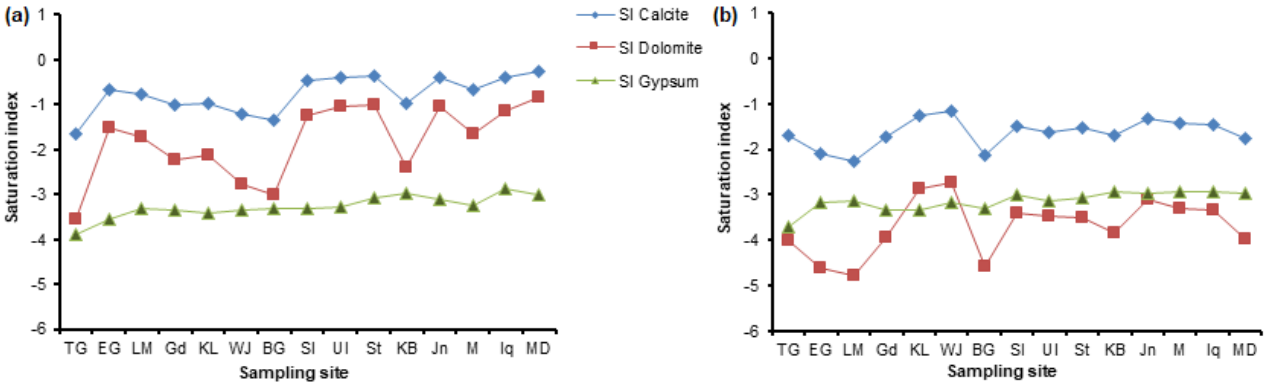

Fig 16. Saturation indexes for some minerals in (a) the dry season and (b) the rainy season 2016

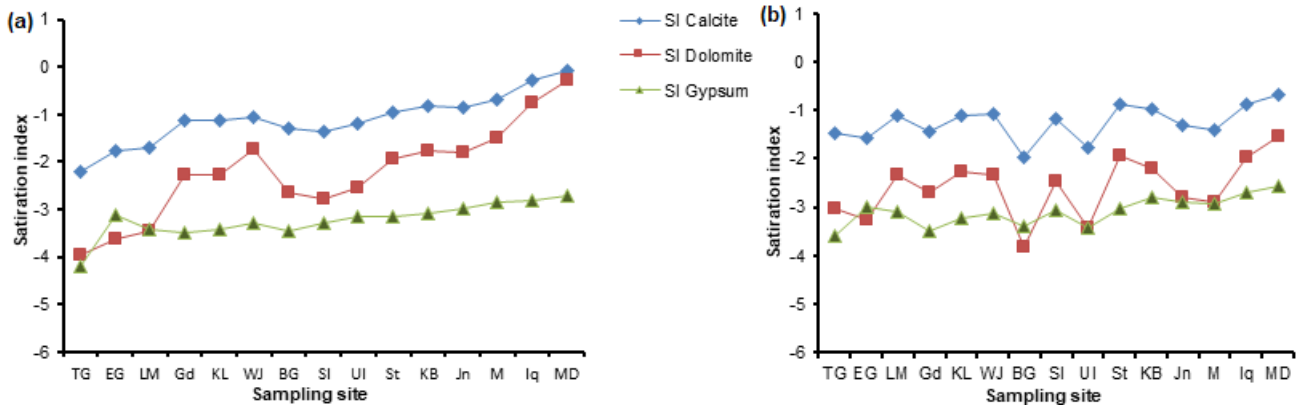

Fig 17. Saturation indexes for some minerals in (a) the dry season and (b) the rainy season 2018

term reflects the character of water with insufficient amount of calcite, dolomite, and gypsum mineral for solution.

Bicarbonate as a dominant anion might have been influenced by the dissolution of calcite and dolomite mineral phases. However, the higher SI for calcite than SI for dolomite showed that more amount of HCO_3^- concentration in the system was dominantly influenced by calcite dissolution. The higher dissolution for calcite was shown from saturated condition (SI = 0) in the Istiqlal site while SI with respect to dolomite still remained at undersaturated (SI < 0) as taken place in 2015. The saturated condition means that the water samples are in equilibrium with respect to the particular minerals [16,27]. Besides dissolved HCO_3^-, calcite also could dissolve in the system by adding Ca^{2+}, whereas dolomite dissolved its Mg^{2+} concentration to the solution. All water samples were undersaturated with respect to gypsum indicated that gypsum also could dissolve in the system by adding Ca^{2+} and SO_4^{2-} to the solution. The much less gypsum SI compared to calcite SI in all water samples implied that Ca^{2+} in the solution might be highly contributed from the dissolution of calcite rather than the dissolution of gypsum minerals.

In 2015, the SI of calcite, dolomite, and gypsum steadily increased related to the decreasing elevation of sampling sites. It meant that the water samples contained more amounts of ion concentrations with more sufficient residence time of water in which was controlled by volume and mechanism of mineral dissolution. In the Mangga Dua site, SI of calcite reached to supersaturated (SI > 1) in both seasons, while SI of dolomite reached to supersaturated in the dry season. A supersaturated condition means that the water sample is incapable of dissolving more of the mineral [16,27]. It implied that both minerals had a great dissolution and strong mineralization that potentially lead to precipitation. The strong mineralization in Mangga Dua could be due to the large influence of minerals from sea water, in addition to the mineral dissolution along with the river flow. The SI for CMD site during the dry season in 2018 reflected a saturated condition with respect to calcite and closed to saturated (SI = -0.22) with respect to dolomite.

■ CONCLUSION

Electrical conductivity (EC), temperature, and pH, which were measured along the Ciliwung River, generally increased with the decreasing elevation lands. The much more amount of rainfall as occurred in 2016 and 2018 than that in 2015 could result in a decrease of EC values in a site near the coast. With the exception of Mangga Dua site, cation concentrations could be ranked as $Ca^{2+} > Na^+ > Mg^{2+} > K^+$ and for anion concentration as $HCO_3^- > Cl^- > SO_4^{2-}$. In general, the hydrochemical facies that could be identified for the Ciliwung River were Ca-Mg-HCO_3 and Ca-Na-HCO_3. In 2015, the introduction of salinity into the river had reached to Mangga Dua shifting its water type to Na-Ca-HCO_3-Cl. The fraction of sea water into Ciliwung River was optimized as much as 2% in the Mangga Dua site during the dry season and decreased to approximately 0.7% during the rainy season. Calculated saturation indexes

with respect to calcite, dolomite, and gypsum minerals showed an increasing trend related to the decreasing elevation land. Mostly, the Ciliwung River water was undersaturated with respect to these minerals, indicating the insufficient amount of these minerals for dissolution. However, the calcite and dolomite saturation indexes in the Mangga Dua site had nearly reached saturated conditions (during the rainy season in 2015 and dry season 2018) and to supersaturated (during the dry season in 2015) representing for a great dissolution and strong mineralization.

■ ACKNOWLEDGMENTS

This study was funded by the Government of Indonesia through the 2015-2019 National Mid-term Development Plan. The sincere thanks were extended to all staff in Hydrology Laboratory - Center for Isotope and Radiation Applications for their assistances during collecting and analyzing samples.

■ REFERENCES

[1] Hendrayanto, 2008, Transboundary watershed management: A case study of upstream-downstream relationships in Ciliwung watershed, *Bull. TERC, Univ. Tsukuba,* 8 (2), 8–11.

[2] Pramono, I.B., 2016, Distribution of water infiltration rate in Ciliwung Watershed, *Forum Geografi*, 30 (1), 24–33.

[3] Mukhaiyar, R., 2017, Digital image and remote sensing image as a data for an identification of a quality of a non-point source pollutant in Ciliwung River-Indonesia, *Int. J. GEOMATE*, 12 (32), 142–151.

[4] Ohte, N., Watanabe, Y., Yoshimizu, C., Kondo, A., Runtunuwu, E., Yamanaka, T., and Tanaka, T., 2010, Stable isotope of nitrate in Ciliwung River, *Bull. TERC, Univ. Tsukuba,* 10 (Suppl. 1), 65–74.

[5] Delinom, R.M., 2010, Geology and hydrogeology of Ciliwung, *Bull. TERC, Univ. Tsukuba,* 10 (Suppl. 1), 27–33.

[6] Sulistyowati, R., Hapsari, R.I., Syamsudin, F., Mori, S, Oishi, S.T., and Yamanaka, M.D., 2014, Rainfall-driven diurnal variations of water level in the Ciliwung River West Jawa-Indonesia, *SOLA*, 10, 141–144.

[7] Irawan, D.E., Silaen, H., Sumintadireja, P., Lubis, R.F., Brahmantyo, B., and Puradimeja, D.J., 2015, Groundwater-surface water interactions of Ciliwung River streams, segment Bogor-Jakarta, Indonesia, *Environ. Earth Sci.*, 73 (3), 1295–1302.

[8] Hui, Q., Peiyue, L., Jia, D., Chao,Y., and Xuedi, Z., 2011, Formation of the river water chemistry in the middle section of Dousitu River-China, *E-J. Chem.*, 8 (2), 727–738.

[9] Birks, S.J., Moncur, M.C., Gibson, J.J., Yi, Y., Fennell, J.W., and Taylor, E.B., 2018, Origin and hydrogeological setting of saline groundwater discharges to the Athabasca River: Geochemical and isotopic characterization of the hyporheic zone, *Appl. Geochem.*, 98, 172–190.

[10] Jiang, L., Yao, Z., Liu, Z., Wang, R., and Wu, S., 2015, Hydrochemistry and its controlling factors of rivers in the source region of the Yangtze River on the Tibetan Plateau, *J. Geochem. Explor.*, 155, 76–83.

[11] Lindell, L., Åström, M., and Öberg, T., 2010, Land-use change versus natural controls on stream water chemistry in the Subandean Amazon, Peru, *Appl. Geochem.*, 25 (3), 485–495.

[12] Duvert, C., Priadi, C.R., Rose, A.M., Abdillah, A., Marthanty, D.R., Gibb, K.S., and Kaestli, M., 2019, Sources and drivers of contamination along an urban tropical river (Ciliwung, Indonesia): Insights from microbial DNA, isotopes and water chemistry, *Sci. Total Environ.*, 682, 382–393.

[13] Rothwell, J.J., Dise, N.B., Taylor, K.G., Allott, T.E.H., Scholefield, P., Davies, H., and Neal, C., 2010, Spatial and seasonal assessment of river water chemistry across North West England, *Sci. Total Environ.*, 408 (4), 841–855.

[14] Wassenaar, L.I., Terzer-Wassmuth, S., Douence, C., Araguas-Araguas, L., Aggarwal, P.K., and Coplen, T.B., 2018, Seeking excellence: An evaluation of 235 international laboratories conducting water isotope-ratio and laser absorption spectrometry, *Rapid Commun. Mass Spectrom.*, 32 (5), 393–406.

[15] Kozaki, D., Ozaki, T., Nakatani, N., Mori, M., and Tanaka, K., 2014, Utilization of ion-exclusion chromatography for water quality monitoring in

suburban river in Jakarta, Indonesia, *Water*, 6 (7), 1945–1960.

[16] Sappa, G., Barbieri, M., Ergul, S., and Ferranti, F., 2012, Hydrogeological conceptual model of groundwater from carbonate aquifers using environmental isotopes (^{18}O, ^{2}H) and chemical tracers: A case study in Southern Latium Region-Central Italy, *J. Water Resour. Prot.*, 4, 695–796.

[17] Central Bureau of Statistics in Bogor Regency, 2016, *Bogor Regency in Figures*, BPS-Statistics of Bogor Regency, BPS Catalog: 1102001.3201.

[18] Central Bureau of Statistics in Bogor Regency, 2017, *Bogor Regency in Figures*, BPS-Statistics of Bogor Regency, BPS Catalog: 1102001.3201.

[19] Central Bureau of Statistics in Bogor Regency, 2019, *Bogor Regency in Figures*, BPS-Statistics of Bogor Regency, BPS Catalog: 1102001.3201.

[20] Purnaini, R., Sudarmadji., and Purwono, S., 2018, Tidal influence on water quality of Kapuas Kecil river downstream, *E3S Web Conf.*, 31, 04006.

[21] Edokpayi, J.N., Odiyo, J.O., Popoola, E.O., and Msagati, T.A.M., 2017, Evaluation of temporary seasonal variation of heavy metals and their potential ecological risk in Nzhelele River-South Africa, *Open Chem.*, 15 (1), 272–282.

[22] Vargas, C.I.C., Vaz, N., and Dias, J.M., 2017, An evaluation of climate change effect in estuarine salinity patterns: Application to Ria de Aveiro shallow water system, *Estuarine, Estuarine Coastal Shelf Sci.*, 189, 33–45.

[23] Anderson, C.J., and Lockaby, B.G., 2012, Seasonal patterns of river connectivity and saltwater intrusion in tidal freshwater forested wetlands, *River Res. Appl.*, 28 (7), 814–626.

[24] Han, D.M., Song, X.F., Currel, M.J., Yang, J.L., and Xiao, G.Q., 2014, Chemical and isotopic constraints on evolution of groundwater salinization in the coastal plain aquifer of Laizhou Bay, China, *J. Hydrol.*, 508, 12–27.

[25] Robinson, C., Gibbes, B., and Li, L., 2006, Driving mechanisms for groundwater flow and salt transport in a subterranean estuary, *Geophys. Res. Lett.*, 33 (3), L.03402.

[26] Aghazadeh, N., and Mogaddam, A.A., 2010, Assessment of groundwater quality and its suitability for drinking and agricultural uses in the Oshnavieh Area, Northwest of Iran, *J. Environ. Prot.*, 1, 30–40.

[27] Etteieb, S., Cherif, S., and Tarhouni, J., 2017, Hydrochemical assessment of water quality for irrigation: A case study of the Medjerda River in Tunisia, *Appl. Water Sci.*, 7, 469–480.

Zinc-Doped Titania Embedded on the Surface of Zirconia: A Potential Visible-Responsive Photocatalyst Material

Azizia Alifi, Rian Kurniawan, and Akhmad Syoufian*

Department of chemistry, Faculty of Mathematics and Natural Sciences, Universitas Gadjah Mada, Sekip Utara, Yogyakarta 55281, Indonesia

** Corresponding author:*

email: akhmadsyoufian@ugm.ac.id

Received: November 5, 2019
Accepted: February 4, 2020

DOI: 10.22146/ijc.51172

Abstract: *The preparation and characterization of zirconia-supported titania with a zinc dopant had been studied. Zinc-doped titania was grown on the surface of zirconia by the sol-gel method. Various zinc contents and calcination temperatures were applied to investigate the zinc doping effect and crystal structure of the zirconia-titania composite. X-ray diffraction method, Fourier-transform infrared spectroscopy, and UV-Vis reflectance spectroscopy were performed to characterize the composite. The morphology of the composite was observed by using a scanning electron microscope, and its composition was analyzed by using energy dispersive spectroscopy. Among various zinc dopant contents and calcination temperatures investigated, doping with 5% zinc (Zn wt./Ti wt.) at 900 °C calcination shows the best result in response to visible light with a bandgap of 2.87 eV and absorption edge wavelength of 432.61 nm.*

Keywords: *titania; zinc; zirconia; sol-gel; doping*

■ INTRODUCTION

TiO_2 has a high photoactivity under ultraviolet light irradiation because of its large bandgap (3.25 eV for anatase). However, solar light consists of 5% UV light (300–400 nm) and 43% visible light (400–700 nm). That is, the UV light only occupies a small portion of the sunlight, and a large part of solar energy cannot be utilized. TiO_2 also shows a higher recombination rate of photogenerated electrons and holes [1]. The photocatalytic performance of TiO_2 can be effectively improved through transition metal doping. Among other metals, Zn has drawn considerable attention because of its superior doping effect on the improvement of TiO_2 photocatalytic performance under visible irradiation [2-3]. Seabra et al. reported that the inhibition of anatase-to-rutile transformation and the increment of specific surface area are responsible for the improvement of TiO_2 photocatalytic performance under visible irradiation by zinc doping [2].

Titania has also been combined with other semiconductors such as zirconium dioxide (ZrO_2). ZrO_2 is a versatile material due to its properties, such as high chemical inertness, photochemical stability, good wear resistance, and a wide bandgap [4]. ZrO_2 has been used in several studies to increase the photocatalytic activity of TiO_2 because the coupling of the two semiconductors can achieve a more efficient charge separation, prolong the lifetime of charge carriers, and significantly minimize the recombination probability between the hole and electron [5-6]. The reported value of ZrO_2 bandgap energy (E_g) is in the range of 3.25 to 5.1 eV, limiting the spectrum of photons that can create electron-hole pairs to participate in oxidation or reduction reactions under the UV light [7-8].

A hybrid of TiO_2 and ZrO_2 has advantageous properties, such as high mechanical strength, high surface area, non-toxicity, corrosion resistance, and photocatalytic activity under sunlight [9]. The combination of TiO_2 and ZrO_2 inhibits the electron-hole recombination process, which enhances the lifetime of charged carriers, thus improving the photocatalytic activity [10]. Fan et al. conducted a photocatalytic degradation of rhodamine B using the TiO_2-ZrO_2 binary system under visible light irradiation. Results showed a promising photocatalytic activity under the visible-light region [11]. The bandgap of titania-zirconia composite

was found to be increasing with a decrease in crystallite and particle size [12-13]. The presence of ZrO_2 in TiO_2 inhibits the anatase-to-rutile phase transformation [14].

Herein, a series of zinc-doped titania was embedded on the zirconia surface by the sol-gel method. Titania was grown on the surface of zirconia to form a composite with higher thermal stability compared to pristine TiO_2. Zinc dopant was incorporated into the TiO_2 structure in order to shift the absorption ability of the composite to the visible range. Sol-gel route was preferred due to its low cost, easy compositional control, and low processing temperature [15]. Various zinc contents (from 1 to 9%) and calcination temperatures (from 500 to 900 °C) were applied to zirconia supported titania to evaluate the absorption shift and crystal structures.

■ EXPERIMENTAL SECTION

Materials

Titanium(IV) tetraisopropoxide (TTIP) (97%, Sigma Aldrich), and zirconia powder (ZrO_2) (Jiaozuo Huasu) were chosen as titania (TiO_2) precursor and supporting material, respectively. Zinc chloride ($ZnCl_2$) (Merck) was used as a dopant source. Absolute ethanol (PA, Merck) and demineralized water (Jaya Sentosa) were used as solvents.

Instrumentation

X-ray powder diffractometer (XRD) PANalytical X'Pert PRO MRD (Cu Kα radiation λ = 1.54 Å, 40 kV, 30 mA) was used to analyze the crystalline structure of composites. Vibrational spectra were measured on a Fourier transform infrared spectrophotometer (FT-IR, Thermo Nicolet Is10). Specular reflectance UV-Vis spectrometer UV 1700 Pharmaspec (SR-UV) was used to analyze the absorption of composites**.** Scanning Electron Microscope-Energy Dispersive X-Ray Spectrometer (SEM-EDX) FLEXSEM1000 with an accelerating voltage of 10 kV was used to analyze the morphology and elemental composition of synthesized composites.

Procedure

First, 2.5 mL of TTIP was diluted into 25 mL of absolute ethanol under mild stirring. Various amounts of $ZnCl_2$ and 1 g of ZrO_2 were mixed in 25 mL of demineralized water. The percentage of zinc dopant was fixed at 1, 3, 5, 7, and 9% to the weight ratio of titanium. The aqueous suspension was then added dropwise into the TTIP solution while being stirred. The mixture was stirred for another 30 min to maximize the reaction. Subsequently, the suspended solid was separated by centrifugation at 2000 rpm for 1 h. The obtained solid was aged in the open air for 24 h followed by the drying process in the oven at 80 °C for another 24 h. Ultimately, the dried solid was calcined under the atmospheric condition at 500 °C for 4 h with a ramp temp of 5 °C/min. Additionally, the composite with 5% zinc content was calcined further at 700 and 900 °C.

■ RESULTS AND DISCUSSION

The UV-Vis absorption spectra of Zn-doped TiO_2 embedded on the surface of ZrO_2 together with pure TiO_2 as a reference are shown in Fig. 1, and the corresponding calculated bandgaps are summarized in Table 1. The UV-Vis absorption of the composite was measured to demonstrate the doping effect of Zn in the TiO_2 structure. The bandgap energy (E_g) value for TiO_2 is 3.12 eV, while Zn-doped TiO_2 on ZrO_2 composites range from 3.08 to 2.87 eV. The increment of Zn content shifted the bandgap energy toward a longer wavelength. The bandgap decreased with the increasing of Zn content until the optimum condition of 5%, which exhibits the lowest bandgap of 2.87 eV. Zinc metal doping

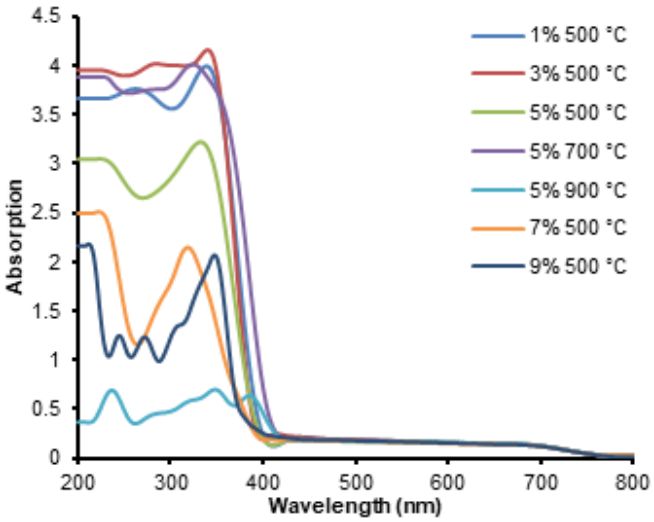

Fig 1. UV-Vis absorption spectra of various Zn-doped TiO_2 on ZrO_2 composites

Table 1. Bandgap data of pure TiO_2 and composites of Zn-doped TiO_2 on ZrO_2

Sample	E_g (eV)
TiO_2 500 °C	3.12
Zn-doped TiO_2-ZrO_2 1% 500 °C	3.07
Zn-doped TiO_2-ZrO_2 3% 500 °C	2.99
Zn-doped TiO_2-ZrO_2 5% 500 °C	2.90
Zn-doped TiO_2-ZrO_2 5% 700 °C	2.89
Zn-doped TiO_2-ZrO_2 5% 900 °C	2.87
Zn-doped TiO_2-ZrO_2 7% 500 °C	2.98
Zn-doped TiO_2-ZrO_2 9% 500 °C	3.08

in TiO_2 structure introduces new energy levels into the bandgap of TiO_2. When zinc is doped into TiO_2 lattice, some of the newly occupied molecular orbitals located below the conduction band (CB) of TiO_2 are formed. Therefore, this redshift and enhanced light absorption are attributed to the charge transfer from the dopant energy level of Zn to the CB of TiO_2 or O 2p to Zn 3d instead of Ti 3d [16]. The absorption of TiO_2-ZrO_2 composite with 7% and 9% of zinc contents returned to the lower wavelength due to the aggregation of ZnO formed during calcination. The increasing calcination temperature from 500 to 900 °C decreased the bandgap energy. It was caused by the phase transformation of TiO_2 from anatase to rutile. The E_g of rutile phase (3.0 eV) is lower than that of the anatase crystal phase (3.2 eV). Thus, the bandgap energy of the sample calcined at 900 °C was lower than samples calcined at 500 and 700 °C.

Fig. 2 shows the surface morphology and corresponding EDX spectra of pure TiO_2 and 5% Zn-doped TiO_2 on the ZrO_2 composite calcined at 500 °C. The elemental composition of the samples obtained from EDX measurements is given in Table 2. The EDX images of elementals distribution of Zn-doped TiO_2 on the ZrO_2 composite calcined at 500 °C are shown in Fig. 3. It can be seen that the undoped TiO_2 particle morphology is spherical in general, and Zn-doped TiO_2 on the ZrO_2 composite looks rougher feature than TiO_2. It is clear from the elemental analysis that 0.95% of the Zn element was present in the doped samples. In addition,

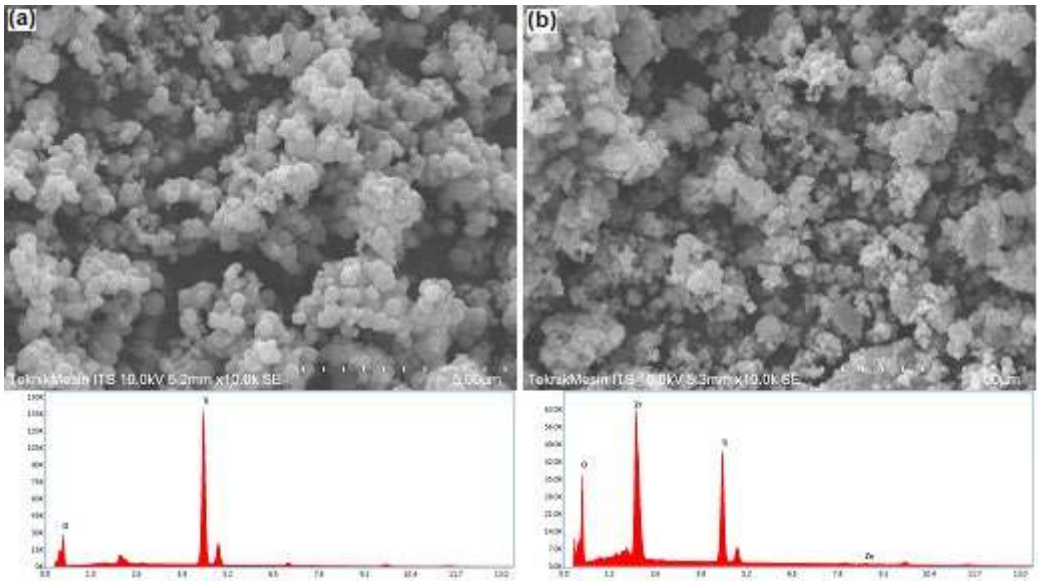

Fig 2. SEM images and EDX spectra of (a) TiO_2 and (b) 5% Zn-doped TiO_2 on ZrO_2 composite calcined at 500 °C

Table 2. Elemental surface composition of TiO_2 and 5% Zn-doped TiO_2 on ZrO_2 composite both calcined at 500 °C

Material	% Mass				
	Zr	O	Ti	Zn	Total
TiO_2	-	36.82	63.18	-	100
5% Zn-doped TiO_2-ZrO_2	31.16	41.51	26.39	0.95	100

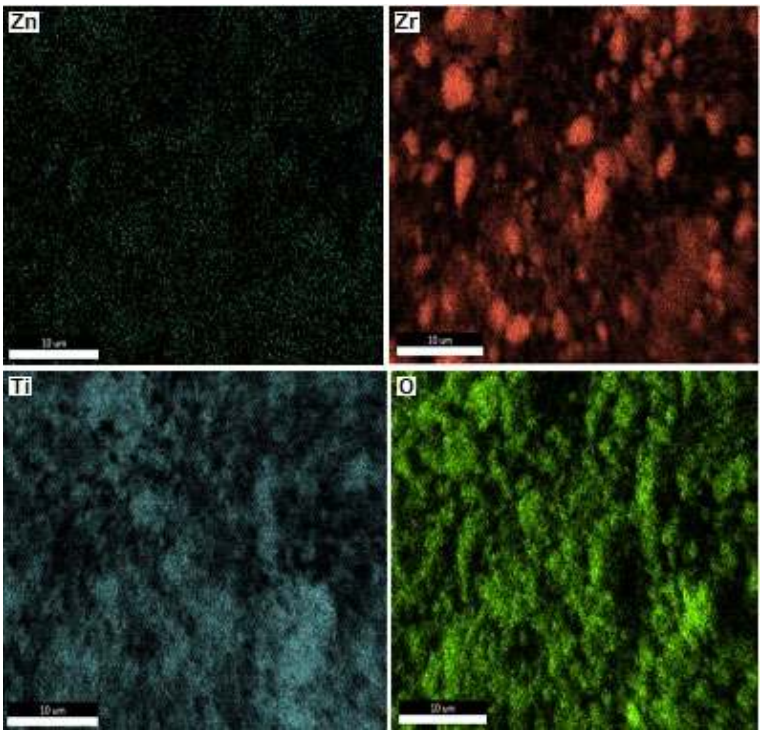

Fig 3. Elemental mapping images of 5% Zn-doped TiO_2 on ZrO_2 composite calcined at 500 °C

it can be revealed from the analysis that Zn had been successfully incorporated on the surface of the TiO_2-ZrO_2 composite. EDX spectra and data confirm that there was no impurity in the samples.

XRD patterns of undoped and Zn-doped TiO_2 on ZrO_2 composites together with pure TiO_2 calcined at 500 °C are shown in Fig. 4. Zn-doped composite calcined at 500 °C exists in two main crystalline forms, anatase and monoclinic, and no peak related to the rutile or any other phase is observed. Two main peaks of anatase TiO_2 are at 2θ of 25° (101) and 48° (200), which is closely matching with ICDD PDF number: 00-002-0387. On the other hand, XRD peaks of ZrO_2 at 2θ of 28° (-111), 31° (111), and 34° (020) are often taken as the characteristic peaks of monoclinic, which is closely matching with ICDD PDF number: 01-074-1200. The presence of the dopant was not found in the XRD patterns, which might be due to either the uniform distribution of dopant in TiO_2 lattice or the low amount of dopant used [17]. The presence of the Zn dopant in the composite was confirmed by EDX analysis, as discussed before. All composites exhibited lower-intensity peaks of anatase at 25° compared to pure TiO_2.

The XRD patterns of 5% Zn-doped TiO_2 on ZrO_2 composites calcined at different temperatures are presented in Fig. 5. XRD pattern of undoped TiO_2 calcined at 500 °C shows only anatase phase at 2θ of 25° (101) and 48° (200), while the XRD pattern of Zn-doped TiO_2-ZrO_2 composite displays a weak anatase peak at 2θ of 25° (101) and strong monoclinic peaks at 2θ of 28° (-111) and 31° (111). XRD pattern of Zn-doped TiO_2-ZrO_2 calcined at 700 °C had an emerging rutile peak at 2θ of 27° (110) and a diminished anatase peak at 25° (101). This suggests that there was a phase transformation from anatase to rutile at about 700 °C, which agrees with the previous experiment [18]. The diffraction peaks at 2θ = 27° (110), 36° (101), 41° (111), and 54° (211) correspond to the rutile phase (ICDD PDF number: 00-004-0551). After calcination at 900 °C, the anatase peak disappeared while the rutile peak became stronger than that at 700 °C. The presence of ZrO_2 and Zn dopant are presumably responsible for inhibiting the transformation of anatase to rutile [14,19-20].

FT-IR spectra of various Zn-doped composites together with pure TiO_2 are presented in Fig. 6. Absorption peaks around 500 and 545 cm^{-1} can be devoted to stretching vibration of the Ti–O bond and

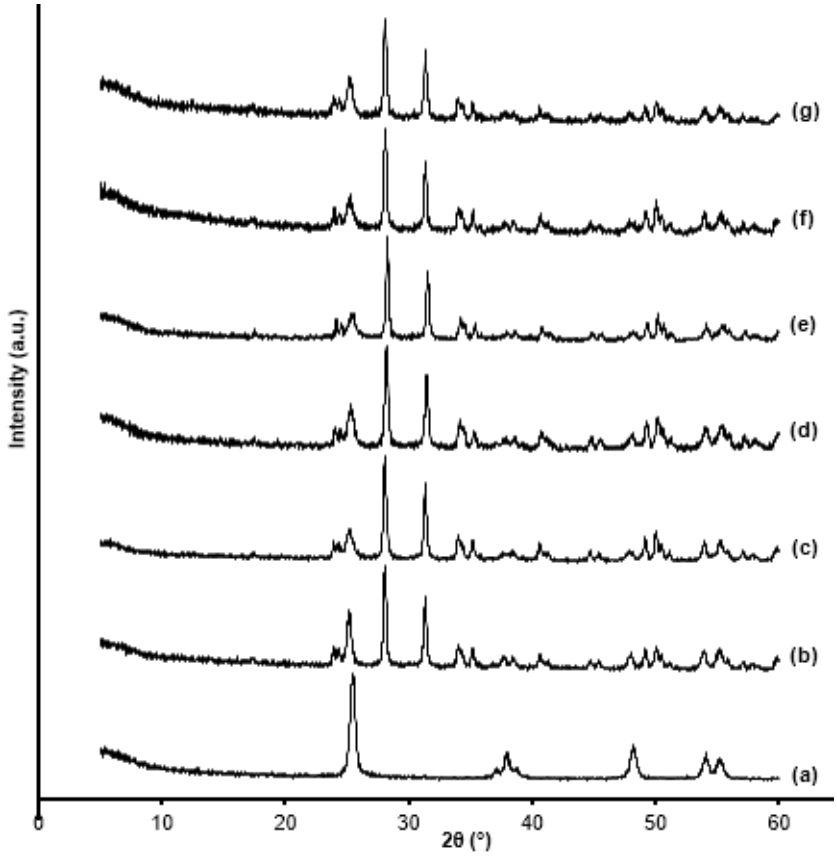

Fig 4. XRD patterns of (a) TiO_2, (b) undoped and Zn-doped TiO_2 on ZrO_2 composites with Zn content of (c) 1, (d) 3, (e) 5, (f) 7, (g) 9% (w/w) calcined at 500 °C

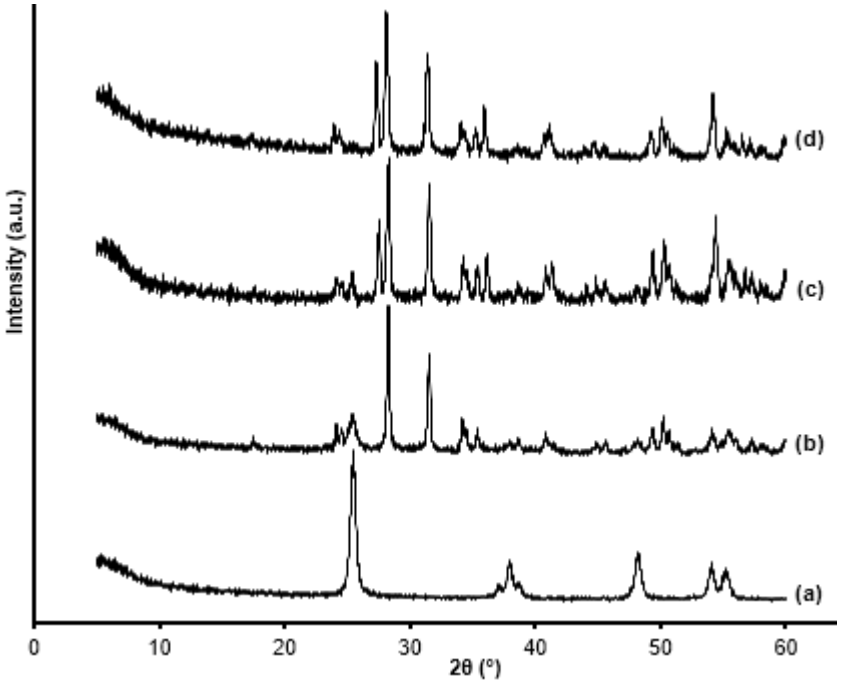

Fig 5. XRD patterns of (a) TiO_2 calcined at 500 °C, 5% Zn-doped TiO_2 on ZrO_2 composites calcined at (b) 500, (c) 700, and (d) 900 °C

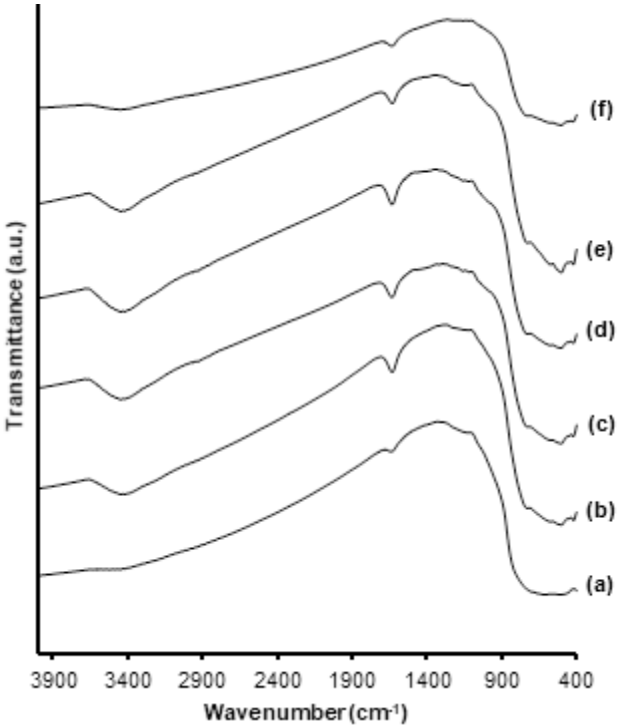

Fig 6. FTIR spectra of (a) TiO_2 and Zn-doped TiO_2 on ZrO_2 composites with Zn content of (b) 1, (c) 3, (d) 5, (e) 7, (f) 9% (w/w) calcined at 500 °C

Zr–O bond, respectively [21-22]. Peaks around 3100–3600 and 1632 cm^{-1} are assigned to stretching and bending vibrations of hydroxyl groups, respectively [23]. The absorption peaks of Ti–O and Zr–O tended to decrease as the Zn dopant content increased. It indicates that zinc metal was successfully doped into the TiO_2 structure. There was a new peak that appeared around 1200 $cm^{-1,}$ which may belong to Zn–O–Ti vibration at the substitutional position.

Fig. 7 shows the FTIR spectra of 5% Zn-doped TiO_2 on ZrO_2 composites calcined at different temperatures, together with TiO_2 calcined at 500 °C as a reference. After calcination at 700 °C, the O–H vibration bands became much weaker than those at 500 °C, indicating the removal of a certain amount of O–H groups during calcination. After heat treatment at a temperature of 900 °C, the spectra show further disappearance of O–H group peaks, indicating a complete elimination of hydroxy groups. The vibration band of Zn–O–Ti around 1200 cm^{-1} decreased when the calcination temperatures were increased. It was caused by dopant that sinters at high temperature [24].

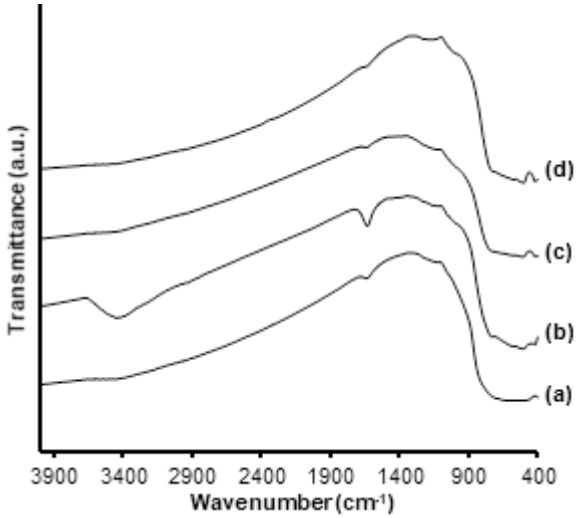

Fig 7. FTIR spectra of (a) TiO_2 calcined at 500 °C, 5% Zn-doped TiO_2 on ZrO_2 composites calcined at (b) 500, (c) 700, and (d) 900 °C

The visible-light-response of the synthesized composite based on UV-Vis spectral data gives an insight that the composite has potential as a photocatalyst. The zinc dopant shifts the absorption edge of TiO_2 to a higher wavelength, thus increasing the photocatalytic activity of TiO_2 hypothetically. Embedding TiO_2 on the surface of ZrO_2 was proven to inhibit the anatase-to-rutile transformation, thus establishing a relatively thermally stable composite compared to TiO_2.

■ CONCLUSION

A series of Zn-doped TiO_2 embedded on the surface of ZrO_2 with various zinc contents were successfully synthesized through the sol-gel method and calcined at different temperatures. Zn doping results in the improvement of photo-response under visible light irradiation. TiO_2-ZrO_2 composite with 5% of zinc content calcined at 900 °C exhibits the lowest bandgap of 2.87 eV with an absorption edge wavelength of 432.61 nm. The presence of ZrO_2 and Zn inhibits the anatase-to-rutile transformation at 700 and 900 °C of calcination temperatures. The experimental results demonstrate that doped TiO_2 embedded on the ZrO_2 surface with optimal Zn content can be considered as a promising photocatalyst under visible light irradiation.

■ ACKNOWLEDGMENTS

We would like to express our gratitude to the Faculty of Mathematics, and Natural Sciences Universitas Gadjah Mada for their support on this works through BPPTNBH 2019 Grant (86/J01.1.28/PL.06.02/2019).

■ REFERENCES

[1] Huang, F., Yan, A., and Zhao, H., 2016, "Influences of doping on photocatalytic properties of TiO_2 photocatalyst" in *Semiconductor Photocatalysis - Materials, Mechanisms and Applications*, Eds. Cao, W., IntechOpen, Rijeka, Croatia.

[2] Seabra, M.P., Salvado, I.M.M., and Labrincha, J.A., 2011, Pure and (zinc or iron) doped titania powders prepared by sol-gel and used as photocatalyst, *Ceram. Int.*, 37 (8), 3317–3322.

[3] Nair, R.G., Mazumdar, S., Modak, B., Bapat, R., Ayyub, P., and Bhattacharyya, K., 2017, The role of surface O-vacancies in the photocatalytic oxidation of methylene blue by Zn-doped TiO_2: A mechanistic approach, *J. Photochem. Photobiol., A*, 345, 36–53.

[4] Yao, N.Q., Liu, Z.C., Gu, G.R., and Wu, B.J., 2017, Structural, optical, and electrical properties of Cu-doped ZrO_2 films prepared by magnetron co-sputtering, *Chin. Phys. B*, 26 (10), 106801.

[5] Jiang, B., Zhang, S., Guo, X., Jin, B., and Tian, Y., 2009, Preparation and photocatalytic activity of CeO_2/TiO_2 interface composite film, *Appl. Surf. Sci.*, 255 (11), 5975–5978.

[6] Zheng, R., Meng, X., and Tang, F., 2009, Synthesis, characterization and photodegradation study of mixed-phase titania hollow submicrospheres with rough surface, *Appl. Surf. Sci.*, 255 (11), 5989–5994.

[7] Polisetti, S., Deshpande, P.A., and Madras, G., 2011, Photocatalytic activity of combustion synthesized ZrO_2 and ZrO_2–TiO_2 mixed oxides, *Ind. Eng. Chem. Res.*, 50 (23), 12915–12924.

[8] Králik, B., Chang, E.K., and Louie, S.G., 1998, Structural properties and quasiparticle band structure of zirconia, *Phys. Rev. B: Condens. Matter*, 57 (12), 7027–7036.

[9] Kubiak, A., Siwińska-Ciesielczyk, K., and Jesionowski, T., 2018, Titania-based hybrid materials with ZnO, ZrO_2 and MoS_2: A review, *Materials*, 11 (11), 2295.

[10] Zhang, J., Li, L., Zhang, J., Zhang, X., and Zhang, W., 2017, Controllable design of natural gully-like TiO_2-ZrO_2 composites and their photocatalytic degradation and hydrogen production by water splitting, *New J. Chem.*, 41 (17), 9113–9122.

[11] Fan, M., Hu, S., Ren, B., Wang, J., and Jing, X., 2013, Synthesis of nanocomposite TiO_2/ZrO_2 prepared by different templates and photocatalytic properties for the photodegradation of Rhodamine B, *Powder Technol.*, 235, 27–32.

[12] Gao, B., Lim, T.M., Subagio, D.P., and Lim, T.T., 2010, Zr-doped TiO_2 for enhanced photocatalytic degradation of bisphenol A, *Appl. Catal., A*, 375 (1), 107–115.

[13] Verma, S., Rani, S., Kumar, S., and Khan, M.A.M., 2018, Rietveld refinement, micro-structural, optical and thermal parameters of zirconium titanate composites, *Ceram. Int.*, 44 (2), 1653–1661.

[14] Andita, K.R., Kurniawan, R., and Syoufian, A., 2019, Synthesis and characterization of Cu-doped zirconium titanate as a potential visible-light responsive photocatalyst, *Indones. J. Chem.*, 19 (3), 761–766.

[15] Kong, L., Karatchevtseva, I., Holmes, R., Davis, J., Zhang, Y., and Triani, G., 2016, New synthesis route for lead zirconate titanate powder, *Ceram. Int.*, 42 (6), 6782–6790.

[16] Wang, Q., Yun, G., An, N., Shi, Y., Fan, J., Huang, H., and Su, B., 2015, The enhanced photocatalytic activity of Zn^{2+} doped TiO_2 for hydrogen generation under artificial sunlight irradiation prepared by sol-gel method, *J. Sol-Gel Sci. Technol.*, 73 (2), 341–349.

[17] Sikirman, A., Krishnan, J., and Mohamad, E.N., 2014, Effect of dopant concentration of N, Fe co-doped TiO_2 on photodegradation of methylene blue under ordinary visible light, *Appl. Mech. Mater.*, 661, 34–38.

[18] Kim, K.H., Park, H., Ahn, J.P., Lee, J.C., and Park, J.K., 2007, HRTEM study of phase transformation from anatase to rutile in nanocrystalline TiO_2 particles, *Mater. Sci. Forum*, 534-536, 65–68.

[19] Jing, L., Xin, B., Yuan, F., Xue, L., Wang, B., and Fu, H., 2006, Effects of surface oxygen vacancies on photophysical and photochemical processes of Zn-doped TiO_2 nanoparticles and their relationships, *J. Phys. Chem. B*, 110 (36), 17860–17865.

[20] Venkatachalam, N., Palanichamy, M., Arabindoo, B., and Murugesan, V., 2007, Enhanced photocatalytic degradation of 4-chlorophenol by Zr^{4+} doped nano TiO_2, *J. Mol. Catal. A: Chem.*, 266 (1-2), 158–165.

[21] Tsiourvas, D., Tsetsekou, A., Arkas, M., Diplas, S., and Mastrogianni, E., 2011, Covalent attachment of a bioactive hyperbranched polymeric layer to titanium surface for the biomimetic growth of calcium phosphates, *J. Mater. Sci. - Mater. Med.*, 22 (1), 85–96.

[22] Tamrakar, R.K., Tiwari, N., Dubey, V., and Upadhyay, K., 2015, Infrared spectroscopy and luminescence spectra of Yb^{3+} doped ZrO_2 nanophosphor, *J. Radiat. Res. Appl. Sci.*, 8 (3), 399–403.

[23] Gao, Y., Masuda, Y., Peng, Z., Yonezawa, T., and Koumoto, K., 2003, Room temperature deposition of a TiO_2 thin film from aqueous peroxotitanate solution, *J. Mater. Chem.*, 13 (3), 608–613.

[24] Kurniawan, R., Sudiono, S., Trisunaryanti, W., and Syoufian, A., 2019, Synthesis of iron-doped zirconium titanate as a potential visible-light responsive photocatalyst, *Indones. J. Chem.*, 19 (2), 454–460.

Properties of Biodegradable Polymer from Terrestrial Mushroom for Potential Enhanced Oil Recovery

Tengku Amran Tengku Mohd[1,2,*], Shareena Fairuz Abdul Manaf[1], Munawirah Abd Naim[1], Muhammad Shafiq Mat Shayuti[1], and Mohd Zaidi Jaafar[2]

[1]*Faculty of Chemical Engineering, Universiti Teknologi MARA, 40450 Shah Alam, Selangor, Malaysia*

[2]*School of Chemical and Energy Engineering, Faculty of Engineering, Universiti Teknologi Malaysia, Skudai, 81310 Johor Bahru, Malaysia*

* ***Corresponding author:***

tel: +603-55436534
email: amran865@uitm.edu.my

Received: December 6, 2019
Accepted: May 28, 2020

DOI: 10.22146/ijc.52254

Abstract: *Polymer flooding could enhance the oil recovery by increasing the viscosity of water, thus, improving the mobility control and sweep efficiency. It is essential to explore natural sources of polymer, which is biologically degradable and negligible to environmental risks. This research aims to produce a biodegradable polymer from terrestrial mushroom, analyze the properties of the polymer and investigate the oil recovery from polymer flooding. Polysaccharide biopolymer was extracted from mushroom and characterized using Fourier Transform Infrared Spectrometer (FTIR), while the polymer viscosity was investigated using an automated microviscometer. The oil recovery tests were conducted at room temperature using a sand pack model. It was found that polymer viscosity increases with increasing polymer concentration and decreases when increase in temperature, salinity, and concentration of divalent ions. The oil recovery tests showed that a higher polymer concentration of 3000 ppm had recovered more oil with an incremental recovery of 25.8% after waterflooding, while a polymer concentration of 1500 pm obtained incremental 22.2% recovery of original oil in place (OOIP). The oil recovery from waterflooding was approximately 25.4 and 24.2% of the OOIP, respectively. Therefore, an environmentally friendly biopolymer was successfully extracted, which is potential for enhanced oil recovery (EOR) application, but it will lose its viscosity performance at certain reservoir conditions.*

Keywords: *biopolymer; mushroom; polymer flooding; viscosity; enhanced oil recovery*

■ INTRODUCTION

Enhanced oil recovery (EOR) includes the mobility-control processes that favor the mobility ratio to improve sweep efficiency [1]. The thickening of water with a biopolymer and reducing gas mobility with foams are such examples. In most cases, biopolymer flooding is used in the EOR process as the thickening agent, which can improve the mobility of oil by increasing the viscosity of water. When the mobility ratio is larger than 1, it results in instability of the flow due to less viscous solvent (water) displacing a more viscous solvent (oil), which will lead to viscous fingering. In contrast, when the mobility is less than 1, improvement can be made by increasing the viscosity of displacing fluid and lowering the viscosity of displaced fluid [2-3]. Therefore, polymers have benefits in enhancing the viscosity of water solution, which in turn reducing the mobility ratio between water and oil, resulting in improvement of sweep efficiency [4]. Besides that, gelled polymer technology could be applied to seal high permeability zones and fractures, resulting in improving sweep efficiency and oil recovery [5]. Another chemical EOR process, which could provide mobility control, is foam flooding, involving the investigation of mobility [6], as well as the improvement of foam stability with the addition of nanoparticles [7-11]. These EOR processes could be monitored using a real-time approach of streaming potential measurement using electrodes permanently installed downhole, which

is the potential to monitor alkaline-surfactant-polymer (ASP) flooding [12-13].

Polymers can be divided into two types, naturally occurred and synthetic. Synthetic polymers such as polyacrylamides are produced from the polymerization of acrylamide monomer, while naturally occurred polymers such as polysaccharides biopolymer are produced by microbial action of organisms. A biopolymer is gaining interest in the EOR process since it possesses stable characteristics at the reservoir condition and only degrades under certain conditions [3]. A biopolymer is an excellent thickening agent at high salinity water. The biopolymer degradation may occur by loss of solution viscosity with time. As a thickening agent, the pivotal feature of the biopolymer is water-soluble. The concentration of the biopolymer solution is dependent on the salinity and the temperature of the reservoir itself. Mohd et al. demonstrated that the properties of several synthetic and natural polymers such as partial-hydrolyzed polyacrylamide (HPAM), polyvinylpyrrolidone, xanthan gum, guar gum, and Arabic gum change significantly with shear rate, polymer concentration, temperature, salinity and divalent ions [14]. Shear thickening and thinning occur at high and low fluid velocities in porous media, respectively. Further increase in velocity could result in polymer degradation due to the rupture of the polymer chain [15]. Hence, optimal polymer rheological properties are important for the polymer flooding process to obtain high oil recovery [16].

Polymer stability is important for polymer flooding. However, some polymers are thermally degraded at high temperature reservoir. Thermal degradation can be accelerated by the presence of dissolved oxygen and iron in the brine. Interestingly, thermal degradation can be reduced by using additives, especially oxygen scavenger [17]. It helps the polymer to remain stable in the reservoir from degradation. From the previous study on polymer concentration, a high salinity reservoir needs a high concentration of polymer for the great efficiency of displacing fluid in the reservoir. Polymers from natural sources have been selected because the raw materials are in abundance, readily available, easy to handle, environmentally friendly, and biodegradable. Their rigid structure and long polysaccharides chains make them suitable to withstand the harsh reservoir conditions. The natural polymers that have been investigated for EOR application at laboratory scale are mushroom and cabbage [18]; *Saccharomyces cerevisiae* [19]; okra [20]; cassava starch [21]; *Detarium microcarpum* [22]; gum Arabic [23]; *Irvingia gabonensis* [21,24]; *Brachystegia eurycoma* [24]; exudate gum [25]; aqueous beans [26] and schizophyllan [27].

However, many synthetic polymers are not biologically degradable, which become threats to some countries. It is essential to explore the natural source of a biopolymer, which is stable at reservoir environment and potential in the EOR application. Terrestrial mushroom has a great potential for a source of biopolymer, which was investigated in this study for potential applications in polymer flooding. Thus, this paper emphasizes the extraction process of biopolymer from the mushroom, analysis of its properties at various reservoir conditions, and determination of oil recovery from polymer flooding.

■ EXPERIMENTAL SECTION

Materials

The material used to produce a polysaccharide biopolymer is the local terrestrial mushrooms. For extraction of polysaccharides, the chemicals used were methanol and ethanol purchased from Merck, sodium hydroxide (NaOH) obtained from Sigma-Aldrich, and distilled water. Other chemicals were sodium chloride (NaCl), calcium chloride ($CaCl_2$), and magnesium chloride ($MgCl_2$) from Vchem used as brine and divalent salts, respectively, for polymer properties measurement, while paraffin oil obtained from Sigma-Aldrich was used for polymer flooding in porous media using sand pack model. Silica sand was obtained from the sea sand at the Pantai Port Dickson, sieved at desired sizes ranging from 150 to 250 μm and purified.

Procedure

Extraction of mushroom polysaccharide

Freeze-dried mushrooms (1 g) were initially extracted with methanol at 65 °C for 8 h to remove soluble

molecules, such as lipids, soluble sugars, or phenolic compounds. Subsequently, polysaccharide extraction was carried out in 30 mL water at room temperature for 24 h prior to separation. The solid was separated by centrifugation at 4 °C for 4000 rpm. The residue was re-extracted with 30 mL of water at 80 °C for 24 h. The extract was centrifuged as a similar previous condition to obtain the solid residue. The remaining solid was added with 30 mL of 1 M NaOH and placed in an oven at 80 °C for 24 h and re-centrifuged. The liquids from each extraction process were precipitated separately by adding ethanol in 2:1 ratio (v/v), and the resulting polysaccharide extracts were re-dissolved in distilled water.

Fourier transform infrared spectroscopy (FTIR) analysis

The FTIR spectra of the extracted polysaccharides were collected by using a Nicolet 6700 FTIR spectrophotometer (Thermo Fisher Scientific, USA). Each sample was scanned in FTIR spectra from 4000 to 400 cm^{-1} with a detector at 2 cm^{-1} resolution.

Properties of mushroom polysaccharide

The polymer was tested using AMVn Automated Micro Viscometer (Anton Paar). The polymer was filled in the capillary tube and inserted into the capillaries of the capillary block. By using the AMVn system, the viscosity reading was recorded four times, and then the average reading was taken. Polymer viscosity was investigated with respect to polymer concentration, temperature, salinity, and concentration of divalent salts. For analysis of polymer concentration, the polymer was investigated in the range of 500 to 5000 ppm, while the temperature effect was analyzed from 15 to 85 °C. The effect of salinity was investigated using sodium chloride (NaCl), ranging from 1000 to 10000 ppm. The same concentration ranges were applied for divalent ion concentration analysis using calcium chloride ($CaCl_2$) and magnesium chloride ($MgCl_2$). The viscosity readings recorded were analyzed and plotted against the respective parameter.

Displacement tests for enhanced oil recovery

The recovery tests were conducted at room temperature of 25 °C. The sand pack model was prepared and packed with local sand homogeneously of sizes ranging from 150 to 250 μm. The porosity and permeability of the sand pack model obtained were 0.394 and 4.7 darcy, respectively, with a pore volume (PV) of 29.7 cm^3. The flooding tests were conducted in a horizontal orientation as the experimental set-up shown in Fig. 1. The sand pack was saturated with 1.0 wt.% brine solution, and then paraffin oil was injected continuously, displacing the brine to initiate the initial reservoir condition. After that, brine was injected at approximately 1 cc/min as a secondary recovery waterflooding process. The brine injection was stopped when the water breakthrough started to occur, and no more oil could be recovered in the process. The volume of oil recovered in the collector was recorded. After that, the co-injection of the polymer was conducted into the sand pack. The injection rate for polymer solution was fixed at 0.5 cc/min, and the volume of oil displaced was recorded at each 0.2 PV of polymer solution injected into the sand pack. The sand pack was cleaned by using methyl alcohol before proceeding with another run of flooding tests.

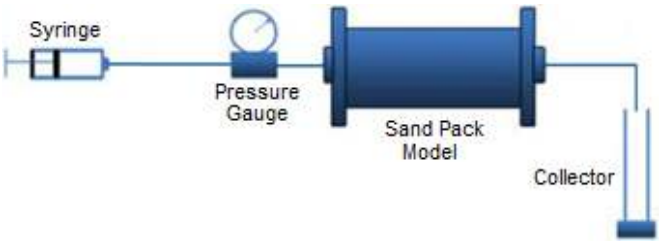

Fig 1. Displacement test set-up

■ RESULTS AND DISCUSSION

Extraction of Mushroom Polysaccharide

A terrestrial edible mushroom was used to produce a polymer solution for this study. Three methods were carried out for the extraction of polysaccharides. The first extraction, which was conducted with water at room temperature, yielded a very low purity of polysaccharide while, the extraction from water and NaOH at 80 °C, yielded more pure polysaccharides [28]. The purity of the obtained polysaccharides can be clearly seen from its color beside FTIR analysis to check the functional group of polysaccharides. Fig. 2 shows the polymer produced from the three extractions, a) water at room temperature, b) water at 80 °C, and c) 1 M NaOH at 80 °C, respectively.

FTIR Analysis

FTIR analysis was conducted to determine the functional group of polysaccharides from the samples, as given in Fig. 3. From all three conditions tested, it was clearly observed that the same functional group has demonstrated a similar pattern with several peaks [29-30].

The presence of functional groups such as O–H stretch (wavelength between 3300–3400 cm^{-1}), C=O stretch (wavelength between 1544–1652 cm^{-1}), and C–O stretch (wavelength of 1048 cm^{-1}) were observed from FTIR as given in Fig. 3, which are belongs to polymer compounds. Hence, it demonstrated that the extraction of polysaccharide in this study has been successful.

Properties of Mushroom Polysaccharide

Viscosity measurement was conducted to analyze the properties of the polymer at various conditions. In this study, the viscosity was investigated at various polymer concentrations, temperature, brine concentration, and divalent ions concentration, as shown in Fig. 4.

Polymer concentration

Fig. 4(a) clearly showed that by raising the polymer concentration has increased the viscosity. The polymer was unstable at lower concentrations due to low viscosity. At 1000 ppm, the polymer started to show stability where the viscosity reading is high at approximately 12.3 cP and

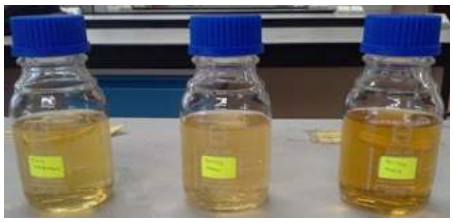

Fig 2. Polysaccharides biopolymer extracted from the mushroom

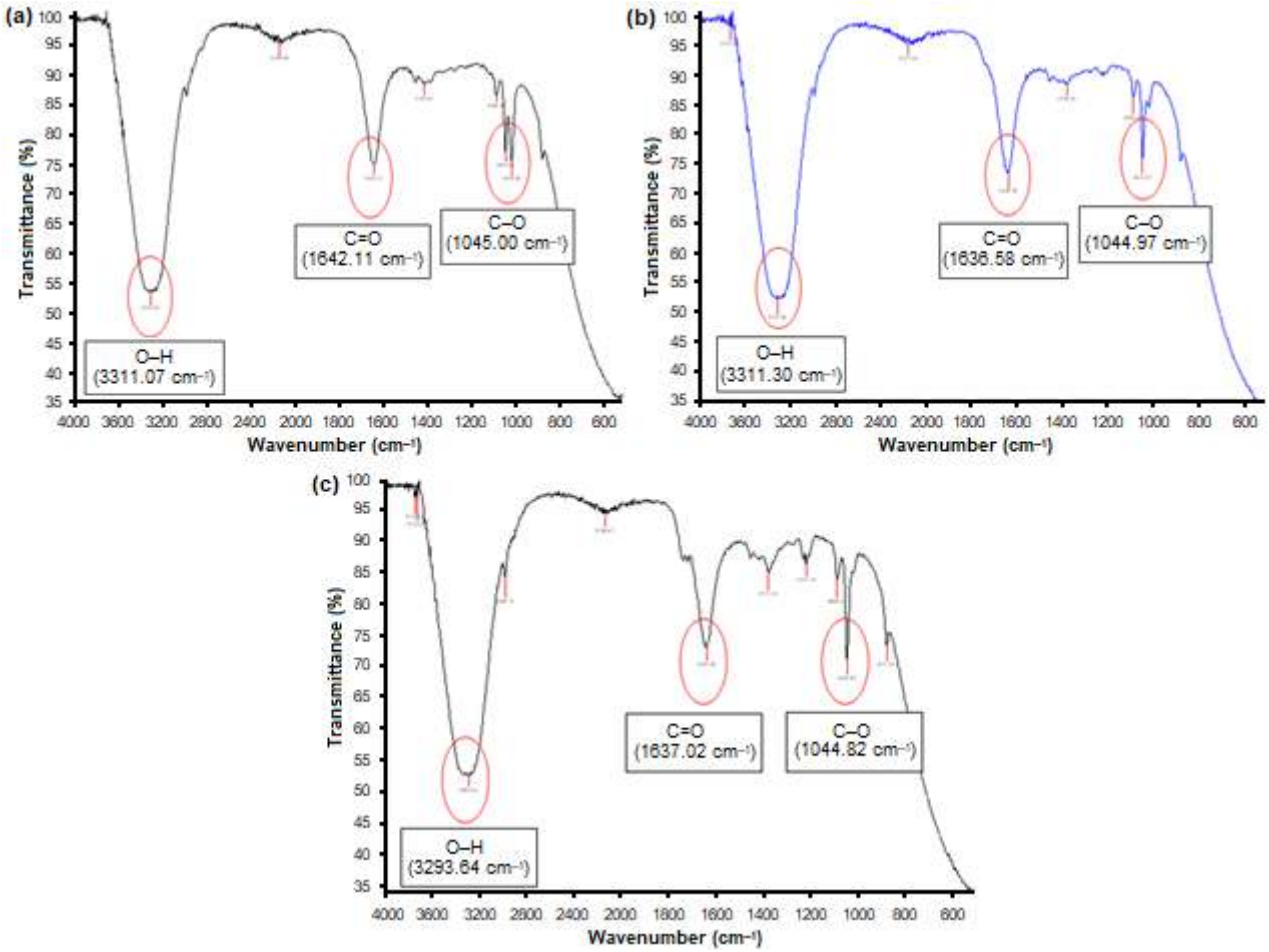

Fig 3. FTIR analysis of sample extracted with (a) water at room temperature, (b) water at 80 °C, (c) 1 M NaOH at 80 °C

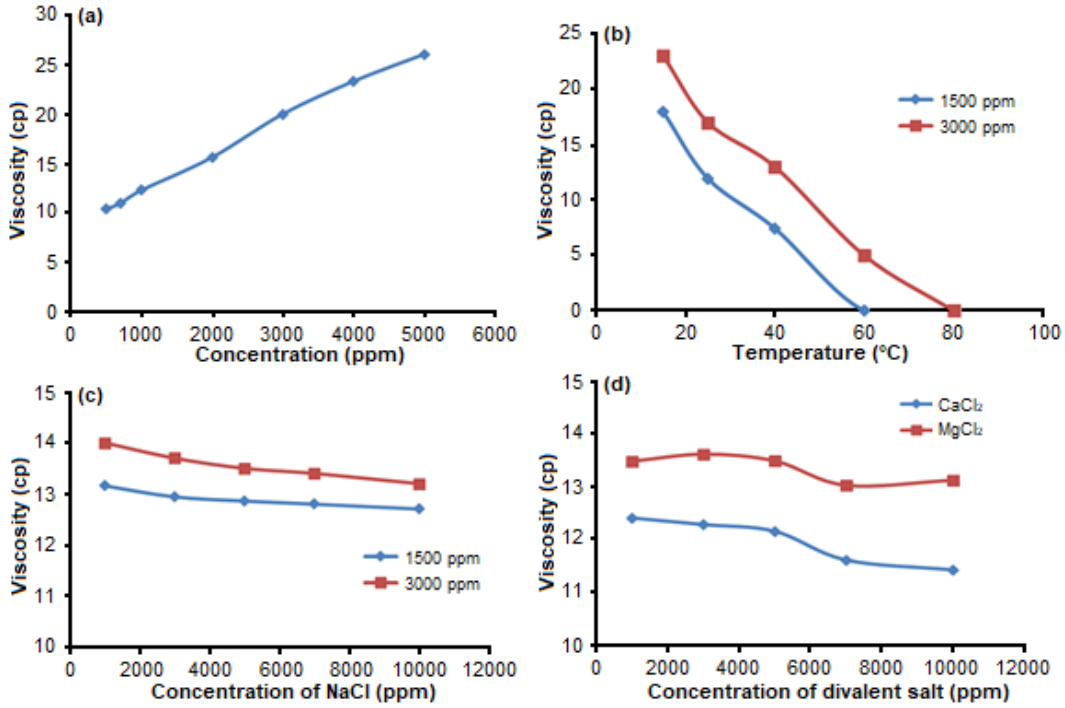

Fig 4. The polymer viscosity at various (a) polymer concentration (ppm), (b) temperature (°C), (c) brine concentration (ppm), (d) divalent ion concentration (ppm)

kept increasing with increase in the polymer concentration. Like other polysaccharides, the viscosity of this extracted biopolymer increases with increasing polymer concentration [31]. The highest polymer viscosity of about 26 cP was obtained at the highest polymer concentration investigated at 5000 ppm. As a polysaccharide, this biopolymer can behave as a non-Newtonian and pseudoplastic fluid, exhibiting shear-thinning behavior like other polysaccharide biopolymers such as *Brachystigia eurycoma* and *Irvingia gabonensis* [24,32] and aqueous beans [26]. From the previous study, a higher concentration of polymer, which could provide higher viscosity is required to recover more oil from the reservoir, as the mobility ratio between the displacing fluid to the displaced fluid is more favorable, resulting in improvement of sweep efficiency [33]. Moreover, a high concentration of polymer can withstand high temperatures and salinity reservoir environments [3,34].

Temperature

Fig. 4(b) shows the results of the temperature effect on the viscosity of extracted biopolymer at 1500 and 3000 ppm. Polymer at 1500 ppm concentration degraded earlier than that at 3000 ppm concentration. In addition, the 3000 ppm polymer can withstand higher temperature up to 80 °C before it was fully degraded, compared to 1500 ppm polymer, which was completely degraded at 60 °C. Viscosity reduction is due to the stronger thermal vibration of water molecules that retard the association effect at high temperatures [4]. Thus, this extracted biopolymer is most applicable at low temperature like xanthan biopolymers, which are mostly limited to applications where the temperature is lower than 60 °C [3]. However, the polymer is likely unstable and immature to react at low temperature, while at high reservoir temperature, the polymer loses its viscosity and degrades [35]. This situation shows that very high polymer concentration is required at high-temperature reservoir conditions to minimize the loss of its viscosity efficiency.

Salinity

Generally, the addition of salt affects the viscosity of the polymer solution. When the salinity is high, the polymer performance decreases as it losses its viscosity. Most of the reservoir is in high salinity condition. Hence, a suitable polymer concentration is important to prevent

viscosity reduction [3]. Based on the test conducted, the result is shown in Fig. 4(c) by using monovalent salt, NaCl. Two concentrations of polymer were tested at 1500 and 3000 ppm. It can be seen that by increasing the concentration of NaCl, the viscosity lost its efficiency. However, the viscosity of the biopolymer is much less affected by the change in salinity compared with a synthetic polymer such as HPAM [3,14], as the viscosity of this biopolymer steadily decreases with increasing NaCl concentration. Small viscosity reductions of 0.8 and 0.5 cP were observed for both 1500 and 3000 ppm polymer concentrations, respectively, when the NaCl concentration increases from 1000 to 10000 ppm. A drastic viscosity reduction could occur to HPAM because when an electrolyte such as NaCl is added to a polymer solution, the repulsive forces are screened by a double layer of electrolytes, and the extension is reduced. As the electrolyte concentration increases, the extension of the polymer chain decreases, resulting in a reduction of the solution viscosity [3]. Therefore, the concentration of polymer was increased to withstand high salinity conditions much longer [34].

Divalent ion

The divalent ions are known to tightly bind the anions along the polyelectrolyte chain because they have higher charge and polarizability, causing the polymer chain to contract to its minimum size and reduce its viscosity. In this study, the extracted biopolymer was kept constant at 1500 ppm to observe the effect at varying divalent ions (Ca^{2+} or Mg^{2+}). Fig. 4(d) shows the result obtained where $CaCl_2$ results in more viscosity reduction than $MgCl_2$ [36]. This situation is slightly similar to the salinity test using NaCl as a monovalent ion effect on viscosity. It was found that the divalent ion contents do not have much effect on the viscosity of biopolymer compared with HPAM [3]. Still, the viscosity reduction is larger than the monovalent ion effect. Therefore, this can be overcome by adding a high concentration of polymer since, in reality, the reservoir is in high salinity condition [33].

Displacement Test for Enhanced Oil Recovery

The test on oil recovery was conducted to determine the percentage of oil recovered from waterflooding, and the incremental oil recovery yielded from polymer flooding. The experiments were performed at room temperature using a sand pack model, as shown in Fig. 1 with different polymer concentrations. Polymer solutions at 1500 and 3000 ppm were prepared to represent low and high polymer concentrations, which were injected into the porous sand pack model to recover the oil. Basically, the higher polymer concentration could provide higher viscosity, resulting in the improvement of sweep efficiency [17]. Fig. 5 and 6 illustrate the results of oil recovery from the displacement test of waterflooding and polymer injection. It was found that polymer could further recover the residual oil, which could not be produced from waterflooding. From Fig. 5, oil recovery from the waterflooding process was approximately 25.4 and 24.2% of the original oil in place (OOIP) for the cases of 3000 and 1500 ppm polymer concentrations, respectively. Water was injected about 2 PVs to ensure that the oil has been fully recovered, and no more oil was produced in the collector. This could minimize the capillary end effects that might exist [37]. After that, the co-injection of the polymer was conducted, resulting in significant incremental oil recovery obtained after the waterflooding process. The percentage of oil recovered also increased with higher polymer concentration. Polymer injection at 3000 ppm has yielded the higher

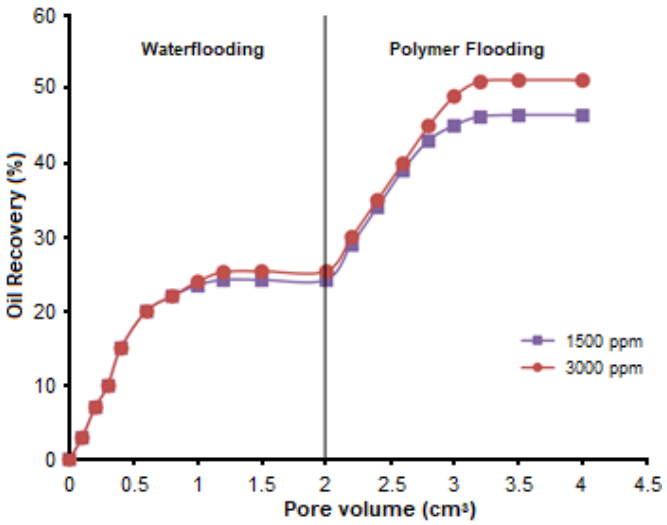

Fig 5. Oil recovery from waterflooding and co-injection of polymer

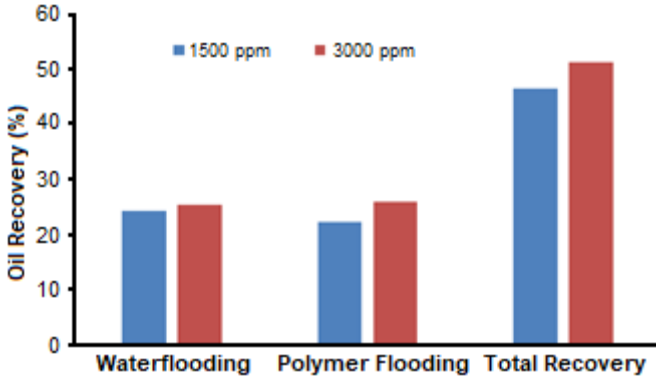

Fig 6. Oil recovery from waterflooding and polymer flooding at different polymer concentrations

incremental oil recovery of 25.8%, while 1500 ppm polymer has produced approximately 22.2% of OOIP, obtained after 2 PVs of polymer injection. These resulted in total recoveries of 51.2 and 46.4% of OOIP, respectively, as shown in Fig. 6. These findings are comparable and supported by biopolymer flooding conducted by Ihebuzor and Onyenkonwu using okra, gum Arabic, and *Irvingia gabonensis* with maximum recoveries of 63.16, 53.01, and 47.37% of OOIP, respectively [32]. Also, Gbonhinbor and Onyekonwu obtained an oil recovery of 44.6% using aqueous beans [26], while Goa found an oil recovery of 55% from schizophyllan biopolymer [27]. When waterflooding is no more effective to recover the trapped oil, subsequent polymer flooding could favor the mobility ratio between the displaced fluid and the displacing fluid compared to the waterflooding, thus improving the sweep efficiency and the cumulative oil recovery. Polymer flooding can improve the macroscopic and microscopic displacement efficiency to enhance oil recovery [38]. Besides reducing the relative permeability within the porous media, the polymer acts in thickening the water, therefore reducing the mobility and minimizes the viscous fingering effect [39]. Reducing the relative permeability of water could also achieve lower mobility through the formation of a layer on the pore walls by the adsorbed polymer, flow pathway segregation of oil and water, wettability alteration, and swelling/shrinkage of the polymer depending on the phase flow. Based on the results, the higher polymer concentration results in a higher viscosity of water, which improves the mobility ratio between the displaced fluid and the displacing fluid, thus minimizing the viscous fingering, improving the sweep efficiency, and enhancing the oil recovery. The introduction of polymer flooding after waterflooding could further recover the residual oil leading to incremental oil recovery [39-40].

■ CONCLUSION

From this research, it can be concluded that polysaccharides biopolymer have been successfully extracted from terrestrial mushroom, where higher purity polysaccharides were yielded from water and sodium hydroxide extraction at 80 °C. In the EOR application, high viscosity polymer is required for a more favorable mobility ratio and improved sweep efficiency. It was found that the viscosity of extracted polymer increased with increasing polymer concentration and decreased with an increase in temperature. The viscosity of the biopolymer was not much affected by the change in salinity and divalent ions compared with a synthetic polymer. However, the presence of divalent ions (Ca^{2+} and Mg^{2+}) have further reduced the polymer viscosity compared to monovalent ion (Na^{+}), while Ca^{2+} provided a more significant reduction effect on polymer viscosity than the Mg^{2+}. The oil recovery tests showed that polymers at a higher concentration of 3000 ppm have recovered more oil with the incremental recovery of 25.8% after waterflooding, while 1500 ppm polymer yielded lower oil recovery with incremental 22.2% of OOIP. The oil recovery from waterflooding was approximately 25.4 and 24.2% of the OOIP, respectively. Therefore, an environmentally friendly biopolymer was successfully extracted, which is potential for enhanced oil recovery (EOR) application, but it will lose its viscosity performance at certain reservoir conditions.

■ ACKNOWLEDGMENTS

This work was financially supported by the Fundamental Research Grant Scheme (FRGS) (600-IRMI/FRGS 5/3 (192/2019)) from the Ministry of Higher Education (MoHE) given to Universiti Teknologi MARA (UiTM).

■ REFERENCES

[1] Bataweel, M.A., and Nasr-El-Din, H.A., 2012, *Rheological study for surfactant-polymer and novel alkali-surfactant-polymer solutions*, North Africa Technical Conference and Exhibition, Cairo, Egypt, 20-22 February 2012.

[2] Seright, R., 2010, Potential for polymer flooding reservoirs with viscous oils, *SPE Reservoir Eval. Eng.*, 13 (04), 730–740.

[3] Green, D.W., and Willhite, G.P., 1998, *Enhanced Oil Recovery*, SPE Textbook Series, Volume 6, Society of Petroleum Engineers, Richardson, Texas.

[4] Niu, Y., Jian, O., Zhu, Z., Wang, G., Sun, G., and Shi, L., 2001, *Research on hydrophobically associating water soluble polymer used for EOR*, SPE International Symposium on Oilfield Chemistry, Houston, Texas, 13-16 February 2001.

[5] Achim, N., Alias, N.H., Ghazali, N.A., Rodhi, M.N.M, Mohd, T.A.T., and Yahya, E., 2015, Polymer gelled technology to improve sweep efficiency in enhanced oil recovery: A literature review, *Adv. Mater. Res.*, 1113, 690–694.

[6] Mohd, T.A.T., Alias, N., Ghazali, N.A., Yahya, E., Sauki, A., Azizi, A., and Yusof, N.M., 2015, Mobility investigation of nanoparticle-stabilized carbon dioxide foam for enhanced oil recovery (EOR), *Adv. Mater. Res.*, 1119, 90–95.

[7] Mohd, T.A.T., Shukor, M.A., Ghazali, N.A., Alias, N., Yahya, E., Azizi, A., Shahruddin, M.Z., and Ramlee, N.A., 2014, Relationship between foamability and nanoparticle concentration of carbon dioxide (CO_2) foam for enhanced oil recovery (EOR), *Appl. Mech. Mater.*, 548-549, 67–71.

[8] Azizi, A., Husin, H., Ghazali, N.A., Khairudin, M.K., Sauki, A., Alias, N.H., and Mohd, T.A.T., 2015, Nanoparticles stabilized carbon dioxide foams in sandstone and limestone reservoir, *Adv. Mater. Res.*, 1119, 170–174.

[9] Mohd, T.A.T., Bakar, N.F.A., Awang, N., and Talib, A.A., 2018, Aqueous foams stabilized with silica nanoparticle and alpha olefin sulfonates surfactant, *J. Mech. Eng. Sci.*, 12 (3), 3759–3770.

[10] Azmi, N.S.M., Roslina, N.R., Mohd, T.A.T., Tan, H.L., and Bakar, N.F.A., 2019, Diffusion coefficient and interfacial tension with addition of silica nanoparticles in CO_2-surfactant-water-hexane for enhanced oil recovery (EOR) using molecular dynamic simulation, *Key Eng. Mater.*, 797, 375–384.

[11] Azmi, N.S.M., Bakar, N.F.A., Mohd, T.A.T., and Azizi, A., 2020, Molecular dynamics simulation on CO_2 foam system with addition of SiO_2 nanoparticles at various sodium dodecyl sulfate (SDS) concentrations and elevated temperatures for enhanced oil recovery (EOR) application, *Comput. Mater. Sci.*, 184, 109937.

[12] Mohd, T.A.T., Jaafar, M.Z., Rasol, A.A.A., and Ali, J., 2017, Review: A new prospect of streaming potential measurement in alkaline-surfactant-polymer flooding, *Chem. Eng. Trans.*, 56, 1183–1188.

[13] Mohd, T.A.T., Jaafar, M.Z., Rasol, A.A.A., and Hamid, M.F., 2017, Measurement of streaming potential in downhole application: An insight for enhanced oil recovery monitoring, *MATEC Web Conf.*, 87, 03002.

[14] Mohd, T.A.T., Taib, N.M., Adzmi, A.F., Ab Lah, N.K.I.N., Sauki, A., and Jaafar, M.Z., 2018, Evaluation of polymer properties for potential selection in enhanced oil recovery, *Chem. Eng. Trans.*, 65, 343–348.

[15] Al Hashmi, A.R., Al Maamari, R.S., Al Shabibi, I.S., Mansoor, A.M., Zaitoun, A., and Al Sharji, H.H., 2013, Rheology and mechanical degradation of high-molecular-weight partially hydrolyzed polyacrylamide during flow through capillaries, *J. Pet. Sci. Eng.*, 105, 100–106.

[16] Zhao, H., Luo, F., Hou, J., Zhang, X., and Cao, L., 2010, *Study on the potential risk appraisal method in polymer flooding*, SPE Hydrocarbon Economics and Evaluation Symposium, Dallas, Texas, USA, 8-9 March 2010.

[17] Kaminsky, R.D., Wattenbarger, R.C., Szafranski, R.C., and Coutee, A., 2007, *Guidelines for polymer flooding evaluation and development*, International

Petroleum Technology Conference, Dubai, U.A.E., 4-6 December 2007.

[18] Alias, N.H., Zulkifli, M.S., Manaf, S.F.A., Yahya, E., Ghazali, N.A., and Mohd, T.A.T., 2014, *Saccharomyces cerevisiae* from baker's yeast for lower oil viscosity and beneficial metabolite to improve oil recovery: An overview, *Appl. Mech. Mater.*, 625, 522–525.

[19] Yahya, E., Alias, N.H., Mohd, T.A.T., Ghazali, N.A., and Ariffin, T.S.T., 2015, Flooding with biopolymer from microbes derived from mushroom and cabbage to enhance sweep efficiency in enhanced oil recovery, *Adv. Mater. Res.*, 1113, 492–497.

[20] Ojo, V.O., Onyekonwu, M.O., Ogolo, N.A., and Ubani, C., 2013, Effect of viscosity of alkaline/surfactant/polymer on enhanced oil recovery in heterogenous sands, SPE Nigeria Annual International Conference and Exhibition, Lagos, Nigeria, 5-7 August 2013.

[21] Ikeagwu, C., and Samuel, A., 2015, The study of local polymers on enhanced oil recovery, *Arch. Appl. Sci. Res.*, 7 (6), 48–55.

[22] Osuji, C., and Onyenkonwu, M., 2012, Using alkaline-surfactant-polymer to improve oil recovery, *Thesis*, Department of Petroleum and Gas, University of Port Harcourt, Nigeria.

[23] Ade, E., and Onyekonwu, M.O., 2012, Experimental study of enhancing oil recovery using local polymers, *Thesis*, Department of Petroleum and Gas, University of Port Harcourt, Nigeria.

[24] Ogolo, N.A., Ogiriki, S., Onyiri, V., Nwosu, T., and Onyenkonwu, M.O., 2015, Performance of foreign and local agents for enhanced oil recovery of Nigerian crude, SPE Nigeria Annual International Conference and Exhibition, Lagos, Nigeria, 4-6 August 2015.

[25] Ajabuego, I., and Onyekonwu, M., 2012, Enhanced oil recovery using local polymer, *Thesis*, Department of Petroleum and Gas, University of Port Harcourt, Nigeria.

[26] Gbonhinbor, J.R., and Onyekonwu, M.O., 2015, Experimental and simulation study on aqueous protein to improve oil recovery, *Int. J. Pet. Eng.*, 1 (4), 271–289.

[27] Gao, C., 2016, Application of a novel biopolymer to enhance oil recovery, *J. Pet. Explor. Prod. Technol.*, 6 (4), 749–753.

[28] Villares, A., García-Lafuente, A., Guillamón, E., and Mateo-Vivaracho, L., 2013, Separation and characterization of the structural features of macromolecular carbohydrates from wild edible mushrooms, *Bioact. Carbohydr. Dietary Fibre*, 2 (1), 15–21.

[29] Cumpstey, I., 2013, Chemical modification of polysaccharides, *ISRN Org. Chem.*, 2013, 417672.

[30] Yadav, H., and Karthikeyan, C., 2019, "Natural polysaccharides: Structural features and properties" in *Polysaccharide Carriers for Drug Delivery*, Eds. Maiti, S., and Jana, S., Woodhead Publishing, Cambridge, UK.

[31] Ndjouenkeu, R., Goycoolea, F.M., Morrisa, E.R., and Akingbala, J.O., 1995, Rheology of okra (*Hibiscus esculentus* L.) and dika nut (*Irvingia gabonesis*) polysaccharides, *Carbohydr. Polym.*, 29 (3), 263–269.

[32] Ihebuzor, N., Onyenkonwu, M.O., 2012, An experimental research on enhanced oil recovery using local polymers, *Thesis*, University of Port Harcourt, Nigeria.

[33] Ayirala, S.C., Uehara-Nagamine, E., Matzakos, A.N., Chin, R.W., Doe, P.H., and van den Hoek, P.J., 2010, *A designer water process for offshore low salinity and polymer flooding applications*, SPE Improved Oil Recovery Symposium, Tulsa, Oklahoma, USA, 24-28 April 2010.

[34] Algharaib, M.K., Alajmi, A.F.F., and Gharbi, R., 2011, *Enhancing recovery in high salinity oil reservoirs through optimized polymer flood*, International Petroleum Technology Conference, Bangkok, Thailand, 15-17 November 2011.

[35] Yang, F., Wang, D., Wang, G., Sui, X., Liu, W., and Kan, C., 2006, *Study on high-concentration polymer flooding to further enhance oil recovery*, SPE Annual Technical Conference and Exhibition, San Antonio, Texas, USA, 24-27 September 2006.

[36] Ward, J.S., and Martin, F.D., 1981, Prediction of viscosity for partially hydrolyzed polyacrylamide

solutions in the presence of calcium and magnesium ions, *SPE J.*, 21 (05), 623–631.

[37] Al Yousef, Z.A., Almobarky, M.A., and Schechter, D.S., 2019, Surfactant and a mixture of surfactant and nanoparticles to stabilize CO_2/brine foam, control gas mobility, and enhance oil recovery, *J. Pet. Explor. Prod. Technol.*, 10 (2), 439–445.

[38] Romero-Zeron, L., 2012, "Advances in enhanced oil recovery" in *Introduction to Enhanced Oil Recovery (EOR) Process and Bioremediation of Oil Contaminants Sites*, Eds. Romero-Zeron, L., IntechOpen, Rijeka.

[39] Kotlar, H.K., Selle, O., and Torsaeter, O., 2007, *Enhanced oil recovery by COMB flow: Polymer floods revitalized*, International Symposium on Oilfield Chemistry, Houston, Texas, USA, 28 February-2 March 2007.

[40] Agi, A., Junin, R., Gbonhinbor, J., and Onyekonwu, M., 2018, Natural polymer flow behaviour in porous media for enhanced oil recovery applications: A review, *J. Pet. Explor. Prod. Technol.*, 8 (4), 1349–1362.

Optimized Synthesis Temperature and Time to Obtain Crystalline Carbon Nitride with Enhanced Photocatalytic Activity for Phenol Degradation

Leny Yuliati[1,2,3,*], Mohd Hayrie Mohd Hatta[4,5], Siew Ling Lee[3,4], and Hendrik Oktendy Lintang[1,2,3]

[1]*Ma Chung Research Center for Photosynthetic Pigments, Universitas Ma Chung, Villa Puncak Tidar N-01, Malang 65151, East Java, Indonesia*

[2]*Department of Chemistry, Faculty of Science and Technology, Universitas Ma Chung, Villa Puncak Tidar N-01, Malang 65151, East Java, Indonesia*

[3]*Center for Sustainable Nanomaterials, Ibnu Sina Institute for Scientific and Industrial Research, Universiti Teknologi Malaysia, 81310 UTM Johor Bahru, Johor, Malaysia*

[4]*Department of Chemistry, Universiti Teknologi Malaysia, 81310 UTM Johor Bahru, Johor, Malaysia*

[5]*Foundation in Science, Faculty of Medicine, ASIA Metropolitan University, 81750, Johor Bahru, Johor, Malaysia*

* ***Corresponding author:***

email: leny.yuliati@machung.ac.id

Received: December 17, 2019
Accepted: March 26, 2020

DOI: 10.22146/ijc.52345

Abstract: *In this work, the crystalline carbon nitride photocatalysts were synthesized by an ionothermal technique with varied synthesis temperature of 500, 550, and 600 °C, and varied synthesis time of 2, 4, and 6 h. Fourier transform infrared spectra showed the successful formation of the prepared carbon nitrides from their characteristic vibration peaks. X-ray diffraction patterns suggested that the same phase of poly(triazine imide) and heptazine could be observed, but with different crystallinity. The optical properties showed that different temperatures and synthesis time resulted in the different band gap energy (2.72–3.02 eV) as well as the specific surface area (24–73 $m^2 g^{-1}$). The transmission electron microscopy image revealed that the crystalline carbon nitride has a near-hexagonal prismatic crystallite size of about 50 nm. Analysis by high-performance liquid chromatography showed that the best photocatalytic activity for phenol degradation under solar light simulator was obtained on the crystalline carbon nitride prepared at 550 °C for 4 h, which would be due to the high crystallinity, suitable low band gap energy (2.82 eV), and large specific surface area (73 $m^2 g^{-1}$). Controlling both the temperature and synthesis time is shown to be important to obtain the best physicochemical properties leading to high activity.*

Keywords: *carbon nitride; crystallinity; phenol degradation; synthesis temperature; synthesis time*

■ INTRODUCTION

Phenol is one of the major organic pollutants that exist in the industry effluents [1]. Even though at low concentration, phenol has high toxicity. An alternative method that offers green and clean technology to treat phenol is the photocatalytic degradation process. Many studies have been focused on the development of titanium dioxide (TiO_2)-based photocatalysts for various photocatalytic degradation reactions [2-4], which are mostly due to the high activity of TiO_2 under ultraviolet (UV) irradiation. However, owing to the large portion of visible light in the sunray, the development of visible light active photocatalysts has been an important task in the photocatalysis field. Since TiO_2 does not absorb visible light, some modifications are required, such as by doping or making a composite with another visible light-active semiconductor [5-7]. In addition to these efforts, studies on the potential materials that are visible light active are still highly required. One of the fascinating choices for the visible light active photocatalysts is

carbon nitride (CN). Even though CN has been investigated for years, many reported literatures showed that the synthesized CN was in the amorphous form [8-14]. While the CN showed photocatalytic activity under visible light, the CN with the amorphous phase has been reported to show lower photocatalytic performance in the catalytic process as compared to the crystalline one. A drastic enhancement in the photocatalytic activity of the CN has been reported to occur over the crystalline CN either for photocatalytic degradation of organic compounds or for hydrogen production [15-19].

In photocatalysis, the directional flow of electrons depends on the organization of the molecules in the structure concerning their crystalline [20-22]. Moreover, the crystalline structure would demonstrate faster electron movement as the direction is confined. The fast rate of electron diffusion would reduce the trapping and de-trapping effect; thus, the rate of electron-hole recombination would be decreased [23]. In the case of crystalline CN, the enhanced photocatalytic activity could also be additionally caused by the improved light absorption due to the extended π-conjugated system and the increased rigidity of the polymer backbones [24]. Since the photocatalytic properties are sensibly affected by the crystallinity of the photocatalyst, constructing a crystalline photocatalyst that is active under natural sunlight is a promising work and highly recommended but can be a challenging task to be achieved.

Several methods to produce the crystalline CN have been examined. Recently, it was reported that the crystalline CN could be synthesized via an ionic melt polycondensation of urea precursor in the presence of potassium chloride-lithium chloride (KCl-LiCl) salt melt [15]. Bhunia et al. produced the crystalline carbon nitride by combining the supramolecular aggregation and polycondensation of an ionic melt using melamine, 2,4,6-triaminopyrimidine, and LiCl/KCl mixture [16]. These two methods produced crystalline CN having not only the structure of graphitic CN but also the poly(triazine imide)-like structure [15-16]. The better-ordered structure of the graphitic CN was observed by using a thermal condensation of melem but must be put under a pure oxygen atmosphere [17]. Another method was also reported involving an additional acidic washing process using hydrogen chloride (HCl) after the polycondensation of melamine in the presence of KCl and LiCl [18]. Another synthesis method, a rapid polymerization of melamine without the early heating process, was proposed to produce the crystalline CN [19]. However, these last-mentioned three methods only produced CN having the structure of graphitic CN with a better order in the interlayer stacking and in-plane repeated units. These semi-crystalline CN materials are usually obtained when the precursor is thermally polymerized [24].

Since we aim to get the crystalline CN, the synthesis method that has been proven to give the structure of crystalline CN shall be employed. Among the techniques mentioned above, the one using ionothermal technique with the help of KCl-LiCl salt melt has been shown to require fewer chemicals to obtain the crystalline CN having the poly(triazine imide)-like structure [15]. Moreover, the resulted crystalline CN was confirmed to give higher photocatalytic activity for phenol degradation under visible light than the amorphous CN. However, a detailed study of the optimized synthesis temperature and time for this method has not been addressed yet. In order to optimize the photocatalytic efficiency of the crystalline CN, in this work, the effects of synthesis temperature and time on the properties and photocatalytic activity of the crystalline CN were investigated. This work demonstrated that the optimized synthesis temperature and time were important parameters to obtain the optimized photocatalytic activity of the crystalline CN. As high as 3.4 times higher photocatalytic activity was observed on the sample synthesized under the optimized conditions than those prepared under the non-optimized one.

■ EXPERIMENTAL SECTION

Materials

For the preparation of CN materials, urea (CH_4N_2O, QRëC, 99%) was used as carbon and nitrogen-rich precursors. Ethanol (C_2H_5OH, HmBG Chemicals, 99.98%) was used as a solvent in the

preparation of CN. For the preparation of crystalline CN, the ionic solvents used were lithium chloride (LiCl, Sigma-Aldrich, 99%) and potassium chloride (KCl, Fisher Chemicals, 99.5%). The model of organic pollutant used for this study was phenol (C_6H_6O, Scharlau Chemie, 99.5%).

Procedure

Synthesis of crystalline carbon nitride

The crystalline carbon nitride was prepared in a similar way to the reported literature [15]. In order to investigate the effect of synthesis temperature (500, 550, and 600 °C), other synthesis parameters including the amount of precursor (2 g), synthesis time (4 h), and amount of salts melt (2.74 g KCl, 2.26 g LiCl) were fixed. The final products were labeled as CN-*T*, which were CN-500, CN-550, and CN-600. The synthesis time was varied to 2, 4, and 6 h to obtain the optimum time. In this part, the amount of precursor (2 g), reaction temperature (550 °C), and amount of salts melt (2.74 g KCl and 2.26 g LiCl) were fixed. The final samples were labeled as CN-*t* in which *t* refers to 2, 4, and 6 h.

Characterizations of crystalline carbon nitride

The prepared CN materials were characterized using several instruments. The structural properties were identified using a powder X-ray diffractometer (XRD). The XRD patterns were recorded using Bruker D8 Advance with CuK_a irradiation (λ = 1.5406 Å). The optical properties were determined by a diffuse reflectance ultraviolet-visible (DR UV-vis) spectroscopy using a Shimadzu UV-2600 DR UV-vis spectrophotometer with wavelength recorded in the range of 220 to 800 nm. The chemical bonds and functional groups were determined by using a Fourier transform infrared spectroscopy (FTIR, Nicolet-iS50). The technique used in the characterization was the KBr pellet technique. The nitrogen (N_2) adsorption-desorption isotherm analysis at –196.15 °C (77K) using a Quantachrome NOVAtouch LX4 instrument was deployed in order to investigate the specific surface area (SA). All the samples were dried at 100 °C in the oven before the measurement. For the degassing part, the samples were heated at 180 °C for 3 h at the ramp of 10 °C/min. The best CN material was also characterized by a transmission electron microscope (TEM, JEOL JEM-2100).

Photocatalytic degradation of phenol

The photocatalyst (0.05 g) was dispersed in 100 mL of a beaker containing 50 mL of 50 ppm phenol. Prior to the photocatalytic reaction, the solution was stirred continuously in the dark condition for 30 min to reach the equilibrium of adsorption-desorption. The photocatalytic reaction was carried out under solar light simulator irradiation (150 W, λ > 230 nm, and I = 110,000 Lux) for 6 h. The final remaining concentration of the solution was determined by using high-performance liquid chromatography (HPLC, Shimadzu, LC-20AT) equipped with a UV detector. The final concentration of phenol was determined using the ratio of degraded phenol to its initial concentration.

■ RESULTS AND DISCUSSION

Effect of Synthesis Temperature

The XRD patterns of the prepared CN-*T* samples are presented in Fig. 1. Based on the spectra, all samples showed crystalline properties with at least one crystalline peak of (210) plane was observed. Two most intense and broad peaks at 2θ of *ca.* 27 and 12° corresponded to an interlayer distance of graphite-like CN and distance of the in-plane arrangement of nitrogen-linked heptazine or poly(triazine imide) units, respectively [8-19,24-31]. Both peaks were observed in all samples. The CN-500 showed at least one crystalline peak, which was observed at 2θ of *ca.* 31.9 (210), indicating the crystallization could be initiated at a temperature of 500 °C.

When the synthesis temperature was increased to 550 °C, more crystalline peaks were visualized, mainly at 2θ of 20.7 (110), 24.5 (200), 29.3 (102) and 32.4° (210), owing to the poly(triazine imide) units [15-16,25-26]. Similar crystalline peaks were also observed when the synthesis temperature was increased to 600 °C, but the resulted CN-600 was composed of the hybrid of heptazine-based and poly(triazine imide) units. The amorphous phase (heptazine-based units) was likely to be induced at a higher temperature as can be seen at 2θ of 27.8°.

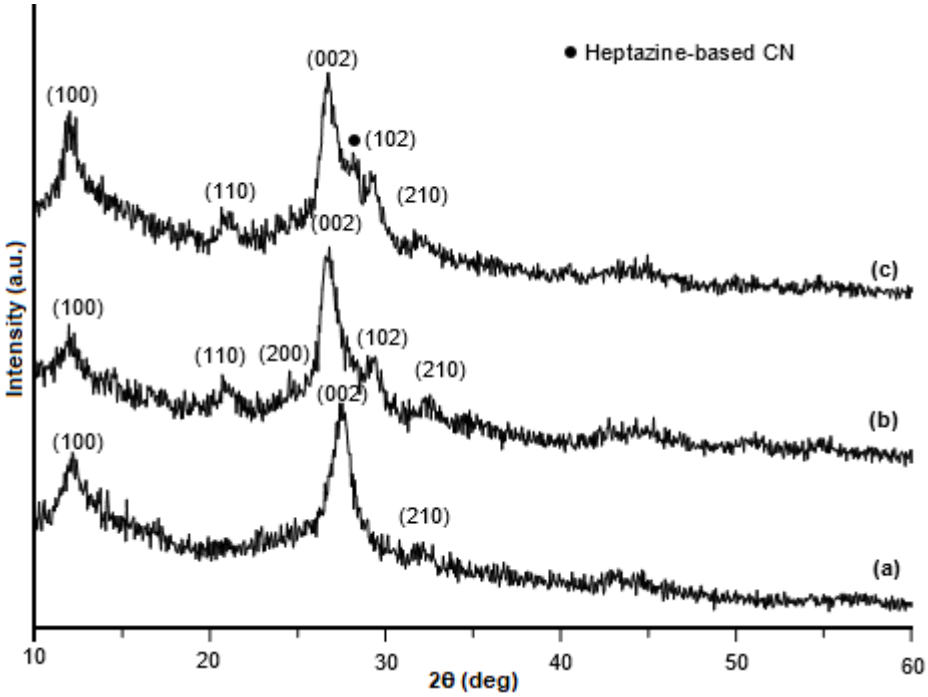

Fig 1. XRD patterns of (a) CN-500, (b) CN-550, and (c) CN-600

It was demonstrated that increasing the synthesis temperature from 500 to 550 °C resulted in the changes in phase structure from heptazine-based units (amorphous CN) to poly(triazine imide) (crystalline CN) with high crystalline phase, owing to its high thermal stability compared to amorphous CN at high temperature in the presence of molten salts. Similar results on the changes of the crystallinity phase were also reported on crystalline CN prepared by urea-based precursor when temperature variation was carried out [27]. The presence of the amorphous phase at a high temperature (600 °C) might be related to the binary phase properties of KCl-LiCl. In ionothermal synthesis, the molten salts were required as the ionic solvent for the growth of crystallization. As the temperature increased, the KCl-LiCl would consist of a mixture of both solid salts and molten salts. Since more solid salts in the eutectic mixture are formed at high temperature, it is believed that the crystallization could not occur, and thus leading to the formation of heptazine-based units. All these XRD results demonstrated that the crystallinity phase could be tuned via controlling the temperature during the ionothermal synthesis.

The optical properties of the prepared CN-*T* photocatalysts were investigated by the DR UV-vis spectrophotometer. Fig. 2 shows the absorption spectra of the CN-500, the CN-550, and the CN-600. Three major peaks were observed in all of the samples. The peak at low region (*ca.* 260 nm) was attributed to C-N indicating the $\pi \rightarrow \pi^*$ transition, while the peak at region *ca.* 320 nm corresponded to the C=O functional group indicating the $\pi \rightarrow \pi^*$ and $n \rightarrow \pi^*$ transitions. The presence of the C=O functional group indicated the less condensation of urea precursor during the polymerization process [28]. Meanwhile, the peak at 366 nm corresponded to the C-N functional group [1,29-31].

The decreased intensity of the C=N and C-N peaks on the CN-500 was due to the incomplete polymerization of CN. It was worthy to note that the CN-550 showed a decreased intensity of the C=O peak, suggesting that the temperature of 550 °C could eliminate the C=O groups and induced the crystallization, forming a highly condensed CN network. When the synthesis temperature was raised to 600 °C, the CN-600 showed the presence of the C=O peak, and the absorption edge was slightly increased to a longer wavelength. As shown in Fig. 2, the CN-600 showed absorption up to 450 nm, while sample CN-550 showed absorption up to 430 nm.

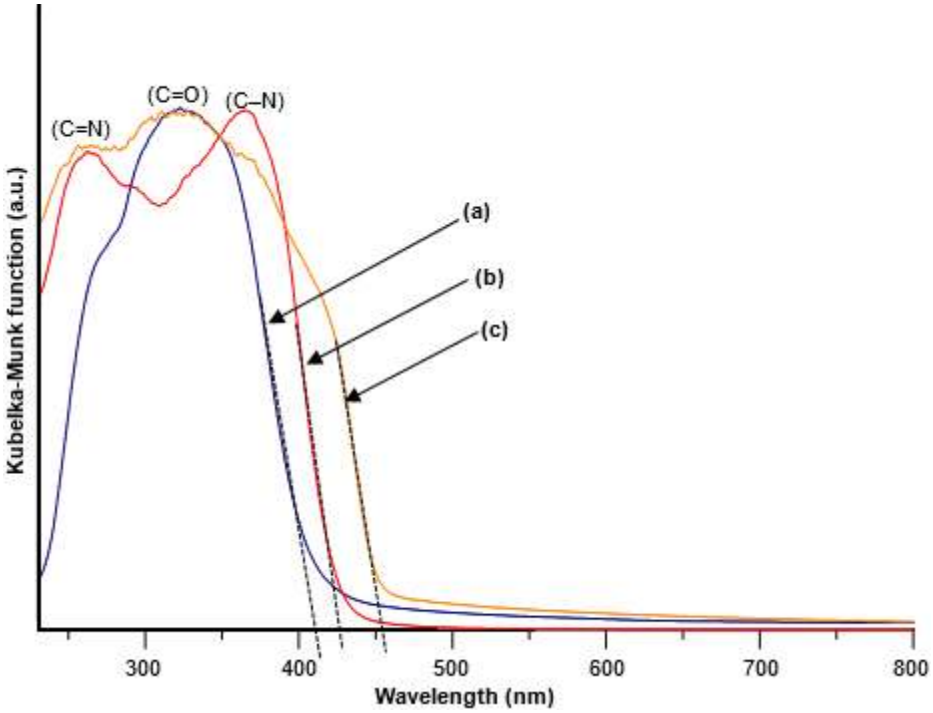

Fig 2. DR UV-vis spectra of (a) CN-500, (b) CN-550, and (c) CN-600

On the other hand, sample CN-500 showed a minimum absorption at region *ca.* 410 nm. This result demonstrated that increasing the synthesis temperature increased the visible light absorption. The altered optical properties might be related to the color changes of the prepared CN samples as the CN-500 showed a pale yellow, while the CN-550 and the CN-600 samples showed a yellowish and brownish yellow color, respectively.

It was revealed that the hybrid of heptazine and poly(triazine imide) CN enhanced the visible light absorption to longer wavelength, indicating a decrease in the band gap energy with increasing the synthesis temperature. Fig. 3 shows the band gap energy of CN-*T* samples estimated from the Tauc plot. The estimated band gap values for CN-500, CN-550, and CN-600 were 3.05, 2.82, and 2.72 eV, respectively. It has been reported that the band gap energy of the material is one of the important properties that can affect the photocatalytic performance [9-10]. Based on Fig. 3, it was shown that the synthesis temperature has a strong impact on the band gap energy values, which could be associated with the photocatalytic activity. As the synthesis temperature increased, the band gap energy of CN-*T* samples was narrowed down, and the visible light absorption was enhanced. These results suggested that the band gap energy of CN can be tuned by controlling the synthesis temperature.

The characteristics of the chemical bonding and functional groups of the CN-*T* samples were studied by FTIR spectrometer. Fig. 4 shows the FTIR spectra of (CN-500, CN-550, and CN-600. From the spectra, it could be noted that increasing synthesis temperature did not result in significant changes in the functional groups. The peaks observed at the regions of 810 and 1200–700 cm^{-1} indicated the successful formation of CN heterocycles, thus, suggesting that the CN material could be synthesized at temperatures ranging from 500 to 600 °C. The peak at *ca.* 810 cm^{-1} corresponded to the bending mode of out-of-plane triazine units, while the multiple bands at *ca.* 1200–1700 cm^{-1} corresponded to the stretching mode of heptazine and/or poly(triazine imide) units [8,11,15,17-21,24-26,28].

On the other hand, the formation of both C≡N and N=C=N at 2170 cm^{-1} was due to the broke of the CN continuity network [8,15,28], owing to the intercalation of lithium and chloride ions that resulted in the formation

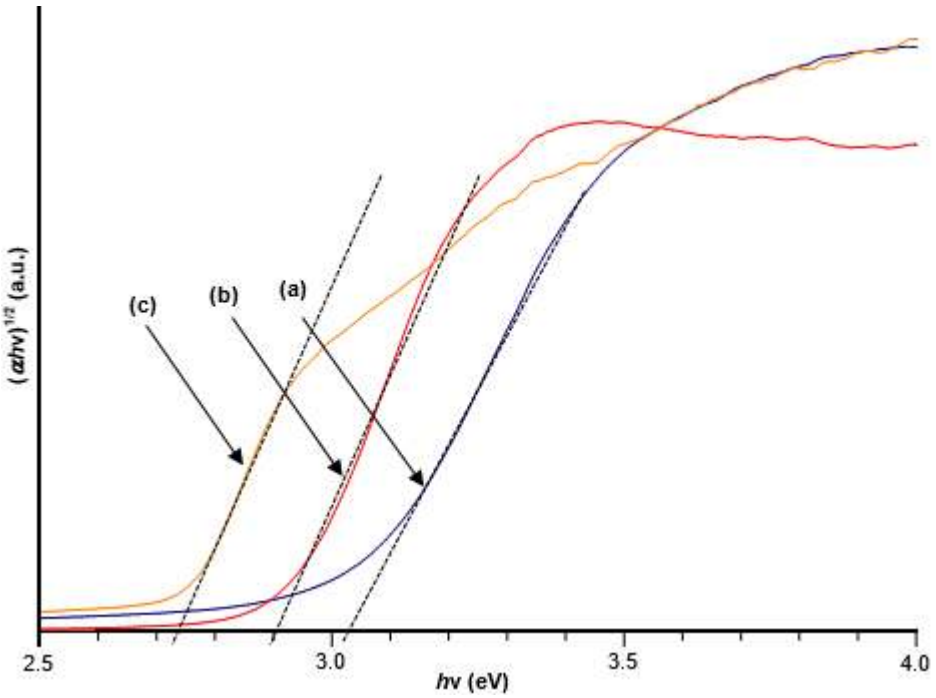

Fig 3. Tauc plots of (a) CN-500, (b) CN-550, and (c) CN-600

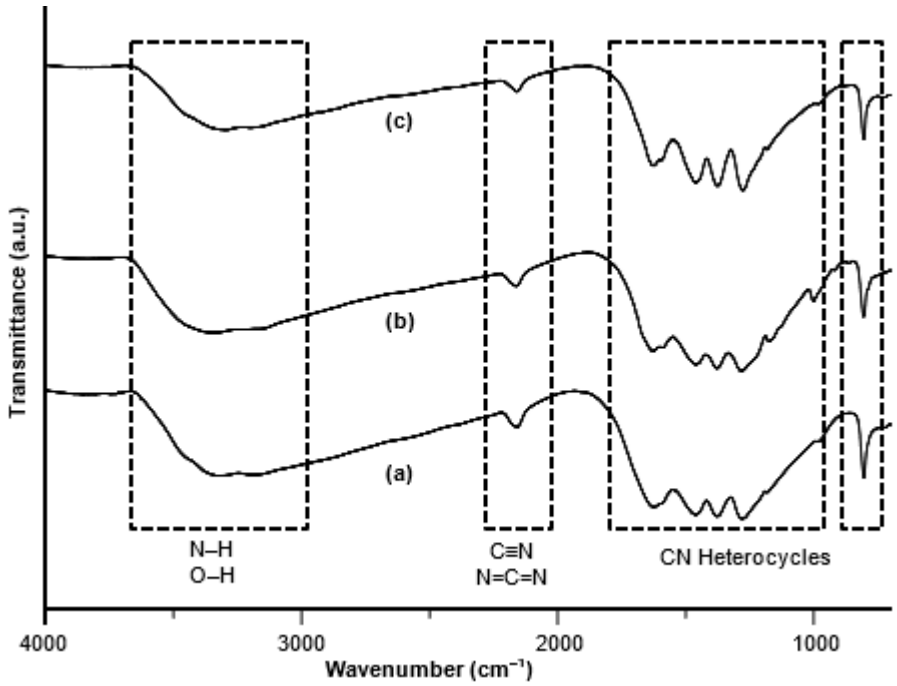

Fig 4. FTIR spectra of (a) CN-500, (b) CN-550, and (c) CN-600

of void channels along with the ABA stacking of poly(triazine imide). Meanwhile, broad bands at around 3000–3700 cm^{-1} were originated from the overlapping of primary amine and secondary amine, N-H and hydroxide, O-H groups, respectively. However, it was observed that the intensity of the broad peak that attributed to the stretching modes of the primary and secondary amines and their intermolecular hydrogen-bonding interactions (3000–3700 cm^{-1}) reduced as the temperature increased, which especially could be

observed on the CN-600 (Fig. 4(c)). This result suggested that the final condensation product obtained in high temperature was lacking in terminal unreacted -NH_2 groups and was cohesive owing to the effect of covalent interactions.

The textural properties and specific surface area were investigated via nitrogen adsorption-desorption analysis. The isotherms and Barrett-Joyner-Halenda (BJH) pore size distribution (inset) of prepared CN-*T* samples are presented in Fig. 5. All samples showed the type IV isotherm with type H3 hysteresis loop according to IUPAC classification, suggesting the formation of the porous structure. The Brunauer-Emmett-Teller (BET) specific surface areas of the CN-500, the CN-550, and the CN-600 were 24, 73, and 65 $m^2 g^{-1}$, respectively. From the BET specific surface area values obtained, it could be suggested that increasing the synthesis temperature from 500 to 550 °C increased the specific surface area. However, the further increase to 600 °C caused a slight decrease in the value of the specific surface area.

The slight decrease in the surface area of the CN-600 might be due to the hybrid composition of heptazine-based CN and poly(triazine imide). On the other hand, the CN-500 and the CN-600 showed a non-uniform pore size distribution (inset), while the CN-550 showed a uniform pore size distribution as only one sharp and intense peak was observed. Taking account of the most intense and sharp peak, the average pore size diameters for the CN-500, the CN-550, and the CN-600 were determined to be 3.62, 3.63, and 3.62 nm, respectively.

On the contrary, the average pore volume of the CN-500, the CN-550, and the CN-600 were 0.06, 0.23, and 0.19 $cm^3 g^{-1}$, respectively. It could be seen that the low specific surface area of CN-500 was due to low pore volume. The CN-600 showed a slight decrease in its surface area, which could be associated with its decreased pore volume. Besides, the slight decrease in the specific surface area of the CN-600 might be related to the structural changes of the poly(triazine imide) to the hybrid composition of poly(triazine imide) and heptazine

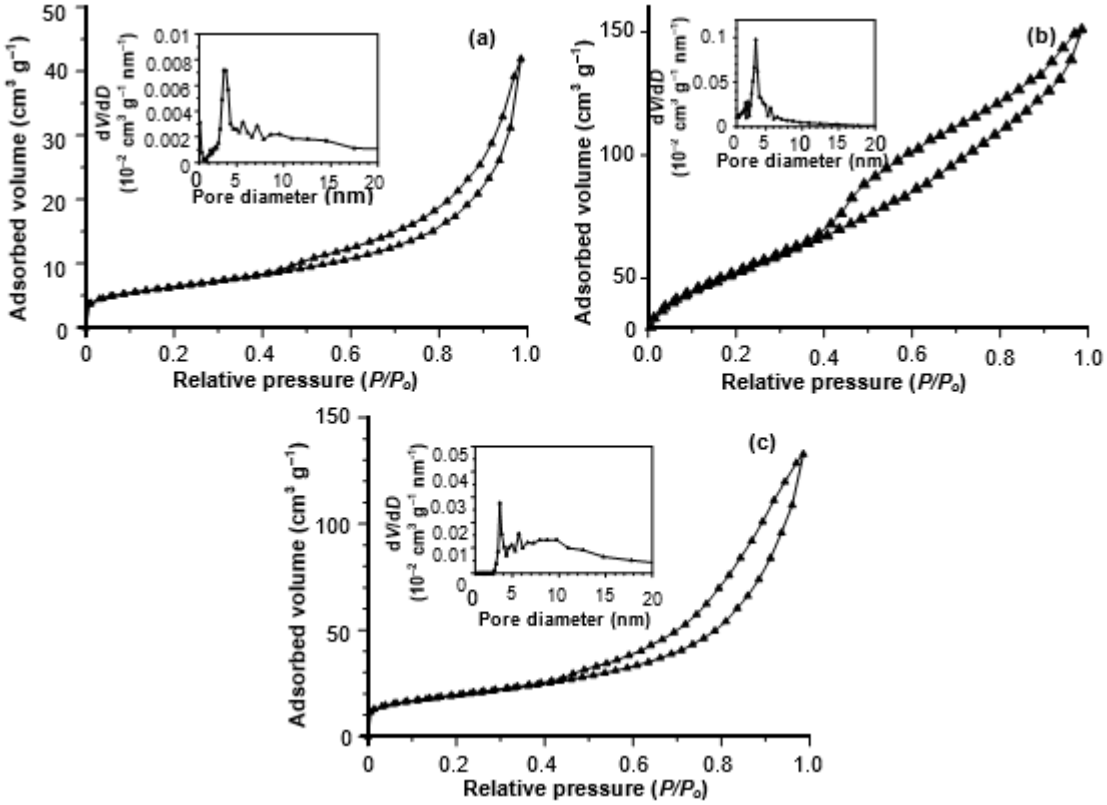

Fig 5. Nitrogen adsorption-desorption isotherms and their respective BJH pore size distribution curves (inset) of (a) CN-500, (b) CN-550, and (c) CN-600

units, considering that the amorphous phase tends to reduce the surface area of the material.

Table 1 shows the percentage of phenol degradation on the prepared CN-*T* samples after 6 h of irradiation under solar light. The CN-500, the CN-550, and the CN-600 showed the photocatalytic activity of 7, 24, and 20%, respectively. The low photocatalytic activity (7%) obtained on the CN-500 sample was clearly due to its large band gap energy, very low crystallinity, and low specific surface area. These properties were mainly due to incomplete polymerization and less condensed structure of CN when synthesized at 500 °C. Meanwhile, the high photocatalytic activity achieved on the CN-550 (24%) was due to its crystallinity and high surface area and might also be associated with the band gap energy value. It could be proposed here that material with a high crystalline phase could lead to an efficient electron charge transfer and provide more active sites for the reaction of photocatalytic oxidation-reduction to occur. On the other hand, the photocatalytic performance of the CN-600 was slightly dropped (20%). As compared to the CN-500 °C, the CN-600 exhibited high photocatalytic activity due to its crystallinity, surface area, and mainly due to its low band gap energy. However, when compared to CN-550 °C, the slightly decreased photocatalytic activity would be due to the decrease in the crystallinity and specific surface area. The decreased band gap energy value of the CN-600 than the CN-550 could not help improving the activity due to such a decrease in crystallinity and surface area. These results demonstrated that the respective chemical and physical properties (crystallinity, band gap energy, and surface area) were significantly dependent on each other. Controlling the synthesis temperature to maintain the chemical and physical properties is needed so that the high photocatalytic performance could be obtained.

Effect of Synthesis Time

The X-ray diffractometer was used to study the structural properties of the prepared CN-*t* samples. The XRD patterns of the prepared CN-2H, CN-4H, and CN-6H were presented in Fig. 6. The two major peaks at a diffraction angle of 2θ of *ca.* 26.9 (002) and 11.9° (100) were referred to an interlayer distance of graphite-like CN and in-plane arrangement of nitrogen-linked heptazine and/or poly(triazine imide) units [8-19,24-31]. It was clear that all samples showed crystalline properties as the planes of (110), (200), (102), and (210) were observed [15-16,25-26].

As shown in Fig. 6(a) and (b), increasing synthesis time from 2 to 4 h increased the crystallinity of the CN. However, a further increase in the synthesis temperature to 6 h resulted in the reduced peak intensity (Fig. 6(c)). The low crystallinity on sample CN-2H might indicate the polymerization or condensation process of CN was not sufficient at a short synthesis time. However, when the synthesis time was prolonged to 4 h, the supersaturation of the salt melt was high and thus, induced the crystallization process as well as forming a more condensed product. The decrease in the peak intensity on the CN-6H sample could be due to the competition between the crystal growth and the dissolution. It was also believed that prolong the synthesis temperature might cause the CN to be partially decomposed. From the XRD patterns, it can be concluded that 4 h was the optimum reaction time required to synthesize crystalline CN with the high crystalline phase.

The optical properties of the prepared CN-*t* photocatalysts were investigated by the DR UV-vis spectrophotometer. The DR UV-vis spectra of the CN-2H, the CN-4H, and the CN-6H are presented in Fig. 7. For all samples, three absorption peaks corresponded to

Table 1. Properties and percentage of phenol degradation after 6 h under solar light irradiation for CN-*T* samples

Sample	Crystallinity	E_g[1] (eV)	S.A[2] ($m^2\ g^{-1}$)	Degradation (%)
CN-500	×	3.02	24	7
CN-550	√	2.82	73	24
CN-600	√	2.72	65	20

[1]Band gap energy values were determined via the Tauc plot

[2]Specific surface area was determined via the BET technique

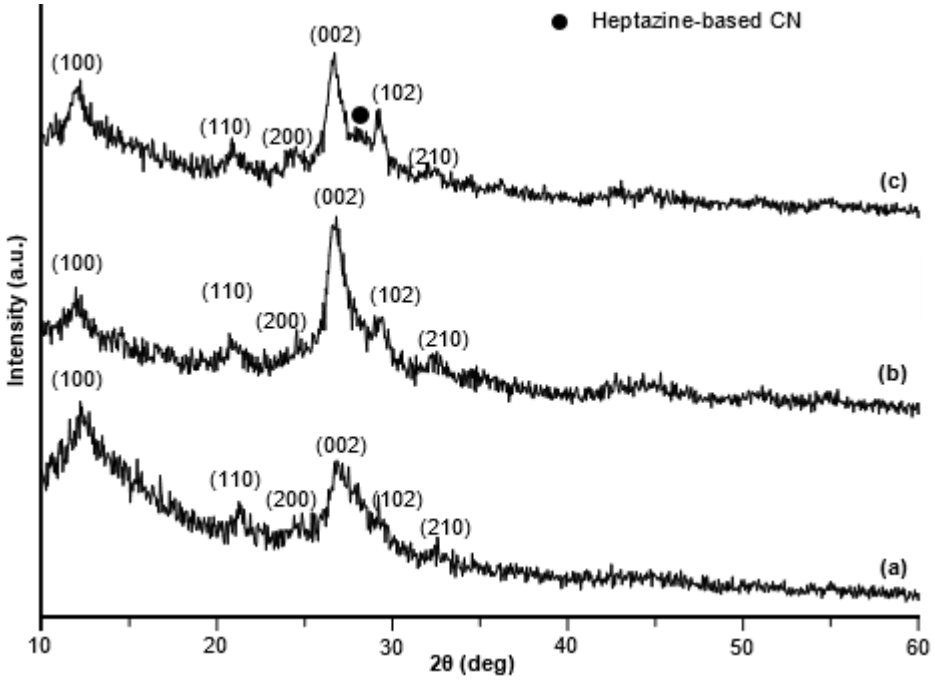

Fig 6. XRD patterns of (a) CN-2H, (b) CN-4H, and (c) CN-6H

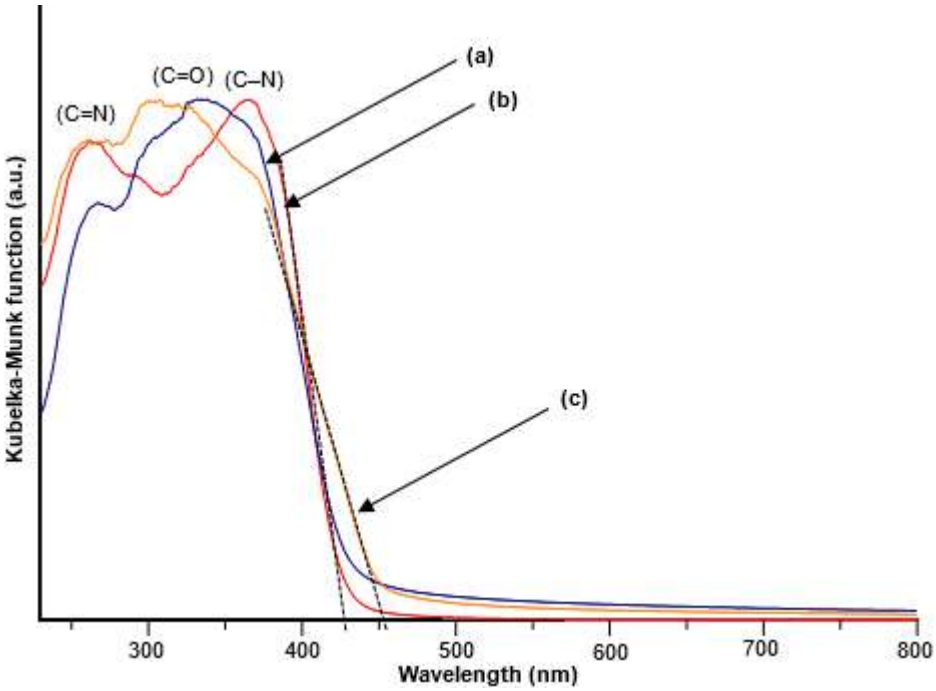

Fig 7. DR UV-vis spectra of (a) CN-2H, (b) CN-4H, and (c) CN-6H

the functional groups of C=N, C=O, and C-O were observed at *ca.* 263, 305, and 360 nm, respectively. Each peak corresponded to $\pi \rightarrow \pi^*$, $\pi \rightarrow \pi^*$ and $n \rightarrow \pi^*$, and $\pi \rightarrow \pi^*$ transitions [8,29-31]. It was observed that the peak of C-N was slightly shifted to a shorter wavelength for the CN-2H. Due to its less condensed and incomplete polymerization, the CN-2H showed a reduced peak intensity, which belonged to the functional group of C=N. The less condensed product of CN might be caused by the short reaction time. While the CN-2H and the CN-

4H have a similar visible light absorption up to 430 nm, the CN-6H showed a slightly shifted absorption toward longer wavelength in the region up to 460 nm. The slight increase in the visible light absorption on sample CN-6H might be due to better crystallinity or CN framework arrangement, as depicted in Fig. 7(c). The enhanced visible light absorption was also due to the increment in the crystallite size owing to the additional formation of heptazine-based units within the CN-6H sample.

Fig. 8 shows the Tauc plots of the CN-2H, the CN-4H, and the CN-6H samples. The estimated band gap energy values for each respective sample were 2.90, 2.87, and 2.76 eV. These band gap values were in good agreement with crystalline CN as reported elsewhere using similar precursor except for the synthesis procedure [27]. While the CN-2H and CN-4H gave a close value to each other, the CN-6H showed a lower band gap energy. The decrease in its band gap energy could be associated with the increase in its crystallite size or quantum size effect. The increased crystallite size was occurred due to phase changes from poly(triazine imide) to the hybrid composition of heptazine-based and poly(triazine imide). These results suggested the need for optimum synthesis time in preparing crystalline CN as shortening the synthesis time would result in less condensed CN while lengthening the reaction time might cause structural and phase changes of the CN.

The characteristics of chemical bonds and functional groups of the prepared CN-*t* photocatalysts were analyzed by FTIR spectrophotometer. Fig. 9 shows the FTIR spectra of the CN-2H, the CN-4H, and the CN-6H samples. The formation of CN heterocycles (heptazine and/or poly(triazine imide)) can be observed in both region at *ca.* 810 and 1200–1700 cm^{-1} [8,11,15,17-20,24-26,28]. The wide and broad peaks at *ca.* 3000–3700 cm^{-1} were originated from the overlapping functional groups of N-H and O-H. The presence of the O-H functional group was due to absorbed water molecules at the ambient pressure. The band at *ca.* 810 cm^{-1} corresponded to the bending mode of out-of-plane heptazine-based and/or poly(triazine imide) units. The bands at 1200–1700 cm^{-1} were attributed to the stretching mode of heptazine and/or poly(triazine imide) units.

The small and intense peak appeared at *ca.* 2170 cm^{-1} on all samples indicated the formation of C≡N and N=C=N that were typical for crystalline CN. The formation of both functional groups was due to the broken of the CN continuity networks [8,15,28], owing to

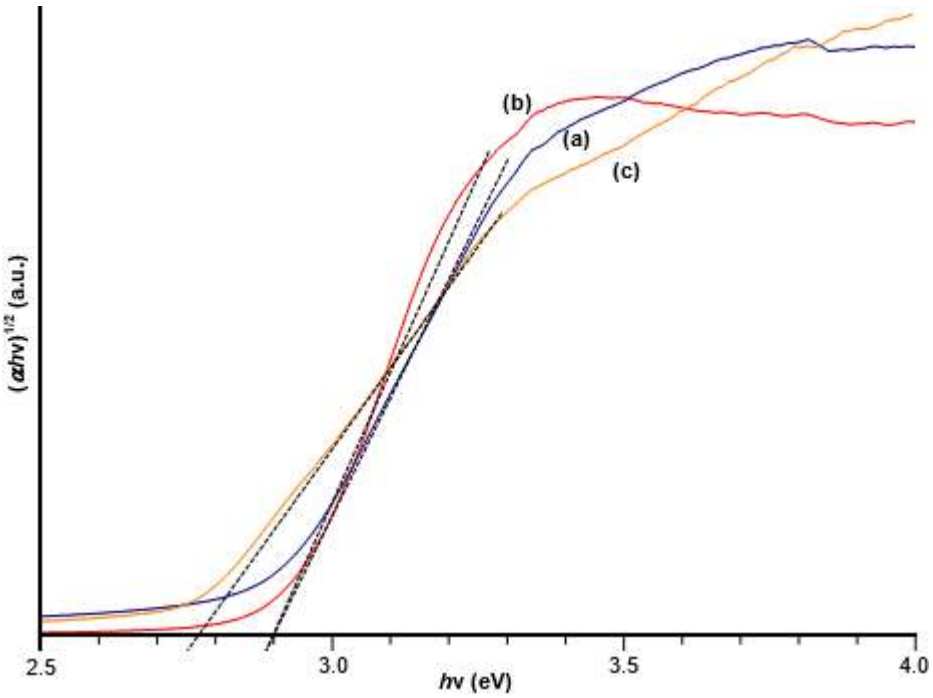

Fig 8. Tauc plots of (a) CN-2H, (b) CN-4H, and (c) CN-6H

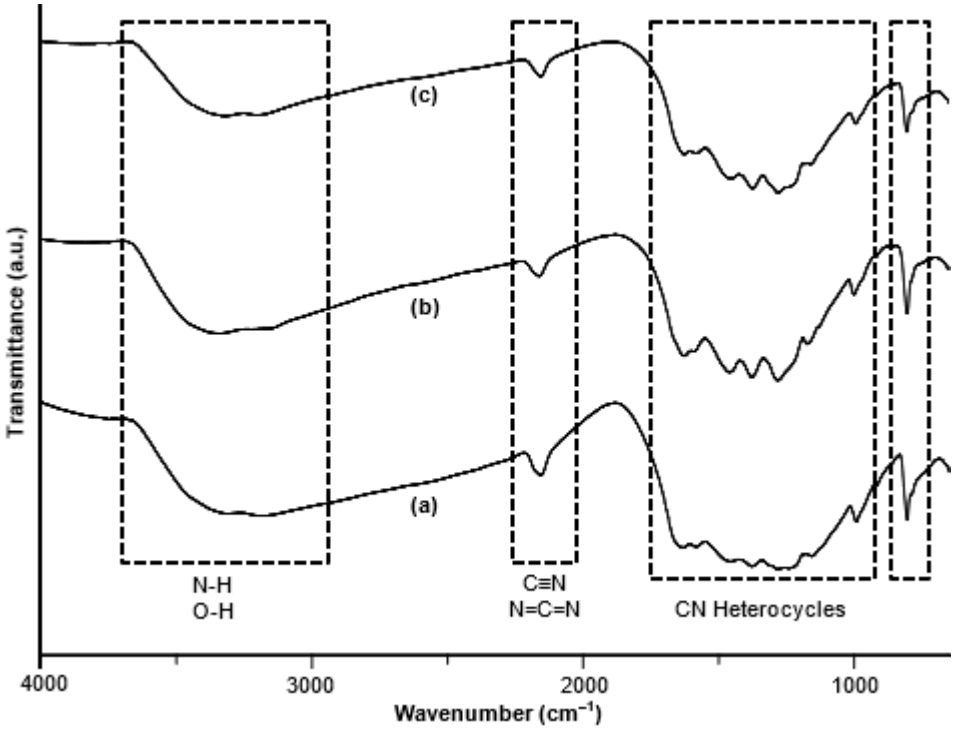

Fig 9. FTIR spectra of (a) CN-4H, (b) CN-6H, and (c) CN-6H

the intercalation of lithium and chloride ions. From the spectra, it can be observed that the less intense peaks of CN heterocycles in the region of 1200–1700 cm^{-1} for the CN-2H sample (Fig. 9(a)) suggested the incomplete formation or less condensed of CN networks due to a short synthesis time. Moreover, increasing synthesis time from 4 to 6 h showed that the CN network structure was decomposed as the peak intensity attributed to CN heterocycles was decreased (Fig. 9(c)). These results demonstrated that short reaction time caused the incomplete formation of CN, while long synthesis time may cause the decomposition of the CN.

The textural properties of the prepared CN-*t* samples were studied via nitrogen adsorption-desorption analysis. The isotherms of each prepared photocatalyst are shown in Fig. 10, while the BJH pore size distribution was shown in the inset of each figure. All samples showed the type IV isotherm with the H3 hysteresis loop, suggesting the presence of the porous structure. From the values of BET specific surface area, increasing synthesis time from 2 to 4 h resulted in the noteworthy increase of the specific surface area from 30 to 73 m^2 g^{-1}, while further increment of synthesis time to 6 h caused the specific surface area was slightly dropped to 55 m^2 g^{-1}.

The low surface area on the CN-2H sample was due to less condensed or incomplete polymerization of CN. This suggested that 4 h of synthesis time was the optimum time to form a highly condensed CN product. In addition, the slightly reduced surface area when prolonging the synthesis time was due to the formation of the hybrid heptazine-based and poly(triazine imide) unit. A similar result was also reported when structural and composition changes were observed [27]. From the insets of the figure, the BJH pore size distribution analysis showed that all samples were uniformly porous with the average sizes of 3.83, 3.62, and 3.62 nm for the CN-2H, the CN-4H, and the CN-6H, respectively. Meanwhile, the average pore volumes calculated via the BJH equation were 0.06, 0.23, and 0.1 cm^3 g^{-1}, respectively. The difference in the pore size between the CN-2H and both the CN-4H and the CN-6H might be due to the limited growth of crystalline CN that was associated with less condensed and incomplete polymerization process.

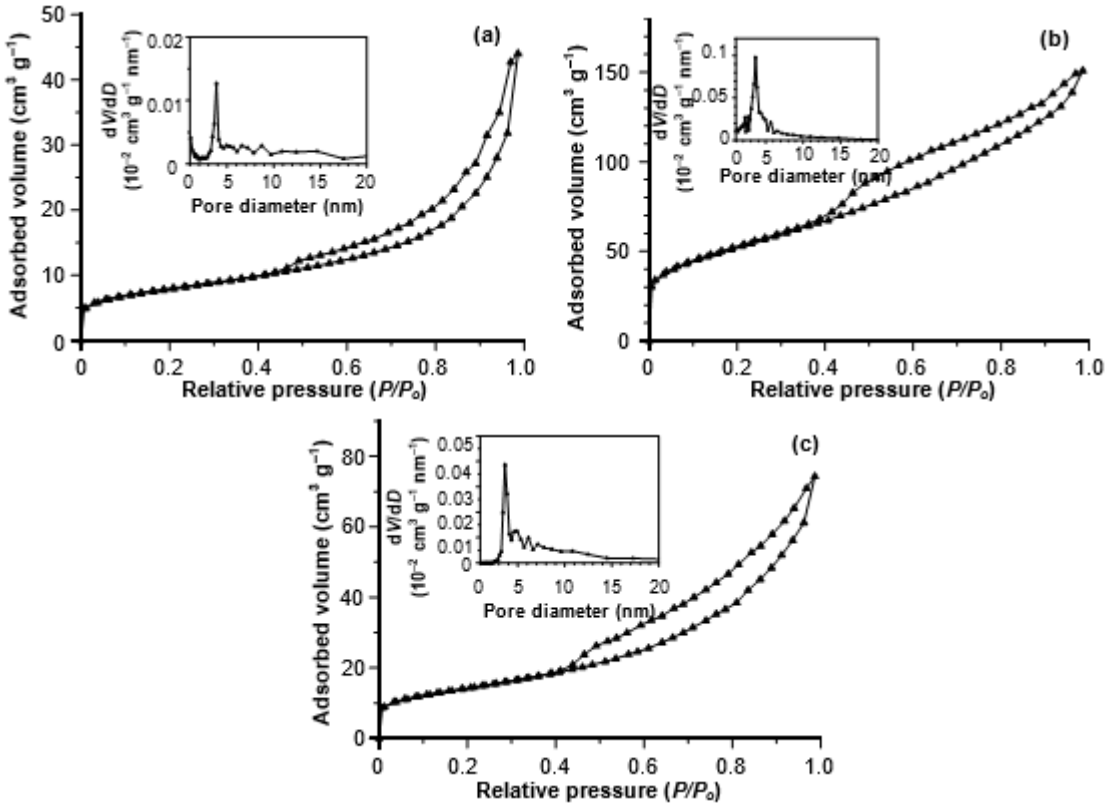

Fig 10. Nitrogen adsorption-desorption isotherms and their respective BJH pore size distribution curves (inset) of (a) CN-2H, (b) CN-4H, and (c) CN-6H

Table 2. Properties and percentage of phenol degradation after 6 hours under solar simulator irradiation for CN-*t* samples

Sample	Crystallinity[1] (%)	E_g[2] (eV)	S.A[3] (m^2 g^{-1})	Degradation (%)
CN-2H	86	2.90	30	17
CN-4H	100	2.82	73	24
CN-6H	90	2.76	55	20

[1]Percentage of crystallinity was calculated via the following formula: Crystallinity (%) = (total area of crystalline peaks)/(total area of all peaks). The percentage of crystallinity of sample CN-4H was taken into account as 100%
[2]Band gap energy values were determined via the Tauc plot
[3]Specific surface areas were determined via the BET technique

Table 2 lists the chemical and physical properties and photocatalytic activity of the CN-*t* samples after 6 h irradiation under solar light. As shown in the table, the high photocatalytic activity was achieved on the CN-4H sample with 24% of phenol degradation within 6 h of irradiation, while the CN-2H and the CN-6H samples showed phenol degradation of 17 and 20%, respectively. Increasing the synthesis time from 2 to 4 h resulted in the lower band gap energy. However, the photocatalytic activity of the CH-6H did not further increase since the surface area decreased from 73 to 55%. The high photocatalytic activity obtained by CN-4H sample compared to CN–2H and CN–6H was coming from the crystallinity of the materials, suitable band gap energy, and high surface area. These results suggested that the synthesis time affected the properties of crystallinity, band gap energy, and surface area. Synthesis time of 4 h was important to obtain a CN sample with improved crystallinity, suitable low band gap energy while maintaining the high surface area to achieve a photocatalyst with high activity.

Optimized Synthesis Temperature and Time

As shown in Table 1 and 2, the optimized synthesis temperature and time that gave optimized photocatalytic activity were 550 °C and 4 h, respectively. Both optimization studies showed that the best photocatalytic activity was obtained when the CN has good crystallinity, enough low band gap energy, and high specific surface area. In order to study the morphology of the crystalline CN obtained under these optimized synthesis conditions, the TEM image was recorded and shown in Fig. 11. It was obvious that the prepared crystalline CN gave a near-hexagonal prismatic crystallite with a size of about 50 nm. This morphology was certainly different from the reported spherical shape or worm structures of the amorphous bulk or mesoporous CN [8].

As we compare the photocatalytic activity of the crystalline CN to the TiO_2 P25 as the benchmark photocatalyst so far [2], the performance of the crystalline CN to degrade phenol could be considered low. However, the activity of the TiO_2 P25 is mainly generated under UV light irradiation, which would be one of the limitations to fully utilize the solar light spectrum. On the other hand, while the crystalline CN could be activated by visible light, its efficiency still needs to be improved. In this work, a clear enhancement in the photocatalytic activity could be achieved, where up to 3.4 times higher degradation percentage was obtained on the crystalline CN synthesized under optimized temperature and time as compared to the ones synthesized under non-optimized conditions. Such improvement was comparable to the reported approach to increase the photocatalytic activity of the amorphous CN, for example, by modifying the interfacial charge transfer of the amorphous CN by reduced graphene oxide, which gave about 2.8 times better performance for photocatalytic degradation of phenol [31]. This study clearly showed that optimizing the synthesis method is an important strategy to optimize the performance of the photocatalyst.

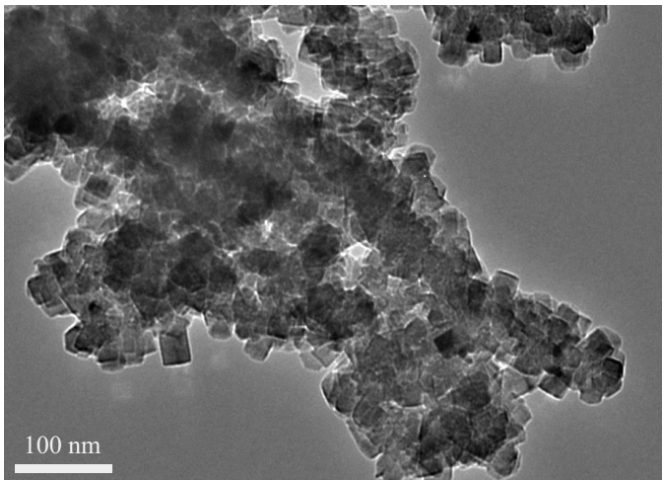

Fig 11. TEM image of crystalline CN prepared at 550 °C and 4 h

■ CONCLUSION

Crystalline CN materials were successfully synthesized at various temperatures (500–600 °C) and various synthesis time (4–6 h). Judging from the photocatalytic performance, the best parameters for synthesis temperature and time were 550 °C and 4 h, respectively. The characterizations by XRD, DR UV-vis, and surface area analyzer revealed that these parameters led to the high crystallinity, enough low band gap energy (2.82 eV), and high specific surface area (73 m^2 g^{-1}), which resulted in up to 3.4 times higher percentage of phenol degradation than the ones synthesized under the non-optimized synthesis conditions.

■ ACKNOWLEDGMENTS

Support from the Directorate General of Strengthening Research and Development, Ministry of Research, Technology, and Higher Education of the Republic of Indonesia via the Fundamental Research scheme (PD 2019, No. 058/SP2H/LT/MONO/L7/2019 and No. 001/MACHUNG/LPPM/SP2H-LIT-MONO/III/2019) is greatly acknowledged.

■ REFERENCES

[1] Villegas, L.G.C., Mashhadi, N., Chen, M., Mukherjee, D., Taylor, K.E., and Biswas, N., 2016, A short review of techniques for phenol removal from wastewater, *Curr. Pollut. Rep.*, 2 (3), 157–167.

[2] Barka, N., Bakas, I., Qourzal, S., Assabbane, A., and Ait-Ichou, Y., 2013, Degradation of phenol in water by titanium dioxide photocatalysis, *Orient. J. Chem.*, 29 (3), 1055–1060.

[3] Fajriati, I., Mudasir, and Wahyuni, E.T., 2014, Photocatalytic decolorization study of methyl orange by TiO_2-chitosan nanocomposites, *Indones. J. Chem.*, 14 (3), 209–218.

[4] Yuliati, L., Roslan, N.A., Siah, W.R., and Lintang, H.O., 2017, Cobalt oxide-modified titanium dioxide nanoparticle photocatalyst for degradation of 2,4-dichlorophenoxyacetic acid, *Indones. J. Chem.*, 17 (2), 284–290.

[5] Kunarti, E.S., Kartini, I., Syoufian, A., and Widyandari, K.M., 2018, Synthesis and photoactivity of Fe_3O_4/TiO_2-Co as a magnetically separable visible light responsive photocatalyst, *Indones. J. Chem.*, 18 (3), 403–410.

[6] Vianney, Y.M., Rosalyn, I., and Angela, S., 2018, Solar based photocatalytic decolorization of four commercial reactive dyes utilizing bound TiO_2-Fe_3O_4 nanocomposite, *Indones. J. Chem.*, 18 (4), 621–631.

[7] Khoriah, K., Wellia, D.V., Gunlazuardi, J., and Safni, S., 2020, Photocatalytic degradation of commercial diazinon pesticide using C,N-codoped TiO_2 as photocatalyst, *Indones. J. Chem.*, 20 (3), 587–596.

[8] Lee, S.C., Lintang, H.O., and Yuliati, L., 2012, A urea precursor to synthesize carbon nitride with mesoporosity for enhanced activity in the photocatalytic removal of phenol, *Chem. Asian J.*, 7 (9), 2139–2144.

[9] Wang, Y., Wang, X., and Antonietti, M., 2012, Polymeric graphitic carbon nitride as a heterogeneous organocatalyst: From photochemistry to multipurpose catalysis to sustainable chemistry, *Angew. Chem. Int. Ed.*, 51 (1), 68–89.

[10] Zhang, Y., Liu, J., Wu, G., and Chen, W., 2012, Porous graphitic carbon nitride synthesized *via* direct polymerization of urea for efficient sunlight-driven photocatalytic hydrogen production, *Nanoscale*, 4 (17), 5300–5303.

[11] Zhao, Y., Zhao, F., Wang, X., Xu, C., Zhang, Z., Shi, G., and Qu, L., 2014, Graphitic carbon nitride nanoribbons: Graphene-assisted formation and synergic function for highly efficient hydrogen evolution, *Angew. Chem. Int. Ed.*, 53 (50), 13934–13939.

[12] Zhu, J., Xiao, P., Li, H., and Carabineiro, S.A.C., 2014, Graphitic carbon nitride: Synthesis, properties, and applications in catalysis, *ACS Appl. Mater. Interfaces*, 6 (19), 16449–16465.

[13] Cui, Y., Huang, J., Fu, X., and Wang, X., 2012, Metal-free photocatalytic degradation of 4-chlorophenol in water by mesoporous carbon nitride semiconductors, *Catal. Sci. Technol.*, 2 (7), 1396–1402.

[14] Zheng, Y., Liu, J., Liang, J., Jaroniec, M., and Qiao, S.Z., 2012, Graphitic carbon nitride materials: Controllable synthesis and applications in fuel cells and photocatalysis, *Energy Environ. Sci.*, 5 (5), 6717–6731.

[15] Hatta, M.H.M., Lintang, H.O., Lee, S.L., and Yuliati, L., 2019, Synthesis of highly active crystalline carbon nitride prepared in various salt melts for photocatalytic degradation of phenol, *Turk. J. Chem.*, 43, 63–72.

[16] Bhunia, M.K., Yamauchi, K., and Takanabe, K., 2014, Harvesting solar light with crystalline carbon nitrides for efficient photocatalytic hydrogen evolution, *Angew. Chem. Int. Ed.*, 53 (41), 11001–11005.

[17] Huang, S., Xu, Y., Ge, F., Tian, D., Zhu, X., Xie, M., Xu, H., and Li, H., 2019, Tailoring of crystalline structure of carbon nitride for superior photocatalytic hydrogen evolution, *J. Colloid Interface Sci.*, 556, 324–334.

[18] Li, Y., Zhang, D., Feng, X., and Xiang, Q., 2020, Enhanced photocatalytic hydrogen production activity of highly crystalline carbon nitride synthesized by hydrochloric acid treatment, *Chin. J. Catal.*, 41 (1), 21–30.

[19] Wang, L., Hong, Y., Liu, E., Wang, Z., Chen. J., Yang, S., Wang, J., Lin, X., and Shi, J., 2020, Rapid polymerization synthesizing high-crystalline g-C_3N_4 towards boosting solar photocatalytic H_2 generation, *Int. J. Hydrogen Energy*, 45 (11), 6425–6436.

[20] Shalom, M., Inal, S., Fettkenhauer, C., Neher, D., and Antonietti, M., 2013, Improving carbon nitride photocatalysis by supramolecular preorganization of monomers, *J. Am. Chem. Soc.*, 135 (19), 7118–7121.

[21] Prins, L.J., Reinhoudt, D.N., and Timmerman, P., 2001, Noncovalent synthesis using hydrogen bonding, *Angew. Chem. Int. Ed.*, 40 (13), 2382–2426.

[22] Seto, C.T., Mathias, J.P., and Whitesides, G.M., 1993, Molecular self-assembly through hydrogen bonding: Aggregation of five molecules to form a discrete supramolecular structure, *J. Am. Chem. Soc.*, 115 (4), 1321–1329.

[23] Çelik, V., and Mete, E., 2012, Range-separated hybrid exchange-correlation functional analyses of anatase TiO_2 doped with W, N, S, W/N, or W/S, *Phys. Rev. B: Condens. Matter*, 86, 205112.

[24] Lin, L., Yu, Z., and Wang, X., 2018, Crystalline carbon nitride semiconductors for photocatalytic water splitting, *Angew. Chem. Int. Ed.*, 58 (19), 6164–6175.

[25] Bojdys, M.J., Müller, J.O., Antonietti, M.A., and Thomas, A., 2008, Ionothermal synthesis of crystalline, condensed, graphitic carbon nitride, *Chem. Eur. J.*, 14 (27), 8177–8182.

[26] Fettkenhauer, C., Weber, J., Antonietti, M., and Dontsova, D., 2014, Novel carbon nitride composites with improved visible light absorption synthesized in $ZnCl_2$-based salt melts, *RSC Adv.*, 4 (77), 40803–40811.

[27] Jin, A., Jia, Y., Chen, C., Liu, X., Jiang, J., Chen, X., and Zhang, F., 2017, Efficient photocatalytic hydrogen evolution on band structure tuned polytriazine/heptazine based carbon nitride heterojunctions with ordered needle-like morphology achieved by an in situ molten salt method, *J. Phys. Chem. C*, 121 (39), 21497–21509.

[28] Liu, J., Zhang, T., Wang, Z., Dawson, G., and Chen, W., 2011, Simple pyrolysis of urea into graphitic carbon nitride with recyclable adsorption and photocatalytic activity, *J. Mater. Chem.*, 21 (38), 14398–14401.

[29] Sam, M.S., Lintang, H.O., Sanagi, M.M., Lee, S.L., and Yuliati, L., 2014, Mesoporous carbon nitride for adsorption and fluorescence sensor of N-nitrosopyrrolidine, *Spectrochim. Acta, Part A*, 124, 357–364.

[30] Alim, N.S., Lintang, H.O., and Yuliati, L., 2015, Fabricated metal-free carbon nitride characterizations for fluorescence chemical sensor of nitrate ions, *Jurnal Teknologi*, 76 (13), 1–6.

[31] Tiong, P., Lintang, H.O., Endud, S., and Yuliati, L., 2015, Improved interfacial charge transfer and visible light activity of reduced graphene oxide-graphitic carbon nitride photocatalysts, *RSC Adv.*, 5 (114), 94029–94039.

Leap Zagreb Connection Numbers for Some Networks Models

Zahid Raza

Department of Mathematics, University of Sharjah, University City, P.O. Box. 27272, Sharjah, United Arab Emirates

* ***Corresponding author:***

tel: +971-568053219
email: zraza@sharjah.ac.ae

Received: January 13, 2020
Accepted: March 24, 2020

DOI: 10.22146/ijc.53393

Abstract: *The main object of this study is to determine the exact values of the topological indices which play a vital role in studying chemical information, structure properties like QSAR and QSPR. The first Zagreb index and second Zagreb index are among the most studied topological indices. We now consider analogous graph invariants, based on the second degrees of vertices, called leap Zagreb indices. We compute these indices for Tickysim SpiNNaker model, cyclic octahedral structure, Aztec diamond and extended Aztec diamond.*

Keywords: *Zagreb connection indices; Tickysim SpiNNaker model; cyclic octahedral; Aztec and extended Aztec diamond*

■ INTRODUCTION

Chemical graph theory is an interdisciplinary field of science which relates chemistry with a branch of mathematical modeling of graphs. In this area of math, one deals with topology of physical structure of a molecule to understand chemical properties of the compounds. A small but significant part of this field is the topic known as topological index where a molecular structure of a chemical formula is scientifically constructed to predict physical and chemical properties of certain molecule. First kind topological index was introduced in 1947 by Wiener. The topological graph is built on atoms as vertices (except for hydrogen atoms and bonds that are always ignored and not considered) and bonds connecting two atoms as edges. There are many different types of topological indices that have been known to exist with vast literature based on them, see for example [5-6,12-14,18-21].

The first Zagreb Index, occurred in an approximate formula for the total π -electron energy [1] and the second Zagreb Index appeared within the study of molecular branching [9]. The first Zagreb connection index and second Zagreb connection index, ZC_1 and ZC_2 respectively, have been put forward in [10] and [11] independently. It has been proved in [10] that the topological index ZC_1 can be written in the form given in Eq. (1). Then Basavanagoud and Praveen Jakkannavar has checked the chemical applicability of ZC_1 and have found that the index has a very good correlation with physical properties of chemical compounds like boiling point, entropy, enthalpy of evaporation, standard enthalpy of vaporization and acentric factor [15] The authors in Ref [10] checked the chemical applicability of ZC_1 and they found that this topological index correlates well with the entropy and acentric factor of octane isomers. Recently, extremal chemical trees with fixed segment length or vertices of degree 2 with respect to modified first Zagreb connection index has been given in Ref. [16] and further extended to general n- vertex tree in [17]. The authors in Ref [2-3] determined some degree base topological indices for diamond like networks and Tickysim SpiNNaker model sheet.

The first connection and second connection index were introduced in 1972 and 1975, respectively. Third connection index is relatively new. These indices are defined as follows for any graph G of order n:

$$ZC_1(G) = \sum_{0\le i\le n-2} c_i(G) * i^2 \quad (1)$$

$$ZC_1(G) = \sum_{0\le i\le n-2} c_i(G) * i^2 \quad (2)$$

$$ZC_1^*(G) = \sum_{0\le i\le j\le n-2} y_{i,j}(G) * (i+j) \quad (3)$$

Here V(G) is the vertex set of graph G, E(G) is edge set of graph G. The c_i denotes the vertex with connection number i and $y_{i,j}$ denotes the number of edges with

connection number i and j. We do not deal with degree of the vertices here so connection number is not to be mistaken with degree of the vertex.

Tickysim SpiNNaker Model

A hexagonal torus that has m vertices in row and n vertices in columns with vertices with total of mn vertices and number of edges equal to 3mn – 2n – 2m + 1. The second of the network topology consists of a set of a hexagonal segments of a hexagonal mesh of nodes. Each node in the simulation represents a SpiNNaker chip that contains a router, packet generator, packet consumer, and a tree of two-input round-robin arbiters which arbitrates between the inputs to the router. The router always consists of a four-stage pipeline. If a packet cannot be forwarded to its requested output after 50 cycles at the head of the router, it is dropped. The packet generator generates packets for each node of the system. If the output buffer is full, the packet generator waits until a space becomes available. The packet consumer receives incoming packets immediately, but the packet consumer will wait 10 cycles before accepting another packet. The arbiter tree is based on SpiNNaker's NoC aspects. In each cycle, the arbiter selects a waiting packet on one of its inputs and forwards it to its output if there is space in the output buffer. For more details, see [4]. The graph TSM sheet is shown in Fig. 1.

Cyclic Octahedral Structure

The Platonic solid known as octahedron with six vertices and 12 edges. An octahedron graph, is a polyhedral graph corresponding to the skeleton of the octahedron, one of the five Platonic solids. The analogy of this structure play vital roles in the field of reticular chemistry, which deals with the synthesis and properties of metal-organic frameworks [7-8]. The different types of octahedral structures arise from the ways that these octahedral can be connected. The cyclic octahedral structure of dimension n is denoted by CYO(n), and it is obtained by arranging n octahedra in cyclic order, as shown in Fig. 2. The cyclic octahedral structure CYO(n) consists of 5n vertices and 12n edges for n > 2.

Aztec Diamond

A diamond shaped graph(see Fig. 3) with insides resembling a domino like structure, is built on square lattices with a vertex in the center of the graph considered as the origin on the x, y plane with half integers taken for x and y.

Extended Aztec Diamond

Extended Aztec diamond (see Fig. 4) is the exact shape and structure as the Aztec diamond but the outer vertices are conjoined by extra edges.

■ RESULTS AND DISCUSSION

The In this section we will present our main results of this paper. In particularly, we compute the leap Zagreb

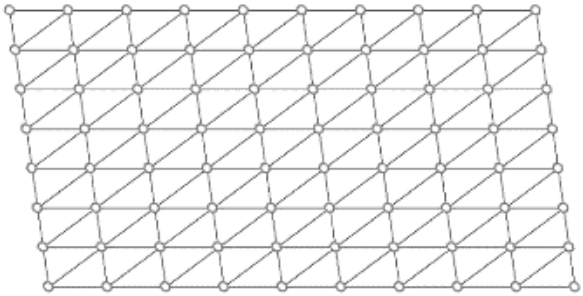

Fig 1. Graph of the TSM sheet for m = 10 and n = 8

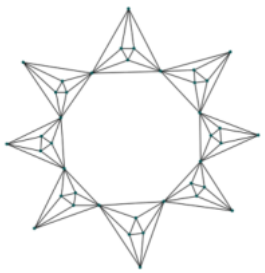

Fig 2. Cyclic octahedral structure (CYO8)

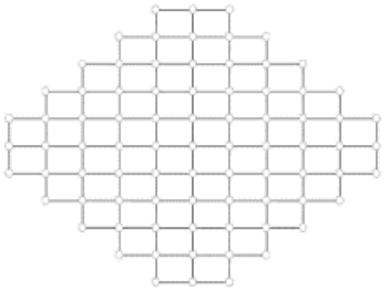

Fig 3. Aztec diamond AZD(n)

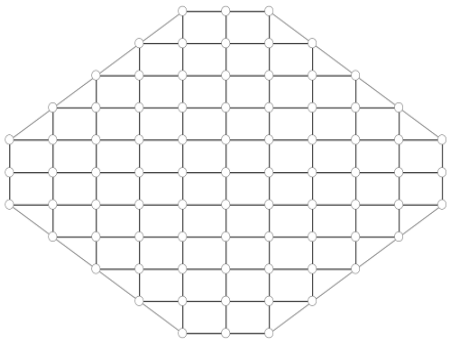

Fig 4. Extended Aztec diamond EAZD(n)

indices of TSM sheet, cyclic octahedral structure, Aztec diamond and extended Aztec diamond and findings presented in this section.

Theorem 1

Let TSM be the graph of Tickysim SpiNNaker model, for n, m ≥ 5. Then the Zagreb connection indices for the TSM are given as:

(1) $ZC_1(TSM) = 670 + 144mn - 316[n+m]$

(2) $ZC_2(TSM) = 2600 + 432mn - 1072[n+m]$

(3) $ZC_1^*(TSM) = 198 + 72mn - 124[n+m]$

Proof

We know the general connection index is $ZC_1(G)=\sum_{0\le i\le n-2} c_i(G)*i^2$. Taking into account the restriction that n ≥ 5 and m ≥ 5, we have the following connection numbers for the TSM sheet. On two diagonal corner ends the connection number c_3 is fixed as the number of vertices from it with distance two are 3. Also, the opposite end corners c_5 is fixed. Where c_3 is always flanked by c_4s on its two on outer surface, c_5 is flanked by c_6 on both outer surface. As m and n increase so do the c_7 on the border between c_4 and c_6.

Therefore c_3, c_4, c_5, c_6 are fixed and c_7 on outer border is given as;

$c_7 = 2(n-4) + 2(m-4)$, $c_3 = 2$, $c_4 = 4$, $c_5 = 2$, $c_6 = 6$.

Moving into the inner parallelogram c_9 that increase with the vertices n, m. Hence; $c_9 = 2(n-4) + 2(m-4)$.

Finally the innermost graph has vertices all the same connection number 12. To have a c_{12} vertex should have at least 2 vertices above it, below it, to its left and to its right. Therefore; $c_{12} = (n-4)(m-4)$.

We know the general connection index is $ZC_1(TSM) = \sum_{0\le i\le n-2} c_i(G)*i^2$, and from vertex partition given in Table 1, we have

$$\begin{aligned} ZC_1(TSM) &= \sum_{0\le i\le n-2} c_i(G)*i^2 = 2.3^2 + 4.4^2 + 2.5^2 + 6.6^2 \\ &\quad + (2n+2m-14)7^2 + (2n+2m-16)9^2 \\ &\quad + (mn-4n-4m+16)12^2 \\ &= 18 + 64 + 50 + 216 + 49(2n+2m-14) \\ &\quad + 81(2n+2m-16) + 144(nm+16-4n-4m) \end{aligned}$$

After simplification of terms, we get put required formula for the connection number for TSM sheet.

$ZC_1(TSM) = 670 + 144mn - 316[n+m]$

For the indices $ZC_2(TSM)$ and $ZC_1^*(TSM)$, we need to partition the edges of the TSN sheet according to the connection numbers of the end points of an edge. It is easy to see that all the edges labelled with their connection number are given in Table 2.

Table 1. Partition of vertex set of TSM sheet

Vertices of type c_i	Number of vertices
c_3	2
c_4	4
c_5	2
c_6	6
c_7	2n + 2m – 14
c_9	2n + 2m – 16
c_{12}	mn – 4n – 4m + 16

Table 2. Partition of edge set of TSM sheet

Edges of type $y_{i,j}(TSM)$	Number of edges
$y_{3,4}$	4
$y_{4,4}$	2
$y_{4,6}$	4
$y_{4,7}$	4
$y_{5,6}$	4
$y_{5,7}$	2
$y_{6,7}$	12
$y_{6,9}$	8
$y_{7,7}$	2m + 2n – 10
y7,9	4m + 4n – 32
$y_{7,12}$	2
$y_{9,9}$	2m + 2n – 18
$y_{9,12}$	4m + 4n – 36
$y_{12,12}$	3mn – 14m – 14n + 65

From Eq. (2) and Table 2, we have the followings:

$$ZC_2(TSM) = \sum_{0\le i\le n-2} y_{i,j}(TSM)^{*}ij$$

$$\begin{aligned} ZC_2(TSM) &= y_{3,4}(3)(4) + y_{4,4}(4)(4) + y_{4,6}(4)(6) \\ &+ y_{4,7}(4)(7) + y_{5,6}(5)(6) + y_{5,7}(5)(7) \\ &+ y_{6,7}(6)(7) + y_{6,9}(6)(9) + y_{7,7}(7)(7) \\ &+ y_{7,9}(7)(9) + y_{7,12}(7)(12) + y_{9,9}(9)(9) \\ &+ y_{9,12}(9)(12) + y_{12,12}(12)(12) \\ &= 12(4) + 16(2) + 24(4) + 28(4) + 30(4) + 35(2) \\ &+ 42(12) + 54(8) + 49(2m + 2n - 10) + 63(4m \\ &+ 4n - 32) + 84(2) + 81(2m + 2n - 18) + 108(4m \\ &+ 4n - 36) + 144(3mn - 14m - 14n + 65) \end{aligned}$$

After simplification of terms, we get the required formula for TSM as:

$$ZC_2(TSM) = 2600 + 432mn - 1072[n + m]$$

From Eq. (3) and Table 2 we have

$$ZC_1^{*}(TSM) = \sum_{0\le i\le n-2} y_{i,j}(TSM)^{*}(i + j)$$

$$\begin{aligned} ZC_1^{*}(TSM) &= y_{3,4}(3+4) + y_{4,4}(4+4) + y_{4,6}(4+6) \\ &+ y_{4,7}(4+7) + y_{5,6}(5+6) + y_{5,7}(5+7) \\ &+ y_{6,7}(6+7) + y_{6,9}(6+9) + y_{7,7}(7+7) \\ &+ y_{7,9}(7+9) + y_{7,12}(7+12) + y_{9,9}(9+9) \\ &+ y_{9,12}(9+12) + y_{12,12}(12+12) \\ &= 7(4) + 8(2) + 10(4) + 11(4) + 11(4) + 12(2) \\ &+ 13(12) + 15(8) + 14(2m + 2n - 10) + 16(4m \\ &+ 4n - 32) + 17(2) + 18(2m + 2n - 18) + 19(4m \\ &+ 4n - 36) + 24(3mn - 14m - 14n + 65) \end{aligned}$$

After simplification of terms, we get the required result for TSM sheet

$$ZC_1^{*}(TSM) = 198 + 72mn - 124[n + m]$$

Remark: We have the following results for fixed value of **m** or **n**

a) If m = 4 and n ≥ 4, then

1. $ZC_1(TSM) = -594 + 260n$
2. $ZC_2(TSM) = -1733 + 674n$
3. $ZC_1^{*}(TSM) = -298 + 164n$

b) If n = 4 and m ≥ 4 then

1. $ZC_1(TSM) = -594 + 260m$
2. $ZC_2(TSM) = -1733 + 674m$
3. $ZC_1^{*}(TSM) = -298 + 164m$

Theorem 2

For n ≥ 3, the Zagreb connection indices for the cyclic octahedron CYO(n) are given as:

(1) $ZC_1(G) = 256n$

(2) $ZC_2(G) = 645n$

(3) $ZC_1^{*}(G) = 176n$

Proof

Total edges are 12n for n cycles and total vertices for n ≥ 3 cycles is 5n. Here there are all three different connection numbers c_5, c_9 and c_{10} when the octahedrons are connected in a cycle. The results follows from Table 3 and Table 4 and from Eq. (1-3).

Theorem 3

Let AZD(n) be the Aztec diamond. Then,

(1) $ZC_1(G) = 128n^2 - 184n - 76$

(2) $ZC_2(G) = 256n^2 - 504n + 52$

(3) $ZC_1^{*}(G) = 64n^2 - 72n - 36$

Proof

We know the general connection index is given by $ZC_1(AZD(n)) = \sum_{0\le i\le n-2} c_i(AZD(n))^{*}$, and from vertex partition given in Table 5, we have

$$\begin{aligned} ZC_1(AZD(n)) &= c_3 3^2 + c_4 4^2 + c_5 5^2 + c_7 7^2 + c_8 8^2 \\ &= 4.3^2 + 8.4^2 + (8n - 20)5^2 + 4.7^2 \\ &+ (2n^2 - 6n + 1)8^2 \end{aligned}$$

After simplification of terms, we get:

$$ZC_1(AZD(n)) = 128n^2 - 184n - 76$$

Table 3. Partition of the vertex set of CYO(n)

Vertices of type c_i	Number of vertices
c_5	3n
c_9	N
c_{10}	N

Table 4. Partition of the edge set of CYO(n)

Edges of type $y_{i,j}$(CYO(n))	No. of edges
$y_{5,5}$	3n
$y_{5,9}$	2n
$y_{5,10}$	4n
$y_{9,10}$	2n
$y_{10,10}$	n

All the vertices with their respective connection numbers are given in Table 5.

For the indices $ZC_2(AZD(n))$ and $ZC_1^*(AZD(n))$, we need to partition the edges of the AZD(n) according to the connection numbers of the end points of an edge. It is easy to see that all the edges labelled with their connection number are given in Table 6.

Table 5. Partition of vertex set of Aztec diamond

Vertices of type c_i	Number of vertices
c_3	4
c_4	8
c_5	8n – 20
c_7	4
c_8	$2n^2$ – 6n + 1

Table 6. Partition of edge set of Aztec diamond AZD(n)

Edges of type $y_{i,j}(AZD(n))$	No. of edges
$y_{3,4}$	8
$y_{3,7}$	4
$y_{4,5}$	8
$y_{5,5}$	8n – 24
$y_{5,7}$	8
$y_{5,8}$	8n – 24
$y_{7,8}$	4
$y_{8,8}$	$4n^2$ – 16n + 12

From the last column of the table we can verify by adding up all the edges to get the total number of edges for all the AZD(n) = $4n^2 - 4$. Also, the restriction is $n \geq 4$ to compute the Zagreb connection index $ZC_2(AZD(n))$ and $ZC_1^*(AZD(n))$. Here using the formula in Eq. (2) and on the last column for all edges in Table 6, we have

$$\begin{aligned} ZC_2(AZD(n)) &= y_{3,4}(3)(4) + y_{3,7}(3)(7) + y_{4,5}(4)(5) \\ &\quad + y_{5,5}(5)(5) + y_{5,7}(5)(7) + y_{5,8}(5)(8) \\ &\quad + y_{7,8}(7)(8) + y_{8,8}(8)(8) \\ &= 12(8) + 21(4) + 20(8) + 25(8n-24) + 35(8) + 40(8n-24) \\ &\quad + 56(8) + 64(4n^2 - 16n + 12) \end{aligned}$$

After simplification of terms, we get the required formula

$$ZC_2(G) = 256n^2 - 504n + 52$$

From Eq. (3) and Table 6 we have the followings:

$$\begin{aligned} ZC_1^*(AZD(n)) &= \sum_{0 \leq i \leq n-2} y_{i,j}(AZD(n))^*(i+j) \\ &= y_{3,4}(3+4) + y_{3,7}(3+7) + y_{4,5}(4+5) \\ &\quad + y_{5,7}(5+7) + y_{5,5}(5+5) + y_{5,8}(5+8) \\ &\quad + y_{7,8}(7+8) + y_{8,8}(8+8) \\ &= 7(8) + 10(4) + 9(8) + 10(8n-24) + 12(8) \\ &\quad + 13(8n-24) + 15(8) + 16(4n^2 - 16n + 12) \\ &= 64n^2 - 72n - 36 \end{aligned}$$

Similarly, we can obtained the Zagreb connection indices for Aztec diamond EAZD(n) in the following theorem.

Theorem 4

The Zagreb connection indices for extended Aztec diamond EAZD(n) are follows;

(1) $ZC_1(EAZD(n)) = 128n^2 + 264n - 492$

(2) $ZC_2(EAZD(n)) = 256n^2 + 524n - 1168$

(3) $ZC_1^*(EAZD(n)) = 64n^2 + 160n - 204$

■ CONCLUSION

In this paper, we computed some topological indices of Tickysim SpiNNaker model TSM, cyclic octahedral structure, Aztec diamond AZD(n) and extended Aztec diamond EAZD(n). The obtained results can be used to predict the certain physio- chemical properties of a molecule as these indices are functions of chemical graphs and can encode many chemical properties such as entropy, boiling point, acentric factor and enthalpy of vaporization. As cited earlier ZC_1 has a very good correlation with physical properties, mainly with the standard enthalpy of vaporization and having a better correlation than the Wiener Index [12]. The Fig. 5, we can take note that all indices raise sharply with n (since all indices are quadratic in terms of order). But the ZC_2 is greater than all other leap indices. Similarly, ZC_1^* correlates well with the acentric factor and entropy and from Fig. 6, we see a similar observation having is predicted to have comparatively much higher values for their eccentric factor with again the former having much larger values than the latter.

It is notable that the obtained results for closed formulas for these networks are all quadratic in terms of order which show that one can build efficient graph algorithms to compute the indices within polynomial time.

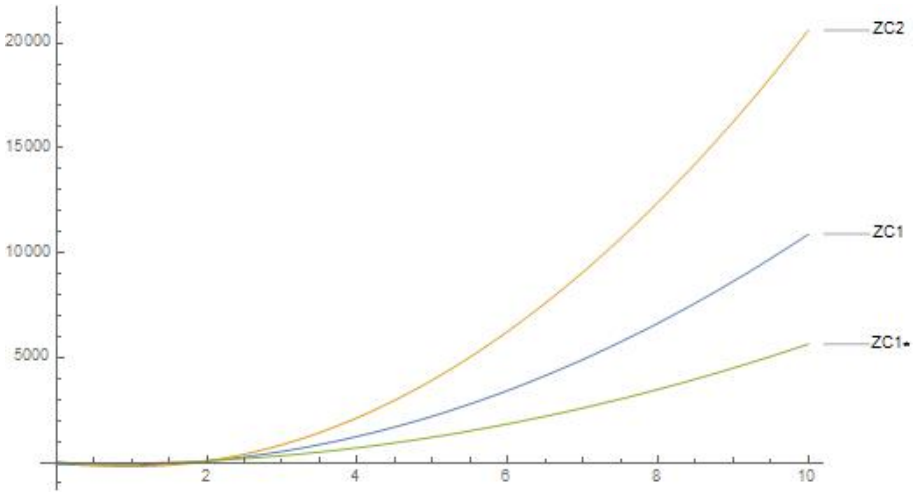

Fig 5. Leap indices for Aztec diamond AZD(n)

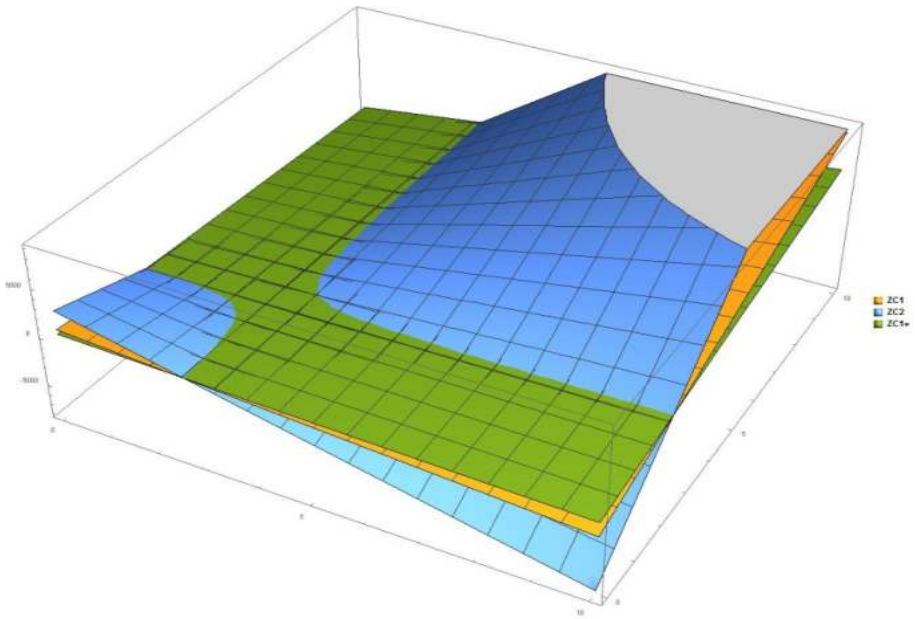

Fig 6. Leap indices for TSM

■ ACKNOWLEDGMENTS

Zahid Raza has been funded during the work on this paper by the University of Sharjah under Project # 1802144068 and MASEP Research Group.

■ REFERENCES

[1] Gutman, I., and Trinajstić, N., 1972, Graph theory and molecular orbitals. Total φ-electron energy of alternant hydrocarbons, *Chem. Phys. Lett.*, 17 (4), 535–538.

[2] Imran, M., Baig, A.Q., Siddiqui, H.M.A., and Sarwar, R., 2017, On molecular topological properties of diamond-like networks, *Can. J. Chem.*, 95, 758–770.

[3] Imran, M., Siddiqui, H.M.A., Ahmed, A., Ali, U., and Hanif, N., 2018, On the degree-based topological indices of the Tickysim SpiNNaker model, *Axioms*, 73 (4), 73.

[4] Stojmenovic, I., 1997, Honeycomb networks: Topological properties and communication

algorithms, *IEEE Trans. Parallel Distrib. Syst.*, 8 (10), 1036–1042.

[5] Zahid, M.A., Baig, A.Q., Naeem, M., and Azhar, M.R., 2018, Eccentricity-based topological indices of a cyclic octahedron structure, *Mathematics*, 6 (8), 141.

[6] Khalid, R., Idrees, N., and Saif, M.J., 2019, Topological characterization of book graph and stacked book graph, *CMC–Comput. Mater. Con.*, 60 (1), 41–54.

[7] Li, M.Y., and Sevov, S.C., 2013, Mellitate-based coordination polymers with a recurring motif: Controlling dimensionality with secondary ligands, *CrystEngComm*, 15 (25), 5107–5113.

[8] Perry IV, J.J., Perman, J.A., and Zaworotko, M.J., 2009, Design and synthesis of metal-organic frameworks using metal-organic polyhedra as supermolecular building blocks, *Chem. Soc. Rev.*, 38 (5), 1400–1417.

[9] Gutman, I., Rui, B., Trinajstić, N., and Wilcox Jr., C.F., 1975, Graph theory and molecular orbitals. XII. Acyclic polyenes, *J. Chem. Phys.*, 62 (9), 3399.

[10] Ali, A., and Trinajstić, N., 2018, A novel/old modification of the first Zagreb index, *Mol. Inf.*, 37 (6-7), 1800008.

[11] Naji, A.M., Soner, N.D., and Gutman, I., 2017, On leap Zagreb indices of graphs, *Commun. Comb. Optim.*, 2 (2), 99–117.

[12] Basavanagoud, B., and Jakkannavar, P., 2018, Computing first leap Zagreb index of some nano structures, *Int. J. Math. Appl.*, 6 (2B), 135–139.

[13] Khalid, K., Kok, I., Ali, A., and Bashir, M., 2019, Zagreb connection indices of TiO_2 nanotubes, *Khimiya*, 27 (1), 86–92.

[14] Ducoffe, G., R. Marinescu-Ghemeci, R., Obreja, C., Popa, A., and Tache, R., 2018, Extremal graphs with respect to the modified first Zagreb connection index, *Proceedings of the 16th Cologne-Twente Workshop on Graphs and Combinatorial Optimization (CTW18)*, Paris, France, 18-20 June 2018, 02011265.

[15] Basavanagoud, B., and Jakkannavar, P., 2018, Computing leap Zagreb indices of generalized xyz - point-line transformation graphs $T^{xyz}(G)$ when z = +, *J. Comput. Math. Sci.*, 9 (10), 1360–1383.

[16] Noreen, S., Bhatti, A.A., and Ali, A., 2020, Extremum modified first Zagreb connection index of n-vertex trees with fixed number of pendent vertices, *Discrete Dyn. Nat. Soc.*, 2020, 3295342.

[17] Noreen, S., Bhatti, A.A., and Ali, A., 2020, Extremal trees for the modified first Zagreb connection index with fixed number of segments or vertices of degree 2, *J. Taibah Univ. Sci.*,14 (1), 31–37.

[18] Raza, Z., 2020, The harmonic and second Zagreb indices in random polyphenyl and spiro chains, *Polycyclic Aromat. Compd.*, 0 (0), 1–10.

[19] Raza, Z., and Sukaiti, M.E., 2020, M-Polynomial and degree based topological indices of some nanostructures, *Symmetry*, 12 (5), 831.

[20] Raza, Z., 2016, The edge version of geometric arithmetic index of polyomino chains of 8-cycles and arbitrary carbon nanocones, *J. Comput. Theor. Nanosci.*, 13 (11), 8455–8459.

[21] Ali, U., Javaid, M., and Kashif, A., 2020, Modified Zagreb connection indices of the T-sum graphs, *Main Group Met. Chem.*, 43, 43–55.

Controlled Release Fertilizer Encapsulated by Glutaraldehyde-Crosslinked Chitosan Using Freeze-Drying Method

Adhitasari Suratman*, Dwi Ratih Purwaningsih, Eko Sri Kunarti, and Agus Kuncaka

Department of Chemistry, Faculty of Mathematics and Natural Sciences, Universitas Gadjah Mada, Sekip Utara, Yogyakarta 55281, Indonesia

* ***Corresponding author:***

email: adhitasari@ugm.ac.id

Received: March 30, 2020
Accepted: May 28, 2020

DOI: 10.22146/ijc.55133

Abstract: *A new encapsulation of NPK fertilizer hydrogel granules made from glutaraldehyde crosslinked chitosan has been successfully fabricated. This designed fertilizer was aimed to maximize the fertilizing process in the soil, as the environmental pollution affected by the excess release of the nutrients can be prevented. The granule was prepared from biodegradable chitosan crosslinked with glutaraldehyde by applying a method of air and freeze-drying. The release test proved that this designed fertilizer showed a good performance as a Controlled Release Fertilizer (CRF) in which the hydrogel granules could absorb and deposit large amounts of NPK. Later on, they could also release large amounts of NPK as well, unlike several types of CRFs. The release percentage of NPK out of the granules tended to decrease with an increase of pH at a range close to the average pH of the soil, which is neutral to base. Comparing two methods, the freeze-drying technique, which yields a bigger pore size, showed a higher release percentage than air-drying. The release kinetics of the granules followed the Korsmeyer-Peppas model.*

Keywords: *hydrogel; controlled release fertilizer; freeze-drying; chitosan; glutaraldehyde*

■ INTRODUCTION

Fertilizers are very important in agriculture, where it is needed by soil to afford essential nutrients required by the plants [1]. However, the fertilizer losses in the soil are still one of the main concerns in the use of fertilizers [2]. Around 40–70% of nitrogen, 80–90% phosphorus, and 50–70% potassium from fertilizers are wasted to the environment without any absorption of the root plant. This problem causes not only economic and resource loss but also causes environmental pollution [3]. Therefore, efficient nutrient absorption from fertilizers to the plants should be increased to avoid nutrient loss during the process in the soil media by controlling the processes in fertilizers, soil media, and plant absorption. In this study, the fertilizer released to the soil media will be observed by controlling the amount of substances such as N, P, K, where adjustment of the release rate of the controlled release fertilizer (CRF) method is used. The granules that are composed of fertilizer and crosslinked chitosan are modified to adjust certain release mechanisms and to regulate the release rate based on the physical characterization of the granules, such as diffusion, swelling, polymer matrix degradation that affects the release pattern of the fertilizer [4-6]. A hydrogel is a type of matrix that is known and used to control the release of fertilizers into the soil [7]. A hydrogel is a 3D-networking hydrophilic polymer that is capable of keeping water in their structure and is dissoluble in water [8-11], therefore it is a good material to be used as a fertilizer media. In addition, the use of hydrogels for fertilizer release can increase efficiency, reduce soil toxicity, and minimalize the potential loss of nutrition, and improve the soil quality [12].

Chitosan, which is a natural polysaccharides obtained from the deacetylation of chitin and formed from β-(1-4)-2-amino-deoxy-β-D-glucose [13], does not dissolve in water, organic solvents, alkaline solutions, and mineral acids at pH above 6.5 [14], and is classified as biodegradable and non-toxic [15], a cationic polymer, and it can form a complex structure with anionic polymers or cross-linking agents [16], such as glutaraldehyde [17]. The solubility of chitosan is affected by the protonation

of the amino groups in the polymer chains [18], and by the crosslinkage with glutaraldehyde that increases the structure stability in acidic solution [19]. Chitosan, a natural and inexpensive source of material found in shrimp and crab, was used in this study as a porous-structure media to keep the NPK fertilizer. Freeze-drying used for the hydrogel formation is based on a dry process in which the solvent media (water) will crystallize at low temperatures and sublimate to the vapor phase [20] in the vacuum [21] and sublimation condition [22]. The shape of pores, pore size distribution, and pore connectivity of the matrix will be formed by ice sublimation during the processes [23]. The benefits of using freeze-drying are long-term-storage use, damage reduction from heat, prevent microorganism activity and excessive stress, and also avoid change of the sample appearance [21,24]. The preparation of porous hydrogels from chitosan using the freeze-drying technique for controlled release fertilizers has not been reported until now. The crosslinking process in chitosan is to afford adequate pores of hydrogel to store and release the NPK fertilizer at different conditions of pH in the soil.

■ EXPERIMENTAL SECTION

Materials

The materials used in this study were chitosan, glacial acetic acid, potassium dihydrogen phosphate, potassium solution 1000 mg/L, ammonium molybdate, ammonium vanadate, glutaraldehyde, potassium hydroxide, citric acid 65%, hydrochloric acid 37% from E. Merck, Germany. NPK fertilizer and deionized water were obtained from a local market.

Instrumentation

Instruments used in this study were Fourier Transform Infrared (FTIR) Spectrometer from Shimadzu Prestige 21, Scanning Electron Microscopy (SEM) from Hitachi SU 3500, UV-Vis spectrophotometer from Thermo Spectronic 20D+, and Atomic Absorption Spectrophotometer (AAS) from Perkin Elmer 3110, and Freeze-dryer from LyoQuest Telstar.

Procedure

Preparation of chitosan hydrogel

The hydrogel was prepared by dissolving chitosan in 10 mL acetic acid solution 0.1 M (2% v/v). One and a half grams of NPK fertilizer was then added into the solution under constant stirring for about 30 min, followed with the addition of 0.16 mL glutaraldehyde solution 25% (0.4% v/v). The hydrogel was dried using the air-drying and freeze-drying method. Hydrogel yielded from freeze-drying was characterized using FTIR and SEM.

The release mechanism of N, P, K

The hydrogel of chitosan crosslinked with glutaraldehyde (1.8 g) was immersed into 20 mL of deionized water for 8 days. The aliquot solution of hydrogel was then filtered. The released amount of nitrogen out of hydrogel was determined with the Kjeldahl method [25]. The released amount of phosphor was determined by UV-Vis Spectrophotometer (at wavelength 426 nm). Aliquot solution of about 0.125 mL was diluted 20 times in water, and about 2.5 mL was taken, added by 5 mL of a complexing solution of vanadomolybdate acid and water until the volume reaches 100 mL. The calibration curve standard was made by absorbance measurement of phosphor standard solution with a concentration of 0.5–2.5 mg/L (interval 0.5 mg/L). Potassium release was determined by diluting aliquot solution up to 8000 times, followed by measurement with Atomic Absorption Spectroscopy (AAS). The calibration curve standard was made by absorbance measurements of potassium standard solution from 1–5 mg/L (interval 0.5 mg/L).

The release mechanism of nitrogen, phosphor, and potassium was determined using zeroth order, the first order, Higuchi and Korsmeyer-Peppas kinetics models (Table 1), where C_t is NPK concentration at the time of t, C_0 is the initial NPK concentration in the hydrogel, Q is the release percentage, M_t and $M\infty$ are amounts of

Table 1. Kinetics model equations for determination of release mechanism of N, P, and K

Kinetics Model	Equation
Zeroth order	$C_t - C_0 = -kt$
First order	$\ln[C] = \ln[C]_0 + kt$
Higuchi	$Q = k\sqrt{t}$
Korsmeyer-Peppas	$\frac{Mt}{M\infty} = kt^n$

nutrient released at a time (t) and at equilibrium, k is a constant of the fertilizer-polymer system, and n is the diffusion exponent characteristic of the release mechanism in which for Quasi-Fickian diffusion is n = 0.5; non-Fickian or anomalous transport n = 0.5–1.0 and case II transport n = 1.0 [26-27]. The calculation result was used to determine the release of N, P, and K with NPK concentration variation.

Swelling ratio of hydrogel at pH variation

The hydrogel was immersed into 20 mL of solution at pH 1; 3; 5; 7; 9 for 120 min. The hydrogel was lifted and weighed every 10 min of immersion. The swelling percentage was calculated using the equation:

$$SR = \frac{Wx - Wd}{Wd} \times 100\%$$

where Wx and Wd refer to the weight of the swollen hydrogel and dried hydrogel, respectively.

NPK release at pH variation

The hydrogel was immersed into 20 mL of solution at pH 1 for 8 days. The aliquot solution was filtered, and NPK content was determined by the Kjeldahl method and measured by UV-Vis spectrophotometer, and AAS. The same procedure was also done at pH 3; 5; and 9.

Air-drying method

Hydrogel made by air-drying was obtained by heating at 70 °C for 24 h in the oven. The hydrogel product was immersed into 20 mL of deionized water for 8 days. The aliquot solution of the immersion was then filtered. The determination of NPK was done with the Kjeldahl method, UV-Vis spectrophotometer, and AAS. The performance of the resulting hydrogel using this method was compared with the freeze-drying method.

■ RESULTS AND DISCUSSION

Physical Characterization of the Glutaraldehyde Crosslinked Chitosan Hydrogel

Hydrogel made by the freeze-drying method is expected to have high stability structures. FTIR data of the hydrogel was used to find material groups to comply with the hydrogel. The spectra is shown in Fig. 1.

FTIR data showed that -OH stretching of the hydrogel product was seen at about 3390 to 3500 cm^{-1} overlapping with N–H stretching (3132 cm^{-1}). The peak at wavenumber of around 1080 and at 1635 cm^{-1} were attributed to the vibrations of –C-O-C glycosidic linkage and N–H bending, respectively. Interaction of the chitosan backbone with glutaraldehyde was indicated by the shifting of N–H bending of uncrosslinked chitosan hydrogel to a lower wavenumber, at 1651 to 1635 cm^{-1}. This wavenumber shifting of a similar crosslinking process was also reported by Akakuru and Isiuku [28].

The SEM images of hydrogel prepared by air-drying and freeze-drying are shown in Fig. 2. It is shown that both hydrogels have clear differences on their surface. The massive surface was seen on the air-drying

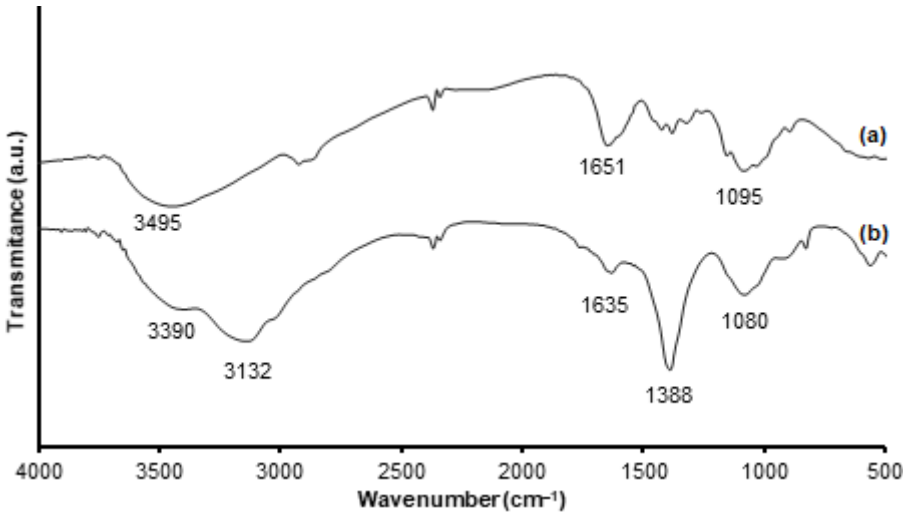

Fig 1. Spectra of (a) chitosan and (b) chitosan crosslinked glutaraldehyde hydrogel

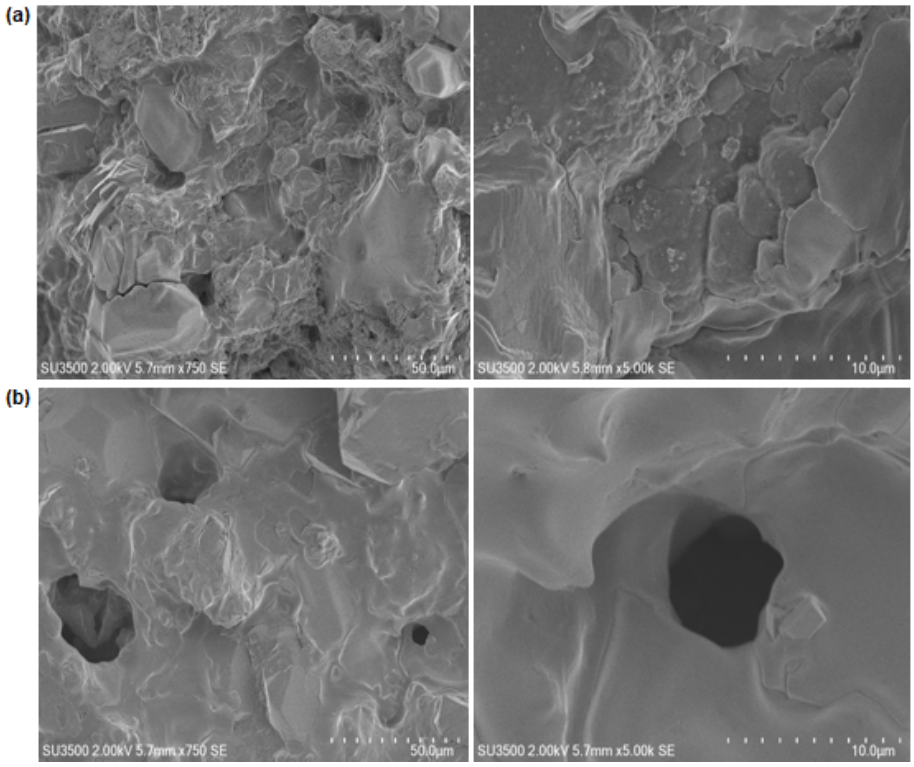

Fig 2. The surface morphology of chitosan hydrogel made with (a) air-drying, and (b) freeze-drying

hydrogel (Fig. 2(a)). The surface with pores was clearly seen on the surface of the hydrogel made by freeze-drying (Fig. 2(b)). The pores on the hydrogel structure was advantageous for the solvent absorption and swelling structure change of the hydrogel.

The Release Kinetics Model of Nitrogen, Phosphor, and Potassium

The release of N, P, and K was studied using fertilizer concentration of 1.5 g that was immersed in deionized water for 8 days. The results are shown in Fig. 3.

From Fig. 3, we can see that the release of N, P, and K from the hydrogel significantly increased until the 5th day and became constant in the following days. The release mechanism of N, P, and K was investigated using zeroth order, first order, Higuchi, and Korsmeyer-Peppas kinetics model. The correlation coefficient (R^2) is shown in Table 2.

Table 2 shows that the release of N, P, and K from the glutaraldehyde crosslinked chitosan hydrogel followed the Korsmeyer-Peppas model, indicated by the regression value, which is close to 1 (0.99). The Korsmeyer-Peppas model explains that the release of N, P, and K is due to the swelling of the hydrogel. The

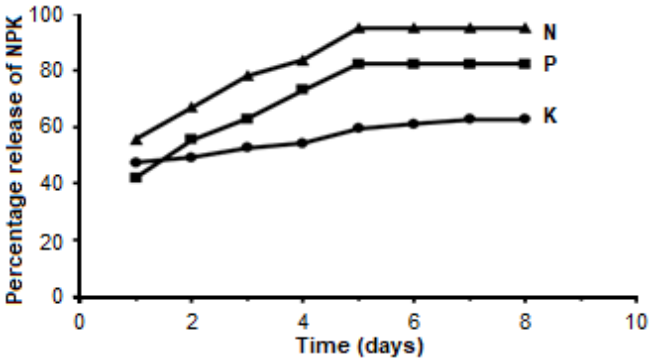

Fig 3. The release of N, P, and K in water until 8 days

Table 2. Correlation coefficient (R^2) of the release kinetics of N, P, and K

Nutrient	Zeroth order	First order	Higuchi	Korsmeyer-Peppas
N	0.94	0.96	0.46	0.99
P	0.98	0.98	0.97	0.99
K	0.97	0.97	0.98	0.99

calculation of the NPK release exponent (n), correlation coefficient (R^2), and release factor (k) of the hydrogel are shown in Table 3.

From Table 3, we can see that the value of n from N, P, and K was smaller than 0.5, indicating that the NPK release followed the Quasi-Fickian diffusion mechanism. It means that the release of NPK from the hydrogel was determined by partial diffusion of swelling and water-filled pores of the hydrogel. The formation of the crosslinked chitosan with glutaraldehyde increased the swellability of the hydrogel because of the increase of density of the hydrogel when compared to the uncrosslinked hydrogel [28].

Effect of Fertilizer Concentration on the Hydrogel

The release of N, P, and K from the freeze-dried hydrogels were performed with fertilizer weight variation of 1; 1.5; and 2 g. This variation is aimed to investigate the effect of NPK fertilizer concentration on the kinetics of N, P, and K releases. The data on the release of N, P, and K are shown in Fig. 4.

Fig. 4 shows that the increase of N, P, and K concentrations in the hydrogel caused the increase of N, P, and K releases. The release mechanism of N, P, and K was investigated using the kinetics model of Korsmeyer-Peppas. The data of the release exponent (n), correlation coefficient (R^2), and release factor (k) with the variation of N, P, and K concentrations are shown in Table 4.

Table 4 shows that the release constants for nitrogen were 34.1; 49.2; 54.5 ppm/day, for fertilizer concentrations of 1, 1.5, and 2 g, respectively. For the same fertilizer concentrations, the release constants for phosphorus were 50.2; 54.7; and 58.2 ppm/day, while the release constants for potassium were 42.1; 42.2; and 50.8 ppm/day.

The data indicates that the reaction rate constant of nitrogen, phosphorus, and potassium increased with the increase of the NPK amount in the hydrogel. This shows that the concentration of the NPK fertilizer in the hydrogel affects the release of nitrogen, phosphorus, and potassium. Meanwhile, the n value of nitrogen, phosphorus, and potassium were smaller than 0.5, indicating that the release of phosphorus and potassium followed the Quasi-Fickian diffusion mechanism [5].

Swelling Ratio of the Hydrogel

The swelling ratio of the hydrogel was studied by immersing the hydrogel in water at pH of 1; 3; 5; 7; and 9 for 120 min (with 10 min interval). Fig. 5 shows the result for the investigation of the swelling of the hydrogel

Table 3. NPK release exponent (n), correlation coefficient (R^2), and release factor (k) of hydrogel

Nutrient	Correlation coefficient (R^2)	Korsmeyer-Peppas	
		n	k (ppm/day)
N	0.99	0.13	49.3
P	0.99	0.27	60.9
K	0.99	0.37	42.2

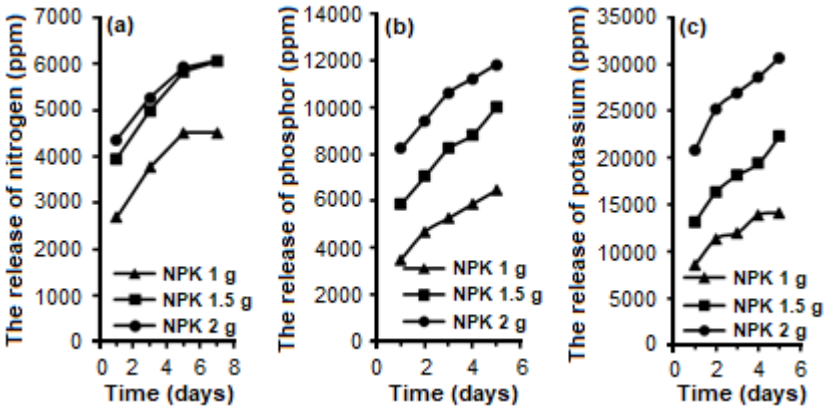

Fig 4. The release of (a) nitrogen, (b) phosphorus, and (c) potassium with fertilizer concentration variation

Table 4. N, P, and K release exponent (n), correlation coefficient (R^2), and release factor (k) with the variation of fertilizer concentration

Nutrient	Concentration of fertilizer	Correlation coefficient (R^2)	Korsmeyer-Peppas	
			n	k (ppm/day)
N	1.0 g	0.97	0.28	34.1
	1.5 g	0.99	0.23	49.2
	2.0 g	0.99	0.18	54.5
P	1.0 g	0.99	0.37	50.2
	1.5 g	0.98	0.32	54.7
	2.0 g	0.99	0.22	58.2
K	1.0 g	0.97	0.31	42.1
	1.5 g	0.98	0.31	42.2
	2.0 g	0.99	0.23	50.8

due to water absorption into the pores of the hydrogel at pH variation. In general, the swellability of the hydrogel is influenced by the presence of hydroxyl groups (–OH) that enhance the hydrophilicity and the presence of amino groups ($–NH_2$) that are protonated in water, mostly in acidic solution. Fig. 5 shows that the lowest swelling of the hydrogel occurred at pH 9. This was due to the $–NH_2$ group of chitosan that was protonated to $–NH_3^+$. This protonation causes chain repulsion and diffusion in the base solution, $-NH_2$ was not protonated.

The NPK Release at Variation of pH Solution

The NPK release of the hydrogel at pH 1; 3; 5; and 9 for 5 days are shown in Fig. 6.

From Fig. 6, it is shown that the lowest NPK release occurred at pH 9, NPK release in the acidic solutions were higher because the acidic pH causes the unreacted $-NH_2$ group to be protonated. The protonation increase the swelling of the hydrogel, causing the solvent to easily enter the pores of the hydrogel resulting in higher NPK release.

The Effect of Drying Method

The effect of the freeze-drying and air-drying methods are shown in Fig. 7.

Fig. 7 shows that the release of N, P, and K from the freeze-dried hydrogels was relatively higher than the

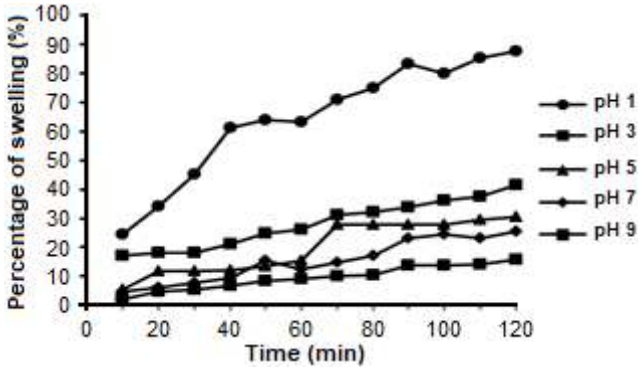

Fig 5. The swelling ratio of hydrogel at pH variation

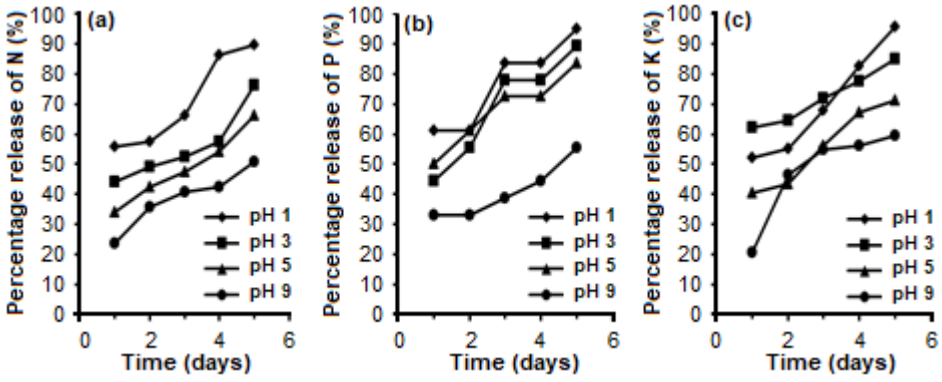

Fig 6. The release of (a) nitrogen, (b) phosphor, (c) potassium at pH 1; 3; 5; 9

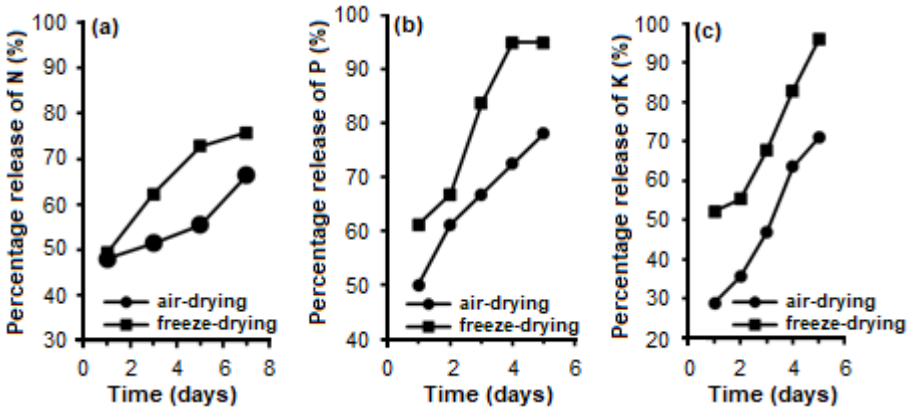

Fig 7. The release (a) nitrogen, (b) phosphor, (c) potassium by freeze, and air-drying method

air-dried hydrogels. It was clear that the pore formation in the freeze-drying method caused the absorption of the solvent leading to higher swelling ratio and caused the diffusion process to be more efficient.

■ CONCLUSION

The NPK release rate increased with the increase of NPK fertilizer concentration that were deposited in the hydrogel structure. The release of NPK from the hydrogel followed the Korsmeyer-Peppas model. The swelling ratio of the hydrogel at acidic pH was higher than at pH 9 due to the protonation of the $-NH_2$ group. The NPK release of the freeze-dried hydrogels showed higher release percentage as more pores in the structure of the hydrogel were formed compared to the air-drying method.

■ REFERENCES

[1] Khan, M.N., Mobin, M., Abbas, Z.K., and Alamri, S.A., 2018, "Fertilizers and their contaminants in soils, surface, and groundwater" in *Encyclopedia of the Anthropocene*, vol. 5, Eds. Dellasala, D.A., and Goldstein, M.I., Elsevier, Oxford, 225–240.

[2] Chen, J., Lü, S., Zhang, Z., Zhao, X., Li, X., Ning, P., and Liu, M., 2018, Environmetally friendly fertilizers: A review of materials used and their effects on the environment, *Sci. Total Environ.*, 613-614, 829–839.

[3] Wu, L., and Liu, M., 2008, Preparation and properties of chitosan-coated NPK compound fertilizer with controlled-release and water-retention, *Carbohydr. Polym.*, 72 (2), 240–247.

[4] Shaviv, A., and Mikkelsen, R.L., 1993, Controlled release fertilizers to increase efficiency of nutrient use and minimize environmental degradation: A review, *Nutr. Cycling Agroecosyst.*, 35, 1–12.

[5] Zhong, K., Lin, Z.T., Zheng, X.L., Jiang, G.B., Fang, Y.S., Mao, X.Y., and Liao, Z.W., 2013, Starch derivative-based superabsorbent with integration of water-retaining and controlled-release fertilizers, *Carbohydr. Polym.*, 92 (2), 1367–1376.

[6] Rashidzadeh, A., Olad, A., Salari, D., and Reyhanitabar, A., 2014, On the preparation and swelling properties of hydrogel nanocomposite based on sodium-alginate-g-poly(acrylic acid-co-acrylamide)/clinoptilolite and its application as slow release fertilizer, *J. Polym. Res.*, 21, 344.

[7] Dehkordi, K.D., and Seyyedboveir, S., 2013, Evaluation of super AB A 200 superabsorbent on water use efficiency and yield response factor of SCKaroun701 corn under deficit irrigation, *Adv. Environ. Biol.*, 7 (14), 4615–4622.

[8] Ahmed, E.M., 2015, Hydrogel: Preparation, characterization, and applications: A review, *J. Adv. Res.*, 6 (2), 105–121.

[9] Sun, Y., Kaplan, J.A., Shieh, A., Sun, H.L., Croce, C.M., Grinstaff, M.W., and Parquette, J.R., 2016, Self-assembly of a 5-fluorouracil-dipeptide hydrogel, *Chem. Commun.*, 52 (30), 5254–5257.

[10] Kim, S.H., Sun, Y., Kaplan, J.A., Grinstaff, M.W., and Parquette, J.R., 2015, Photo-crosslinking of a self-assembled coumarin-dipeptide hydrogel, *New*

J. Chem., 39 (5), 3225–3228.

[11] Verhulsel, M., Vignes, M., Descroix, S., Malaquin, L., Vignjevic, D.M., and Viovy, J.L., 2014, A review of microfabrication and hydrogel engineering for micro-organs on chips, *Biomaterials*, 35 (6), 1816–1832.

[12] Rajakumar, R., and Sankar, J., 2016, Hydrogel: Novel soil conditioner and safer delivery vehicle for fertilizers and agrochemicals – A review, *Int. J. Appl. Pure Sci. Agric.*, 2 (9), 163–172.

[13] Ray, S.S., 2013, *Environmentally Friendly Polymer Nanocomposites*, Series in Composites Science and Engineering, Woodhead Publishing, Cambridge, United Kingdom.

[14] Nguyen, T.T.T., Hosh, C., Hwang, S.G., Tran L.D., and Park, J.S., 2013, Characteristics of curcumin-loaded poly (lactic acid) nanofibers for wound healing, *J. Mater. Sci.*, 48, 7125–7133.

[15] Kean, T., and Thanou, M., 2010, Biodegradation, biodistribution, and toxicity of chitosan, *Adv. Drug Delivery Rev.*, 62 (1), 3–11.

[16] Ahmadi, F., Oveisi, Z., Samani, S.M., and Amoozgar, Z., 2015, Chitosan based hydrogels: Characteristic and pharmaceutical applications, *Res. Pharm. Sci.*, 10 (1), 1–16.

[17] Jose, S., Fangueiro, J.F., Smitha, J., Cinu, T.A., Chacko, A.J., Premaletha K., and Souto, E.B., 2012, Cross-linked chitosan microspheres for oral delivery of insulin: Taguchi design and in vivo testing, *Colloids Surf., B*, 92, 175–179.

[18] Shelma, R., and Sharma, C.P., 2010, Acyl modified chitosan derivatives for oral delivery of insulin and curcumin, *J. Mater. Sci. - Mater. Med.*, 21, 2133–2140.

[19] Jamelaa, S.R., and Jayakrishnan, A., 1995, Glutaraldehyde cross-linked chitosan microspheres as a long acting biodegradable drug delivery vechicle: Studies on the *in vitro* release of mitoxantrone and *in vivo* degradation of microspheres in rat muscle, *Biomaterials*, 16 (10), 769–775.

[20] Ratti, C., 2012, "Freeze drying process design" in *Handbook of Process Design*, Eds. Ahmed, J., and Rahman, M.S., John Willey & Sons, Hoboken, New Jersey, USA, 621–647.

[21] Adams, G.D., Cook, I., and Ward, K.R., 2015, The principles of freeze-drying, *Methods Mol. Biol.*, 1257, 121–143.

[22] Shukla, S., 2011, Freeze drying process: A review, *Int. J. Pharm. Sci. Res.*, 2 (12), 3061–3068.

[23] Wang, W., Chen, M., and Chen, G., 2012, Issues in freeze drying of aqueous solutions, *Chin. J. Chem. Eng.*, 20 (3), 551–559.

[24] Day, J.G., and Stacey, G., 2007, *Cryopreservation and Freeze-Drying Protocols*, Springer Science and Business Media, Berlin.

[25] Anonymous, 2005, *Water and waste water – Part 52: Test methods of nitrogen organic content by macro Kjedahl and titration*, National Standardization Agency, Indonesian National Standard (SNI) 06-6989.52-2005.

[26] Jamnongkan, T., and Kaewpirom, S., 2010, Controlled release fertilizer based on chitosan hydrogel: Phosphorus release kinetics, *Sci. J. UBU*, 1, 43–50.

[27] Rasool, A., Ata, S., Islam, A., Rizwan, M., Azeem, M.K., Mehmood, A., Khan, R.U., Qureshi, A.R., and Mahmood, H.A., 2020, Kinetics and controlled release of lidocaine from novel carrageenan and alginate-based blend hydrogels, *Int. J. Biol. Macromol.*, 145, 1–30.

[28] Akakuru, O.U., and Isiuku, B.O., 2017, Chitosan hydrogels and their glutaraldehyde-crosslinked counterparts as potential drug release and tissue engineering systems – Synthesis, characterization, swelling kinetics and mechanism, *J. Phys. Chem. Biophys.*, 7 (3), 1–7.

Preparation, Electronic Properties, and Powder-XRD Structure Analysis of 3,5-Bis(pyridin-2-yl)-H-1,2,4-triazoledichloridocopper(II)

Kristian Handoyo Sugiyarto[1,*], Isti Yunita[1], and Harold Andrew Goodwin[2]

[1]*Department of Chemistry Education, Universitas Negeri Yogyakarta, Jl. Colombo No. 1, Yogyakarta 55281, Indonesia*

[2]*School of Chemistry, UNSW, Sydney, NSW 2052, Australia*

* ***Corresponding author:***

tel: +62-8157935534
email: sugiyarto@uny.ac.id

Received: April 22, 2020
Accepted: May 30, 2020

DOI: 10.22146/ijc.55600

Abstract: *Salt of [Cu(*bptrzH*)Cl$_2$], (*bptrzH *= 3,5-bis(pyridin-2-yl)-H-1,2,4-triazole) has been prepared and characterized its electronic spectral and magnetic properties. This salt is paramagnetic with magnetic moment, μ_s, being 1.77–1.78 BM at 293 K, but decreased significantly with decreasing temperature to be 0.60–0.63 BM at 90 K, indicating antiferromagnetic nature. This is associated with Cu–Cu magnetic interactions at low temperatures, and suggests that the salt adopt an octahedrally polymeric structure. The electronic spectrum of this salt reveals a strong ligand field band centered at about 13,000 cm^{-1} and a very strong charge transfer absorption at about 23,000–24,000 cm^{-1}. The spectrum is better resolved at lower temperature and this is parallel to the slight change in color from yellowish-green at room temperature to bright green at low temperature (90 K). The powder XRD of this complex was refined by Le Bail method of Rietica program and found to be fit as triclinic symmetry of space group P$\bar{1}$ with the figure of merit: R_p = 5.02; R_{wp} = 7.95; R_{exp} = 5.40; Bragg R-Factor = 0.05; and GOF = 2.166.*

Keywords: *magnetic moment; copper(II);* bptrzH*; antiferromagnetic; spectrum; Rietica*

■ INTRODUCTION

The coordination chemistry of Cu(II) is of interest for many researchers, particularly due to the various 4-6 coordination numbers, its magnetism associated with ferro-/antiferro-magnetic property, the ability to form bi-poly nuclear compound, and strong Jahn-Teller distortion. In four coordination as in $[(C_2H_5)_2NH_2]_2[CuCl_4]$, the tetrachloridocuprate(II) was reported an interesting thermochromism from bright green at room- to low-temperatures to yellow on heating above 43 °C [1-2]. This is associated with the geometrical phase transition, square-planar (green) $\rightleftharpoons$ tetrahedral (yellow) in anionic tetrachloridocuprate(II). The phase transition is confirmed primarily due to organic counter-part change arrangement [3]. The driving force for this geometric transition is believed because of the cationic counterpart movements of particular organic species [2], while the thermochromic nature according to Bhattacharya et al., is evident due to the Jahn-Teller effects of Cu(II) and NH···Cl hydrogen bonds [4]. Since then, other studies also reported the thermochromic properties in other copper(II) compounds. Fabbrizzi et al. [5] observed continuous and discontinuous thermochromism of copper(II). The role of the organic counterpart cation to the tetrachloridocuprate(II) is then confirmed in other numerous compounds [6-11].

Another characteristic of copper(II) species is its ability to form numerous di-/poly-nuclear compounds which usually lead to typical magnetic interaction effect, that is ferro-/anti-ferromagnetic properties [12-15]. The d^9 system of Cu(II) is also well known to show structurally Jahn-Teller distortion as it has been observed in octahedral, trigonal bipyramidal, square-planar, and tetrahedral geometries, accompanying the phase transition and thus the importance in functional molecular and inorganic materials is of interest [16]. It should also be noted that the Cu(II) complexes discussed might involve bridging system Cu(II)-ligand-Cu(II) as well as interligand hydrogen bonds which might be considered to account of magnetic interactions. The organic compound, 3,5-bis(pyridine-2-yl)-1,2,4-triazole,

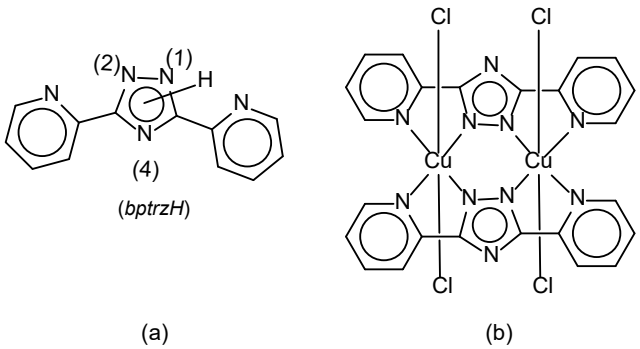

Fig 1. Possible asymmetrically flanking *bptrzH* (a) and dinuclear double bridging framework with $CuCl_2$ (b)

bptrzH (Fig. 1(a)) has been known as a ligand that can provide bridging-coordination to transition metal compounds due to conformation of the ligand [17]. Thus *bptrzH* might coordinate through N^2 and N^4 donor atoms leading to dinuclear single bridging (N^2, N_{py}, N^4, N_{py}') complex. It might also be possible to coordinate through N^1 and N^2 donor atoms leading to dinuclear double bridging (N_{py}, N^1-N^2, N_{py}')$_2$ when both pyridine rings are symmetrically flanking to the triazole ring (Fig. 1(b)). However, mononuclear meridional tris-bidentate, N_{py}, N^2, is also possible to occure [18-19].

Therefore, preparation of a complex containing this organic ligand with copper(II) chloride which has not been studied, is very promising characteristics at least associated with ferro and antiferro magnetic properties for the bridging complex. Moreover, the chloride ion may also act as a bridging anionic ligand. Hence, the combination of the two species, *bptrzH* and chloride ion is expected to produce Cu(II) complex with interesting properties.

■ EXPERIMENTAL SECTION

Materials

The main chemicals of picolinic acid hydrazide, 2-cyanopyridine, methanol, and $CuCl_2{\cdot}2H_2O$, were purchased from Sigma-Aldrich. All the reagents were used without initial purification.

Procedure for Preparation of the Complex

Preparation of ligand

The compound (*bptrzH*) was synthesized according to method of Kubota et al. [20]. A mixture of picolinic acid hydrazide, 6.857 g (0.05 mol), and 2-cyanopyridine, 52.055 g (0.5 mol, in excess), were heated together at 220–225 °C for about 10 h. After cooling, the solid was filtered, washed with cold ethanol, and dried in a vacuum desiccator. Recrystallization from ethanol resulted in white solid (mp. 196 °C uncorrected, lit. 209–211 °C).

*Preparation of complex [Cu(*bptrzH*)Cl_2]*

Into a well stirred methanolic solution of $CuCl_2{\cdot}2H_2O$, 0.341 g (2 mmol), was added dropwise of a methanolic solution of *bptrzH*, 0.233 g (1 mmol), whereupon the finely greenish-yellow powders came out readily. It was carefully filtered, washed with cold methanol, and then dried in aeration. (Sample 1 and 2 were separately prepared).

Instruments and Procedure of Physical Measurements

Physical characterization

Magnetic measurements. The magnetic data for solid samples were obtained using a Newport variable temperature Gouy balance equipped with cryostat containing liquid nitrogen for low-temperature measurements and calibrated with $CoHg(NCS)_4$. All data have been corrected for diamagnetism calculated using Pascal's constants. Molar susceptibilities (χ_M) were quoted in $cm^3\ mol^{-1}$ and the magnetic moments were calculated according to the relationship $\mu_{ef} = 2.828\ \sqrt{(\chi_M.T)}$ BM.

Electronic spectral measurements. Electronic spectra were recorded on a Zeiss PMQII spectrophotometer equipped with a diffuse reflectance accessory. Solid (powder) samples were spread on white filter paper and their spectra were calibrated against magnesium oxide. For low-temperature measurement a special brass attachment with silica glass windows was used. The fitting was sealed and a stream of cold nitrogen gas was passed over the assembly to prevent condensation. The fitting was then placed in contact with the base of an insulated brass dewar filled with liquid nitrogen and low-temperature measurement was made. In the measurement of spectra of the sample at room- and low-temperatures, the sample mounting was

not changed and hence any measured changes in intensities at different temperatures are significant even though the actual values for intensities are not.

Powder X-ray diffraction. The diffractogram of the complex was recorded by using a Rigaku Miniflex 600 40 kW 15 mA Benchtop Diffractometer, with CuK_α, λ = 1.5406 Å. The powdered sample was spread on the glass plate and then was placed on the cell holder. The reflection data were recorded in a scan mode at 2–80 (degree of 2θ) with interval of 0.04 steps per 4 sec for 2 h. The recorded diffractogram was then analyzed with the Rietica program of Le Bail method (5–80 degree of 2θ) which was run within 30 cycles.

■ RESULTS AND DISCUSSION

Elemental Analysis of *bptrzH* and the Complex

BptrzH was isolated as white solid having melting point (196 °C) close to the literature (209–211 °C). The elemental analysis was found to be C = 64.79 (64.56), H = 3.84 (4.06), and N = 31.05 (31.37)%, with calculated figures in the bracket for $C_{12}H_9N_5$. ^{1}H-NMR spectrum of this compound confirms the corresponding formula, showing four strong resonances at 7.3, 7.8, 8.4, and 8.8 ppm by integration ratio of 1:1:0.9:1 respectively. Thus, this corresponds to the four different positions of hydrogen atoms in pyridine rings. The weak and broad resonance at 13.6 ppm is believed to be due to the only one H(N) in the triazole ring [20].

Direct interaction of copper(II) chloride with *bptrzH* ($C_{12}H_9N_5$) in methanol resulted in greenish-yellow finely powder. The C–H–N elemental analysis, C = 38.90 (39.19), H = 1.97 (2.46), N = 18.71 (19.28)%, with calculated figures in the bracket for [Cu($C_{12}H_9N_5$)Cl_2], signify this complex formula.

Magnetic Moment

The effective magnetic moment for the complex at room temperature, μ_{293K}, is 1.77–1.78 BM. This is remarkably close to the spin-only value for one unpaired electron (μ_s = 1.73 BM) in d^9-octahedral configuration. The effective magnetic moment, however, is significantly temperature dependent, being gradually decreased with decreasing temperature to about 0.61–0.63 BM at 89–99 K, and increased with increasing temperature to about 1.85–1.92 BM at 353–373 K. The change in moment was found to be reversible as shown by the magnetic data listed in Table 1 which were recorded according to the order of measurements. The trend of decrease in the moment as displayed in Fig. 2 suggests the possibility of further decreases at very low temperatures.

The decreasing magnetic moment within the experimental temperatures in this compound is associated with the antiferromagnetic behavior due to the interaction of metal atoms, Cu-Cu. No effect of externally magnetic field is observed as shown by the moment values recorded with 15 A at 176–90 K (sample 1) and at 156–89 K (sample 2). As temperature is gradually lowered the Cu(II)-Cu(II) distance in the molecule becomes gradually shorter, and the interaction of the one unpaired electron in Cu(II)-Cu(II) becomes stronger. The magnetic interaction should be then an anti-parallel couple spin of electron, and as a result the magnetic moment is lowered. The reproducibility of this behavior in this complex is confirmed by magnetic data from the two samples (sample 1-2) which were separately prepared in different batch. This antiferromagnetic behavior is much the same as the plot of magnetic susceptibility with temperature in another octahedral dimer, [Cu(*bptrzH*)(CF_3SO_3)H_2O]$_2$ [18]. Such typical behavior

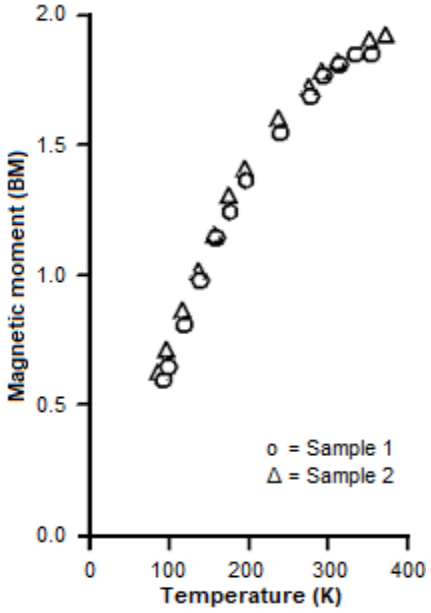

Fig 2. Magnetic moment of [Cu(*bptrzH*)Cl_2]

Table 1. Magnetic moment of [Cu(*bptrzH*)Cl_2] at various temperatures

Sample 1			Sample 2		
T/K	$\chi_M/10^{-6}$	μ_{ef}/BM	T/K	$\chi_M/10^{-6}$	χ_M/BM
293.2	1336	1.77	293.2	1359	1.78
176.3	1115	1.25	237.2	1346	1.60
176.3 (**15A**)*	1175	1.28	156.5	1072	1.16
90	500	0.60	156.5 (**15A**)*	1081	1.16
90 (**15A**)*	518	0.61	89	551	0.63
99	531	0.65	89 (**15A**)*	550	0.63
118.1	689	0.81	99	632	0.71
137.2	878	0.98	118.1	785	0.86
156.5	1052	1.15	137.2	952	1.02
195.8	1194	1.37	176.3	1219	1.31
237.2	1273	1.55	195.8	1272	1.41
275	1304	1.69	275	1352	1.72
313.2	1304	1.81	313.2	1326	1.82
333.2	1288	1.85	353.2	1286	1.90
353.2	1209	1.85	373.2	1245	1.92

* The moment was measured in different (electro)magnetic fields, by applying electric current 15 A vs 10 A, and it turned out to give relatively the same results, indicating that the magnetic properties do not depend on external magnetic field strength

in magnetism is very common for poly- or di-nuclear copper(II) with ligand other than *bptrzH* due to Cu-Cu interaction and the role of counterion [12-14,21], ferromagnetic-antiferromagnetic coupling [15-16] and ferromagnetic domain [22]. Thus, this complex is proposed to be dimer [Cu(*btrzH*)Cl_2]$_2$ (as in Fig. 1(b)) following Prins et al. [18].

Electronic Spectrum

The electronic spectrum of this complex, [Cu(*bptrzH*)Cl_2], as shown in Fig. 3, reveals two well resolved of absorption bands. The peak at lower energy which is relatively asymmetrical band centered at around 13,000 cm^{-1} should be the octahedral ligand-field band attributed as $^2E_g \rightarrow {}^2T_{2g}$ while the one centered at much higher energy, around 23,000–24,000 cm^{-1} might be associated with the "charge-transfer" band of metal-ligand, π-π*, and this is what dominates the greenish yellow color of this species. A very clear shoulder band at around 16000 cm^{-1} might be associated with Jahn-Teller distortion [16,23-24] due to primarily asymmetrical electronic configuration in e_g^3 orbitals.

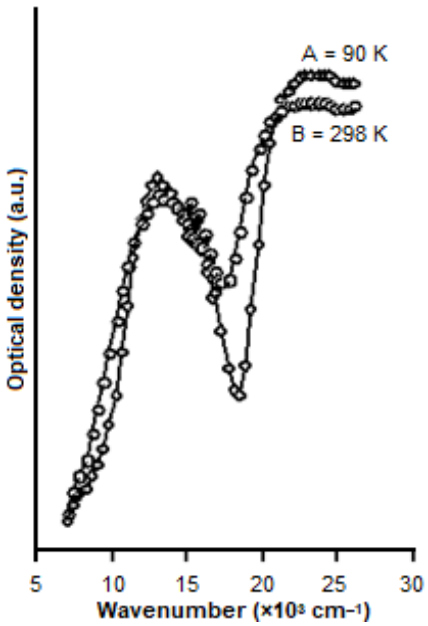

Fig 3. Electronic spectra of [Cu(*bptrzH*)Cl_2]

Structural Analysis

The complex compound resulted from interaction of copper(II) chloride and *bptrzH* apparently does not dissolve in a various commonly known solvents, water,

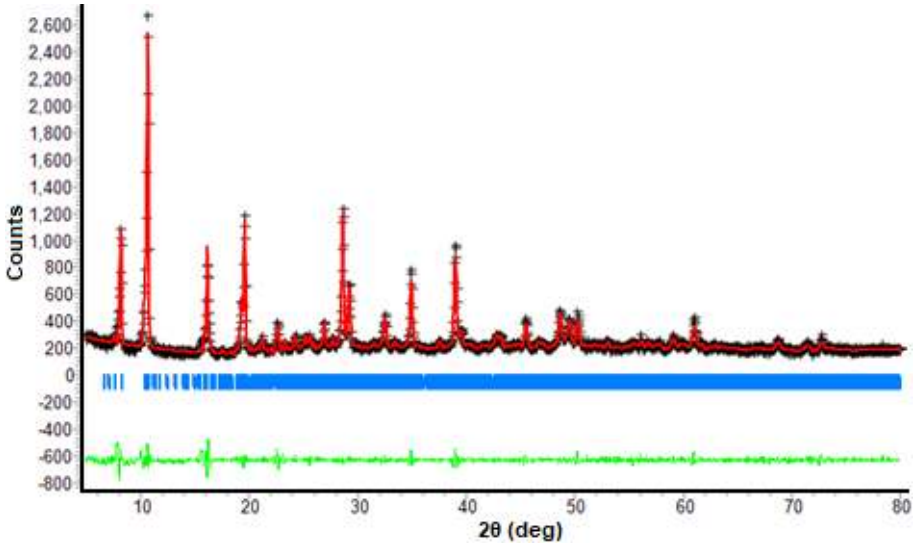

Fig 4. Diffractogram of [Cu(*bptrzH*)Cl_2]. The black signs (+) represent the observed-experimental data, the red full line is the calculated refinement at 5–80° of 2θ for the expected model of triclinic symmetry of space group PĪ which are the blue bar-lines, and the green curve-line indicates the differences between the observed diffractogram and the refinement

nitromethane, ethanol, methanol, acetone, acetonitrile, and so far attempt to grow a single crystal was unsuccessful. Structural analysis was then performed from its powder XRD. This is quite common for the oxides compounds following Rietveld method [e.g. 25-27]. However, it has been applied to that of iron(II) complex [28] quite recently and found to be a significant result. Since then, referring to the suggestion by Toby as well [29], application of this method has been extensively performed to some powdered complexes [30-38] and the results were found to be reasonably acceptable.

For these reasons, the powder X-ray diffraction of this complex was then recorded and the diffractogram together with its refinement following Le Bail method of Rietica program is shown in Fig. 4. It is obvious that the calculated red full line does almost pass through the black experimentally observed data, and this is confirmed by the almost linear green-curve line which reflects the tiny difference between both data. This suggests that the refinement is considerably fit for triclinic symmetry of space group PĪ with Goodness of Fitting (GOF) 2.166, derived Bragg R-Factor 0.05, and low figures of merit: R_p = 5.02, R_{wp} = 7.95, and R_{exp} = 5.40. The detailed cell parameters are: a = 10.83314 Å; b = 13.5746 Å; c = 14.5156 Å; α = 112.3884°; β = 86.0523°; γ = 94.8069°; V = 1965.1938 Å^3; and Z = 2 (Table 2).

Table 2. Detailed cell parameters of (a), [Cu(*bptrzH*)$_2$$Cl_2$], and (b)

Compound	(a)	(b) [18]
Symmetry	Triclinic	Triclinic
Space Group	PĪ	PĪ
a (Å)	10.8331	8.841(3)
b (Å)	13.5746	14.132(6)
c (Å)	14.5156	14.382(6)
V (Å^3)	1965.1938	1606(1)
α (°)	112.3884	112.58(3)
β (°)	86.0523	92.23(3)
γ (°)	94.8069	102.45(3)
R_p	5.02	
R_{wp}	7.95	
R_{exp}	5.40	
Z	2	2 (dimer)
GOF: χ^2	2.166	
R_{Bragg}	0.05	

(b) [Cu(*bptrzH*)(CF_3SO_3)(H_2O)]$_2$

The antiferromagnetic interaction of Cu(II) at lower temperatures suggests that this complex is likely to adopt a dimer of [Cu(*bptrzH*)Cl_2]$_2$ (Fig. 1(b)) following the structure of [Cu(*bptrzH*)(CF_3SO_3)(H_2O)]$_2$ [18]

which is known as dinuclear double bridging as also observed in spin crossover system of $[Fe_2(bptrz)_2Cl_4]$ [19].

■ CONCLUSION

The complex of [Cu (*bptrzH*)Cl_2] has been successfully isolated as greenish-yellow finely powder from the reaction of copper(II) chloride with the *bptrzH* ligand which is insoluble in some common solvents. The complex shows antiferromagnetic Cu-Cu interactions with magnetic moment of 1.78 BM at 293 K and gradually down with temperatures to 0.63 BM at 90 K. It is believed to have a geometrical structure of dinuclear double bridging octahedral coordination.

■ ACKNOWLEDGMENTS

Thanks to the Department of Inorganic Chemistry, the School of Chemistry, UNSW - Australia, which provided this research facility

■ REFERENCES

[1] Willett, R.D., Haugen, J.A., Lebsack, J., and Morrey, J., 1974, Thermochromism in copper(II) chlorides. Coordination geometry changes in $CuCl_4^{2-}$ anions, *Inorg. Chem.*, 13 (10), 2510–2513.

[2] Willett, R.D., Ferraro, J.R., and Choca, M., 1974, Pressure studies on the thermochromic salt $[(CH_3)_2CHNH_3]_2CuCl_4$, a compound with three phases containing distinctly different $CuCl_4^{2-}$ stereochemical configurations, *Inorg. Chem.*, 13 (12), 2919–2921.

[3] Ding, J., Li, H.S., Wen, L.W., Kang, X.B., Li, H.D., and Zhang, J.M., 2013, Electronic and magnetic properties of an organic multiferroic: $(C_2H_5NH_3)_2CuCl_4$, *J. Magn. Magn. Mater.*, 346, 91–95.

[4] Bhattacharya, R., Ray, M.S., Dey, R., Righi, L., Bocelli, G., and Ghosh, A., 2002, Synthesis, crystal structure and thermochromism of benzimidazolium tetrachlorocuprate: $(C_7H_7N_2)_2[CuCl_4]$, *Polyhedron*, 21 (25-26), 2561–2565.

[5] Fabbrizzi, L., Micheloni, M., and Paoletti, P., 1974, Continuous and discontinuous thermochromism of copper(II) and nickel(II) complexes with *N,N*-diethyl ethylenediamine, *Inorg. Chem.*, 13 (12), 3019–3021.

[6] Hamdi, M., Oueslati, A., Chaabane, I., and Hlel, F., 2012, Characterization and electrical properties of $[C_6H_9N_2]_2CuCl_4$ compound, *ISRN Condens. Matter Phys.*, 2012, 750497.

[7] Lee, C.H., Lee, K.W., and Lee, C.E., 2003, Quasi-two-dimensional magnetism in $(C_nH_{2n+1}NH_3)_2CuCl_4$ studied by electron paramagnetic resonance, *Curr. Appl. Phys.*, 3 (6), 477–479.

[8] Zolfaghari, P., de Wijs, G.A., and de Groot, R.A., 2013, The electronic structure of organic-inorganic hybrid compounds: $(NH_4)_2CuCl_4$, $(CH_3NH_3)_2CuCl_4$ and $(C_2H_5NH_3)_2CuCl_4$, *J. Phys. Condens. Matter*, 25 (29), 295502.

[9] Aldrich, E.P., Bussey, K.A., Connell, J.R., Reinhart, E.F., Oshin, K.D., Mercado, B.Q., and Oliver, A.G., 2016, Crystal structure of the thermochromic bis(diethylammonium) tetrachloridocuprate(II) complex, *Acta Cryst. E*, 72 (1), 40–43.

[10] Vishwakarma, A.K., Kumari, R., Ghalsasi, P.S., and Arulsamy, N., 2017, Crystal structure, thermochromic and magnetic properties of organic-inorganic hybrid compound: $(C_7H_7N_2S)_2CuCl_4$, *J. Mol. Struct.*, 1141, 93–98.

[11] Kapustyanyk, V.B., and Korchak, Y.M., 2000, Thermochromic phase transition in $[NH_2(C_2H_5)_2]_2$ $CuCl_4$ crystals, *J. Appl. Spectrosc.*, 67 (6), 1045–1049.

[12] Zhang, L., Bu, W.M., Yan, S.P., Jiang, Z.H., Liao, D.Z., and Wang, G.L., 2000, Weaker magnetic interactions of oxalato-copper(II) binuclear compounds: Synthesis, spectroscopy, crystal structure and magnetism, *Polyhedron*, 19 (9), 1105–1110.

[13] Julve, M., Gleizes, A., Chamoreau, L.M., Ruiz, E., and Verdaguer, M., 2017, Antiferromagnetic interactions in copper(II) μ-oxalato dinuclear complexes: The role of the counterion, *Eur. J. Inorg. Chem.*, 2018 (3-4), 509–516.

[14] Gusev, A.N., Nemec, I., Herchel, R., Shul'gin, V.F., Ryush, I., Kiskin, M., Efimov, N., Ugolkova, E., Minin, V., Lyssenko, K., Eremenko, I., and Linert, W., 2019, Copper(II) self-assembled clusters of bis((pyridin-2-yl)-1,2,4-triazol-3-yl)alkanes. Unusual

rearrangement of ligand upon reaction condition, *Dalton Trans.*, 48 (9), 3052–3060.

[15] Chaudhuri, P., Wagner, R., and Weyhermüller, T., 2007, Ferromagnetic *vs* antiferromagnetic coupling in bis(μ-phenoxo)dicopper(II) complexes. Tuning of the nature of exchange coupling by remote ligand substituents, *Inorg. Chem.*, 46 (13), 5134–5136.

[16] Halcrow, M.A., 2013, Jahn-Teller distortions in transition metal compounds, and their importance in functional molecular and inorganic materials, *Chem. Soc. Rev.*, 42 (4), 1784–1795.

[17] Chen, J.C., Hu, S., Zhou, A.J., Tong, M.L., and Tong, Y.X., 2006, Synthesis, crystal structures, and magnetic properties of three new iron complexes derived from 3,5-bis(pyridin-2-yl)-1,2,4-triazole, *Z. Anorg. Allg. Chem.*, 632 (3), 475–481.

[18] Prins, R., Birker, P.J.M.W.L., Haasnoot, J.G., Verschoor, G.C., and Reedijk, J., 1985, Magnetic properties of dimeric disubstituted-triazole copper(II) compounds. X-ray structure of bis[μ-3,5-bis(pyridin-2-yl)-1,2,4-triazolato-*N*',*N*^{1},*N*^{2},*N*'']-bis[aqua(trifluoro methanesulfonato-*O*)copper(II)], *Inorg. Chem.*, 24 (24), 4128–4133.

[19] Kitchen, J.A., and Brooker, S., 2008, Spin crossover in iron(II) complexes of 3,5-di(2-pyridyl)-1,2,4-triazoles and 3,5-di(2-pyridyl)-1,2,4-triazolates, *Coord. Chem. Rev.*, 252 (18-20), 2072–2092.

[20] Kubota, S., Uda, M., and Nakagawa, T., 1975, 1,2,4-Triazoles. V. Nuclear magnetic resonance study of *N*-methyl derivatives of 1,2,4-triazoles, *J. Heterocycl. Chem.,* 12 (5), 855–860.

[21] Zhou, J.H., Cheng, R.M., Song, Y., Li, Y.Z., Yu, Z., Chen, X.T., Xue, Z.L., and You, X.Z., 2005, Syntheses, structures, and magnetic properties of unusual nonlinear polynuclear copper(II) complexes containing derivatives of 1,2,4-triazole and pivalate ligands, *Inorg. Chem.*, 44 (22), 8011–8022.

[22] Aqeel, A., Akhtar, N., Polyakov, A.O., Rudolf, P., and Palstra, T.T.M., 2018, Magnetic functionality of thin film perovskite hybrids, *APL Mater.*, 6 (11), 114206.

[23] Conradie, J., Conradie, M.M., Tawfiq, K.M., Coles, S.J., Tizzard, G.J., Wilson, C., and Potgieter, J.H., 2018, Jahn-Teller distortion in 2-pyridyl-(1,2,3)-triazole-containing copper(II) compounds, *New J. Chem.*, 42 (19), 16335–16345.

[24] Scăeţeanu, G.V., Chifiriuc, M.C., Bleotu, C., Kamerzan, C., Măruţescu, L., Daniliuc, C.G., Maxim, C., Calu, L., Olar, R., and Badea, M., 2018, Synthesis, structural characterization, antimicrobial activity, and in vitro biocompatibility of new unsaturated carboxylate complexes with 2,2′-bipyridine, *Molecules*, 23 (1), 157.

[25] Aughterson, R.D., Lumpkin, G.R., de los Reyes, M., Sharma, N., Ling, C.D., Gault B., Smith, K.L., Avdeev, M., and Cairney, J.M., 2014, Crystal structures of orthorhombic, hexagonal, and cubic compounds of the $Sm_{(x)}Yb_{(2-x)}TiO_5$ series, *J. Solid State Chem.*, 213, 182–192.

[26] Lüdtke, T., Weber, D., Schmidt, A., Müller, A., Reimann, C., Becker, N., Bredow, T., Dronskowski, R., Ressler, T., and Lerch, M., 2017, Synthesis and characterization of metastable transition metal oxides and oxide nitrides, *Z. Kristallogr. Cryst. Mater.*, 232 (1-3), 3–14.

[27] Purwaningsih, S.Y., Rosidah, N., Zainuri, M., Triwikantoro, T., Pratapa, S., and Darminto, D., 2019, Comparation of X-ray diffraction pattern refinement using Rietica and MAUD of ZnO nanoparticles and nanorods, *J. Phys. Conf. Ser.*, 1153, 012070.

[28] Grosjean, A., Négrier, P., Bordet, P., Etrillard, C., Mondieig, D., Pechev, S., Lebraud, E., Létard, J.F., and Guionneau, P., 2012, Crystal structures and spin crossover in the polymeric material $[Fe(Htrz)_2(trz)](BF_4)$ including coherent-domain size reduction effects, *Eur. J. Inorg. Chem.*, 2013 (5-6), 796–802.

[29] Toby, B.H., 2006, R factors in Rietveld analysis: How good is good enough?, *Powder Diffr.*, 21 (1), 67–70.

[30] Sugiyarto, K.H., Saputra, H.W., Permanasari, L., and Kusumawardani, C., 2017, Structural analysis of powder complex of $[Mn(phen)_3](CF_3SO_3)_2{\cdot}6.5H_2O$, *AIP Conf. Proc.*, 1847, 040006.

[31] Kusumawardani, C., Permanasari, L., Fatonah S.D., and Sugiyarto, K.H., 2017, Structural analysis of

powder complex of tris(1,10-phenanthroline) copper(II) trifluoromethane sulfonate dihydrate, *Orient. J. Chem.*, 33 (6), 2841–2847.

[32] Kusumawardani, C., Kainastiti, F., and Sugiyarto, K.H., 2018, Structural analysis of powder complex of $[Cu(bipy)_3](CF_3SO_3)_2(H_2O)_x$ (x = 0.5, 1), *Chiang Mai J. Sci.*, 45 (4),1944–1952.

[33] Sutrisno, H., Kusumawardani, C., Rananggana, R.Y., and Sugiyarto, K.H., 2018, Structural analysis of powder tris(phenanthroline)nickel(II) trifluoro acetate, *Chiang Mai J. Sci.*, 45 (7), 2768–2778.

[34] Sugiyarto, K.H., Kusumawardani, C., Sutrisno, H., and Wibowo, M.W.A., 2018, Structural analysis of powdered manganese(II) of 1,10-phenanthroline (phen) as ligand and trifluoroacetate (TFA) as counter anion, *Orient. J. Chem.*, 34 (2), 735–742.

[35] Sugiyarto, K.H., Kusumawardani, C., and Wulandari, K.E., 2018, Synthesis and structural analysis of powder complex of tris(bipyridine) cobalt(II) trifluoromethanesulfonate octahydrate, *Indones. J. Chem.,* 18 (4), 696–701.

[36] Sugiyarto, K.H., Kusumawardani, C., Wigati, H., and Sutrisno, H., 2019, Structural study of the powder complex of Cu(II)-1,10-phenanthroline-trifluoroacetate, *Orient. J. Chem.*, 35 (1), 325–331.

[37] Louise, I.S.Y., Nabila, S., and Sugiyarto, K.H., 2019, Complex of tris(phenanthroline)cobalt(II) trifluoro acetate: Characterisation and powder XRD analysis, *Orient. J. Chem.*, 35 (5), 1500–1507.

[38] Sugiyarto, K.H., Louise, I.S.Y., and Wilujeng, S.S., 2020, Preparation and powder XRD analysis of tris (2,2'-bipyridine)nickel(II) trifluoroacetate, *Indones. J. Chem.*, 20 (4), 833–841.

Supplementary Data

This supplementary data is a part of paper entitled "Virtual Screening of the Indonesian Medicinal Plant and Zinc Databases for Potential Inhibitors of the RNA-Dependent RNA Polymerase (RdRp) of 2019 Novel Coronavirus".

Table S1. Hydrogen bond occupancy of between ligand and receptor

Remdesivir (RDM)

Acceptor	Donor	Percentage (%)	Distance (Å)	Angle
TYR_560@O	LIG_1079@H34: @O33	97.5	2.6466	158.6022
ASP_559@OD2	LIG_1079@H42: @O41	87.73	2.6095	164.6033
ASP_701@OD1	LIG_1079@H36: @O35	65.33	2.572	167.4986
ASP_559@OD1	LIG_1079@H40: @O39	61.66	2.5706	168.1091
ASP_701@OD2	LIG_1079@H36: @O35	33.79	2.5828	167.1641
LIG_1079@O37	ARG_496@HH22: @NH2	18.55	2.8256	156.0252
LIG_1079@O33	CYS_563@H: @N	14.74	2.922	159.5935
LIG_1079@O37	ARG_496@HH12: @NH1	12.22	2.8363	154.439
ASP_559@OD1	LIG_1079@H42: @O41	10.71	2.5992	166.0198

ZINC1529045114

Acceptor	Donor	Percentage (%)	Distance (Å)	Angle
LIG_1079@O11	ARG_496@HH11: @NH1	45.55	2.8161	160.3069
LIG_1079@N7	ARG_565@HH21: @NH2	30.18	2.8914	151.6928
ASP_701@OD1	LIG_1079@H23: @O15	29.6	2.6544	162.9622
ASP_393@OD2	LIG_1079@H26: @N9	29.58	2.8336	154.8585
ASP_564@OD2	LIG_1079@H15: @N4	28.95	2.7219	159.6432
ASP_559@OD1	LIG_1079@H7: @O7	23.96	2.6534	165.5095
ASP_701@OD2	LIG_1079@H21: @O14	22.52	2.7076	159.0275
ASP_701@OD1	LIG_1079@H21: @O14	19	2.7394	158.8832
LIG_1079@O15	SER_700@HG: @OG	17.66	2.783	158.7613
LIG_1079@O17	ARG_565@HH11: @NH1	13.74	2.914	159.1019
ASP_393@OD1	LIG_1079@H26: @N9	13.26	2.8326	157.1251
TYR_560@O	LIG_1079@H5: @O6	12.98	2.712	158.0925
ASP_564@OD1	LIG_1079@H16: @N4	12.92	2.7262	161.7094
ASP_559@OD2	LIG_1079@H16: @N4	12.63	2.7354	162.14
ASP_564@OD1	LIG_1079@H15: @N4	12.57	2.7371	159.6196
ASP_564@OD1	LIG_1079@H23: @O15	12.47	2.6626	161.8866
ASP_559@OD2	LIG_1079@H15: @N4	12	2.742	163.0233

ZINC169730811

Acceptor	Donor	Percentage (%)	Distance (Å)	Angle
ASP_702@OD2	LIG_1079@H7: @O7	80.78	2.6585	163.4954
ASP_702@OD2	LIG_1079@H5: @O6	45.58	2.6486	162.1343
LYS_492@O	LIG_1079@H25: @N4	32.53	2.8454	160.469
LIG_1079@N5	SER_490@HG: @OG	25.2	2.839	158.8034
ARG_494@O	LIG_1079@H24: @N4	22.69	2.8325	151.8958
LIG_1079@N3	SER_490@HG: @OG	22	2.7854	158.4971
ARG_494@O	LIG_1079@H21: @O11	18.99	2.6927	162.3982
ASP_701@O	LIG_1079@H5: @O6	18.38	2.7158	161.0261
LIG_1079@O1	ARG_777@HH21: @NH2	17.89	2.817	153.8028
LIG_1079@O1	ARG_777@HH11: @NH1	17.45	2.8169	153.3582
LIG_1079@O7	SER_755@H: @N	17.21	2.9072	150.621

9-Ribosyl-trans-zeatin

Acceptor	Donor	Percentage (%)	Distance (Å)	Angle
GLU_752@O	LIG_1079@H3*: @O3*	37.66	2.7351	162.4237
GLU_752@O	LIG_1079@H2*: @O2*	29.31	2.7178	160.6939
ASP_702@OD2	LIG_1079@H3*: @O3*	23.14	2.6916	164.9356
TRP_558@O	LIG_1079@H5*: @O5*	15.34	2.7385	158.6033
ASP_702@OD2	LIG_1079@H2*: @O2*	15.24	2.6704	159.5671

Table S2. The results of cluster analysis

Remdesivir (RDM)

#Cluster	Frames	Frac	AvgDist	Stdev	Centroid	AvgCDist
0	20000	1	1.696	0.337	10516	0

ZINC1529045114

#Cluster	Frames	Frac	AvgDist	Stdev	Centroid	AvgCDist
0	20000	1	1.788	0.32	8765	0

ZINC169730811

#Cluster	Frames	Frac	AvgDist	Stdev	Centroid	AvgCDist
0	20000	1	1.834	0.385	13887	0

9-Ribosyl-trans-zeatin

#Cluster	Frames	Frac	AvgDist	Stdev	Centroid	AvgCDist
0	20000	1	1.821	0.472	14033	0

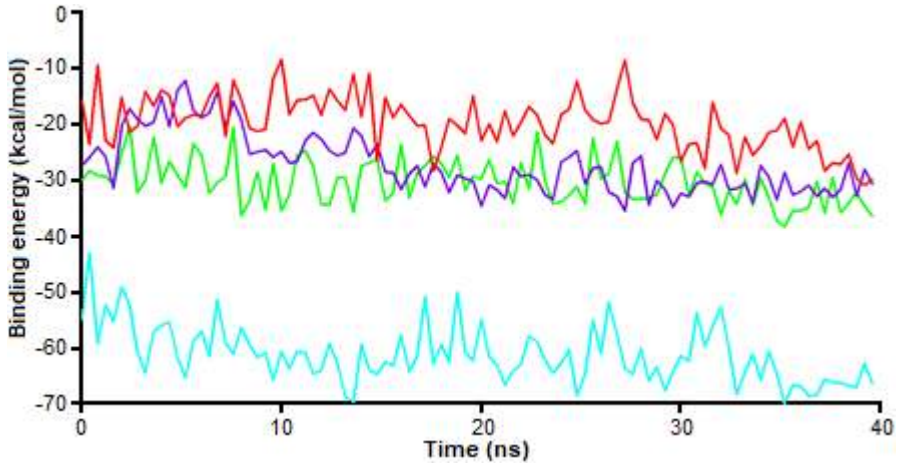

Fig S1. Plot of MM-PBSA binding energy (kcal/mol) versus time in which RDM, ZINC1529045114, ZINC169730811, and 9-Ribosyl-trans-zeatin assigned as red, green, blue, and purple, respectively

Virtual Screening of the Indonesian Medicinal Plant and Zinc Databases for Potential Inhibitors of the RNA-Dependent RNA Polymerase (RdRp) of 2019 Novel Coronavirus

Muhammad Arba[1,*], Andry Nur-Hidayat[1], Ida Usman[2], Arry Yanuar[3], Setyanto Tri Wahyudi[4], Gilbert Fleischer[5], Dylan James Brunt[5], and Chun Wu[5,]**

[1]*Faculty of Pharmacy, Universitas Halu Oleo, Kendari 93232, Indonesia*

[2]*Department of Physics, Universitas Halu Oleo, Kendari 93232, Indonesia*

[3]*Faculty of Pharmacy, Universitas Indonesia, Depok 16424, Indonesia*

[4]*Department of Physics, IPB University, Bogor 16680, Indonesia*

[5]*Department of Molecular & Cellular Biosciences, College of Science and Mathematics, Rowan University, Glassboro, New Jersey 08028, United States*

* ***Corresponding author:***

email: muh.arba@uho.ac.id; wuc@rowan.edu***

Received: May 16, 2020
Accepted: August 3, 2020

DOI: 10.22146/ijc.56120

Abstract: *The novel coronavirus disease 19 (Covid-19) which is caused by severe acute respiratory syndrome coronavirus 2 (SARS-CoV-2) has been a pandemic across the world, which necessitate the need for the antiviral drug discovery. One of the potential protein targets for coronavirus treatment is RNA-dependent RNA polymerase. It is the key enzyme in the viral replication machinery, and it does not exist in human beings, therefore its targeting has been considered as a strategic approach. Here we describe the identification of potential hits from Indonesian Herbal and ZINC databases. The pharmacophore modeling was employed followed by molecular docking and dynamics simulation for 40 ns. 151 and 14480 hit molecules were retrieved from Indonesian herbal and ZINC databases, respectively. Three hits that were selected based on the structural analysis were stable during 40 ns, while binding energy prediction further implied that ZINC1529045114, ZINC169730811, and 9-Ribosyl-trans-zeatin had tighter binding affinities compared to Remdesivir. The ZINC169730811 had the strongest affinity toward RdRp compared to the other two hits including Remdesivir and its binding was corroborated by electrostatic, van der Waals, and nonpolar contribution for solvation energies. The present study offers three hits showing tighter binding to RdRp based on MM-PBSA binding energy prediction for further experimental verification.*

Keywords: *Covid-19; herbal; ZINC; RdRp,* in silico*; coronavirus*

■ INTRODUCTION

The novel coronavirus disease in 2019 (Covid-19) which is caused by severe acute respiratory syndrome coronavirus 2 (SARS-CoV-2) has been declared as a pandemic across the world as it impacts all countries worldwide with more than two million people infected and hundred thousand fatalities [1]. The current situation still has the potential to elevate considering its rapid contagious nature and no drug or vaccine for this particular coronavirus has been found until recently. This necessitates the urgent effort to find small molecules with the potential to inhibit specific proteins of the coronavirus.

Antiviral drug discovery including the 2019 novel coronavirus is subjected to the specific proteins responsible for the viral life cycle continuation. One of the druggable proteins with the potential to target is RNA-dependent RNA polymerase (RdRp) which belongs to the nucleic acid polymerase. The crucial function of RdRp is its role in catalyzing the synthesis of the viral

RNA which is required for viral replication [2-3]. The protein exists in the virus and fortunately not in the host (human body). Therefore, targeting RdRp is considered to have a high potential to inhibit the coronavirus life cycle.

Several small molecules that target RdRp have been reported such as Remdesivir and Sofosbuvir. Remdesivir is a nucleoside analog prodrug and it is reportedly to inhibit SARS-CoV and MERS-CoV [4-5]. Sofosbuvir, on the other side, is a nucleotide analog prodrug, which targets the hepatitis C virus (HCV) infection through HCV NS5B RdRp [6-7]. As it is known that the 2019 nCov-2 coronavirus is a single-strand RNA virus that shares structural similarity with RdRp of Hepatitis-C-Virus (HCV), Ebola, dengue virus, and rhinoviruses, those drugs were also projected for the treatment of the 2019 nCoV-2. However, since the coronavirus is well known for its highly adaptive capability for modified nucleotide analog, the need for novel prompt SARS-CoV-2 antiviral drug discovery was inevitable. Here we performed *in silico* screening based on the pharmacophore features of Remdesivir to find potential compounds for inhibiting RdRp protein. The obtained hits were subjected to molecular docking and molecular dynamics simulation confirmation. We identified several hits molecules with better affinities than Remdesivir according to Molecular Mechanics-Poisson Boltzmann Surface Area (MM-PBSA) protocol.

■ COMPUTATIONAL METHODS

Pharmacophore modeling was performed with the aid of LigandScout 4.3 [8] and the Pharmit web server [9]. In both applications, the structure of Remdesivir (RDM) was used to model pharmacophore. Several pharmacophore features were selected based on the RDM structure and its interaction with the RdRp 2019 nCov2. The 'Max hits per conf' was set to 1 in case of using the Pharmit web server. The selected features were used for screening against the Indonesian Herbal Database (http://herbaldb.farmasi.ui.ac.id/) [10-11] and ZINC [12] databases and the retrieved molecules were submitted for molecular docking. The iDock [13] software was employed for the docking study. The iDock essentially uses the AutoDock Vina machine while adding some features which enable automatic docking of a large compound library. The PDB structure of the RdRp of 2019 novel coronavirus was retrieved from the RCSB protein database using PDB ID 6M71 [14]. Protein structure preparation including adding polar hydrogen atoms and assigning Kollman charges was carried out by using the AutoDock tool (ADT) and the structure was saved in PDBQT format. The grid box for the docking study was defined by following the study of Gao et al. (2020) [14] who indicated the interaction of RDM with the 2019 coronavirus RdRP structure with a grid box size of (x = 40, y = 40, z = 40) and center of (x = 116.02, y = 118.37, z = 127.80) was set which encompass the Remdesivir (RDM) binding site. All ligands were converted to PDBQT format using Open Babel version 2.4.1. Docking analysis was conducted with the Discovery Studio Visualizer 2016.

Prediction of ADME (Absorption, Distribution, Metabolism, Excretion) properties for the two best compounds from ZINC and one compound from HerbalDB databases was performed by using the SwissADME web server (http://www.swissadme.ch) which is developed by the Swiss Institute of Bioinformatics [15]. Each SMILE file of the compound was submitted to the webserver to generate the ADME properties.

The top docked molecules in complex with RdRp and native RdRp were subjected to molecular dynamics (MD) simulation for 40 ns using Amber16 with a time step of 2 fs, periodic boundary conditions, Lennard-Jones (LJ) cutoff of 0.9 nm, and the particle mesh Ewald by following our previous procedure [16]. The ff14SB [17] and GAFF2 [18] were used to assign protein and ligand, respectively. Neutralization was done by introducing sodium ions, while solvation was conducted using the TIP3P water model. Energy minimization was carried out in three steps. The first minimization was carried out using 6000 steps consisting of 500 steepest descent and 5500 steps of the conjugate gradient with protein restrained. Second and third minimization was done using the same steps as the first minimization with the main atoms of protein restrained and without restraint, respectively. After minimization, the system was heated

to 300 K in 150 ps, which was followed by 200 ps equilibration. The final production step was done for 40 ns in the NPT ensemble using pmemd.cuda module of Amber16. Root Mean Square Deviation (RMSD), Root Mean Square Fluctuation (RMSF), hydrogen bond analysis was done using the cpptraj module [19] of Amber16. Also, we performed cluster analysis based on the DBScan algorithm to evaluate the consistency of the initial conformation during the 40 ns MD simulation using the cpptraj module. We used 15 *minpoints* as a threshold to form a cluster with *epsilon* 2.5 Å as distance cutoff for forming a cluster. The PDB structure with the highest chance of occurrence was extracted and employed it as the conformation during 40 ns MD simulation. Finally, the MD trajectory was employed for binding free energy calculation during 40 ns using Molecular Mechanics-Poisson Boltzmann solvent accessible surface area (MM-PBSA) method [19-21] as implemented in MMPBSA.py module of Amber16 software. Considering the highly charged binding interface of ligand-RdRp complex, we employed the solute dielectric constant 4 in the MM-PBSA binding energy calculation.

■ RESULTS AND DISCUSSION

The study was initiated with the analysis of the structure of Remdesivir (RDM). It is known that RDM is a prodrug and when binding to RdRp, it is converted to its tri-phosphate form. Therefore, the active form of RDM was used for further analysis. Fig. 1 displays the structure of RDM and its active form.

The pharmacophore features of RDM consisted of one aromatic ring, five hydrogen bond donor, sixteen hydrogen bond acceptor, three negative ions (phosphate atoms), and one hydrophobic feature. However, only five features were selected in LigandScout 4.3 to increase the potential hit molecules gain, which includes one aromatic, one hydrogen bond donor, and three hydrogen bond acceptors. Screening against the Indonesian Herbal database resulted in 151 hit molecules gain. The same features were employed when screening using the Pharmit web server, in which screening against the ZINC database retrieved 14480 hit molecules. Fig. 2 displays the selected features of pharmacophore in the LigandScout 4.3 and Pharmit web server.

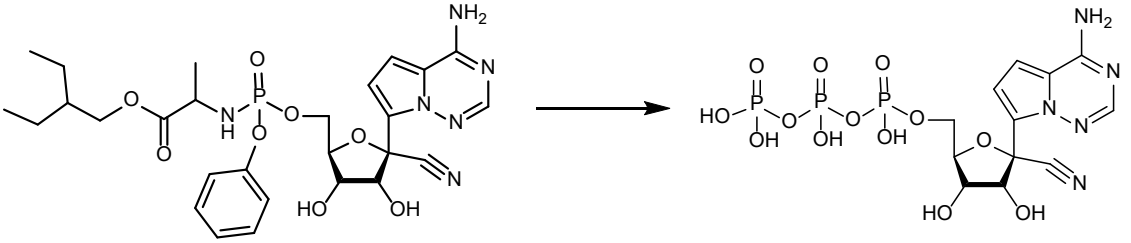

Fig 1. The 2D structures of Remdesivir (left) and its active form (right)

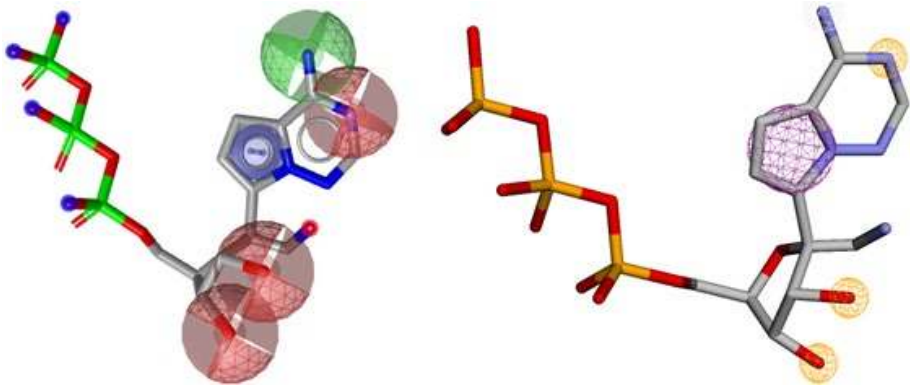

Fig 2. The pharmacophore features selected for screening with one aromatic (blue and purple circles), one hydrogen bond donor (green and white circles), and three hydrogen bond acceptors (red and yellow circles) features employed for screening in LigandScout and Pharmit web server, respectively

Molecular docking of 14480 hits molecules and 151 molecules retrieved from ZINC and Indonesian Herbal databases, respectively, was performed in the putative of the binding site of RDM. It is known that the structure of RNA-dependent RNA polymerase of SARS-CoV-2 form "right hand" conformation and contains three domains, which is similar to the structure of SARS coronavirus (SARS-CoV) [14,20-21]. A finger subdomain spans from Ser397 to Ala581 and Lys621 to Gly679, a palm subdomain is located at Thr582 to Pro620 and Thr680 to Gln815, while the thumb subdomain was positioned at His816 to Glu920. The active site of the 2019 SARS-CoV-2 is located in the palm domain which consisted of motif A, B, C, D, E, F, and G. The binding model of RDM to the RdRp is supposedly surrounded by Asp618, Asp623 (motif A), Thr680, Ser682, Asn691 (motif B), Ser759, Asp760, and Asp761 (motif C) [14]. The binding site of RDM is depicted in Fig. 3. This site was also identified as the top 1 site by the SiteMap module of the Schrodinger Package (Release 2019-4).

The docking of RDM at the supposed binding site gave the binding energy of −6.96 kcal/mol, while docking of 14480 hit molecules yielded binding energies from −4.42 kcal/mol to −12.36 kcal/mol. On the other hand, docking 151 molecules gave binding energies between −5.2 and −10.65 kcal/mol. All docking results were analyzed for their ligand structures and interactions with RdRp and based on the structural comparison between hit molecules and Remdesivir for mimicking nucleotide structure, we selected one compound from the Indonesian Herbal Database and two compounds from the ZINC database for subjecting to 40 ns MD simulation. Fig. 4 displays the two-dimensional best docked hit molecules.

The best docked hit molecules show a similar interaction with Remdesivir (RDM). Table 1 tabulates the binding energy and interactions with RdRp.

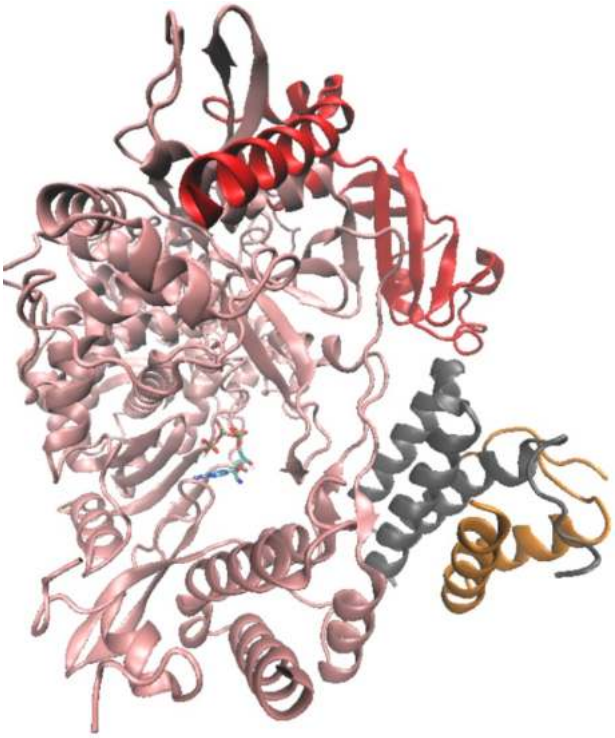

Fig 3. The putative ligand-binding site of RDM to RdRp, in which carbon and oxygen atoms of active RDM were colored blue and red, respectively

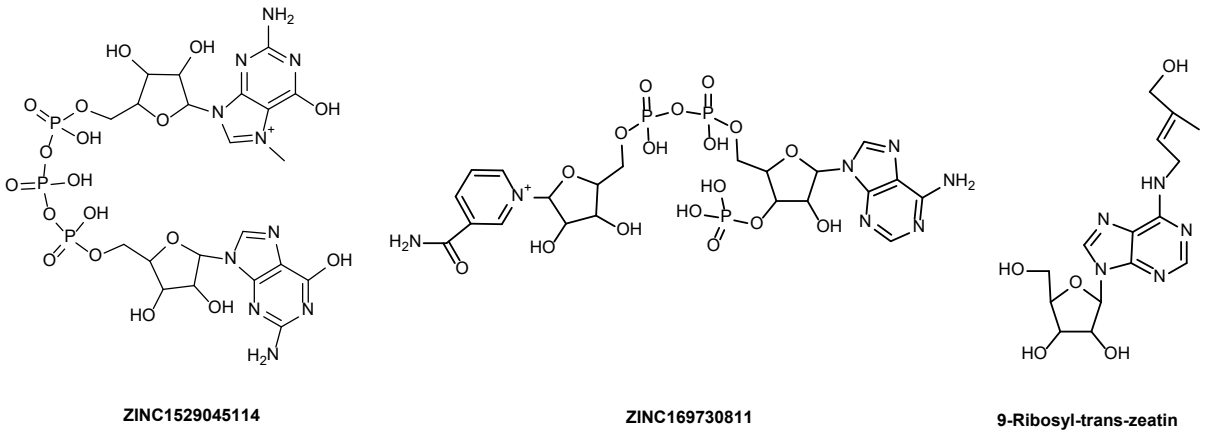

Fig 4. The two-dimensional best docked hit molecules

Table 1. The binding affinities and interactions between hit molecules and RdRp

Ligand	Binding affinities (kcal/mol)	H-bond (distance, Å)	Electrostatic interactions	Hydrophobic
RDM	−6.96	Tyr619 (3.22) Ser814 (3.12) Asp760 (2.32) Asp761 (2.21) Glu811 (3.36) Lys798 (2.72)	Asp618 Asp760 Asp761 Glu811	
ZINC1529045114	−8.07	Lys621 (2.87) Arg624 (3.06) Thr687 (2.69) Asn691 (3.26) Asp452 (3.37) Asp623 (3.04)	Asp623 Asp760	Arg555
ZINC169730811	−8.04	Tyr619 (3.32) Cys622 (3.10) Glu811 (3.26)	Arg624 Asp623	Lys798
9-Ribosyl-trans-zeatin	−10.65	Asp761 (2.34) Glu811 (2.43) Tyr619 (2.64) Asp760 (2.84)		Cys622

Interaction of ZINC1529045114 was supported by hydrogen bonds between the oxygen atom of the phosphate group with Lys621, as well as the nucleoside group with Thr687, Asn691, Asp452, Asp623, and Arg624. The purine group also contributed to the electrostatic interactions through pi-anion interactions with Asp623 and Asp760. In the meantime, the interaction of ZINC169730811 was based on the hydrogen bond interactions with Tyr619 through the oxygen atom of the phosphate group, as well as with Cys622 through the oxygen of the oxolane group. The hydrogen bond interaction was also observed with Glu811, while electrostatic interactions between pi-electron of purine group and Arg624 and Asp623 were observed. Also, hydrophobic interaction with Lys798 was noted. While hydrogen bonding interactions for 9-Ribosyl-trans-zeatin occurred with Asp761, Glu811, Tyr619, and Asp760. In the meanwhile, Remdesivir (RDM) showed hydrogen bonding interactions with Tyr619, Ser814, Asp760, Asp761, Glu811, and Lys798. Electrostatic interactions with Asp618, Asp760, Asp761, and Glu811 were observed between RDM and RdRp. Fig. 5 displays the interaction of each hit molecule with the RdRp.

Prediction of ADME Properties

Table 2 shows the predicted ADME properties for the three compounds. The ZINC1529045114, ZINC169730811, and 9-Ribosyl-trans-zeatin show low intestinal absorption properties with no chance for distribution into the brain. The three compounds also could not be inhibitors for the subtypes of cytochrome P450 enzymes (CYPs) including CYP1A2, CYP2C19, CYP2C9, CYP2D6, and CYP3A4, which indicated that the two compounds could not probably be metabolized. Compound 9-Ribosyl-trans-zeatin fulfill the conditions of drug-likeness properties without any violation of Lipinski rule of five including MV < 500, calculated octanol-water partition coefficient (LogP) ≤ 5, some hydrogen bonding acceptors ≤ 10, as well as several hydrogen bonding donors ≤ 5. All the three compounds have a minor *in silico* ADME properties for oral administration, which indicated their favorable use in prodrug form.

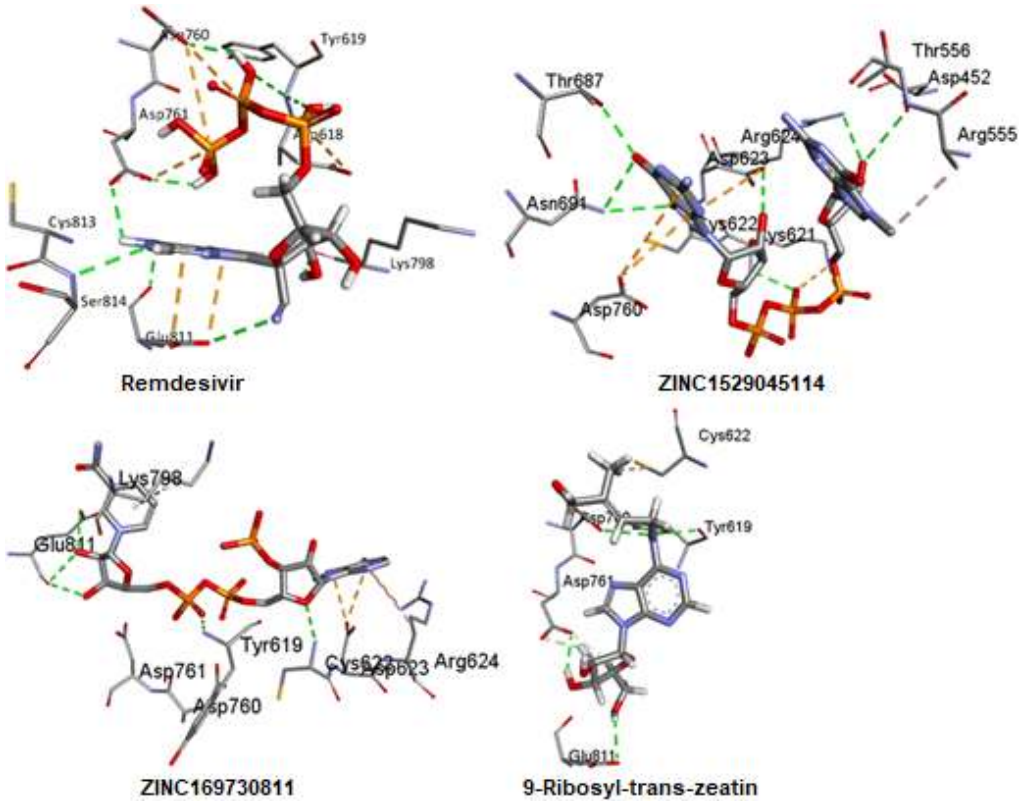

Fig 5. The interaction of each hit molecules with RdRp. The green, orange, and purple dashed lines represent hydrogen bond, electrostatics, and hydrophobic interactions, respectively

Table 2. The predicted ADME properties

Compound	GI absorption	BBB permeant	CYP1A2	CYP2C19	CYP2C9	CYP2D6	CYP3A4	Lipinksi rule
RDM	Low	No	No	No	No	No	No	3 violations (MW>500, N or O>10, NH or OH>5)
ZINC1529045114	Low	No	No	No	No	No	No	3 violations (MW>500, N or O>10, NH or OH>5)
ZINC169730811	Low	No	No	No	No	No	No	2 violations (MW>500, N or O>10)
9-Ribosyl-trans-zeatin	Low	No	No	No	No	No	No	0 violation

Molecular dynamics simulation was performed to analyze the impact of ligand binding to the RdRp stability, which was estimated using the RMSD values of the receptor backbone atoms. Fig. 6 displays the RMSD values for receptor backbone atoms of each complex and native apo RdRp (without ligand) as a function of 40 ns simulation time. It is noted that the native apo RdRp and protein-ligand complexes reached equilibrium during the 40 simulations. The RMSD values of 9-Ribosyl-trans-zeatin were higher than those of other compounds. ZINC1529045114, ZINC169730811, and RDM display fluctuation in the early 20 ns especially for RDM and ZINC169730811. However, those three complexes become stable after around 25 ns and the curve fluctuation of ZINC169730811 was lower than those two ligands, which implied that ZINC169730811 could form a more stable complex with RdRp.

On the other hand, residue fluctuation during ligand binding was recorded as RMSF values of the native apo RdRp and four complexes as shown in Fig. 7.

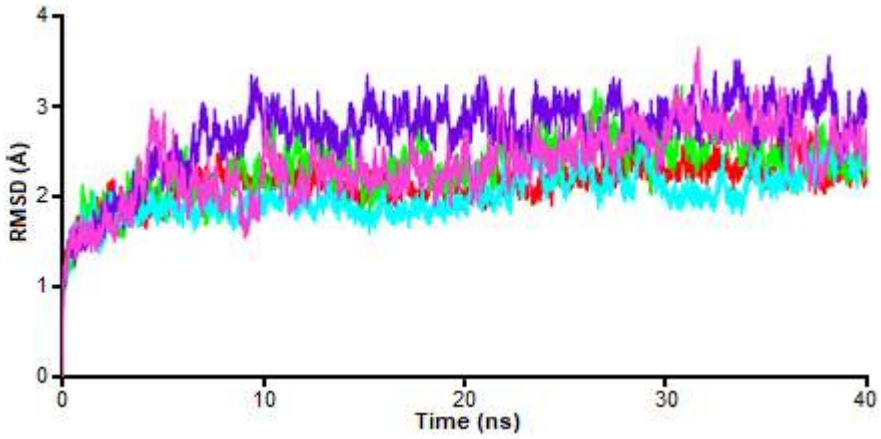

Fig 6. The RMSD values for the receptor backbone atoms of each complex of RDM (red), ZINC1529045114 (green), ZINC169730811 (blue), 9-Ribosyl-trans-zeatin (purple), and native apo RdRp (pink)

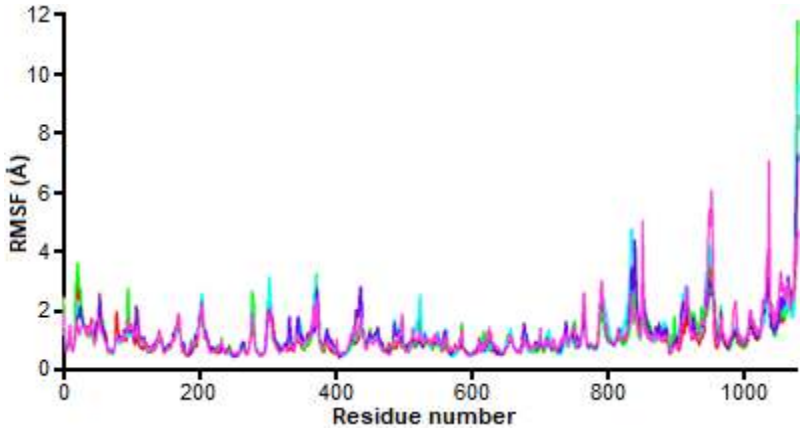

Fig 7. A plot of residue fluctuation during ligand binding was recorded as RMSF values as RDM (red), ZINC1529045114 (green), ZINC169730811 (blue), 9-Ribosyl-trans-zeatin (purple), and receptor only (pink)

The RMSF values indicated that the higher RMSF values, the more fluctuation amino acid residues during MD simulation. As shown in Fig. 7, the highest peak was located at residue 1078 which was corresponded to the amino-terminal region of the protein, which is typical in all protein fluctuation. Peaks around 810 and 980, 300, 380, and 20 have more fluctuated around 4 Å than other regions, which is attributable to residues in tails. The amino acids involved in the ligand-binding including Tyr560 (Tyr619), Lys562 (Lys621), Cys563 (Cys622), Asp564 (Asp623), Arg565 (Arg624), Thr628 (Thr687), Asn632 (Asn691), Asp701 (Asp760), Asp702 (Asp761), Glu752 (Glu811) as well as the rest of residues was stable enough under 3 Å and each ligand-induced the similar pattern of RMSF fluctuation.

Trajectory clustering was employed to identify the most populated structure for each complex. It is found out that the percentage of clusters was 100% in each complex (Table S2). Fig. 8 displays the single-populated structure of each ligand and their superimposition, while Fig. 9 depicts their detailed interactions. The single populated structure of RDM resulted in tight interactions with key residues of RdRp such as Asp701 (Asp760) and Asp559 (Asp618). The most abundant structure of ZINC1529045114 was also involving key residues of RdRp such as Asp564 (Asp623), Asp701 (Asp760), and Thr621 (Thr680). Similar interactions were also observed in the most abundant structure of ZINC169730811 which include Arg496 (Arg555), Asp564 (Asp623), and Asp702 (Asp761). While the most abundant of the 9-Ribosyl-trans-zeatin structure includes interactions with Asp564 (Asp623), Asp559

(Asp618), and Arg496 (Arg555). As Zhao et al. (2020) [14] reported the key residues of Asp618, Asp623, Asp760, Asp761, Thr680, Arg555, and Asn691, was supposed to interact with Remdesivir (RDM).

Additionally, the hydrogen bond occupancies were also monitored during the trajectory period of the MD run. Table S1 shows the hydrogen bonding profile for each complex. The complex of ZINC169730811 showed hydrogen bonding higher occupancies than that of ZINC1529045114 and 9-Ribosyl-trans-zeatin. The highest occupancy was observed between ZINC169730811 and Asp702 (Asp761) with 80.78%, followed by moderate occupancies with Lys492 (Lys551) (32.53%). While the highest hydrogen bonding occupancy occurring in ZINC1529045114 was detected with Arg496 (Arg555) (45.55%), followed by hydrogen bonding moderate occupancy with Arg565 (Arg624) (30.18%) and Asp701 (Asp760) (29.6%) and Asp564 (Asp623) (28.95%). While those observed in 9-Ribosyl-trans-zeatin occurred with low occupancies, for example, occupancies of hydrogen bonding with Glu752 (Glu811) and Asp702 (Asp761) were 37.66% and 23.14%, respectively. From the data shown, it can be concluded that ZINC169730811 has better binding stability than ZINC1529045114 and 9-Ribosyl-trans-zeatin.

Binding Free Energy Calculation

The enthalpy terms of binding affinities of hit molecules were calculated using MM-PBSA methods as reflected in Table 3, while due to complexity, the entropy part was not calculated. The MM-PBSA binding energy offers a good compromise between accuracy and computational cost [22-25].

The ZINC169730811 displays the lowest total interaction energies (ΔE_{PBTOT} = −57.73±4.49 kcal/mol), followed by ZINC1529045114 (−30.29±4.38 kcal/mol), 9-Ribosyl-trans-zeatin (−20.79±4.19 kcal/mol) and RDM (−17.87±4.19 kcal/mol). The electrostatic energy value (ΔE_{ELE} = −45.31±7.30 kcal/mol) was favorable for the binding of ZINC169730811 as in the case of ZINC1529045114 (ΔE_{ELE} = −46.46±7.84 kcal/mol), RDM (−39.29±4.78 kcal/mol), and 9-Ribosyl-trans-zeatin (−14.06±4.60 kcal/mol). The favorable energy terms were also contributed by the lower van der Waals energy (ΔE_{VDW} = −58.77±4.29 kcal/mol), ZINC1529045114 (ΔE_{VDW} = −37.05±4.49 kcal/mol), 9-Ribosyl-trans-zeatin (ΔE_{VDW} = −21.75±5.57 kcal/mol) and RDM (ΔE_{VDW} = −15.72±5.29 kcal/mol). The binding of ligands was also corroborated by lower nonpolar contribution for solvation energy (ΔE_{PBSUR} = −6.22±0.26 kcal/mol), −4.56±0.20 kcal/mol, −3.56±0.32 kcal/mol, and −3.34±0.31 kcal/mol for ZINC169730811, ZINC1529045114, RDM, and 9-Ribosyl-trans-zeatin, respectively. The superiority of the binding energy of ZINC169730811 to other ligands was also reflected in Fig. S1 which shows the plot of MM-PBSA binding energy

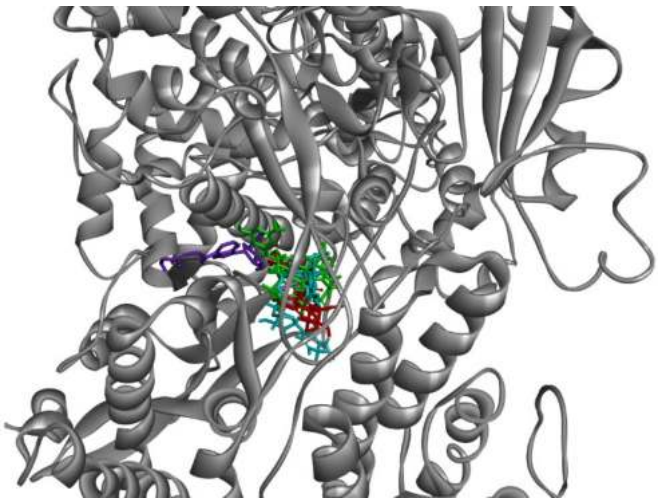

Fig 8. The superimposition of single populated structures in which RDM, ZINC1529045114, ZINC169730811, and 9-Ribosyl-trans-zeatin are colored as red, green, blue, and purple, respectively

Table 3. The binding energy for the last 10 ns predicted by MM-PBSA protocol.

Ligand	ΔE_{ELE} (kcal/mol)	ΔE_{VDW} (kcal/mol)	ΔE_{PB} (kcal/mol)	ΔE_{PBSUR} (kcal/mol)	ΔE_{PBTOT} (kcal/mol)
ZINC1529045114	−46.46±7.84	−37.05±4.49	57.78±6.42	−4.56±0.20	−30.29±4.38
ZINC169730811	−45.31±7.30	−58.77±4.29	52.58±5.36	−6.22±0.26	−57.73±4.49
9-Ribosyl-trans-zeatin	−14.06±4.60	−21.75±5.57	18.36±3.19	−3.34±0.31	−20.79±4.19
RDM	−39.29±4.78	−15.72±5.29	40.71±4.02	−3.56±0.32	−17.87±4.19

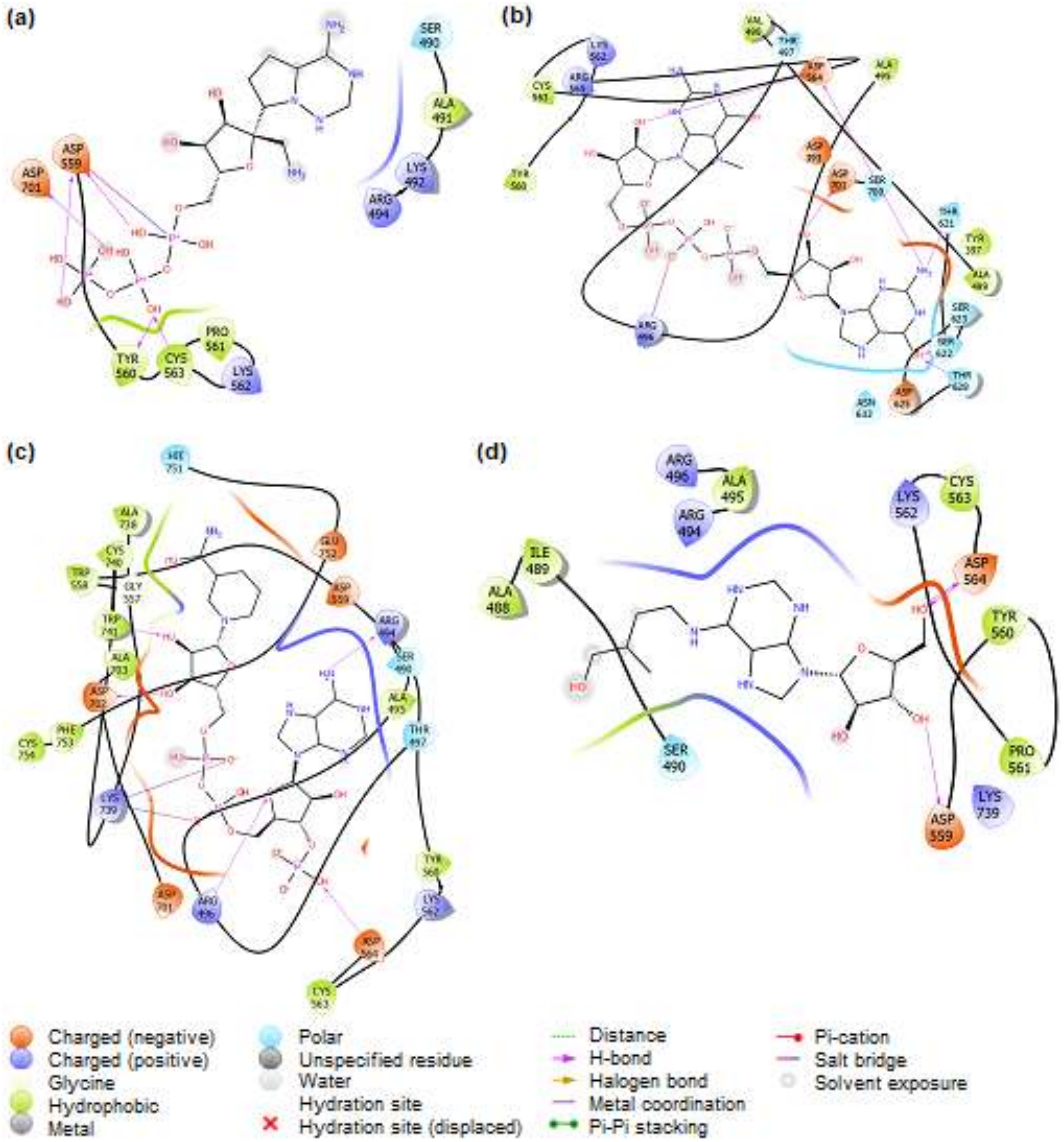

Fig 9. The single populated pose of each ligand. (a) RDM (b) ZINC1529045114 (c) ZINC169730811 (d) 9-Ribosyl-trans-zeatin

throughout simulation time, in which ZINC169730811 has the lowest binding energy in the whole simulation time. It is worth to note that the three-hit molecules display lower binding energies than that of RDM, which is indicated their tighter affinities toward the RdRp protein.

■ CONCLUSION

In brief, the present study employed pharmacophore modeling for identifying hit molecules from both Indonesian herbal and ZINC databases potential for binding to RNA-dependent RNA polymerase (RdRp) of SARS-CoV-2. One hit from herbal and two hits from ZINC databases was selected for MD simulation, and the three hits showing tighter binding to RdRp based on MM-PBSA binding energy prediction. The present study suggests the three hits as potential inhibitors of RdRp, however, further experimental verification is required.

■ ACKNOWLEDGMENTS

This study was supported by the Ministry of Research and Technology/National Board of Research and Innovation, the Republic of Indonesia. C.W. also acknowledges the support from US National Science

Foundation under Grants NSF RUI-1904797 and XSEDE MCB 170088. We acknowledge Prof. Rao for offering us the cryo-EM structure of RdRp (PDB ID: 6M71) before its availability from the Protein Data Bank.

■ AUTHOR CONTRIBUTIONS

MA, AH, and IU design and experimented, AY support the herbal database, GF and DJB wrote the manuscript, CW supervised the experiment. All authors agreed to the final version of this manuscript.

■ REFERENCES

[1] World Health Organization, 2020, *Coronavirus Disease (COVID-2019): Situation Reports, 94*, World Health Organization, Geneva, 12.

[2] Dolan, P.T., Whitfield, Z.J., and Andino, R., 2018, Mechanisms and concepts in RNA virus population dynamics and evolution, *Annu. Rev. Virol.*, 5 (1), 69–92.

[3] Jia, H., and Gong, P., 2019, A structure-function diversity survey of the RNA-dependent RNA polymerases from the positive-strand RNA viruses, *Front. Microbiol.*, 10, 1945.

[4] Agostini, M.L., Andres, E.L., Sims, A.C., Graham, R.L., Sheahan, T.P., Lu, X., Smith, E.C., Case, J.B., Feng, J.Y., Jordan, R., Ray, A.S., Cihlar, T., Siegel, D., Mackman, R.L., Clarke, M.O., Baric, R.S., and Denison, M.R., 2018, Coronavirus susceptibility to the antiviral Remdesivir (GS-5734) is mediated by the viral polymerase and the proofreading exoribonuclease, *MBio*, 9 (2), e00221-18.

[5] Gordon, C.J., Tchesnokov, E.P., Feng, J.Y., Porter, D.P., and Götte, M., 2020, The antiviral compound Remdesivir potently inhibits RNA-dependent RNA polymerase from Middle East respiratory syndrome coronavirus, *J. Biol. Chem.*, 295 (15), 4773–4779.

[6] Götte, M., and Feld, J.J., 2016, Direct-acting antiviral agents for hepatitis C: Structural and mechanistic insights, *Nat. Rev. Gastroenterol. Hepatol.*, 13 (6), 338–351.

[7] Gane, E.J., Stedman, C.A., Hyland, R.H., Ding, X., Svarovskaia, E., Symonds, W.T., Hindes, R.G., and Berrey, M.M., 2013, Nucleotide polymerase inhibitor sofosbuvir plus ribavirin for Hepatitis C, *N. Engl. J. Med.*, 368 (1), 34–44.

[8] Wolber, G., and Langer, T., 2005, LigandScout: 3-D pharmacophores derived from protein-bound ligands and their use as virtual screening filters, *J. Chem. Inf. Model.*, 45 (1), 160–169.

[9] Sunseri, J., and Koes, D.R., 2016, Pharmit: interactive exploration of chemical space, *Nucleic Acids Res.*, 44 (W1), W442–W448.

[10] Yanuar, A., Mun'im, A., Lagho, A.B.A., Syahdi, R.R., Rahmat, M., and Suhartanto, H., 2011, Medicinal plants database and three dimensional structure of the chemical compounds from medicinal plants in Indonesia, *Int. J. Comput. Sci. Issues*, 8 (5), 180–183.

[11] Arba, M., Pangan, A., and Yanuar, A., 2020, The search for peptide deformylase inhibitor from Indonesian medicinal plant database: An *in-silico* investigation, *Biointerface Res. Appl. Chem.*, 10 (2), 5117–5121.

[12] Irwin, J.J., Sterling, T., Mysinger, M.M., Bolstad, E.S., and Coleman, R.G., 2012, ZINC: A free tool to discover chemistry for biology, *J. Chem. Inf. Model.*, 52 (7), 1757–1768.

[13] Li, H., Leung, K.S., and Wong, M.H., 2012, idock: A multithreaded virtual screening tool for flexible ligand docking, *IEEE Symposium on Computational Intelligence in Bioinformatics and Computational Biology (CIBCB)*, San Diego, United States, 9-12 May 2012, 77–84.

[14] Gao, Y., Yan, L., Huang, Y., Liu, F., Zhao, Y., Cao, L., Wang, T., Sun, Q., Ming, Z., Zhang, L., Ge, J., Zheng, L., Zhang, Y., Wang, H., Zhu, Y., Zhu, C., Hu, T., Hua, T., Zhang, B., Yang, X., Li, J., Yang, H., Liu, Z., Xu, W., Guddat, L.W., Wang, Q., Lou, Z., and Rao, Z., 2020, Structure of the RNA-dependent RNA polymerase from COVID-19 virus, *Science*, 368 (6492), 779–782.

[15] Daina, A., Michielin, O., and Zoete, V., 2017, SwissADME: A free web tool to evaluate pharmacokinetics, drug-likeness and medicinal chemistry friendliness of small molecules, *Sci. Rep.*, 7, 42717.

[16] Arba, M., and Nurmawati, O., 2020, Identification of potential inhibitors for Bruton's Tyrosine Kinase (BTK) based on pharmacophore-based virtual screening, *Biointerface Res. Appl. Chem.*, 10 (3), 5472–5477.

[17] Maier, J.A., Martinez, C., Kasavajhala, K., Wickstrom, L., Hauser, K.E., and Simmerling, C., 2015, ff14SB: Improving the accuracy of protein side chain and backbone parameters from ff99SB, *J. Chem. Theory Comput.*, 11 (8), 3696–3713.

[18] Wang, J., Wolf, R.M., Caldwell, J.W., Kollman, P.A., and Case, D.A., 2004, Development and testing of a general amber force field, *J. Comput. Chem.*, 25 (9), 1157–1174.

[19] Roe, D.R., and Cheatham III, T.E., 2013, PTRAJ and CPPTRAJ: Software for processing and analysis of molecular dynamics trajectory data, *J. Chem. Theory Comput.*, 9 (7), 3084–3095.

[20] Appleby, T.C., Perry, J.K., Murakami, E., Barauskas, O., Feng, J., Cho, A., Fox, D., Wetmore, D.R., McGrath, M.E., Ray, A.S., Sofia, M.J., Swaminathan, S., and Edwards, T.E., 2015, Structural basis for RNA replication by the hepatitis C virus polymerase, *Science*, 347 (6223), 771–775.

[21] Deval, J., Symons, J.A., and Beigelman, L., 2014, Inhibition of viral RNA polymerases by nucleoside and nucleotide analogs: Therapeutic applications against positive-strand RNA viruses beyond hepatitis C virus, *Curr. Opin. Virol.*, 9, 1–7.

[22] Rifai, E.A., Ferrario, V., Pleiss, J., and Geerke, D.P., 2020, Combined linear interaction energy and alchemical solvation free-energy approach for protein-binding affinity computation, *J. Chem. Theory. Comput.*, 16 (2), 1300–1310.

[23] Kollman, P.A., Massova, I., Reyes, C., Kuhn, B., Huo, S., Chong, L., Lee, M., Lee, T., Duan, Y., Wang, W., Donini, O., Cieplak, P., Srinivasan, J., Case, D.A., and Cheatham, T.E., 2000, Calculating structures and free energies of complex molecules: Combining molecular mechanics and continuum models, *Acc. Chem. Res.*, 33 (12), 889–897.

[24] Srinivasan, J., Cheatham, T.E., Cieplak, P., Kollman, P.A., and Case, D.A., 1998, Continuum solvent studies of the stability of DNA, RNA, and phosphoramidate–DNA helices, *J. Am. Chem. Soc.*, 120 (37), 9401–9409.

[25] Arba, M., Ruslin, Ihsan, S., Tri Wahyudi, S., and Tjahjono, D.H., 2017, Molecular modeling of cationic porphyrin-anthraquinone hybrids as DNA topoisomerase IIβ inhibitors, *Comput. Biol. Chem.*, 71, 129–135.

Supplementary Data

This supplementary data is a part of the paper entitled "Synthesis and Certification of Lanthanum Oxide Extracted from Monazite Sand".

Supplement 1 (S-1). Homogeneity test of macroelement (La concentration) in the ten lanthanum oxide subsamples

La-Oxide Sub-sample	Test Results of La (%) A	B	Xt	Xt-Xr	$(Xt-Xr)^2$	Wt	Wt^2
1	77.016	77.116	77.0660	-0.9867	0.9736	0.1000	0.0100
2	78.706	78.082	78.3940	0.3413	0.1165	0.6240	0.3894
3	76.636	75.622	76.1290	-1.9237	3.7006	1.0140	1.0282
4	76.890	75.958	76.4240	-1.6287	2.6527	-0.9320	0.8686
5	81.372	78.846	80.1090	2.0563	4.2284	2.5260	6.3807
6	79.810	78.232	79.0210	0.9683	0.9376	1.5780	2.4901
7	80.316	79.118	79.7170	1.6643	2.7699	-1.1980	1.4352
8	79.676	77.718	78.6970	0.6443	0.4151	1.9580	3.8338
9	76.220	77.738	76.9790	-1.0737	1.1528	1.5180	2.3043
10	79.070	76.912	77.9910	-0.0617	0.0038	2.1580	4.6569
		Xr	**78.0527**				
			Total		16.9510		23.3972
				Sx	0.9417	Sw	0.5849
				Sx^2	0.8868	Sw^2	0.3421
						$Sw^2/2$	0.1711
						$Sx^2 - (Sw^2/2)$	0.7158
						Ss	**0.3579**

In Supplement 1, La concentration measured of 78.0527% or 0.780527. Log 0.780527 = -0.106, then 1 - 0.5 log 0.780527 = -1.0538. The value of σ = 2.0760, so the value of 0.3 σ = 0.6228. The value of Ss = 0.3579. The concentration of La has been homogeneous, because of Ss < 0.3 σ.

Supplement 2 (S-2). Homogeneity test of microelement (Sm concentration) in the ten lanthanum oxide subsamples

La-Oxide Sub-sample	Test Results of Sm (%) A	B	Xt	Xt-Xr	$(Xt-Xr)^2$	Wt	Wt^2
1	0.116	0.110	0.1130	-0.01015	0.0001	-0.0060	3.60×10^{-5}
2	0.104	0.116	0.1100	-0.01315	0.0002	-0.0120	1.44×10^{-4}
3	0.128	0.126	0.1270	0.00385	1.5×10^{-5}	0.0020	4.00×10^{-6}
4	0.125	0.119	0.1220	-0.00115	1.3×10^{-6}	-0.0060	3.60×10^{-5}
5	0.113	0.125	0.1190	-0.00415	1.7×10^{-5}	-0.0120	1.44×10^{-4}
6	0.137	0.136	0.1365	0.01335	0.0002	0.0010	1.00×10^{-6}
7	0.132	0.129	0.1305	0.00735	5.4×10^{-5}	-0.0030	9.00×10^{-6}
8	0.145	0.132	0.1385	0.01535	0.0002	0.0130	1.69×10^{-4}
9	0.119	0.118	0.1185	-0.00465	2.2×10^{-5}	-0.0010	1.00×10^{-6}
10	0.117	0.116	0.1165	-0.00665	4.4×10^{-5}	0.0010	1.00×10^{-6}
		Xr	**0.12315**				
			Total		0.0008		5.45×10^{-4}
				Sx	4.7×10^{-5}	Sw	1.36×10^{-5}
				Sx^2	2.2×10^{-9}	Sw^2	1.86×10^{-10}
						$Sw^2/2$	9.28×10^{-11}
						$Sx^2 - (Sw^2/2)$	2.10×10^{-9}
						Ss	$\mathbf{1.05 \times 10^{-9}}$

In Supplement 2, the Sm concentration measured of 0.123% or 0.00123. Log 0.00123 = -2.9096. The value of σ = 5.4823, so the value of 0.3 σ = 1.6447. The value of Ss = 1.05×10^{-9}. The concentration of Sm has been homogenous, because of Ss < 0.3 σ.

Supplement 3 (S-3). Homogeneity test of microelement (Y concentration) in the ten lanthanum oxide subsamples

La-Oxide Sub-sample	Test results of Y (%)		Xt	Xt-Xr	$(Xt-Xr)^2$	Wt	Wt^2
	A	B					
1.	0.101	0.099	0.1000	-0.00165	2.7×10^{-6}	-0.002	4.0×10^{-6}
2.	0.096	0.101	0.0985	-0.00315	9.9×10^{-6}	-0.005	2.5×10^{-4}
3.	0.106	0.103	0.1045	0.00285	8.1×10^{-6}	0.003	9.0×10^{-6}
4.	0.100	0.103	0.1015	-0.00015	2.2×10^{-8}	0.003	9.0×10^{-6}
5.	0.105	0.125	0.1150	0.01335	1.8×10^{-4}	-0.020	4.0×10^{-4}
6.	0.095	0.100	0.0975	-0.00415	1.7×10^{-5}	-0.005	2.5×10^{-5}
7.	0.099	0.097	0.0980	-0.00365	1.3×10^{-5}	-0.002	4.0×10^{-6}
8.	0.094	0.099	0.0965	-0.00515	2.6×10^{-5}	-0.005	2.5×10^{-5}
9.	0.104	0.103	0.1035	0.00185	3.4×10^{-6}	-0.001	1.0×10^{-6}
10.	0.102	0.101	0.1015	-0.00015	2.2×10^{-8}	0.001	1.0×10^{-6}
		Xr	**0.10165**				
			Total		2.6×10^{-4}		5.0×10^{-4}
				Sx	1.4×10^{-5}	Sw	1.2×10^{-5}
				Sx^2	2.1×10^{-10}	Sw^2	1.6×10^{-10}
						$Sw^2/2$	7.9×10^{-11}
						$Sx^2 - (Sw^2/2)$	1.3×10^{-10}
						Ss	6.4×10^{-11}

In Supplement 3, the Y concentration measured of 0.10165% or 0.0010165. The value of σ = 5.6429, so the value of 0.3 σ =1.6929. The value of Ss = 6.4×10^{-11}. The concentration of Y has been homogenous, because of Ss < 0.3 σ.

Supplement 4 (S-4). Stability test of macroelement (La concentration) in the three lanthanum oxide subsamples

La-Oxide Sub-sample	The concentration of La after 6 months (%)		Y_T (%)
	Y_A	Y_B	
1	77.066	79.980	78.957
4	76.424	79.160	77.792
9	76.979	78.330	77.655
	Yr (%)		**78.135**

In Supplement 1 (S-1) the concentration of La was obtained Xr = 78.0527% and in supplement 4 (S-4) the stability test data of La was obtained Yr = 78.1350%, the value of |Xr – Yr| = 0.0828**,** the value of 0.3 σ = 0.6228, so the concentration of La in lanthanum oxide is stable, because of |Xr – Yr| ≤ 0.3 σ namely 0.0828 < 0.6228.

Supplement 5 (S-5). Stability test of microelement (Sm concentration) in the three lanthanum oxide subsamples

La-oxide Sub-sample	The concentration of Sm after 6 months (%)		**Y_T (%)**
	Y_A	Y_B	
1	0.113	0.127	0.120
2	0.110	0.119	0.115
7	0.131	0.126	0.129
	Yr (%)		**0.121**

In Supplement 2 (S-2) the Sm concentration was obtained, Xr = 0.123% and on the stability test data in Supplement 5 (S-5) the Sm concentration was obtained Yr = 0.121%, the value of |Xr - Yr| = 0.002, and the value of 0.3 σ = 1.6447, so the concentration of Sm in lanthanum oxide was stable because of |Xr - Yr| ≤ 0.3 σ namely 0.002 < 1.6447.

Supplement 6 (S-6). Stability test of microelement (Y concentration) in the three lanthanum oxide subsamples

La-oxide Sub-samples	The concentration of Y after 6 months (%)		Y_T (%)
	Y_A	Y_B	
3	0.105	0.101	0.103
7	0.098	0.100	0.099
4	0.101	0.099	0.100
	Yr (%)		**0.1007**

In the Supplement 3 (S-3) the Y concentration was obtained, Xr = 0.10165% and on the stability test data, in Supplement 6 (S-6) the Y concentration was obtained Yr = 0.1007%, the value of |Xr – Yr| = 0.0095, and the value of 0.3 σ = 1.6919, so the concentration of Y in lanthanum oxide was stable because of |Xr - Yr| ≤ 0.3 σ namely 0.0095 < 1.6919.